JP0150822

JAERI-Review
2001-039

TIARA Annual Report 2000

November 2001

Advanced Radiation Technology Center

日本原子力研究所
Japan Atomic Energy Research Institute

本レポートは，日本原子力研究所が不定期に公刊している研究報告書です。
入手の問合わせは，日本原子力研究所研究情報部研究情報課（〒319-1195 茨城県那珂郡東海村）あて，お申し越しください。なお，このほかに財団法人原子力弘済会資料センター（〒319-1195 茨城県那珂郡東海村日本原子力研究所内）で複写による実費頒布をおこなっております。

This report is issued irregularly.
Inquiries about availability of the reports should be addressed to Research Information Division, Department of Intellectual Resources, Japan Atomic Energy Research Institute, Tokai-mura, Naka-gun, Ibarakiken 319-1195, Japan.

©Japan Atomic Energy Research Institute, 2001
編集兼発行　日本原子力研究所

JAERI-Review 2001-039

TIARA Annual Report 2000

Advanced Radiation Technology Center

Takasaki Radiation Chemistry Research Establishment
Japan Atomic Energy Research Institute
Watanuki-cho, Takasaki-shi, Gunma-ken

(Received October 4, 2001)

This annual report describes research and development activities which have been performed with the JAERI TIARA (Takasaki Ion Accelerators for Advanced Radiation Application) facilities from April 1, 2000 to March 31, 2001. Summary reports of 103 papers and brief descriptions on the status of TIARA in the period are contained. A list of publications, the type of research collaborations and organization of TIARA are also given as appendices.

Keywords: JAERI TIARA, Ion Accelerators, Solid State Physics, Radiation Effects in Materials, Materials for Space, Semiconductors, Organic Materials, Inorganic Materials, Nuclear Fusion Reactor, Functional Materials, Radiation Chemistry, Radiation Biology, Nuclear Medicine, Biotechnology, Radioisotope Production, Nuclear Chemistry, Radiation Shielding, Materials Analysis, Microbeam Technology, Accelerator Technology, Safety Control

(Eds.) Masahiro SAIDOH, Akio TORAISHI, Hideki NAMBA, Hisayoshi ITOH, Shigeru TANAKA, Hiroshi NARAMOTO, Toshiaki SEKINE ,Atsushi TANAKA, Yasuhiko KOBAYASHI, Kazuo ARAKAWA, Michiaki OTSUBO, Satoshi TAJIMA and Susumu TANAKA

原研イオン照射研究施設（ＴＩＡＲＡ）平成１２年度年次報告

日本原子力研究所高崎研究所
放射線高度利用センター

(2001年10月 4日受理)

本年次報告は、原研イオン照射研究施設で、2000年4月1日から2001年3月31日までの間に行われた研究活動の概要をまとめたものである。1）宇宙用半導体、2）バイオテクノロジー、3）放射線化学及び有機材料、4）無機材料、5）材料解析、6）核科学およびラジオアイソトープ製造、7）マイクロビーム応用、8）加速器施設の放射線遮蔽、9）加速器技術の９部門にわたる１０３編の研究報告に加えて、施設の運転保守・利用状況、公表された文献、企業・大学等との研究協力関係、研究開発・施設運営組織を収録する。

高崎研究所：〒370-1292 群馬県高崎市綿貫町 1233
編集委員：西堂雅博、虎石昭雄、南波秀樹、伊藤久義、田中　茂、楢本　洋、関根俊明、田中　淳、小林泰彦、荒川和夫、大坪道朗、田島　訓、田中　進

PREFACE

This report covers research and development activities which have been conducted with TIARA(Takasaki Ion accelerators for Advanced Radiation Application) during the period from April 2000 to March 2001, and also gives an outline of the operation of TIARA in the same period.

All accelerators in TIARA, the AVF cycrotron, the 3MV tandem accelerator, the 3MV single-ended accelerator and 400kV ion implanter, have been operated steadily since the construction were completed in 1993, and have supplied the beam-time to the research programs as had been recognized in advance by the Subcommittee of TIARA of Advisory Council for JAERI's Research Facilities. In the same time, available species and energy ranges of ions have been widened to meet requirements from users, and the quality of ion beams have been improved gradually.

In the R & D of semiconductor devices for space applications, the radiation tolerance of newly developed. InGaP/GaAs/Ge multi-junction solar cells have been characterized. Three different modes of multiple bit upsets were found in highly integrated memory devices like 16Mbit DRAMs. To investigate mechanisms behind single event phenomena, a new measurement system was applied for obtaining transient currents induced in junction diodes by a single heavy ion. In the development of SiC devices, SiC-based field effect transistors(MOSFETs) fabricated with hot-implantation exhibited quite high resistance against radiation compared with Si-MOSFETs.

In biotechnology, three areas: mutation induction in plants; plant physiology using the positron emitting tracer imaging system(PETIS); and heavy-ion-microbeam application were continued. A novel flower mutant featuring serrated petals and sepals was isolated *in Arabidopsis thaliana* by means of carbon-ion irradiation. Using PETIS, a lot of data were obtained on plant uptake and translocation of water, NO_3^- ion, F^- ion, metallic ions and photoassimilates. In microbeam application, a method for the detection of ion-hit points on a target was developed for the study of cellular effects of low dose radiation, especially aimed at single-ion-hit experiments.

In the field of radiation chemistry and organic materials, research works on ion track structures and the synthesis of new materials have been studied by irradiation of heavy ions. Space environment durability of newly developed polymeric materials was estimated for spacecraft. The ion track filters were developed for separation of peptide molecules. Thin film-dosimeter was applied to measure the dose distribution of ion beams with the accuracy of 1 μm region. The studies on cross-linking of polydimethylsiloxane and poly(methyl)phenylsilane in ion track show that the ion beam irradiation is unique and powerful technique to produce nanowires. The effect of LET on primary process was studied by ion pulse radiolysis with polystyrene solution in cyclohexane and by measurement of energy deposition with photon counting method in irradiated gaseous nitrogen.

In the field of nuclear fusion materials, various kinds of experimental studies were perfomed. Especially, in order to simulate the effects of He and H produced through (n, α) and (n, p) transmutation reactions in the fusion reactor materials, dual or triple ion-beams including He^+ ions and/or H^+ ions were widely irradiated onto the candidate fusion materials. Effects of implanted helium and/or hydrogen atoms on physical, chemical properties and thermo-mechanical properties as well as microstructure evolution by irradiation damage were intensively investigated with the support of calculation codes, TRIM/SRIM.

In the R & D of inorganic materials, the formation mechanism and thermal stability of carbon-based materials have been intensively investigated. The formation processes of carbon onions in copper and gold were elucidated through simultaneous TEM observation under C ion irradiation. The optimum growth conditions have been successfully obtained for preparation of high quality C_{60}, diamond-like carbon, and nanocrystalline diamond by means of ion beam assisted deposition. As for the development of highly efficient photo-catalyst TiO_2, it has been demonstrated that high quality anatase and rutile films can be grown

epitaxially by pulsed laser deposition. Ion implantation of F into TiO_2 has also been performed to improve its photo-reactivity.

In the ion beam analysis studies have been performed based on various different moyivations. The secondary electrons spectroscopy combined with ion shadowing was developed further by comfirming non-diffraction effect. The in-situ analysis of solid-liquid interface was successfully employed to determine the reaction kinetics in leaching process of nuclear waste materials. The interactions of cluster ions with solids have been made in polymeric materials and crystalline solids, and the non-linear effect seems to be influential in the radiation damage and also in the beam counting.

In nuclear science and radioisotope production, development of biomedical radioisotopes has been continued. Excitation functions for no-carrier added production of ^{186}Re that is expected to be used in radioimmunotherapy have been measured for deuteron-induced reactions on a tungsten target. Using an isotope separator on-line, a search was made to find a proposed ^{126}La isomer in measurement of internal conversion electrons. A candidate transition for the isomer has been obtained. A laser ion source for an isotope separator on-line has been developed; ionization of a short-lived aluminum isotope was enhanced by photoionization. An isotope separator has been used for the first time to produce endohedral ^{133}Xe-fullerene.

In the field of ion beam engineering, the fluoride concentration and distribution in the teeth were measured by using proton induced gamma-ray emission in the micro beam system. In the in-air micro-PIXE analysis system, success of elemental distribution mapping in a human leukemia cells and of single fog droplets with spatial resolution of 1 μ m are worthy of note.

In the field of radiation shielding for accelerator facilities, three experiments have been performed aiming to contribute to the radiation safety of the accelerators facilities. The first one is on the formation of radioactive aerosols under high-energy radiation fields and the results were discussed in terms of the attachment model. The second is on the measurements of dose distribution and microdosimetric spectra on and inside a plastic phantom behind iron shield with a tissue equivalent detector. The third one is on the comparison of the liquid scintillators responses with and without boron loading in order to improve a neutron detector.

The sources of instability of cycrotron beam intensities were analyzed as the function of elapse time after switching-on the AVF cycrotron. It is conformed that the cause of beam instability is correlated closely to the change of magnetic field through the temperature change of the magnet yokes and pole tips. Constructing the temperature control system for the cycrotron magnet successfully stabilized the magnetic field strength.

The reception of users, general management of the facilities, safety management of the radiation controlled areas, support on utilization of facilities, and other duties have been also practiced smoothly.

The tenth TIARA Research Review Meeting was held on June 18 –19, 2001 in Takasaki, of which subjects were reported in this issue, 8 keynote and one invited lectures as well as one memorial lecture were presented. Three hundred twenty seven persons participated in the meeting. In contrast with the earlier meetings, numerous results of TIARA utilization were presented, suggesting the TIARA is now becoming a fruitful facility.

We owe the progress mentioned above to advices of the Consultative Committee for the JAERI-Universities Joint Research Project, Advisory Council JAERI's Research Facilities and their subcommittees.

Masahiro Saidoh, Director
Advanced Radiation Technology Center
Takasaki Radiation Chemistry Research Establishment

Contents

1. Semiconductors for Space 1
1.1 Radiation Tolerance of Multi-junction Space Solar Cells 3
1.2 Analysis of Single-ion Multiple-bit Upset in Commercial High-density DRAMs 6
1.3 Angular Dependence of Ion-induced Current Measured by TIBIC System 9
1.4 Development of Collimated Swift Heavy-ion Micro-beams for Investigation of Single Event Phenomena 12
1.5 Analysis of Failure Caused by Cosmic Rays in High-voltage High-power Semiconductor Devices 14
1.6 Radiation Tolerance of Silicon Carbide Metal-oxide-semiconductor Transistor with Annealed Gate Oxide 17
1.7 Study of Proton- and Electron-irradiation Effects on $CuInSe_2$ Thin Films 20
1.8 Pulsed-ESR Characterization of Diamond implanted with High Energy Phosphorus Ions at High Temperature 23

2. Biotechnology 27
2.1 Differential G-value of Oxidation of Phenylalanine in Aqueous Solution Irradiated with Energetic Heavy Ions 31
2.2 The Influence of C Ion Beam Irradiation on Nuclear DNA Content in Plants Regenerated from Irradiated Leaf Explants in Chrysanthemum 34
2.3 Effects of $^{12}C^{5+}$ Ion Beams on Germination and Leafing of Seed in Chrysanthemum (*Dendranthema Grandiflora Tzvelev.*) 36
2.4 Development of Cell Surgery Technique by Ion Microbeam 38
2.5 Effects of Ion Beam Irradiation on the Growth of Netted Melon (*Cucumis Melo* L.) 40
2.6 Carbon and Helium Ion Beam Irradiation Effects on Seedling and Plant Characters of Tomato cv. First 42
2.7 Induction of Mutation in Spiraea by Ion Beam Irradiation —Effects of Ion Beams on Germination of Spiraea Seed— 45
2.8 Isolation and Characterization of the Ion-beam-induced New Arabidopsis Floral Mutant,*Frill 1* 47
2.9 Mutation Breeding using Ion-beam Irradiation in Aster 50
2.10 Mutation Generation in Carnation Plants Regenerated from in Vitro Leaf Cultures Irradiated with Ion Beams 52
2.11 Mutation Induced by Ion Beam Irradiation to Hinoki Cypress Shoot Primordia 55
2.12 Mutation Induction with Ion Beam Irradiation in Garlic(*Allium Sativum* L.) 57
2.13 Mutation Breeding of Rice,Eggplant and Gloriosa by Ion Beam Irradiation 59
2.14 Production of Mutants that have High Ability to Assimilate Nitrogen Dioxide by the Irradiation of Ion Beams in *Ficus Stipulata.* 62

2.15 Induction of Somatic Mutation by Ion Beam Irradiation in Lethal Chlorophyl Mutant of Rice 64
2.16 Genetic Screening of Antiauxin Mutants in *Arabidopsis Thaliana* 67
2.17 Isolation of Response Deficient Mutants to Environments from Plant Seeds Irradiated with Ion-beam 70
2.18 System of Cell Irradiation with a Precise Number of Heavy Ions 73
2.19 Effects of Locally Targeted Heavy Ions to the Zygotic Nuclei During Early Development of the Silkworm,*Bombyx Mori* 76
2.20 Ion Beam Mutagenesis in a Model Legume *Lotus Japonicus* 79
2.21 Effects of Ion Beam Irradiation on Sweetpotato Callus and Chrysanthemum Leaf Discs 82
2.22 Effects of Helium Ions and Gamma Rays Irradiation of Sexual Plant Reproductive Stages on Seed Production and Postembryonic Leaf Development in *Brassica Napus* L. 85
2.23 Development of the Pollen Transformation System and Analysis of Apoptosis Induction by Local Damage, using Penetration Controlled Irradiation with Ion Beams 87
2.24 Utilization of Ion Beam-irradiated Pollen in Plant Breeding 88
2.25 Dynamical Study on Influence of CO_2 Enrichment to the Transportation of Photoassimilates using Positron Imaging 90
2.26 Analysis of Nitrogen Absorption and Translocation by Soybean Grown in Different Conditions for Phosphorus Supply 93
2.27 Zinc Translocation Oscillates in a Leaf of Zinc-deficient Rice 96
2.28 Effects of Environmental Stress on ^{11}C Distribution in Rice Plants Detected by PETIS Detector 99
2.29 Water and Trace Element Behavior in a Plant 102
2.30 Uptake of ^{18}F-water ^{15}O-H_2O and $^{13}NO_3^-$ in Tomato Plants 105
2.31 Single-hit Effects and By-stander Effect on Cells by Heavy-ion Microbeams 107
2.32 Fundamental Study on Radiotherapy of Tumors to Beneficial Companion Animals using Heavy Ion Beam 110

3. Radiation Chemistry/Organic Materials 113
3.1 Study on Space Environment Durability of Newly Developed Polymeric Materials for Spacecraft (II) 115
3.2 Preparation of Ion Track Membranes and Their Separation Characteristics of Peptide Molecules 118
3.3 Application of Thin Film Dosimeters to Measurement of Ion Beam Dose Distribution II 120
3.4 Cross-linking of Polydimethylsiloxane in Heavy Ion Tracks 122
3.5 Nano-wire Formation along Ion Projectiles in Polysilane Thin Films 125

3.6 Primary Process of Radiation Chemistry Studied by Ion Pulse Radiolysis ····· 129
3.7 Measurement of Energy Deposition Around the Heavy Ion Trajectory by Photon Counting Method ····· 131

4. Inorganic Materials ····· 133
4.1 He Ions Implantation Effect on the Thermal Diffusivity of CVD-SiC ····· 135
4.2 Effects of Helium Embrittlement on Fatigue Properties of Reduced Activation Ferritic/Martensitic Steel ····· 138
4.3 Effects of Triple Beams on Microstructural Evolution in Ferritic/Martensitic Steels ····· 141
4.4 Investigation of the Resonant Vibration Modes of Self Interstitial Atoms in Metals by Low Temperature Specific Heat Measurement ····· 144
4.5 Study of Ion-induced Structural Changes in Li_2TiO_3 Ceramics ····· 146
4.6 Damage Evolution in High Energy Multi Ion-irradiated BCC Metals and the Interaction between Gas Atoms(H and He) and Damage Defects ····· 149
4.7 Dose Rate Effects on Microstructural Evolution in Austenitic Stainless Steels under Ion Irradiation ····· 152
4.8 Effect of Simultaneous Ion Irradiation on Microstructural Change of SiC/SiC Composites at High Temperature ····· 155
4.9 Radiation Induced Cavity Formation in F82H with Various Heat and Mechanical Treatments ····· 158
4.10 Comparison of Cavity Formation Behavior in RAF/M Steels Irradiated with Dual Beams of Fe +He Ions as Observed in the Depth Dependent Damage Structure ····· 161
4.11 Investigation of Hardness Changes on Helium-ion Implanted Iron by Ultra-micro-hardness Testing ····· 164
4.12 Effect of Ion Irradiation on Corrosion Behavior of Austenitic Stainless Steel ····· 167
4.13 Effect of Radiation on Microstructures and Corrosion Resistance of Austenitic Stainless Steels ····· 170
4.14 Nucleation and Growth of Carbon Onions in Cu and Au under Ion Implantation ····· 173
4.15 Thermal Response of the Metal/Fullerite Hybrid Assembly ····· 176
4.16 Deposition and Characterization of Carbon Films Prepared by Ion-bombardment-assisted Method ····· 179
4.17 Evolution of Co+C_{60} Structures during Co-deposition and Subsequent Annealing ····· 181
4.18 Modification of Carbon Related Films with Ion Beams ····· 183
4.19 Formation Process and Stability of Radiation-induced Non-equilibrium Phase in Silicon ····· 186
4.20 Improvement in Surface Roughness of Nitrogen-implanted Glassy Carbon by Hydrogen Doping ····· 188
4.21 Temperature Dependence of Growth Process of C_{60} Thin Films on a KBr(001)

Surface ····· 190
4.22 Thermal Relaxation of Hydrogen Disordering in Palladium-hydrogen System Irradiated with Energetic Electrons ····· 193
4.23 Anomalous Change in Electrical Resistivity in $EuBa_2Cu_3O_y$ Superconductor Irradiated with Energetic Electrons ····· 195
4.24 Defect Accumulation in Nanocrystalline Gold Irradiated with Electrons at Low Temperature ····· 197
4.25 Epitaxial Anatase and Rutile TiO_2 Films Prepared by Pulsed Laser Deposition ····· 199
4.26 Effect of Fluorine-ion Implantation in TiO_2 Rutile Single Crystals ····· 201

5. Material Analysis ····· 205
5.1 In-situ Observation of Growth Processes of Transition Metal Compound Thin Films by Carbon-implantation ····· 207
5.2 Development of In-situ Ion Beam Analysis of Adsorbate Atoms at the Solid-liquid Interface ····· 210
5.3 Carbon KVV Auger Electron Emission from HOPG Bombarded by Fast Protons ····· 212
5.4 Characterization of Defects and Hydrogen Absorption in Pd Irradiated with Protons ····· 215
5.5 Chemical Modifications of Polycarbonate by C_n^+ Cluster Irradiation ····· 218

6. Nuclear Science and RI Production ····· 221
6.1 Development of a Laser Ion Source with an Ohmic-heating Ionizer for the TIARA-ISOL ····· 223
6.2 Internal Conversion Electron Measurements in the Decay of the Proton-rich Isotope ^{126}Ce using an On-line Mass Separator ····· 226
6.3 Synthesis of Endohedral ^{133}Xe-fullerene by Ion Implantation ····· 228
6.4 Excitation Functions of Rhenium Isotopes on the ^{nat}W(d,xn) Reactions and Production of No-carrier-added ^{186}Re ····· 230

7. Microbeam Application ····· 233
7.1 Evaluation of Three Dimensional Microstructures on Silica Glass Fabricated by Ion Microbeam ····· 235
7.2 Development of High Performance Buffer Materials —Sorption Mechanism of Europium by Apatite and Smectite Mixture using RBS and Micro-PIXE— ····· 238
7.3 Development of In-air Micro-PIXE System for High-efficiency Elemental Analyses ····· 241
7.4 Fluoride Uptake Measurement using Microbeam PIGE ····· 244
7.5 Application of In-air Micro-PIXE Camera to Bovine Aortic Endothelial Cells and Human Leukemia Cells ····· 247
7.6 Application of Micro-PIXE to the Analysis of Single Fog Droplets ····· 250
7.7 In-air Micro-PIXE Analysis of Ascitic Hepatoma Tissue Slices ····· 253
7.8 Redistribution of Elements between Minerals in Rocks —Analysis of Uranium

Distribution in Rocks by μ-PIXE— ····· 256
7.9 Radiation Damage in Si PIN Diodes Induced by Heavy Ion Microbeam Single Hits ····· 259
7.10 Development of a High-energy Microbeam Single Ion Hit Technique for Bio-medical Applications ····· 262

8. Radiation Shielding for Accelerator Facilities ····· 265
8.1 Study of Particle Size Distribution of Radioactive Aerosols Formed by Irradiation of 65 MeV Quasi-monoenergetic Neutrons ····· 267
8.2 Measurement of Neutron Dose behind Iron Shield with Tissue Equivalent Proportional Counter ····· 270
8.3 Development of Neutron Monitor using a Liquid Scintillator ····· 273

9. Accelerator Technology/TIARA General ····· 277
9.1 Beam Energy Measurement by the Time-of-flight Technique ····· 279
9.2 Study of Beam Energy Spreads for the Single-ended Accelerator using Nuclear Resonance Reactions (II) ····· 281
9.3 Measurement of MeV Energy Cluster Ion Beam Current ····· 283
9.4 Development of Transparent-type Beam Current Monitor ····· 285
9.5 Development of the Sub-micron Ion Beam System at keV Range ····· 287
9.6 Temperature Control of Cyclotron Magnet for Stabilization of Magnetic Field Strength ····· 290
9.7 Present Status of JAERI AVF Cyclotron System ····· 293
9.8 Renewal of Computer Control System of the 3MV Tandem Accelerator ····· 296

10. Status of TIARA 2000 ····· 299
10.1 Utilization of TIARA Facilities ····· 301
10.2 Operation of the Electrostatic Accelerators ····· 303
10.3 Operation of JAERI AVF Cyclotron System ····· 304
10.4 Radiation Control & Radioactive Waste Management in TIARA ····· 305

Appendix ····· 309
Appendix 1. List of Publication ····· 311
Appendix 2. Type of Research Collaboration ····· 325
Appendix 3. Organization and Personnel of TIARA ····· 327

This is a blank page.

1. Semiconductors for Space

1.1 Radiation Tolerance of Multi-junction Space Solar Cells ····· 3
O.Anzawa, S.Kawakita, K.Aoyama, M.Imaizumi, S.Matsuda, T.Ohshima, T.Hirao, H.Itoh, M.Saito, and Y.Matsumoto,

1.2 Analysis of Single-ion Multiple-bit Upset in Commercial High-density DRAMs ····· 6
H.Shindou, A.Makihara, T.Aburaya, S.Kuboyama, S.Matsuda, T.Hirao, T.Ohshima, M.Yoshikawa , and H.Itoh

1.3 Angular Dependence of Ion-induced Current Measured by TIBIC System ····· 9
H.Mori, T.Hirao, J.S.Laird, S.Onoda, and H.Itoh

1.4 Development of Collimated Swift Heavy-ion Micro-beams for Investigation of Single Event Phenomena ····· 12
S.Onoda, T.Hirao, H.Mori, and H.Itoh

1.5 Analysis of Failure Caused by Cosmic Rays in High-voltage High-power Semiconductor Devices ····· 14
H.Matsuda, I.Omura, Y.Sakiyama, K.Shibata, H.Ohashi, T.Hirao, T.Ohshima, J.S.Laird, H.Itoh, H.Mori, and S.Onoda

1.6 Radiation Tolerance of Silicon Carbide Metal-oxide-semiconductor Transistor with Annealed Gate Oxide ····· 17
T.Ohshima, H.Itoh, and M.Yoshikawa

1.7 Study of Proton- and Electron-irradiation Effects on $CuInSe_2$ Thin Films ····· 20
A.Yoshida, H.S.Lee, H.Okada, A.Wakahara, T.Ohshima, H.Itoh, S.Kawakita, M.Imaizumi, and S.Matsuda

1.8 Pulsed-ESR Characterization of Diamond implanted with High Energy Phosphorus Ions at High Temperature ····· 23
J.Isoya, T.Ohshima, Y.Morita, and H.Itoh

This is a blank page.

1.1 Radiation Tolerance of Multi-junction Space Solar Cells

Osamu Anzawa, Shiro Kawakita, Kazuhiro Aoyama, Mitsuru Imaizumi, Sumio Matsuda, Takeshi Ohshima*, Toshio Hirao*, Hisayoshi Itoh*, Masashi Saito, Yusuke Matsumoto**
National Space Development Agency of Japan (NASDA), Department of Material Development, JAERI*, Advanced Engineering Service(AES) corporation**

1. Introduction

It is important to improve radiation tolerance of space solar cells, which play a role of power source of satellites, in order to extend the mission life time of satellites. Therefore, evaluation of radiation degradation of space solar cells is necessary in developing new type cells like multi-junction cells.

An InGaP/GaAs/Ge triple-junction solar cell is formed by stacking three different sub cells (InGaP top cell, GaAs middle cell, and Ge bottom cell) on a Ge substrate. The triple-junction solar cell shows extremely high conversion efficiency, because the InGaP top cell, the GaAs middle cell and the Ge bottom cell effectively convert short, middle and long wavelength light into electricity, respectively.

The output current of the multi-junction solar cell is limited by the lowest photocurrent generated at among the three sub cells. In order to improve radiation tolerance of the multi-junction solar cell, it is necessary to obtain degradation characteristics of each sub cell by irradiation. In this study, proton irradiation experiments with various energy have been carried out for the triple-junction solar cell and its degradation characteristics have been evaluated.

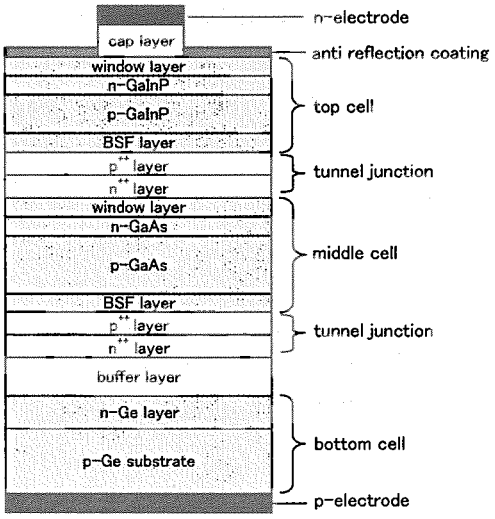


Fig.1 Schematic cross-section of an InGaP/GaAs/Ge triple-junction solar cell

2. Experiments

Schematic cross section of the InGaP/GaAs/Ge triple-junction solar cell evaluated in this study is shown in Fig. 1. P type single crystal Ge of 140 μm thickness was used as a substrate. The Ge bottom cell was made by formation of an n-type Ge layer due to thermal diffusion of As donors. The GaAs middle cell and the InGaP top cell were grown epitaxially on the Ge bottom cell using metalorganic chemical vapor deposition (MOCVD) technique. The adjacent sub cells were electrically connected through tunnel junctions. The cell size is 2×2 cm^2. Table 1 shows the condition of irradiation tests. Proton irradiation to the cells was carried out at JAERI Takasaki by using an AVF cyclotron, a tandem accelerator, and an ion implanter. 1MeV electron irradiation tests were also performed using an electron accelerator No.1 at JAERI. The current-voltage (I-V)

Table 1 Irradiation test condition

condition	particle	energy [MeV]	fluence [particle/cm^2]	accelerator (port)
1	proton	0.05	1×10^{10} - 1×10^{12}	Ion implanter (IA1)
2		1	3×10^{10} - 3×10^{12}	Tandem accelerator (TA1)
3		3		
4		10	8×10^{9} - 3×10^{13}	Cyclotron (LD1)
5	electron	1	1×10^{15} - 1×10^{17}	Electron accelerator No.1

characteristics of the cells were measured under light illumination from an AM0 solar simulator at NASDA. The temperature of the cells was kept at 28 °C during the I-V measurements. The quantum efficiency (QE) of each sub cell was individually measured at 28 °C. During the measurement of QE of a sub cell, the sample cell was illuminated by color bias light in order to activate the other sub cells. An appropriate electric bias was applied between the electrodes of the sample cell in order to measure QE for each sub cell under zero bias (short circuit) condition.

3. Results and Discussion

Figure 2 shows the degradation characteristics of short circuit current (Isc), open circuit voltage (Voc) and maximum power (Pmax) of the triple-junction solar cell irradiated with 10MeV protons. In this figure, the degradation characteristic of a GaAs single-junction solar cell fabricated on a GaAs substrate using liquid phase epitaxy (LPE) technique is also shown. The degradation of Voc of the triple-junction cell is almost equivalent to that of the single-junction cell. On the other hand, higher radiation tolerance of Isc and Pmax of the triple-junction cell is found compared with the single-junction cell. While the remaining factor of Isc of the single-junction solar cell at a fluence of 3×10^{12} p/cm^2 is about 85%, that of the triple-junction solar cell is about 100%. As shown in Fig. 3, the QE of the GaAs middle cell and Ge bottom cell degrade by irradiation of 10 MeV protons, although the InGaP top cell scarcely degrades.

Generally, in the case of multi-junction solar cells, it is possible to control the photocurrent generated at each sub cell by adjusting the its base layer thickness. The current generated at the Ge bottom cell is always largest among the three sub cells because the thick Ge substrate is used. In contrast to the Ge sub cell, it is feasible to adjust the photocurrent of the GaAs middle cell equal to that of the InGaP top cell after degradation due to irradiation by designing the generation current of GaAs middle cell larger than that of InGaP top cell at before degradation. As a result, radiation tolerance of the triple-junction cell is expected to be improved.

The degradation characteristics of Pmax due to various energy proton irradiation and 1MeV electron irradiation are shown in Fig. 4. The ratio of the 1MeV electron fluence to the 10MeV proton fluence, at which the same remaining factor of Pmax is obtained, is approximately 700. On the other hand, the fluence ratio for a conventional GaAs solar cell was reported to be about 1000[1]. In proton irradiation, the degradation becomes severer when the proton energy lowers. The relative damage coefficients are obtained from comparison of proton fluences, which give a remaining factor of 75%, to be 4, 9 and 24 for 3MeV, 1MeV and 0.05MeV proton irradiation, respectively.

4. Conclusion

It is feasible that radiation tolerance of Isc and Pmax of the InGaP/GaAs/Ge triple-junction solar cell is drastically improved by adjusting the photocurrent generated at each sub cell after irradiation, as compared with a single-junction GaAs solar cell. The relative damage coefficients, which are necessary for predicting degradation of solar cells in space, have been obtained.

References

1)B.E.Anspaugh,"GaAs Solar Cell Radiation Handbook", JPL Publication 96-9, 1996

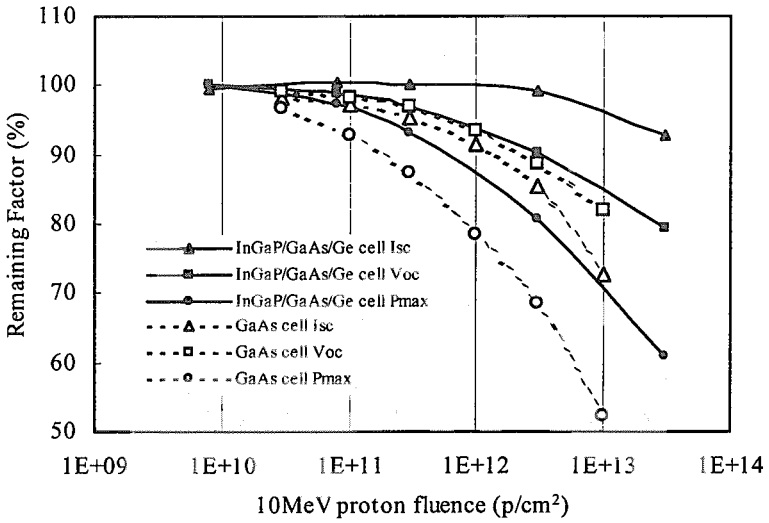


Fig.2 Degradation characteristics by 10 MeV proton irradiation

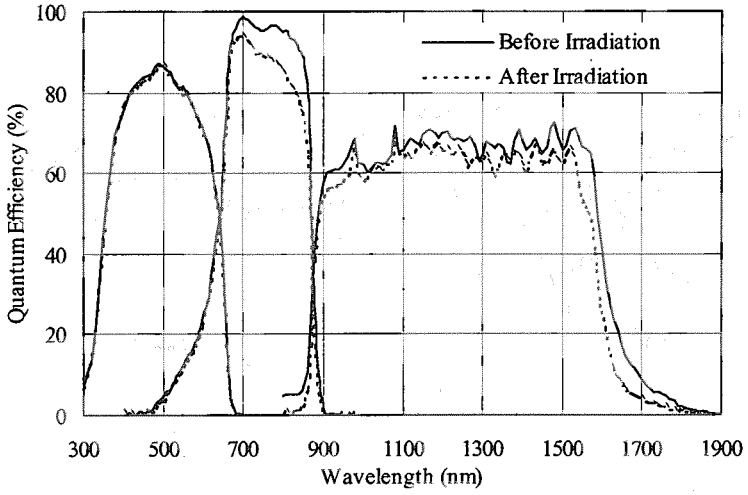


Fig.3 Quantum efficiency of InGaP/GaAs/Ge triple junction solar cell before and after 10 MeV proton irradiation (fluence = 3×10^{12} p/cm^2)

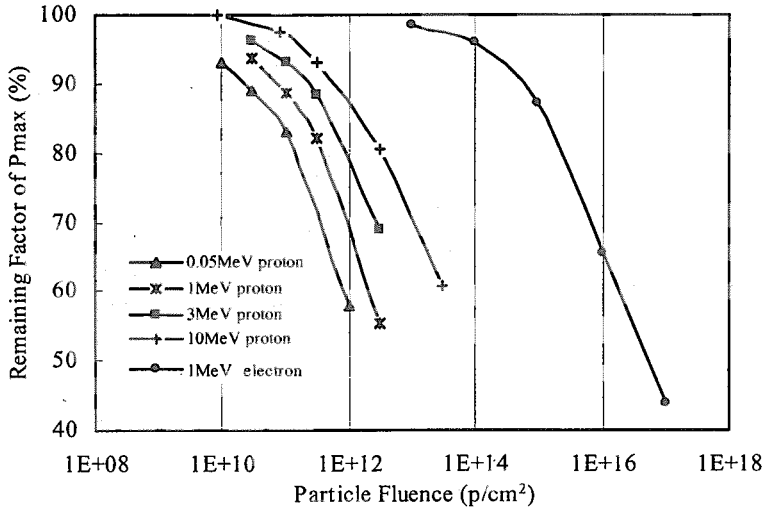


Fig.4 Degradation characteristics of Pmax by various energy proton irradiations

1.2 Analysis of Single-Ion Multiple-Bit Upset in Commercial High-Density DRAMs

H.Shindou[1], A.Makihara[1], T.Aburaya[1], S.Kuboyama[1], S.Matsuda[1], T.Hirao[2], T.Ohshima[2], M.Yoshikawa[2] and H.Itoh[2]
[1] National Space Development Agency of Japan (NASDA)
[2] Depertment of Materials Development, JAERI

1. Introduction

High-density Dynamic Random Access Memories (DRAMs) are very attractive devices for mass memory systems, such as Solid State Recorders (SSRs) intended for space applications. It is well known that DRAMs are very sensitive to Single Event Upsets (SEUs) caused by high-energy protons and heavy ions in space[1]. Error-Correction Code (ECC) is an essential element to correct the data errors caused by SEUs. For example, the Hubble Space Telescope (HST) SSRs used 16Mbit DRAMs with a powerful ECC encoding scheme known as Reed-Solomon. It is also shown that in high-density DRAMs, several types of Multiple-Bit Upsets (MBUs) modes occurs besides the normal single-bit SEUs[1][2]. In order to design effective ECC in the electronic system used in space, it is indispensable to clarify the mechanisms behind the MBUs.

In this study, we have characterized the MBU modes caused by heavy ions in high-density DRAMs. New types of MBU modes have found in 16Mbit and 64Mbit DRAMs. The mechanism responsible for the new modes is discussed based on detailed physical bit-map analysis.

2. Exprimental

2.1 Sample Devices

The sample devices used in the experiments were 16Mbit (2M word x 8bit, uPD4217800) and 64Mbit (8M word x 8bit, uPD4264800) DRAMs manufactured by NEC[3][4]. The information summaries of these devices are quoted in Table 1. These devices were specially assembled in ceramic packages. The general DRAM cell structure is shown in Fig.1. The MOSFET is turned on or off by the word line and the capacitor is charged or discharged through the bit line. In DRAMs, binary information is stored in a one-transistor cell as the presence or absence of charge on the capacitor [1].

Table 1. Design Information for DRAMs

	16Mbit DRAM (uPD4217800)	64Mbit DRAM (uPD4264800)
Technology	CMOS, bulk	CMOS, bulk
Process rule	0.45μ m	0.28μ m
Memory cell Size	2.48x1.24 =3.075μm²	0.65x1.30 =0.84μm²
Capacitance	27fF	25fF

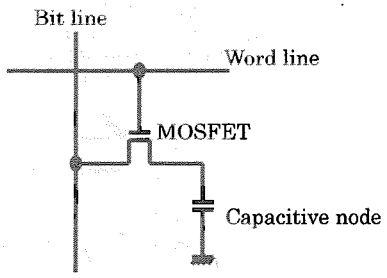


Fig.1 General DRAM cell structure

2.2 Test Setup

The devices were controlled by a small MPU card. Specific data were written to the DRAMs prior to irradiation and refreshed during irradiation using only row address strobing(RAS). The supply voltage was fixed to its minimum recommended value. Upsets of memory cells are usually caused by discharging the capacitor [1]. Therefore, most of the upsets are observed in cells in the charged state. On the other hand, specific types of upsets are also observed in cells in the discharged state. To evaluate the extent of the disturbance caused by an incident ion, most of the experiments were conducted on the devices in which all cells were in either a charged or a discharged state. The

experiments were performed with mono-energetic ions obtained from accelerators at Japan Atomic Energy Research Institute (JAERI) and Brookhaven National Laboratory (BNL).

3. Results and discussion

Fig.2 and Fig.3 show typical MBU clusters in the charged state of the 16Mbit and 64Mbit DRAMs, respectively. It is clear that the MBU clusters spread along the incident ion tracks. Upsets of the cells in the discharged state were not observed in a previous study [1]. However, upsets were also observed in the discharged state for both 16Mbit and 64Mbit DRAMs. Typical pattern of the MBU clusters is shown in Fig.4. Most of the upsets in the discharged state took place at a single bit and several at multiple bits. The cross-sections of the MBU events as a function of ion species and incident angle in the charged and discharged state are shown in Table 2. It seems that the cross section of the MBU in the discharged state was about two or three orders of magnitude smaller than that of the charged state. Entire word-line upsets were also observed in the discharged state as shown in Fig. 5. In this figure, The solid circles indicates the position of the upsets. The entire word line MBUs were observed in 8 memory blocks simultaneously. This result suggests that

Table 2 MBU event cross-section [cm^2/bit] as a function of ion species and incident angles in the charged and discharged state for 16Mbit and 64Mbit DRAMs.

Species of Ion			Angle of Incidence [deg.]					
			MBU on charged cells			MBU on discharged cells		
			0	60 (word)	60 (bit)	0	60 (word)	60 (bit)
	16Mbit DRAM	I	2.6×10^{-9}	1.8×10^{-9}	2.2×10^{-9}	1.2×10^{-11}	1.2×10^{-11}	1.6×10^{-11}
		Br	3.0×10^{-9}	2.5×10^{-9}	3.5×10^{-9}	5.9×10^{-12}	8.4×10^{-12}	9.1×10^{-12}
		Ni	3.4×10^{-9}	2.5×10^{-9}	2.8×10^{-9}	2.6×10^{-12}	5.1×10^{-12}	5.4×10^{-12}
	64Mbit DRAM	I	7.3×10^{-10}	1.3×10^{-9}	9.7×10^{-10}	7.7×10^{-12}	1.2×10^{-11}	1.0×10^{-11}
		Br	1.1×10^{-9}	8.0×10^{-10}	1.1×10^{-9}	7.9×10^{-12}	1.2×10^{-11}	1.0×10^{-11}
		Ni	1.1×10^{-9}	1.2×10^{-9}	1.1×10^{-9}	4.7×10^{-12}	1.2×10^{-11}	8.4×10^{-12}

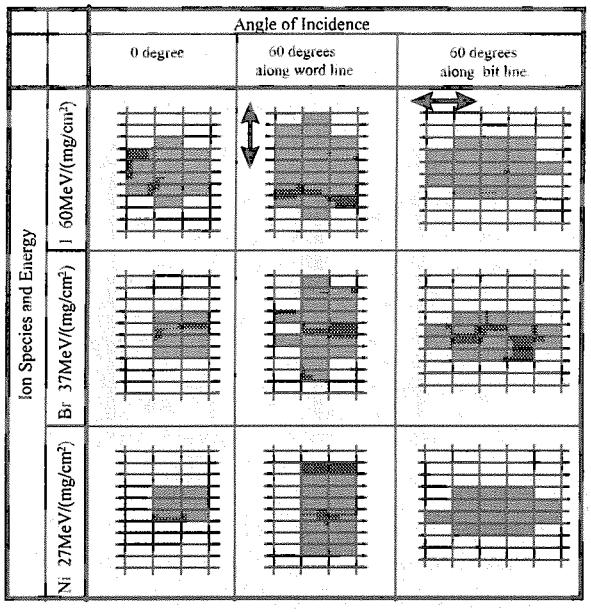


Fig.2 MBU clusters in the charged state of 16Mbit DRAMs

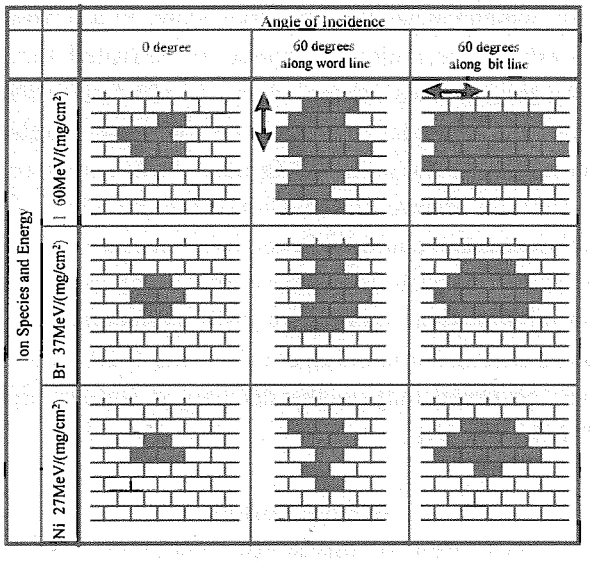


Fig.3 MBU clusters in the charged state of 64Mbit DRAMs

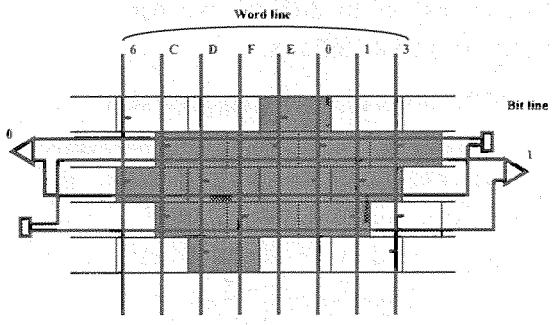


Fig.4 MBU clusters generated in the discharged state of 64Mbit DRAMs by I ion irradiation at 60deg. along the bit line.

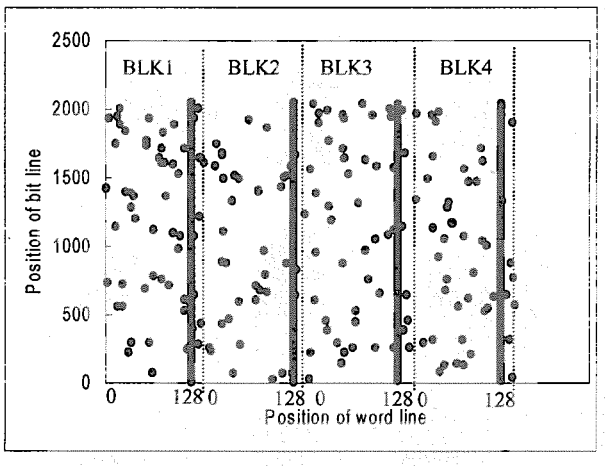


Fig.5 Entire word line MBU created by I ion I irradiation at 60 deg. along bit lines in the discharged state of 16Mbit DRAM.

the address decorder is disturbed by incident ions and, which causes the erroneous state. In a refresh sequence, the address decorder is activated first, then the bit lines are pre-charged, and finally the gates of the access transistors are turned on via the word line. If the gates of the access transistors are turned on before the bit lines are pre-charged, unknown data could be stored in the memory cells. This MBU mode would be a fatal error for SSRs because a great number of cells connected to a word line upset simultaneously. This MBU mode was observed only in the discharged state of the 16Mbit DRAMs.

4. Conclusions

As a result of this study, three MBU modes have been found in highly integrated DRAMs, i.e., 16Mbit and 64Mbit DRAMs. We consider that the MBUs are caused by different mechanisms, which are summarized as follows.

(a) MBU observed in the charged state

To discharge a capacitor, it is necessary that the carriers created by an incident ion are collected by the diffusion volume of the active transistor connected to the capacitor. MBU clusters in charged cells result from direct ion strikes to the cell area because their shapes are spread along the incident ion tracks.

(b) MBU observed in the discharged state

This MBU takes place by single ion hit to the precharge or sense amplifier circuit. Although this MBU mode can also be caused even in the charged state, the rate is relatively low.

(c) Entire word line MBU

The MBU occurs as a result of miss operation of the address decorder induced by incident ions. Since this type of MBU occurs in several memory blocks simultaneously, depending on the construction of the memory, it is likely that the MBU leads to serious errors in electronic systems.

References

[1] L.W.Massengill et al.,"Cosmic and Terrestrial Single-Event Radiation Effects in Dynamic Random Access Memories," IEEE Trans. Nucl. Sci., Vol. NS43, No.2, pp. 576-593 (1996).

[2] K.A.LaBel et al.,"Anatomy of an In-Flight Anormaly:Investigation of Proton Induced SEE Test Results for Stacked IBM DRAMs," IEEE Trans. Nucl. Sci., Vol.45, No.6, pp.2898-2903 (1998).

[3] S.Koshimaru et al.,"2nd generation 16Mbit DRAM," NEC Technical Journal, Vol.46, No.2, pp.90-93 (1993).

[4] S.Tsukada et al.,"Development of 64Mbit DRAM (3rd generation)," NEC Technical Journal, Vol.50, No.3, pp.23-27 (1993).

1.3 Angular Dependence of Ion-Induced Current Measured by TIBIC System

H. Mori*, T. Hirao, J. S. Laird, S. Onoda* and H. Itoh

*Graduate School of Engineering, Tokai University
Department of Materials Development, JAERI

1. Introduction

Single-event phenomena (SEP) are known to be malfunctions of electronic devices caused by the impact of high-energy particles in space environments. Among SEP, single event upset (SEU) is accompanied with data errors in memory devices. SEUs occur when the amount of electric charge induced by an energetic ion exceeds the critical charge required to maintain the memory state of a cell. Ion-induced carriers migrate promptly in a picosecond time scale via the drift and funneling processes. Migration of carriers also takes place through the diffusion process in a time range longer than 1 nanosecond.

Recent progress in large-scale integration of memory devices has made them more susceptible to SEUs because the critical charge is reduced by such integration. In highly integrated memory devices, a number of memory cells upset simultaneously due to impingement of a single ion, which is called multiple bit upset (MBU). When an angled ion strikes on such devices, the MBU clusters were reported to spread along the incident ion track [1,2]. The results can be ascribed to a spread of carrier distribution formed by the incident ion. However, the fundamental processes behind MBU have not yet been fully clarified. In this paper, we evaluate the amount of the collected charge in diodes as a function of incident ion angle to investigate the influence of angled ion hit on the generation of MBU clusters.

2. Experimental

The heavy ions used in this study were 15 MeV silicon (Si) of which linear energy transfer (LET) and the projected range in Si are 14.3 MeV/(mg/cm^2) and 6.46 μm, respectively. For ion irradiation, a microbeam of about 1μm in diameter was formed using a heavy ion microbeam system connected to a 3 MV tandem accelerator at JAERI Takasaki TIARA facility. The test devices were low-capacitance Si p^+n junction diodes with a substrate doping level of 4 x 10^{14} cm^{-3} or 5 x 10^{15} cm^{-3} (phosphorus donors) and a junction area of 50 μm in diameter. The p^+ region was formed by boron implantation at 30 keV at a dose 1 x 10^{15} cm^{-2}. At an applied bias of - 20 V the depth of the depletion region for the two diodes are 8.3 μm and 2.3 μm, respectively. The test devices were mounted on a chip carrier with 50 Ω double-ended micro-striplines. They were fixed at an angle of 0°, 15°, 30° and 45° to the incident ion. The experimental setup is schematically shown in figure 1. The transient current waveforms were observed with a 3 GHz bandwidth oscilloscope (Tektronix model TDS 694C).

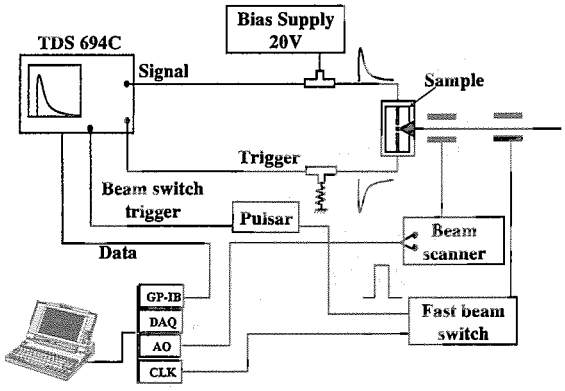


Figure 1. Schematic representation of the transient current measurement system.

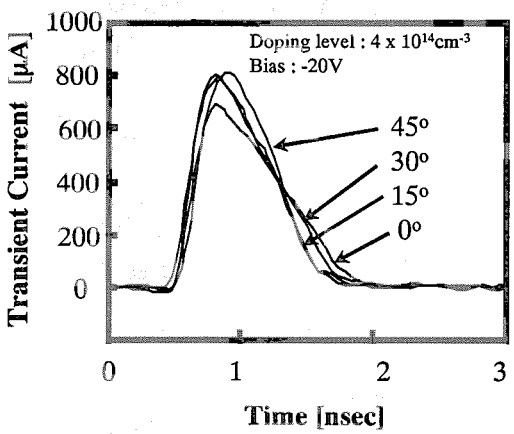


Figure 2. Waveforms of the transient current induced by a 15 MeV Si-ion at different incident angles for the test device with a substrate doping level of 4 x 10^{14} cm^{-3}. Transient currents were measured at a reverse bias of 20 V.

To reduce radiation damage, TIBIC (Transient Ion Beam Induced Current) system, by which the transient currents can be obtained by irradiation of a single ion, was used [3].

3. Results and Discussion

Figure 2 shows the waveforms of the transient current induced by a 15 MeV Si-ion under a reverse bias of 20 V in the Si p^+n junction diode with the substrate doping level of 4 x 10^{14} cm^{-3}. As shown in figure 2, the waveforms of the transient current changed with the angle. As the angle increased the charge collection time became short. When the angled ion passes near the diode electrode, ion-induced charges were collected rapidly due to a high electric field nearby the electrode. The amount of the collected charge is estimated by simply integrating the current transient to be approximately 500 fC. Assuming that all charges generated by an ion are collected at the diode electrode, the amount of the collected charge is estimated from the energy loss and the projected range of the ion to be about 570 fC. This value agrees well to the experimentally obtained one. For the test device with the substrate doping level of 4 x 10^{14} cm^{-3}, the incident ions always stop in the depletion region. In this case, ion-induced charge is drifted with a built-in potential and corrected at the diode electrode. Thus the amount of the collected charge is independent of the incident angle of ions.

Figure 3 shows the waveforms of the transient current induced by a 15 MeV Si-ion under a reverse bias of 20 V in the Si p^+n junction diode with the substrate doping level of 5 x 10^{15} cm^{-3}. In this figure, the waveforms of the transient current are almost the same. The amount of the collected charge is estimated by simply integrating the current transient to be approximately 520 fC. When the projected range of an ion is longer than the depth of the depletion region, it is necessary to consider not only the drift effect but also the funneling one. The former occurs in the depletion region, the latter beyond the depletion region. It was reported that the total charge collection length including the

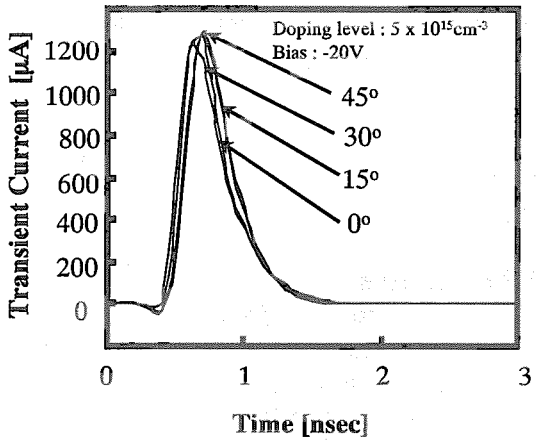


Figure 3. Waveforms of the transient current induced by a 15 MeV Si-ion at different incident angles for the test device with a substrate doping level of 5 x 10^{15} cm^{-3}. Transient currents were measured at a reverse bias of 20 V.

drift and funneling lengths is twice as long as the depth of the depletion region [4]. Taking account of the energy loss of 15 MeV Si-ions in the electrode, the penetration length of the ions in the device is estimated to be 5.7 μm, which is approximately twice as long as the depth of the depletion region. According to a previous paper [4], almost all charges should be collected at the diode electrode even in the case of normal incident of ions. Since an angled ion penetrate to a shallow position compared with a normal incident ion, most of ion-induced charges are probably collected at the electrode. It accounts for the result that the transient current was independent of the incident angle of ions.

Summary

We have examined the relationship between the amount of collected charge and the incident angle of ions. It was found that the amount of collected charge is independent of the incident ion angle when the projected range of ions was not longer than the charge collection length, which is twice as long as the depth of the depletion region of junction diodes.

Acknowledgements

The authors would like to acknowledge JAERI Electrostatic Accelerator group for their cooperation with the experiments.

Reference

[1] A.B.Cambell, et al., IEEE Trans. on Nucl. Sci., Vol. 45, No. 3, 1603, (1998).
[2] A.Makihara, et al., IEEE Trans. on Nucl. Sci., Vol. 47, No. 6, 2400, (2000).
[3] J.S.Laird, et al., JAERI-Review 2000-204, 11 (2000).
[4] T. Hirao, et al., Ionizing Radiation (Hoshasen), Vol. 23, No. 1, 35 (1997).

1.4 Development of Collimated Swift Heavy-ion Micro-beams for Investigation of Single Event Phenomena

S. Onoda*, T. Hirao, H. Mori* and H. Itoh
*Graduate School of Engineering, Tokai University
Department of Materials Development, JAERI

1.Introduction

Semiconductor devices used in artificial satellites are exposed to high-energy particles. When these particles penetrate into devices, dense electron-hole pairs are created and induce Single-Event Phenomena (SEP). Because SEP lead to system failures, it is necessary to raise SEP tolerance to increase the reliability of electronic systems in artificial satellites. To simulate SEP of device used in space, it is important to use ion beams, having high Liner Energy Transfer (LET). Focus such an ion beam on a SEP sensitive region in semiconductor device, the size of the beam has to be smaller than the sensitive area. Therefore, we have been developing the technique of micro-beam formation using micro-collimators, and applying it to measure single event transient currents as a function of LET.

2.Experiments

The scattered beam irradiation method, witch is shown schematically in figure 1, provides ion beams with a low intensity and homogeneous flux[1]. The heavy ion beam used in this study is 150 MeV $^{40}Ar^{8+}$ accelerated with an AVF cyclotron at JAERI Takasaki TIARA facilities.

The direct beam from cyclotron is scattered by an Au thin film (1μm in thickness), and the scattered beam goes into the SEP chamber placed at angle of 40 degrees. The scattered beam is collimated with micro-collimators made of Mo with a diameter of 2 mm or 20 μm. The angle of the micro-collimator to the incident beam direction can be adjusted to an accuracy of 0.1° so as to minimize the ion scattering on the inner wall of the collimator. The collimated beams are evaluated from the energy spectra measured with a silicon surface barrier detector (SSD) and a multi channel analyzer (MCA). For

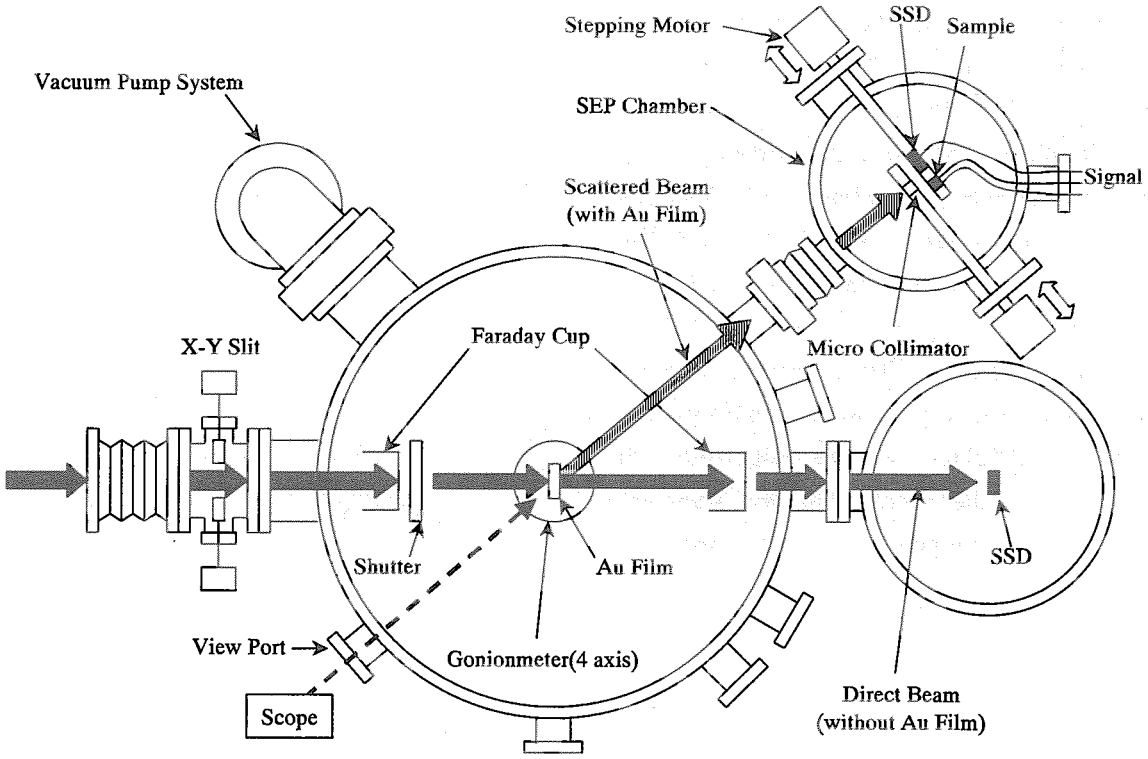


Figure 1.Scattered-beam irradiation method with micro-collimator for SEP testing.

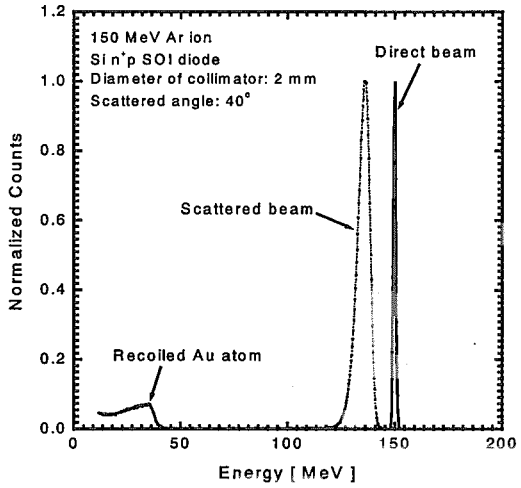


Figure 2. Normalized energy spectra of the direct Ar ion beam and the beam scattered with 1-μm thick Au film.

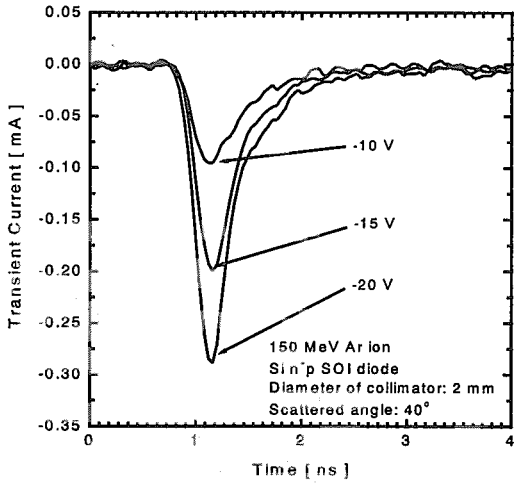


Figure 3. Bias dependence of the single event transient currents. The negative biases of 10, 15 or 20 V is applied to the sample diode.

comparison, the energy spectrum of the direct beam is also measured.

The silicon on insulator (SOI) n^+p diodes are used in this study. The thickness of the top silicon layer and the diode area are 6 μm and 50 μm, respectively. The single event transient currents are measured using a high bandwidth oscilloscope. To minimize the effect of defects induced by ions, the measurement is performed under single ion hit.

3. Results and Discussion

Figure 2 shows energy spectra of a 150 MeV Ar ion beam (direct beam) and a scattered beam obtained with the Au film and the collimator with 2mm in diameter. In the case of the scattered beam, a peak due to scattered Ar ions and a small peak due to recoiled Au atoms are obtained. Although Au atoms could be eliminated using a thin absorber[1], we do not apply this method because the transient currents induced by recoiled Au atoms are negligibly small compared with that by scattered Ar ions. The peak energy and FWHM of the scattered Ar ions are 136 MeV and 6.4 MeV, respectively. Those of the direct Ar beam are 150 MeV and 0.9 MeV, respectively. The scattered Ar ions lose their energy by about 14 MeV and their energy purity becomes poor. However, the LET value does not spread much since the LET is not a strong function of the particle energy. Therefore, the beam formed by this method could be used to examine the LET dependence.

Figure 3 show the transient currents induced by scattered Ar ions when the collimator with 2 mm diameter is used. The applied negative biases to the SOI diodes are 10, 15 and 20 V. The absolute value of the peak current increases with increasing negative bias. Analysis of the carrier transportation in the SOI diode is now in progress. The transient current depends on the position of an ion incident on the sample diode. The current value becomes small when an ion impinges at an edge region of the diode. To reduce the edge effects, it is important to aim the ion beam at central junction area of the diode. When the collimator with a 20 μm is used, the beam flux is too low to measure the transient current. The flux is approximately ~10^{-5} cpm. To obtain the transient currents by using the narrow collimator, further increase of the beam flux is necessary.

4. Summary

The scattered beam irradiation method is applied to obtain the single event transient currents in semiconductor devices. The beam energy of the scattered beams is found to be high sufficient to evaluate the single event transient currents as a function of LET. By using this method the transient currents are successfully obtained in the SOI n^+p diodes. For detailed experiments on transient currents, the beam focus on the central area of diode junctions will be performed.

References

1) I. Nashiyama, et al. "Scattered-Beam Irradiation Method for SEU Testing", TIARA Annual Report, 1992, pp. 3-6.

1.5 Analysis of Failure Caused by Cosmic Rays in High-Voltage High-Power Semiconductor Devices

Hideo Matsuda[1)], Ichiro Omura[1)], Yoko Sakiyama[1)],
Kunihiko Shibata[1)], Hiromichi Ohashi[2)],
Toshio Hirao[3)], Takeshi Ohshima[3)],
Jamie S.Laird[3)], Hisayoshi Itoh[3)],
Hideki Mori[4)], Shinobu Onoda[4)]

[1)] Toshiba Corporation, Semiconductor Company
[2)] Toshiba Corporation, R&D Center
[3)] Department of Material Development, JAERI
[4)] Graduate School of Engineering, Tokai University

1. Introduction

High power semiconductor devices have been widely used in key industries, for instance, traction, transmission, etc. A failure of such power devices induced by cosmic rays at the sea level has been recently observed(1). At the present stage it is considered that high power devices fail or breakdown by reaction between Si and cosmic rays, e.g., high energy neutrons and protons. Since the experimental technique to measure radiation induced failures in high power devices is not established, the mechanisms behind the failures have not yet been clarified. As for the tests of high power semiconductor devices by irradiation of neutrons and protons using accelerators, it has been reported that the failure rate depended on the device structure and that the rate at nominal voltage was lower than that extrapolated from the data obtained at higher voltage (2)(3).

The aims of this work is (1):to verify the equivalence between the failure rates obtained by proton irradiation and those by actual cosmic rays and (2):to examine the failure rates for various devices at their nominal voltage, which are quite useful for designing high power devices having high performance as well as high reliability. In order to clarify the failure mechanisms, we have investigated the failure points generated in power devices by heavy ion irradiation.

2. Experiments

2.1 Proton irradiation

An AVF-cyclotron at TIARA has been used for proton irradiation. Parameters are proton energy and fluence. The failure rate of high power devices was derived from the number of failures divided by proton fluence. The test block diagram is schematically shown in Fig.1.

2.2 Heavy ion irradiation

An 3MV-tandem-accelerator has been used for heavy ion irradiation. A micro-beam of 15MeV-C was scanned on the test devices at 2 microns per pitch. The test block diagram is shown in Fig.2.

3. Results and discussion

3.1 Proton irradiation

The test devices suddenly failed by proton irradiation during voltage blocking.

The phenomenon is very similar to the failure caused by actual cosmic rays. Fig.3 shows the failure rate as a function of supplied electric field. The horizontal axis represents the maximum electric field in the devices. The vertical axis represents the failure rate divided by irradiated particle fluence. A solid line in the figure exhibits the data reported in reference (2), in which the data was obtained by irradiation of neutrons in an energy range of 1MeV to 800MeV. The slope of the failure rate obtained in this test is similar to that of reference (2) whereas some deviations in the absolute value are obtained. Detailed analysis of the experimental data is now in progress.

3.2 Heavy ion irradiation

The test devices also suddenly failed by heavy ion irradiation during voltage blocking. Details are now under investigation.

4. Conclusion

A preliminary examination of failures in high power devices due to proton and heavy ion irradiation has been performed. The test results obtained by proton irradiation are similar to those reported previously. It shows the propriety of our measurements for device failure. Further investigations are necessary to clarify the failure mechanisms.

References

(1)H.Matsuda, et al, "Analysis of GTO Failure Mode During DC Voltage Blocking", Proc. of the 6th ISPSD, (1994) pp221-225.

(2)H.R.Zeller, "Cosmic Ray Induced Failures in High Power Semiconductor Devices", Microelectron. Reliab., 37, (1997)pp1711-1718.

(3)P. Voss, "Irradiation Experiments with High-voltage Power Devices as a Possible Means to Predict Failure Rates due to Cosmic Rays", Proc. of the 9th ISPSD, (1994) pp169-172.

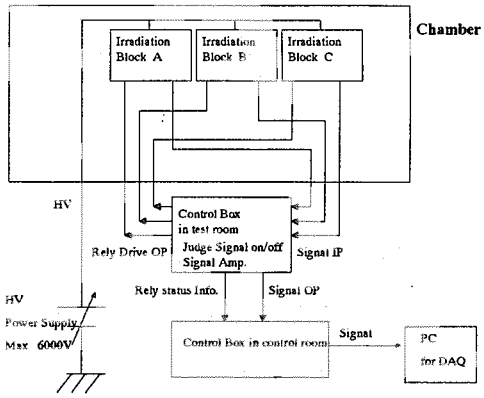


Fig.1a Proton Irradiation Test Diagram

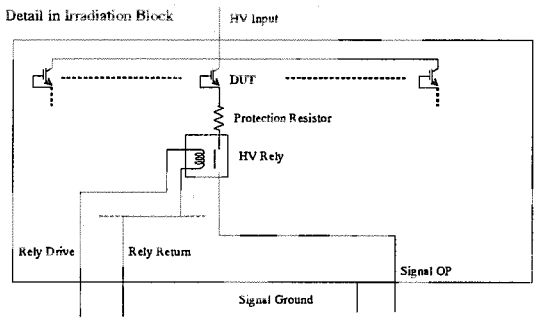


Fig.1b Proton Irradiation Test Diagram (Details of the Irradiation Block in Fig.1a)

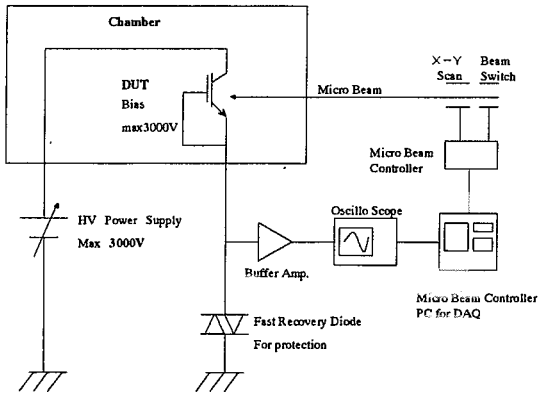


Fig.2 Heavy Ion Irradiation Test Diagram

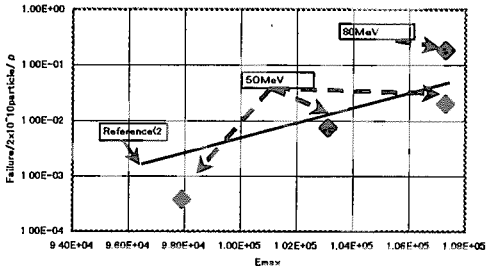


Fig.3 Dependence of Failure Rate
on Electric Field

1.6 Radiation Tolerance of Silicon Carbide Metal-Oxide-Semiconductor Transistor with annealed gate oxide

Takeshi Ohshima, Hisayoshi Itoh, and Masahito Yoshikawa
Department of Material Development, JAERI

1. Introduction

Silicon carbide (SiC) is regarded as a promising candidate for electronic devices used in harsh radiation environments (Rad-hard devices) as well as high-power and high-frequency electronic devices. For the development of rad-hard devices, it is important to understand the effect of various types of irradiation on the electrical characteristics of SiC devices. Recently, we have demonstrated that the electrical characteristics of SiC metal-oxide-semiconductor field effect transistor (MOSFET) before irradiation can be improved by hydrogen (H_2) annealing of the gate oxide during the fabrication process.[1] In this study, we investigate the gamma-ray (γ-ray) irradiation effects on SiC MOSFETs with H_2-annealed gate oxides (SiC(H_2) MOSFETs).

2. Experiments

The MOSFETs used in this study were fabricated on p-type epitaxial 6H-SiC films (4μm thick) grown on 6H-SiC substrates (3.5° off, Si-face). The net acceptor concentration of the epitaxial films ranges from $5x10^{15}$ to $1x10^{16}$ /cm^3. The source and drain of the MOSFETs were formed using phosphorous implantation at 800 °C and subsequent annealing at 1500 °C for 20 min in an Ar atmosphere. The gate oxide was fabricated by pyrogenic oxidation (H_2:O_2 = 1:1) at 1100 °C for 60 min. Hydrogen annealing was performed at 700 °C for 30 min at a pressure of 20 Torr. The gate length and width of the MOSFETs are 10 μm and 200 μm, respectively. Gamma-ray irradiation was performed up to 530 kGy (SiO_2) at a rate of 8.8 kGy/h at room temperature (RT). No electrical bias was applied to the gate , the drain and the source during the irradiation. The electrical characteristics were measured at RT under dark conditions. The channel mobility (μ) of the MOSFETs was derived from the linear region of the drain current (I_D) versus drain voltage (V_D) curves. The value of μ before irradiation was obtained to be 52 cm^2/Vs. The threshold voltage (V_{th}) is determined from the curve of the square root of I_D versus V_G in the saturation region. Before irradiation, V_{th} was measured to be 1.37 V.

3. Results and discussion

Figure 1 shows I_D versus gate voltage (V_G) curves in the subthreshold region (subthreshold-current curves) for the SiC(H_2) MOSFET before and after irradiation at four different radiation doses. The voltage marked with a cross on each curve corresponds to V_{th} .

McWhorter and Winokur reported the technique for separating the effects of interface traps and oxide-trapped charges from the change of subthreshold curves by irradiation[2]. According to their study, the entire subthreshold-current curve is simply translated by the generation of oxide-trapped charge because the contribution of trapped-oxide charge to the shift of V_{th} is independent of gate bias. On the other hand, interface traps interact with carriers in semiconductor, and the density of interface traps capturing carriers depends on gate bias. Thus, the subthreshold-current curve is stretched by the generation of interface traps. As a result, the shift of the threshold voltage by irradiation (ΔV_{th}) is described as $\Delta V_{ox}+\Delta V_{it}$, where ΔV_{ox} and ΔV_{it} are the voltage shifts due to the generation of oxide-trapped charges and interface traps, respectively. The shift of the midgap voltage (ΔV_{mid}) upon irradiation represents the shift owing to the formation of trapped-oxide charges only ($\Delta V_{ox} = \Delta V_{mid}$). Since the subthreshold-current curve between the midgap (V_{mid}) and the threshold voltages is stretched by the generation of interface traps, ΔV_{it} can be determined from $\Delta V_{it} = (V_{th} - V_{mid})_{post}-(V_{th} - V_{mid})_{pre}$, where "post" and "pre" denote after and before irradiation, respectively. Detailed analysis is described in ref. 2.

The net number of radiation-induced interface traps (ΔN_{it}) is obtained from ΔV_{it}

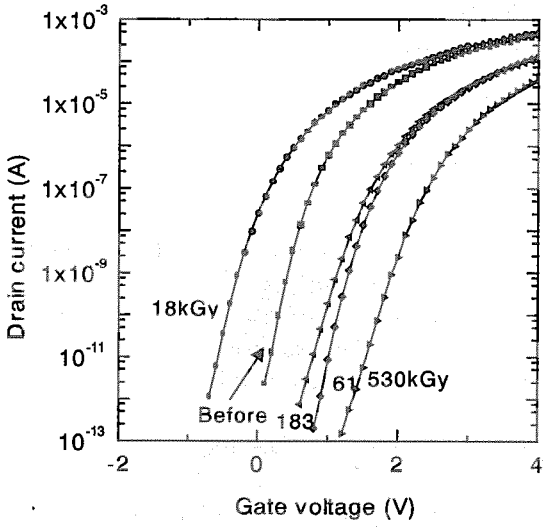


Fig. 1 Subthreshold-current curves for $SiC(H_2)$ MOSFETs irradiated with γ-rays. The bias of 12 V was applied between source and drain during the measurement. The values of absorbed dose are shown in the figure. The result before irradiation is also shown for comparison.

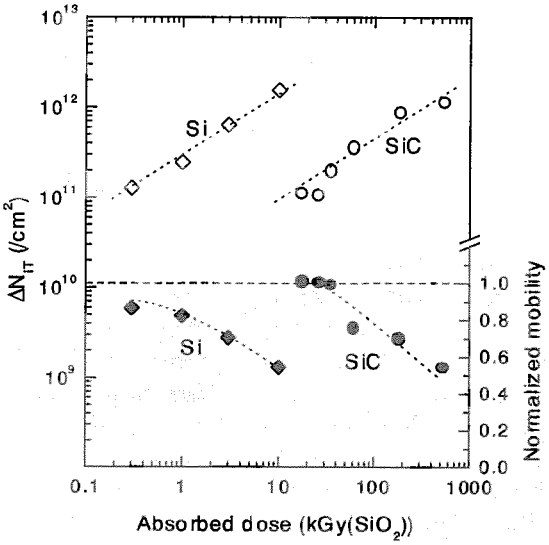


Fig2.Absorbed dose dependence of ΔN_{IT} and the channel mobility for $SiC(H_2)$ MOSFETs. The channel mobility is normalized to the pre-irradiation value. Open and closed circles represent ΔN_{it} and the normalized mobility, respectively. The reported ΔN_{it} and the normalized channel mobility for Si MOSFET[2, 3] are shown as open and closed diamonds, respectively.

by

$$\Delta N_{it} = |\Delta V_{it}| C_{OX}/q, \qquad (1)$$

where C_{OX} is equal to ε_{OX}/t_{OX}, and ε_{OX} and t_{OX} are the relative dielectric constant of SiO_2 and the thickness of gate oxide, respectively. The absorbed dose dependence of ΔN_{it} (open symbols) and the normalized channel mobility (closed symbols) for $SiC(H_2)$ MOSFETs are shown in Fig. 2. For comparison, the result reported for Si MOSFETs[2, 3] is also shown in the figure. The values of ΔN_{it} for $SiC(H_2)$ MOSFET are lower than that in the Si MOSFETs. As for the absorbed dose dependence, ΔN_{IT} for the $SiC(H_2)$ MOSFETs increases with increasing the absorbed dose with an exponent of approximately 2/3. The 2/3 power-law dependence is also found in Si whose gate oxide was formed using dry oxidation[2, 3]. The power-law dependence relates to the generation mechanism of interface traps. Regarding μ, the value for $SiC(H_2)$ MOSFETs decreases at doses above 60 kGy(SiO_2), and becomes 50 % of the unirradiated case at 530 kGy(SiO_2). In the case of Si MOSFET,[14] the channel mobility degrades to 50% at a dose of only 10 kGy(SiO_2). Thus we conclude that $SiC(H_2)$ MOSFETs are extremely radiation resistant compared to Si based MOSFETs.

Sexton et al.[3] reported that a decrease of μ in Si MOSFET was able to be fitted as a function of ΔN_{it} using

$$\mu = \mu_0 / (1 + \alpha \Delta N_{it}), \qquad (2)$$

where μ_0 and α are the channel mobility before irradiation and a constant (= 7.0 ± 1.3 x 10^{-13}), respectively. Figure 3 shows the relationship between the normalized mobility and ΔN_{it} for $SiC(H_2)$ MOSFETs (closed cilcles). The open circles and the solid line in the figure are the reported results for Si MOSFETs[3] and the result calculated using eq. (2), respectively. Although the generation of interface traps for $SiC(H_2)$ MOSFETs by irradiation takes place at extremely low rate in comparison with that for Si MOSFETs, the relationship between channel mobility and ΔN_{it} for both

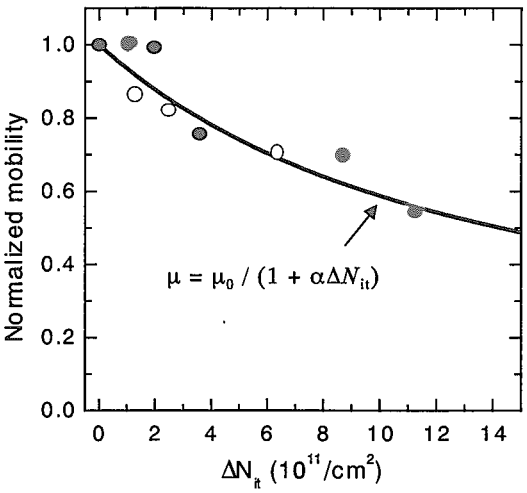


Fig.3 Relationship between the normalized mobility and ΔN_{IT} for SiC(H_2) MOSFETs (closed circles). The reported result for Si MOSFETs is also plotted as open circles for comparison. The solid line represents the results calculated using eq. (2).

MOSFETs can be described using eq. (2). It is noticed that because interface traps in the middle region of the bandgap of 6H-SiC act just as trapped-oxide charges owing to extremely long charge release times at RT,[4] ΔN_{it} obtained in this analysis is thought to be the density of radiation induced interface traps existing near the conduction band edge. Thus, the obtained results suggest that the channel mobility in SiC MOSFETs decreases mainly due to the generation of interface traps existing near the conduction band edge. Schörner et al.[5] reported that the channel mobility in unirradiated 6H-SiC MOSFETs is affected by acceptor like traps existing near the conduction band edge.

4. Summary

Enhancement-type *n*-channel MOSFETs with H_2-annealed gate oxide have been fabricated on 6H-SiC substrates. These devices were irradiated with γ-rays up to 530kGy(SiO_2) at RT. Based on changes in the subthreshold-current curve with irradiation, the relationship between the generation of interface traps and the decrease of channel mobility in the MOSFETs was evaluated. The net number of radiation-induced interface traps for the SiC MOSFETs with H_2-annealed gate oxide is lower than that for Si MOSFETs. The dependence of channel mobility on the generation of interface traps in SiC MOSFETs with H_2-annealed gate oxide can be fitted using the relationship obtained for Si MOSFETs whereas interface traps in SiC MOSFETs with H_2-annealed gate oxide are generated at an extremely low rate as compared to that in Si MOSFETs.

References

1) T. Ohshima, M. Yoshikawa, H. Itoh, K. Kojima, S. Okada, I. Nashiyama, Mat. Sci. Forum **338-342** (2000) 1299 .
2) P. J. McWhorter, P. S. Winokur, Appl. Phys. Lett. **48** (1986) 133.
3) F. W. Sexton, J. R. Schwank, IEEE Trans. Nucl. Sci. **NS-32** (1985) 3975 .
4) M. Yoshikawa, K. Saitoh, T. Ohshima, H. Itoh, I. Nashiyama, S. Yoshida, H. Okumura, Y. Takahashi and K. Ohnishi, J. Appl. Phys. **80** (1996) 282.
5) R. Schörner, P. Friedrichs, D. Peters, IEEE Trans. Electron Devices **46** (1999) 533.

1.7 Study of proton- and electron-irradiation effects on $CuInSe_2$ thin films

A. Yoshida[1], H.S. Lee[1], H. Okada[1], A. Wakahara[1], T. Ohshima[2], H. Itoh[2], S. Kawakita[3], M. Imaizumi[3] and S. Matsuda[3]
[1] Department of Electrical and Electronic Engineering, Toyohashi University of Technology, [2] Department of Material Development, JAERI
[3] National Space Development Agency of Japan

1. Introduction

$CuInSe_2$ (CIS)-related chalcopyrite materials have received considerable attention because of their potentials for solar cell application[1]. In addition, CIS-related thin film solar cells have also been expected to use in space area because of their superior irradiation hardness[2], low cost and low mass[3]. In order to use in space area under high-energy electrons, protons and other particles, it is important to evaluate the property of damages generated by irradiation in solar cells and cell materials. A few reports have been published for irradiation effect on CIS-based thin film solar cells. Recently, NASDA[4] performed the irradiation of 1MeV electrons and 10MeV protons to CIS solar cells. The electrical characteristics were not decreased after irradiation of electrons up to a fluence of 5×10^{16} cm^{-2} and remained at 80% of the initial efficiency after irradiation of protons up to a fluence of 1×10^{13} cm^{-2}. CIS-based thin film solar cells have more superior irradiation hardness, compared with other solar cells, such as Si and GaAs solar cells[4,5]. However, the property of damage generated by irradiation in CIS thin film itself is not yet clear.

In this work, in order to clarify the mechanism of damages generated by irradiation in CIS solar cells, and to improve their performance, we have studied for the proton- and electron-irradiation effects on the electrical properties of CIS thin films.

2. Experimental procedure

The CIS thin films were fabricated by radio frequency sputtering on semi-insulating GaAs (001) substrates at 400~450℃. The thickness of CIS thin films was 6000Å. The process of making a target material for sputtering was described in another report in more detail[6]. The substrate was cleaned ultrasonically by organic solvents, and etched in H_2SO_4 solution for 1min. In addition, the substrate was cleaned by Ar plasma for 10min to remove the native oxide on the surface of the GaAs substrate before growth.

The proton irradiation was performed at the ion-injector for 380keV proton and Tandem accelerator for 1MeV proton of the Japan Atomic Energy Research Institute (JAERI). The electron irradiation was also performed at the Cockcraft-Walton type accelerator for 2MeV electron and dynamitron accelerator for 3MeV electron. The fluences of proton and electron were in the range of $1\times10^{13}\sim5\times10^{14}cm^{-2}$ and $1\times10^{15}\sim6\times10^{17}cm^{-2}$, respectively. The electron concentration and mobility of CIS thin films were determined between 80 and 300K by van der Pauw method before and after irradiation.

3. Results and Discussion

3.1 Electrical properties of CIS thin films before irradiation

The CIS thin films were confirmed to be grown epitaxially from the Reflection High Energy Electron Diffraction (RHEED) pattern shown in Fig. 1. The samples showed n-type conduction, and the carrier concentration (n_0) and mobility were in range of $4\times10^{16}\sim1\times10^{17}cm^{-3}$ and 85~120 $cm^2/V.sec$, respectively.

3.2 Calculation of carrier removal rate with irradiation fluence

To discuss about irradiation hardness of CIS thin films quantitatively, carrier removal rate, R_c, was estimated. Theoretically, the change in carrier concentration Δn in the CIS thin films with irradiation fluence is expressed by[7]

$$\Delta n = n_0 - n_\phi = \sum I_{ij} f(E_{ij})\phi \approx R_c \cdot \phi \quad (1)$$

where n_0 and n_ϕ indicate the carrier concentration of CIS thin films before and after

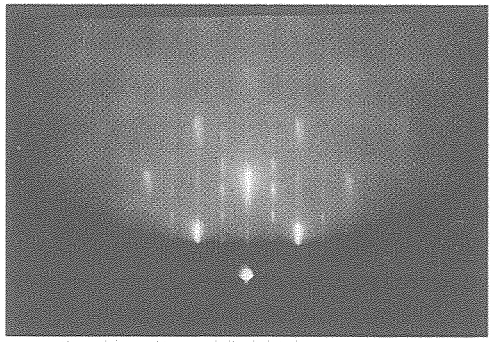


Fig. 1 RHEED patterns of CIS thin film. Electron beam is incident to [-100] direction of (001) GaAs.

irradiation, respectively, I_{ij} is the introduction rate of j-th majority carrier trap center by irradiation, $f(E_{ij})$ is the capture rate of majority carriers by the j-th trap center, R_C is the carrier removal rate, and ϕ is the irradiation fluence. Carrier concentration n_ϕ after irradiation is approximated, under the condition of small ϕ, from eq. (1) as follows:

$$n_\phi = n_0 \exp(-R_C\phi / n_0) \qquad (2)$$

3.3 Carrier removal behavior after proton- and electron-irradiation

Figure 2 shows the dependence of carrier concentration in CIS thin films on 380keV and 1MeV proton fluence. In Fig.2, as the proton fluence exceeded 1×10^{13}cm^{-2}, the carrier concentration was decreased. From these results, the electrical properties of CIS thin films were strongly dependent on proton fluence. The carrier concentration calculated from the eq. (2) was fitted with experimental data as shown in Fig.2. Consistent fitting was obtained below 1×10^{14} cm^{-2}. Although good fitting was not found in higher fluence region, eq. (2) is valid in lower fluence region. Further study is needed to clarify the carrier removal behavior after higher proton irradiation. Judging from the fitting in the lower fluence region, R_C was estimated to be about 1000cm^{-1}, which is comparable with other solar cells, such as InP[8] and GaAs[9] where R_C is 1800cm^{-1} and 700~1500cm^{-1}, respectively. In this study, little significant change in the carrier removal rate was observed as a function of proton energy.

Figure 3 shows the dependence of carrier concentration in CIS thin films on 2MeV and 3MeV electron fluence. In Fig.3, as the electron fluence exceeded 1×10^{17}cm^{-2}, the carrier concentration was decreased. From these results, the electrical properties of CIS thin films were strongly dependent on electron fluence. The carrier concentration calculated from the same formula in Fig.2 was fitted with experimental data as shown in Fig.3. From these results, R_C was estimated to be about 1cm^{-1}, which is lower than other solar cells, such as InP[10] and GaAs[11] where the R_C are 2~10cm^{-1} and 1.2~4cm^{-1}, respectively. However, no significant change in the carrier removal rate was observed as a function of electron energy.

The irradiation hardness of solar cells is explained by their higher absorption coefficients, shorter minority carrier diffusion lengths, and lower carrier removal rate. Therefore, CIS thin films are likely to have more irradiation hardness than other materials because the carrier removal rate in CIS is lower, compared with Ⅲ - Ⅴ compound in this study[12].

3.4 Investigation of irradiation induced defects

Figure 4 shows the temperature dependence of carrier concentration which was measured before and after 380keV proton irradiation. To investigate fundamental properties of irradiation induced defect, comparisons between experiment and theory were made. Theoretically, the carrier density of CIS thin films, n, was calculated from the charge balance equation for a donor and compensated acceptor before irradiation. Here, we found N_D, N_A and E_D to obtain the best fit in the unirradiated case. Namely, N_D=9.5 × 10^{16}cm^{-3}, N_A=3.7 × 10^{16}cm^{-3} and E_D=21meV were obtained. This activation energy is in agreement with the result of 5~20meV, which is attributed to In_{Cu} in n-type $CuInSe_2$[13].

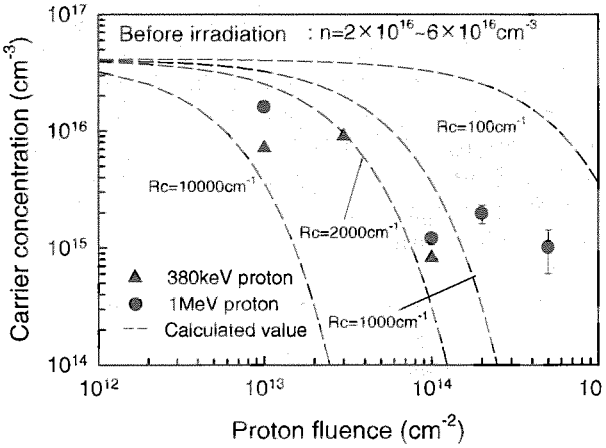


Fig. 2 Dependence of carrier concentration in CIS thin films on proton fluence.

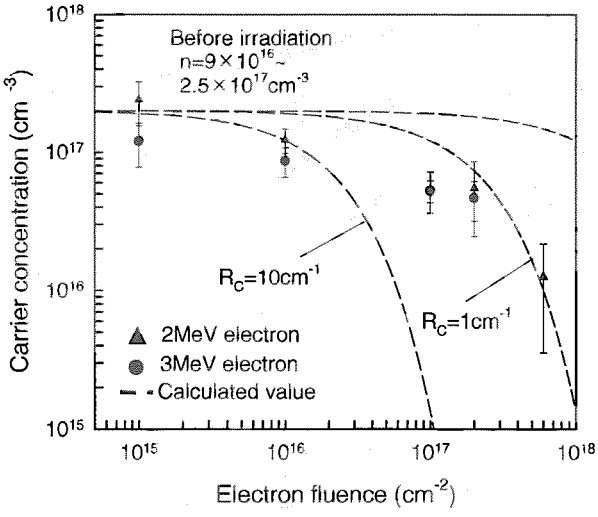


Fig. 3 Dependence of carrier concentration in CIS thin films on electron fluence.

After irradiation, the slope of the temperature dependence was increased. This suggests that some defects would be formed in CIS thin films by irradiation. At a fluence of $1\times10^{14}cm^{-2}$, the activation energy of 95meV was obtained from fitting the data in agreement with result of V_{Se} defect. Although it has been reported that many kinds of defects are formed by irradiation, we assumed that defects of 95meV energy level, which acted as the electron trap, are mainly produced in CIS thin films. Then, at a fluence of $3\times10^{13}cm^{-2}$, the density of a defect, N_T, and the defect level, E_T, were created by irradiation. Based on the charge balance equation, it is also possible to evaluate the defect density (N_T) and the activation energy of the defect (E_T) induced by irradiation. We fitted again to the experimental data by using a charge balance equation in which a defect was included. In this calculation of the carrier density, we assumed that a single defect with the activation energy of 95meV was produced in CIS thin films by irradiation and that the defect density was increased with proton fluence. After that, the same procedure was also made to the data of a fluence of $1\times10^{14}cm^{-2}$. As seen in Fig.4, a good agreement is reproduced with experimental data. From these results, $N_T = 1\times10^{17}cm^{-3}$ for a fluence of $3\times10^{13}cm^{-2}$ and $N_T = 5.7\times10^{17}cm^{-3}$ for a fluence of $1\times10^{14}\ cm^{-2}$ were obtained. New defect, which acted as an electron trap, was due to proton irradiation, and the defect density was increased with proton fluence.

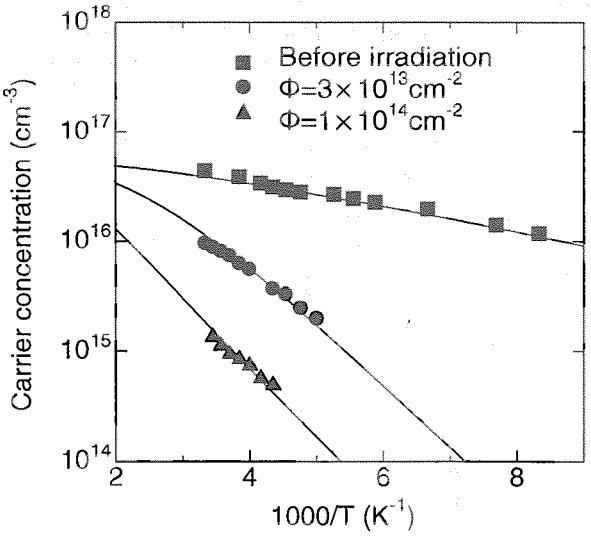


Fig. 4 Dependence of carrier concentration on temperature as a function of 380keV proton fluence. Solid lines: fitting curve to experimental data.

4. Summary

We have studied for proton- and electron-irradiation effect on the electrical properties of CIS thin films. As the proton and electron fluence was increased, the carrier concentration was decreased. The carrier removal rate with proton and electron fluence was estimated to be about $1000cm^{-1}$, and $1cm^{-1}$, respectively. In this study, significant change in the carrier removal rate was not clearly observed as a function of proton and electron energy. The electrical properties of CIS thin films before and after proton irradiation were also studied between 80 and 300K. A defect level was created by proton irradiation, and the density of defect induced by irradiation was evaluated.

Acknowledgment

This study was carried out as a part of "Ground Research Announcement for Space Utilization" promoted by Japan Space Forum.

References

1) R.M. Burgess et al., Proc.20th IEEE Photov. Spec. Conf. 1988.
2) C.F. Gay, R.R. Potter, D.P. Tanner, B.E. Anspaugh, Proc.17th IEEE Photov. Spec. Conf. 1984, p. 151.
3) B. Basol, Proc. 25th IEEE Photov. Conf. 1996, p. 157.
4) T. Hisamatsu, T. Aburaya, and S. Matsuda, Proceedings of 2nd World Conference of Photovoltaic Energy Conversion 1998, (IEEE Service Center, New York, 1998) p. 3568.
5) H.W. Schock, and K. Bogus, Proceedings of 2nd World Conference of Photovoltaic Energy Conversion 1998, (IEEE Service Center, New York, 1998) p. 3586.
6) T. Tanaka, Y. Demizu, T. Yamaguchi, and A. Yoshida, Jpn. J. Appl. Phys. 35 (1996) 2779.
7) M. Yamaguchi, S.J. Taylor, M.J. Yang, S. Matsuda, O. Kawasaki, and T. Hisamatsu, Jpn. J. Appl. Phys. 35 (1996) 3918.
8) I. Weinberg, C.K. Swartz, D.J. Brinker, D.M. Wilt, Conference Record of the Twenty First IEEE Photov. Spec. Conf. 1990, p. 1235.
9) M. Kitagawa, T. Fujino, K Morimoto, Annu. Rep. Radiat. Cent. Osaka Prefect. 1985, p. 29.
10) M. Yamaguchi, C. Uemura, A. Yamamoto, A. Shibukawa, Jpn. J. Appl. Phys. 23 (1984) 302.
11) M. Yamaguchi, and C. Amano, J.Appl.Phys. 57 (1985) 537.
12) M. Yamaguchi, J. Appl. Phys. 78 (1995) 1467.
13) H. Neumann, V.N. Nguyen, H.J. Hobler, and G. Kuhn, Solid State Commun. 25 (1978) 889.

1.8 Pulsed-ESR Characterization of Diamond Implanted with High Energy Phosphorus Ions at High Temperature

J. Isoya, T. Ohshima*, Y. Morita* and H. Itoh*
University of Library and Information Science, Department of Material Development, JAERI*

1. Introduction

Diamond is a promising material for electronic devices for high-speed, high-power applications and those used in a harsh environment. In CVD growth of homoepitaxial diamond film, n-type conductivity has been achieved by phosphorus doping[1]. In the process technology of silicon LSI, ion implantation is widely used for impurity doping. In ion implantation doping, annealing which reduces lattice-damages accumulated during implantation and drives the implant into the required lattice site is critically important. Since diamond is a metastable state of carbon under ambient pressure, annealing temperature accessible is far below the melting point. Since the atomic radius of phosphorus is considerably larger than that of carbon, the solubility of phosphorus in diamond is expected to be small. Thus, the phosphorus doping by ion implantation in diamond is much more complicated than that in silicon.

We have been searching a condition for n-type doping by using high-energy (9-21 MeV) phosphorus ions. By using the high-energy and by varying the energy of implantation, phosphorus ions are implanted into a wide depth range from 2 to 4 μm. Electron spin resonance (ESR) technique is used to identify both the radiation-induced defects and the defects remaining after annealing.

Firstly, conditions that should increase the concentration of phosphorus without increasing the concentration of defects excessively need to be obtained. In room temperature implantation, even at a low fluence of 4×10^{12} cm^{-2}, microscopic amorphous particles which are consisting of ~30 carbon atoms are formed with a rate of 2.5×10^{2} particles/ion[2]. Although the amorphous phase disappeared after the annealing at 1800°C under high pressure of 6 GPa, the electric activation of implants seems to be difficult. The formation of amorphous phase was suppressed by using high target temperatures, 700°C, 1000°C and 1500°C.

The ESR-active defects remaining after high-temperature implantation are vacancy-clusters of a chain-type. Since dangling bond having an unpaired electron is located at each end of the vacancy-chain, the ESR spectra are characterized with 2-lines separated by zero-field splitting of S=1. With the increase of the fluence, the vacancy-clusters of a larger size are increased. Under the same fluence for the target temperatures, 700°C, 1000°C and 1500°C, the concentration of defects decreases and the fraction of vacancy-chain of longer length increases with the increase of the temperature.

After the implantation at 1800°C, the implanted layer turned to non-diamond phase of black color. Since there is a limitation on elevating the target temperature, the defects formed by implantation at the temperature below ~1500°C need to be annealed by heating the crystal to an elevated temperature under high pressure. In the present work, we have studied the annealing behaviour of the vacancy-clusters of a large size.

The zero-field splitting of vacancy-chains having S=1 decreases with the increase of the chain length. The signals from vacancy-clusters of larger sizes overlap with the signal of S=1/2 species with the g-value close to that of free electron. We have developed a convenient method to discriminate S=1/2 signal(s) from S=1 signal(s) by applying pulsed technique.

2. Experimental

Synthetic diamond crystals of type IIa were irradiated using a 3 MV tandem accelerator with phosphorus ions of nine different energies between 9 MeV and 21 MeV. The samples had a shape of regular

plate with a size, typically, of 3×3×1 mm^3. The implantation was carried out along the [100] axis. For the high temperature implantation experiments, diamond crystals were heated through direct contact with a graphite heater of an electric furnace.

The ESR spectra were recorded on a Bruker ELEXSYS E580 spectrometer.

3. Results and Discussion

As mentioned above, the defects produced by high temperature implantation are mainly vacancy-chains with S=1. Since vacancy-chains of various lengths are formed, ESR spectrum of the implanted crystal has many peaks. We have applied a nutation method of pulsed technique to discriminate the signals of S=1/2 species from those of S=1 species. The rotation of the magnetization around the microwave magnetic field B_1 is called nutation. The microwave pulse is characterized by the turning angle θ_p, through which the microwave magnetic field B_1 turns the electron spins: $\theta_p=\varpi_n t_p$, where ϖ_n is the nutation frequency and t_p is the pulse width. When only one of the $\Delta M_S=\pm 1$ transitions of S=1 spin is excited, the effective rotation is $2^{1/2}$ times that for an S=1/2 spin[3]. We use a three- pulse sequence in which the echo formed by the second and the third pulses monitors the z-component of the magnetization rotated by the first pulse. By varying the pulse width of the first pulse, nutation is observed as a periodic variation of the echo amplitude.

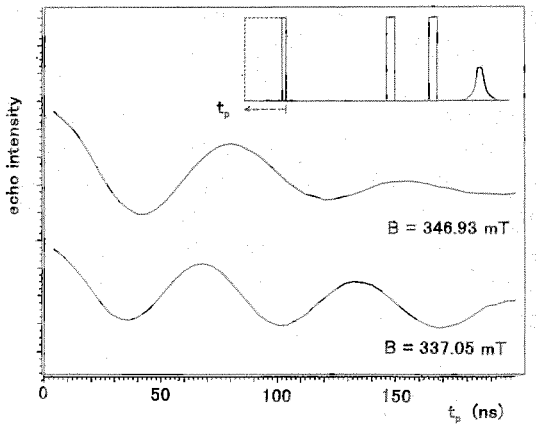


Fig.1. Spin nutations of two signals in the ESR spectrum (20 K, B//[100]) of type-IIa diamond crystal implanted with phosphorus ions (1000°C, 4×10^{13} ions/cm^2 × 9 steps of the energy between 9 and 21 MeV)

In Fig.1, the spin nutations for two signals in the ESR spectrum of a crystal which had been implanted at 1000°C with phosphorus ions with a fluence of 4×10^{13} ions/cm^2 for each of 9 steps of the energy between 9 and 21 MeV are demonstrated. Each of two time domain spectra was taken with the external magnetic field fixed at each signal position. From the difference in the nutation frequency, it is determined that effective spin for the two signals are S=1/2 and S=1, respectively. To obtain 2-dimensional spectrum, the time domain spectra (t_p of the first pulse: 4(k-1) ns where k=1,···, 64) were measured as a function of the magnetic field (B_0+B(j-1), j=1,···,512). At each magnetic field, the time domain spectrum was Fourier-transformed to give nutation frequencies and corresponding relative intensities. As shown in Fig.2, a counter map representation which indicates the assignment of the nutation frequency to each signal in the spectrum was obtained.

Field-swept spectrum which corresponds to an integrated form of conventional ESR-spectrum is obtained by measuring the intensity of the echo created by the above three-pulse sequence as a function of the magnetic field. If a suitable value of the pulse width of the first pulse is selected, response from either S=1 or S=1/2 spin is selectively collected. Fig.3 demonstrates the spectra that are constructed predominantly from the response of S=1/2 and S=1, respectively. If a small pulse width for the first pulse is employed, responses of both S=1 and S=1/2 spins are collected. The spectra shown in Fig.4 were taken with this setting (t_p = 4 ns). While either the spectrum of S=1/2 or that of S=1 species is selectively extracted in Fig.3, Fig.4 (b) corresponds to total spectrum of the same sample. The presence of the S=1/2 signal, which might not be evident in Fig.4(b), is clearly shown in Fig.3(a).

For a low fluence of 2×10^{12} cm^{-2}, the S=1/2 signal shown in Fig.3(a) was not observed. It is likely that the S=1/2 signal is originating from extended defects which are formed by accumulation of defects under high fluence implantation at high temperature. It should be noted that, comparing to the S=1 signal, the S=1/2 signal exhibits considerably faster damping,

indicating shorter relaxation time. This shorter relaxation time is likely to be caused by an extended character of the defect.

The crystal implanted at 1000°C (4×10^{13} ions/cm^2 × 9 steps) was annealed at 1700°C for 14 hrs under high pressure of 6 GPa. As shown in Fig.4, the vacancy-clusters (S=1 species) decreased the concentration and changed the structure since both the peak heights and the peak positions were changed. It should be noted that the intensity of the S=1/2 species grew considerably by the annealing. When the fluence is increased at high temperature implantation, extended defects not only start to be produced during implantation but also are formed considerably by post-implantation annealing. Since phosphorus ions captured by extended defects are not likely to be electrically activated, it is required to lower the concentration of the extended defects. By the post-implantation annealing with accessible temperature and pressure, the recovery of crystallinity is limited. An excessive accumulation of defects by high fluence need to be avoided. It is suggested that the increase of the concentration of phosphorus without increasing the concentration of defects should be attained by a repetition of cycle of low-fluence implantation followed by annealing at elevated temperature. Combination of carbon ion implantation which should fill the vacancy-clusters might be useful.

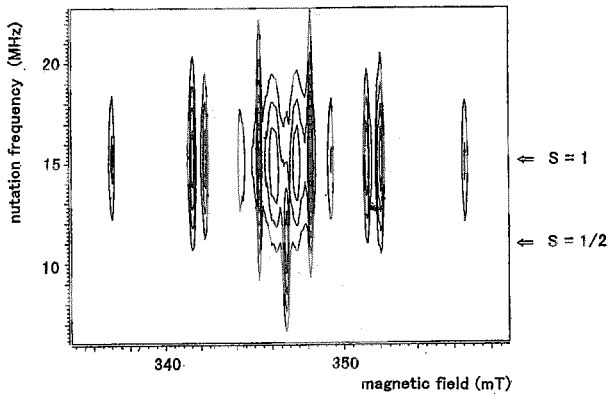


Fig.2. 2-dimentional nutation spectrum (20 K, B//[100]) of type-IIa diamond crystal implanted with phosphorus ions (1000°C, 4×10^{13} ions/cm^2 × 9 steps of the energy between 9 and 21 MeV)

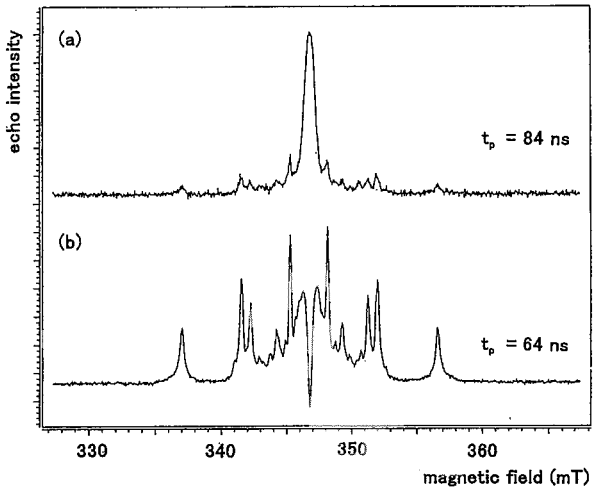


Fig.3(a) ESR spectrum in which the responses of S=1/2 species are selectively collected.
(b) S=1 spectrum

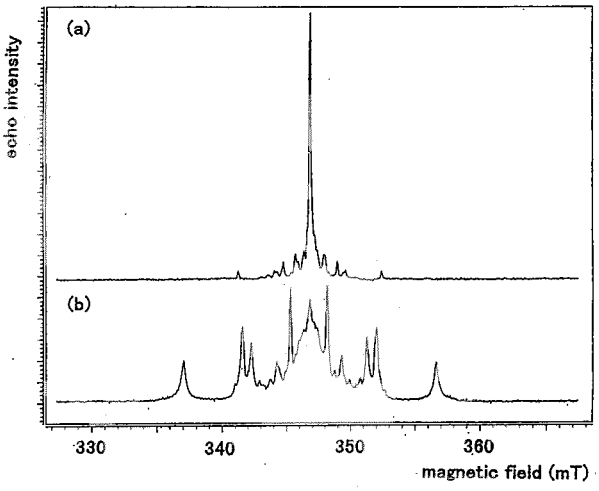


Fig.4 Echo-detected ESR spectrum (20 K, B//[100])
(a) after post-implantation annealing at 1700°C (14 hrs under high pressure of 6 GPa)
(b) as-implanted (1000°C, 4×10^{13} ions/cm^2 × 9 steps of the energy between 9 and 21 MeV)

Acknowledgments

The type-IIa synthetic diamond crystals used in the present work were supplied from Sumitomo Electric Industries. The annealing at 1700°C was carried out by Dr. Hisao Kanda (National Institute for Materials Science).

Reference

1) S. Koizumi, M. Kamo, Y. Sato, H. Ozaki and T. Inuzuka, Appl. Phys. Lett. 71, 1065 (1997)
2) J. Isoya, H. Kanda, I. Sakaguchi, Y. Morita and T. Ohshima, Radiat. Phys. Chem. 50, 321 (1997)
3) J. Isoya, H. Kanda and Y. Uchida, Phys. Rev. B 42, 9843 (1990)

This is a blank page.

2. Biotechnology

2.1 Differential G-value of Oxidation of Phenylalanine in Aqueous Solution Irradiated with Energetic Heavy Ions ····· 31
M.Taguchi, Y.Kobayashi, K.Hayano, and H.Hiratsuka

2.2 The Influence of C Ion Beam Irradiation on Nuclear DNA Content in Plants Regenerated from Irradiated Leaf Explants in Chrysanthemum ····· 34
H.Yamaguchi, T.Morishita, K.Degi, A.Tanaka, Y.Hase, and N.Shikazono

2.3 Effects of $^{12}C^{5+}$ Ion Beams on Germination and Leafing of Seed in Chrysanthemum *(Dendranthema Grandiflora Tzvelev.)* ····· 36
T.Nakahara, K.Hirashima, H.Murakami, A.Tanaka, N.Shikazono, S.Hase, and H.Watanabe

2.4 Development of Cell Surgery Technique by Ion Microbeam ····· 38
M.Yamaguchi, Y.Yokota, S.Kitamura, M.Inoue, Y.Hase, and A.Tanaka

2.5 Effects of Ion Beam Irradiation on the Growth of Netted Melon (*Cucumis Melo* L.) ···· 40
H.Katai, M.Taneishi, A.Tanaka, N.Shikazono, Y.Hase, and H.Ohtsuka

2.6 Carbon and Helium Ion Beam Irradiation Effects on Seedling and Plant Characters of Tomato cv. First ····· 42
M.Masuda, S.G.Agong, A.Tanaka, N.Shikazono, and Y.Hase

2.7 Induction of Mutation in Spiraea by Ion Beam Irradiation —Effects of Ion Beams on Germination of Spiraea Seed — ····· 45
M.Iizuka, N.Kudo, Y.Kimura, Y.Hase, and A.Tanaka

2.8 Isolation and Characterization of the Ion-beam-induced New Arabidopsis Floral Mutant,Frill 1. ····· 47
Y.Hase, and A.Tanaka

2.9 Mutation Breeding using Ion-beam Irradiation in Aster ····· 50
T.Baba, F.Nakamura, H.Nishi, Y.Yoshida, A.Tanaka, N.Shikazono, Y.Hase, and H.Watanabe

2.10 Mutation Generation in Carnation Plants Regenerated from in Vitro Leaf Cultures Irradiated with Ion Beams ····· 52
M.Okamura, M.Ohtsuka, N.Yasuno, T.Hirosawa, A.Tanaka, N.Shikazono, Y.Hase, and M.Tanase

2.11 Mutation Induced by Ion Beam Irradiation to Hinoki Cypress Shoot Primordia ····· 55
K.Ishii, Y.Hase, N.Shikazono, and A.Tanaka

2.12 Mutation Induction with Ion Beam Irradiation in Garlic(*Allium Sativum* L.) ····· 57
T.Tashiro, Y.Yamamoto, A.Tanaka, N.Shikazono, and Y.Hase

2.13 Mutation Breeding of Rice,Eggplant and Gloriosa by Ion Beam Irradiation ····· 59
M.Mizobuchi, M.Okada, M.Matsumoto, A.Iwasaki, A.Tanaka, N.Shikazono, and Y.Hase

2.14 Production of Mutants that have High Ability to Assimilate Nitrogen Dioxide by the Irradiation of Ion Beams in *Ficus Stipulata.* ····· 62
M.Takahashi, S.Kohama, M.Hakata, Y.Hase, N.Shikazono, A.Tanaka, and H.Morikawa

2.15 Induction of Somatic Mutation by Ion Beam Irradiation in Lethal Chlorophyl Mutant of Rice ····· 64

M.Maekawa, A.Tanaka, N.Shikazono, and Y.Hase
2.16 Genetic Screening of Antiauxin Mutants in *Arabidopsis Thaliana* ····· 67
C.Ooura, E.T.Aspuria, Y.Oono, Y.Hase, Y.Kobayashi, and H.Uchimiya
2.17 Isolation of Response Deficient Mutants to Environments from Plant Seeds Irradiated with Ion-beam ····· 70
Y.Sasuga, Y.Kami, M.Ooshima, G.Takata, Y.Kobayashi, Y.Sakata, Y.Oono, Y.Kobayashi, S.Tanaka, and H.Takenaga
2.18 System of Cell Irradiation with a Precise Number of Heavy Ions ····· 73
Y.Kobayashi, T.Funayama, M.Taguchi, S.Wada, M.Tanaka, T.Kamiya, W.Yokota, H.Watanabe, and K.Yamamoto
2.19 Effects of Locally Targeted Heavy Ions to the Zygotic Nuclei During Early Development of the Silkworm,*Bombyx* Mori ····· 76
K.Kiguchi, H.Tamura, R.Harata, K.Shirai, R.Kanekatsu, Y.Kobayashi, and H.Watanabe
2.20 Ion Beam Mutagenesis in a Model Legume *Lotus Japonicus* ····· 79
K.Tateno, M.Kawaguchi, Y.Watanabe, N.Shikazono, A.Tanaka, T.Haga, and K.Miura
2.21 Effects of Ion Beam Irradiation on Sweetpotato Callus and Chrysanthemum Leaf Discs ····· 82
K.Shimonishi, S.Nagayoshi, K.Ueno, Y.Hase, N.Shikazono, and A.Tanaka
2.22 Effects of Helium Ions and Gamma Rays Irradiation of Sexual Plant Reproductive Stages on Seed Production and Postembryonic Leaf Development in *Brassica Napus* L ····· 85
H.Minami, N.Sakurai, N.Shikazono, A.Tanaka, and H.Watanabe
2.23 Development of the Pollen Transformation System and Analysis of Apoptosis Induction by Local Damage, using Penetration Controlled Irradiation with Ion Beams ····· 87
Y.Hase, A.Sakamoto, S.Wada, S.Kitamura, and A.Tanaka
2.24 Utilization of Ion Beam-irradiated Pollen in Plant Breeding ····· 88
S.Kitamura, M.Yamaguchi, M.Inoue, Y.Hase, and A.Tanaka
2.25 Dynamical Study on Influence of CO_2 Enrichment to the Transportation of Photoassimilates using Positron Imaging ····· 90
S.Matsuhashi, S.Watanabe, N.S.Ishioka, C.Mizuniwa, T.Ito, and T.Sekine
2.26 Analysis of Nitrogen Absorption and Translocation by Soybean Grown in Different Conditions for Phosphorus Supply ····· 93
N.Ohtake, T.Ohyama, K.Sueyoshi, T.Kawachi, H.Fujikake, A.Momose, T.Suganuma, A.Osa, M.Koizumi, S.Hashimoto, N.Ishioka, S.Watanabe, T.Sekine, S.Matsuhashi, T.Ito, C.Mizuniwa, H.Uchida, and A.Tsuji
2.27 Zinc Translocation Oscillates in a Leaf of Zinc-deficient Rice ····· 96
H.Nakanishi, S.Kiyomiya, M.Yoshimura, S.Watanabe, S.Matsuhashi, N.S.Ishioka, T.Itoh, C.Mizuniwa, H.Uchida, A.Tsuji, S.Hashimoto, T.Sekine, and S.Mori
2.28 Effects of Environmental Stress on ^{11}C Distribution in Rice Plants Detected by PETIS Detector ····· 99
H.Hayashi, H.Mano, N.Suzui, S.Matsuhashi, C.Mizuniwa, T.Ito, S.Hashimoto, N.Ishioka, T.Watanabe, T.Sekine, A.Osa, H.Uchida, and A.Tsuji

2.29 Water and Trace Element Behavior in a Plant ····· 102
T.M.Nakanishi, J.Furukawa, K.Tanoi, H.Yokota, N.Ikeue, S.Hashimoto, S.Matsuhashi, T.Sekine, T.Itoh, T.Mizuniwa, N.S.Ishioka, S.Watanabe, A.Osa, H.Uchida, and A.Tsuji
2.30 Uptake of ^{18}F-water ^{15}O-H_2O and $^{13}NO_3^-$ in Tomato Plants ····· 105
A.Tsuji, H.Uchida, T.Yamashita, S.Matsuhashi, T.Ito, C.Mizuniwa, N.S.Ishioka, S.Watanabe, S.Hashimoto, and T.Sekine
2.31 Single-hit Effects and By-stander Effect on Cells by Heavy-ion Microbeams ····· 107
Y.Furusawa, N.Yasuda, CL.Shao, M.Aoki, K.Sato, K.Takakura, T.Funayama, and Y.Kobayashi
2.32 Fundamental Study on Radiotherapy of Tumors to Beneficial Companion Animals using Heavy Ion Beam ····· 110
S.Wada, M.Natsuhori, N.Ito, Y.Kobayashi, T.Funayama, and K.Yamamoto

This is a blank page.

2.1 Differential G-value of oxidation of phenylalanine in aqueous solution irradiated with energetic heavy ions.

Mitsumasa Taguchi[1)], Yasuhiko Kobayashi[1)], Kazuki Hayano[2)], and Hiroshi Hiratsuka[2)]

[1]Department of Radiation Research for Environment and Resources, JAERI,

[2]Department of Chemistry, Gunma University.

1.Introduction

It is well known that the yields of transient species, *e.g.*, OH radical and hydrated electron, depend on the kind of ionizing radiations used. The differential *G*-values (the yield at a particular energy or LET of an ion in the sample solution) of OH radical decreased with the LET value of heavy ions having a few hundred MeV/n energy[1)]. Though low LET radiations form spurs sparsely, heavy ions form spurs densely along their trajectories. The transient species are so near as to interact easily with each other in the track. Therefore, the decrease of the *G*-value will be due to the increase of reactions of OH radical with other transient species.

The productions of *p*-, *m*-, and *o*-tyrosine, which are the adducts of one hydroxyl group on phenyl ring of phenylalanine, were reported after γ-ray irradiation of aqueous phenylalanine solution[2)]. In the present report, we investigated the differential *G*-value of production yields of tyrosine isomers by the irradiations of He- or O_2-saturated aqueous phenylalanine solution with several hundreds MeV C, Ne, and Ar ions.

2.Experimental

Aqueous phenylalanine solutions (13 mM) were saturated with He or O_2 gas, and put into an aluminum cell, which has an aluminum window of 15-μm thickness for the irradiation. The volume of the sample solution was 4.7 ml and its depth was about 4 mm.

Irradiations were performed with 220-MeV $^{12}C^{5+}$, 350-MeV $^{20}Ne^{8+}$, and 460-MeV $^{40}Ar^{13+}$ ions using Irradiation Apparatus for Seed[3,4)] in TIARA facility. Energy of the ion was attenuated by a set of aluminum foils (10- to 500-μm thickness) installed on the cell. The incident energies (*E0*), the energies of the ion at the surface of the sample solution after penetrating the aluminum foils and the windows, were calculated by the TRM code[5)]. Penetration depth of the ion was less than 1.1 mm in water. Therefore, the sample solution was stirred during the irradiation by a magnetically coupled stirrer chip to keep the homogeneity. The sample solution was also irradiated with γ-ray as a low LET radiation.

The irradiated solutions were analyzed by High Performance Liquid Chromatography (HPLC) with a reversed phase column at 40 ℃. Water with 3-% acetonitrile was used as an eluent and its flow rate was 0.8 ml/minute.

3.Results and discussion

The productions of *p*-, *m*-, and *o*-tyrosine were confirmed on the HPLC chromatogram after the γ-ray and heavy ion irradiations. Yields of the productions of these tyrosine isomers (Tyrs) increased linearly with an increase of dose. *G*-value of the production of total tyrosine isomers by γ-ray irradiation was estimated to be 0.30 (He-saturated) and 1.35 (O_2-saturated). *G*-values obtained by heavy ion irradiations were not constant for the different incident energies of the ions, for example, *G*-values varied from 0.32 at 207 MeV to 0.19 at 67.6 MeV of the incident energy of the C ion. This means that the yield of total Tyrs along the trajectory decreases with decreasing energy of the ions.

We estimated the number of total molecules of Tyrs (N_T) produced by the single ion irradiation from

the fluence dependence of the concentration of Tyrs:

$$N_T = C \times 0.0047 \times N_A / F . \quad (1)$$

where C is the concentration of tyrosine isomers estimated, and F and N_a are the fluence of the ion and the Avogadro number, respectively. All the used ions stop completely in the sample solution so that N_T is the number of molecules of Tyrs integrated over the trajectory. N_T increased steeply with $E0$. N_T corresponds to the value of the Differential G-value (G'), the G-value at a particular energy of the ion in the sample solution, integrated over the trajectory:

$$N_T = \int_0^{E0} G' \, dE \times 100. \quad (2)$$

The G'-value of OH radical increases with the energy of C ion having 419- to 1022-eV/nm LET[6]. Therefore, as the first approximation, the production yield of Tyrs along the trajectory was assumed to be linearly proportional to the energy of the ion in the region up to 300 MeV:

$$G' = a + bE \quad (3)$$

where E is the energy of the ion in the sample solution, and a and b are parameters for fitting the experimental results. The G'-values were estimated by differentiating the fitted curve of N_T as a function of E. The G'-values estimated for each E value were plotted against LET as shown in Figure 1. The G'-value decreases with increasing LET value of the same ion. Furthermore, the G'-value appears to increase with increasing atomic number of the ion at the same LET value. Different track structure for heavy ions would induce such a characteristic LET dependence of G'-value.

The G'-values obtained by all ions was larger than the G-value for γ-ray irradiation in the low LET region used for the He-saturated solutions, though the G'-values are smaller than the G-value in all LET region for the O_2-saturated solutions. The G'-values of transient species were estimated in aqueous formic acid solutions irradiated with C ions in the 419- to 1022-eV/nm LET region[6]. The G'-value of OH radical decreased monotonously with the LET value as the same as the G'-value of Tyrs. However, G'-values of HO_2

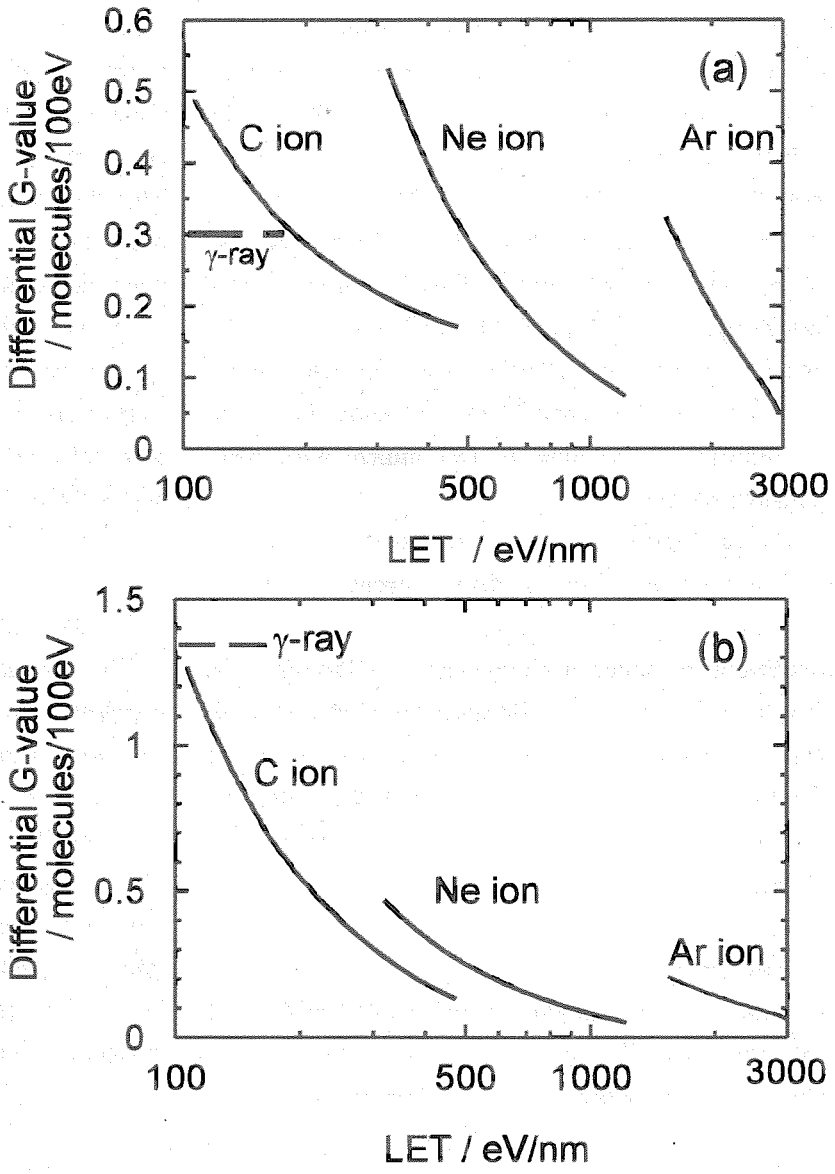


Figure 1
Differential G-value of total tyrosine isomers as a function of LET for the aqueous phenylalanine solutions saturated with He (a) and O_2 gas (b).

radical and H_2O_2 increased monotonously with the LET value in water, because these species would be produced by the recombination of transient species in the track[6]. The production of Tyrs will be principally induced by OH radical. Assuming that the *G'*-value of OH radical for all the ions used here decreases similarly to the *G'*-value of OH radical in formic acid solution, the *G'*-values of Tyrs will decrease with the LET value from 0.3 for He-saturated and 1.35 for O_2-saturated solutions obtained by the γ-ray irradiation. However, partly greater *G'*-values than that expected are observed for only He-saturated solutions. The oxidizing agents such as O_2 and $Fe(CN)_6^{3-}$ increase the oxidation of Phe. The *G*-value of total Tyrs in the O_2-saturated aqueous Phe solution was estimated to be about four times of that in the absence of oxygen after the irradiation with γ-ray. The ions produce the oxidizing species, *e.g.*, O_2 molecule and HO_2 radical, which are rarely produced by the γ-ray irradiation and increase with the LET value. The partly greater *G'*-value would be caused by the oxidizing species produced in the track for the He-saturated aqueous Phe solution.

References

1) A. Appleby, E.A. Christman, and M. Jayko, *Radiat. Res.*, **104**, 263 (1985).

2) O.H. Weeler and R. Montalvo, *Radiat. Res.*, **40**, 1 (1989).

3) M. Kikuchi *et al.*, *TIARA Annual Report* **1**, 159 (1992).

4) M.Taguchi *et al.*, *Radiat. Phys. Chem.*, **60**, 263 (2001).

5) J.F. Ziegler, *et al.*, The Stopping Power and Range of Ions In Solid, vol. 1, Pergamon Press, New York, 1985.

6) J.A. LaVerne, *Radiat. Phys. Chem.*, **34**, 135 (1989).

2.2 The influence of C ion beam irradiation on nuclear DNA content in plants regenerated from irradiated leaf explants in chrysanthemum

H. Yamaguchi, T. Morishita, K. Degi,
A. Tanaka*, Y. Hase* and N. Shikazono*.
Institute of Radiation Breeding, NIAS, Department of Radiation Research for Environment and Resources, JAERI *

1.Introduction

It is the problem in mutation breeding that the mutation occurs not only in the trait aimed to improve, but also in other traits and the infection by irradiation. Ichikawa et al.[1] reported that some shoots produced after gamma ray irradiation had lower chromosome number than the control plants and the reduction of chromosome number was correlated with the size of inflorescence in chrysanthemum.

The flow cytometry easily enabled to measure the nuclear DNA content and it was indicated that nuclear DNA content related to the plant size in sugar cane [2]. Therefore, we considered that the utilization of nuclear DNA content as the index of the degree of infection by irradiation might be possible.

In this study, we investigate the influence of carbon ion beam irradiation on nuclear DNA content of plants regenerated from irradiated leaf explants in chrysanthemum.

2. Materials and Methods

The chrysanthemum cultivar 'Taihei' was used for this study. Leaf explants were plated on callus induction media (MS media supplemented with 4 μM BA, 1 μM NAA, 2% sucrose and 0.9% agar). They were irradiated with various doses of accelerated $^{12}C^{5+}$ (220 MeV, 0.02 nA) ion particles using an AVF Cyclotron in JAERI. After irradiation, the explants were plated on new media, and then plated on regeneration media three weeks later. The regeneration rate was investigated six weeks later. The regenerated plants were established and the nuclear DNA contents were measured.

The nuclear DNA content was measured with flow cytometric analysis. Leaf of garden pea (*Pisum sativum* cv. Narikoma Sanjunichi) was used as standards and the ratio of nuclear DNA content in a sample to that in garden pea was calibrated. The measurements were repeated two times using two different leaves from a plant.

3.Results and Discussion

The influence of C ion beam irradiation on the regeneration from leaf explants was showed on Fig 1. The regeneration rates were about 70 % with 2 Gy, about 50 % with 3 Gy and 10% with 5 Gy.

Figure 2 shows that the influence of C ion beam irradiation on nuclear DNA content. The mean of nuclear DNA content of 52 plants regenerated from leaf explants without irradiation, only with in vitro culture, was 2.271, while the mean of the 65 times measurements on the control plants maintained by herbaceous cutting was 2.263. Therefore, it was

suggested that the in vitro culture method used in this study did not cause the variation of the nuclear DNA content of regenerated plants.

In the plants derived from the explants irradiated with 2 Gy, there appeared the plant, the nuclear DNA content of which decreased to 96 % of that of the control plants. In 5 Gy irradiation, large variations in nuclear DNA content were observed and in the plant with the least content that decreased to 94 %. The means of the nuclear DNA content were fewer than that of the control plants in both irradiated doses. Therefore, it was suggested that C ion beam irradiation to leaf explants affects to the nuclear DNA contents of the regenerated plants.

We investigate further the affects at lower doses with which the influence of irradiation on the regeneration was hardly observed. For the mutation breeding with ion beam irradiation, we develop the possibility of the utilization of nuclear DNA content as the index of the degree of infection by irradiation in investigating the relationship between the nuclear DNA content and the plant size.

References

1) S, Ichikawa, et al., Radiation Botany 10 1970, 557-562.
2) S, Nagatomi, et al., Breed. Sci. 48 (Supple.2) 1998,334.

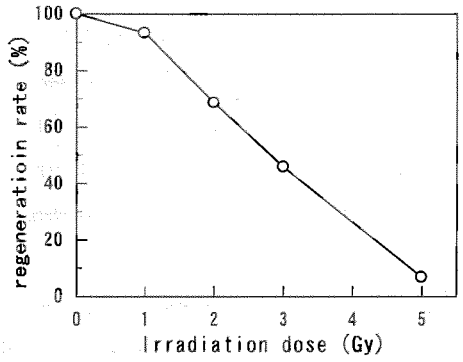


Fig. 1 The influence of C ion beam irradiation on the regeneration from leaf explants.

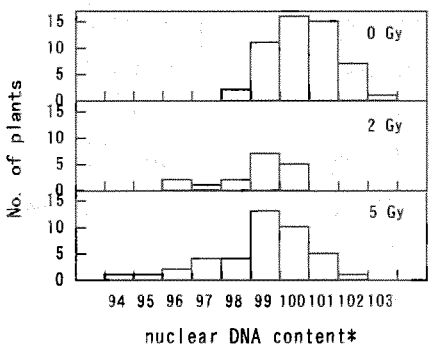


Fig. 2 The influence of C ion beam irradiation on nuclear DNA content.

2.3 Effects of $^{12}C^{5+}$ Ion Beams on Germination and Leafing of Seed in Chrysanthemum (*Dendranthema grandiflora* Tzvelev.)

T. Nakahara[1], K. Hirashima[1], H. Murakami[1], A. Tanaka[2], N. Shikazono[2], S.Hase[2] and H.Watanabe[2]

Fukuoka Agricultural Research Center[1]

Department of Radiation Research for Environment and Resources, JAERI[2]

1. Introduction

In the field of plant breeding ion beams are expected the useful method owing to high LET (linear energy transfer) .
Ion beams have been irradiated to seeds, meristem tip, callus and protoplast in order to induce mutation. Recently they have been irradiated to many species of plant and many mutants were acquired[1)] . In many cases, seeds were Arabidopsis, tabacco, rice, strawberry, tomato, hydrangea, melon, etc. Therefore we tried to irradiate seeds of chrysanthemum in addition to protoplast in order to breed mutant with various floral color.

2. Experimental methods

Seeds of spray type chrysanthemum cultivar 'Pretty parade' selfpollinated were used for the experiments. One hundred seeds were fixed on a thick paper in petri dish with glue. These petri dishes were covered with Kapton film. The seeds were irradiated with 220 MeV $^{12}C^{5+}$ ion beams from the AVF cyclotron in JAERI. In the experiment I, doses were set in the range from 0 to 75 Gy at three levels. On the other hand, in the experiment II, doses were set in the range from 0 to 40 Gy at eleven levels. Triple petri dishes were used for each dose. The experiments were performed twice. Thereafter the seeds were sown on peat moss in plastic trays and kept at greenhouse. The rate of germination and leafing were investigated after 30 days of seedling.

3. Results and Discussion

In experiment I, the rate of germination were performed 100 per cent at 75 Gy . On the other hand, the rate of leafing was decreased abruptly at 25 Gy. The leafing was not obserbed higher than 50 Gy at all.

The dose response curve showed similar tendency in experiment II. The rate of germination were maintained higher than 80 per cent between 0 Gy and 40 Gy. While the rate of leafing were decreased abruptly higher than 10 Gy. Only a few leafing were obserbed at 30 Gy. No leafing was observed at 40 Gy.

It seems that the sensitivity of germination to ion beams is obviously different from that of leafing. The seeds irradiated with ion beams at higher than approximately 40 Gy are maintained ability to germinate, but the next leafing are not maintained. It is thought that a certain

damage is probably received. It is considered that the dose is deduced lower than around 15 Gy to produce useful mutant.

Further investigation is nessesary to solve the effects of C and He ion beams on leafing in chrysanthemum seedling. Now the traits of the seedlings are being examined outdoors.

References

1) S.Nagatomi, A.Tanaka, A.Kato, H.Yamaguchi, H.Watanabe and S.Tano, TIARA Annual Report 6:41-43 (1998)

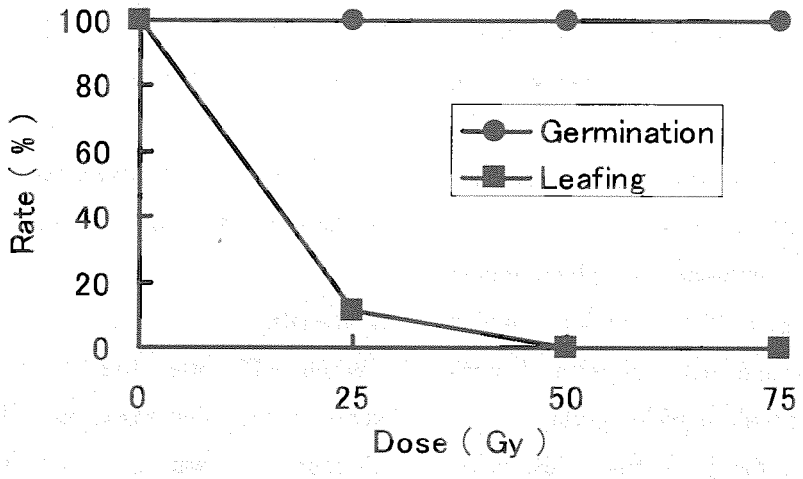


Fig.1 Effect of C ion beams on germination and leafing of chrysanthemum seeds (exp.I)

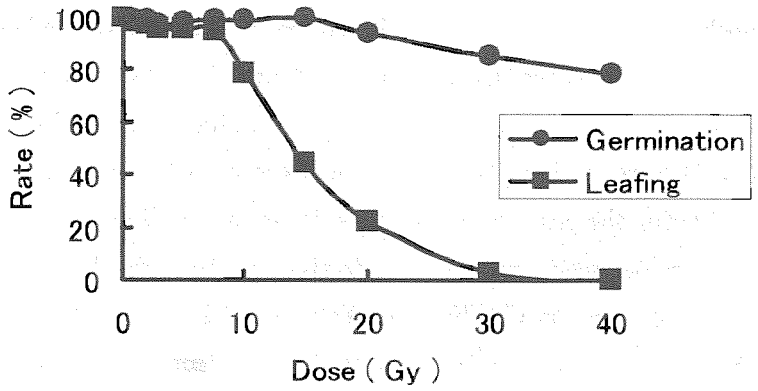


Fig.2 Effect of C ion beams on germination and leafing of chrysanthemum seeds (exp.II)

2.4 Development of Cell Surgery Technique by Ion Microbeam

M. Yamaguchi[1)], Y.Yokota[1)], S. Kitamura[1)], M. Inoue[1)], Y. Hase[2)] and A. Tanaka[2)]

[1)]Faculty of Agriculture, Kyoto Prefectual University, [2)]Department of Radiation Reserch for Environment and Resources, JAERI

1. Introduction

Ion beam has a peculiar pattern of energy transfer along the track, and its penetration depth in the target material can be controlled. Accordingly, a lot of energy can be deposited on the focused point of material exposed, suggesting that ion microbeam can be used for surgical treatment of plant cells.

We have alredy reported the phenomenon specific for ion beam, "leaky pollen", which seemed to be resulted from physical lesions induced in the outer wall of pollen grain[1,2)].

Here, we describe the preliminary results on the relationship between LET and RBE of C ion, and biological effects of C ions in tobacco callus and protoplast for the purpose of development of cell surgery in plant cells.

2. Materials and Methods

Nicotiana tabacum L. cv TUKUBA-1 was used in the present experiments.

Seeds were fixed on CR-39 plates and exposed to 220 MeV C ions. Considering the penetration range and LET of C ions in the seed embryo obtained from the results on etching on CR-39 and ELOSS code, seeds were exposed under different LETs, in combination of Ni absorber. Simultaneously, seeds were irradiated with gamma rays, and RBE was obtained on the basis of the chromosome aberration frequency in root tip cells and survival rate of seedlings.

Callus($1\times1\times1mm^3$) derived from leaf explant and mesophyll protoplast were embedded in the agarose medium (thickness 1 mm), and exposed to 220 MeV C ions (LET 111 keV/μm, penetration depth 1 mm). Irradiation of electrons (LET 0.2 keV/μm) was also performed. Growth rate in callus and the colony formation rate in protoplasts were determined.

3. Results

When LET was fixed in C ion exposure, survival rate decreased and the chromosome aberration frequency increased, with the increase of dose. On the other hand, survival reduction and the chromosome aberration frequency increased with the increase of LET, resulting in the increase of RBE value. However, the highest RBE was found at 226 keV/μm, based on 37 % survival reduction and 50 % chromosome aberration frequency (Fig. 1).

The dose-response curve for the growth rate in callus exposed to C ions, electrons and gamma-rays is shown in Fig. 2. C ions were more effective on the growth reduction than other radiations. RBE for C ions based on the RD_{50} was 6.2 to electrons. When protoplasts were exposed to C ions, colony formation rate decreased with the increase of dose (Fig. 3). However, under the present experimental conditions, clear dose-response curve was not obtained.

References

1)M. Inoue, H. Watanabe, A. Tanaka and A. Nakamura, TIARA Ann. Rep., 2 (1992) 50-53

2)A. Tanaka, H. Watanabe, S. Shimizu, M. Inoue, M. Kikuchi, Y. Kobayashi and S. Tano, Nucl. Instr. and Meth. In Phys. Res., B129 (1997) 42-48

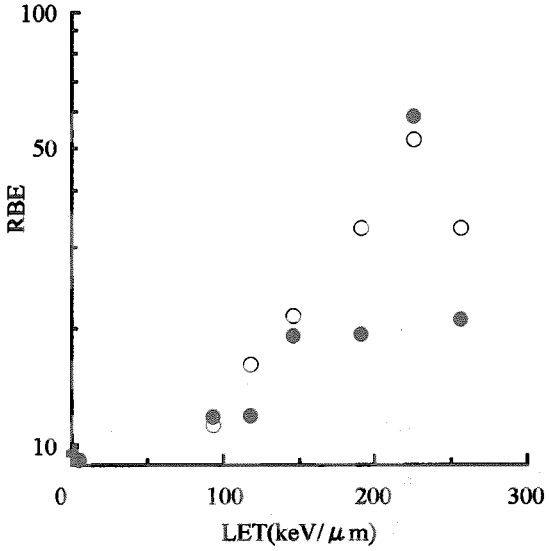


Fig. 1 Relationship between LET and RBE on the chromosome aberration frequency and survival rate.
○, 37% survival reduction
●, 50% chromosome aberration frequency

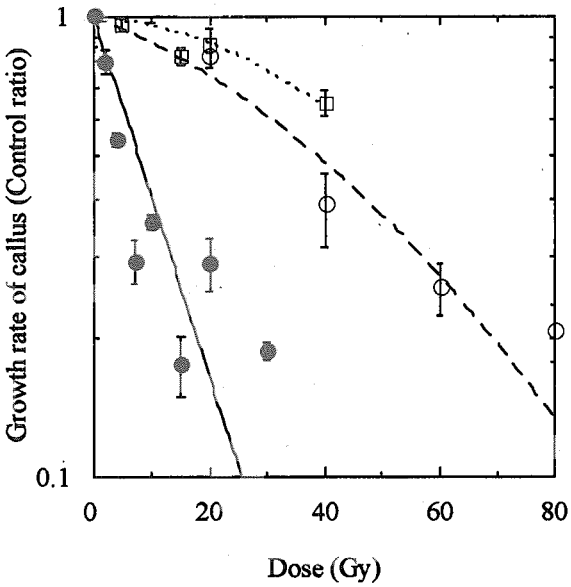


Fig. 2 Dose-response curve for growth rate in callus exposed to carbon ions(●), electrons(○) and gamma rays(□).

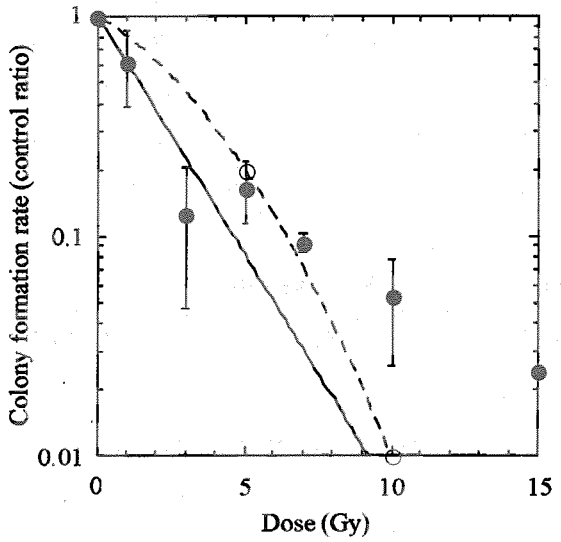


Fig. 3 Dose-response curve for colony formation rate in protoplasts exposed to carbon ions(●) and electrons(○).

2.5 Effects of ion beam irradiation on the growth of netted melon (*Cucumis melo* L.)

H.Katai[1)], M.Taneishi[1)], A.Tanaka[2)], N.Shikazono[2)], Y.Hase[2)] and H.Ohotsuka[1)]

[1)] Shizuoka Agricultural Experiment Station

[2)] Department of Radiation Research for Environment and Resources, JAERI

1.Introduction

Netted melon (*Cucumis melo* L.) is cultivated as an important fruit in Shizuoka.

In comparison with gamma and X rays, ion beams, which have higher LET (linear Energy Transfer) and deposit their energies quite locally are considered to be an efficient mutagenic agent applicable to mutation breeding of melon.

The final goal of this study is to develop high fruit-thickening ability lines by ion beam irradiation to melon seeds.

In this paper, we report the effects of ion beam irradiation on the growth of M1 plants.

2.Materials and Methods

Melon cultivar 'Earls Favorite Kenon Fuyu2' was used in this study.

The dry seeds were irradiated with 220 MeV carbon ion beams from the TIARA AVF cyclotron in JAERI.

After the irradiation, seeds were allowed to germinate under dark place at 30℃.

Survival rate of the irradiated seeds was determined at 60 days after germination.

Secondly, we investigated percentage of pollen germination, fruit set, and fertility seeds in M1 plants.

3.Results and Discussion

The influence of ion beam irradiation on germination and survival was shown in Fig.1

Carbon ion beam irradiation up to 200Gy did not affect on germinating rate at 8 days after imbibition.

Survival rate was rapidly decreased at higher than 80Gy and the median lethal dose (LD50) was estimated to be around 110Gy.

In M1 plants, pollen germinating rate and fruit setting rate were decreased as dose increased (Fig.2).

Especially, above 40Gy, fruit setting rate showed an marked decrease, and plants with no fruit set were frequently observed.

As shown in Fig.3, rates of fertility seeds following exposure at 20Gy and 50Gy were 65.0% and 48.1%, respectively.

From these results, we adopted 40Gy as adequate dosage to obtain mutants efficiently.

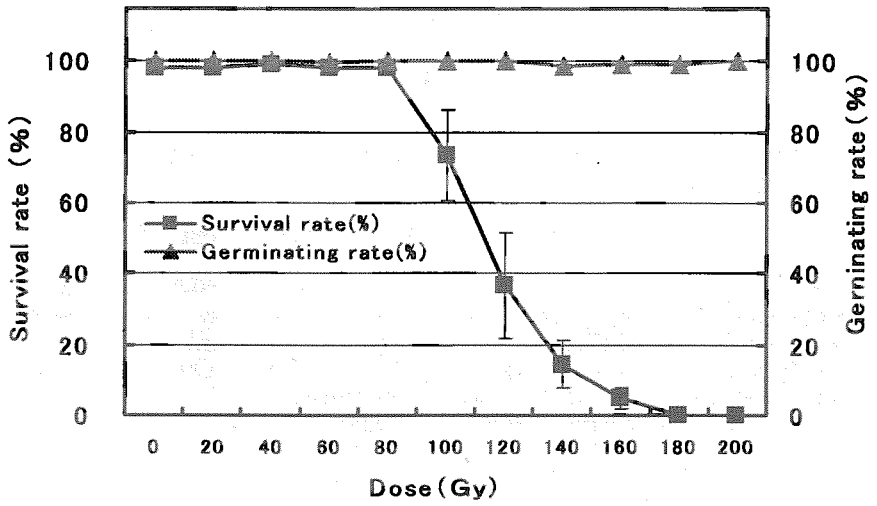


Fig.1 Dose response of germination and survival of netted melon

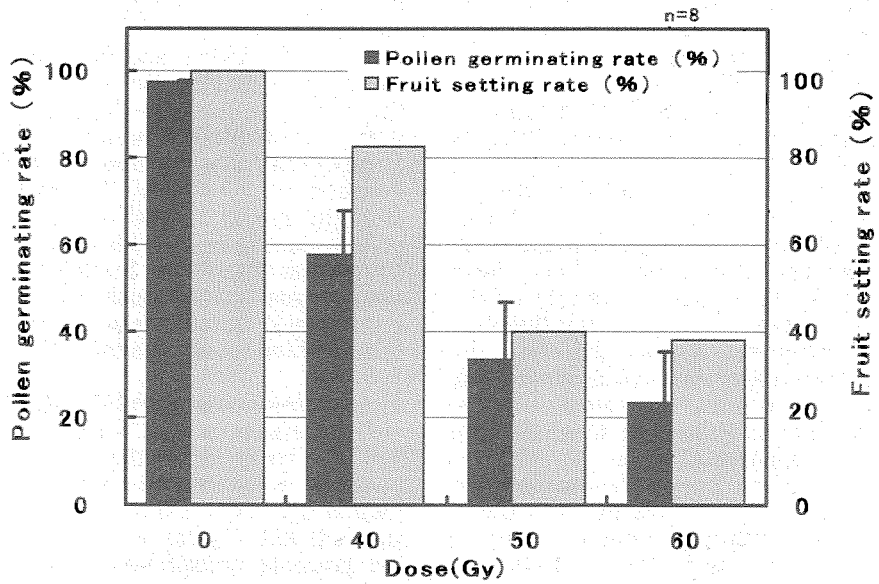


Fig.2 Effect of C ion beam on pollen germination and fruit set in M1 plants

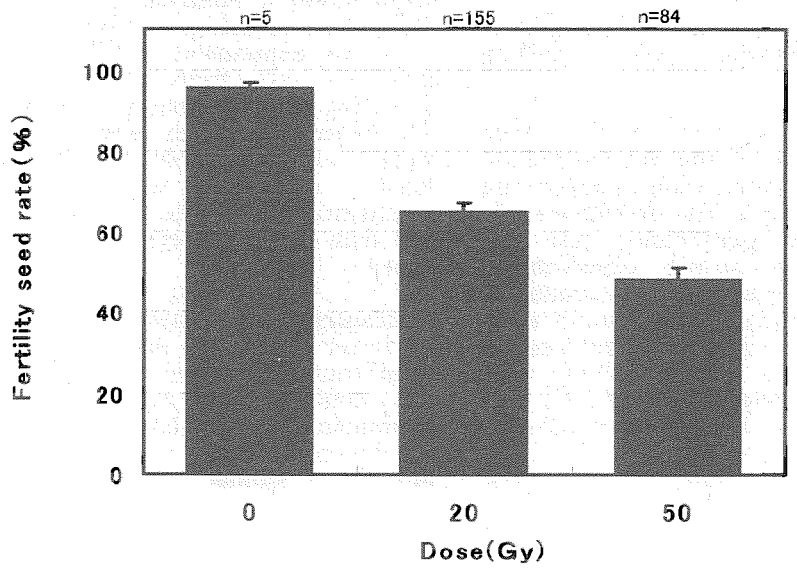


Fig.3 Effect of C ion beam on fertility seeds rate in M1 fruits

2.6 Carbon and helium ion beam irradiation effects on seedling and plant characters of tomato cv. First

M. Masuda [1], S.G.Agong [1], A. Tanaka [2], N.Shikazono [2], Y.Hase [2]
[1]Department of Eco-physiology for Crop Production, Faculty of Agriculture, Okayama University
[2]Department of Radiation Research for Environment and Resources, JAERIE

1. Introduction

Early tomato improvement work was dependent greatly on the availability of useful mutants especially in the understanding of the genetics and breeding of the crop (Stube,1972). With the increasing demand and the changing human taste preferences, there is a continuous drive to generate new tomato cultivars for the modern production and consumer purposes. However, the efficiency of mutation for the genetic improvement of tomato largely depends on the identification of stable and homogenous tomato genotypes, for example the Japanese breeding line, cv. First which is a high yielding breeding line but lacks resistance to many damaging biotic and abiotic stresses (Masuda et al.,1998).

Ion beam, a recently innovated technique has been shown to produce a new type of mutant in Arabidopsis thaliana (Tanaka et al. 1997a). However, no attempts have been made to expand the genetic diversity of the less variable cultivated tomato using this new mutagenic procedure. It was therefore the objective of this study to investigate on the effects of ion beams in tomato seeds, seedlings and plants following irradiation of seeds as a fundamental basis for tomato genetic advancement. Future development in the tomato industry following successful generation of mutants would involve selection for suitable agriculturally important characteristics.

2. Materials and methods

Experiment 1: C and He irradiation effects on seed germination and seedling characters

1) Seed material

Irradiated tomato seeds of cv. First were used in this study. Soon after the irradiation, seeds were kept under room temperature conditions for one week. The irradiated seeds were subjected to germination test and subsequent seedling growth observations. Irradiation of the tomato seeds was conducted according to the procedures of Tanaka et al. (1997a). Irradiation system, comprised of Irradiation Apparatus for Seed (IAS) with installation conforming to the JAERI. The IAS was connected to a vertical beam line of the AVF-cyclotron in conjunction with a 220-MeV carbon or 50-MeV helium ion irradiation. About 100 dry seeds were sandwiched between kapton films (7.5 μm thickness, 50 x 50 mm, Toray-Dupont Co. Ltd.) to make a monolayer of seeds for homogenous irradiation. The seeds were irradiated for about 3 minutes for all doses under atmospheric pressure.

2) Seed germination

The seeds were placed on Whatman No. 1 filter papers in 9-cm petri dishes. Two and a half milliliters of distilled deionized water was initially added, and followed by additions of 1m ℓ as needed. Seeds were incubated for two weeks in the growth chamber conditions with controlled environmental factors. Temperature was maintained at 28 ℃ in the duration of 12-h day/12-h night. The light strength was at 10,000 lux (cool homolux inflorescent lamp, which is close to the solar strength and a relative humidity of 100%. The seeds were continuously observed for the growth and development of radicle and till the termination of the experiment.

3) Seedling growth and development

Germinated seeds were transferred into seedling trays for further observation on the possible morphological injuries and physiological disorders. Data was taken on seedling survival rate (%) as well as observations on the possible conspicuous mutants expressed at the seedlings.

Experiment 2: Analysis of Mutants in the M2 tomato seedlings and plants.

In this experiment, seedlings originating from the M1 fruits (M2) were studied following direct seeding in vermiculite.
All germinated seeds were grown at the stages where possible to observe unique feature associated with the irradiation treatments. Again the experimental design and data analysis were as already outlined above.

3. Results and Discussion

At lower irradiation dosages (<50 Gy), no significant differences were noted between the control and the irradiated seeds germination. On the contrary, almost double the dosage rate that of C was necessary for inflicting similar inhibition of seed

germination in the He-ion beam irradiated tomato seeds (Fig.1).

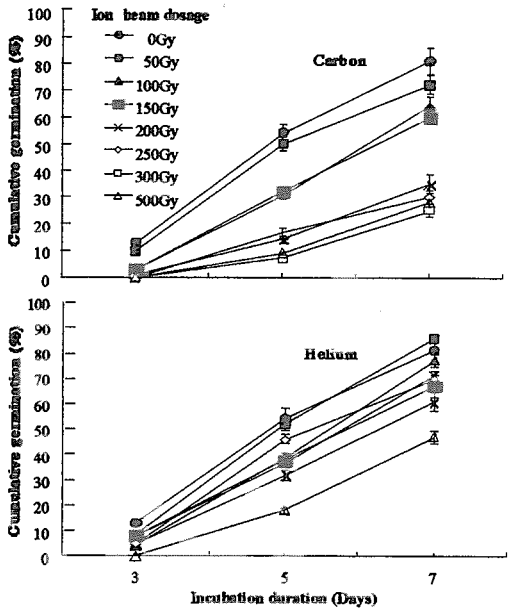


Fig. 1. Effect of C and He ion beam irradiation of tomato cv First seeds on cumulative germination percentage.

Of the seedling parameters observed, radicle length proved to be very effective in detecting obvious irradiation dosage injury effects even in cases where insignificant germination capacities between irradiation dosages were recorded (Fig.2). Notably, a C-ion beam irradiation of 50 Gy gave rise to a significantly retarded radicle compared to that of control whereas in the case of He, the difference of irradiation effect could only be detected as from 200 Gy in comparison to the control. Seedling survival rates recorded in this study suggest that the optimum irradiation dosage could be C-50 Gy and He-150～200 Gy, respectively (Fig.3)

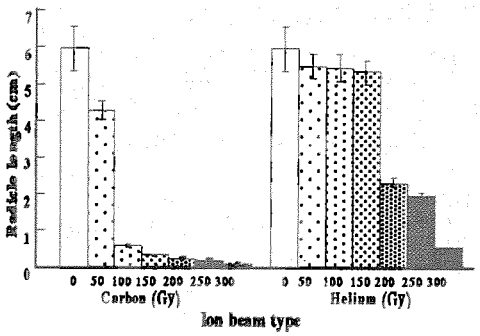


Fig. 2. Effect of C and He ion beam irradiation of tomato cv. First seeds on radicle length.

Analysis of the abnormalities in M1 seedlings raised from ion beams irradiated seeds, showed that ion beams resulted extremely in very low number of individual seedlings (Table1). Stunted growth and normal plants without selfed seeds were recorded in M1 seedlings. Further more other traits like parthenocarpic fruit development were recorded for He-300 Gy but lacked in the C ion beam irradiated treatments.

Analysis of the mutation spectrum of the M2 progenies derived from seeds irradiated with ion beams revealed a series of mutants (Table 2).

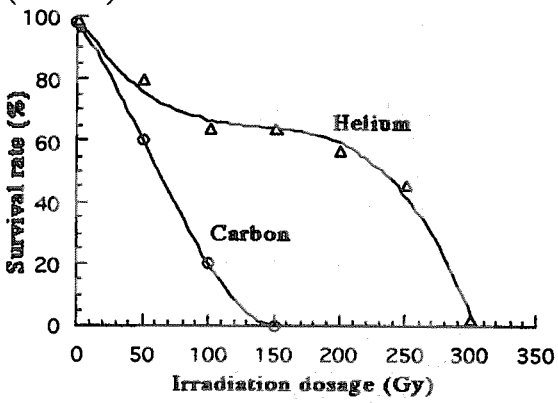


Fig.3. Survival rate of seedlings as affected by carbon and helium ion beam irradiated tomto seeds.

The rate of the occurance in chlorophyll mutants due to C- ion beam irradiation of the tomato seeds was relatively low. On the other hand, He ion beam irradiation of tomato seeds prolifically resulted into several mutants namely: albino. viridis, xantha and broad leaf form. Mutants were notably detectable on seeds irrariated with He ion beam dosage of between 50 and 300 Gy. He-100 Gy or lower dosages were ineffective for the generation of morphologically detectable mutants.

On the other hand, all seedlings derived from 200 and 250 Gy He-ion beam irradiation dosage survived whereas except for two, the seedlings derived from treatment of >300 Gy died after about four weeks of growth under similar conditions indicated above. Hence 300 Gy is likely to be the upper irradiation dosage within which total elimination of the seed does not occur.

Closer evaluation of the M2 generation indicated that C- 50 Gy as well as He-150 Gy are likely to produce important tomato mutants. Elsewhere, ion beam of varying irradiation dosages have been shown to produce a mutant with spotted pigmentation in testa of Arabidopsis thaliana (Tanaka et al. 1997b). Thus this technology is going to revolutionise tomato genetic improvement with a short run.

Conclusively, C-50 Gy and He-150 Gy are considered to be likely the optimum dosages for irradiating tomato seeds with the possibility of generating tomato mutants without causing excessive injury to the embryo.

Table 1. Analysis of abnormalities in M1 seedlings raised from ion beam irradiated seeds

Category of abnormality	Carbon (Gy)		Helium (Gy)				
	50	100	100	150	200	250	300
No. of survived seedlings [Z]	63	21	67	67	61	48	2
Normal plants with selfed-seeds	39	0	62	55	48	16	0
Stunted plants with selfed seeds	1	15	4	6	1	19	1
Normal plants without selfed-seeds	13	0	0	0	0	2	1[Y]
Stunted plants without selfed-seeds	10	6	1	6	12	11	0
Normal growth with narrow leaf and parthenocarpic friuit	0	0	0	0	0	0	1[Y]
Normal growth with chimera on leaf	0	0	1	0	1	0	0

Z : to see in Fig.1.
Y : this plant is same.

4. Summary

Tomato seeds were irradiated with carbon (C) and helium (He) ion beams and thereafter, the performance of the irradiation on tomato seed germination, seedling and plant characters monitored. This investigation was prompted based on the fundamental reason that various agriculturally important tomato mutants are expected from this research. Potential ion beam irradiation effects were noted via an extremely reduced radicle elongation in both C (>50 Gy) and He (>200 Gy) irradiation dosages. The radicle is a suitable organ for the detection of irradiation effects even where germination would not offer precise indication.

C-ion beam irridintion severly affected the survival rate of the seedlings with C-100 Gy giving rise to only 20% survival compared to 64% at He-100 Gy. Several abnormalities: stunted growth, failure of pollen production and failure to complete plant life cycle were observed in the M1 seedlings and plants.

In the M2 seedlings and plants, albino, viridis xantha and broad leaf forms were detected in the plants. Conclusively, C-50 Gy and He-150 Gy are likely to be optimum dosages for irradiating tomato seeds with the possibility of generating tomato mutants without causing excessive injury to the embryo.

5. References

1) M. Masuda, M., T. Furuichi, and Y. Takeda. J. Japan. Soc. Hort. Sci. 67: 93–98 (1998)
2) A. Stevens and C.M Rick. Genetics and breeding. In Atherton, J.G. and the late J. Rudich (eds.) The Tomato Crop, pp 35-100. Chapman and Hall, London, New York (1986)
3) A.Tanaka, N. Shikazono, Y. Yokota, H. Watanabe and S. Tano. Int. J. Radiat. Biol. 72 : 121-127 (1997a)
4) A.Tanaka, S,Tano,T.Thanes,Y.Yokota, N.Shikazono and H.Watanabe. Genes and Genetic Systems 72 :141-148 (1997b)

Table 2. Mutation spectrum of M2 progenies derived from seeds irradiated with ion beam

Radiation dosage (Gy)	No. of M1 seeds with mutation apperance in M2 progeny						No. of M1 seeds used for M2 progeny
	Alb.	Xan.	Viri.	Broad leaf	Short internode	Self-topping	
C- 50		1			1		40
100	1						15
He-100	1						66
150		3		1			61
200	2	2	3			1	49
250		1	1	1			18
300							1

Z: Forty seeds were used for each lot of M2 progeny .

2.7 Induction of Mutation in Spiraea by Ion Beam Irradiation; —Effects of Ion Beams on Germination of Spiraea Seed—

Masahide IIZUKA[1],Nobuhiro KUDO[1], Yasuo KIMURA[1],
Yoshihiro HASE[2] and Atushi TANAKA[2]
[1]Gumma Horticultural Experiment Station,
[2] Department of Radiation Research for Environment and Resources, JAERI.

Introduction

Ion beams, which have a higher linear energy transfer (LET) than X and gamma rays, is one of efficient mutagenic agents, applicable to mutation breeding of many horticultural crops. However, there have been few studies on the effects of ion beam irradiation on induction of mutation in vegetables and ornamental crops. The lethal dose of the $^{4}He^{2+}$ and $^{12}C^{5+}$ ion beam irradiation to strawberry and hydrangea seed became clear [1),2)]. And ion beams are irradiated in the strawberry, and a fungal pathogen (Glomerella cingulata) resistance is individualy selected[3)].

We have the mutation breeding of the garden plants.Spiraea (Spiraea thunbergii) is important flowering trees and shrubs.An ion beam was irradiated in spiraea for the purpose of variation of the flower color. We examined effects of ion beam irradiation on germination of spiraea seed.

Materials and Methods

Seeds of Spiraea 'Pinkey' (Spiraea tunbergii) were used in this study. Seeds were irradiated with ion beam (220 MeV $^{12}C^{5+}$) at various doses (5 to 140 Gy). Irradiated seeds were surface-sterized with 70% ethanol and 1% sodium hypochlorite solution and washed three times in sterile water. They were cultured on a modified 1/2 MS medium(Murashige and Skoog,1962) containing 3% sucrose and 0.8% at 25 °C and 16 hr-photoperiod. Germination rate was investigated after 30 days culture. Survival seedlings were acclimatized and transferred in soil. Morphological changes of the seedlings were investigated.

Results and Discussion

When the dosage of irradiation increased, the germination rates of the seed decreased. And at the dose of more than 100Gy, a germination rate, decreased rapidly(Fig.1).

After germination, many individuals which showed dwarf type and acute leaf type mutations were recognized in the irradiated seedlings(Table.1).We are performing cytological studies to investigate horticultural values of the mutants and are screening mutants of flower color variation in the growth plants.

References

1)N. Kudo et al. TIARA Ann. Rep., 16:62-64. (1998)
2)M. Iizuka et al. TIARA Ann. Rep., 2.3:30-31. (1999)

3)M. Iizuka et al. TIARA Ann. Rep.,
2.4:33-34. (2000)

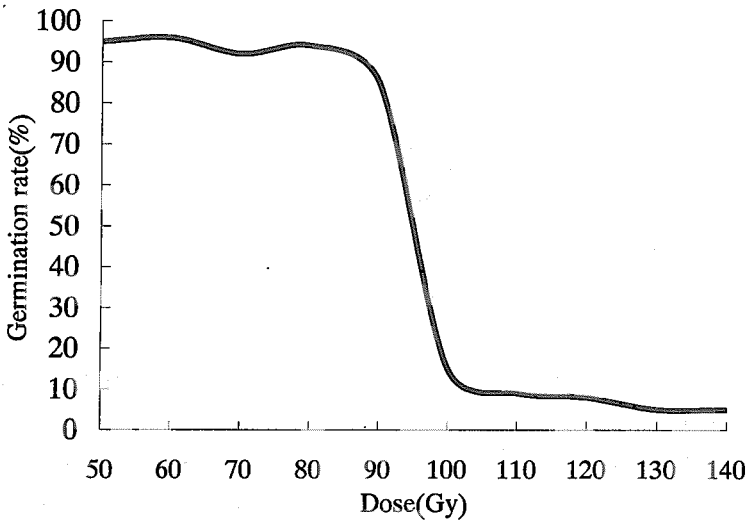


Fig.1.Effect of carbon ion beam on the germination of spiraea seed

Table 1. The number of dwarf type and acute leaf type mutants with carbon ion beam irradiation

Dose (Gy)	No.of irradiated seeds	No.of dwarf type mutants	No.of acute leaf type mutants
90	458	3	1
80	412	2	2
70	388	3	1
60	425	1	0
50	436	2	0

2.8 Isolation and characterization of the ion-beam-induced new Arabidopsis floral mutant, *frill1*

Yoshihiro Hase and Atsushi Tanaka
Department of Radiation Research for Environment and Resources, JAERI

1. Introduction

New plant mutants such as UV-resistant Arabidopsis and Chrysanthemum with novel flower colors and shapes have been obtained using ion beams as a mutagen[1, 2]. These results strongly suggest that ion beams provide the possibilities of finding a lot of new mutants valuable not only for the plant breeding but also for the primary botanical research.

Now that the Arabidopsis genome project has finished, mutant isolation is becoming more important because wide varieties of mutants are indispensable for functional analysis of respective genes. We have been trying to isolate new Arabidopsis mutants defect in organ development in order to analyse how and by which genes plant organ formation is regulated. In this report, we describe a new Arabidopsis floral mutant, *frill1* (*frl1*), and its phenotypical analyses[3].

2. Materials and Methods

2.1 Isolation of mutant

Dry seeds of Arabidopsis ecotype Columbia were exposed to 220 MeV carbon ion beams with a dose of 150 Gy. Irradiated M1 seeds were sown and selfed to obtain M2 seeds. About 12,000 M2 plants derived from 1,500 M1 plants were grown and visible mutants were selected. One of them, named the *frl1* mutant, was backcrossed twice with wild-type Columbia and has been maintained by self-pollination.

2.2 Mapping analysis

The *frl1* mutant was crossed with wild-type Lansberg erecta. Approximately 400 plants of selfed F2 progeny were used for gene mapping as described by Konieczny and Ausubel[4].

2.3 Phenotypical observation

Epidermal cells of mature petals were observed under an optical microscope after soaking in 70% ethanol for 2 days for clarification. For observation of nuclei, the petals cleared were dyed in 1 μg/ml DAPI solution. Sections of the petals were made using Technovit 7100 resin and dyed by toluidine blue.

3. Results and Discussion

From the screening of 12,000 M2 plants derived from the ion-beam-irradiated M1 seeds, more than 50 visible mutants were selected (data not shown). Among them, the *frill1* (*frl1*) mutant has serrated petals and sepals but the other floral and vegetative organs are not affected (Fig. 1). Mutants like *frl1* have not been reported before and this mutant is thought to be important to understand plant morpho-genesis because it has a highly organ-specific phenotype.

In the wild-type petal, we can see a well-ordered radial cell lineage from the base toward the tip (Fig. 2). However, the cell lineage in the *frl1* petals was disordered, especially in the distal region of the petal (Fig. 2). Furthermore, the number of petal epidermal cells in the distal region was

decreased and their size was variable and relatively larger in the *frl1* petal, as compared with those in the wild-type petal (Fig. 2). Nuclear size was also larger and variable in the *frl1* petal but not in the wild-type petal. These observations suggest that abnormal endo-reduplication occurred in the distal region of *frl1* petal (Fig. 2). In contrast, no significant phenotypical defect was observed in the basal region of *frl1* petal.

Morphological observations throughout the petal development revealed that *frl1* petals were normal before stage 9 of Arabidopsis floral development and the *frl1* phenotype became apparent at stage 10 (stage 10 corresponds to the middle stage of petal development) (data not shown). From these results, it is thought that *FRL1* acts in the latter half of petal development, and that *FRL1* is an important factor to attain normal cell division and expansion especially in the distal region of Arabidopsis petals.

Now we are isolating *FRL1* gene using a map-based approach (Fig. 3). *FRL1* is mapped in the 105-kb region at the middle of the upper arm of chromosome 1. Complementation analysis is in progress.

References

1) A.Tanaka et al., TIARA Ann.Rep.1995 (1996) 32-34.
2) S.Nagatomi et al., TIARA Ann. Rep. 1997, JAERI-Review 98-016 (1998) 41-43.
3) Y.Hase et al., Plant Journal, 24 (2000) 21-32.
4) A.Konieczny and F.M.Ausubel., Plant Journal, 4 (1993) 403-410.



Figure 1 Flower of *frill1* mutant.

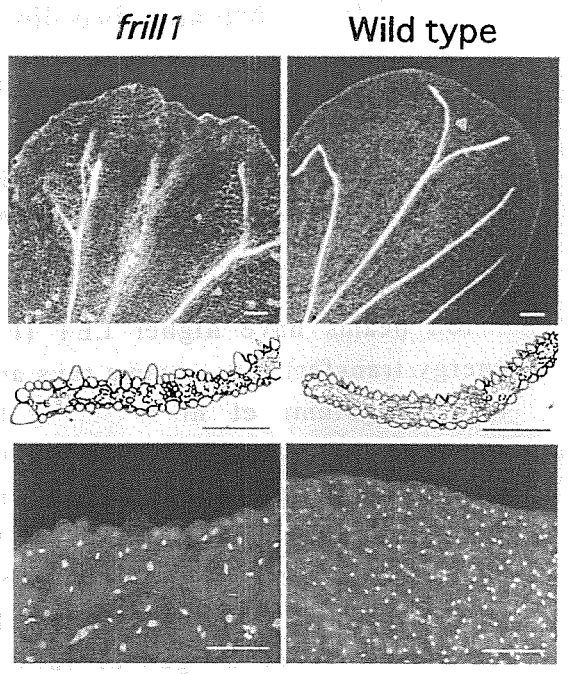


Figure 2 Comparison of petal epidermal cells. (Upper) Distal region of mature petals. Bars=100mm. (Middle) Cross sections of petal tip. Bars =100mm. (Lower) DAPI images of petal tip. Bars =50mm.

Chromosome I

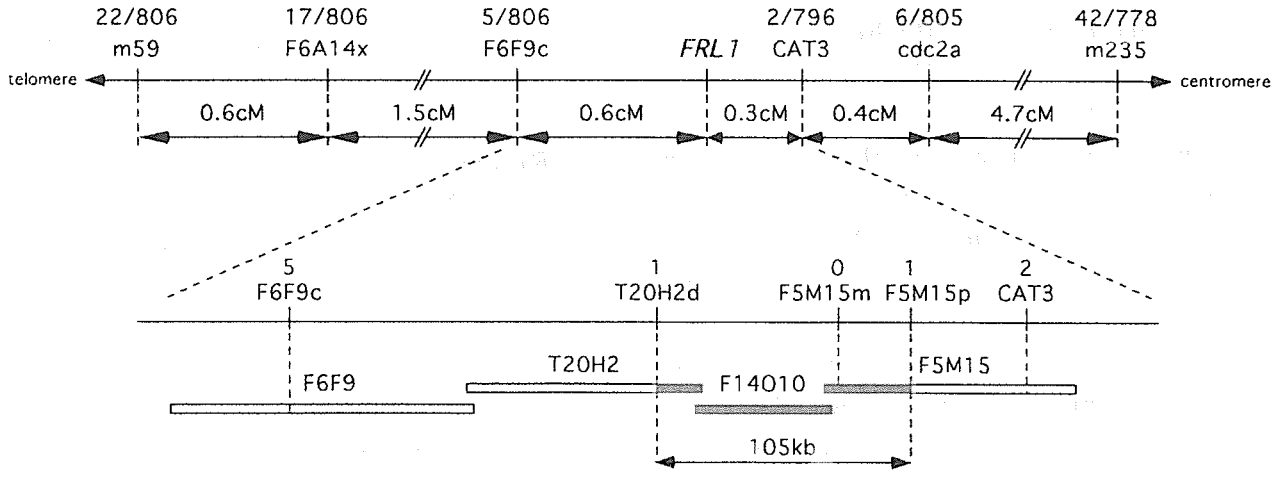


Figure 3 Map position of the *FRL1* gene.

2.9 Mutation breeding using ion-beam irradiation in aster

T.Baba[1], F. Nakamura[1], H. Nishi[1] and Y.Yoshida[1],
A.Tanaka[2], N.Shikazono[2], Y.Hase[2] and H.Watanabe[2]
Fukuoka Pref. Federation of Agricultural Co-operative Association[1]
Department of Radiation Research for Environment and Resources, JAERI[2]

1. Introduction

Ion beams have higher LET (linear energy transfer) than gamma rays and X rays. Nagatomi et al.[1) 2)], have reported that specific chrysanthemum mutants such as complex and stripe flower color mutants were induced by a combined method of ion-beam irradiation with *in vitro* culture, which were not induced by gamma rays. We expect that ion beam irradiation will be a new mutation- breeding method for many horticultural plants.

We supposed that ion beam induced specific mutation not only flowers color but also flower shape. The purpose of this study is to investigate the effects of ion beam on the mutant of flower shape.

2. Materials and Methods

Aster cultivar, 'Yae - purple' of *A. hybrida Hort* (purple color and double flower) was used in this study. The explants of leaf was placed in petri dish containing M S media (Murashige and Skoog) supplemented with 2mg/l benzylaminopurine (BA), 1mg/l naphtalene acetic acid (NAA), 30g/l sucrose and 2g/l gellan gum for callus induction. The samples covered with Kapton film were irradiated with 220MeV carbon and 50MeV helium ion beams from the TIARA AVF cyclotron. After irradiation, the sample was transferred to the same fresh callus induction medium and was incubated under dark place at 25℃ for 7 days and then incubated under 2500~3000 lux at 25℃. The cultured callus was transferred onto MS medium supplemented with 0.3mg/l BA, 15g/l sucrose, and 2g/l gellan gum in order to induce shoot regeneration. The regenerated plants potted with vermiculite were acclimated, and grown plants were cultivated in the greenhouse.

3. Results and Discussion

In this study, we obtained 35 regenerated plants (1.75%) from 2000 explants of leaf, but it was not enough to investigate to the effects of ion beam on the mutant of flower shape. We think their results were caused by regeneration and acclimation method. After the solution of each problem, we would like to progress this study.

References

1) S.Nagatomi, A.Tanaka, A.Kato, H.Watanabe and S.Tano, TIARA Annual Report 5:50-52(1996)
2) S.Nagatomi, A.Tanaka, H.Watanabe and S.Tano, TIARA Annual Report 6:48-50(1997)
3) T.Baba, S.Tanaka, S.Haraguchi, A.Tanaka, N.Shikazono and H.Watanabe
TIARA Annual Report 2:48-49(1999)



Carbon Helium Control

Fig.1. Plant regenerated from leaf explants irradiated with ion beams, In June 2001.

2.10 Mutation Generation in Carnation Plants Regenerated from in vitro Leaf Cultures Irradiated with Ion Beams

M. Okamura[1)], M. Ohtsuka[1)], N. Yasuno[1)], T. Hirosawa[1)].
A. Tanaka[2)], N. Shikazono[2)], Y. Hase[2)] and M. Tanase[2)]
[1)]Plant Laboratory, Agribio business company, Kirin Brewery Co., Ltd.
[2)]Department of Radiation Research for Environment and Resources, JAERI

1. Introduction

Most of mutagens used for mutation breeding of crops in the world are gamma rays and X-rays. Ion beams have higher linear energy transfer (LET) and bring on plant cells intensive relative biological effectiveness (RBE) as compared with gamma rays and X-rays[1)]. Therefore ion beams could be utilized widely as a new mutagen. By the irradiation with heavy ion beams, specific flower color mutants were induced in chrysanthemum[2)] and new flower shape mutant was induced and analyzed in *Arabidopsis*[3)].

A combined method of irradiation with plant cell and tissue culture is useful to enhance mutation frequency[2-4)], and to obtain commercial varieties in a short period of time[5)].

In this study, we investigate the efficiency of mutation generation by means of a combined method of ion beam irradiation with tissue cultures, and characterize the feature of mutation breeding using ion beam irradiation in carnation.

2. Materials and Methods

Carnation cultivar, 'Vital' (spray type, cherry pink flowers with frilly petals), was used for the experiment. The leaf segments were placed in petri dish containing Murashige and Skoog medium supplemented with 2mg/l Zeatin, 30g/l sucrose and 7g/l agar (MSZ medium). The samples covered with Kapton film were irradiated with 220 MeV carbon ($^{12}C^{5+}$) and 50 MeV helium ($^{4}He^{2+}$) ion beams from the TIARA AVF cyclotron (JAERI, Takasaki). After irradiation, the leaf segments were transferred onto fresh MSZ medium and cultured in the growth chamber. The frequency of adventitious shoot regener-ation was examined two months after irradiation. The regenerated plants were acclimatized in the greenhouse and their flower color and shape were investigated. The regeneration frequency of adventitious shoots from the leaf cultures irradiated with gamma rays was examined in order to compare the RBE of ion beams with that of gamma rays.

On the other hand, the regenerated plants from the leaf cultures irradiated with X-rays by soft X-ray unit, and the plants derived from 0.3% EMS (ethyl methanesulfonate)-treated buds for 5 hours were also established and examined as comparison.

3. Results and Discussion

The dose response curves of adventitious shoot regeneration by ion beam irradiation were shown in Figure 1, and that by gamma ray irradiation in Figure 2. In $^{4}He^{2+}$ ion beams, regeneration frequency decreased gradually with increasing dose and the median re-generation dose (RD50) was estimated at 40 Gy. In $^{12}C^{5+}$ ion beams, regeneration frequency also decreased with increasing dose and RD50 was estimated at 15 Gy. In gamma rays, RD50 was around 60Gy. The RBE of $^{12}C^{5+}$ ion beams relative to gamma rays was estimated to be 3-4.

The mutants in flower color and/or shape in the plants regenerated from leaf cultures irradiated with $^{12}C^{5+}$ ion beams were shown in Table 1, and those with X-rays in Table 2. The mutation rates of flower color are 2.3% and 1.3% in $^{12}C^{5+}$ ion beams and X-rays, respectively. Flower color mutants such as pink, light pink and red were obtained by

X-ray irradiation, whereas the color spectrum of the mutants obtained by $^{12}C^{5+}$ ion beam irradiation was wide such as pink, dark pink, light pink, salmon, red, complex and striped types (Figure 3). In EMS-treated plants, flower color mutants such as pink, red and striped type were observed. However the striped color of EMS mutants was vague as compared with that of $^{12}C^{5+}$ ion-induced mutants. The examination of the plants derived from gamma ray irradiation is ongoing.

In carnation variety tested, new mutants in flower color such as salmon, clear striped type, complex type and in flower shape such as wild *Dianthus* type petals have been obtained from the plants regenerated from $^{12}C^{5+}$ ion beam-irradiated leaf cultures. The results correspond with the report in chrysanthemum[2] in that the color spectrum of the ion beam-induced mutants was wider than that of the mutants induced by low LET radiations and the specific mutants such as complex and striped color types were obtained. High frequency rearrangements of the DNA such as inversion, insertion and translocation were reported in carbon ion-induced mutants[6]. These results suggest that ion beams have different effect from low LET radiations on mutation generation of crops.

References

1) A. Tanaka, N. Shikazono, Y. Yokota, H. Watanabe and S. Tano, Int. J. Radiat. Biol 72 (1997), 121-127
2) S. Nagatomi, A. Tanaka, H. Watanabe and S. Tano, JAERI-Review 97-015 (1997), 48-50
3) Y. Hase, A. Tanaka, T. Baba and H. Watanabe, The Plant J.24 (2000), 21-32
4) H. Yamaguchi, S. Nagatomi, A. Tanaka, N. Shikazono, T. Morishita and K. Degi, JAERI-Review 2000-024 (2000), 41-42
5) M. Okamura, In: Bajai YPS ed. Biotechnology in Agriculture and Forestry, vol 27: Springer-Verlag (1994), pp209-223
6) N. Shikazono, A.Tanaka, H. Watanabe and S. Tano, Genetics 157 (2001), 379-387

Table 1. No. of mutants in plants regenerated from leaf cultures irradiated by $^{12}C^{5+}$ ion beams

Dose (Gy)	No. lines tested	Mutants in flower color and/or shape (No.)	Mutation (%) in flower color
5	230	Round petals (2)	0
10	254	Pink (1), Dark Pink (1), Light Pink (2), Salmon (2), Red (1), Striped type; pink and white (2), *Dianthus* type petals (2)	3.5
15	185	Pink (1), Pink / Round petals (1), Red (1), Red / Round petals (1), Complex type; pink and white (2)	3.2
30	36	Striped type; pink and white (1)	2.8
Total	705	Color mutants (16)	2.3

Table 2. No. of mutants in plants regenerated from leaf cultures irradiated by soft X-rays (Soft X-ray unit: Ohmicron® OM60R: 60kVp, 5mA)

Dose (Gy)	No. lines Tested	Mutants in flower color and/or shape (No.)	Mutation (%) in flower color
40	115	Pink (1)	0.9
80	78	Pink (2)	2.6
90	172	Pink (2), Light pink (1)	1.7
130	191	Red (1)	0.5
Total	556	Color mutants (7)	1.3

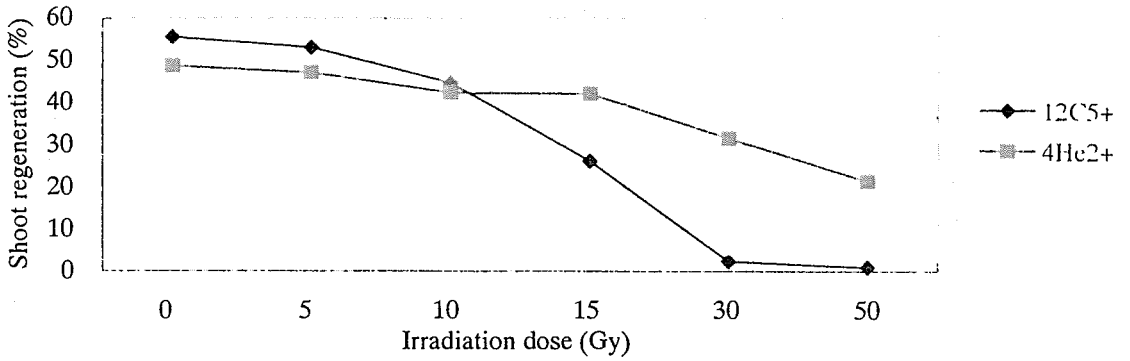


Figure 1. The influence of ion beams on leaf cultures in carnation

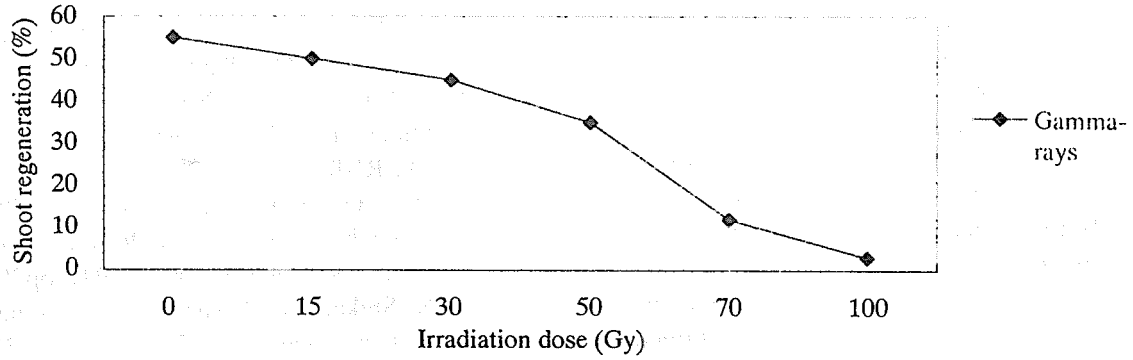


Figure 2. The influence of gamma-rays on leaf cultures in carnation

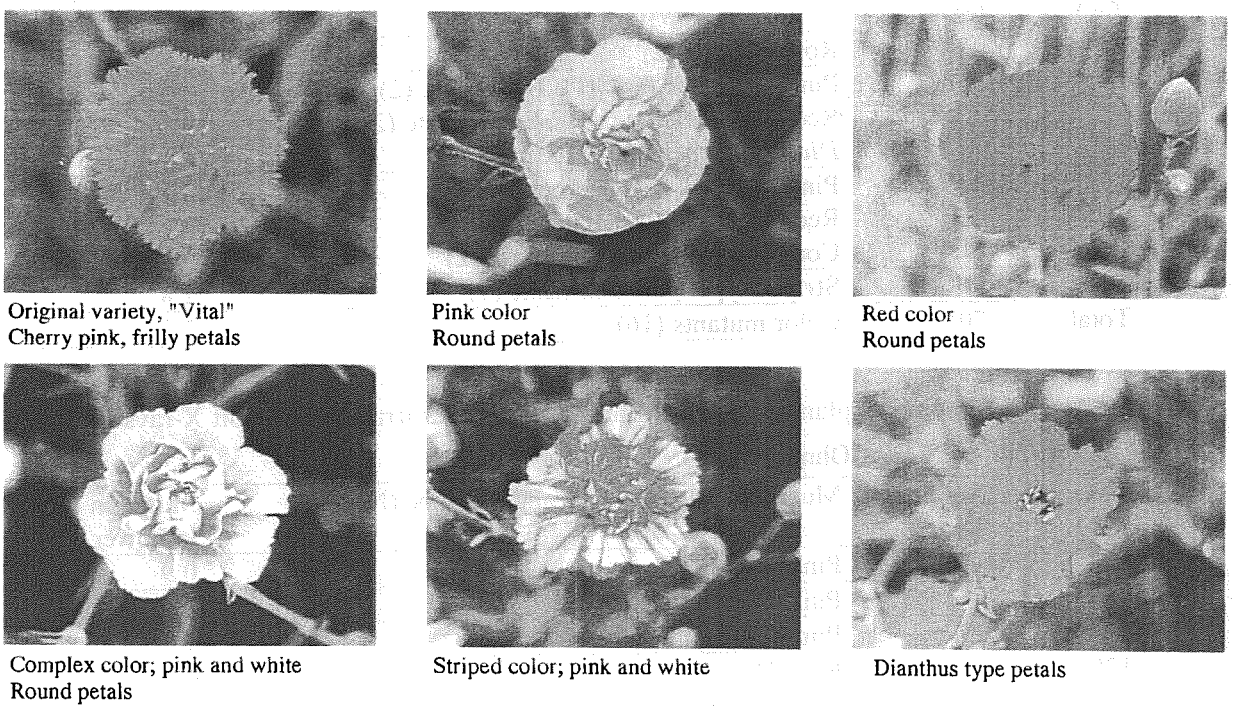


Fig. 3. Carnation mutants regenerated from in vitro leaf cultures irradiated with 12C5+ ion beams

2.11 Mutation Induced by Ion Beam Irradiation to Hinoki Cypress Shoot Primordia

K. Ishii[1], Y. Hase[2], N. Shikazono[2], and A. Tanaka[2]

[1]Department of Molecular and Cell Biology, Forestry and Forest Products Research Institute, [2]Department of Radiation Research for Environment and Resources, JAERI

1. Introduction

Hinoki cypress (*Chamaecyparis obtusa* Sieb. et Zucc.) is the most important endemic forest conifer in Japan. It covers 24 % of the plantation area. Hinoki cypress produces the highest quality wood and can be grown throughout Japan, excluding Hokkaido and the Ryukyu Island. In forest tree species, many mutants were obtained by Gamma-rays radiation breeding. However, in Hinoki cypress, only a juvenile leaf-form mutant was obtained and reported[1].

Ion beam is expected to increase the mutation frequency and wide spectrum, since it has a high LET (linear energy transfer). The combination of ion beams irradiation and tissue culture was sometimes beneficial for high frequent mutation induction[2][3][4]. Tissue culture of Hinoki cypress was reported first for micropropagation[5].

In this study, we conducted irradiation of the shoot primordia of Hinoki cypress with $^{4}He^{2+}$ and $^{12}C^{5+}$ heavy ion beams to regenerate mutant trees.

2. Experimental procedure

Shoot primordia of Hinoki cypress was used for the experiments. They are cultured on CD medium[6] supplemented with 2.25 mg/l 6-benzylaminopurine and 0.005 mg/l naphthalene acetic acid (NAA). Fresh shoot primordia were subcultured on the same medium in petri dish (35 x 10 mm) which were covered with Kapton film. They were irradiated with 50 MeV $^{4}He^{2+}$ or 220 MeV $^{12}C^{5+}$ ion beam from AVF cyclotron in JAERI. After irradiation the shoot primordia were subcultured to the new CD media containing 0.005 mg/l NAA for shoot differentiation.

3. Results and Discussion

In $^{4}He^{2+}$ ion beam, the survival rate of Hinoki cypress shoot primordia decreased as the amounts of irradiation increased (Fig. 1) when the diameter of shoot primordium cluster was less than 2 mm. The lethal dose with helium and carbon beams was about 80 Gy after 9 weeks cultivation.

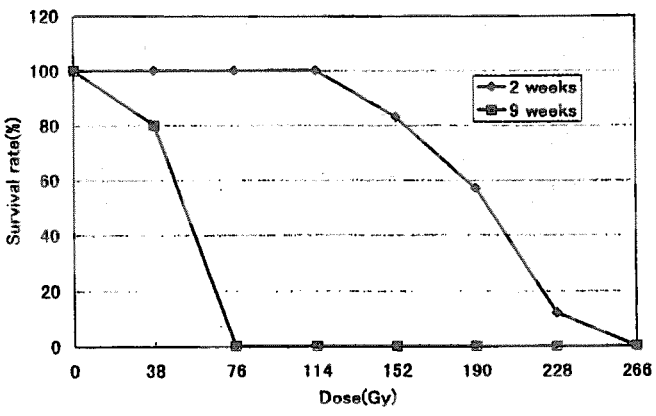


Fig.1 Dose-response curve for survival rate of Hinoki cypress shoot primordia exposed to 50 MeV 4He2+

However, when shoot primordium clusters more than 3 mm diameter were irradiated, there were surviving shoot primordia even above 80 Gy irradiation. We observed albino, xanta and wax rich type mutation shoots regeneration from these irradiated shoot primordia (Table 1). There were no correlation among frequency of the mutants, types and dosage of the irradiation. Even in the low dosage of irradiation, there appeared the mutation.

4. Summary

Combination of ion beam irradiation and tissue culture was effective to induce mutation of Hinoki cypress. Size of the tissue was important factor for determination of the lethal dosage.

References

1)T. Kondo, Forest Tree Breeding 167(1993)12-15.

2)S. Nagatomi, A. Tanaka, A. Kato, H. Watanabe and S. Tano, TIARA Annual Report 5(1996)50-52.

3)S. Nagatomi, A. Tanaka, H. Watanabe and S. Tano, TIARA Annual Report 6(1997) 48-50.

4)T. Nakahara, K.Hirashima, M. Koga, A. Tanaka, N. Shikazono and H. Watanabe, TIARA Annual Report 1998(1999)28-29.

5)K. Ishii, Plant Cell Tissue and Organ Culture 7(1986)247-255.

6)R.A. Campbell and D.J. Durzan, Can J. Bot. 53(1975)1652-1657.

Table 1 $^{4}He^{2+}$ ion beam induced shoot mutation in tissue cultured Hinoki cypress
(After 8 months cultivation on shoot elongation medium)

intensity(Gy)	no of mutants / petri dish		
	albino	xanta	wax rich
0	0	0	0
38	2	35	0
76	5	36	1
114	0	1	2
152	3	26	4
190	6	20	0
228	3	18	0
266	0	15	1

2.12 Mutation Induction with Ion Beam Irradiation in Garlic (*Allium sativum* L.)

T.Tashiro*, Y.Yamamoto*, A.Tanaka**, N.Shikazono**, Y.Hase**
University Farm, Faculty of Bioresource, Mie University*, Department of Radiation Research for Environment and Resources, JAERI**

1. Introduction

There is a great demand for garlic recently because garlic is one of the remarkable health foods. Garlic belongs to a group of the Allium family and doesn't have flower. It is difficult to breed positively because of the propagation method by bulbs. Therefore, the consumer and the producer could not satisfy the breeding in garlic.

Ion beams have higher LET (linear energy transfer) than gamma rays. We expect that ion beam irradiation will be a new mutation-breeding method for garlic. We supposed that ion beam induced specific mutation not only morphological character but also chemical composition.

The purpose of this study is to investigate the effects of ion beam on the mutant of volatile sulfur compounds of garlic. In this paper, we report the effects of ion beam on callus proliferation and shoot regeneration from the irradiated callus induced from basal plate[2] of garlic bulb, and bulblet induction from explants of basal plate bulb.

2.Materials and Methods

Garlic cultivars, 'Fukuchi-white' treated sterilely was used for the experiments. We obtained the compact and granular callus like embryogenic callus, which were induced from bulb basal plates on MS (Murashige & Skoog) medium supplemented with plant growth regulators (2,4-dichlorophenoxy acetic acid) [1]. The callus prepared in 1～2mm thickness were covered with Kapton film and irradiated with 50 MeV $^{4}He^{2+}$ and 320 MeV $^{12}C^{6+}$ ion beams from the TIARA AVF cyclotron in JAERI.

The other hand, the explants of bulb basal plates, thin section prepared 1mm thickness, was placed in petri dish containing LS media, 30g/l sucrose and 3g/l gellan gum for shoot induction[2]. They were covered with Kapton film and irradiated with 320MeV carbon ion beams. After irradiation, the both samples were transferred to the fresh shoot induction medium and was incubated under 3000 lux at 25℃.

3.Results and discussion

The effect of helium ion beam irradiation on the callus proliferation and shoot regeneration was shown in Table 1. Both callus proliferation and shoot regeneration ratio decreased with as increasing dose and almost suppressed at higher than 2Gy. This result suggests that the dose to obtain mutants efficiently is 0.25-0.5 Gy with helium ion. The effect of carbon ion beam irradiation on the shoot regeneration ratio and bulblet induction from explants was shown in Table 2. The shoot regeneration ratio decreased with increasing dose and the median lethal dose (LD50) was estimated 0.5-1.0 Gy. However, the relation between irradiation dose and bulblet induction from survival explants was not apparent.

We investigate further the efficient irradiation dose for the obtainment of mutants.

References

1) Y.Yamamoto, T.Tashiro, International Plant Propagators' Society 7: 17-18 (2000)
2) M.Ayabe, S.Sumi, Plant Cell Reports 17: 773-779 (1998)

Table 1 Effects of helium ion beam on proliferation of callus and regeneration of shoot from callus induced basal plate of garlic bulb

Dose	Callus weight(g)		B/A	Number of callus colonies with
Gy	A	B		regenerated shoots per petri dish
	Day 0	Day 38	(%)	Day 143
10	0.677	0.665	98.2	7.7
5	0.652	0.644	98.8	3.7
2	0.581	0.566	97.4	2.0
1.5	0.594	0.613	103.2	7.7
1	0.492	0.558	113.4	11.7
0.5	0.636	0.660	103.8	8.7
0.25	0.654	0.718	109.8	11.0
0	0.754	0.984	130.5	23.8

Table 2 Effects of carbon ion beam on induction of shoot and bulblet from basal plate of garlic bulb

Dose	Numbe of survived	Number of explantns with	B/A	Numbe of survived	Number of	D/C
Gy	explants(A)*	induced shoots(B)		explants(C)	bulblets(D)	
	Day 20	Day 40	%	Day 60	Day 60	
10	16	3	18.8	2	2	1.0
5	14	4	28.6	2	0	0.0
2	14	6	42.9	7	4	0.6
1	11	4	36.4	5	9	1.8
0.5	18	9	50.0	9	12	1.3
0.2	12	10	83.3	12	16	1.3
0.1	13	12	92.3	11	25	2.3
0.05	22	21	95.5	20	28	1.4
0	8	7	87.5	8	15	1.9

* : There were 24 replicates for each treatment.

2.13 Mutation Breeding of Rice, Eggplant and Gloriosa by Ion Beam Irradiation

M. Mizobuchi, M. Okada, M. Matsumoto, A. Iwasaki, A. Tanaka*, N.Shikazono*, Y. Hase*

Kochi Prefectual Agricultural Research Center , Department of Radiation Research for Environment and Resources, JAERI*

1. Introduction

In Kochi Prefecture, we are carrying out mutation breeding of rice, eggplant and gloriosa. Though we have used γ -rays and MNU as mutagens, we attempt to use ion beams in this study. Because the linear energy transfer (LET)and relative biological effectiveness (RBE) of ion beams are extremely higher than those of γ -rays. Thus, seeds of rice, eggplant, and gloriosa were irradiated with ion beams and several biological effects were examined. Moreover, we selected individuals that have excellent mutant characters. We used helium(He) and carbon(C) ions that were accelerated by using the AVF cyclotron in Takasaki, JAERI .

2. Materials and Methods

In rice, dry seeds of variety 'Tosapika' were irradiated. In order to examine the effects of ion beams, germination rates and survival rates were measured. Then the adequeate irradiation dosages were determined.

In eggplant, we irradiated ion beams to seeds, and sow them to determine the adequate doses of the beams by observing the survival rates.

Range of ion beams are about 1-1.5 mm, so that ion beams can not penetrate large seed of gloriosa. Because we could not determine the position of embryo, ion beams were irradiated with both the hilum side and the opposite side (the back side) of seeds.

3. Results and Discussions

In rice, the survival rate became 0% by the irradiation of 220MeV C with the dose of 60Gy. LD50 was about 25Gy. It is thought that the adequate irradiation dose for mutation induction is the dose in which survival rate becomes 70% of the control. In the case of 220MeV C, the adequate dose was thought to be about 20Gy(Fig. 1). In the irradiation of 50MeV He, the survival rate became 0% at 300Gy, and the LD50 was about 200Gy. Then the adequate dose was about 150Gy in the case of 50MeV He. Irradiations of 320MeV C and 100MeV He are being examined at present.

In eggplant 'Ryouma' , LD50 of 220MeV C ions was about 35Gy, and that of 'Wase-shinkuro' was about 55Gy. The adequate dose for mutation induction was thought to be 30-50Gy (Fig. 3). LD50 of 50MeV He in 'Wase-shinkuro' was about 225Gy, and the adequate dose was 150-200Gy (Fig4)

In gloriosa, when C ions were irradiated with the back side of seed, the germination rate much more decreased than with the hilum side. Moreover, a lot of abnormal

individuals were observed. These includes narrow leaves, leaves with picotee or stripe variegation, and late growth. The effect of the irradiation to the back side was higher than to the hilum side. In an irradiation with 80Gy of 50MeV He ions, differences of germination rates, survival rates, abnormal rates of individuals were observed between strains. Differences of the maturational degree of seeds was thought to be one of these causes (Table 1).

4. Reference

1)A.Tanaka et al.,TIARA Ann Rep.,1998,p39

2)H.Yamaguchi et al.,TIARA Ann Rep.,1998,p42

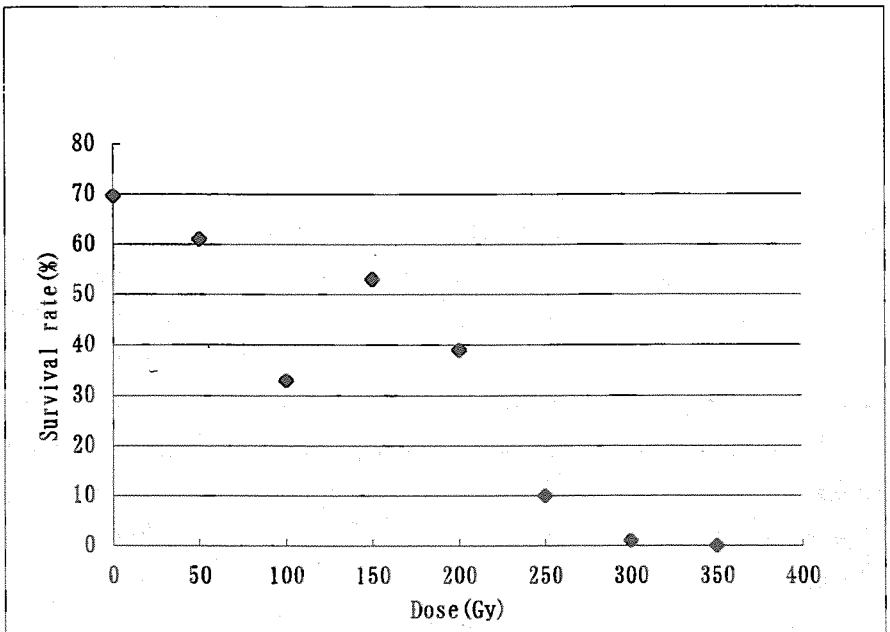


Fig. 2 Survival rate of Tosapika in Helium(50MeV) irradiation

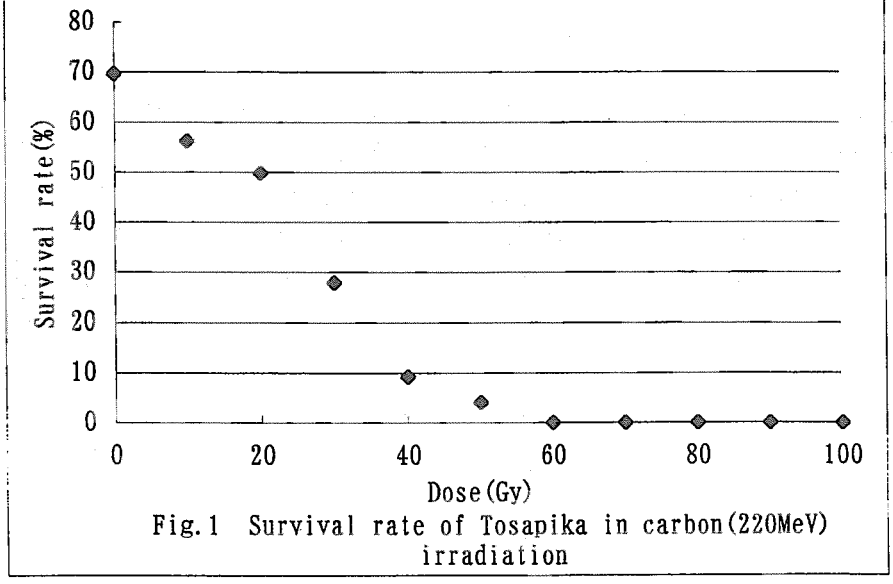


Fig. 1 Survival rate of Tosapika in carbon(220MeV) irradiation

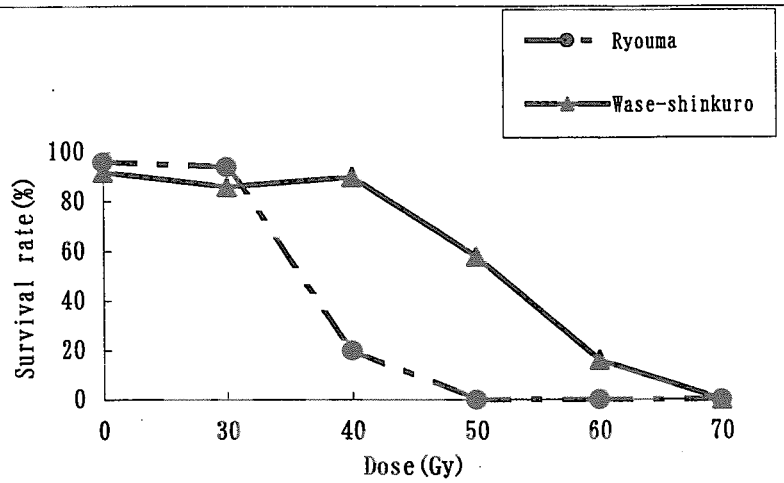


Fig. 3 Survival rate of eggplant in carbon(220MeV) irradiation

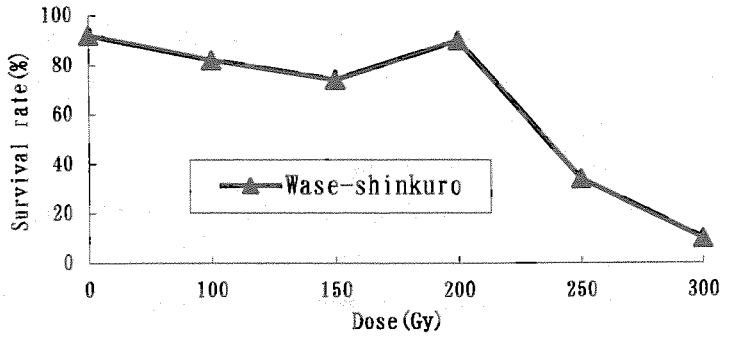


Fig. 4 Survival rate of eggplant in helium(50MeV) irradiation

Table 1 The effect of ion beam [1] on the dry seed of gloriosa

No.	Kind and system	Number of seeds	Germination [2] rate (%)	Survival [3] rate (%)	Abnormal [3] stock rate (%)
No.3	Misato-aka-kouben	51	65	85	45
No.33	K163	20	30	75	17
No.37	South-africa	30	3	33	100
No.51	*G-lutea*	50	38	70	21
No.62	r・K	50	50	88	38

[1] Irradiation condition : $^{4}He^{2+}$ 50MeV、80Gy、Irradiation side Back side.

[2] Investigation period : 2000.11.20 ～ 2001.2.4

[3] Investigation 2001.2.4. (number of surviving plants ／ number of germinated seeds) × 100

2.14 Production of Mutants that Have High Ability to Assimilate Nitrogen Dioxide by the Irradiation of Ion Beams in *Ficus stipulata*

M. Takahashi[1)], S. Kohama[1)], M. Hakata[1)], Y. Hase[2)], N. Shikazono[2)], A. Tanaka[2)], and H. Morikawa[1)]

[1)]Department of Mathematical and Life Sciences, Graduate School of Science, Hiroshima University, [2)] Department of Radiation Research for Environment and Resources, JAERI

Nitrogen dioxide (NO_2), a major air pollutant that causes acid rain, reacts with volatile organic compounds in the atmosphere to produce photooxidants, including ozone. Plants take up NO_2[1)] and assimilate its nitrogen through a primary nitrate assimilation pathway[2)].

We discovered that among naturally occurring 217 taxa of the higher plants, including 50 wild herbaceous plants (42 genera of 15 families) collected from roadsides, 60 cultivated herbaceous plants (55 genera of 30 families), and 107 cultivated woody plants (74 genera of 45 families), there is more than 600-fold variation in the ability to assimilate NO_2[3)]. We also reported that the overexpression of a chimeric nitrite reductase gene (derived from spinach) resulted in a 1.8-fold higher NiR activity than that of wild-type and 1.4-fold higher capability to assimilate NO_2 than the wild-type plants[4)].

Ficus stipulata Thunb. (= *Ficus thunbergii*), "Hime-itabi" is an evergreen, climber roadside tree that belongs to Moraceae, the mulberry family. This tree will be useful to cover highway corridors, building surfaces and roof tops to cleanup nitrogen dioxides and other air pollutants.

Materials and methods

Five millimeter long explants containing shoot apices or 1 mm long explants containing nodes were cut from aseptically-grown *Ficus stipulata* Thunb. (= *Ficus thunbergii*) plants using a surgical blade.

The explants were placed on filter paper on shoot formation medium that was consisted of woody plant medium (WPM) supplemented with 3% sucrose, 0.6% Gellan gum, 44.4 μ M benzyl adenine (BA) and 100 nM thidiazuron (TDZ) (pH 5.6). They were then cultured at 25℃ in the light (30 to 40 μ mol/s/m^2). After culture for 3 to 4 days, explants were irradiated with $^{12}C^{5+}$ (220 MeV) and $^{4}He^{2+}$ (50 MeV) ion beams from the AVF cyclotron in JAERI. The irradiated explants were transferred to fresh shoot formation medium and cultured for up to three months.

Results and Discussion

Fig. 1 shows the effect of the irradiation with the $^{4}He^{2+}$ ion beam on the regeneration frequency of explants of the *Ficus* tree. The dose of the

irradiation was changed from 20 to 200 Gy, and the regeneration frequency was determined one, two and three months after irradiation. The data shows the average of three dishes containing 20 explants each. The irradiation higher than 100 Gy drastically decreased the regeneration frequency; only ca. 20% of irradiated explants formed shoots. Based on the study by Tanaka et al.[5], we consider that the dose of around 75 Gy with $^{4}He^{2+}$ ion beam will be strong enough to induce mutation in this *Ficus* tree.

With the $^{12}C^{5+}$ ion beam, the irradiation of 30 to 100 Gy gave about 30% of the regeneration frequency as shown in Fig. 2. With this particular ion bean, the dose higher than 30 Gy strongly inhibited the formation of shoots from the explants. We therefore concluded that the dose of around 20 Gy with $^{12}C^{5+}$ ion beam will be strong enough to induce mutation in this *Ficus* tree.

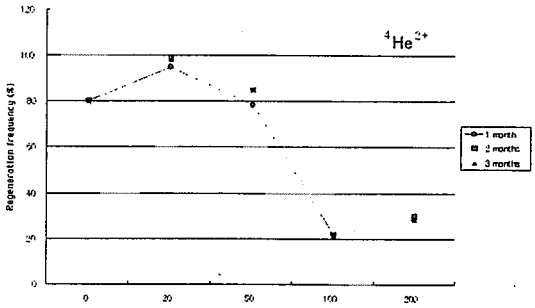


Fig. 1. The effect of the irradiation with the $^{4}He^{2+}$ ion beam on the regeneration frequency of explants of *Ficus stipulata* Thunb. (= *Ficus thumbergii*).

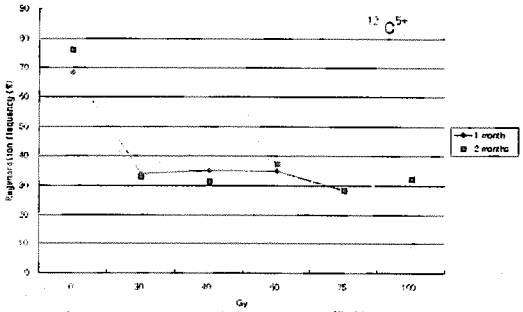


Fig. 2. The effect of the irradiation with the $^{12}C^{5+}$ ion beam on the regeneration frequency of explants of *Ficus stipulata* Thunb. (= *Ficus thumbergii*).

References

1) A.C. Hill, J. Air Pollut. Contr. Ass., 21 (1971) 341-346.

2) T. Yoneyama, H. Sasakawa, Plant Cell Physiol., 20 (1979) 263-266.

3) H. Morikawa, A. Higaki, M. Nohno, M. Takahashi, M. Kamada, M. Nakata, G. Toyohara, Y. Okamura, K. Matsui, S. Kitani, K. Fujita, K. Irifune, N. Goshima, Plant Cell Environ., 21 (1998) 180-190.

4) M. Takahashi, Y. Sasaki, S. Ida, H. Morikawa, Plant Physiol., 126 (2001) 731-741.

5) A. Tanaka, S. Tano, T. Chantes, Y. Yokota, N. Shikazono, H. Watanabe, Genes Genet. Syst., 72 (1997)141-148.

2.15 Induction of Somatic Mutation by Ion Beam Irradiation in Lethal Chlorophyl Mutant of Rice

M. Maekawa[1)], A. Tanaka[2)], N. Shikazono[2)] and Y. Hase[2)]

[1)]Research Institute for Bioresources, Okayama University
[2)]Department of Radiation Research for Environment and Resources, JAERI

1. Introduction

Transposon (mobile element) is very useful for gene isolation in several plant species. Since so far, any class II type transposons have not been discovered in rice, *Ac/Ds* system in maize was introduced into rice and was tried to be applied for gene-tagging[1)]. If an endogenous transposon was discovered in rice, it could be used easily as a powerful tool for gene-tagging in open environments. As *Mu* in maize[2)], transposons may be found in mutagenized rice. As ion beams are a type of high linear energy transfer (LET) radiation and can deposit high energy on a target compared to low LET radiations, the novel mutants or large DNA rearrangements are expected to be induced by ion beam irradiation[3)]. So, it is expected that transposon may be induced by ion beam irradiation. Visualization of transposon activity is made by variegation in chlorophyl mutant or anthocyanin accumulation. Maekawa[4)] found a variegated chlorophyl mutant in F2 of the cross between distantly related rice varieties. Although a near isogenic line (NIL) for this mutant gene with T-65 genetic background was bred, this line did not show any variegations through generations. So, if variegation could be induced by mutation in this NIL, it is highly expected that this mutant line carries transposon. Thus, this study aims to induce somatic mutation at M1 in this stable chlorophyl mutant line by ion beams.

2. Experimental procedure

Seeds of a chlorophyl mutant (referred yl) were derived from a yl-stble (stable yl) plant in T-65 yl-stb BC3F2. Ion beams used were helium and carbon. Irradiated seeds were sterilized with 70% EtOH and sown in planters containing commercial substrate. After three weeks, presence/absence of variegations were examined because yl mutants start withering from this time.

3. Results and Discussion

Carbon ion beam irradiation drastically reduces germination rates of T-65 yl-stb plants irradiated with increasing dose and the median lethal dose with carbon ion was estimated to be 30 Gy (Tab.1). In M1 plants irradiated with 50 Gy of 220 MeV C ions, a variegated yl plant generated as shown in Fig.1-b. This plant showed small or large sectors in leaves expanded laterly (Fig. 1-c and d). As a result, out of 992 M1 plants germinated one variegated plant was obtained. On the other hand, helium ion beam irradiation slightly reduces germination rate of yl-stb plants with increasing dose of 50 Gy to 150 Gy and the median lethal dose was estimated to be over 150 Gy. In M1 plants irradiated with 100 MeV $^{4}He^{2+}$, any yl plants showing clear variegation were not observed though 9 vague-typed yl plants were generated totally (Tab.1). These vague-typed yl plants were also obtained with the frequencies of 0.1 % in control. The frequency of vague-typed yl plants generated with helium ion beam irradiation was 0.3 %. This frequency was slightly higher than that in

control, suggesting that helium ion beam irradiation might induce vague type variegation.

The variegated yl plant at M1 bore 9 panicles. The frequencies of clear variegation were examined in panicle-row lines. Spikelet fertilities in 9 panicles were low, varying from 0 % to 41.7 %. Most of panicle-row lines, no.2 to 6 and no.9, segregated variegated (Fig.2-a and b) and stable yl (Fig.2-c) plants (Tab.2). In no.5 line, 2 revertants were segregated (Fig.2-d). Totally, the ratio of variegated to stable yl plants was good fitness to 3:1, suggesting that mutable dominance gene conversion might be induced by carbon ion beam irradiation. In addition, no.2 and 5 lines segregated albino. On the other hand, all yl plants showing vague-typed variegation obtained by helium ion beam irradiation segregated only stable yl pedigrees at M2 (data not shown). This result showed that vague-typed variegations observed at M1 plants by helium ion beam irradiation were transient.

These results indicated that clear variegation induced by carbon ion beam irradiation at M1 plants is heritable and conversion of *yl* to *Yl* is mutable. This suggested that stable yl phenotype might be caused by inactivation of a transposon.

Tab.1 Germination rates and frequencies of variegated yl plants in ion beam irradiated T-65 yl-stb M1 plants

Radiation	Energy (MeV)	Absorbed dose(Gy)	No. of seeds sown	No. of plants germinated	Germ. rate(%)	No. of var. yl plants
$^{12}C^{5+}$	220	30	772	372	48.2	0
		40	773	324	41.9	0
		50	791	204	25.8	1 [1]
		60	784	90	11.5	0
		70	748	2	0.3	0
		80	768	0	0.0	0
		90	752	0	0.0	0
		100	758	0	0.0	0
		Total	6146	992	16.1	1 [1]
$^{4}He^{2+}$	100	50	566	405	71.6	1 [2]
		75	569	345	60.6	2 [2]
		100	575	182	31.7	0
		125	575	352	61.2	0
		150	572	326	57.0	6 [2]
		Total	2857	1610	56.4	9 [2]
Control			2804	2439	87.0	3 [2]

[1]; Clear type. [2]; Vague type.

Tab.2 Segregation of yl phenotype in M2 plants derived from the variegated yl plants generated at carbon ion-irradiated M1 plants

	Spik. fert.(%)	yl phenotype			
Panicle no. of M1 plant		Normal	Variegated	Stable	Albino	Total
1	0.0	0	0	0	0	0
2	41.7	0	12	3	2	17
3	7.7	0	1	1	0	2
4	9.8	0	1	2	0	3
5	17.0	2	3	1	1	7
6	9.1	0	3	2	0	5
7	3.3	0	1	0	0	1
8	3.9	0	2	0	0	2
9	16.2	0	4	1	0	5
Total		2	27	10	3	42

References

1)T. Izawa, T. Ohnishi, T. Nakano, N. Ishida, H. Enoki, H. Hashimoto, K. Itoh, C. Wu, C. Miyazaki, T. Endo, S. Iida and K. Shimamoto, Plant Mol. Biol. **35** (1997) 219.

2)D. S. Robertson, Mutat. Res. **51** (1978) 21.

3)A. Tanaka, Gamma Field Symposia **38** (1999) 19.

4)M. Maekawa, Modification of Gene Expression and Non-Mendelian Inheritance. eds. K. Oono and F. Takaiwa.(Natl. Inst. Agr. Res.) (1995) 379.

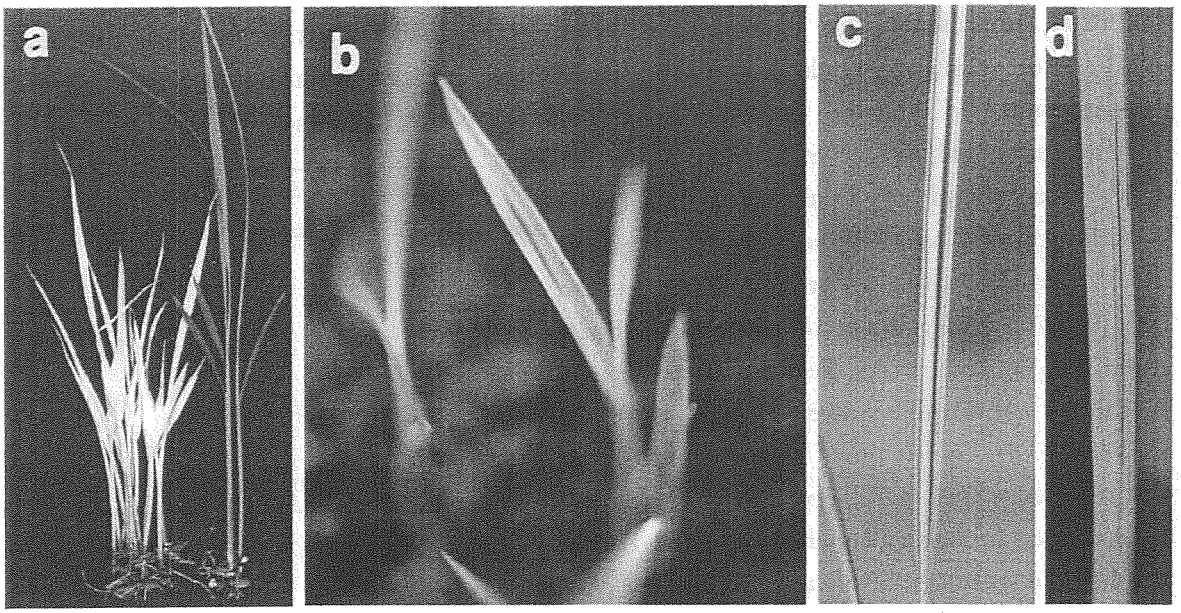


Fig.1 Stable yl plants and a variegated plant generated at carbon ion-mutagenized M1 population. a; Normal (right) and yl-stb(left). b; Variegated plant at seedling stage. c,d; Large and small sectors observed in the variegated plant (b), respectively.

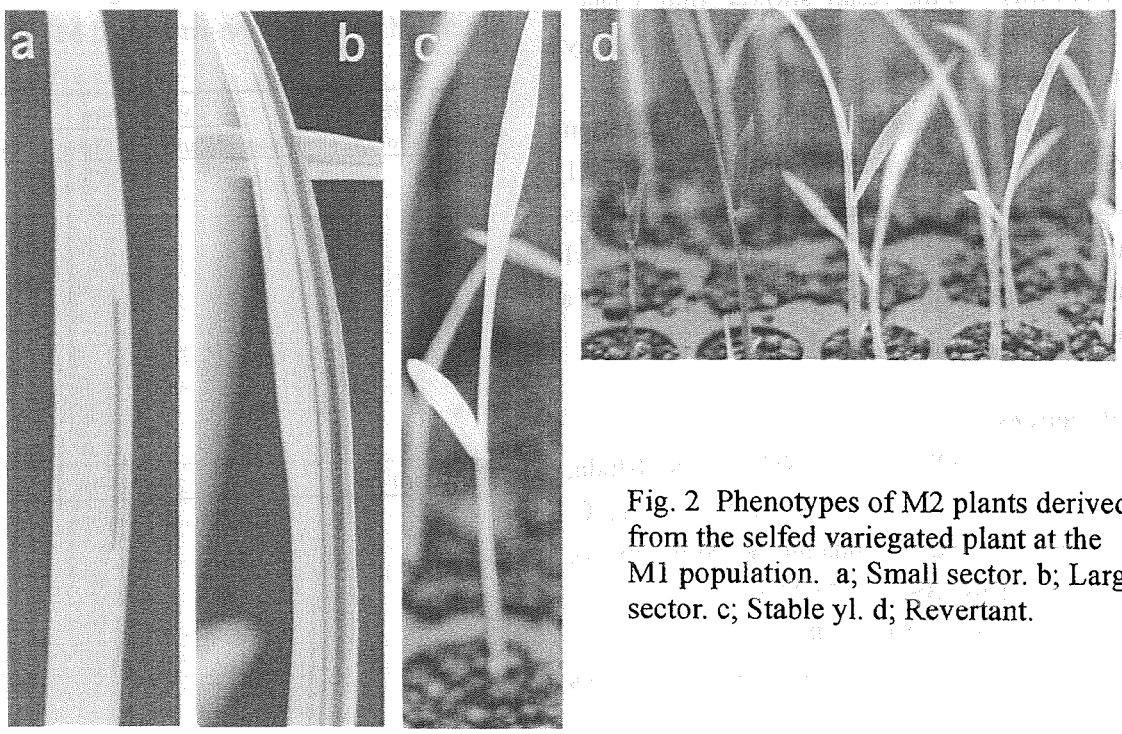


Fig. 2 Phenotypes of M2 plants derived from the selfed variegated plant at the M1 population. a; Small sector. b; Large sector. c; Stable yl. d; Revertant.

2.16 Genetic screening of antiauxin mutants in *Arabidopsis thaliana*

C. Ooura[1], E.T. Aspuria[1),4)], Y. Oono[1),2)], Y. Hase[2)], Y. Kobayashi[1),2)], H. Uchimiya[1), 3)]

[1)] Advanced Science Research Center, JAERI

[2)] Department of Radiation Research for Environment and Resources, JAERI

[3)] Institute of Molecular and Cellular Biosciences, The University of Tokyo

[4)] Dept. of Horticulture, University of the Philippines at Los Banos

1. Introduction

Auxins, typified by indole-3-acetic acid, are plant hormones that regulate many physiological and developmental phenomena by controlling cell division, cell elongation and cell differentiation in plants. Genetic screening followed by characterization of auxin-related mutants has contributed to the elucidation of the molecular mechanism of auxin biosynthesis, transport and response to stimuli [1-3]. However, no mutant defective in an auxin receptor gene has yet been isolated to date. Recently, Shikazono *et al.* [4] reported that the ion beams, characterized by high linear energy transfer (LET), as compared to X-rays or γ-rays, induced point mutations as well as large deletions at higher frequency. These significant findings prompted us to use ion beams for screening novel auxin-related mutants as it may generate new type of mutants that have never been obtained through other mutagens. In addition, the use of chemicals such as antiauxins was also adapted for screening novel auxin-related mutants. Antiauxins have similar structure to auxins but do not exhibit auxin activity [5]. They are believed to inhibit the auxin action by competing with auxin in the binding site of the auxin receptor, although the detailed mechanism of inhibition is unknown. Antiauxins could be powerful tools to elucidate molecular mechanism of auxin perception, assuming that the hypothesis for the inhibitory mechanism of antiauxins is legitimate. This report demonstrates the characterization of the effects of antiauxin on root growth of *Arabidopsis thaliana*, and the isolation of antiauxin resistant mutants from ion beam-irradiated *Arabidopsis* seed population.

2. Experiments

Arabidopsis thaliana (L.) Colombia ecotype was used throughout the experiments. The ion beam-irradiated *Arabidopsis thaliana* lines were generated with $^{12}C^{5+}$ beams (220 MeV, 150 Gy) accelerated by the AVF cyclotron at the TIARA facility in JAERI TAKASAKI. The EMS-treated lines were purchased from LEHLE SEEDS (Round Rock TX, USA). T-DNA insertional lines were obtained from Nottingham *Arabidopsis* Stock Center (Nottingham, UK). BA3 line, a transgenic line harboring *AuxRD* (auxin responsive domain)-GUS, is described in Oono et al., [6]. Surface-sterilized seeds were plated

onto germination medium (GM; 0.5x Murashige and Skoog salts [Giboco BRL, Gaithersburg, MD, USA], 10% sucrose, 1xB5 vitamins, and 500 μg ml^{-1} MES, pH 5.8 solidified with 0.8% Bacto agar [Difco, Detroit, MI, USA]) containing various concentration of auxin and/or anti-auxin, *p*-chlorophenoxyisobutyric acid (PCIB). Seedlings were grown vertically under continuous light at 23 °C. For screening of mutants, seeds were germinated and grown on GM containing 20 μM PCIB. Putative mutants whose root growth was not inhibited by PCIB were isolated, grown on pots containing a mixture of Metro-Mix® 350 (Scotts, Marysville, OH, USA), vermiculite and perlite at a ratio of 1:1:1 and maintained in the greenhouse.

3. Result and discussion

Physiological experiments with *Arabidopsis* roots showed that PCIB had antagonistic effects on auxin-induced lateral root formation and GUS expression in the root tip of BA-3. PCIB inhibited root elongation by itself and did not restore root elongation from auxin-induced inhibition. The distinct root morphology caused by PCIB and auxin suggested each compound acts independently on root elongation (data not shown).

PCIB resistant mutants that showed relatively longer roots compared to wild type in the presence of 20 μM PCIB were screened from a total of 59,000 ion beam-, EMS-, and T-DNA-mutagenized M2 seeds. As shown in Table 1, seventy-six putative mutants were isolated in the primary screening. Twenty of 76 lines showed the reproducible PCIB resistant phenotype in M3 population, although the phenotype in M3 is segregated in all the lines except one (#183). The mutant line #183, which was isolated from the ion beam-irradiated seed population, exhibited slightly longer hypocotyls and shorter roots than the wild type line in the medium containing neither auxin nor PCIB (Figure 1). The length of main roots of seven-day-old wild type and #183 seedlings grown on the medium containing 20 μM PCIB were 51% and 71 % shorter than those of the untreated seedlings, suggesting that #183 was PCIB resistant with respect to root elongation (Figure 1). The auxin dose response curve in root elongation of the #183 line was similar to that of the wild type. However, the #183 line required higher auxin concentration than wild type to form lateral roots (data not shown). The root gravitropism of the #183 line seemed to be weaker than that of the wild type. PCIB caused loss of gravitropism in the #183 as in the wild type line (data not shown). These results suggest that the #183 line is an auxin-related mutant that has pleiotropic morphological phenotypes characteristic of several other auxin-related mutants.

4. Summary

The effects of PCIB, an antiauxin, on *Arabidopsis* root system were investigated. PCIB acted as auxin antagonist on auxin-induced gene expression and lateral root formation; it inhibited root elongation independently to auxin. Furthermore, an

antiauxin resistant mutant was successfully isolated using ion beam as a new type of mutagen. The isolated mutant exhibited pleiotropic morphological phenotypes characteristic to several other auxin-related mutants.

Table1. Summary of the screening of PCIB resistant mutants.

Mutagen	Number of M1 (T1) seeds	Number of M2 (T2) seeds screened	Number of putative mutants isolated in the primary screening	Number of putative mutant lines (M3 or T3) in the secondary screening
Ion beam	6700	25000	52	1/6*
EMS	8300	34000	14	0/4*
T-DNA	3900	16000	11	0/11*
Total	15300	59000	76	1/20*

*(number of lines in which all the seedlings showed mutant phenotype in the M3 population)/(number of lines in which several seedlings showed mutant phenotype in the M3 population)

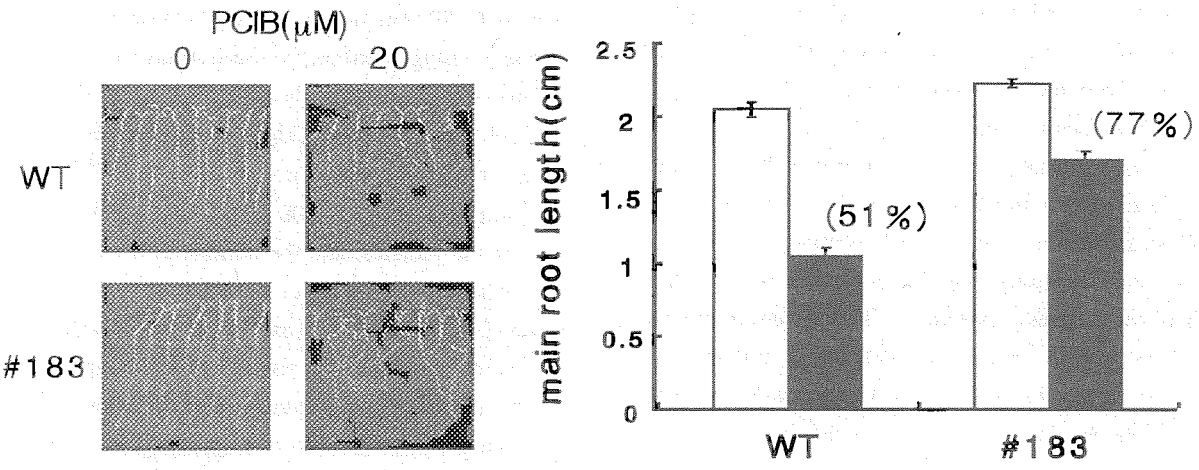


Figure1. Phenotype of the PCIB resistant mutant, #183. Seeds were sowed on GM containing 0 μM (open bars) or 20 μM PCIB (solid bars) and grown under the continuous light for 7 days at 23 °C.

References

1) Bartel B. (1997) *Annu. Rev. Plant Physiol. Plant Mol. Biol.* 48: 51-66.
2) Dolan L. (1998) *Genes Develop.* 12: 2091-2095.
3) Leyser O. (1998) *Current Biol.* 8: R305-R307.
4) Shikazono N, Tanaka A, Watanabe H, Tano S. (2000) *JAERI-Review* 2000-024: 38-40.
5) McRae DH, Bonner J. (1953) *Physiol. Plant.* 6: 485-510.
6) Oono Y, Chen QG, Overvoorde PJ, Köhler C, Theologis A. (1998) *Plant Cell* 10: 1649-1662.

2.17 Isolation of response deficient mutants to environments from plant seeds irradiated with ion-beam

[$]Y. Sasuga, Y. Kami, M. Ooshima, G. Takata, Y. Kobayashi, Y. Sakata, *Y. Oono, ** Y. Kobayashi, S. Tanaka, and H. Takenaga
Faculty of Applied Bioscience, Tokyo University of Agriculture, *Advanced Science Research Center, JAERI, **Department of Radiation Research for Environment and Resources, JAERI.

1. Introduction

A living organism has developed various kinds of sensors for the adaptation to circumstances. It is obvious that animals including mankind have the senses of sight, smell, hearing, taste, and touch. Plants are also known to have their own sensing systems. For instance, they have photoreceptors, such as phytochrome and cryptochrome, to adjust themselves to light environment. On the other hand, little is known about sensors in the subterranean parts of plants, although roots have many essential functions such as absorption, transport, and storage of water and nutrition. The sessile nature of plants may have promoted the development of the sensing system by which the roots manage to survive in all sorts of soil conditions.

In this respect, we have examined the responses of *Arabidopsis thaliana* radicles to chemical and physical factors (*e.g.* water, nutrition, temperature, and contact), suggesting that growing radicles have their own sensing systems to several environmental factors. The response deficient mutants to environmental factors may provide valuable tools for research in the molecular mechanisms of plant sensing system.

Ion-beam irradiation characterized by high linear energy transfer and relative biological effectiveness is expected to be a powerful mutagen. Studies on the structural alteration of the DNA in ion-induced mutants demonstrated that ion-beam irradiation caused genetic changes enough to produce various mutants.

[$]Present address: Department of molecular physiology, Tokyo Metropolitan Institute of Medical Science

In the present study, we devised a bioassay by using two-tier medium to evaluate primary root curvature to contact (thigmotropism), and screened mutants disordered in thigmotropism from *Arabidopsis thaliana* seeds irradiated with carbon ion.

2. Materials and Methods

1) Bioassay of *Arabidopsis thariana* radicles for evaluation of thigmotropism

Arabidopsis thaliana (Col-0) seeds were surface-sterilized with 70% ethanol and 1% solution of NaOCl and inoculated on a two-tier medium in a petri dish (90 mm in diameter). The lower layer was prepared using various concentrations of phytagel (0.2 to 0.7%), whereas the upper layer consisted of 0.3% phytagel medium (Figure 1A). The inoculated seeds were maintained for 4 days at 24±3℃ under white light condition (2500 lux, 16 h light, 8 h dark) to grow the radicles, and the number of seedlings that bent their growing radicles horizontally on boundary between two layers was counted. Among the concentrations tested, we usually used a simple assay system (upper layer phytagel concentration, 0.3%; lower layer, 0.5%), named thigmotropism research system (TRS), for the screening of thigmotropism deficient mutants.

2) Screening of thigmotropism deficient mutants

The mature dry seeds of *Arabidopsis thaliana* (Col-0) were sandwiched between kapton films and irradiated with carbon ion (220 MeV) at a dose of 100-200 Gy at TIARA. The irradiated seeds were grown and the self-pollinated seeds (M2 seeds) harvested. The M2 seeds were used for the screening of mutants by means of TRS. The seedling whose radicle penetrated the lower layer of 0.5% phytagel was grown to yield the self-pollinated seeds (M3

seeds). The M3 seeds were used for further genetic analysis.

3. Results and Discussion

1) Characterization of thigmotropism in *Arabidopsis thaliana* radicles

The percentage of root curvature increased with increasing concentrations of phytagel in the lower layer. The curvature was observed by 30-50% at the concentrations of 0.2-0.3%. At higher concentrations, however, all radicles bent to the boundary between two-tier media (Figure 1B). These results suggest this simple assay system (TRS) is of use for the investigation of thigmotropic responses in roots and screening of mutants disordered in contact sensing and signal transduction.

It has been reported that a phytohormone, auxin, is involved in deviation growth of plants caused by gravitropism and phototropism [1, 2]. We investigated whether or not auxin participated in thigmotropism with the aid of auxin inhibitors. Two days after germination, either of auxin antagonist, PCIB, or an inhibitor of auxin transport, TIBA, was added to the medium at concentrations of 10-60 μM. The radicle curvature (%) decreased by 40 and 25% by the treatments of PCIB (60 μM) and TIBA (60 μM), respectively (data not shown). These results suggest auxin may participate in thigmotropic response as well as gravitropism in plant roots.

2) Isolation of thigmotropism deficient mutants

About 12,000 M2 seeds from *ca.* 2,000 carbon-ion mutagenized M1 seeds of *Arabidopsis thaliana* were screened by using TRS (lower layer phytagel concentration: 0.5%). Out of 12,000 seeds, 37 mutants that struck their radicles deep into the lower layer were obtained (Figure 1C). In M3 generation, only 6 lines (K-14, 16, 36, 38, and 41) were found to be penetrative. However, all seedlings of M3 generation were not penetrative, but most showed curvaceous phenotype. Penetrative and curvaceous mutants of M3 generation were observed to occur at a segregation ratio of 1 to 40-70 (Table 1). In M4 generation, K-14 and 16 lines demonstrated higher frequency of penetrative phenotype at a segregation ratio of 1 to 0.6-0.9 (data not shown).

3) Analysis of a thigmotropism deficient mutant, K-14

In M5 generation of K-14 line, there was a new phenotype that the radicle crept on surface of upper layer, whereas M4 generation of K-14 line exhibited only two phenotypes (penetrative and curvaceous). In F2 population derived from crosses between M4 plants of K-14 and wild type, moreover, there was still another phenotype that the radicles penetrated lower layer after crept on surface of upper layer. The segregation ratios of phenotypes in M5 generation and F2 population were shown in Table 2. These data suggest that K-14 line possess multiple gene disruption. Therefore, it is necessary that back-cross with wild type is repeated. Further studies are now in progress to repeat back-cross and identify mutate position on genome.

4. References

1) Ferrari S et al., Plant Sci. 158: 77-85 (2000)
2) Fujita H and Syono K, Plant J. 12: 583-595 (1997)

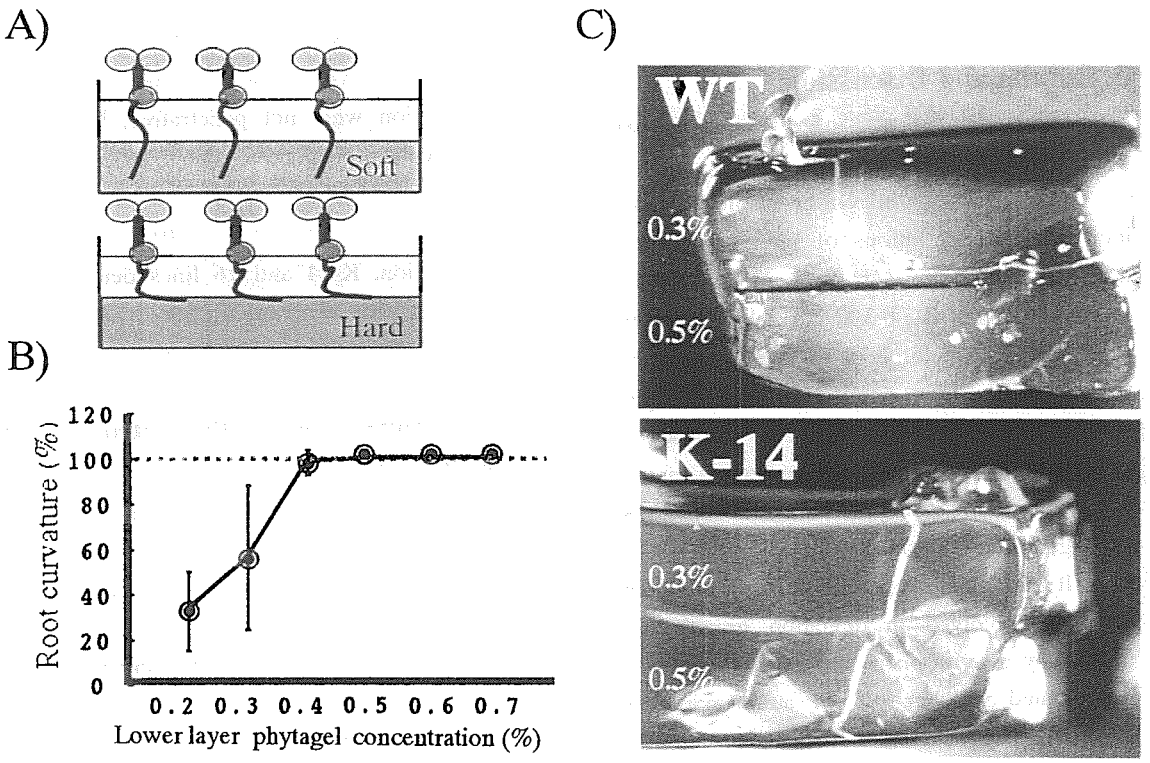


Figure 1. Thigmotropism research system (TRS). A) A diagram of TRS. B) Changes of root curvature ratio in various phytagel concentration of lower layer. Phytagel concentration of upper layer: 0.3%. C) Photograph of radicle thigmotropic responses. Upper panel: wild type, Lower panel: a thigmotropism deficient mutant (K-14).

Table 1. Segregation ratio of thigmotropism deficient mutants in M3 generation

Line	Number of plants		Ratio
	P	Cu	
WT	3	475	1: 158
K-7	—	—	—
K-14	283	165	1: 0.6
K-16	143	125	1: 0.9
K-36	3	185	1: 62
K-38	4	201	1: 50
K-41	6	208	1: 35

P: penetrative Cu: curvaceous

Table 2. Segregation ratio of K-14 mutants in M5 generation or F2 population crossed with wild type.

Line	Ratio			
	P	Cr	Cu	Cr P
WT	1	—	158	—
K-14 a	1	1	0.5	—
K-14 b	1	0.7	0.5	—
K-14 c	1	1	0.4	—
K-14 (F2)a	1	3	2	0.4
K-14 (F2)b	1	5	6	0.5
K-14 (F2)c	1	3	2	1

P: penetrative Cr: creepy Cu: curvaceous
Cr P: creepy and penetrative

2.18 System of Cell Irradiation with a Precise Number of Heavy Ions

Y. Kobayashi[1)], T. Funayama[1)], M. Taguchi[1)], S. Wada[1,2)], M. Tanaka[1,3)], T. Kamiya[4)], W. Yokota[4)], H. Watanabe[1)] and K. Yamamoto[1,3)]

[1)]Department of Radiation Research for Environment and Resources, JAERI, [2)]Department of Veterinary Medicine, Kitasato University, [3)]Department of Biomolecular Sciences, Graduate School of Life Sciences, Tohoku University, [4)]Advanced Radiation Technology Center, JAERI

1. Introduction

A microbeam is a source of focused or collimated radiation localized to micron-sized area of the specimen. The use of heavy ion microbeams provides a unique way to control precisely, the number of ions traversing individual cells and the localization of dose within the irradiated cell. In recent years there has been an increasing interest in the use of microbeams to study a number of important radiobiological processes in ways that cannot be achieved using conventional "broad-field" irradiation[1-3].

Heavy ions transfer their energy to biological organisms through high-density ionization and excitation of molecules and atoms along the particle trajectories. Populations of cells exposed to very low doses of high-LET heavy ions contains a few cells which have been hit by a particle, while the majority of the cells receive no radiation damage. At somewhat higher doses, a few cells receive two or more events according to the *Poisson* distribution of ion injections. Using microbeams, we will be able to overcome this limitation by delivering an exactly counted number of ions to each cell.

A microbeam can be used for selective irradiation of individual cells, which can be subsequently observed to ascertain what changes have occurred to that cell and to neighboring un-irradiated cells. The use of microbeam allows direct investigation of cell-to-cell communications such as "bystander effects", that is, radiation effects of heavy ions transmitted from irradiated cells to neighboring un-irradiated cells.

Furthermore, a microbeam with sufficient resolution will be useful for analyzing cellular spatial sensitivity, the interaction of damages produced by separate events, the dynamics of cellular repair, and the intra-cellular process such as *apoptosis*; by means of highly localized irradiation of a part of a nucleus or cytoplasm.

Therefore, we have developed a cell irradiation system for targeting cells individually with a precise number of high-LET heavy ions to elucidate radiobiological effects of exactly one particle and to investigate the interaction of damages produced by separate events.

2. Experimental setup

The cell irradiation system was incorporated into the high-energy heavy ion microbeam apparatus[4] which has been installed under a vertical beam line of the AVF cyclotron at the TIARA of JAERI-Takasaki.

Figure 1 shows a schematic diagram of the connections between the off-line microscope control system for cell-finding, the on-line microscope control system for cell-targeting, and the beam shutter control system for

delivery of counted heavy ions, 13.0 MeV/u $^{20}Ne^{7+}$ and 11.5 MeV/u $^{40}Ar^{13+}$. Chinese hamster ovary cells (CHO-K1) were attached to the cell dish, the bottom of which was made of 100 μm thick ion track detector Harzlas TNF-1 (modified CR-39). Positional data of the individual cells were obtained by microscopically searching at the off-line microscope in the preparation room before irradiation.

A local-area-network connects the *On-line Local* PC, the *On-line Remote* PC, and the *Off-line* PC, allowing the object database created by the *Off-line* PC to be used by the cell-targeting system at other PCs.

3. Irradiation procedure

Just before irradiation, the medium was removed to make ions penetrate the cells and the bottom of cell dish. Then the sample holder was transported from the off-line microscope to the on-line microscope in the beam room.

Using the object database, targeting and irradiation at the on-line microscope were carried out quickly. However, the positioning accuracy was not sufficient for automatic targeting of mammalian cells. Therefore, the cells, once targeted according to the object database, needed to be observed at the on-line microscope, and to be re-targeted remotely from the *On-line Remote* PC console. To obtain phase-contrast image of CHO-K1 cells for adjustment of the targeting, a ring-light was newly attached around the microaperture, from which the collimated ions were extracted.

Then the object lens was replaced with a plastic scintillator coupled to a photomultiplier tube (PMT) assembly mounted on the on-line microscope turret. The collimated ions were detected with the PMT assembly after passing through a target cell and the bottom of the cell dish, that is 100 μm thick ion track detector Harzlas TNF-1. The energy spectrums of collimated ions were measured with a multi-channel analyzer by analyzing scintillation light pulses. The number of ions having traversed the sample was counted with a constant fraction discriminator coupled to a preset counter/timer. Every irradiation was terminated by the action of beam shutter, which was controlled by the preset counter/timer module or manually. Recently, a P-chopper in the injection system of the cyclotron has also been used as a fast beam switch.

4. Detection of ion tracks at irradiation time

Immediately after irradiation, the cell dish was refilled with medium, and then the bottom was etched from the opposite side of the cells with alkaline-ethanol solution at 37°C for 15 minutes. After a rinse with distilled water, the bottom of the cell dish was observed microscopically for evaluation of the targeting accuracy. The almost all ion track pits were concentrated within the collimated diameter range. The cells were then incubated at 37°C continuously to check the effect of etching treatment on the cell growth. No significant effect of the etching treatment on the cell growth was observed.

5. Conclusion

Detection of the ion tracks provides us with accurate information about the spatial distribution of irradiated ions just after irradiation time. By this method, we can observe the number of ion hits and their positions on and around the target cells at the beginning of the post-irradiation incubation of the cell samples. This method will be quite useful because the accuracy of irradiation

information is important to study low dose effect, especially the effects of exactly one particle.

It is known that an average of about 2-5 α-particle traversals is required to kill a cell. Does single hit of high-LET heavy ions in a nucleus really kill the entire cell? This question will soon be answered.

References

1) C. R. Geard, D. J. Brenner, G. Randers-Pehrson, and S. A. Marino, *Nucl. Instr. and Meth.* **B54**, 411-416 (1991)
2) L. A. Braby, *Scanning Microscopy*, **6**, 167-175 (1992)
3) M. Folkard, B. Vonjnovic, K. M. Prise, A. G. Bowey, R. J. Locke, G. Schettino, and B. D. Michael, *Int. J. Radiat. Biol.* **72**, 375-385 (1997)
4) Y. Kobayashi, H. Watanabe, M. Taguchi, S. Yamasaki and K. Kiguchi, "MICRODOSIMETRY An Interdisciplinary Approach", Proceedings of the 12th Symposium on Microdosimetry, Oxford, 1996; D. T. Goodhead and P. O'Neill, Eds., pp. 343-346, The Royal Society of Chemistry, Cambridge (1997)

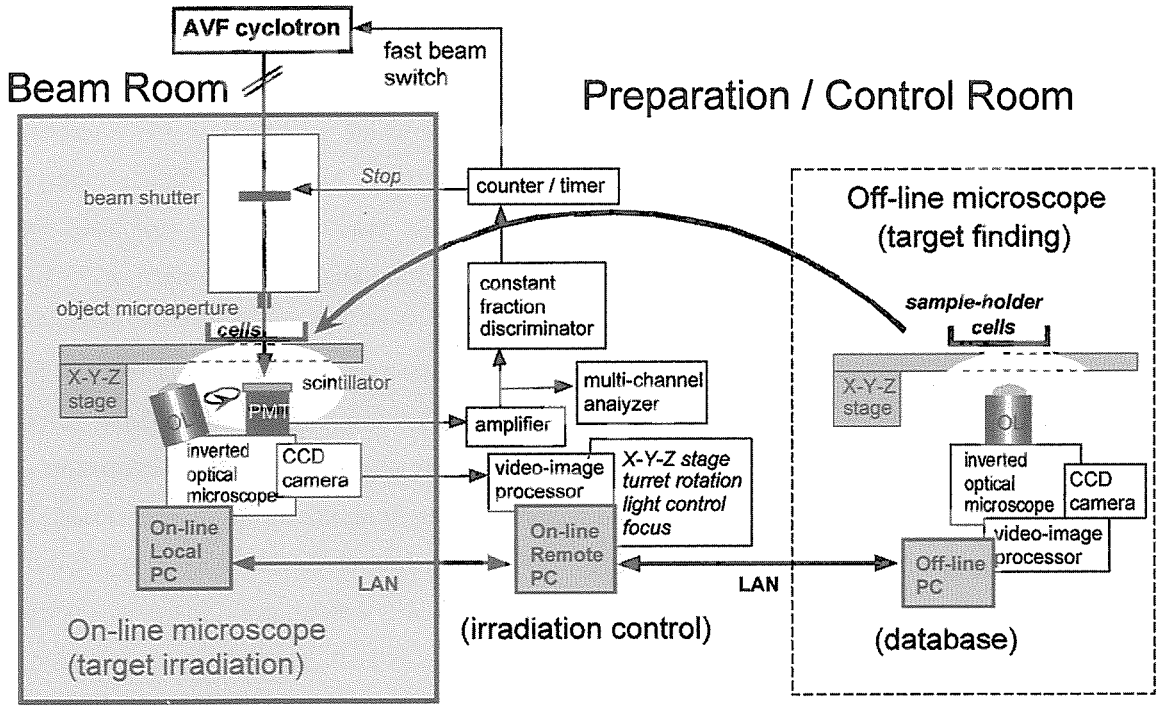


Figure 1. Schematic diagram of the connections between the microscope control system for target finding and the beam shutter control system for delivery of counted heavy ions. Before irradiation at the beam room, positional data of the individual cells were obtained at the Off-line microscope in the preparation/control room by microscopically searching on the sample dish, the bottom of which was made of 100 μm thick ion track detector Harzlas TNF-1.

2.19 Effects of Locally Targeted Heavy Ions to The Zygotic Nuclei During Early Development of The Silkworm, *Bombyx mori*

K. Kiguchi[1)], H. Tamura[1)], R. Harata[1)], K. Shirai[1)], R. Kanekatsu[1)], Y.Kobayashi[2)] and H. Watanabe[2)]

[1)] Faculty of Textile Science and Technology, Shinshu University

[2)] Department of Radiation Research for Environment and Resources, JAERI

1. Introduction

To develop a better risk evaluation system of cosmic radiation in spaceflight environment, it is essential to derive an understanding of the biological effects of low-fluence high-energy heavy particles. In JAERI-Takasaki, a novel heavy ion microbeam system has been installed under the vertical beam line of an AVF cyclotron. This made it possible to target and irradiate the desired region of small biological samples. Using this system, we have been studying the effects of heavy ions on the embryonic development in the silkworm, *Bombyx mori* (Kiguchi *et al.*, 1997, 1998, 1999, 2000). In this report we describe the effect of irradiation targeted to zygotic nucleus or nuclei during early development.

2. Materials and Methods

Eggs of the *pnd* mutant strain of the silkwrom, *Bombyx mori*, were used as experimental animal. The eggs were subjected to carbon or neon ions ($^{12}C^{5+}$, 18.3 MeV/u, range in water = 1.2mm; $^{20}Ne^{8+}$, 17.5 MeV/u, range = 0.7 mm) through various size apertures during the early development. After irradiation, eggs were kept at 25℃ and fixed for 2 hrs in Carnoy's fixative at desired stages. The embryos were then stained with 0.01 % toluidine-blue, and observed by means of a light microscope connected to a CCD camera. Some of eggs were allowed to develop, and the morphology of the resultant embryos was examined carefully under a dissecting microscope.

3. Results and Discussion

1) Local irradiation to the zygotic nucleus at fertilization stage

Fertilization occurs about 2 hrs after oviposition at 25 ℃. Zygotic nucleus was aimed to irradiate with carbon ion microbeams (150 μ m ϕ , 500 Gy). Since embryonic development was completely inhibited when eggs were irradiated at the position of 55 % egg width and 90 % egg length (55/90) as shown in Fig.1, position of irradiation was fixed at 55/90 in the following experiments. Dose response experiments showed that 50 % inhibition dose for hatching is about 10 Gy. Lower doses [1 Gy and 0.1 Gy (about 10 ions/150 μmϕ)] did not affect their hatching. However, survival percentages at each larval molting, pupation and adult emergence were significantly lower than the non-irradiated control (Fig. 2), indicating that the irradiation to the zygotic nucleus shortly after fertilization has some delayed effects which appear during the post-embryonic development. These results suggest that the fertilization stage is the most critical stage for exposure to low-fluence high-energy particles.

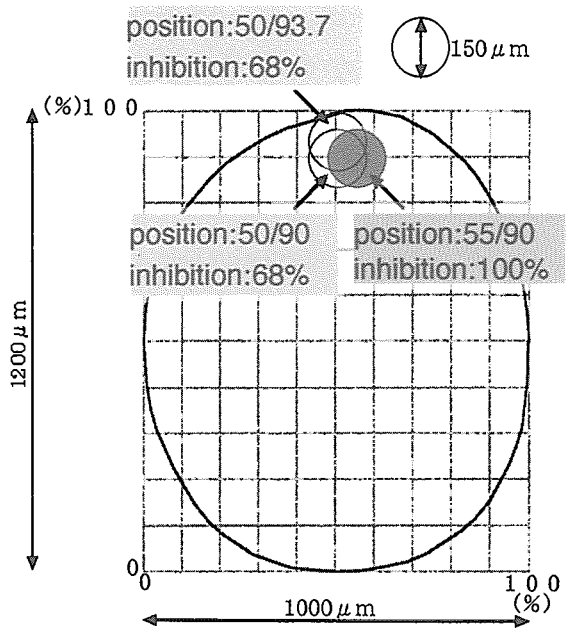


Fig.1 Locally targeted irradiation of carbon ion microbeams (150 μm φ, 500Gy) to the zygotic nucleus at the fertilization stage.

It was shown that embryogenesis is completely inhibited in the egg irradiated at the position of 55 % egg width and 90 % of egg length.

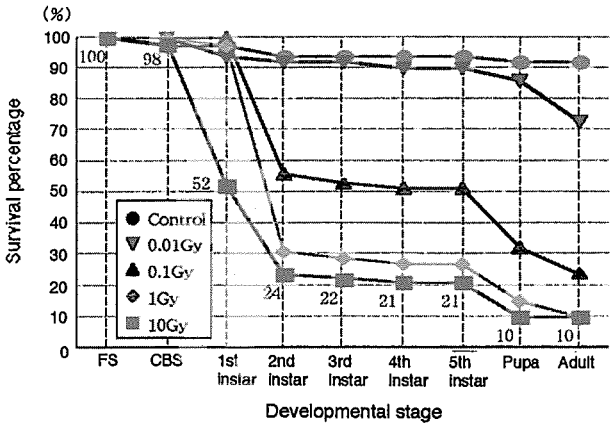


Fig.2 Effects of locally targeted irradiation of carbon ion beams(150 μm φ) to the zygotic nucleus on the embryonic and post-embryonic devepoment in the silkworm, *Bomby mori*.

Irradiated position : 55/90

No. of eggs used : 50-60

FS: fertilization stage

CBS: cellular blastderm stage

2) Local irradiation at the intralecithal cleavage stage

After fertilization, cleavage proceeds through a succession of synchronous mitotic divisions of the zygotic nucleus and its daughter nuclei. The cleavage energids (nuclei and their associated cytoplasm) form an elliptical assemblage (Fig. 3). Eggs of this intralecithal cleavage stage (8 hrs after oviposition) were irradiated with neon ion microbeams (250 μm φ, 500Gy) at the position of 15/65, 50/40 and 50/90, 85/65 (Fig.3). As shown in Fig. 4, abnormal morphology was induced at high frequency only when the ventral side of the

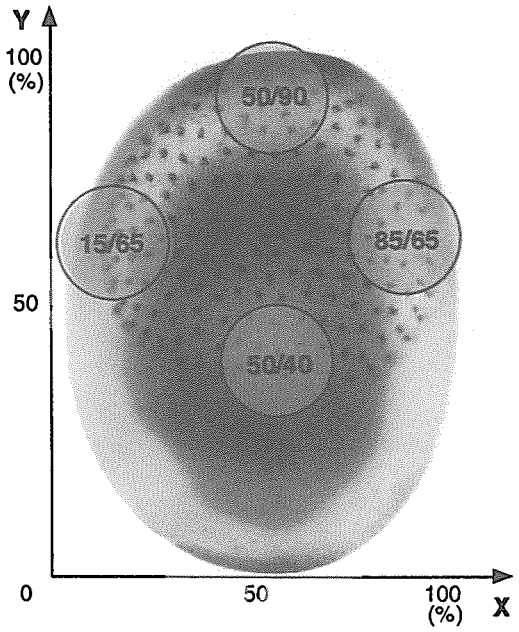


Fig.3 Positions of irradiation at intraleicithal cleavage stage (8 hrs after oviposition)

X: egg width

Y: egg length

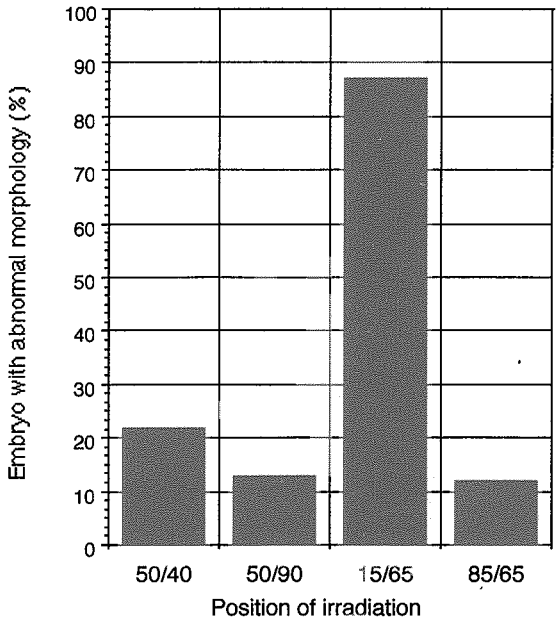


Fig. 4 Effect of local irradiation at intralecithal cleavage stage
Neon ion microbeams (250 μ m ϕ, 500Gy) were irradiated at each indicated position.

assemblage was (15/65) irradiated, but most of eggs irradiated at the other positions hatched normally and became larvae with normal morphology. To answer the question why the effects were different depending on the irradiated position, morphology and fate of the irradiated nuclei were examined. The results indicated that the irradiated nuclei stop their cleavage and hypertrophy, and that the resultant enlarged nuclei move out to the extra-embryonic regions (anterior, dorsal and posterior periplasm). On the other hand, when irradiated at the position of 15/65, a mass of the enlarged nuclei reached to the embryonic region (ventral periplasm). From these results, it is considered that local irradiation to dividing nuclei during intralecithal cleavage stage would have little effect in case affected nuclei move out to the extra-embryonic region.

4. References

1) K.Kiguchi, S.Yamasaki, Y.Kobayashi and H.Watanabe, JAERI-Review, 97-015,45-47(1997)

2) K.Kiguchi, S.Yamasaki, Z.L.Tu, Y.Kinjoh, Y.Kobayashi and H.Watanabe, JAERI-Review, 98-016, 38-40(1998)

3) K.Kiguchi, T.Shima, Y.Kinjoh, Z.L.Tu, S.Yamasaki, Y.Kobayashi, M.Taguchi, H.Watanabe, JAERI-Review, 99-025, 53-55(1999)

4) K.Kiguchi, Y.Kinjoh, K.Masahashi, Z.T.Tu, H.Tamura, K.Shirai, K.Kanekatsu, Y.Kobayashi, M.Taguchi and H.Watanabe, JAERI-Review, 2000-024, 51-53(2000)

2.20 Ion beam mutagenesis in a model legume *Lotus japonicus*

Kumiko Tateno, Masayoshi Kawaguchi*, Yuichiro Watanabe*,
Naoya Shikazono**, Atsushi Tanaka**, Tatsuya Haga, Kinichiro Miura

Institute for Biomolecular Science, Gakushuin University. *Department of Life Sciences, Graduate School of Arts and Sciences, University of Tokyo. **Department of Radiation Research for Environment and Resources, JAERI.

1. Introduction

Leguminosae is one of the largest families in angiosperms. The family exhibits a remarkable biodiversity which includes many of the agronoically significant crop species. Furthermore most of leguminous plants have an ability of symbiotic nitrogen fixation in response to rhizobia. In order to understand the biodiversity and the biological interactions at a molecular level, *Lotus japonicus* has been selected as a model system [1]. In a couple of years the infrastructure such as a large-scale EST analysis [2], genome analysis [3] and construction of high-linkage map has started in *L. japonicus*. Paralell to the infrastructure, generation of a large-scale mutant seed pool would significantly facilitate molecular genetic analysis in legumes. Prior to a large-scale mutagenesis, it would be of imporance to evaluate which kinds of mutagenesis work on *L. japonicus* systemically. In this report we compared the frequency in emergence of symbiotic mutants isolated by ion beam mutagenesis with that by EMS mutagenesis which we have conducted [4, 5, Kawaguchi et al. in submssion].

2. Materials and Methods

2.1. Plant material

An early flowering accession of *L. japonicus* 'Miyaojima' MG-20 [6] was used for ion beam mutagenesis. M1 seeds were sown on Power Soil (Kanto Hiryo Kogyo, Japan) in a biotron LH-300 (Nippon Medical & Chemical Instruments, Japan). Plants were grown under the 18 h/ 6 h day/night cycle, a light intensity of 150 $\mu Esec^{-1}m^{-2}$, at 25 °C, 70-90% humidity condition. Fifty to 500 M1 plants were bulked to obtain M2 seeds.

2.2. Irradiation by carbon and helium ions

Dry seeds of 'Miyakojima' MG-20 covered with a Kapton film were irradiated with various doses of C^{5+} (50 to 300 Gy at the intervals of 50 Gy) and He^{2+} ions (100 to 600 Gy at intervals of 100 Gy). The energy of carbon and helium ions was 220 MeV and 50 MeV, respectively.

2.3. Genetic analysis

Mutants with stable phenotypes were crossed with *L. japonicus* 'Miyakojima' MG-20 or a different species *L. burttii* B-303. F2 seedlings were grown in a nitrogen-free B & D media containing a true symbiont of *L. japonicus*, *Mesorhizobium loti* 303099. The nodulating phenotype was evaluated one month after inoculation. Allelism tests were done between a hypernodulating mutant isolated from F2 population mutagenized by irradiation of helium ions and another hypernodulating mutant *Ljsym78* which had been isolated by EMS mutagenesis.

3. Results and Discussions

M2 seeds were bulked from 50 - 500 M1 plants. No M2 seeds were obtained from M1 plants mutagenized with 500 Gy and 600 Gy helium ions. Unfortunately due to a careless mistake, we failed to draw a survival curve using seeds irradiated by a various doses of ion beam. Therefore we evaluated the emergence of symbiotic mutants in M2 population. Nodulation phenotype was evaluated from 4,884 M2 seedlings (200 Gy of carbon ions), 3,505 seedlings (250 Gy) and 3,352 seedlings (300 Gy), and some of mutant candidates were isolated. However no stable mutants were obtained at M3 generation. In contrast the emergence frequency of symbiotic mutants is approximately one-to-thousand ratio with respect with EMS mutagenesis (kawaguchi et al in submission). The genome mutation derived from this kind of carbon ion appeared to be very weak in *L. japonicus*.

On the other hand, we succeeded to isolate one hypernodulating mutant from 345 M2 seedlings irradiated by 300 Gy dose of helium ions. The hypernodulating mutant (tentatively named LjHe300-1) exhibited pleiotropic phenotypes shown in Figure 1. In addition to dramatically enhanced nodulation on the root (Fig. 1C), an increased number of flowers were observed at the top of peduncle (Fig. 1A). Flowering time was much later than that of wild type (data not shown). Noteworthy is the leaflet of LjHe300-1 plant (Fig. 1B). In general leaf veins develop near the bottom of leaflets. However the veins of the mutant plant develop near a leaflet surface, and consequently the back of the leaflets appeared to emerge on the surface in the LjHe300-1 mutant. These pleiotropic traits were cosegregated stably to M3 generation with hypernodulating phenotype. Backcrosses with *L. japonicus* 'Miyakojima ' MG-20 or *L. burttii* allowed us to know that the mutant phenotypes were inherited in a recessive manner. Then we crossed LjHe300-1 with a hyernodulating mutant *Ljsym78* derived from EMS mutagenesis. The hypernodulating phenotype was clearly complemented in F1 seedling, indicating that LjHe300-1 defines a new locus.

As far as we examined, helium ion beam mutagenesis seemed to be effective in *L. japonicus* to some extent. However the effects of ion beam irradiation and the genome structure of the mutants including LjHe300-1 remains mysterious and unclear. For example it is rather difficult to think that the highly pleiotropic traits of LjHe300-1 are regulated by only single gene. Because there are few molecular data on the ion beam mutagenesis, it would be of value to accumulate the molecular information in *L. japonicus*. A large-scale mutagenesis and subsequent generation of a large mutant pool should be avoided at present.

Reference

[1] K.Handberg and J. Stougaard, Plant J., 2, 487, 1992.
[2] E.Asamizu et al., DNA Res., 7, 127, 2000.
[3] D. Cyranoski, Nature 409, 272, 2001.
[4] H.Imaizumi-Anraku et al., Plant Cell Physiol., 38, 871, 1997.
[5] MZ. Solaiman et al., J. Plant Res. 113, 443, 2000.
[6] M. Kawaguchi, J. Plant Res., 113, 497, 2000.

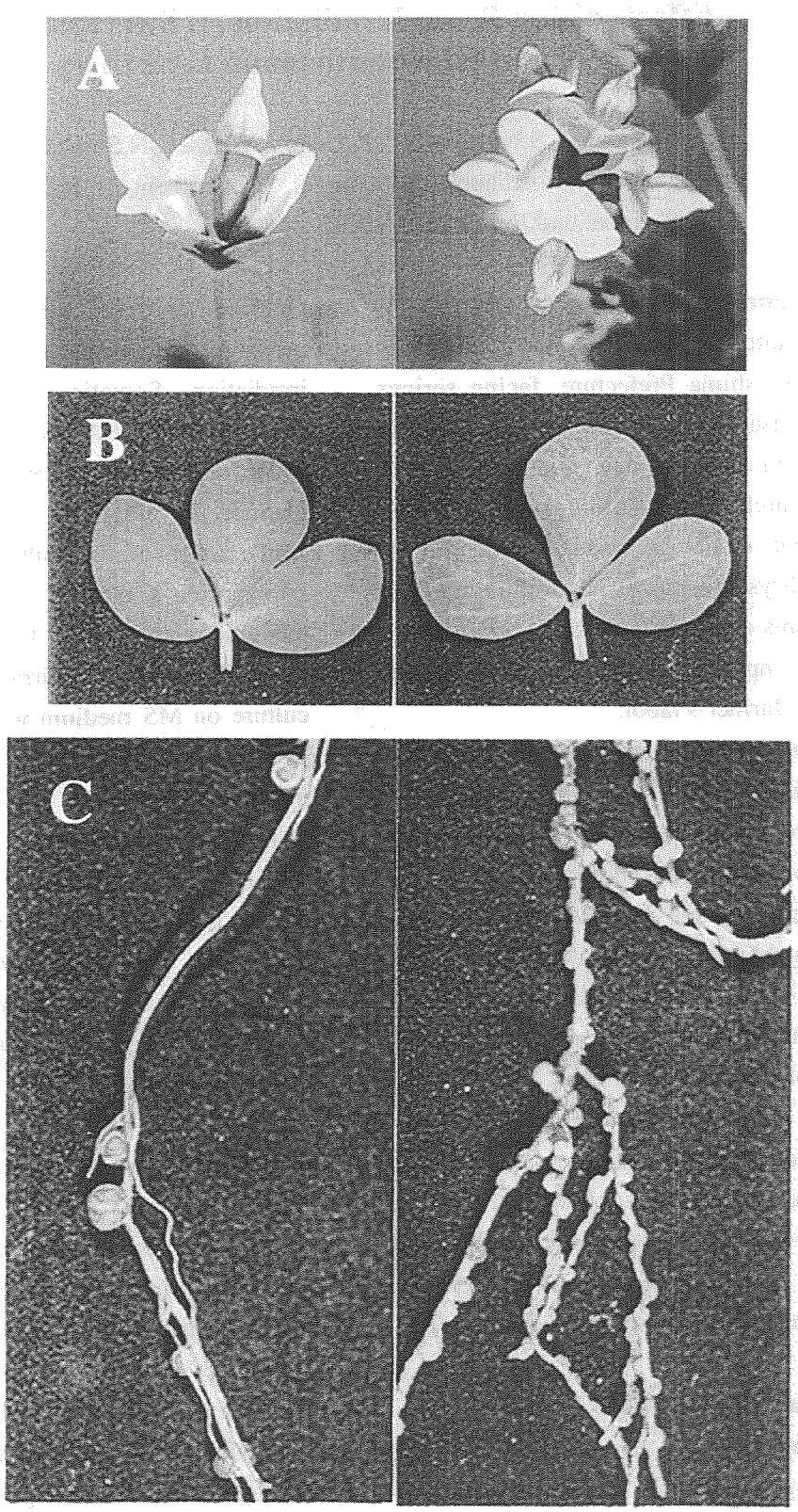


Figure 1. Phenotypes of LjHe300-1 mutant. A, Papilionaceous flowers; B, Compound leaves; C, Nodules induced by the infection of *M. loti* 303099. Wild type (left), LjHe300-1(right).

2.21 Effects of Ion Beam Irradiation on Sweetpotato Callus and Chrysanthemum Leaf Discs

K.Shimonishi[1)], S.Nagayoshi[1)], K.Ueno[1)], Y.Hase[2)], N.Shikazono[2)] and A.Tanaka[2)]
[1)]Kagoshima Biotechnology Institute, [2)]Department of Radiation Research for Environment and Resources, JAERI

1. Introduction

Sweetpotato is one of the most important crops in Kagoshima Prefecture, facing serious situations caused by increasing imports of cheap starch, which require new type variety of different starch composition such as high amylose that could be used for degradable plastics. Chrysanthemums are important cut flowers in this area and have some agronomical traits to be improved such as reducing axillary buds to save farmer's labor.

Mutation breeding is suitable for minor improvement of existing varieties especially for heterogeneous crops of high polyploidy such as sweetpotato and chrysanthemum, remaining most of their original characteristics. Now, ion beams, available at TIARA, have high LET and high RBE compared to traditional radiations. Therefore, they are considered to be the most suitable tool for their advantages above and are expected as a promising new mutagen.

The objectives of our research are to develop effective method for mutation with these crops using ion beams and to obtain needed variants. In this paper, we describe effects of ion beam irradiation on cultures of these crops.

2. Materials and Methods

1) Plant materials

Embryogenic callus of sweetpotato (cv. *Koukei-14* and other three cultivars) was induced from meristematic tissue and was subcultured on MS medium[1)] with 1 mg/L picloram or 0.05 mg/L 2,4-D. Callus was prepared around ϕ1-2 mm in size prior to irradiation. Somatic embryos were induced using 4 mg/L ABA and 1 mg/L GA_3 followed by transfer to MS hormone free medium for plantlet development. Chrysanthemum (cv. *Jimba* and two other cultivars) leaves were cut into approx. 4 mm × 2 mm and cultured on MS medium with 5 mg/L IAA and 1 mg/L BA prior to 3-6 days of irradiation, followed by culture on MS medium with 0.01 mg/L NAA and 0.05 mg/L BA for adventitious shoot development.

2) Ion beam irradiation

Callus and leaf discs were irradiated with helium (50 MeV / 100 MeV) ions and carbon (220 MeV / 320 MeV) ions accelerated by AVF cyclotron at JAERI at doses of 20-1000 Gy for sweetpotato and 1-10 Gy for chrysanthemum.

3. Results and discussions

1) Sweetpotato

The dose response of sweetpotato callus has not been yet clear especially with 220 MeV C ions which reach just 1.1mm depth. Fig.1 shows influence of 50 MeV He ions on callus growth of two cultivars, suggesting low dose (possibly lower than 100 Gy) could be suppressive. Although influence on regeneration from callus is also unclear, regeneration frequency and developing stage were both tended to be repressed as dose increased in case of

Koukei-14 (Table 1).

So far, plantlets were regenerated from the callus irradiated with 220 MeV C and 50 MeV He ion particles, even irradiated with C ions at high as 200 Gy. Some plantlets showed morphological abnormality with vitrificated narrow leaves, which are sometimes seen via simple embryogenesis without any artificial mutation treatments. Plantlets obtained from high dose of 220 MeV C could be derived from unaffected part of callus because of thickness of the specimen, although lethal damages were not visible on the callus surface just after the irradiation. Further studies to clear the dose response are needed.

2) Chrysanthemum

Chrysanthemum, especially "*Jimba*", was supposed to be sensitive to radiation from data of X-ray irradiation, therefore, specimens were irradiated at up to 10 Gy of He ions. *Jimba* has high ability to produce adventitious shoots: around 400 per an initial ϕ6 cm Petri dish. Irrradiration by 50 MeV He ions suppressed adventitious shoot induction at 3 Gy or higher dose, and 100 MeV He ions did not seem to have affected at 5 Gy (Table 2). However, elongation of adventitious shoot was suppressed at 5 Gy. An interesting result was an effect of preculture period prior to irradiation. Both the number of adventitious shoot induction and development was higher when precultured 6 days, suggesting developing stage of culture could affect regeneration frequency from irradiated tissue in chrysanthemum.

Regenerated plants, which were acclimated and transplanted in a greenhouse, flowered ten months after irradiation. Analysis and selection of these variants is needed as well as further investigation into effects of carbon ion irradiation.

Refferences

1) T. Murashige and F. Skoog, *Physiologia Plantarum* 15 (1962), 473-497.

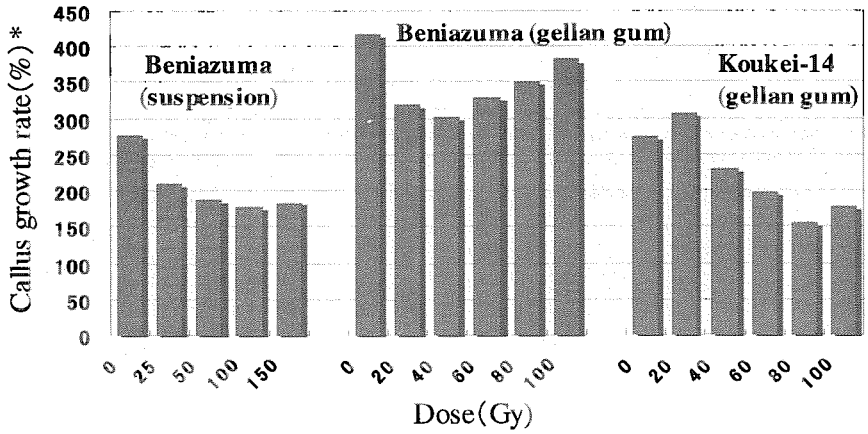


Fig. 1 Influence of 50MeV-He ion beam irradiation to callus growth of sweetpotato.

* Callus growth rate : Fresh weight of 4 weeks after irradiation/ Fresh weight of just after irradiation.

Table 1. Regeneration from callus irradiated by 50 MeV-He ions in sweetpotato.

Cultivar	Dose (Gy)	Regeneration indicators	
		Frequency [y]	Developing stage [z]
Beni-azuma	20	0.0	0.0
	40	1.5	1.5
	60	2.0	2.5
	80	0.5	1.0
	100	0.5	0.5
Koukei-14	25	2.5	1.5
	50	1.0	1.0
	100	0.5	0.5
	150	0.0	0.0
	200	0.0	0.0

y) Classified to five levels by ratio of regenerating (pro-embryo or later) area: 0 (none) - 4 (all)

z) Classified to five levels of developing stage: 0 (staying calllus) - 4 (development of somatic embryos)

Table 2. Adventitious shoot (AS) formation from leaf discs irradiated by helium ion beams in chrysanthemum cv. Jimba

50 MeV-He ions			100 MeV-He ions				
Dose (Gy)	AS Formation		Dose (Gy)	Preculture period (day)	AS Formation		
	Frequency (%)	# Shoots induced			Frequency (%)	# Shoots induced [y]	# Shoots developed [z]
1	84.3	16.8	0	6	100	206	30
2	31.7	7.2	1	6	100	146	43
3	51.8	10.0	2	6	99	164	39
5	15.0	3.0	5	6	95	168	19
10	7.1	1.4	2	3	90	82	14
			10	3	89	70	5

y) Number of visible shoot primordia induced. Numbers are per one Petri dish with 20 leaf discs.

z) Number of shoots developed or elongated. Numbers are per one Petri dish with 20 leaf discs.

2.22 Effects of Helium Ions and Gamma Rays Irradiation of Sexual Plant Reproductive Stages on Seed Production and Postembryonic Leaf Development in *Brassica napus* L.

H.Minami,N.Sakurai*,N.Shikazono**,A.Tanaka**and H.Watanabe**

Ohsima Horticultural Research Center, Tokyo Metropolitan Agricultural Station; *Radiation Laboratory, Tokyo Metropolitan Industrial Technology Institute; **Department of Radiation Research for Environment and Resources, JAERI

1.Introduction

The effects of gamma rays on whole plants in sexual reproductive stages have been intensively examined in plant mutation breeding. It is especially important in mutation breeding to increase mutation ratio. The ratio varies in life stages in which plant was irradiated. It is well known that reproductive organs ranging from differentiation to development and immature embryo during embryogenesis are more radiosensitive than the other organs[1].

Lardon *et al*[2]. made the flower culture method for developing an isolated whole flower (a flower with a pedicel) of *Brassica napus* into a mature pod within 50 days after pollination. The embryogenesis in sexual reproductive stages proceeds synchronously.

The purpose of this study is to investigate the effects of ion beams in sexual reproductive stages on embryogenesis and postembryogenic plant development of *B. napus* through flower culture method. In this paper, we report the effects of helium ions and gamma rays of the flowers ranging from the stage just before pollination to in torpedo embryo on seed production or postembryonic leaf development of *B. napus*.

2.Materials and Methods

2.1 Plant

B. napus cv. Lisandra were grown at 15/10℃ under natural daylight. Flowers of the terminal racemes were used and cultured through flower culture method. Whole flowers, which were unpollinated on the morning of anthesis during middle flowering period, were collected to be transferred on 1.5 ml tube (eppendorf) in Murashige and Skoog's macro and micro elements medium[3] supplemented with 3 % sucrose pH 5.8 using a procedure modified from that of Lardon *et al*..

2.2 Stages and Irradiation

The fertilization and early embryo stages were observed one day and four days, respectively, after pollination. The early globular and globular embryos were observed five days and six days, respectively, after pollination. The torpedo embryo was observed 10 days after pollination.

Seed production

Whole flowers were irradiated just before pollination at day of anthesis, one

day and four days after pollination at 17, 32, 57 and 87 Gy dose using gamma rays. Mature seeds were counted 50 days after pollination.

Postembryonic leaf development

Whole flowers were irradiated five days after pollination at 30 Gy dose using helium ions (AVF cyclotron) and gamma rays (^{60}Co). Whole flowers were irradiated 10 days after pollination at 30 Gy dose using gamma rays.

Mature seeds were collected 50 days after pollination. Those seeds were cultivated to be observed the first leaves.

3.Results and Discussion

The flowers irradiated at 57 Gy in unpollinated and early embryo stages reduced the numbers of mature seeds to 30% and 20% of that of unpollinated flowers, respectively and at 87 Gy hardly produced the mature seeds(Table 1). On the other hand, the flower irradiated in stage of fertilization began to reduce the number of mature seeds at 17 Gy and dropped the number to 15% of that the unirradiated flower at 32 Gy. The flower hardly produced the mature seeds at 57 and 87 Gy.

It is well known that the major reason for abortion of seed is the failure of development of embryo after successful fertilization. Mericle et al. also reported that the zygote of barley is more radiosensitive for survival ratio than the early embryo. In our experiment, the flower shortly after fertilization of *B.napus* was more radiosensitive for mature seed production than that in early embryo.

The helium ions and gamma rays irradiation of early globular embryos showed some drastic effects on first true leaf development. Those effects were classified into four types: cup-shaped, funnel-shaped, shrunk and the other varied leaves. The types were observed in 40 % of plants developed first true leaf. On the other hand, the irradiation of gamma rays of torpedo embryo had not stronger effects than that of globular embryo, while caused sectors lacking chlorophyll in some first true leaves.

We investigate the effects of ion beams irradiation of further developed embryo on postembryonic development through flower culture of *Brassica napus* in progress.

4. References

1) H. Gaul: Radiation Bot. 4(1964)155-232
2) A. Lardon, A.M. Triboi-Blondel and C. Dumas: Sexual Plant Reproduction 6(1993) 52-56
3) T. Murashige and F. Skoog: Physiologia Plantarum 15(1962)473-497
4) L.W.Mericle and R.P.Mericle Radiat. Bot 1(1962)195-202

Table 1. Effects of gamma rays on mature seed production of whole flower of *B. napus*

Stages	Dose(Gy)				
	0	17	32	57	87
	Number of matured seeds/pod				
Unpollination	6.0	4.4	4.7	1.2*	0.2*
Fertilization	8.7	5.6*	1.3*	0.1*	0.1*
Early embryo	8.2	5.4	8.4	2.7*	0.3*

* Significantly different from the control at the 5% level (Least Significant Level)

2.23 Development of the pollen transformation system and analysis of apoptosis induction by local damage, using penetration controlled irradiation with ion beams

Y. Hase, A. Sakamoto, S. Wada, S. Kitamura and A. Tanaka
Department of Radiation Research for Environment and Resources, JAERI

There are several gene transfer techniques in plants such as *Agrobacterium*-mediated transformation and direct gene introduction by electroporation. However, the range of applicable plant species is restricted by the host range in the *Agrobacterium*-transfection method, and also plant species that are capable of regeneration from protoplast are limited in the electroporation method. If pollen can be used as a carrier of DNA vector, a large part of these disadvantages could be surmounted. However, no stable method in pollen transformation has been established before.

We have reported that the transient GUS expression was observed at a high frequency (55.1%) when tobacco pollen was incubated in a DNA (pBI221) solution, following ion-beam irradiation of pollen at the penetration depth of 4 μm[1, 2]. Although tobacco pollen has an endogenous GUS-like activity, the GUS expression frequency increased as the concentration of DNA solution increased[1]. Those results suggest that the foreign DNA can be efficiently introduced into the pollen using penetration-controlled irradiation with ion beams. The amount of seeds obtained by the pollination of the DNA-introduced pollen did not decrease significantly[2]. However, any apparent transformant was not found in the screening of more than 10,000 seeds. We mentioned three possible reasons why transformants had not been obtained in our system[3]. One is nucleases released from pollen, the second is the bimembrane structure of the pollen and the last is DNA incorporation frequency into the generative nuclei[3]. In order to examine these problems, we subjected pollen to the Agrobacterium transfection. However, any transformant has not been obtained yet. Recently, it was reported that the target of Arabidopsis *in planta* transformation method is the ovule and is not the pollen[4-6]. In their reports, the GUS expression rate in pollen was zero or extremely low as compared with that in ovules. Furthermore, a transformant was obtained only by genetic crosses using Agrobacterium-treated pistils were used as a recipient of the untreated pollen, but was not obtained in the reciprocal treatment. These results suggest that the pollen transformation can not be achieved only by raising the transient GUS expression frequency and that the nature of pollen, such as bimembrane structure and DNA incorporation capability may be fundamental problems in a pollen transformation system.

In another work, we are developing a experimental system to analyse the local irradiation effect on the apoptosis induction. Actually, apoptosis is induced by the damage on DNA. However, some evidence suggests that damage in cell membrane is also involved in the apoptosis induction. Now we are investigating the frequency of apoptosis induced cells following ion beam irradiation at different penetration depth.

References

1) A. Tanaka et al., *JAERI Rev.* 97-015:21-23(1997).
2) Y. Hase et al., *JAERI Rev.* 98-016:81-83(1998).
3) Y. Hase et al., *JAERI Rev.* 99-025:82-83(1999).
4) Guan-Ning Ye et al., *Plant Journal* 19: 249-257 (1999).
5) C. Desfeux et al., Plant Physiology 123: 895-904 (2000).
6) N. Bechtold et al., Genetics 155: 1875-1887 (2000).

2.24 Utilization of Ion Beam-irradiated Pollen in Plant Breeding

Satoshi Kitamura[1,2], Muratoshi Yamaguchi[1], Masayoshi Inoue[1],
Yoshihiro Hase[2] and Atsushi Tanaka[2]
1. Faculty of Agriculture, Kyoto Prefectural University. 2. Department of Radiation Research for Environment and Resources, JAERI.

Introduction

Pollen is indispensable to sexual reproduction in different plant species. We have been analyzing biological effects of ion beam on the pollen[1, 2, 3]. Previously, we revealed that pollen exposed to ion beam was available for overcoming cross-incompatibility[2]. Furthermore, we found a unique phenomenon, "leaky pollen", which was specific for the ion beam exposure. This ion beam-specific phenomenon seemed to be resulted from physical lesions induced in outer wall of pollen grain[1]. In C ion exposure, the most effective penetration depth for inducing leaky pollen was around 4 μm[4].

We are developing the gene transfer system using the pollen exposed to ion beam.

Materials and Methods

Nicotiana tabacum L. cv. Bright Yellow 4 was used in this experiment. Dry mature pollen was monolayered on a Kapton film or plastic plate. The samples were set in a beam line of 3MV tandem accelerator, where the penetration depth of ion particles could be controlled[4], and exposed to 18 MeV C ion (LET, 800 keV/μm) with the penetration depth of 7.4 μm.

Pollen germination rate was determined on a solid medium containing 20% sucrose, 100 μg/ml boric acid and 0.8% agar.

After exposure, pollen was suspended in a liquid medium (20% sucrose and 100 μg/ml boric acid) and pollinated to the emasculated flowers. Based on seed weight per capsule, seed fertility was determined. Transient GUS assay was performed in the pollen suspended in the liquid medium with pBI221. Separately, pollen was suspended in the liquid medium with pCH (harboring hygromycin resistance gene), and pollinated according to the methods described above. The seeds obtained were allowed to grow in MS medium with 6% sucrose, 0.8% agar and 5 ppm hygromycin. Survival seedlings were subjected to PCR amplification of the hygromycin resistance gene.

Results and Discussion

Pollen germination rate was reduced with the increase of dose, and resulted in about 60% of the control in the 1000 Gy regime. However, up to the 1000 Gy exposure, a significant reduction of seed fertility was not observed.

Transient GUS expression was observed in the pollen grain and pollen tube. GUS expression rate in the exposed was 2~4 times higher than that in the non-exposed. In the 1000 Gy regime, GUS expression rate was about 30%. Considering pollen germination rate and transient GUS expression rate, the 1000 Gy of C ion seemed to be mostly available for the pollen mediation.

Pollen exposed to 1000 Gy of C ion was suspended in the medium with pCH and used

for pollination. Consequently, a number of seeds were obtained. After screening on the medium containing hygromycin, several seedlings were survived. However, after PCR amplification specific for the resistance gene, a corresponding band was not detected in any survival seedlings.

It is known that pollen releases nuclease during the developmental stage[5]. It was reported that the nuclease activity in pollen was removed by replacement of the liquid medium[6] or treatment of chelating reagents such as EDTA[7]. We also found that nuclease activity was strong in mature tobacco pollen, resulting in the degradation of exogenous plasmid DNA suspended in the medium. This degradation was, to a limited extent, weakened by washing with the medium solution. Application of 50 mM EDTA into the medium was mostly effective for suppressing the nuclease activity, but, simultaneously, pollen germination was greatly reduced.

As mentioned above, it is conceivable that exogenous gene can be incorporated into pollen through the opening induced by ion beam exposure. To establish the gene transfer system using the pollen exposed to ion beam, it is necessary to develop another procedure reducing nuclease activity in pollen.

References

(1) Inoue, M., H. Watanabe, A. Tanaka and A. Nakamura (1992) *TIARA Annual Report* 2: 50-52.

(2) Yamashita, T., M. Inoue, H. Watanabe, A. Tanaka and S. Tano (1995) *TIARA Annual Report* 5: 44-46.

(3) Nishimura, H., M. Inoue, A. Tanaka and H. Watanabe (1997) *Can. J. Bot.* 75: 1261-1266.

(4) Tanaka, A., H. Watanabe, S. Shimizu, M. Inoue, M. Kikuchi, Y. Kobayashi and S. Tano (1997) *Nuc. Instr. Meth. Phys. Res.* B129: 42-48.

(5) Vischi, M., and S. Marchetti (1997) *Theor. Appl. Genet.* 95: 185-190.

(6) Matousek, J., and J. Tupy (1983) *Plant Sci. Lett.* 30: 83-89.

(7) Negrutiu, I., E. H. Bors and I. Potrykus (1986) *Biotechnology and Ecology of pollen.* Springer Verlag, pp 65-70.

2.25 Dynamical study on influence of CO_2 enrichment to the transportation of photoassimilates using positron imaging

S. Matsuhashi, S. Watanabe, N. S. Ishioka, C. Mizuniwa, T. Ito and T. Sekine
Department of Radiation Research for Environment and Resources, JAERI

Introduction

Burning of a large amount of fossil fuel by humans after the Industrial Revolution causes markedly increasing of the carbon dioxide (CO_2) concentration in the air, and the present CO_2 concentration is about 350 ppm[1]. In general, it is known that plants increase their photosynthesis rate for a while as a short period response to CO_2 enrichment[2]. This conclusion was deduced from yield measurement. Detailed studies have not been done yet, especially on dynamical aspects on the translocation of photoassimilates from source to sink.

The present paper reports the first positron-imaging measurement using ^{11}C-labeled carbon dioxide ($^{11}CO_2$) on the influence of CO_2 enrichment to behavior of photoassimilates in a broad bean plant. This plant was chosen because of its broad leaves absorbing much $^{11}CO_2$.

Experiment

Seeds of broad bean (*Vicia faba*) were immersed in a water flow until a radicle (enbryonic root) broke through testa (seed coat). The seeds were transplanted from water to a vermiculite bed after germination. After a shoot appeared on the soil, the plant was transplanted to a plastic cultivation pot filled with vermiculite. The beds and pots were kept in an illuminated incubator. A commercial nutrient solution (HYPONeX 8-12-6, HYPONeX Japan Co.) was fed to the plants every week. A broad bean with the 6th under-growing foliage leaf on the plant was selected for the present experiment. For positron imaging measurement, the plant was placed in a chamber conditioned at 350-ppm CO_2. The pair of the 4th foliage leaves were inserted into a quvet for feeding $^{11}CO_2$ which is a clear acrylic box (with dimensions: 12 cm in length x 8 cm in width x 1 cm in depth). The quvet was sealed at the petiole of the 4th foliage leaves with dental filling, and connected to the $^{11}CO_2$ gas circulating system. The CO_2 concentration in the quvet was controlled at 350- or 1000-ppm CO_2 by introducing fresh air or a CO_2 standard gas (air containing 1000-ppm CO_2) at a flow rate of 60 ml/min. The $^{11}CO_2$ gas was supplied to the quvet for 1-2 minutes[3]. Immediately measurments with the positron-emitting tracer imaging system (PETIS) and positron multi-points measurement system (PMPS) were started[4]. After the $^{11}CO_2$ gas was drained from the quvet, fresh air was sent to the box. Three hours later, the CO_2 concentration in the quvet was changed from 350-ppm to 1000-ppm, and kept at the same CO_2 concentration for approximately 2 hours. The next PETIS and PMPS measurements were done by labeling the same leaves with $^{11}CO_2$ gas, followed by supplying a 1000-ppm-CO_2 standard gas until the end of the measurements.

Results and discussion

Figure 1 shows the PETIS images of ^{11}C-labeled photoassimilates from the 4th foliage leaves to the stem through the petiole in a broad bean plant. As seen from Fig.1 (b), the first

outflow of photoassimilates from the leaves at 350-ppm CO_2 was observed 13 minutes after labeling with $^{11}CO_2$. The photoassimilates flowed toward the bottom of the plant. On the other hand, the outflow of photoassimilates from the leaves at 1000-ppm CO_2 was observed 8 minutes after labeling, as seen from Fig. 1. (c), which was 5 minutes faster than that at 350-ppm CO_2. The results suggest that the increase of CO_2 concentration at leaves accelerates the translocation of photoassimilates from the leaves.

Figure 2 shows the time-course change of the amount of ^{11}C-labeled photoassimilates at the stem. The sets of PMPS detectors 1 and 2 were placed between the 2nd and 3rd foliage leaves, and between the 4th and 5th foliage leaves, respectively. At 350-ppm CO_2, the ^{11}C-labeled photoassimilates took approximately 20 minutes to reach the detector 1, while it took more than 70 minutes to the detector 2. The amount of ^{11}C-labeled photoassimilates after 2 hours at the detector 2 was 1/5 of that at the detector 1. At 1000-ppm CO_2, the arrival of photoassimilates at the detector 1 was observed 15 minutes from labeling, which was 5 minutes earlier than that at 350-ppm CO_2.

The results obtained suggest that high concentration of CO_2 in the air not only increases the yield of photoassimilates, but also accelerates the transportation of photoassimilates. Observation of the translocation of ^{11}C-labeled compounds by PETIS gives us possibilities of finding changes on the transportation of photoassimilates in a plant under different CO_2 concentrations.

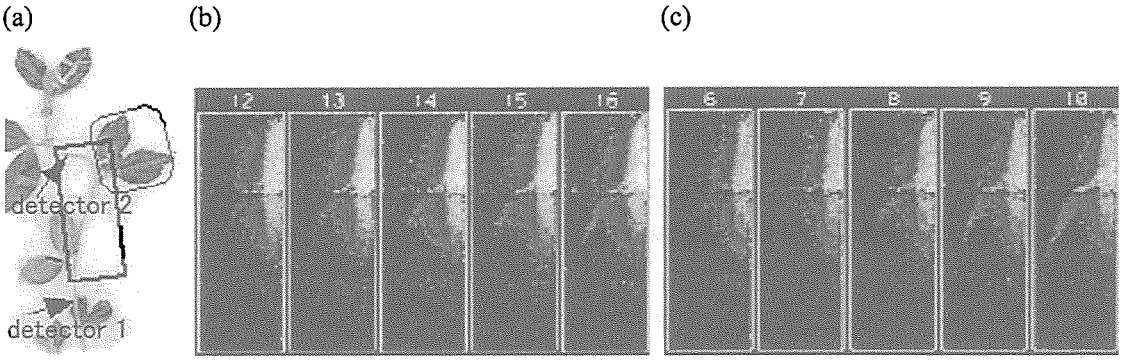


Fig. 1. Visualization of transportation of photoassimilates in a broad bean plant under different CO_2 concentrations of the air. (a) The broad bean plant used for the PETIS and PMPS measurements. The CO_2 concentration was controlled for the 4th foliage leaves as shown by the round square. The field of view of the PETIS is shown by the rectangle. The PMPS-detector positions are shown by the two arrows. (b) Images of translocation of [^{11}C]-photoassimilates from the leaves kept in the air containing 350-ppm CO_2. Among the images accumulated for 1 min each, the 12th to 16th ones after labeling with $^{11}CO_2$ are shown. (c) Same as (b) except for the fact that the leaves were kept in the air containing 1000-ppm CO_2 . The 6th to 10th images are shown.

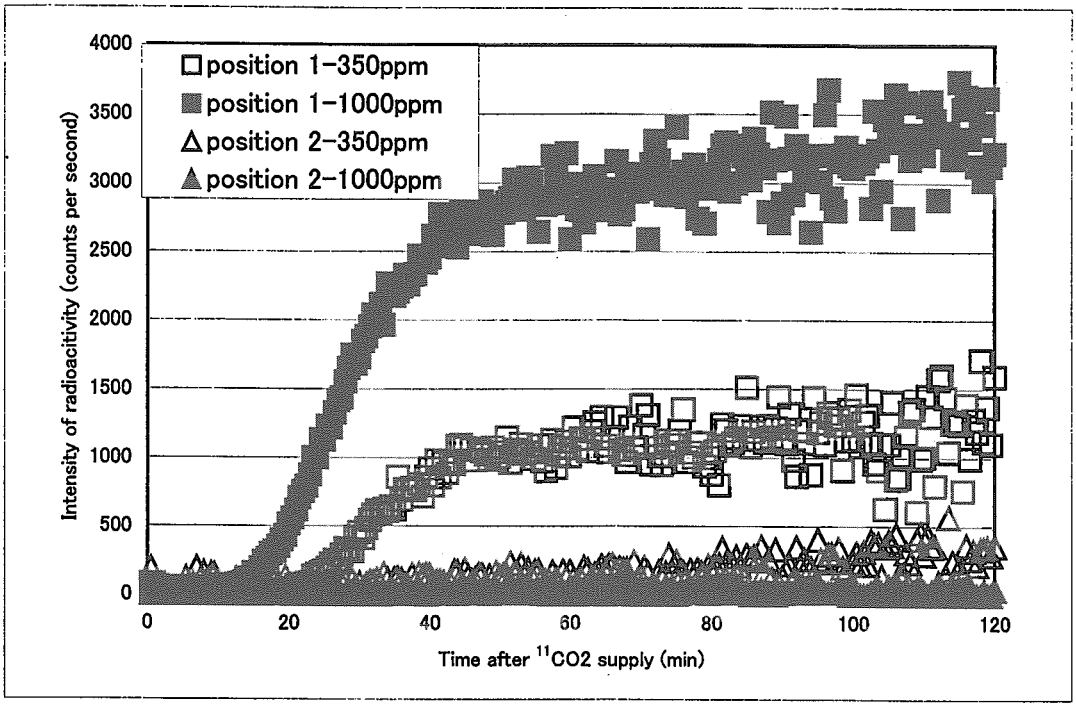


Fig. 2. Time-course study of the translocation of [^{11}C]-photoassimilates from the leaves kept in the air of different CO_2 concentrations. Counts from the PMPS detectors set as shown in Fig. 1 are plotted.

References

1) IPCC Third Assessment Report - Climate Change 2001 A report of Working Group I of the Intergovernmental Panel on Climate Canges, IPCC (2001).

2) A. Makino, Journal of Plant Research, 107 (1994) 79-84.

3) N. S. Ishioka, H. Matsuoka, S. Watanabe, A. Osa, M. Koizumi, T. Kume, S. Matsuhashi, T. Fujimura, A. Tsuji, H. Uchida, T. Sekine, Journal of Radioanalytical and Nuclear Chemistry, 239 (1999) 417-421.

4) H. Uchida, T. Omura, T. Suzuki, A. Tsuji, T. Yamashita, T. Fujimura, S. Matsuhashi, T. Kume, Radiation and Industries, 80 (1998) 6-10.

2.26 Analysis of Nitrogen Absorption and Translocation by Soybean Grown in Different Conditions for Phosphorus Supply

N. Ohtake, T.Ohyama, K. Sueyoshi. T. Kawachi, H. Fujikake, A. Momose, T. Suganuma, A. Osa*, M. Koizumi *, S. Hashimoto**, N.Ishioka*, S. Watanabe*, T Sekine*, S. Matsuhashi**, T. Ito**, C. Mizuniwa**, H.Uchida*** and A. Tsuji***

Faculty of Agriculture, Niigata University, * Department of Material Science, JAERI, ** Department of Radiation Research for Enviroment and Resources, JAERI ,*** Hamamatsu Photonics Co.

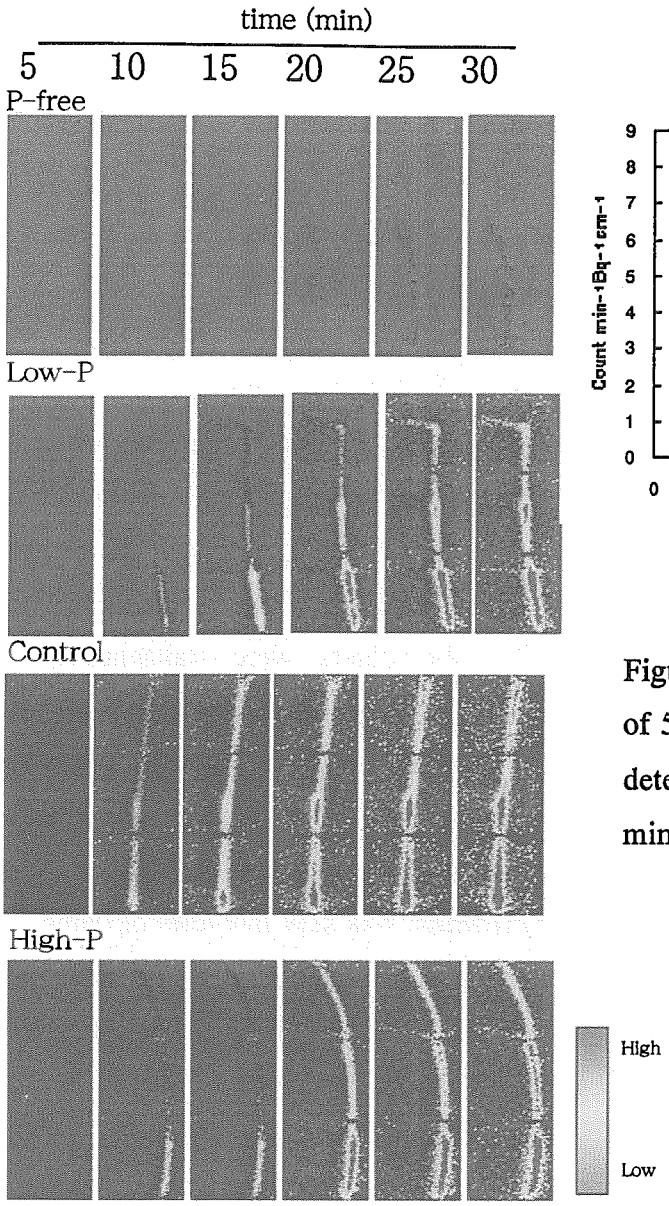
1. Introduction

Because the phosphate is easily absorbed by in soil, especially volcanic ash soils, P fertilizer is important for crop growth together with N fertilizer. Generally, the phosphate requirement of plants is in a relatively narrow range. The phosphorus requirement for optimal growth is in a range of 0.3-0.5% of the plant dry matter during the vegetative stage of growth[1]. On the other hand, the probability of phosphorus toxicity increases at contents higher than 1% in the dry matter[1]. The purpose of this study was to investigate the nitrate absorption, translocation and accumulation by non-nodulating soybean plants grown under different P levels using $^{13}NO_3^-$ or $^{15}NO_3^-$ as tracer.

2. Materials and methods

Non-nodulating soybean seeds (T201) were sown in vermiculite. Ten days after sowing (DAS), the plants were transplanted to culture in a 800mL glass bottle with 600mL of the hydroponics culture solution containing 2mM $NaNO_3$ and grown in a growth chamber (LX-3000, Taitec Co. Japan) which was kept in cycles of being 12 hours light (336 μmol $m^{-2}s^{-1}$) at 28℃, and 12 hours dark at 18 ℃. The chemical composition of the culture solution except for P was as follows (mg l^{-1}): K_2SO_4 (109), KCl (7.854), $CaCl_2 \cdot 5H_2O$ (184), $MgSO_4 \cdot 7H_2O$ (123), H_3BO_4 (0.367), $CuSO_4 \cdot 5H_2O$ (0.032), $MnSO_4$ (0.189), $ZnSO_4 \cdot 7H_2O$ (0.144), $(NH_4)_6Mo_7O_{24}$ (0.004), $NiSO_4 \cdot 6H_2O$ (0.0035), $EDTANa_2$ (14.6), $FeSO_4 \cdot 7H_2O$ (14.9). Four levels of phosphate contents was applied as sodium hydrogen phosphate (adjusted at pH 6.0) at 0 μM (P-free), 10 μM (Low-P), 50 μM (Control) or 250 μM (High-P).

The ^{13}N-tracing experiment was conducted 34 and 35 days after planting.



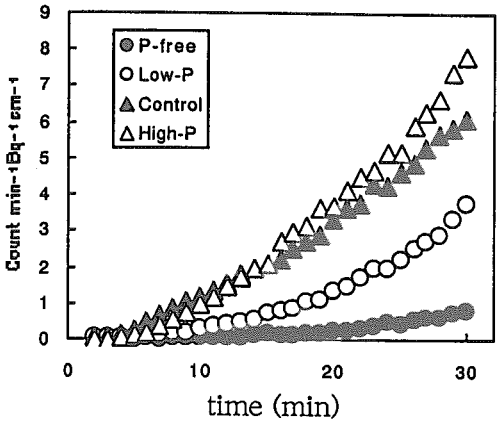


Figure 1 ^{13}N accumulation image integrate of 5 min image and radioactivity per area of detected area. Data were collected for every minute until 30min after $^{13}NO_3^-$ addition.

Each treated plant were transferred to a 50 mL of culture solution with aeration. The nitrate labeled with ^{13}N was added to the culture solution. The radioactivities in the shoot were observed by PETIS. Data were collected for every minute until 30min after $^{13}NO_3^-$ addition. The ^{15}N-tracing experiment was conducted 36 days after planting. The plant was supplied with 2mM $Na^{15}NO_3$ (70.7 atom%) for 60 min and then the root was washed 3 times in deionized water. Plants were frozen with liquid nitrogen and freeze-dried. The ^{15}N abundance in each organ was determined by an emission spectrometry.

3. Results and discussion

Soybean plants grown in P-free and Low-P condition showed P-deficient symptoms such as dark leaf color and long thin root. High-P treated plants showed P-excess

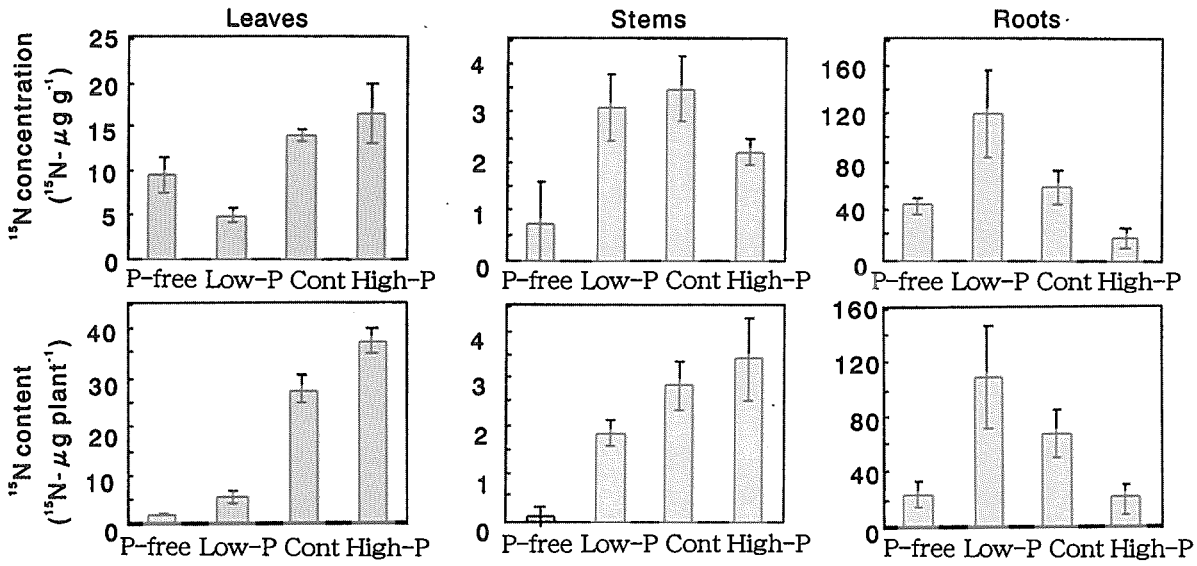


Figure 2 ^{15}N concentration (upper) and content (lower) in each of organs. $Na^{15}NO_3$ was applied during 60 min for the plants (36 days after planting).

symptoms such as spindly growth of shoot.

Images of ^{13}N accumulation in shoot were shown in Figure 1. The plant treated High-P accumulated a relatively higher amount of ^{13}N than control plants and the plant treated Low-P accumulated about half of that by control plants. For the P-free treated plant ^{13}N signals were scarcely detected.

For quantitative analysis, experiments were performed using ^{15}N-labeled nitrate in almost the same way as mentioned above. The ^{15}N concentration and content were found to have the same tendency as the results of ^{13}N experiments. The ^{15}N concentration and content in leaves and stems increased with increasing P supply, while those in roots were decreased with increasing P supply.

These results indicated that the nitrate transport from root to shoot is enhanced by increasing P supply, while the N accumulation of root is decreased. The same tendency was reported regarding total N and P concentrations[2]. The present paper reports the first visualized experiment that showed enhanced N transporting from root to shoot by increasing P supply.

References

1) Marschner H. Mineral nutrition of higher plants. Academic Press, 275-277 (1995)

2) Israel D.W. and Rufty JR. Crop Sci., 954-960 (1988)

2.27 Zinc Translocation Oscillates in a Leaf of Zinc-deficient Rice

H. Nakanishi[1], S. Kiyomiya[1], M. Yoshimura[1], S. Watanabe[2], S. Matsuhashi[2], N. S. Ishioka[2], T. Ito[2], C. Mizuniwa[2], H. Uchida[3], A. Tsuji[3], S. Hashimoto[2], T. Sekine[2] and S. Mori[1]

[1] Department of Applied Biological Chemistry, The University of Tokyo

[2] Department of Radiation Research for Environment and Resources, JAERI

[3] Central Research Laboratory, Hamamatsu Photonics K. K.

1. Introduction

Zinc (Zn) is an essential catalytic component of many enzymes and also plays a critical structural role in many proteins. Despite the importance of Zn as an essential micronutrient for plant growth, relatively few studies have examined the mechanisms and regulation of Zn absorption and translocation by plants. A γ-ray emitting nuclide, ^{65}Zn, is the only available radioactive isotope of Zn and experiments have been done using this isotope in plants, especially Zn movement in developing wheat grains[1]. It has been impossible to conduct time course studies with the same intact plants reproducibly. The use of γ-rays emitted on positron-annihilation has been adopted in plant nutrition research. We have already reported the visualization of real time ^{11}C-methionine movement in barley plants[2), 3)], $^{13}NH_4^+$ and $H_2{}^{15}O$ translocation in rice plants[4), 5)] by a Positron Emitting Tracer Imaging System (PETIS). ^{62}Zn also emits positrons. Here we used ^{62}Zn and visualized the real time ^{62}Zn translocation in rice plants by PETIS.

2. Experimental procedure

2.1 Plant material

Rice (*Oryza sativa* L. cv. Nipponbare) seeds were germinated on paper towels and cultured hydroponically in a growth chamber with a 14-h light (30°C) / 10-h dark (25°C) regime and a photon flux of 320 μmol m^{-2} s^{-1}. For Zn deficiency, plants were transferred to Zn-deficient medium two weeks before beginning experiments. The ^{62}Zn absorption experiments were performed after one month of germination.

2.2 Production of ^{62}Zn

^{62}Zn was produced in the $^{63}Cu(p, 2n)^{62}Zn$ reaction by bombarding a 500 μm thick copper foil with a 30 MeV proton beam from the TIARA AVF cyclotron. Using a beam current of 1 μA for 30 min, about 50 MBq of ^{62}Zn was produced. The radiochemical separation of the ^{62}Zn from the target was carried out with a method described by Bormans et al.[6] For the elution of ^{62}Zn in anion exchange chromatography, 0.005 M HCl was adopted instead of 0.25 M H_2SO_4, because a solution with a low ionic strength must be supplied to plants. The first 5 mL effluent of 0.005 M HCl with a relatively high radioactivity was supplied for succeeding experiments on plants. The chemical form of ^{62}Zn in the final solution was determined as Zn^{2+} from its behavior in anion exchange chromatography.

2.3 Experimental set up for ^{62}Zn translocation in the plant

A single rice plant was supplied with 20 mL of culture solution in a polyethylene bag. The plant and the bag were fixed between two acrylic boards and placed midway between a

pair of PETIS detectors. ^{62}Zn (5~10 MBq, carrier-free in 0.5 mL) was added to the nutrient solution. The data was automatically corrected using 9.186 h as the half-life of ^{62}Zn. Three pairs of positron multi-probe system (PMPS) detectors were used for time-course tracer analysis of ^{62}Zn. The PETIS and PMPS detectors were calibrated as follows: ^{22}Na (1 mm radius, 370 kBq) was put at the center between a paired detectors, radioactivity was counted for 10 min, and the counting efficiency for each detector pairs was evaluated. The values obtained by PETIS and PMPS were calculated using these efficiency values. The maximum value was set to 100.

After a 6 h PETIS analysis, the plant was removed from the polyethylene bag and the roots were gently washed for 1 min in 100 mL of complete culture solution. Then the plants were placed under a Bio-imaging plate (Fuji Film, Tokyo, Japan) inside a cassette. After an appropriate time, the plate was read by an image-analyzing system (BAS-1500, Fuji Film, Tokyo, Japan).

The experiment was repeated at least three times to confirm the reproducibility of the results.

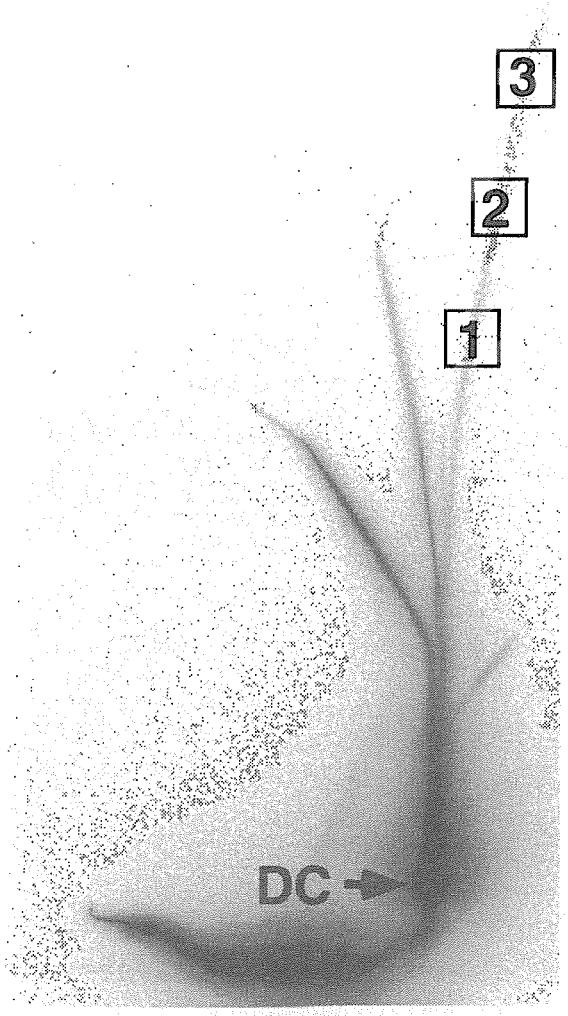


Fig. 1 ^{62}Zn distribution after 6 h absorption experiment in Zn-deficient rice.

3. Results and Discussion

In rice plants, root-supplied ^{62}Zn was translocated to the whole plant parts after 6 h absorption experiment (Fig. 1). The ^{62}Zn absorbed from the root was first trasnlocated and accumulated to the discrimination center[2), 3), 4), 5)] (DC in Fig. 1), and re-translocated from here to other parts of the plant. In Zn-deficient rice, ^{62}Zn radioactivity was detected in the DC about 30 min after the supply of ^{62}Zn (Fig. 2A), and the ^{62}Zn accumulation to the DC after 6 h was about 10 times higher than that in the control plants(data not shown). Three pairs of PMPS detectors were set on the second youngest leaf with 4.7 cm intervals (Fig. 1), and ^{62}Zn signals were measured (Fig. 2B, C). The first arrival of ^{62}Zn to the position 1 was about 60 min after the supply of ^{62}Zn and ^{62}Zn accumulated gradually with time. Interestingly, the amount of existing ^{62}Zn at position 1 oscillated (Fig. 2B). The same wave-like pattern was also obtained at position 2. A more precise observation shows that the cycle of the waves were about 20 min in both position 1 and position 2 (Fig. 2C). The time difference of the waves of position 1 and position 2 was

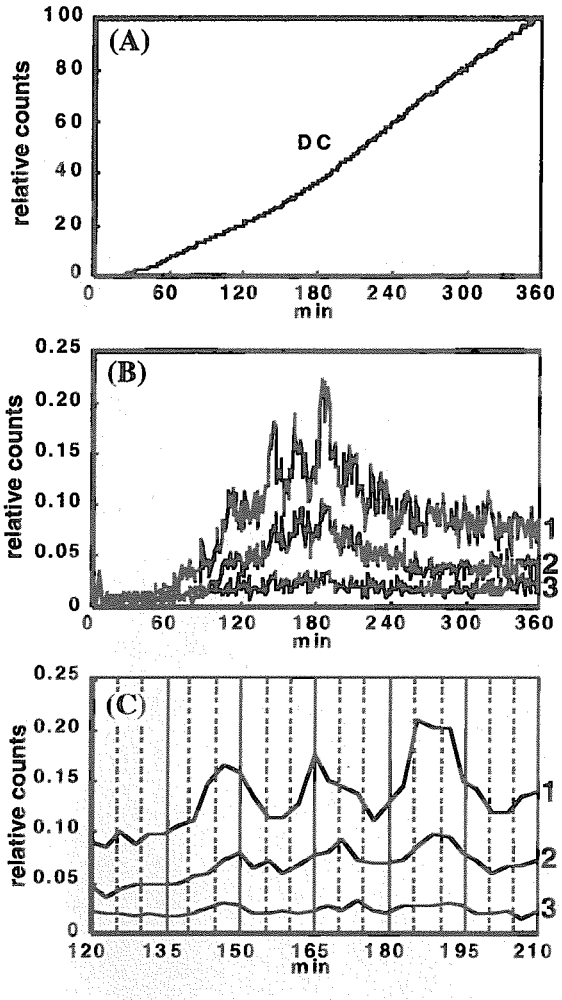


Fig. 2 Time-course study of the translocation of ^{62}Zn into the discrimination center (DC) and leaf. (A) Accumulation of ^{62}Zn at the DC. (B) ^{62}Zn radioactivity curves at the numbered positions in Fig. 1. (C) Precise observation of B from time 120 min to 210 min.

about 5 min. Because the PMPS detectors were set with 4.7 cm intervals, the ^{62}Zn translocation speed from position 1 to position 2 was calculated about 1 cm min^{-1}. At position 3, the amount of ^{62}Zn was very low, but the same pattern was obtained. This wave-like translocation was observed only in Zn-deficient rice plants, but not in control plants. This pattern was not found in the cases of ^{11}C-methionine, $^{13}NH_4^+$, $H_2{}^{15}O$ and ^{52}Mn, and specific for ^{62}Zn. At this moment, we can assign no reason for this phenomenon. We should emphasize again that the DC has a critical role for determination of the distribution of minerals and nutrients. From *Arabidopsis thaliana*, seven Zn transporter genes (*ZIP1~ZIP6*, *ZAT1*) were isolated[7], and some of them were upregulated under Zn-deficiency. Almost the same number of genes are expected to exist in rice, and some of them may be upregulated by Zn-deficiency and participating in the Zn transport at the DC.

References

1) J. N. Pearson, Z. Rengel, C. F. Jenner, R. D. Graham, Australian Journal of Plant Physiology 25 (1998) 139-144.

2) H. Nakanishi, N. Bughio, S. Matsuhashi, N. S. Ishioka, H. Uchida, A. Tsuji, A. Osa, T. Sekine, T. Kume and S. Mori, Journal of Experimental Botany 50 (1999) 637-643.

3) N. Bughio, H. Nakanishi, S. Kiyomiya, S. Matsuhashi, N. S. Ishioka, S. Watanabe, H. Uchida, A. Tsuji, A. Osa, T. Kume, S. Hashimoto, T. Sekine and S. Mori, Planta (2001) in press.

4) S. Kiyomiya, H. Nakanishi, H. Uchida, A. Tsuji, S. Nishiyama, M. Futatsubashi, H. Tsukada, N. S. Ishioka, S. Watanabe, T. Ito, C. Mizuniwa, A. Osa, S. Matsuhashi, S. Hashimoto, T. Sekine and S. Mori, Plant Physiology 125 (2001) 1743-1753.

5) S. Mori, S. Kiyomiya, H. Nakanishi, N. S. Ishioka, S. Watanabe, A. Osa, S. Matsuhashi, S. Hashimoto, T. Sekine, H. Uchida, S. Nishiyama, H. Tsukada and A. Tsuji, Soil Science and Plant Nutrition 46 (2000) 975-979.

6) G. Bormans, A. Janssen, P. Adriaens, D. Crombez, A. Witsenboer, J. De Goeilj, L. Mortelmans and A. Verbruggen, Applied Radiation and Isotopes 43 (1992) 1437.

7) M. L. Guerinot, D. Eide, Current Opinion in Plant Biology 2 (1999) 244-249.

2.28 Effects of environmental stress on ^{11}C distribution in rice plants detected by PETIS detector

H. Hayashi[1], H. Mano[1], N. Suzui[1], S. Matsuhashi[2], C. Mizuniwa[2], T. Ito[2], S. Hashimoto[2], N. Ishioka[2], T. Watanabe[2], T. Sekine[2], A. Osa[3], H. Uchida[4], A. Tsuji[4]

[1]Department of Applied Biological Chemistry, Univ. Tokyo, [2]Department of Radiation Research for Environment and Resources, JAERI, [3]Department of Material Science, JAERI, [4]Central Research Laboratory, Hamamatsu Photonics Co.

1. Introduction

Sieve tubes are the main roots for long distance transport of photoassimilates in plants. This phloem transport process of photoassimilates is highly affected by the surrounding conditions, such as temperature and light condition as this process is an energy dependent process. Sucrose, most important photoassimilate translocating in sieve tubes, is loaded into sieve tubes through cell membrane from apoplast by the energy dependent process, so called phloem loading. Sucrose in the sieve tubes at the site of photosynthesis is unloaded and reloaded along sieve tubes repeatedly, and is finally transported to the sink position.

To know this process deeply, we have established the experiments for detailed analysis of phloem transport, such as speed of translocation by the positron-emitting tracer imaging system (PETIS).

2. Experiments

Rice plants (Oryza sativa L. var. Nipponbare) were grown in a complete nutrient solution. The plants of the 9th-leaf stage were used for the experiments.

Around 135 MBq of $^{11}CO_2$ was applied to the small absorption chamber containing the tip of 7th leaf blade of rice plant for 10 min. Just after the absorption started, the ^{11}C-compounds distribution were detected by PETIS at the leaf sheath position. To detect the effect of temperature, several positions of the leaf sheath which absorbed $^{11}CO_2$ were cooled down to 5 °C by cooling blocks.

3. Results and discussion

The results show that this PETIS provides a convenient system for displaying ^{11}C-compounds movements in plants even though the spatial detection limit is 2 mm and measurement lasting more than 60 minutes may be difficult because of fast decay of ^{11}C.

Figure 1 shows the BAS image of the absorption and translocation of ^{11}C-compounds at the end of experiment. The absorbed ^{11}C-compounds at the leaf blade were transported only to the leaf sheath direction, namely to the leaf sheath, roots and another leaves, not to the tip of the leaf blade. These results suggest that phloem transport is one-way traffic at the leaf blade level.

Detailed images of PETIS are presented in figure 2. The absorbed $^{11}CO_2$ were metabolized at the leaf blade and translocated to the leaf sheath within 17 min (Figure 2-1, Position B). The distance between A and B in the leaf sheath was 5.25 cm and the time delay of ^{11}C-compound arrival was 5.0 minute. From these data, the rate of phloem transport at the leaf sheath of rice plants was calculated as 63 cm/hour. From the data of position B and C, the rate was calculated
as 48 cm/hour. These figures of phloem transport rate are consistent with another examples of phloem transport of other plants, which was evaluated by different methods.

The effects of low temperature on the phloem transport rate were also analyzed by the same PETIS. We tried several times to detect the effects of low temperature. In some experiments, the delay of ^{11}C-compounds arrival was detected (data not shown). However, low temperature (5 °C) did not stop the phloem transport in our experiments.

These data of phloem transport of ^{11}C-compounds measured by PETIS are very useful to discuss the effects of environmental stress on the long distance phloem transports of photoassimilates, specially the rate of transport. In our experiments, the rate of phloem transport was calculated directly based on the data by PETIS.

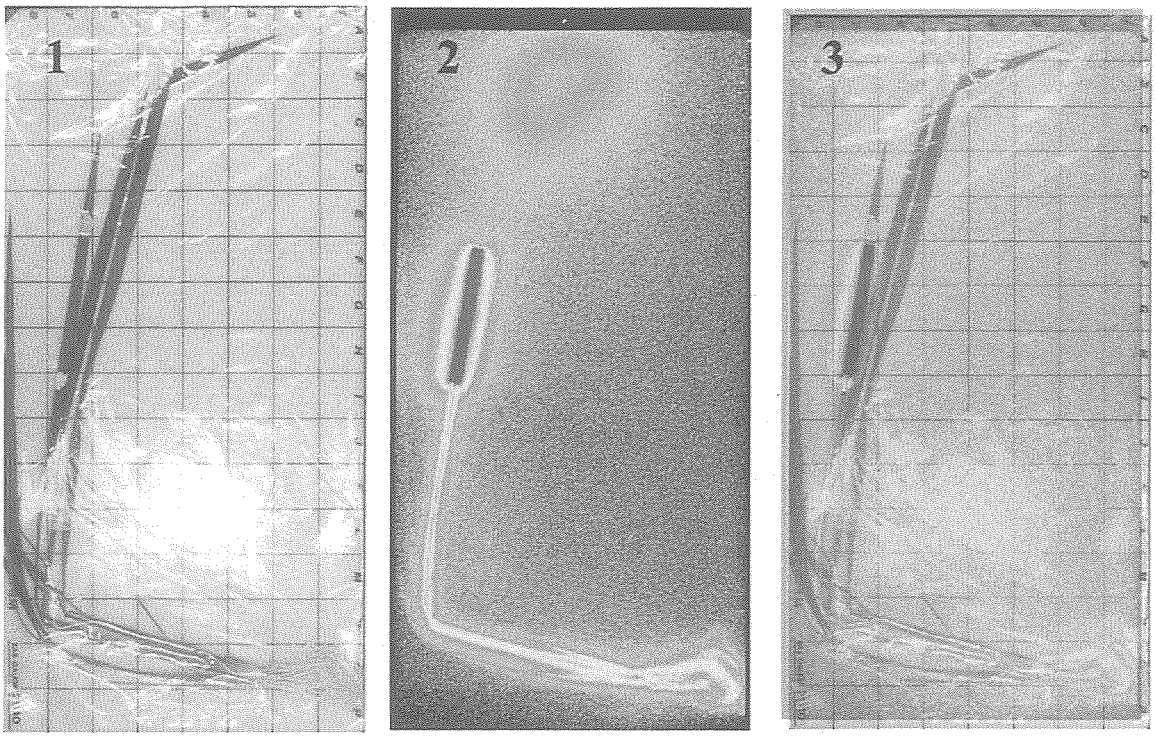


Figure 1 BAS images of ^{11}C- absorbed rice plant.

1:Photograph of ^{11}C- absorbed rice plant. 2: BAS image. 3: 1+2.

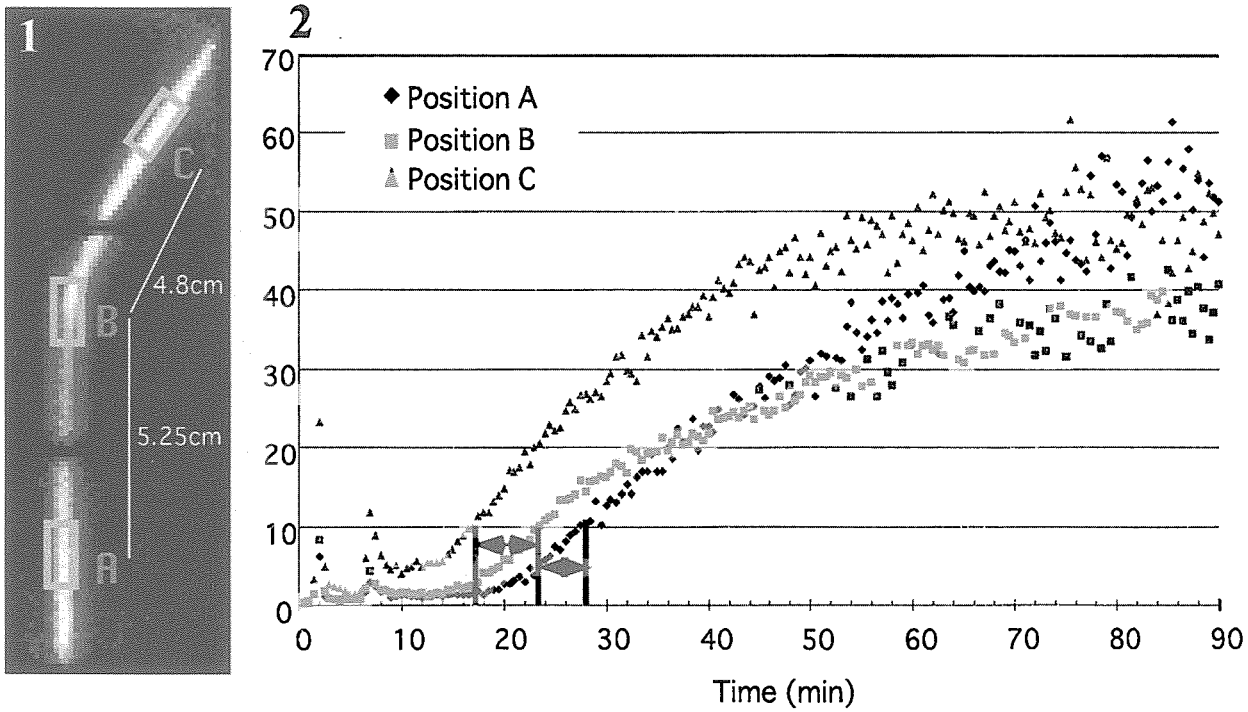


Figure 2 Detection of ^{11}C movements in rice plant by PETIS.

1:Cumulative image of ^{11}C activity in rice plant for 90 min..

2: Changes of ^{11}C activity at the positons A, B, and C.

2.29 Water and Trace Element Behavior in a Plant

T. M. Nakanishi[1)], J. Furukawa[1)], K. Tanoi[1)], H. Yokota[1)], N. Ikeue[1)], S. Hashimoto[2)], S. Matsuhashi[2)], T. Sekine[2)], T. Ito[2)], T. Mizuniwa[2)], N. S. Ishioka[2)], S. Watanabe[2)], A. Osa[3)], H. Uchida[4)], A. Tsuji[4)]
[1)] Graduate School of Agricultural and Life Sciences, The University of Tokyo
[2)] Department of Radiation Research for Environment and Resources, JAERI
[3)] Department of Materials Science, JAERI
[4)] Hamamatsu Photonics, Co., Ltd.

1. Introduction

Water movement, which plays an important role in chemical processes, has not been studied in detail. McKay *et al.* applied a positron emission tomography (PET) for neurological research of laboratory animals to the study of long distance transport of ^{18}F-water in plants[1)]. The paper suggested the advantage of PET for the study of physiological functions of plants. The positron-emitting tracer imaging system (PETIS) using positron-emitting nuclides has enabled us to detect the real time radioactivity movement in living plants[2, 3,4,5)]. So we employed PETIS to know the real time water uptake[6, 7,8,9,10)].

2. Material and Methods

2.1 Production of ^{18}F-water

^{18}F (half-life 110min) was produced by the reaction ^{16}O(α, pn)^{18}F by bombarding a frozen-water target with a 1.0 μA beam of 50MeV protons using the TIARA AVF cyclotron[11)]. After 40min irradiation, about 100MBq of ^{18}F was produced in 6ml of water, and the ^{18}F-water was purified through a cation exchange column.

2.2 Plant materials

Seeds of soybean plant (*Glycine max* cv. Tsurunoko) were germinated in wet vermiculite for three days. Then the seedlings were grown in a MGRL water culture solution in a phytotron at 25℃ for two weeks under sufficient light (2,000 μ mol m^{-2} s^{-1} for 12h) with 70% humidity[12)]. The culture solution was renewed with freshly prepared one every week. To measure the ^{18}F-water absorption from the bottom part of the stem, the root was cut off in distilled water. Then the labeled water was supplied to perform PETIS analysis.

2.3 Measurement of ^{18}F uptake by PETIS

The gamma-ray camera especially prepared for PETIS consisted of a pair of $Bi_4Ge_3O_{12}$ scintillator arrays to detect real time movement of labeled compounds in the target area (Figure 1)[13)]. To measure the ^{18}F-water uptake from root, the root of a plant was put into the vinyl bag that contained 10ml of culture solution. The plant and the bag were fixed on an acrylic board, and set in the middle of the two gamma-ray detectors. Before measurement the culture solution in the vinyl bag was removed and 5ml of the ^{18}F-water (15 MBq/ml) was supplied. The gamma-ray data was automatically collected every 30 s.

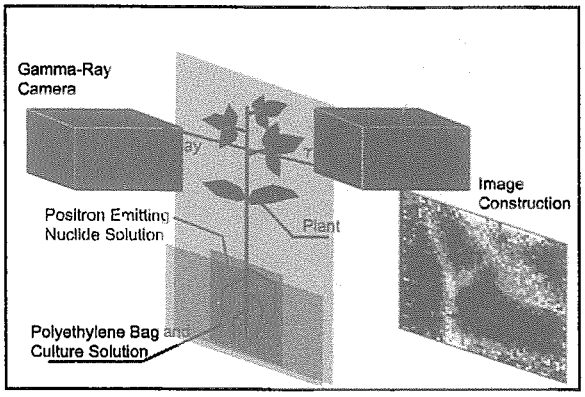


Fig.1 Overview of PETIS

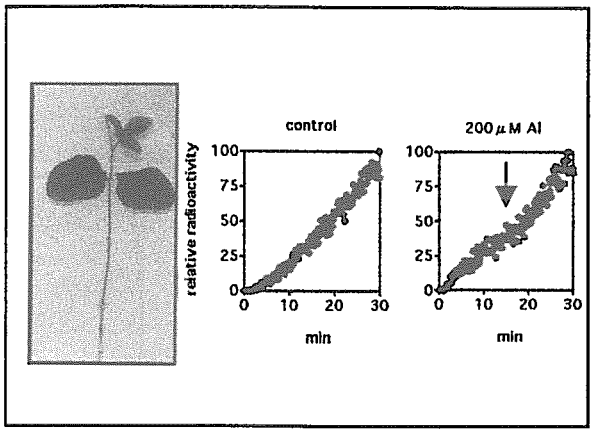


Fig.2 Al effect on ^{18}F-water uptake from a root

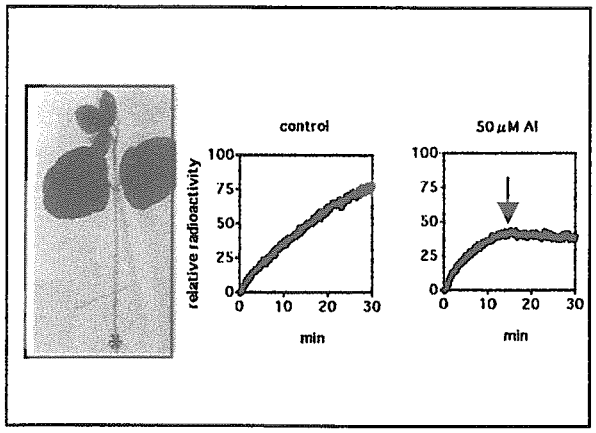


Fig.3 Al effect on ^{18}F-water uptake from a stem

2.4 ^{18}F distribution by BAS (Bio-imaging Analyzer System)

The bottom part of a stem was put into a vinyl bag where 10 MBq/ml ^{18}F-water was put. After 10 min, the plant was taken from the solution and placed on an IP (Imaging Plate) in a cassette. After 30min of exposure the image on IP was taken by BAS (BAS-1500, Fuji Film, Tokyo, Japan).

3. Results and Discussion

Figure 2 shows ^{18}F-water uptake from a root with addition of 200 μ M $AlCl_3$ into the ^{18}F-water 15min. after the beginning of measurement. In this experiment, we measured the ^{18}F radioactivity at an internode between the root and the first leaves. It was shown that Al treatment for 15min did not show any change in ^{18}F-water uptake.

In Figure 3 ^{18}F-water supplied from the bottom part of a stem, ^{18}F-water uptake was stopped by the addition of 50 μ M $AlCl_3$, suggesting that Al induced some damage in the ^{18}F-water uptake activity.

Because of the restricted area detected by a gamma-ray camera, we performed radiography using IP. Figure 4 is the BAS image of a soybean plant treated with 400 μ M $AlCl_3$ for 5min. From the BAS image, one can see that a small amount of ^{18}F was translocated to the first leaves compared with that in control plant.

Considering the decrease of the ^{18}F-water uptake, it was suggested that the root of the plant played an important role to protect the shoot from toxic substances.

Recently we tried a PETIS measurement using ^{15}O-labeled water and found that there was a difference in uptake behavior between ^{18}F-water and ^{15}O-water[14, 15]. However ^{15}O-water uptake activity was decreased a few minutes after 400 μ M Al was added from the bottom part of a stem.

It has been shown that PETIS is an effective tool for analyzing the environmental and soil conditions through analyzing water absorption and translocation in plants. We hope that PETIS will develop further for studying the living plant physiology.

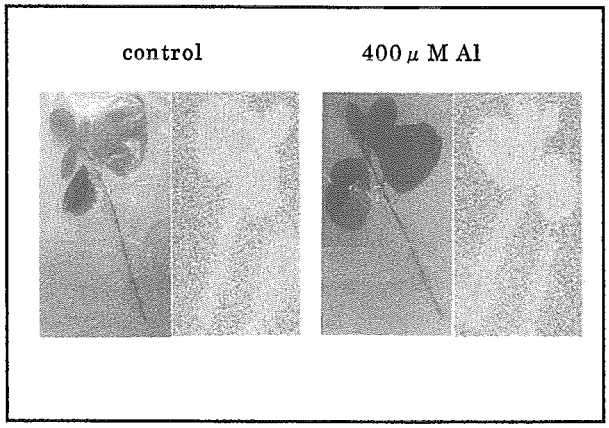


Fig.4 ^{18}F-water distribution (BAS image)

4. Summary

To know the effect of Al on a soybean plant, we performed real time ^{18}F-water uptake measurement by PETIS. We also measured the distribution of ^{18}F in a

whole plant by BAS. Aluminum treatment for 15min did not show any change in ^{18}F-water uptake from the root. When a soybean plant was treated with Al at the bottom of the stem, the total amount of ^{18}F-water absorption was found to be drastically decreased and the BAS image showed that only a small amount of ^{18}F was translocated to the first leaves.

References

1) R.M.L.McKay, G.R.Palmer, X.P.Ma, D.B.Layzell and B.T.A.McKee, Plant Cell and Environment 11 (1988) 851-861.
2) H.Hayashi, Y.Okada, M.Mano, T.kume, S.Matsuhashi, N.S.Ishioka, H.Uchida and M.Chino, Plant Soil 196 (1988) 233-237.
3) H.Matsunami, Y.Arima, K.Watanabe, N.S.Ishioka, S.Watanabe, A.Osa, T.Sekine, H.Uchida, A.Tsuji, S.Matsuhashi, T.Itoh and T.Kume, Soil Sci. Plant Nutr. 45 (1999) 955-962.
4) H.Nakanishi, N.Bughio, S.Matsuhashi, N.S.Ishioka, H.Uchida, A.Tsuji, A.Osa, T.Sekine and S. Mori, J. Exp. Bot. 50 (1999) 637-643.
5) T.Sato, N.Ohtake, T.Ohyama, N.S.Ishioka, S.Watanabe, A.Osa, T.Sekine, A.Tsuji, S.Matsuhashi, T.Itoh and T.Kume, Radioisotopes 48 (1999) 12-19.
6) J.Furukawa, H.Yokota, K.Tanoi, S.Ueoka, S.Matsuhashi, N.S.Ishioka, S.Watanabe, H.Uchida, A.Tsuji, T.Itoh, T.Mizuniwa, A.Osa and T.M.Nakanishi, Radioanal. and Nucl. Chem. in press.
7) T.M.Nakanishi, J.Furukawa, K.Tanoi, H.Yokota, S.Ueoka, N.S.Ishioka, S.Watanabe, A.Osa, T.Sekine, T.Itoh, T.Mizuniwa, S.Matsuhashi, S.Hashimoto, H.Uchida and A.Tsuji, J. Radioanal. Nucl. Chem. in press.
8) T.M.Nakanishi, T.Kataoka, J.Furukawa, K.Tanoi, H.Yokota, S.Ueoka, N.S.Ishioka, S.Watanabe, A.Osa, T.Sekine, T.Itoh, T.Mizuniwa, S.Matsuhashi, S.Hashimoto, H.Uchida and A.Tsuji, Radioanal. Chem.-MARC V (2000) 158.
9) J.Furukawa, H.Yokota, K.Tanoi, S.Ueoka, N.S.Ishioka, S.Watanabe, A.Osa, T.Sekine, T.Itoh, T.Mizuniwa, S.Matsuhashi, S.Hashimoto, H.Uchida, A.Tsuji and T.M.Nakanishi, Radioanal. Chem.-MARC V (2000) 157.
10) T.M.Nakanishi, J.Furukawa, K.Tanoi, H.Yokota, S.Ueoka, N.S.Ishioka, S.Watanabe, A.Osa, T.Sekine, T.Itoh, T.Mizuniwa, S.Matsuhashi, S.Hashimoto, H.Uchida and A.Tsuji, Proc. of 12th International Conference on Methods and Applications of Radioanal. Chem. (2000) 157.
11) N.S.Ishioka, H.Matsuoka, S.Watanabe, A.Osa, M.Koizumi, T.Kume, S.Matsuhashi, T.Fujimura, A.Tsuji, H.Uchida and T.Sekine, J. Radioanal. Nucl. Chem. 239 (1999) 417-421.
12) T.Fujiwara, M.Y.Hirai, M.Chino, Y.Komeda and S.Naito, Plant Physiol. 99 (1992) 263-268.
13) T.Kume, S.Matsuhashi, M.Shimazu, T.Itoh, T.Fujimura, K.Adachi, H.Uchida, N.Shigeta, H.Matsuoka, A.Osa and T.Sekine, Appl. Radiat. Isot. 48 (1997) 1035-1043.
14) T.M.Nakanishi, H.Yokota, K.Tanoi, J.Furukawa, N.Ikeue, Y.Ohkuni, H.Uchida and A.Tsuji, Radioisotopes 50 (2001) 163-168.
15) T.M.Nakanishi, H.Yokota, K.Tanoi, N.Ikeue, Y.Ohkuni, J.Furukawa, N.S.Ishioka, S.Watanabe, A.Osa, T.Sekine, S.Matsuhashi, T.Itoh, T.Kume, H.Uchida and A.Tsuji, Radioisotopes 50 (2001) 265-269.

2.30 Uptake of ^{18}F-Water ^{15}O-H_2O and $^{13}NO_3^-$ in Tomato Plants

A.Tsuji, H.Uchida, T.Yamashita, S.Matsuhashi*, T.Ito*, C.Mizuniwa*, N.S.Ishioka*, S.Watanabe*, S.Hashimoto*, T.Sekine*
Central Research Lab., Hamamatsu Photonics K.K.,
*Department of Radiation Research for Environment and Resources, JAERI,

1.Introduction

Conventionally, behavioral observation of water and other compounds has in plants mainly been carried out by static methods such as autoradiography and other methods of image measurement using RI. We have developed a dynamic image measurement method using positron emitting nuclides, which allows us to investigate the biological functions of plants from a new angle.

The Positron Emitting Tracer Imaging System (PETIS) which we have developed is comprised of two planar detectors, which detect annihilation γ rays. From this measurement method dynamic movements of substances within a plant can be observed as a two-dimensional image without contacting the sample plant.

Using this method, we have carried out the fundamental research such as the observation of the uptake and transport of water, minerals and nutrients. Those data are compiled in the present report togetheer with additional experimental data.

2.Experiments

The PETIS used this experiment consists of two-dimensional block detectors which are composed of a $Bi_4Ge_3O_{12}$ scintillator array coupled to a position sensitive photomultiplier tube (PS PMT; Hamamatsu R3941-2). The mosaic BGO array is formed with 27(X) x 23(Y) array of 2 mm square cross section x 20 mm deep BGO pillars, where each segment is placed with 2.2 mm pitch.

$^{18}F^-$ and $^{13}NO_3^-$ were produced by the TIARA AVF cyclotron. And ^{15}O was produced by the $^{14}N(d,n)^{15}O$ reaction in a nitrogen gas target. The target gas contained 0.5% oxygen as carrier and was kept as a continuous a flow with flow rate of 500ml/min at a pressure of 3kg/cm^2. The gas in the target chamber was irradiated with a 10 MeV deuteron beam at a current of 15 μA using the cyclotron (SUMITOMO CYPRIS-HM) at Hamamatsu Photonics PET Center.

Tomato plants were grown in vermiculite from seeds at 27°C and maintained in a controlled environmental chamber. The plants cultivated for 4~6 weeks (about 40 cm high) were used for the present experiment.

The water containing ca. 10 MBq/ml of ^{18}F-water, ca. 200Mbq/ml of ^{15}O-H_2O or 10 MBq/ml of $^{13}NO_3^-$ was fed to the root or a leafstalk of the plants. Under dark and bright conditions, ^{18}F-water and ^{15}O-H_2O uptake were observed and was similarly increased.

3. Results and discussion

Figure 1 shows time course curves of ^{15}O-H_2O tracer activity at a tomato stem. The uptake velocity of ^{15}O-H_2O was 2.0~2.5 cm min^{-1} at a bright condition. There was slight uptake under a dark condition as expected. Figure 2 shows the relation between ^{18}F-water and ^{15}O-H_2O at a bright condition. ^{18}F-water uptake was rapid compared to that of ^{15}O-H_2O, and the shape of

the curve was different from each other. The first ^{18}F-water signal was noticed 2 minute after beginning the experiment. But, ^{15}O-H_2O signal was noticed 5 minute after beginning the experiment.

To study $^{13}NO_3^-$ retranslocation, $^{13}NO_3^-$ was provided from the cut end of the 5th or 6th leafstalk of a tomato. In the case of feeding to the 5th leafstalk, the image of the lower stem appeared 4 min after beginning the experiment, and then the images the upper stem appeared after next 7 min later (Figure 3). In contrast, in case of fed to the 6th leafstalk, only the image of the lower stem appeared (Figure 4).

These results suggest that ^{18}F-water uptake only shows "$^{18}F^-$ ion uptake" but not "water uptake". And these results show the difference between source and sink of tomato.

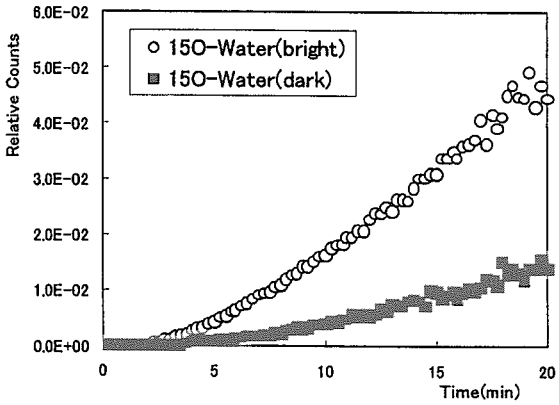


Figure 1 Time course study of ^{15}O-H_2O uptake at the tomato stem.

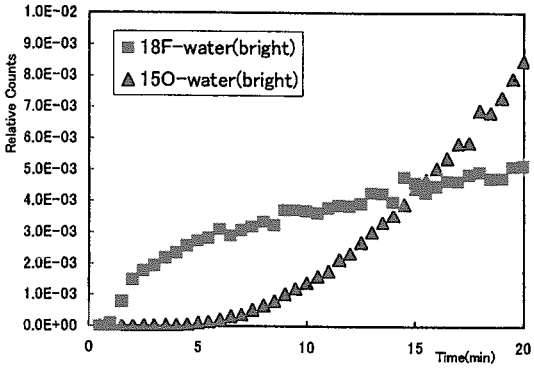


Figure 2 Time course study of ^{15}O-H_2O and ^{18}F-water uptake under bright condition.

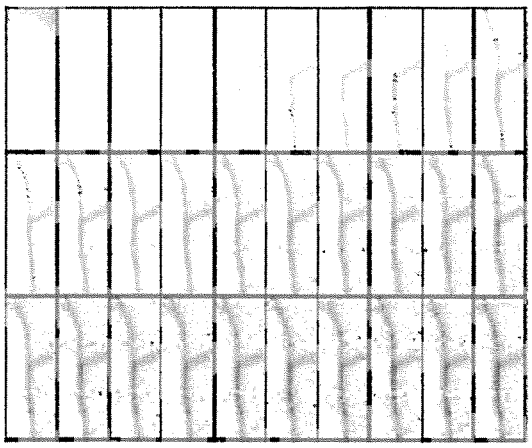


Figure 3 Images of $^{13}NO_3^-$ uptake for feeding to the 5th leafstalk of a tomato. (Images cllected each for one minute were shown)

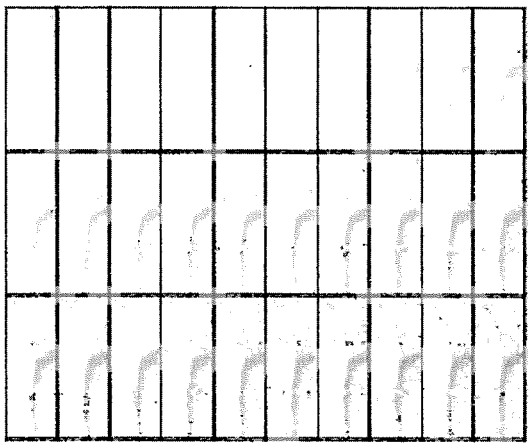


Figure 4 Same as Fig.3 except for feeding to the 6th leafstalk. (Image were shown every minute)

2.31 Single-hit Effects and By-stander Effect on Cells by Heavy-ion Microbeams

Y. Furusawa[1], N. Yasuda[2], CL. Shao[1,3], M. Aoki[1], K. Sato[4], K. Takakura[4], T. Funayama[5], and Y. Kobayashi[5]

[1] Research Center for Charged Particle Therapy, NIRS

[2] International Space Radiation Laboratory, NIRS

[3] Institute of Plasma Physics, Chinese Academy of Sciences

[4] Laboratory of Biophysics, International Christian University

[5] Advanced Radiation Technology Center, JAERI

1. Introduction

Radiobiological responses induced by radiation are different with the radiation quality. The distributions of the energy transfer especially by charged particles in a matter are not uniform in contrast with X-rays or gamma-rays. The truck structure has a defined distribution of ionization density that depends on the effective charge or velocity of the accelerated ions. In addition, the probability to hit the cells is dispersed with time and space, and the energy deposition in the cell is different by the geometrical relationship between the positions of the cell and the ion traversal at exposure. The cells may shows different radiobiological responses among cell that received different doses and qualities of the radiation which depend on the type of hit, e.g. by directly or by glancingly. It is generally thought that the cellular response is mainly caused by the radiation energy absorption in the cell nuclei. However it is also reported that a cell escaped from the direct hit of radiation show some radiobiological effects, and it is called as "bystander effect". To make clarify the bystander-effects, a selected cell (or cell nuclei) will be handled as a target, and radiobiological effects by single-ion hit or by non-ion hit (miss the target on purpose) will be analyzed. To realize this radiobiological experiment, we tried to improve the single-ion exposure system of HZ-1 at TIARA, and establish to detect radiobiological endpoints of bystander effects such as inhibition of cell proliferation, induction of micronuclei, apoptosis, proteins, DNA breakage, and so on.

2. Experimental

During the experiments, 460 MeV (11.5 MeV/u) $^{40}Ar^{+13}$ and 260 MeV (13 MeV/u) $^{20}Ne^{+7}$ beams were used at HZ-1 and HY-1 experiment ports at TIARA, JAERI. Also 3.5 GeV (290 MeV/u) $^{12}C^{+6}$ and 28 GeV (500 MeV/u) $^{56}Fe^{+26}$ beams were used at biology experiment port at HIMAC, NIRS.

Development of an Illumination System: Cells grown on a Mylar film (t = 5μm) and covered with the same film to prevent dry-up during the exposure were tried to observe with a microscope installed at the HZ-1 irradiation port. However it was difficult to obtain a clear image of cells with a reflected illumination system that installed in the microscope. Positioning of the cell onto the microbeam was thought to be impossible. Thus we have newly developed another illumination system for the microscope. We found a light guided ring-illumination device shows a better

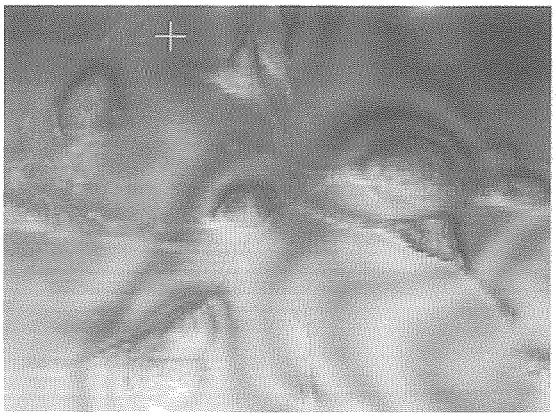


Fig.1. Microscopic image of cells by newly

image when the light coming from a defined angle which defined by numerical aperture of an objective lens of the microscope. We developed very small ring-illumination device using white-photodiodes, and fitted on to the collimated outlet having 3 mm of the diameter at the HZ-1 beam line. The image looks like a phase contrast microscope or a differential interference microscope (Fig.1).

Reference Data by the Spread Beams: Dose-response curves for induction of apoptosis were obtained at HY-1 beam port as a reference data of HZ-1 microbeam. Detection of micronucliated cells were successfully performed with X-rays from preliminary experiments, it was tested at HY-1 port.

Detection of Bystander Effects: It is reported that non-irradiated cells show at least some radiobiological responses (bystander effects) through signals from irradiated cells. The signal of bystander effects may communicate directly through the cell-cell gap-junction and/or indirectly by cytokines through liquid mediated way between cells. Detection of the liquid mediated bystander effects on non-irradiated cells from irradiated cells were tried by means of co-culture method in this period. X-rays were used and, measurement of cell proliferation and induction of micronuclei were tested as the end point of detection of bystander effects in the preliminary experiments[1]. Cell number of the non-irradiated sample (recipient cells) increased with the radiation dose on irradiated cells (donor cells), and existence of participation by liquid mediated factor was suggested. The increase of the cell number was suppressed when 0.1 mM PTIO (2-Phenyl-4,4,5,5-tetramethylimidazoline-1-oxyl 3-oxide), a nitric oxide (NO) inhibitor, was added in the co-culture medium. When DMSO, a radical scavenger was added, there was no response to the addition. A possibility that the NO or its derivatives may be a cytokine of the proliferation was suggested. Another dose-response relationship was observed upon micronuclei experiment. The dose-response increased up to 4 Gy, showed a maximum, and decreased with father dose. A good fitting of the dose-response curve in micronuclei induction was given using a compound equation, under assumption that the induction of micronuclei in the non-irradiated cells increase linear-quadratic manner with the concentration of the cytokine, number of survivors of irradiated cells which produce and release the cytokine. This good fit of dose-response curve suggests the cytokine is released only from surviving cells.

Investigation of Pseudo-microbeam Exposure Method: To analyze the bystander effects by exposure of selected cells, development of the other possible microbeam exposure system was carried out using energetic heavy-ion beams at HIMAC. The system is briefly approved ideas as follows. Cells were grown on a CR-39 truck detector having landmarks by primary sparse exposure of ion beams with slightly etching. The cells were irradiated by low-flux heavy-ion beams, and cultured. Three microscopic images at same geometrical position in a sample area, i.e. 1) just after the cell irradiation, 2) after the cell culture, and 3) after the father etching of CR-39 to detect irradiated ions were obtained. The images were superimposed, and cell proliferation and number of ion traversals for each cell were measured.

In a experiment, prior to use for the cell culture, CR-39 plates were irradiated with $5x10^3$ p/cm^2 of carbon beam and etched with 7N-NaOH for appropriate time at 70 °C to produce landmarks. HSG cells were seeded and attached on a CR-39 plate having landmarks 4-6 hours prior to cell exposure. The cells were irradiated with 0.1 or 0.4 Gy of 500 MeV/u $^{56}Fe^{+26}$ randomly spread ion-beam, and images; 1) of the cells together with landmarks were obtained. The cells were cultured in a CO_2-incubator for 2-3 days, fixed, and then the cell images; 2) was taken with the landmark. The CR-39 plates were etched again in 7N-NaOH for 0.5-1 hour at 70 °C to produce the trucks at the cell irradiation. Images; 3) of the etch-pits by the irradiation, together with landmarks were obtained.

Cell numbers increased by the proliferation started from each irradiated cell were identified by superimpose to meet with the images 1) and 2) using the landmarks. The number of traversals, or the number of direct-hits in each irradiated cells was obtained from the images 1) and 3). Relationship between the number of hits and the proliferation were obtained. We could observe from 0.4 Gy exposure samples any micro-colony which consists of more than 5 cells from 2- or more traverse (>2 direct-hit) cells at the irradiation, however approximately 10 % colonies which consists 6-10 cells from 1-traversal (1 direct-hit) cells. In addition, from 0.1 Gy exposure samples, approximately 25 % colony that consists of 6-10 cells was observed. This means in case of 0.4 Gy exposure samples, even if it is one direct-hit cells, they may received more radiation dose from the glancing type hit, and suppress the cell prolife-ration. Another hand, micro-colonies with zero direct-hit cells that consists 1-5, 6-10, and more than 11 cells were found in 55, 40, and 5 %, respectively. This result also indicates if the cells did not receive any direct hit by 0.1 Gy exposures, they may receive some dose through the glancing hit.

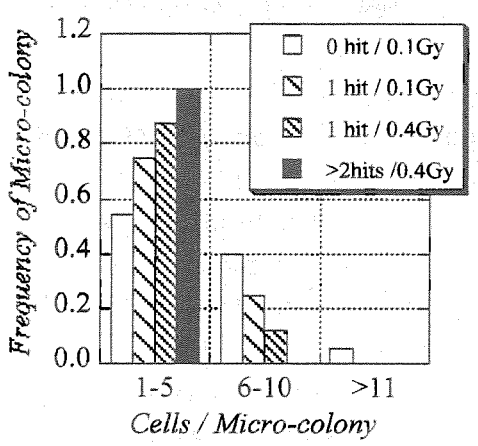


Fig.2. Number of proliferated cells in one micro-colony after heavy-ion exposure with the pseudo-microbeam system. The nunber of hits to each cell and the average dose to the whole sample were indicated in the figure.

3. Conclusion

A possible illumination system for the online microscope that equipped at the HZ-1 microbeam port was developed to observe cells.

A bystander effect on un-irradiated cells from irradiated cells can be observed by a cell co-culture system both with X-rays and HIMAC carbon-ion beams. The induction of micronuclei in an un-irradiated cell may be caused by a signal transduction through nitric-oxide (NO), because the effects were suppressed by an addition of PTIO (NO scavenger).

A pseudo-microbeam exposure method was developed using CR39 truck detector and microscopic image analyzing system with HIMAC random heavy-ion beams, and a preliminary experiment was performed. Suppression of cell proliferation upon individual cells was observed as results of "direct-hit effect" and "glancing-hit effect" with this method.

References

[1] Shao C. L. et al.: Medium-mediated bystander effects on HSG cells co-cultivated with the cells irradiated by X-rays and 290 MeV/u carbon ions. *J. Radiat. Res.* 2001, (submitted)

[2] Furusawa Y, and Aoki M.: Relationship between radiation quality and radiobiological effects on cells – LET and ions –. In: *Proc. 11th Symp Beam Engineering and Advanced Material Synthesis*, pp.159-162, Org Comm 11th Beam Engineering Symp, Tokyo, 2000.

[3] Kazufumi Sato: Thesis, International Christian University. 2001.

2.32 Fundamental Study on Radiotherapy of Tumors to Beneficial Companion Animals using Heavy Ion Beam

S.Wada[a], M.Natsuhori[a], N.Ito[a]
Y.Kobayashi[b] T.Funayama[b], K.Yamamoto[b]
[a]Department of Veterinary Medicine,Kitasato University
[b]Department of Radiation Research for Environment and Resources, JAERI

1.Introduction

Recently, beneficial companion animals that assist the people both mentally and physically, and that highly contribute to the people in many occasions have risen in their estimation. As companion animals can live much longer than before because of improvement of their breeding condition and preventive medicine, the incidence of aging-related disorders and neoplasm formation are increasing. So the application of radiotherapy in the veterinary medicine increases as one of treatments against tumor. But different tumor types have different radiosensitivity[1] respectively. It is important to determine the intrinsic radiosensitivity of its tumor to individual patient in advance for curing of tumor effectively, increasing local control and reducing morbidity. Especially there are not biological fundamental data enough on the radiotherapy against canine and feline tumor by using ion beam. It is essential for effective radiotherapy with high LET radiation as well as low LET to establish the predictive assay and biological parameters that can rapidly evaluate radiosensitivity of the tumors. To examine the correlation between the double-strand breaks (DSB) and the cell survival as radiation effect, we measured DSB by using the single cell gel electrophoresis (comet assay) that is rapid and easy method.

2.Materials and methods

Cell lines used for this experiment were squamous cell carcinomas, fibrosarcoma and hemangiopericytoma that originated from spontaneously generated canine tumor. Cell lines were kept and grown in MEM medium with 10% serum supplemented. These were incubated at 37 ℃ in humidified atmosphere of 95% air and 5% carbon dioxide mixture. These cells were irradiated ^{12}C ion beams at 220 MeV (108 keV/μm) or γ ray radiation (^{60}Co-γ source) at a dose rate of 2.0 Gy/min. The survival rates were fitted to the linear-quadratic model, and the survival fraction at 2Gy (SF2) as the index of the cell killing by radiation was calculated from the survival curves[1].

On the irradiation of γ-rays, 1×10^5 cell/ml cells suspended in medium were irradiated. On the irradiation of carbon

ion beams, cells mixed into agarose on the slide grass were irradiated for initial damage assessment, and monolayer of cells on the culture dish were irradiated for residual damage assessment. Samples for the residual damage assessment were incubated at 37 ℃ for 4hr after irradiation and then re-suspended. The cell suspension was mixed with agarose and was layered on the slide glass. The slides were placed immediately in a chilled lysing solution. The slides were placed on a horizontal gel electrophoresis platform and covered with chilled neutral buffer solution (pH 8) for evaluating DSB. Electrophoresis was conducted in dark for 30 min at 25 V (0.85 V / cm). Slides were stained with 50μl ethidium bromide. Cells were examined with a fluorescence microscope (Fig.1). Images of the cells were analyzed by the kinetic image analysis software (Kinetic image Inc.) and we used tail moment as the parameter that reflected DNA damage.

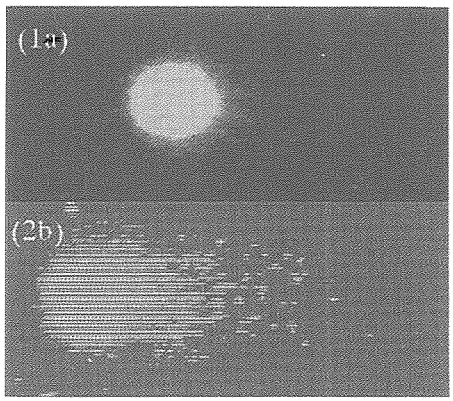


Fig.1 DNA fragments of squamous cell carcinoma. (1a) control. (1b) exposure to 4 Gy of carbon beam. DNA broken by radiation migrated from the nucleus in electric field.

3.Result and Discussion

As some dose-response curves for initial and residual radiation-induced DNA damage were obtained for three canine tumor cell lines and were fitted by linear regression, they were well described by a linear fit. Because the slope angles (tail moment/Gy) obtained from the linear regression analysis of initial and residual DNA damage dose-response curves showed difference between three canial tumor cell lines we regarded that the three tumor cell lines have different sensitivities respectively on initial and residual radiation-induced DNA damage. In case of irradiation of carbon beams, the hemangiopericytoma indicated the highest slope angle, the squamous cell carcinoma indicated the lowest one and the middle is the fiborsarcoma on both initial and residual DNA damage. In case of irradiation of gamma-rays, the same tendency was observed. Table 1 indicates slopes from liner regression analysis of the initial and residual dose-response curves and SF2 (the survival fraction at 2Gy) that was conventionally used as index for evaluating radio-sensitivity. Table1 indicates that the hemangiopericytoma was highly sensitive and the squamous cell carcinoma was radioresistant in the clonogenic assay, the difference of the slopes evaluating initial and residual DNA damage accorded to clonogenic radio-sensitivity. Fig.2 indicates that the relationship between SF2 and radiation-induced initial and residual DNA damage. Fig.2 indicates good correlation between gamma-rays and carbon beam-induced initial and residual DNA damage and SF2 of clonogenic radio-sensitivity.

After all those indicated that it was

possible to predict the survival fraction (radio-sensitivity) of tumor by evaluating radiation-induced DNA damage of its tumor with comet assay. The clonogenic assay consumes away more than a week. However, as the comet assay can yield a result within several hours, it is considered that comet assay is beneficial as rapid predictive test for radio-sensitivity of tumor in radiotherapy.

Reference

1) S.Wada, Y.Kobayashi, T.Funayama, M.Natsuhori, K.Yamamoto, N.Ito, JAERI- review 2000-024, 80-82.

Table 1 slopes (tail moment/Gy) from liner regression analysis of the initial and residual damage and SF2

	Cell line	SF2	Initial damage	Residual damage
Carbon beam	Squamous cell carcinoma	0.140±0.014	0.763±0.144	0.120±0.065
	Fibrosarcoma	0.109±0.004	0.858±0.077	0.254±0.059
	Hemangiopericytoma	0.089±0.009	1.343±0.204	0.327±0.071
γ ray	Squamous cell carcinoma	0.562±0.044	0.458±0.054	0.033±0.009
	Fibrosarcoma	0.458±0.006	0.704±0.028	0.064±0.017
	Hemangiopericytoma	0.360±0.033	0.832±0.027	0.081±0.009

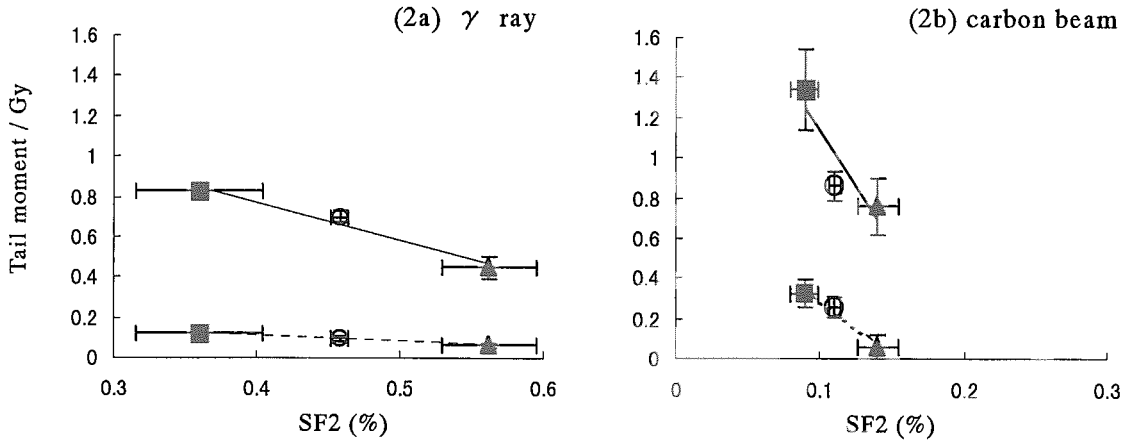


Fig.2 Relationship between slopes (tail moment / Gy) of initial (—) and residual (···) DNA damage and SF2 that was conventionally used as index for evaluating radiosensitivity. (2a) gamma ray. (2b) carbon beam. Squamas cell carcinoma (▲), fibrosarcoma(○),Hemangiopericytoma (■).

3. Radiation Chemistry/Organic Materials

3.1 Study on Space Environment Durability of Newly Developed Polymeric Materials for Spacecraft (II) ····· 115
F.Imai, M.Iwata, Y.Nakayama, K.Imagawa, M.Sugimoto, N.Morishita, and S.Tanaka

3.2 Preparation of Ion Track Membranes and Their Separation Characteristics of Peptide Molecules ····· 118
M.Asano, H.Koshikawa, Y.Maekawa, M.Yoshida, T.Kume, and K.Ogura

3.3 Application of Thin Film Dosimeters to Measurement of Ion Beam Dose Distribution II ····· 120
T.Kojima, H.Sunaga, H.Takizawa, H.Hanaya, and H.Tachibana

3.4 Cross-linking of Polydimethylsiloxane in Heavy Ion Tracks ····· 122
H.Koizumi, M.Taguchi, Y.Kobayashi, and T.Ichikawa

3.5 Nano-wire Formation along Ion Projectiles in Polysilane Thin Films ····· 125
S.Seki, K.Maeda, Y.Yoshida, S.Tagawa, M.Sugimoto, and S.Tanaka

3.6 Primary Process of Radiation Chemistry Studied by Ion Pulse Radiolysis ····· 129
Y.Yoshida, S.Seki, A.Saeki, K.Okamoto, S.Tagawa, M.Taguchi, and H.Namba,

3.7 Measurement of Energy Deposition Around the Heavy Ion Trajectory by Photon Counting Method ····· 131
M.Taguchi, H.Namba, and S.Ohno

This is a blank page.

3.1 Study on Space Environment Durability of Newly Developed Polymeric Materials for Spacecraft (II)

F. Imai,[1] M. Iwata,[1] Y. Nakayama,[1] K. Imagawa,[1]
M. Sugimoto,[2] N. Morishita,[2] and S. Tanaka[2]
[1] Office of Research and Development, NASDA
[2] Department of Material Development, JAERI

1. Introduction

Many kinds of polymeric materials have been developed as thermal control materials for the International Space Station (ISS), Space Shuttle, satellites, and so on. Polyimides and fluoropolymers are typical polymeric materials used for these spacecraft. However, the performance of these polymers is degraded in the space environment. For example, although polyimide film (KAPTON®) is stable against electron beam (EB) and ultraviolet rays (UV) exposure, it exhibits low durability against atomic oxygen (AO). In contrast, although fluoropolymers are stable against AO due to the high dissociation energy of the C-F bond compared with other polymeric materials, durability against ions, EB, and UV is not so good. To improve these vulnerabilities, polyimides with high durability against AO[1] and cross-linked PTFE[2] have been developed. Recently, we have developed a new type of polyimide films. One of the samples, for example, has a polyimide-siloxane layer on its surface and is expected to have high durability against AO. To evaluate the performance of these new materials, it is important to irradiate them with ions, EB, UV, and/or AO at ground simulation test facilities for the space environment and to analyze the physical or chemical effects by using thermo-optical property measurement (solar absorptance α_S and normal infrared emittance ε_N), surface analysis techniques, and so on.

We irradiated thermal control materials with ions (H^+, Fe^+, and C^+) and EB and evaluated the change of thermo-optical properties or mechanical properties.[3] In the present work, we will report the results of ions (H^+, O^+, and He^+) and EB irradiation of polyimides and fluoropolymers.

2. Experimental

Materials used for this study are shown in Table 1.

Table 1 Specimen

Name	Composition
PI2	Polyimide: coating ca. 3000nm of polyimide-siloxane layer on UPILEX-R standard
PI6	Polyimide: UPILEX-R (BPDA-ODA) standard, thickness 0.05mm
PI7	Polyimide: UPILEX-S (BPDA-PDA) standard, thickness 0.05mm
X-PTFE	Fluoropolymer: Cross-linked PTFE, thickness ca. 0.5mm (Cross-linking was performed with ca. 100kGy of EB irradiation at around melting point)
PTFE	Fluoropolymer: PTFE standard, thickness ca. 0.5mm

BPDA-ODA: [biphenyl tetra carboxylic dianhydride]-[4,4'oxydianiline]
BPDA-PDA: [biphenyl tetra carboxylic dianhydride]-[para phenylene diamine]
PTFE: poly tetra fluoro ethylene

We irradiated materials with ions or EB in vacuum at room temperature and evaluated the properties. Ion irradiation was performed at the TIARA facility under experimental conditions shown in Table 2. EB irradiation was performed at NASDA's Combined Space Effects Test

Facility ("Facility-D") at an energy of 200keV, current of 2mA, irradiation time of 600s, fluence of 8.37E+13e/cm^2, and absorbed dose of 45kGy. The fluence of EB is the same as the space environment of the ISS orbit at an altitude of 407km for about 25 years.

Table 2 Irradiation conditions

Ion	Energy	Fluence [cm^{-2}]	
H^+	10MeV	2.0E+10	6.0E+10
		2.0E+11	2.0E+12
He^+	1MeV	6.6E+9	2.0E+10
		6.6E+10	6.6E+12
		2.0E+13	6.6E+13
O^+	1MeV	6.0E+9	1.8E+10
		6.0E+10	6.0E+12
		2.5E+12	1.8E+13
		6.0E+13	

The fluence in a geostationary orbit for 10 years is H 2.0×10^{11} cm^{-2}, He 6.6×10^{9} cm^{-2}, and O 2.0×10^{8} cm^{-2}.

We analyzed specimens by thermo-optical property measurement, XPS, FT-IR, ^{19}F-NMR, indentation hardness test, nano-indentation, and so on.

3. Results and Discussion

3.1 Ion irradiation

Measured values of solar absorptance (α_S) and normal infrared emittance (ε_N) of the specimens irradiated with 1MeV O^+ ions are shown in Fig. 1 (a) and (b) as functions of fluence. Although a slight

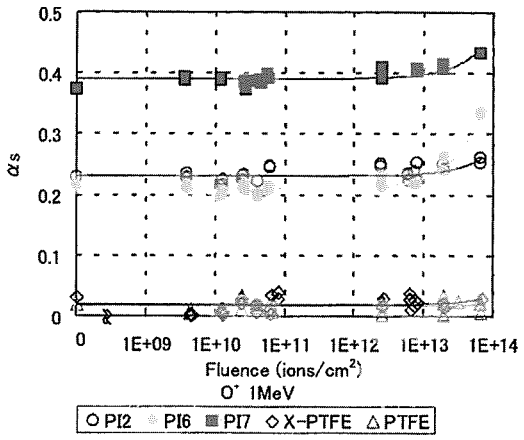


Fig. 1(a) Changes of solar absorptance (α_S) of specimens irradiated with 1MeV O^+ ion.

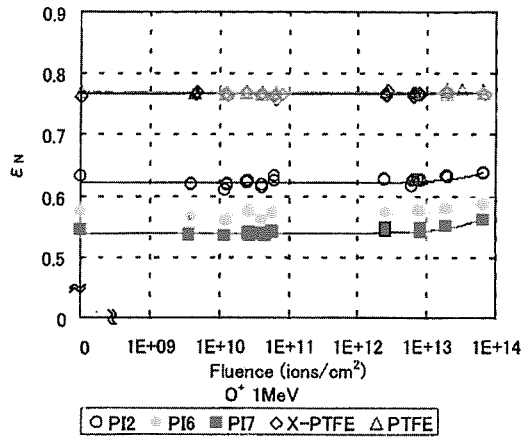


Fig. 1(b) Changes of normal infrared emittance (ε_N) of specimens irradiated with 1MeV O^+ ion.

increase in α_S is observed for polyimides at higher fluences as shown in Fig. 1 (a), there is no substantial influence on thermo-optical properties since the lowest fluence of 6.0E+9 cm^{-2} is equivalent to 300 years. However, increases in α_S at fluences exceeding 1E+13 cm^{-2} are observed. The change in α_S of PI6 is higher than that of PI7 and can be attributed to the difference of molecular stability for radiation doses. All the specimens irradiated with H^+ and He^+ also show excellent stability.

3.2 EB irradiation

There was no change in thermo-optical properties of each specimen before and after irradiation with EB.

We applied two indentation tests to PI6 and PI7. One is a nano-indentation test that is sensitive to surface regions of some tens of nanometers. The other is an indentation hardness test that is suitable for characterizing a several-micrometer thick region. There was no change of the depth profile of nano-indentation test for either specimen.

The indentation hardness test revealed that the indentation depth of PI6 film irradiated with EB increased compared to non-irradiated film. This indicates that a structural change occurred in the material irradiated with EB. The indentation depth of non-irradiated PI2 was 1/6 (ca.0.4μm) of that of the non-irradiated PI6. This reflects the hardness of the polyimide-siloxane layer on the surface of PI2. The indentation depth of irradiated PI2 was almost the same as that of the non-irradiated film, so PI2 is more stable than PI6. No structural change of PI7 was observed in the indentation tests. Little change was observed between the irradiated and non-irradiated specimens of PI2, PI6, and PI7 for XPS, FT-IR, or NMR. The durability of polyimide films for EB can thus be summarized as PI2 ≧ PI7 > PI6.

Regarding fluoropolymers, the indentation depth of non-irradiated X-PTFE is larger than that of PTFE. Although the depth of non-irradiated PTFE and irradiated one is almost same, that of X-PTFE decreased by 7% (Fig. 2).

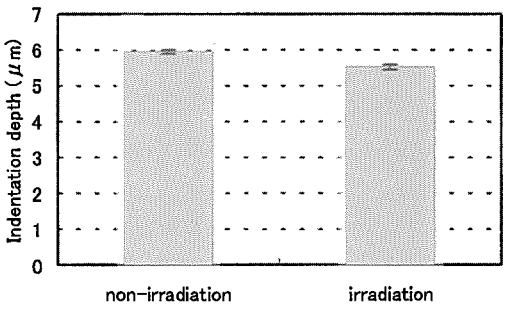


Fig. 2 Indentation depth of X-PTFE

The radiation-induced cross-linking and grafting of PTFE depend on the dose of EB, and the molecular chain of PTFE cut by EB irradiation forms molecule radicals.[4] These radicals recombine with cross-linking points of PTFE. This structural change hardens the specimen. The decrease of the indentation depth in the hardness test is attributable to the reaction described above.

The energy distribution of electrons in PTFE is calculated with EDMULT Version 6.3 and shown in Fig. 3. The

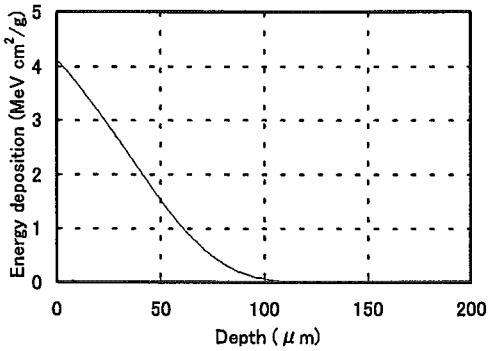


Fig. 3 Electron energy deposition in PTFE

depth-dose curve is similar to this figure, thus the range of EB in PTFE used in this experiment is estimated to be 0.116mm, which is smaller than the thickness of PTFE specimen. Hence, the absorbed dose is the highest at the surface. The functional group ratio of X-PTFE analyzed with NMR was almost the same as that of PTFE.

To investigate the details of structural changes, we plan to vary the absorbed dose of specimens. X-PTFE with a higher cross-linking factor will also be examined.

References

1) M. R. Reddy, J.Mater.Sci.30(1995)281.
2) E. Katoh, H. Sugisawa, A. Oshima, Y. Tabata, T. Seguchi, and T. Yamazaki, Radiat.Phys.Chem.54(1999)165.
3) Y. Nakayama, H. Seino, K. Imagawa, M. Sugimoto, H. Kudoh, N. Morishita, and Y. Morita, TIARA Annual Report 1999, 87.
4) Y. Tabata, S. Ikeda, and A. Oshima, Nuclear Instruments and Methods in Phys. Res. Sec. B, to be published.

3.2 Preparation of ion track membranes and their separation characteristics of peptide molecules

M. Asano[1], H. Koshikawa[1], Y. Maekawa[1], M. Yoshida[1], T. Kume[1], and K. Ogura[2]

[1]Department of Material Development, JAERI

[2]College of Industrial Technology, Nihon University

1. Introduction

Heavy ion-beam deposits energy locally concentrated along the ion-path through the materials. This induces nanoscopic damage sufficient for the ion-path to be susceptible to development in an etchant, resulting in the formation of through-holes with uniform size. These membranes are used as the separation filters for radioactive wastes of nuclear power plants. Since their pore sizes are easily controlled by the kind of ion particles and etching conditions, these membranes are further expected to be applied to precisely controlled selective separation membranes. We reported that polyethylene terephthalate (PET) membranes with different pore diameters are applied to size-exclusion membranes; the polyethylene glycols with the molecular weight of 106 to 70,000, are clearly separated to each other by changing the pore diameter[1]. In this report, we describe the preparation of the PET and diethyleneglycol-bis-allylcarbonate (PEGAC) membranes with nanometer scale pore diameters using highly diluted alkaline etchant and their application to separate the proteins in blood, albumin (BSA) and γ - globulin (IgG).

2. Experimental

The PEGAC film was prepared according to a conventional cast polymerization with 3 wt% of di-2-propylperoxydicarbonate (IPP) as a radical initiator at 70 °C for 24 hours. The films are irradiated with Xe and Ar ions with the energy of 450 and 520 MeV, respectively, using TIARA cyclotron of Japan Atomic Energy Research Institute (Takasaki, Japan) and Au ions with the energy of 11.4MeV/n using UNILAC of GSI (Darmstadt, Germany). The irradiated films were etched in 0.1 – 0.3 N NaOH at 70 °C. The samples were etched in a conductometric cell made of Teflon. The etching was monitored by simultaneous measurements of the electric conductivity using a conductometer (712, Metrohm Ltd., Switzerland) to determine the breakthrough time of pore through membranes. The pore diameters were determined using a scanning electron microscope (SEM). The separation experiments of the blood proteins were performed using a permeation measurement apparatus "Demonstrator" developed by collaboration of GSI and JAERI; the permeation of the proteins through the membranes was determined by a gel permeation chromatography (GPC).

3. Results and Discussion

3.1 Preparation of ion track membranes

Figure 1 shows the pore diameter of PET (38 μm thickness), as a function of etching time in 0.1, 0.2, and 0.3 N NaOH at 70 °C. The PET membranes were irradiated with Xe ions (450 MeV, 1.0 x 10^{10} ions/cm^2 fluence) before etching. The plots of the pore diameter to the etching time exhibited two linear relation

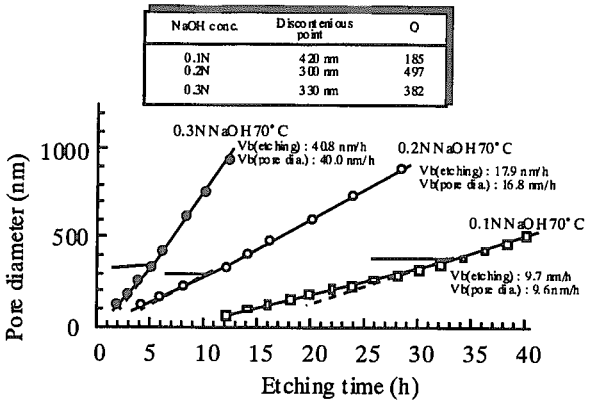


Fig. 1 Pore diameters as a function of time at different etchalant concentrations; (□) 0.1N, (○)0.2N, (●)0.3N. Ion beam:129Xe,450MeV

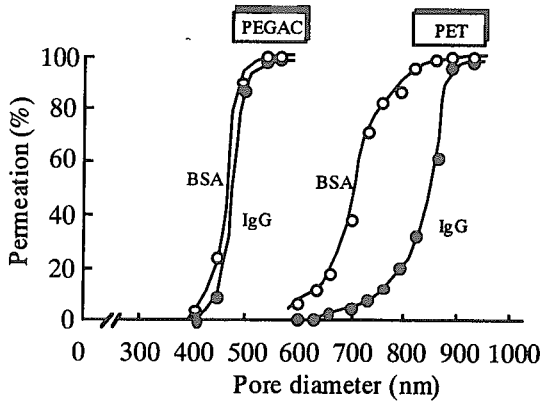


Fig. 2 Permeation of BSA and IgG as a function of pore diameter of ion-track membranes.

regions separated by a discontinuous point (DP). The etching rates at the etching time longer than DPs corresponded to the etching rates of unirradiated PET films. As shown in Figure 1, the pore diameter of DPs of the PET films etched in 0.1, 0.2, and 0.3 N NaOH were 420, 300, and 330 nm, respectively.

Since the damaged region induced by the energy and kind of particles of ion beam the different pore diameters at the DP were considered to be not caused directly by the undamaged regions during etching. On the other hand, the diameter of the DP decreased with the increase of the film sensitivity against the ion beam irradiation (Q value). Therefore, we assume that the DP is probably related to the change in a pore shape, e.g., conical to cylindrical shapes.

3.2 Separation characteristic of peptide molecules of ion track membranes

Permeation experiments of BSA and IgG were performed using the PET membranes prepared by irradiation of Xe ions (450 MeV, 3.0 x 10^6 ions / cm^2 fluence), followed by etching in 0.2 N NaOH at 70 °C. Figure 2 shows the permeation of BSA and IgG through the PET membranes with different pore diameters from 300 to 900 nm. Both peptides can permeate through PEGAC membranes with pore diameter less than 500 nm. However, in the case of PET membranes even with 600-700nm of the pore diameter, the permeations of BSA and IgG are lowed than 20%.

As shown in Figure 2, we can not see any permeation selectivity through PEGAC; permeation of both peptides started at 400 nm and reached to 100 % at about 500 nm in the pore diameter of the membranes. However, with the PET membranes at the 730 nm of pore diameter, the permeation of BSA is 72%, while the permeation of IgG is only 8.3%. In the words, PET membranes shows 9 times higher permeability of BSA to that of IgG.

References

1)M. Asano, Y. Maekawa, R. Spohr and M. Yoshida, International Symposium on "Prospects for Application of Radiation towards the 21st century",P-125~126, March 13-17, Tokyo,Japan(2000)

3.3 Application of Thin Film Dosimeters to Measurement of Ion beam Dose Distribution II

T. Kojima, H.Sunaga, H.Takizawa, H.Hanaya and H.Tachibana
Advanced Radiation Technology Center, JAERI

1. Introduction

Ion beams at the TIARA AVF cyclotron (e.g. $^{1}H^{+}$: max. 90 MeV) have been extensively applied to various material science and biological studies. In these research field, evaluation of absorbed dose and/or dose distribution is essential for interpretation of radiation effects of ion beams on materials or biological substances, taking into account of radiation qualities and non-homogeneity of energy deposition in an interested volume.

Dosimetry required in these research works should cover the dose range of 5 Gy–200 kGy with the precision of ±5% (1σ) and the spatial resolution better than about 1 μm. Thin film dosimeters of about 10-200 μm thick, e.g. alanine-PE and Gafchromic film, have been well-characterized for ^{60}Co γ –rays or MeV electrons and applied also to ion beams[1, 2]. The dose response characteristics of these dosimeters have been studied in the uniform-fluence radiation field under scanning beams as the function of the mass stopping power, involving development of real-time fluence monitoring. The coefficients to convert γ -ray dose/electron dose to ion-beam dose were estimated for values of up to about 10,000MeV/(g/cm^2). The Ion beam dosimetry using film dosimeters has established covering almost all the ions delivered from the cyclotron with overall uncertainty of better than ±5%(1σ), which was estimated by combining uncertainty components in fluence measurement ±2% and film dosimetry ±4% (1σ) in quadrature.

One of these characterized films, the Gafchromic film (MD-1260) having 7-μm thick radiation-sensitive layer on the surface was applied to measure lateral dose distribution.

A potentiality of dose distribution measurement with high spatial resolution of 1-μm was demonstrated by means of feasibility of reading-out of optical density values using analyzing light with 1-μm in diameter.

2.Experimental

The detailed experimental procedure of ion irradiation of films is found in elsewhere[1, 2]. Gafchromic films were irradiated by 450-MeV $^{129}Xe^{23+}$ ions to

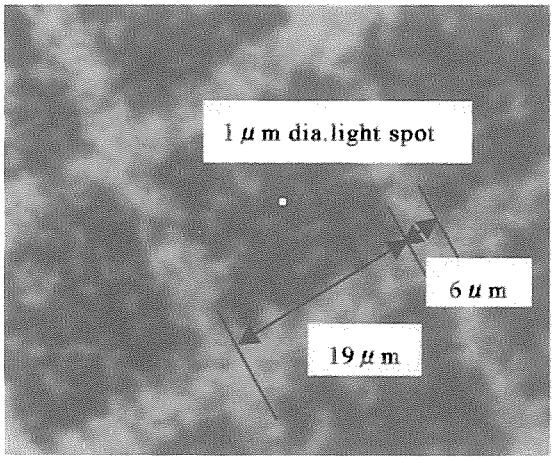


Fig.1.Color change pattern on the Gafchromic film irradiated with 450-MeV $^{129}Xe^{23+}$ ions through the 10-μm thick Cu foil mask.

40-120 Gy through the 10-μm thick Cu foil mask having mesh pattern (line width:6 μm, line-line inner distance: 19μm). $^{129}Xe^{23+}$ ions were chosen because they stop completely in the thin mask. Color of Gafchromic films was analyzed using a microscopic spectrophotometer (HITACHI, U-6500) which has analyzing spot light of 1-μm in diameter.

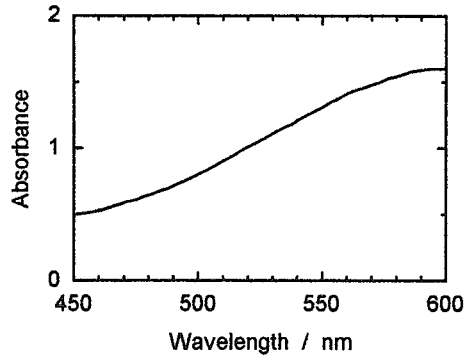


Fig.2 The absorption spectrum of the Gafchromic film(120Gy), which is obtained using 1-μm dia. analyzing light.

3.Results and discussion

The color change pattern on the Gafchromic film irradiated to 120 Gy (about 10^6 ions/cm^2 equivalent) with 450 MeV $^{129}Xe^{23+}$ ions is shown in Fig.1, as an example. Color change patterns relevant to irradiated areas (dark part in Fig.1) were identified with sufficient sharpness of the line edge. The film has a potential to know irradiated area, e.g. nucleus in a cell, with the spatial resolution of about 1μm. Unhomogeneity in coloration may be due to non-uniformity of dye dispersion in a film and/or a few number of ions in 1μm^2.

Analysis of color distribution pattern on a Gafchromic film using the microscopic spectrophotometer with analyzing light of 1-μm in dia. was tried as the base of dose distribution measurement. One example of measured absorption spectra is shown in Fig.2 over the wavelengths of 450-600 nm. The absorbance values were measurable with the precision same as that of a common spectrophotometer having analyzing light of bigger than 50μm in diameter, though they associated with the rather high background absorbance value over the measuring wavelength range. These absorbance values are converted into absorbed doses on the basis of the above -mentioned conversion coefficients.

3.Conclusion

In this study, feasibility of dose distribution measurement with the spatial resolution of 1-μm was demonstrated using Gafchromic films and the microscopic spectrophotometer, though the X-Y scanning system for color profile measurement should be necessary for lateral dose mapping.

The dosimetry technique developed so far meets accuracy and spatial resolution demands for ion beam dosimetry in material science and biological research using a TIARA cyclotron.

References

1)T.Kojima et al.: *Radiat.Phys.Chem.*, **53**, (1998) 115

2)T.Kojima et al.:IAEA-TECDOC-1070 (1999) 197.

3)K.Hata and H.Baba: JAERI-M 88-184 (1988)

4)J.F.Ziegler, J.P.Biersack and U. Littmark : "The stopping power and range of ions in solids", Vol.1(1985) (Permagon Press, Oxford).

5)T.Kojima et al.:JAERI-Conf 2000-1 (2000), 31

3.4 Cross-linking of Polydimethylsiloxane in Heavy Ion Tracks

H. Koizumi, M. Taguchi*, Y. Kobayashi* and T. Ichikawa
Division of Molecular Chemistry, Graduate School of Engineering, Hokkaido University; *Department of Radiation Research for Environment and Resources, JAERI

1. Introduction

Ion beam deposits energy along their ion tracks with high density. The high local dose cause chemical effects differnet from those by γ-rays and fast electrons[1-3]. The high local dose in the ion tracks is higher than the gelation dose for polydimethylsiloxanes. Gelation can hence occur in each ion track, and "gel string" is generated[4-6].

In this study, we have elucidated the relationship between the weight of the gel strings and initial molecular weight of the polymers[6].

2. Experimental

Polydimethylsiloxanes (KF 96, KF 96H) supplied by Shin-Etsu Chemical Co., Ltd. were degassed under vacuum. They were put in metal cells with an aluminum window of 25 μm thickness. 460 MeV $^{40}Ar^{13+}$, 350 MeV $^{20}Ne^{8+}$ and 220 MeV $^{12}C^{5+}$ ions from the cyclotron of JAERI TIARA were irradiated at the HY1 port. The depth of liquid polydimethylsiloxane was made sufficiently larger than the range of the ion beams.

The irradiated samples were dissolved in hexane. The insoluble residue was separated with membrane filters (Millipore LSWP04700, pore size 10.0 μm), and the weight of insoluble residue was measured.

3. Results and Discussion

The weight of the insoluble residue of polydimethylsiloxane irradiated with 256 MeV Ar ion is shown in Fig.1 as a function of the ion fluence. The weight is proportional to the ion fluence. This dependence is different from that for γ-rays and fast electrons: the gel fraction: the gel fraction irradiated with the low LET radiations is negligible below the gelation dose, and increase from the dose and reaches to a constant value.

These results indicate that the gelation occurs in each ion tracks. The number of the gel strings increases with increasing the number of the irradiated ions. The yield of the insoluble residue are tabulated in table 1.

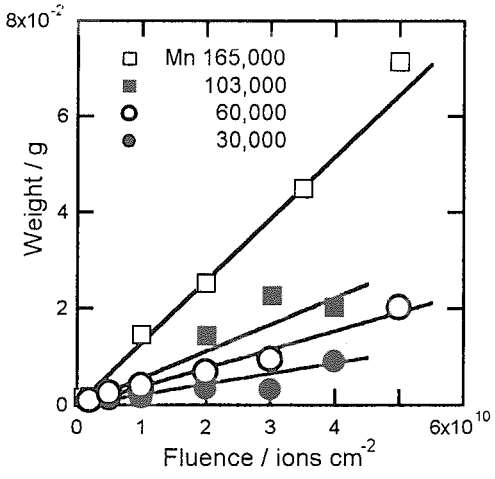


Figure 1. Weight of insoluble residue obtained from polydimethylsiloxanes irradiated with 256 MeV Ar ions. The irradiated area is 19.6 cm^2.

The weight of the insoluble residue increases with increasing the initial molecular weight (M_n) of the polymers. It arises from an increase in the radius of the gel string (r) with increasing M_n. The values of r are calculated with assuming that the length of the gel strings is the range of the ions and the radius is constant over the range. They are shown in table 1. The gelation dose decreases with increasing M_n. Since the dose in an ion track decreases with increasing the distance from the center of the ion track, the area higher than the gelation dose in the ion tracks then increases with decreasing the gelation dose. The radius of the gel strings hence increases.

The radii of the gel strings are estimated from the local dose distribution in the ion tracks and the dose-yield relationship for low-LET radiation. A gel string is generated in each ion tracks due to high local dose in the ion tracks. We assume that the gelation in the ion tracks occurs with the same dose relationship for low-LET radiation[8].

Table 1. Dose of gelation (D_{gel}) and Dose of 90 % gelation ($D_{90\%gel}$) in the radiolysis of polydimethylsiloxanes by low-LET radiation, yield of insoluble residue per ion (Y), and radius of gel strings (r) obtained in the radiolysis by 256 MeV Ar ions.

Viscosity / $mm^2\ s^{-1}$	M_n [a]	L / nm [b]	D_{gel} / Gy [c]	$D_{90\%gel}$ / Gy [d]	Y / g ion^{-1}	r / nm [e]	M_{gel} / g [f]
1,000	30,000	110	3.58×10^{4}	9.20×10^{4}	1.1×10^{-14}	5.1	1.8×10^{-14}
10,000	60,000	230	1.79×10^{4}	4.60×10^{4}	2.0×10^{-14}	6.9	3.6×10^{-14}
100,000	103,000	390	1.04×10^{4}	2.70×10^{4}	2.8×10^{-14}	8.3	6.0×10^{-14}
1,000,000	165,000	630	6.51×10^{3}	1.70×10^{4}	6.6×10^{-14}	13	9.6×10^{-14}

[a] Number-average molecular weight.

[b] The polymer length calculated with the degree of polymerization and the bond length of Si-O.

[c] Gelation dose calculated with G-value of 3.0 for crosslinking G(X) and that of 0.75 for mainchain scission G(s).

[d] Dose of 90% gel fraction.

[e] Value calculated with assuming that the length of the gel strings is the range of 256 MeV Ar ion in polydimethylsiloxane (133 μm), and the radius is constant over the range. The density of the gel strings was assumed to be the same as that of the polymers (0.975 g cm^{-3}).

[f] Weight of a gel string calculated from the radii in Fig. 4 and the density of the polymers (0.975 g cm^{-3}).

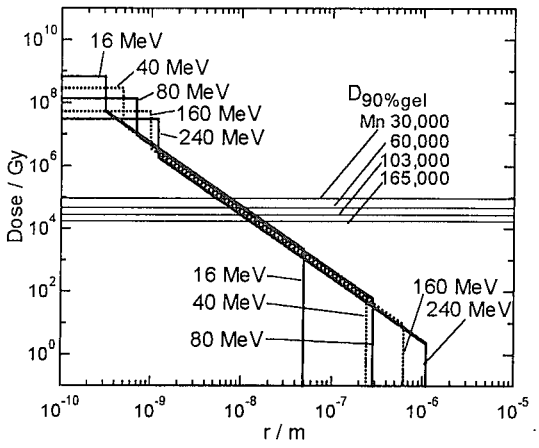


Figure 2. Radial dose distribution for Ar ions in polydimethylsiloxane. Dose of 90 % gelation ($D_{90\%gel}$) for low-LET radiation are indicated.

Radial dose distribution for Ar ions in polydimethylsiloxane is shown in Fig.2. It is calculated with the equation proposed by Chatterjee and Schaefer[9]. Dose of 90 % gelation for low-LET radiation are also indicated. The radii of the 90 % gelation were calculated with the dose distribution, and were plotted in Fig. 3. The radii were comparable with the experimental radii of the gel strings.

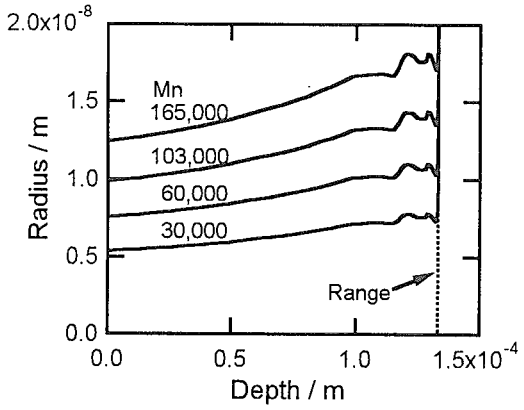


Figure 3. Radius at which dose in the ion tracks becomes the dose of 90 % gel fraction plotted as a function of depth from the surface of the polymer.

The weight of the gel strings generated by 350 MeV $^{20}Ne^{8+}$ and 220 MeV $^{12}C^{5+}$ ions was 5-10 times larger than that by the Ar irradiation. It will arise from the larger range of the ions. The radii of the gel strings were smaller than the radius for the Ar irradiation: 2-5 nm for the polymers with M_n of 60,000.

References

1) H. Koizumi, M. Taguchi, H. Namba, T. Ichikawa, H. Yoshida, Nucl. Instr. and Meth. B, **132** (1997) 633.

2) H. Koizumi, T. Ichikawa, H. Yoshida, H. Namba, M. Taguchi, and T. Kojima, Nucl. Instr. and Meth. B, **117** (1996) 431.

3) H. Koizumi, T. Ichikawa, H. Yoshida, H. Shibata, S. Tagawa, and Y. Yoshida, Nucl. Instr. and Meth. B, **117** (1996) 269.

4) H. Koizumi, M. Taguchi, and T. Ichikawa, TIARA Annual Report 1998, JAERI-Review 99-025 (1999) 93.

5) H. Koizumi, M. Taguchi, Y. Kobayashi, and T. Ichikawa, TIARA Annual Report 1999, JAERI-Review 2000-024 (2000) 91.

6) H. Koizumi, M. Taguchi, Y. Kobayashi, and T. Ichikawa, Nucl. Instr. and Meth. B **179**(2001) 530.

7) C. G. Delides, Radiat. Phys. Chem. **16** (1980) 345.

8) A. Chatterjee and H. J. Schaefer, Radiat. Environ. Biophys. **13** (1976) 215.

3.5 Nano-wire Formation along Ion Projectiles in Polysilane Thin Films

S. Seki[a], K. Maeda[a], Y. Yoshida[a], S. Tagawa[a], M. Sugimoto[b], and S. Tanaka[b]
[a]The Institute of Scientific and Industrial Research, Osaka University.
[b]Department of Material Development, JAERI, Takasaki

Introduction

Polysilane derivatives are themselves one dimensional semiconducting wires that exhibit interesting features such as thermo- and solvato-chromism [1,2], nonlinear optical property [3], and photoconductivity [4]. These features of polysilanes have been ascribed to the σ electrons delocalized along the skeleton. The UV-light induced reactions in polysilanes have been widely studied because of their high efficiency of main chain scission [5]. We reported the radiation effects of ion beams on polysilanes and the dependence of reaction processes on LET (linear energy transfer: energy deposition rate of incident particles per unit length) of the characteristic radiation [6]. Polymers seem to be cross-linked by high LET ion beam irradiation. On the other hand a main chain scission reaction was predominantly seen for low LET radiation. The difference in radiation induced reactions was ascribed to a variation of density of reactive intermediates. The spatial distribution of deposited energy by charged ions played a significant role in promoting chemical reactions in the target materials [7-11], and we suggested that the ion beam produced a non-homogeneous field of chemical reactions, where the reactive intermediates produced by an incident ion are radially distributed from the projectile. The size of the field depended not only on LET but also on the kind of reactive intermediate species. It is called as "chemical track radii" which should be defined for each target materials.

Experimental

poly(methylphenylsilane) (PMPS) was synthesized by the reaction of methylphenyldichlorosilane with sodium in refluxing toluene or *n*-undecane (Kipping method). The reaction was carried out under an atmosphere of predried argon with or without 12-crown-4 ether. The PMPS was fractionated by separatory precipitation leading to **PS1** (Mn = 4.6 ~ 2.2 x 10^5), **PS2** (Mn = 1.5 ~ 1.1 x 10^5), **PS3** (Mn = 2.6 ~ 2.1 x 10^4), **PS4** (Mn = 1.0 x 10^4 ~ 9.0 x 10^3), and **PS5** (Mn = 5.0 ~ 4.0 x 10^3) with small dispersion less than 1.5. PMPS was spin-coated on Si substrate which had been treated by NaOH solution in ethanol/water = 1/1 during 5 min. These films were irradiated in a vacuum chamber (< 1 x 10^{-6} hPa) with ion beams listed in the table from a cyclotron accelerator at Japan Atomic Energy Research Institute, Takasaki Radiation Chemistry Laboratory. The irradiated films were developed by acetone, diethylether, dibutylether, and benzene in this order, respectively for 2 min. AFM measurements were performed at RT and in air using Seiko Instruments SPI-3800.

Results and discussion

Cross-linking reactions in a polysilane thin film is revealed to occur within chemical track, which

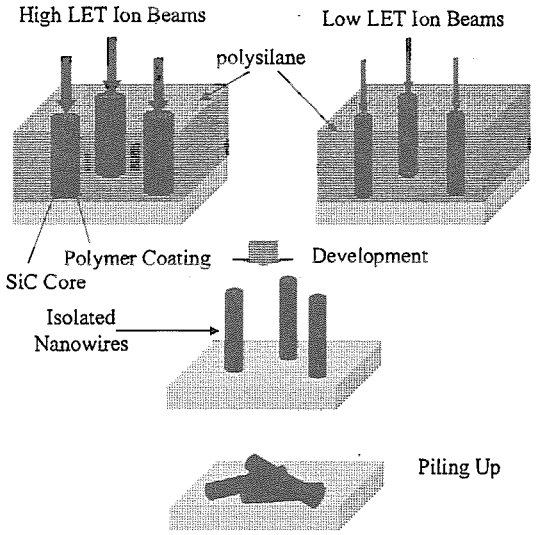


FIG 1. Schematic view showing the formation of nanowires in a polysilane thin film. Development gives individual nanowires and the number density of wires.

renders the film insoluble against any kinds of solvents. The following equations give good interpretation to the gelation in polysilane films [6],

$$s = \{1-(r+\delta r)\}^f$$

$$g = 1-\{1-(r+\delta r)\}^f$$

where s and g denote the fraction of sol and gel, respectively, r is the radius of a chemical track determined by the energy deposition rate of an incident ion, δr is the differential radius of the track which depends on the shape and size of a individual polymer molecule, and f is the fluence of the incident ion beams. The schematic of the gelation in the polymer system is presented in figure 1. An incident ion densely deposits its energy within a limited area, and a cross-linked, cylinder-like polymer gel is formed along the projectile. The uncross-linked part of a film is washed by solvent, leading to the isolated nanowires of cross-linked polysilanes. The wires are piled up by the procedures when the film is irradiated at high fluence of ion beams, thus we can determine the size of a nanowire by trace of the gel fraction. The estimated values of the nanowire radii are summarized in the table for PMPSs.

Table Chemical core sizes in PMPS with different molecular weights for a variety of ion beams.

Ion Beams	LET	$r+dr$ [a] (nm)				
	(eV/nm)	PS1	PS2	PS3	PS4	PS5
450 MeV Xe	8500	13.4	-	9.3	-	7.4
520 MeV Kr	4100	10.2	-	8.9	-	6.7
175 MeV Ar	2200	6.3	5.9	-	5.1	4.3

a $r+dr$ denotes the radius of a chemical track, i.e., the radius of a nanowire formed by each ion beam.

The radii apparently increase with an increase in the LET of ion beams and the molecular weight of a target polymer: PMPS, representing that the diameter of a nanowire is perfectly under control. The IR spectra of the irradiated products showed the typical features of β-SiC ceramics [12], however the ratio of β-SiC conversion did not reach to 100 % for all the specimens (~25 % for **PS1** and ~65 % for **PS5** upon irradiation to 450 MeV $^{129}Xe^{23+}$). Thus the β-SiC ceramic structure is formed only at the center part of each nanowire because of the extremely high energy density. The conversion ratio also estimates the corresponding size of SiC core for PS1 (11.8 nmϕ) and PS5 (12.4 nmϕ). This suggests that the β-SiC core size: r depends only on LET, and the thickness of the cross-linked polymer coating: δr can be individually controlled by the molecular weight of the polymer.

The variation of δr in **PS1-PS5** is discussed based on the theoretical aspects on the physical interaction of ion beams to a matter. The following formulas were already given on the values of the coaxial energy in an ion track [12],

$$\rho_c(r) = \frac{LET}{2}\left[\pi r_c^2\right]^{-1} + \frac{LET}{2}\left[2\pi r_c^2 \ln\left(\frac{e^{1/2} r_p}{r_c}\right)\right]^{-1} \qquad r \le r_c$$

$$\rho_p(r) = \frac{LET}{2}\left[2\pi r^2 \ln\left(\frac{e^{1/2} r_p}{r_c}\right)\right]^{-1} \qquad r_c < r \le r_p$$

where ρ_c and ρ_p are the deposited energy density at core and penumbra area, respectively, r_c and r_p are the radii of core and penumbra area, e is an exponential factor. The equations give a value of deposited energy density at a boundary of a nanowire by using its radii. The density is estimated as 1.2 ~ 1.6 eV/nm^3 for all the ion beams in **PS5**. The small discrepancy in the density indicates that the radial distribution of deposited energy influences the size of a nanowire and its surface structure. The density (~1 g/cm^3) and molecular weight of **PS5** give the volume of a molecule roughly as 10^2 nm^3. The deposited energy per molecule is ~150 eV indicating that the ion beams form only a few cross-linking points at the boundary because the G-value of cross-linking (number of reactions per absorbed 100 eV) has been already reported as 0.5~1. Thus simple cross-linking of polymer molecules occurs at the nanowire surface. It suggests the structure of a nanowire having a β-SiC core lapped by the cross-linked polysilanes.

Figure 2 shows a scanning electron microscope (SEM) image for the nanowires formed on a Si substrate. We have already reported the formation of nanowires of which shape was noodle-like (warm-like) one on Si substrate [13], however the structure turns into rigid rod-like one by changing the polymer molecular weight and the target film

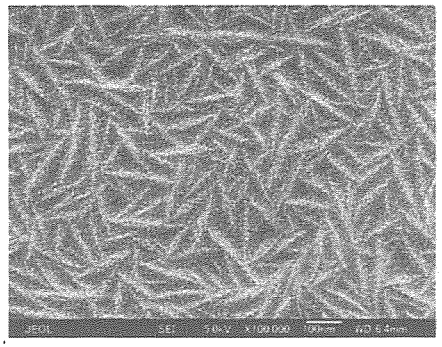


FIG 2. A SEM image of standing nano-wires on a Si substrate. The nano-wires were formed by the 450 MeV $^{128}Xe^{23+}$ irradiation to a poly(methylphenylsilane) thin film (200 nm thick) at 3.2 x 10^8 ions/cm^2.

thickness as displayed in the figure. The nanowires are also controlled as standing on the substrate even after the development by the solvent, which is shown in figure 3. Control in the aspect ratio plays a significant role to realize the standing nanowires, and the ratio is kept below 4/1 in the present system. Almost all the other nanowires are laid on the substrate after the development when the ratio exceeds ~ 4/1. The adhesion of the nanowires to the substrates will be the important feature of the present technique in view of their application on the nano-fabrication. The number of observed nanowires in a unit area shows good agreement with that of incident particles. In spite of a development procedure by solvents, the wires remain adhered to the Si substrate and the nanowires remain isolated from each other. This indicates that

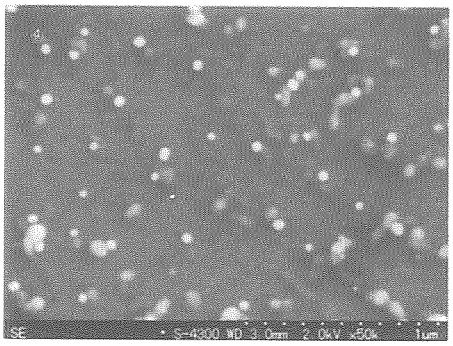


FIG 3. A SEM image of standing nano-wires on a Si substrate. The nano-wires were formed by the 450 MeV $^{128}Xe^{23+}$ irradiation to a poly(methyl phenylsilane) thin film (80 nm thick) at 3.2 x 10^8 ions/cm^2.

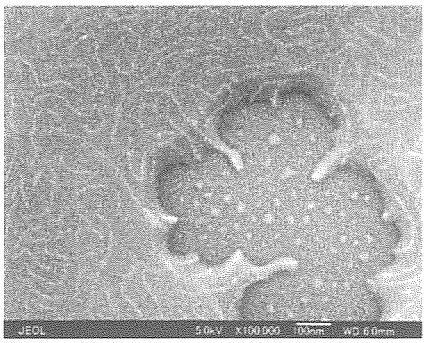


FIG 4. A SEM image of nano-wires on a Si substrate. The nano-wires were formed by the 450 MeV $^{128}Xe^{23+}$ irradiation to a poly(methyl phenylsilane) film (~1 μm thick) at 1.9 x 10^8 ions/cm^2. The image was recorded on the way of the development procedure by benzene.

one end of the wire is tightly connected to the substrate by chemical bonds. Figure 4 indicates the structure of long-nanowires which is recorded on the way of the development procedure. The image clearly shows the bonding structures of one end to the Si substrate, and it is concluded that the adhesion prevents the nanowires from the desertion during the developments, and also from the aggregation of themselves.

Conclusion

The ion beam irradiation is very unique and powerful technique to produce nano-sized cylindrical structures as displayed in the present study. It not only produces isolated nanowires on Si surface but also controls their size and length of wires. The size-controllability is also supported by the theoretical models of an energy distribution in a single ion track. We believe that the present technique has the potential to be developed for producing nano-structure materials other than SiC nanowires in the future.

References

1) Trefonas III, P., Damewood, J. R., & West, R. *Organometallics* **4**, 1318-1319 (1985).
2) Harrah, L. A. & Zeigler, J. M. *J. Polym. Sci., Polym. Lett. Ed.* **23**, 209-211 (1985).
3) Kazjar, F., Messir, J., & Rosillio, C. *J. Appl. Phys.* **60**, 3040-3044 (1986).
4) Kepler, R. G., Zeigler, J. M., Harrah, L. A., & Kurtz, S. R. *Phys. Rev.* **B35**, 2818-2822 (1987).

5) Trefonas III, P., West, R., & Miller, R. D. *J. Am. Chem. Soc.* **107,** 2737-2742 (1985).
6) Seki, S., et al. *J. Phys. Chem.* **B103**, 3043-3048 (1999).
7) Magee, J. L. & Chattarjee, A. Kinetics of Nonhomogenious Processes, G. R. Freeman Ed., Chapter 4, p.171-214 (1987).
8) LaVerne, J. A. & Schuler, R. H. *J. Phys. Chem.* **98**, 4043-4049 (1994).
9) Kobetich E. & Katz, R Phys. Rev. **170**, 391-396 (1968).
10) Wilson, W. E. *Radiat. Res.* **140**, 375-381 (1994).
11) Varma, M. N., Baum, J. W., & Kuehner, A. J. *Radiat. Res.* **62**, 1-11 (1975).
12) Seki, S., et al. *Radiat. Phys. Chem.* **48**, 539-544 (1996).
13) Seki, S. et al. *Adv. Mater.* in press.

3.6 Primary Process of Radiation Chemistry Studied by Ion Pulse Radiolysis

Y.Yoshida[1], S. Seki[1], A. Saeki[1], K. Okamoto[1], S. Tagawa[1], M. Taguchi[2], H. Namba[3]

[1]ISIR, Osaka University.

[2]Department of Radiation Research for Environment and Resources, JAERI

[3]Department of Material Development, JAERI

1. Introduction

Radiation effect of high energy high LET ion beams on the material is very interesting and was investigated by many researchers, because the highly-densed irradiation makes the different effect from that by low-LET radiation, such as γ rays. We have been studied the primary process of the ion beam-induced radiation chemistry by using the technique of ion beam pulse Radiolysis for emission spectroscopy[1-3].

The lifetime of excimer in solid polystyrene was a constant (20ns), which did not depend on the values of LET. However, the lifetimes of polystyrene excimer were changed in the liquid phase. Figure 1 shows the time-dependent behavior of the emission from polystyrene excimer obtained in 520 MeV Kr^{+20} ion pulse radiolysis of 3, 10, and 100 mM polystyrene solutions in cyclohexane monitored at 330 nm [1]. The emission intensities at various concentrations were normalized at the ion pulse end. In 100 mM solution, the lifetime of polystyrene excimer was 20 ns, which was agreement with the lifetime of solid polystyrene excimer. In 10 and 3 mM, the fast and the slow decay components were observed. The lifetimes of the slow components corresponded to 20 ns. The ratio of emission intensity of the fast component to that of the slow component increased with decreasing of the concentration of polystyrene.

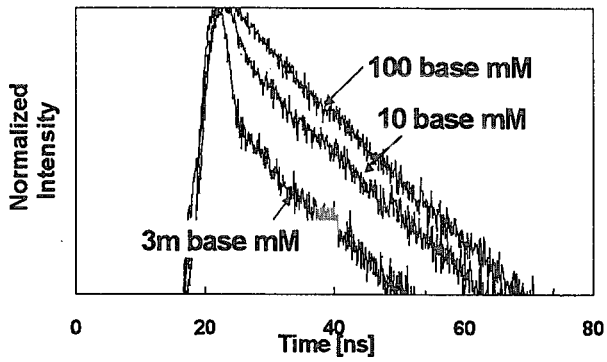


Fig. 1 Time-dependent behavior of polystyrene excimer obtained in 520 MeV Kr^{+20} pulse radiolysis of polystyrene solution in cyclohexane monitored at 330 nm

If the fast and slow components are given by polystyrene excimer, the difference can be explained by a reaction of polystyrene excimer with other short-lived intermediates. To confirm the reaction, ion beam-induced emission spectra in polystyrene-cyclohexane system were observed by using a streak camera with a monochorometor. The spectra showed the polystyrene excimer as well as solid polystyrene. Therefore, polystyrene excimer in cyclohexane reacts with other short-lived intermediates in the short time region.

In this paper, the primary process of radiation chemistry on the LET effect is discussed base on the date obtained in the ion beam pulse radiolysis.

2. Results and Discussion

In solid polystyrene, polystyrene excimer is produced in the following reaction scheme as shown in Fig. 2. The polystyrene excimer (PS_2^*) is formed through monomer excited state (PS^*) or through the geminate ion recombination of an electron and dimmer a cation radical of polystyrene ($PS_2^{\cdot+}$). Although yields of polystyrene excimer should be changed by the LET effect, the quantitative experiment has not been done in the ion beam pulse radiolysis. However, It means that polystyrene excimer does not react with other polystyrene excimer, because the polystyrene excimer is very stable in solid phase. Therefore, the LET effect on the lifetime of the polystyrene excimer was not observed.

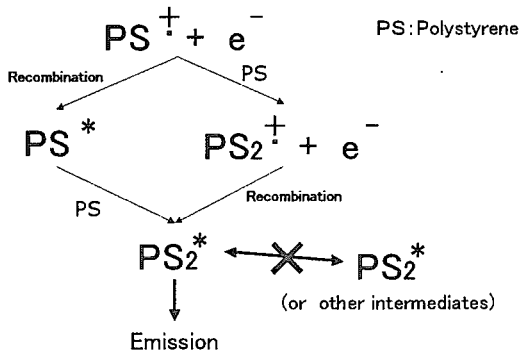


Fig.2 Reaction Mechanism in Solid Polystyrene.

On the hand, the reaction mechanism of polystyrene is very complicated in alkane liquid, as shown in Fig. 3. There are two formation processes of polystyrene excimer (PS_2^*) from excited state (PS^*) and through dimmer cation radical ($PS_2^{\cdot+}$) as well as in solid polystyrene. The PS^* is partially formed by the energy transfer from the excited state of alkane (RH^*) which is mainly produced through the geminate ion recombination of $RH^{\cdot+}$ and electron.

The LET effect on the time-dependent behavior of polystyrene excimer as shown in Fig. 1 should be caused by following reaction.

$$X + PS_2^* \rightarrow ? \quad (1)$$

Where, X means an unknown short-lived intermediate such as RH^*. The Polystyrene excimer does not react other polystyrene excimer, because the reactivity is not so high even in liquid phase.

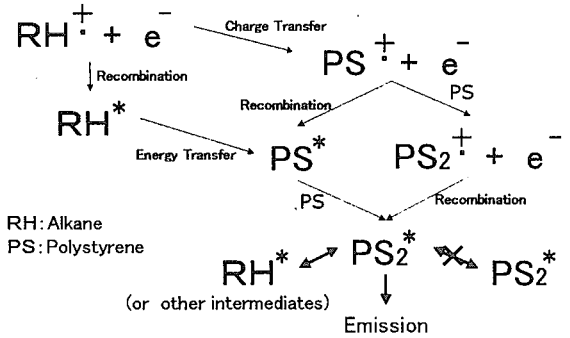


Fig.3 Reaction Mechanism in Polystyrene −alkane solution.

To discuss the whole process of the LET effect on ion beam-induced reaction, the behavior of electron and cation radical are very important which are first intermediates produced by ion beam, because the higly-densed excitation effect is decreased with the time by the diffusion motion.

The geminate ion recombination in a spur has been studied by using subpicosecond and picosecond pulse radiolysis. The kinetics of the recombination can be analyzed by the Smoluchowski equation based on the diffusion theory. However, the theory can not be applied to the truck model. The new theory will be necessary to elucidate the problem. Recently, the simulation method for the multi-ion pair model has been developed to analyze the pulse radiolysis date. The LET effect can be analyzed by using the simulation technique.

Although the LET effects on the geminate ion recombination are very important phanomena, the experiment has not been done. Only by ion beam pulse radiolysis for absorption spectroscopy will make a clear of the primary process. There are many problems for the absorption spectroscopy, such as the ion beam intensity, the penetration of the ion beam into material, the light source, and so on. To solve the problem, we will start the preliminary experiment near future.

References

1) H. Shibata et al. Nuclear. Instrum. Meth.,A327, 53, 1993
2) Y. Yoshida et al., Nuclear. Instrum. Meth, A327, 41, 1993
3) H. Shibata et al., Nucl. Instrum. Meth., B105, 42, 1995

3.7 Measurement of energy deposition around the heavy ion trajectory by photon counting method.

M.Taguchi[a], H.Namba[b], and S.Ohno[c]
[a]Department of Radiation Research for Environment and Resources, JAERI,
[b]Department of Material Development, JAERI,
[c]Theoretical Radiation Research Laboratory.

1.Introduction

It is well known that irradiation effects of heavy ions on chemical substances and living things are more complicated than that of low LET radiations. The characteristic irradiation effects of heavy ions are considered to be caused by heterogeneous and high-dense energy distribution around heavy ion trajectory. We have been studying on spatial distribution of energy deposited by high energy heavy ions traveling through matters[1,2]. The distribution of deposit-energy for various ions can be estimated by the theoretical equations in water, which is the main component of living bodies.

In the present report, we measured numbers of photons from the gaseous nitrogen irradiated with 330-MeV Ar^{11+} ions by the photon counting system to estimate the contribution of total and low energy electrons to energy deposition in order to understand track structure in detail.

2.Experimental

Ion irradiation and light emission measurement were performed at the beam port of HX-1 in TIARA facility, which is called the Experimental Apparatus for Basic study of Radiation Chemistry with Heavy Ions (EA-BRACHI)[1,3]. Ar^{11+} ions with 330-MeV energy were induced through a tantalum collimators with 2 mm hole, which was sealed with Kapton film (7.5 μm thick) to keep the gas pressure in the target chamber, set on the upper streams of the ion beam to the target chamber. The pressure of nitrogen gas was controlled to 100-360 Torr at ambient temperature, using pressure sensors, a throttling valve, pressure controller and mass flow controller that previously described[3]. The fluence of the Ar ion was measured by counting photons from plastic scintillators induced by one Ar ion irradiation, or counting Ar ions directory by channeltron detector before and after the photon counting measurements, and was 1×10^6 ions/sec. Optical system was constructed with lens and three slits to collect photons of the excited nitrogen molecules from the restricted area. The space resolution of the area was 2 mm. The distance of the restricted area from the center of the ion beam was changed with moving target chamber itself. The optical system was placed at the radial distance of from –2 mm to 50 mm. The photons were measured by a single photon counting system with a photomultiplier tube (PMT).

3.Results and Discussion

Figure 1 shows light emission spectrum of gaseous nitrogen at 760 Torr irradiated with 330 MeV Ar^{11+} ions. Several emission bands are clearly observed in the spectrum. Similar bands of nitrogen have been observed in the electron irradiation experiment[4]. All these light emission bands measured here could be ascribed to either the second positive transitions of nitrogen molecules ($C^3\Pi_u$-$B^3\Pi_g$) or the first negative transitions of nitrogen molecular ions. The (0,0) transition of the first negative system of nitrogen molecular ion observed at the wavelength of 429 nm has an excitation cross section proportional to the total ionization cross section[5]. Therefore, the analysis of this transition will be important to evaluate the yields of total ion pairs, which corresponds to the ionization measurements performed previously[1,2]. On the other hand, the

(0,0) transition of the second positive system of nitrogen molecules observed at 337.1 nm is known to be induced exclusively by low energy electrons at about 20 eV[6]. Thus it is suitable for estimation of the contribution to the energy deposition from the low energy electrons.

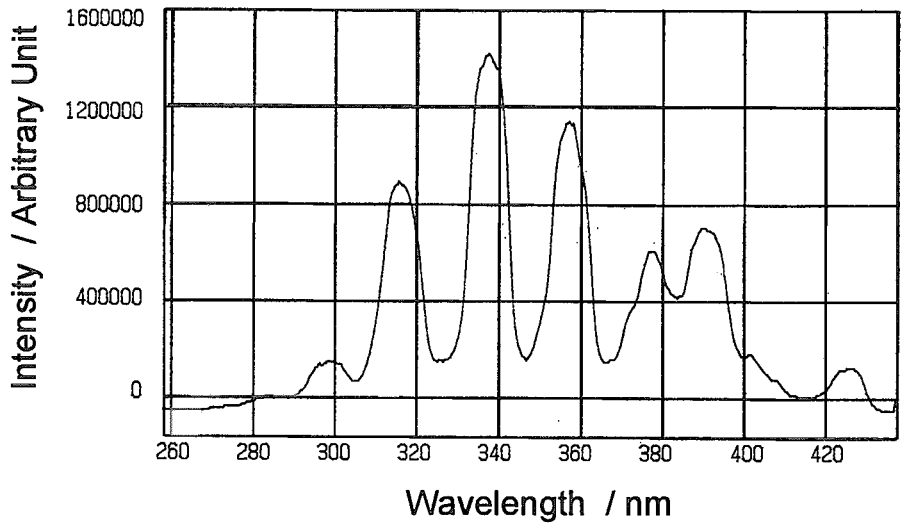


Figure 1 Fluorescence spectrum of gaseous nitrogen irradiated with 330-MeV Ar^{11+} ions.

The distance from the ion beam reduced to the unit density, r (mm), is expressed with the distance from the ion beam in gas, r_{gas} (mm)

$$r = r_{gas} \times \rho_{gas} / \rho_{water} \quad (1)$$

where ρ_{gas} is the density of the gas and r_{water} is the unit density ($1 g/cm^3$). The relative emission density at distance r, D(r), is expressed as follows:

$$D(r) = N_p / F_i / \rho_{gas} \times (\rho_{water} / \rho_{gas})^2 \quad (2)$$

where N_p is number of photons measured by the photomultiplyer, F_i is ion fluence.

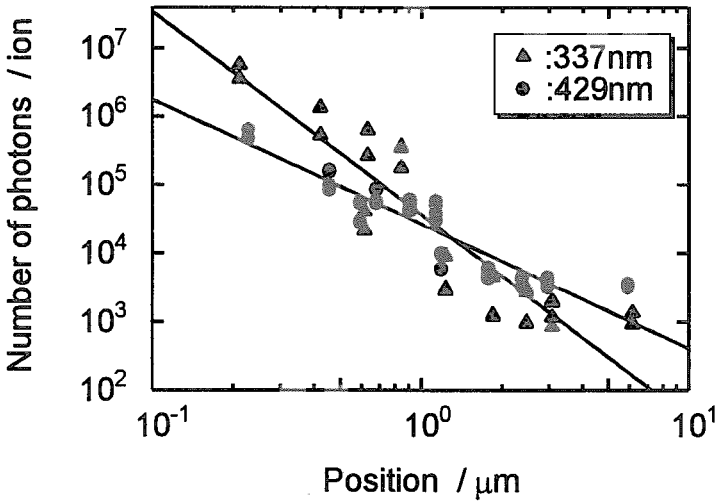


Figure 2 Distribution of intensities of light emissions at 337 and 429 nm around 330 MeV Ar ion trajectory in nitrogen at unit density.

Figure 2 shows the relative emission density in water of low energy secondary electron around the trajectory of 330-MeV Ar ion obtained with the equations. D(r) of 429-nm light emission decreased as the reciprocal square of the normalized distance. This slope is almost the same as that of dose measured by ionization chambers[1,2]. D(r) of 337-nm light emission decreased steeper than that of the total ionization.

References

1) M.Taguchi, *et al.*, *Radiat. Phys. Chem.*, **55**, 511 (1999).

2) S.Ohno, *et al.*, *Radiat. Phys. Chem.*, **55**, 503 (1999).

3) M.Taguchi, *et al.*, *JAERI-Review*, **2000-024**, 99 (2000).

4) P.P.Panta, *et al.*, *Radiat. Phys. Chem.*, **46**, 1259 (1995).

5) M.Imai and W.L.Borst, *J. Chem. Phys.*, **61**, 1115 (1974).

6) W.L.Borst and E.C.Zipf, *Phys. Rev.*, **A1**, 834 (1970).

4. Inorganic Materials

4.1 He Ions Implantation Effect on the Thermal Diffusivity of CVD-SiC ····· 135
T.Taguchi, N.Igawa, and S.Jitsukawa
4.2 Effects of Helium Embrittlement on Fatigue Properties of Reduced Activation Ferritic/Martensitic Steel ····· 138
T.Hirose, H.Tanigawa, M.Ando, E.Wakai, Y.Miwa, S.Jitsukawa, Y.Katoh, A.Kohyama, and M.Narui
4.3 Effects of Triple Beams on Microstructural Evolution in Ferritic/Martensitic Steels····· 141
E.Wakai, T.Sawai, A.Naito, K.Kikuchi, S.Jitsukawa, S.Yamamoto, H.Naramoto, S.Yamashita, Y.Masumoto, K.Oka, and S.Ohnuki
4.4 Investigation of the Resonant Vibration Modes of Self Interstitial Atoms in Metals by Low Temperature Specific Heat Measurement ····· 144
M.Watanabe
4.5 Study of Ion-induced Structural Changes in Li_2TiO_3 Ceramics ····· 146
T.Nakazawa, V.Grismanovs, D.Yamaki, Y.Katano, T.Aruga, A.Iwamoto, and S.Jitsukawa
4.6 Damage Evolution in High Energy Multi Ion-irradiated BCC Metals and the Interaction between Gas Atoms (H and He) and Damage Defects ····· 149
Y.Shimomura, I.Mukouda, D.Yamaki, T.Nakazawa, T.Aruga, and S.Jitsukawa
4.7 Dose Rate Effects on Microstructural Evolution in Austenitic Stainless Steels under Ion Irradiation ····· 152
N.Sekimura, T.Okita, A.Kurui, Y.Hashimoto, S.Jitsukawa, T.Sawai, Y.Miwa, S.Hamada, S.Saitoh, and K.Kikuchi
4.8 Effect of Simultaneous Ion Irradiation on Microstructural Change of SiC/SiC Composites at High Temperature····· 155
T.Taguchi, E.Wakai, N.Igawa, S.Nogami, A.Hasegawa, L.L.Snead, and S.Jitsukawa
4.9 Radiation Induced Cavity Formation in F82H with Various Heat and Mechanical Treatments ····· 158
T.Sawai, E.Wakai, T.Tomita, A.Naito, and S.Jitsukawa
4.10 Comparison of Cavity Formation Behavior in RAF/M Steels Irradiated with Dual Beams of Fe +He Ions as Observed in the Depth Dependent Damage Structure ····· 161
A.Naito, S.Jitsukawa, E.Wakai, T.Sawai, I.Ioka, and H.Tanigawa
4.11 Investigation of Hardness Changes on Helium-ion Implanted Iron by Ultra-micro-hardness Testing····· 164
H.Tanigawa, S.Jitsukawa, H.Abe, T.Iwai, and Y.Katoh
4.12 Effect of Ion Irradiation on Corrosion Behavior of Austenitic Stainless Steel····· 167
I.Ioka, S.Hamada, M.Futakawa, A.Naito, K.Kiuchi, S.Kuroiwa, S.Miyamoto, and K.Ogura
4.13 Effect of Radiation on Microstructures and Corrosion Resistance of Austenitic Stainless Steels ····· 170
S.Hamada, A.Naito, C.Kato, and K.Kiuchi
4.14 Nucleation and Growth of Carbon Onions in Cu and Au under Ion Implantation····· 173
H.Abe, S.Yamamoto, A.Miyashita, and H.Itoh
4.15 Thermal Response of the Metal/Fullerite Hybrid Assembly ····· 176
J.Vacik, H.Naramoto, K.Narumi, Y.H.Xu, S.Yamamoto, and H.Abe

4.16 Deposition and Characterization of Carbon Films Prepared by Ion-bombardment-assisted Method ····· 179
X.D.Zhu, Y.H.Xu, H.Naramoto, K.Narumi, A.Miyashita, and K.Miyashita
4.17 Evolution of Co+C_{60} Structures during Co-deposition and Subsequent Annealing ····· 181
V.Lavrentiev, H.Abe, S.Yamamoto, H.Naramoto, K.Narumi, and K.Miyashita
4.18 Modification of Carbon Related Films with Ion Beams ····· 183
H.Naramoto, Y.Xu, K.Narumi, X.Zhu, J.Vacik, S.Yamamoto, and K.Miyashita
4.19 Formation Process and Stability of Radiation-induced Non-equilibrium Phase in Silicon ····· 186
M.Takeda, T.Suda, S.Watanabe, S.Ohnuki, and H.Abe
4.20 Improvement in Surface Roughness of Nitrogen-implanted Glassy Carbon by Hydrogen Doping ····· 188
K.Takahiro, N.Takeshima, K.Kawatsura, S.Nagata, S.Yamamoto, K.Narumi, and H.Naramoto
4.21 Temperature Dependence of Growth Process of C_{60} Thin Films on a KBr(001) Surface ····· 190
K.Narumi, and H.Naramoto
4.22 Thermal Relaxation of Hydrogen Disordering in Palladium-hydrogen System Irradiated with Energetic Electrons ····· 193
K.Yamakawa, Y.Chimi, K.Adachi, N.Ishikawa, and A.Iwase
4.23 Anomalous Change in Electrical Resistivity in $EuBa_2Cu_3O_y$ Superconductor Irradiated with Energetic Electrons ····· 195
N.Ishikawa, Y.Chimi, A.Iwase, H.Wakana, T.Hashimoto, and O.Michikami
4.24 Defect Accumulation in Nanocrystalline Gold Irradiated with Electrons at Low Temperature ····· 197
Y.Chimi, A.Iwase, N.Ishikawa M.Kobiyama, T.Inami, and S.Okuda
4.25 Epitaxial Anatase and Rutile TiO_2 Films Prepared by Pulsed Laser Deposition ····· 199
S.Yamamoto, T.Sumita, T.Yamaki, H.Abe, A.Miyashita, and H.Itoh
4.26 Effect of Fluorine-ion Implantation in TiO_2 Rutile Single Crystals ····· 201
T.Yamaki, T.Sumita, S.Yamamoto, H.Abe, A.Miyashita, and H.Itoh

4.1 He ions implantation effect on the thermal diffusivity of CVD-SiC

T.Taguchi, N.Igawa and S.Jitsukawa
Department of Materials Science, JAERI/Tokai

1. Introduction

Ceramic matrix composites show excellent mechanical properties at high temperature. These composites, therefore, are expected to be used for structural applications at high temperatures. In particular, SiC/SiC composite is expected to be used for first wall and blanket components in a fusion reactor because of low activation. In the fusion reactor, the material has to have high thermal diffusivity for heat exchange and thermal shock.

Under fusion conditions, He and H are produced by 14MeV neutron-induced transmutation reactions which are (n, α) and (n,p), respectively. These transmutation rates in SiC are larger than those in other candidate materials such as ferritic steels and vanadium alloys.[1,2] It is important to investigate He and/or H effects on the thermal and mechanical properties. In this study, we investigated He ions implantation effect on the thermal diffusivities of CVD-SiC.

2.Experimental procedure

2.1 Materials

The β -SiC was fabricated by Chemical Vapor Deposition method and obtained from Toshiba Denko Co. Ltd., Japan. The density was 3.21 g/cm^3. The specimen size was 10mm in diameter and 0.7 mm in thickness.

2.2 Measurement of thermal diffusivity and thermal conductivity

The thermal diffusivity of the specimens was measured in the temperature range from 15 to 1100 ℃ using a laser flash thermal diffusivity analyzer (PS-2000, Rigaku Co. Ltd., Japan) with a ruby laser of 20 J in the maximum power. The transient temperature response at the rear surface of the specimen was monitored with an IR detector. The thermal diffusivity, α , was obtained by $t_{1/2}$ method using the following equation:

$$\alpha = 1.388L^2/\pi^2 t_{1/2} \quad (1)$$

where $t_{1/2}$ is the time required to reach half of the total temperature rise on the rear surface of the specimen, and L is the specimen thickness.

2.3 Implantation

An irradiation apparatus was installed in Light Ion Room No.2 of cyclotron facility at TIARA. β -SiC was irradiated by 50 MeV He ions for 19 hours with this apparatus using an Al-foil energy degrader in order to obtain the uniform He distribution in the specimens.

The distribution of He concentration was calculated by TRIM code[3] (see Fig.1). In this study, the beam current was about 0.4 μ pA/cm^2 and the irradiation time was about 19

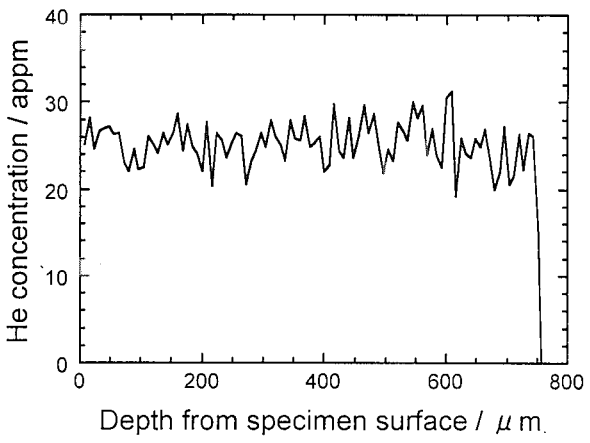


Fig.1 Depth distribution of He in CVD-SiC calculated by TRIM code.

hours. It was found that He^- ions could be implanted uniformly in the specimen toward the depth of about 760 μ m. He ions were implanted up to approximately 25.5 appm.

3. Results

Figure 2 shows the measured results of thermal diffusivities of the CVD-SiC. The thermal diffusivities of CVD-SiC decreased after implantation of He^- ions. He atoms combine with lattice defects easily and become stable because they are not soluble in SiC. Consequently the thermal diffusivities of He implanted specimens decreased. The thermal diffusivity of CVD-SiC measured in the 2nd run was higher than that measured in the 1st run. It is reported that He release from SiC started at 500 ℃ and tended to increase with increasing temperature[4]. The specimen was heated up to 1100 ℃ during the 1st measurement. Therefore, the thermal diffusivity of the 2nd measurement was higher than that of 1st measurement. However, the thermal diffusivity of 2nd measurement was lower than those of as-received CVD-SiC. By annealing at temperature higher than 1100 ℃, it is expected that the thermal diffusivity of specimen increases.

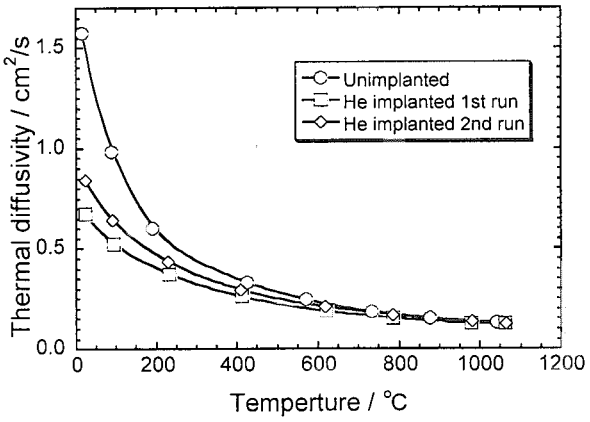


Fig.2 The thermal diffusivities of as-received CVD-SiC and He implanted CVD-SiC as functions of temperature.

4. Discussion

The thermal conductivity K is calculated from the thermal diffusivity α by the following equation:

$$K = \alpha \rho C_P \quad (2)$$

where ρ is the density and C_P is the specific heat capacity at constant pressure. Because heat conduction in SiC takes place by phonon-phonon scattering, K is also given as Debye equation:

$$K = 1/3 C_V V l \quad (3)$$

where l is the mean free path of phonons, C_V is the heat capacity per unit volume and V is the mean phonon velocity. C_V is expressed by the following equation,

$$C_V = \rho C_P. \quad (4)$$

We assume that the mean phonon velocity V is equal to the velocity of sound in SiC. In this study V is given by the following equation:

$$V = \sqrt{E/\rho} \quad (5)$$

where E is the elastic modulus of the SiC. By setting eqn(2)=eqn(3), we obtain

$$l = 3\alpha / V. \quad (6)$$

In this study, it is assumed that phonon scattering propagates in only one direction, which is the same direction as that of heat propagating. The linear density of scattering points of phonons in a solid is defined as X and given by the following equation:

$$X = 1/l. \quad (7)$$

When additional phonon scattering by defects is introduced into a solid after irradiation, the linear density of scattering points is increased from $X_{unimplanted}$ to $X_{implanted}$. The linear density of scattering points attributable to irradiation-induced defects, X_{defect}, is approximated by:

$$X_{defect} = X_{implanted} - X_{unimplanted}. \quad (8)$$

Finally, the defect linear density induced by irradiation, X_{defect}, is calculated from α by the following equation,

$$X_{defect}=1/l_{implanted}-1/l_{unimplanted} \quad (9)$$
$$=\frac{V}{3}\left(\frac{1}{\alpha_{implanted}}-\frac{1}{\alpha_{unimplanted}}\right).$$

Figure 3 shows the X_{defect} calculated from equation (9) as a function of temperature. In the result, the X_{defect} calculated from 2nd run data was lower than that from 1st run. The reason for this is that the induced defects partly disappear when the specimens were heated up to 1100 ℃ during the 1st measurement. In the 1st run the X_{defect} was decreased rapidly in the region of the temperature up to 700 ℃.

5. Conclusion

He ion implantation effect on the thermal diffusivities of CVD-SiC was investigated. The results obtained in this study are summarized as follows:

(1) The thermal diffusivities of CVD-SiC decreased after implantation of He ions.

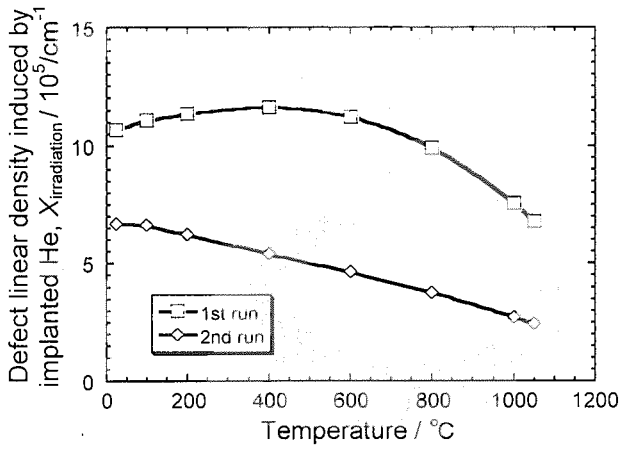


Fig.3 The relationship between defect linear density induced by implanted He and temperature.

(2) The thermal diffusivity measured in the 2nd run was higher than that measured in the 1st run because He was released from SiC during the 1st run.

(3) The defect linear density induced by irradiation, X_{defect}, was estimated. In the 1st run the X_{defect} was decreased rapidly in the region of the temperature up to 700 ℃.

References

1) L.L.Snead et al., Journal of Nuclear Materials, **233-237** (1996) 26-36.

2) T.Noda et al., Journal of Nuclear Materials, **233-237** (1996) 1491-1495.

3) J.F.Ziegler et al., The Stopping and Ranges of Ions in Matter, vol.1, Pergamon Press, New York, 1985.

4) K.Sasaki, T.Yano, T.Maruyama and T.Iseki, Journal of Nuclear Materials, **179-181**(1991) 407-410.

4.2 Effects of Helium Embrittlement on Fatigue Properties of Reduced Activation Ferritic/Martensitic Steel

T. Hirose[1),4)*], H. Tanigawa[1)*], M. Ando[2)], E. Wakai[1)], Y. Miwa[3)],
S. Jitsukawa[1)], Y. Katoh[4)], A. Kohyama[4)] and M. Narui[5)]
[1)] Department of Material Science, [2)] Department of Fusion Engineering Research,
[3)] Department of Nuclear Energy System, JAERI,
[4)] Institute of Advanced Energy, Kyoto University,
[5)] Institute for Materials Research, Tohoku University,

1. Introduction

Reduced activation ferritic steel, RAFs, is the leading candidate material for the first wall and blanket structures of the future D-T fusion reactors[1)]. Among the engineering issues of concern, fatigue properties are realized to be an important issue to be studied including neutron irradiation and transmutation He effect.

The objective of this work is to evaluate fatigue properties under fusion reactor condition. Helium implantations to RAFs were carried out utilizing AVF Cyclotron accelerator in TIARA facility. And low temperature neutron irradiation was also carried out to distinguish the helium embrittlement from irradiation hardening. Post-implantation and post-irradiation fatigue tests were performed at ambient temperature in the air.

2. Experimental procedure

2.1 Specimen

The material used was F82H IEA heat (Fe-8Cr-2W-0.2V-0.04Ta). The more detail of the steel was found in elsewhere[2)].

Miniaturized hourglass type fatigue specimen, so called SF-1 specimen was used in this work. Figure 1 shows dimensions of SF-1 specimen. The hourglass potion of SF-1 specimens was finished electrolytically.

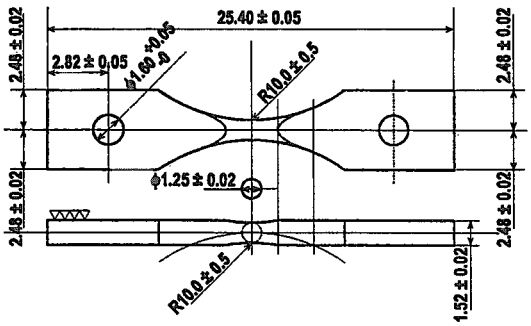


Figure 1. The dimensions of SF-1 specimen

2.2 Helium Implantation

Helium implantation to F82H was carried out with AVF cyclotron accelerator at the TIARA facility. SF-1 specimens were implanted with energy-degraded 50MeV helium ions at the temperature below 393K[3)]. Helium ion was implanted on opposite two sides. The maximum helium content in F82H was estimated to be 100appm by TRIM-95. Figure 2 shows helium distribution on the minimum diameter plane of SF-1. As shown in this figure, helium was homogeneously implanted from the surface to ~400μm depth, except for the small area where helium was implanted twice.

2.3 Neutron Irradiation

Neutron irradiation was carried out using the Japan Materials Testing Reactor (JMTR). Miniaturized hourglass fatigue specimens, SF-1 were irradiated at temperature below 363K using water rabbit capsule. The fluence was 3.1×10^{19}n/cm^2 (E>1.0MeV) and irradiation damage was estimated to be 0.02dpa. Some miniaturized sheet tensile specimens (SS-J) were also irradiated in the same capsule to evaluate the amount of irradiation hardening[4)].

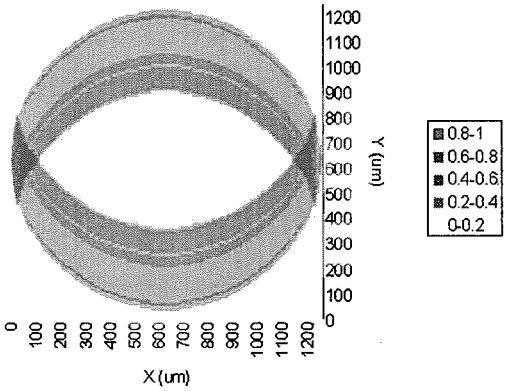


Figure 2. Helium distribution on the minimum diameter cross-section of SF-1

* Present affiliation: Department of Fusion Engineering Research

2.4 Fatigue Test Condition

Diametral strain controlled fatigue tests were carried out with a triangular strain waveform and a total diametral strain range, $\Delta\varepsilon_d$ of 0.2% ~ 3.0%. The diametral strain rate was 0.04%/s, the stress condition was push-pull. The number of cycles to failure, N_f, was defined as a point where a tensile peak stress decreased by 25% from an extrapolation curve of the tensile peak stress against number of cycle[5]. All tests were performed at an ambient temperature in the air.

3. Results and Discussion

The irradiation damage induced by neutron irradiation caused significant hardening. Figure 3 shows effects of neutron irradiation on fatigue lifetime of F82H.

In Figure 4 and 5, changes in the total stress amplitude and the total plastic strain range are plotted as a function of the number of cycles of both unirradiated and neutron-irradiated samples. F82H demonstrated cyclic softening even after neutron irradiation. Increase of stress amplitude related to irradiation hardening was observed. The increase in initial peak tensile/compressive stress was as well as the increase in the yield stress. Plastic strain range of irradiated sample was reduced to 50~70% of unirradiated sample. The plastic range did not change much during fatigue test except near the fracture. The cycle dependence of plastic strain range was not affected by neutron irradiation. Although stress amplitude of irradiated samples undergoes cyclic softening and falls below stress amplitude of the unirradiated one, the hardening was sufficiently high to decrease number of cycles to failure, N_f. The reduction of N_f was significant for large strain tests.

SEM micrographs of fatigue-fractured F82H irradiated samples were presented in figure 6.

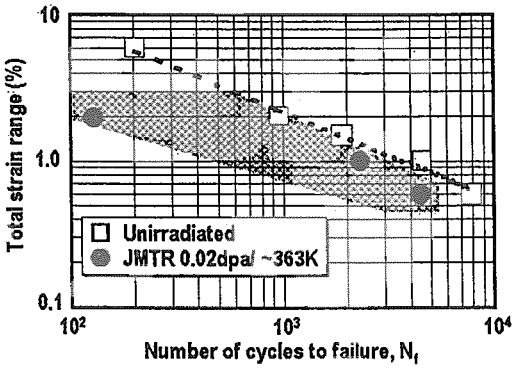


Figure 3. Effects of neutron irradiation on the fatigue lifetime of F82H

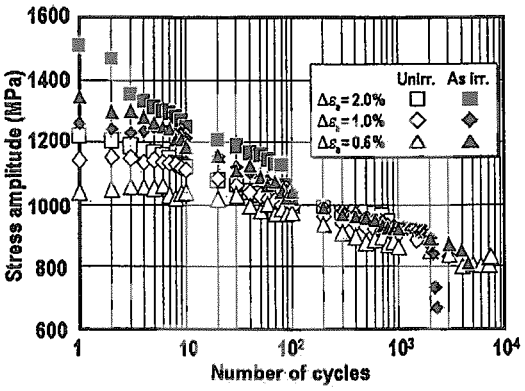


Figure 4. Cyclic stress responses before and after irradiation.

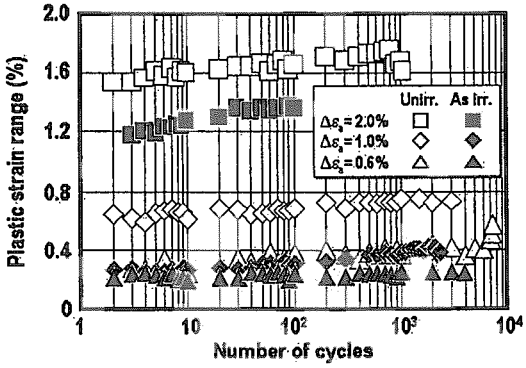


Figure 5. Plastic strain ranges before and after irradiation.

The analyses of fracture surface revealed this significant reduction of N_f was caused by local brittle fracture. Unirradiated specimens had ductile fracture surface, and some specimen had striation pattern. Any brittle fracture was not observed on the unirradiated samples. On the other hand, brittle fracture due to loss of

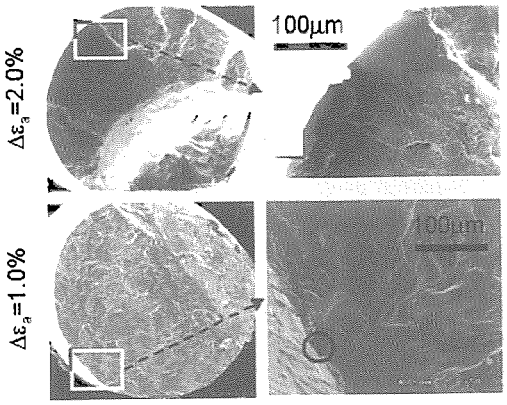


Figure 6. SEM micrographs of fatigue fractured F82H irradiated samples. TEM foil was fabricated from solid circle.

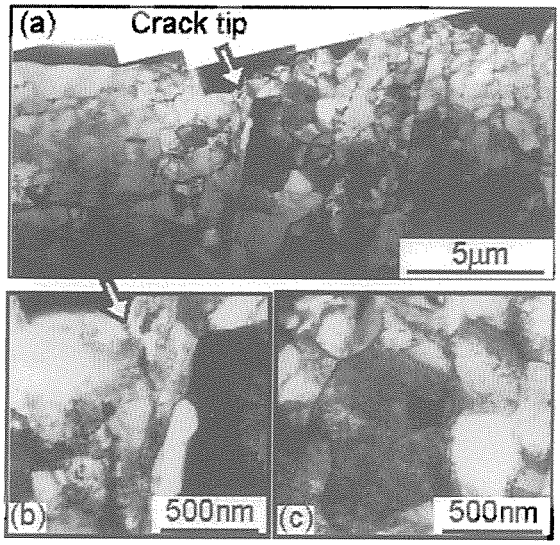


Figure 7. TEM micrographs of fatigue fractured F82H unirradiated sample. ($\Delta\varepsilon_a$: 1.5%, N_f: 1.8×10^3)
(a) Whole of TEM foil, (b) crack tip and deformation structure, (c) typical cell structure.

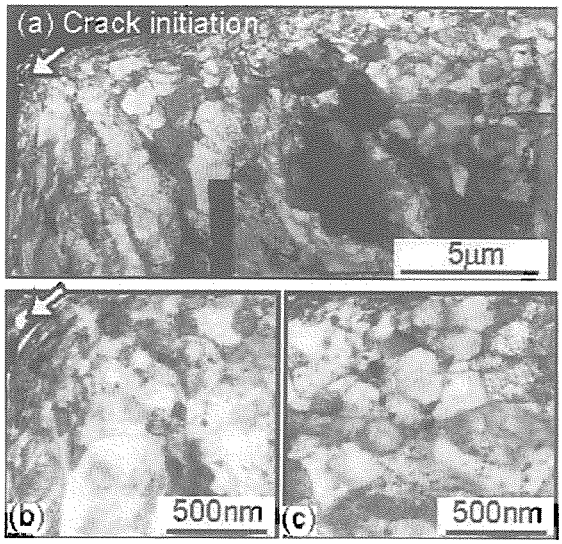


Figure 8. TEM micrographs of fatigue fractured F82H irradiated. ($\Delta\varepsilon_a$: 1.0%, N_f: 2.3×10^3)
(a) Whole of TEM foil, (b) crack initiation site, (c) typical cell structure.

ductility was observed on all irradiated samples. In case of $\Delta\varepsilon_a$=2% test, fracture surface had large brittle regions. The brittle fracture accelerated crack propagation. It is considered that this rapid crack propagation reduced the N_f. On the other hand, in case of small strain tests, crack was initiated in brittleness, however the crack propagated with ductile manner.

Figure 7 shows TEM micrographs of fatigue fractured F82H unirradiated sample.
TEM foil was pick-upped from near the fatigue crack tip. As shown in this figure, crack was initiated and propagated along with prior austenite grain boundary[6]. Typical lath structure was diminished and cell structure was formed whole of foils. Cell structure was formed during cyclic deformation. Especially, peculiar shaped cell was formed along with prior austenite grain boundary. Cyclic softening was considered to be caused by this cell structure, which contains less dislocation density[7].

Figure 8 shows TEM micrographs of fatigue fractured F82H neutron-irradiated sample. Cell structure was observed. Peculiar shaped cell structure was spread from crack-initiated point. Neutron irradiation did not have significant effects on fatigue-damaged structure.

4. Summary

Reduced activation ferritic/martensitic steel F82H was irradiated in the JMTR. Post irradiation fatigue tests and microstructural analysis on fatigue-damaged structure were carried out.

1. The increase in yield stress of F82H was almost 150MPa. This increase affected the peak tensile and compressive stress of fatigue tests.
2. Plastic strain range was decreased to less than 75% of unirradiated samples.
3. Cyclic softening and stability of plastic strain range were observed even after neutron irradiation. The reduction of N_f was caused by brittle crack initiation.
4. Neutron irradiation in this work did not have significant effects on fatigue-damaged structure.

References

1) A. Kohyama, et al., J. Nucl. Mater., 233-237 (1996) 138-147.
2) K. Shiba et al., JAERI-Tech 97-038 (1997).
3) T. Hirose et al., JAERI-Review, TIARA annual report 1999.
4) Y. Kohno, et al., J. Nucl. Mater., 283-287 (2000) 1014.
5) A. Nishimura, et al., J. Nucl. Mater., 283-287 (2000) 677-680.
6) J. Bertsch, et al., J. Nucl. Mater. 283-287 (2000) 832-837.
7) T. Hirose, et al., presented in ASTM symposium on SSTT, to be published in ASTM STP 1418.

4.3 Effects of Triple Beams on Microstructural Evolution in Ferritic/Martensitic Steels

E. Wakai[1], T. Sawai[1], A. Naito[1], K. Kikuchi[1], S. Jistukawa[1], S. Yamotomo[2], H. Naramoto[2], S. Yamashita[3], Y. Masumoto[3], K. Oka[3], and S. Ohnuki[3]

[1]Tokai Establishment, JAERI, [2]Takasaki Establishment, JAERI
[3]Graduate School of Engineering, Hokkaido University

1. Introduction

Low-activation ferritic/martensitic steels are first prominent of structural material in fusion nuclear reactor[1)] and also expected as the target structural material in the spallation neutron source (SNS). The high-energy neutrons produced in the D-T fusion reaction induce displacement damage and generate gaseous atoms from (n, p) and (n, α) reactions in the materials. In the SNS system, the steel vessel containing a liquid Pb-Bi target as neutron source is subjected to intense-pulsed protons. The target vessel will be damaged by atomic displacements due to primary protons, spallation neutrons, recoil atoms and accumulate high concentration transmutation products such as He and H atoms.

Helium and hydrogen accumulations due to transmutation and implantation in these systems have been considered as a potential cause for embrittlement[2)] and swelling[3)] in ferritic/martensitic steels. Purpose of this study is to investigate (1) the effect of triple ion beams (iron, helium, and hydrogen ions) and dual beams (iron and helium ions) on swelling behavior in F82H ferritic/martensitic steel and (2) the diffusion of hydrogen atom in the steel irradiated by the triple beams.

2. Experimental procedure

Specimens were F82H (Fe-8Cr-2W-0.2V-0.04Ta-0.1C) steel, F82H-40%CW, Fe-9Cr, Fe-12Cr, and oxide dispersive 12Cr-ferritic steel (ODS). Irradiations were performed under triple or dual beam ions in the TIARA facility. The size of the specimen used for the irradiation was about 0.3 mm-thick, 6 mm-long and 3 mm-wide. The area of 0.3 mm-thick and 2mm-long within 6mm-long was irradiated. A set of many specimens were simultaneously irradiated with a simultaneous triple or dual ions consisting of 10.5 MeV Fe^{3+} ions, 1.05 MeV He^{+} ions, and 0.38 MeV H^{+} ions or the Fe^{3+} and He^{+} ions to 50dpa(displacement per atoms) at 1 μm depth in the TIARA(Takasaki Ion Accelerators for Advanced Radiation Application) facility of JAERI as given in Fig. 1. The damage peak of Fe^{3+} ion was about 1.75 μm, and the irradiation of helium and hydrogen atoms was controlled to implant in the depth range from 0.5 to 1.3 μm using two energy degraders with aluminum foil,

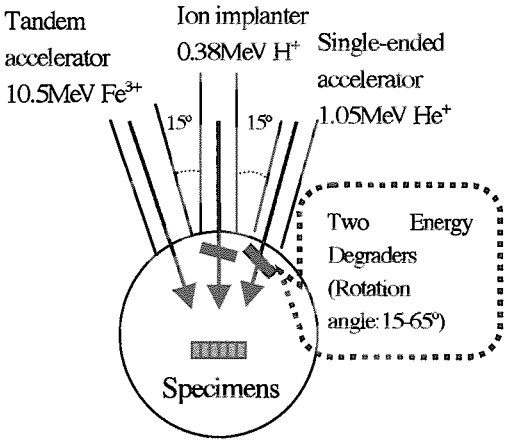


Fig. 1 Schematic configuration of three beam lines, two energy degraders and specimens.

which were calculated by using SRIM97 code, respectively. The ratios of hydrogen and helium concentrations to dpa (appm/dpa) in fusion reactor and SNS target conditions were about 40 appmH/dpa and 10 appmHe/dpa, and about 2000 appm/dpa and 100 appmHe/dpa, respectively.
The irradiation dose rate was about 1.6×10^{-3} dpa/s. After the irradiation, the specimens were thinned by using a FIB(Focused Ion Beam) with Ga ion gun operated at 30 kV equipped with micro-pick up system, Hitachi FB-2000A, and the microstructures were examined by transmission electron microscope. An example of FIB thin foil specimen is included in Fig. 2. Hydrogen concentrations in the specimens were measured from the surface to 2 μm depth by using $^{1}H(^{15}N, \alpha\gamma)^{12}C$ nuclear resonance reaction after the multiple-irradiation.

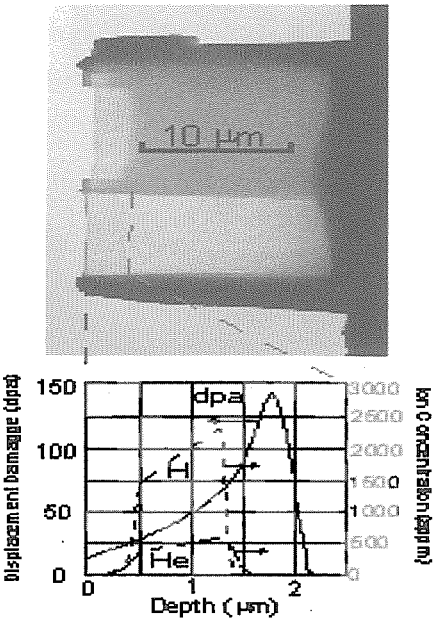


Fig. 2 Depth profiles of displacement damage, hydrogen and helium concentrations in F82H steels irradiated by triple beams (lower figure). The rates of He and H to dpa in fusion condition are shown. The foil specimen was prepared by FIB (upper figure).

3. Results and discussion

Cavities were formed in the F82H steels irradiated at 450°C to 50 dpa by triple and dual beams as shown in Fig. 3. Many small cavities with size of about 5 nm were formed in the specimen irradiated by dual beams with Fe^{3+} and He^{+} ions under 10appmHe/dpa as shown in Fig. 3(a). In the case of triple beams with Fe^{3+}, He^{+} and H^{+} ions, larger cavities of 20 -30 nm and small cavities of 5nm were formed under 10 appmHe/dpa and 40 appmH/dpa as seen in Fig.

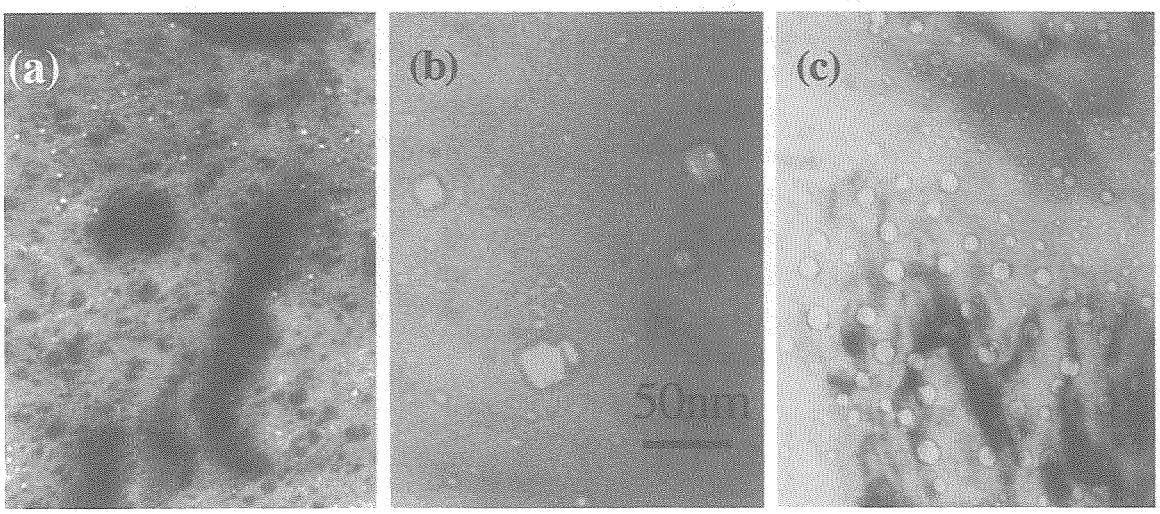


Fig. 3 (a) appmHe/dpa=10, appmH/dpa=0, (b) appmHe/dpa=10, appmH/dpa=40, (c) appmHe/dpa=100 appmH/dpa=2000
Cavities (objects with white contrast) formed in F82H irradiated at 430°C to 50 dpa under dual/triple beams.

3(b). In the condition of 100 appmHe/dpa and 2000 appmH/dpa, higher density cavities with sizes from about 5 to 15 nm were formed as shown in Fig. 3(c). The triple beams enhanced the growth of cavities. In the case of Fe-9Cr and -12Cr, the similar results were obtained for the dual and triple experiments. Therefore, the implanted hydrogen atoms under triple beams affected strongly on the microstructural evolution. In order to reduce cavity growth, the effect of dislocation density on swelling was also examined, and it was shown that the cavity size of F82H-CW was smaller than F82H-std, as shown in Fig.4. The high density dislocations in cold-worked specimen somewhat suppressed the growth of cavities.

To examine the diffusion of hydrogen atoms in the F82H, hydrogen concentration in F82H steels irradiated at 430 or 80°C with the triple beams or dual beams of helium and hydrogen ions implanted at 80°C were examined. The implanted hydrogen concentrations in these irradiations were about 4-8at%. An example of hydrogen concentration measured by using $^{1}H(^{15}N, \alpha\gamma)^{12}C$ nuclear resonance reaction at ambient temperature is given in Fig. 5. The hydrogen concentrations in all case were less than the detection level (~1at%).

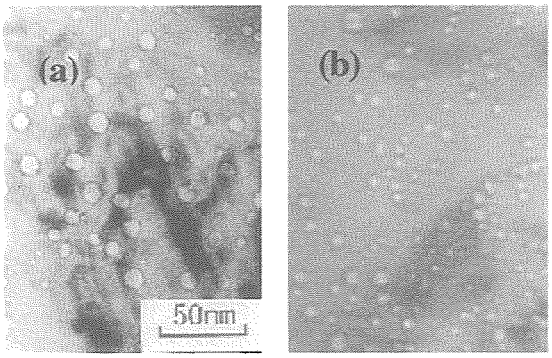


Fig. 4 Cavities formed in F82H-std (a) and F82H-40%CW (b) irradiated at 430°C to 50 dpa by triple beams of target condition.

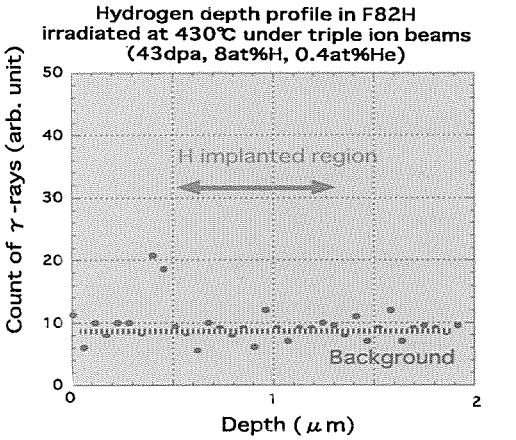


Fig.5 Hydrogen concentration profile measured by $^{1}H(^{15}N, \alpha\gamma)^{12}C$ nuclear resonance reaction in F82H steel irradiated at 430°C with triple beams of target condition.

4. Conclusions

The effect of triple ion beams (iron, helium, and hydrogen ions) and dual beams (iron and helium ions) on swelling behavior of F82H ferritic/martensitic steel irradiated to 50 dpa has been examined. The diffusion of hydrogen atom in the steel is also examined. It was found that the triple beams affected strongly on microstructural evolution, i.e., the growth behavior of cavities under triple beams was clearly different from that under dual beams. However, the implanted hydrogen concentration could not be detected in the F82H steels implanted to 4 - 8 at % hydrogen with the triple beams at 80 or 430°C or dual beams of helium and hydrogen ions.

References

1. B. van der Schaaf, et al., Journal of nuclear materials, 283-287(2000)52-59.
2. R. L. Klueh, et al., Journal of nuclear materials, 283-287(2000)478-482.
3. E. Wakai, et al., Journal of nuclear materials, 283-287(2000)799-805.

4.4 Investigation of the resonant vibration modes of self interstitial atoms in metals by low temperature specific heat measurement

M.Watanabe
Department of Materials Science, JAERI

1.Introduction

Some theories[1] predict the resonant vibration modes due to self interstitial atoms in metals, which have large amplitudes and low frequencies. These kinds of modes for a single defect present an important problem for physics of lattice defect. The resonant vibration modes have an important influence on properties of phonons. To verify the existence of these modes, we measured the specific heat of electron-irradiated fcc metal(Cu) and bcc metals(Mo, W) at low temperatures.

2.Experimental

The specimens used in this work were Cu, Mo and W single crystals with dimensions of $12\times12\times0.5$ mm^3, 12$^{\Phi}\times0.5$ mm^3 and 8.8$^{\Phi}\times0.5$ mm^3. The irradiations with 2-MeV electrons to the dose of 7.73×10^{17}/cm^2, 6.49×10^{17}/cm^2 and 9.54×10^{17}/cm^2 at 19K, 23K and 25K, respectively, were performed by using the a low temperature irradiation facility interfaced to TIARA 3MV single-ended accelerator. Before and after irradiation, we measured the specific heat of the specimen under the adiabatic condition between 2K-60K[2].

3.Results and discussion

Fig. 1 shows the specific heat change in Cu<100> after irradiation to the dose of 7.73×10^{17}/cm^2 at 19K and subsequent 60K annealing[2]. Two peaks of specific heat changes were found. This temperature range is lower than that at the first stage of the recovery.

Figs. 2 and 3 show the specific heat change in Mo<100> after irradiation to the dose of 6.49×10^{17}/cm^2 at 23K and 300K annealing, respectively. Fig. 4 show the specific heat change in W<100> after irradiation to the dose of 6.49×10^{17}/cm^2 at 25K.

The specific heat change in Mo<100> and W<100> after irradiation well corresponded to recovery stage by the electric resistance measurement.

The specific heat which changed by the irradiation is recovered with increasing anneal temperature.

For Mo<100> and W<100>, the peaks of the specific heat change were observed, which originated from the resonance mode vibration similarly to that for Cu<100>.

The resonant modes couple strongly to distortions of the local environment. Fig.5 shows the reaction of the dumbbell to a crystal deformation[3]. The resonant E_g mode couples to the <100>-shear but neither to the <110>-shear nor to the compression. These resonance effects also pertain to interstitial clusters where some resonance frequencies might even be lower[3] and couple strongly to some phonon branches[4].

4.Summary

To verify the existence of the resonant vibration modes, we measured the specific heat of electron-irradiated metals at low temperatures. For fcc metal(Cu) and bcc metals(Mo, W), the peaks of the specific heat change were observed, which originated from the resonance mode vibration.

Reference

1) A.Scholz and Chr.Lehmann, Phys.Rev. B6(1972)813.
2) M.Watanabe, TIARA Annual Report 1999, p141(2000)
3) P.H.Dederrichs, C.Lehmann, H.R.Scholz and R.Zeller, J.Nucl.Mater.69/70(1978)176
4) R.F.Wood and M.Mostoller, Phys. Rev. Lett. 35(1975)45

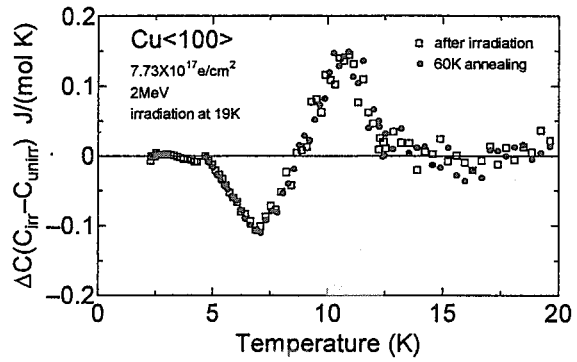


Fig.1. Specific heat change in Cu<100> after irradiation to the dose of 7.73×10^{17}e/cm^2 at 19K and 60K annealing.

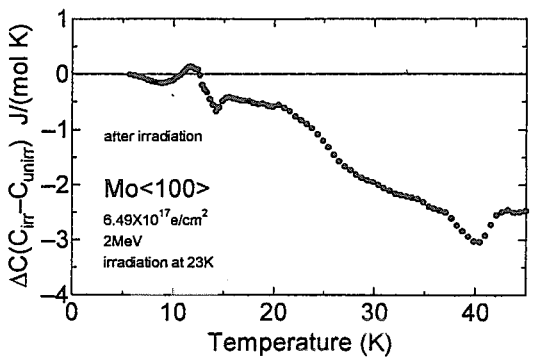


Fig.2. Specific heat change in Mo<100> after irradiation to the dose of 6.49×10^{17}e/cm^2 at 23K.

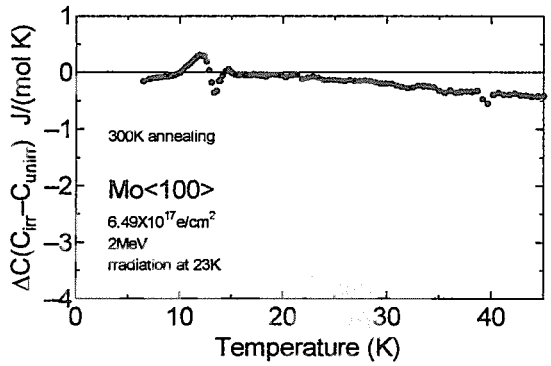


Fig.3. Specific heat change after 300 K annealing in Mo<100> irradiation to the dose of 6.49×10^{17}e/cm^2 at 23K.

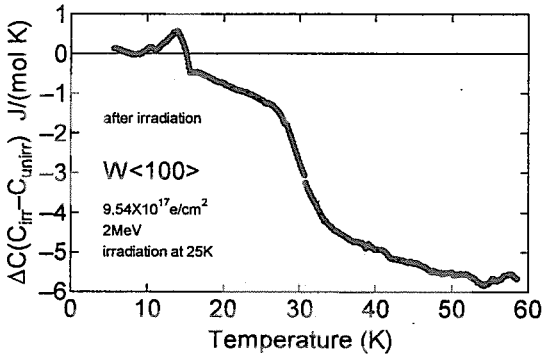


Fig.4. Specific heat change in W<100> after irradiation to the dose of 9.54×10^{17}e/cm^2 at 25K.

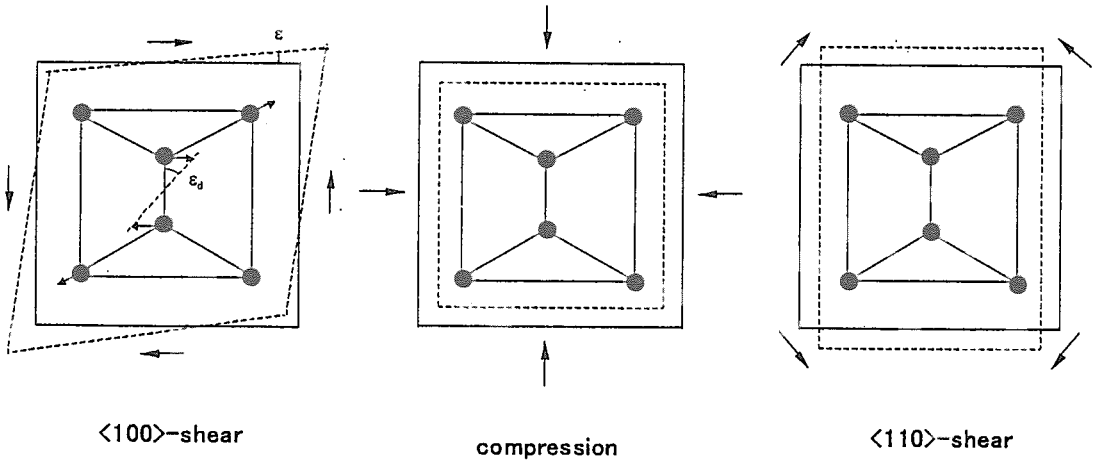


Fig.5.Homogeneous deformation of a crystal containing a <100>-dumbbell interstitial in fcc metals.

4.5 Study of ion-induced structural changes in Li_2TiO_3 ceramics

T. Nakazawa[1], V. Grismanovs[2], D. Yamaki[1], Y. Katano[3], T. Aruga[1], A. Iwamoto[1] and S. Jitsukawa[1]
[1] Department of Materials Science, JAERI
[2] OECD Halden Reactor Project
[3] Nippon Advanced Technology Co., Ltd

1. Introduction

The Li_2TiO_3 ceramics is regarded as one of the most suitable candidate for the solid tritium breeder material of D-T fusion reactors[1]. It is known that in an operating fusion reactor, the radiation damage in Li_2TiO_3 will be produced by fast neutrons, energetic tritons (2.7 MeV) and helium ions (2.1 MeV) generated by $^6Li(n,\alpha)\,^3H$ reaction. The damage caused by ionising radiation may result in the microstructure changes and hence may have an impact on the tritium release behaviour, thermal and mechanical properties of Li_2TiO_3. Thus, the study of irradiation defects and damage microstructure in Li_2TiO_3 is essential in order to evaluate its irradiation performance.

2. Experimental procedure

The Li_2TiO_3 ceramics have been fabricated from 99% pure powder purchased from CERAC, Inc. The powder was cold pressed at 300 MPa into cylinders subsequently sintered at 1223 K for 6 h in an Ar atmosphere. The obtained Li_2TiO_3 ceramics have approximately 78% of theoretical density (3.43 g/cm^3)[1]. The specimens were machined from the cylinders to the form of disks with diameter of 10 mm and thickness of around 1.0 mm.

The Li_2TiO_3 ceramic samples were irradiated at various temperatures (343-873 K) with the triple ion beams (0.25 MeV H^+, 0.6 MeV He^+ and 2.4 MeV O^{2+}) up to identical fluences for each ion estimated at 1.0×10^{21} ion/m^2. The ion energies were so chosen that the projected ranges of the incident ions might be about 2.2 μm.

Then irradiated samples were examined by Raman spectroscopy and X-ray diffraction (XRD) technique.

The isochronal annealing of Li_2TiO_3 samples irradiated by the triple ion beam has been carried out in an Ar atmosphere at various temperatures to study the recovery of radiation damage.

3. Results and Discussion

The formation of the anatase (TiO_2) layer on the surface of Li_2TiO_3, after its exposure to the triple ion beams (H^+, He^+ and O^{2+}), has been shown by both Raman spectroscopy and XRD analysis[2].

The obtained results of the XRD analysis are presented in Fig. 1. The reference XRD patterns of the Li_2TiO_3 ceramic pellet (B) and of the anatase powder (A) are also shown in Fig.1. The XRD patterns of irradiated Li_2TiO_3 ceramics (C,D,E) include several additional signals compared with the reference XRD pattern of Li_2TiO_3 (B). One can see that a peak at an angle 2θ equal to 25.2 is common for all irradiated Li_2TiO_3 samples. Beyond a doubt, this signal corresponds to the most intense peak in the XRD pattern of anatase. This fact suggests that the surfaces of irradiated samples include some traces of anatase. The computer simulation of the XRD patterns of irradiated Li_2TiO_3 samples also proved that they are the superposition of the XRD patterns of pure Li_2TiO_3 and anatase.

The Raman spectra of Li_2TiO_3 ceramics irradiated by triple ion beams are displayed in Fig. 2. The reference spectra of Li_2TiO_3 ceramics and anatase are shown in Fig. 3. On Raman spectrum of TiO_2, a peak observed at 640cm^{-1} is assigned to the Ti-O stretching in

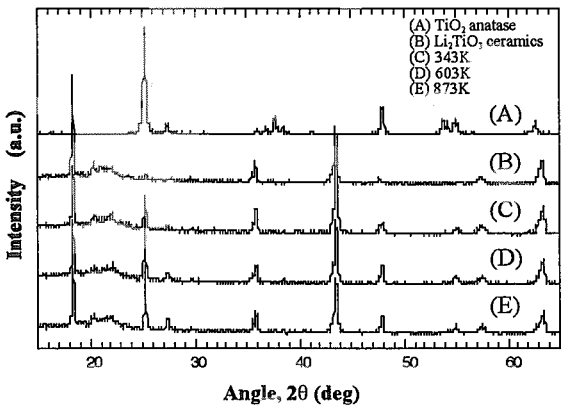


Fig.1. XRD patterns of Li_2TiO_3 ceramics irradiated by triple ion beam at 343, 603 and 873 K, and of non-irradiated Li_2TiO_3 ceramics and anatase powder.

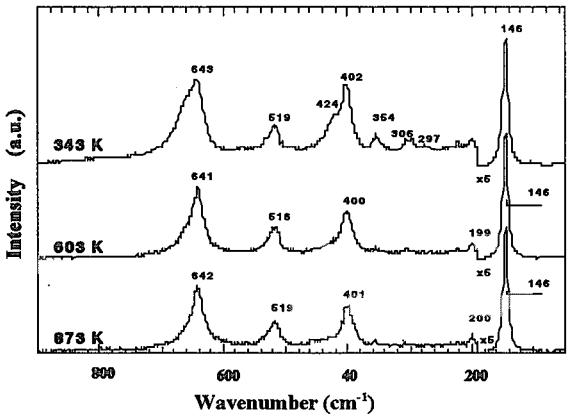


Fig. 2. Raman spectar of Li_2TiO_3 ceramics irradiated by triple ion beam at various temperatures. Intensities of the spectra lying over 190 cm^{-1} are multiplied by a factor five.

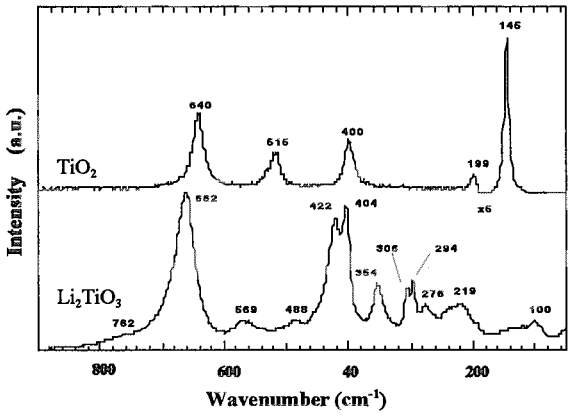


Fig. 3. Reference Raman spectra of anatase (TiO_2) and Li_2TiO_3 ceramics. The intensity of anatase spectrum lying over 190cm^{-1} is multiplied by a factor five.

the TiO_6 octahedron. The Ti-O stretching is observed at 662cm^{-1} for Li_2TiO_3 ceramics. The Ti-O stretching of Li_2TiO_3 is shifted from 662 to near 640 cm^{-1} because of the irradiation at various temperatures. One can see that the Raman spectra of Li_2TiO_3 irradiated at 603 and 873 K quite resemble to that of anatase. However, the Raman spectrum of the sample irradiated at 343 K seems to be a superposition of the Li_2TiO_3 and anatase spectra. This fact clearly points to the temperature effect on the formation of anatase on the surface of Li_2TiO_3; the higher the temperature is, the more efficient the formation of anatase phase is. One can deduce the same tendency from the XRD patterns in Fig. 1.

In such a manner the irradiation of Li_2TiO_3 ceramics by H^+, He^+ and O^{2+} ions causes the formation of anatase on its surface. The rough

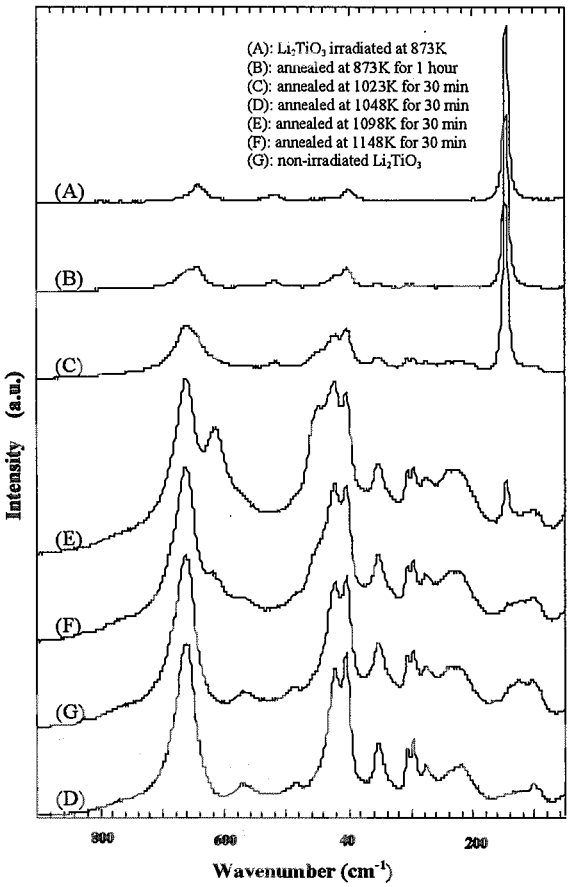


Fig. 4. Raman spectra of Li_2TiO_3 ceramics irradiated by triple ion beam at 873K and then annealed at indicated temperatures.

estimation of a thickness of anatase layer can be done from the following consideration:

The radiation source of XRD apparatus is X-rays of CuKα line with λ=1.54 nm; the penetration of such radiation into Li_2TiO_3 sample can be estimated below 1 μm, less than penetration depth of the incident ions (v.s., 2.2 μm). In view of the fact that the XRD patterns of irradiated Li_2TiO_3 samples represent the superposition of signals from the anatase and Li_2TiO_3, the anatase layer can be estimated under 1 μm.

The formation of the anatase phase is probably due to the displacement damage and electronic energy deposition in Li_2TiO_3 by energetic incident ions. The TRIM code[3] was used to estimate the damage parameters. The maximum damage level for the irradiation with fluence of $1.0x10^{21}$ ion/m^2 is calculated to be about 9 displacement per atom (dpa) at the depth of 2.2 μm assuming the threshold energy of 40 eV for displacement of Li, Ti and O atoms. The accumulated radiation dose

by the electronic energy deposition for the triple irradiation is calculated to be 1000GGy in the near surface layer of about 0.5 μm.

The observed temperature effect on the formation of anatase phase is most likely connected with the enhancement of the diffusion of displaced atoms with temperature. And, the atoms are also more easy to displace with the rise of temperature since the increased lattice vibrations could help in net effect of the displacement of its atoms by incident ions[4].

The heat treatment of irradiated samples was conducted in order to evaluate a temperature of the thermal annealing of introduced structural defects. The results of examination by Raman spectroscopy after the isothermal annealing are presented in Fig. 4. One can see that after the heat treatment at 1148 K the Raman spectrum of annealed sample became almost identical to that of non-irradiated Li_2TiO_3. The temperature of about 1050 K can be estimated as a starting point of the efficient surface recovery from the traces of anatase. This temperature is close to the one required for the synthesis of Li_2TiO_3 powder with the soild reaction[5]. The heat treatment at its temperature is a practical way for the recovery of the structural defects in Li_2TiO_3 ceramics caused by the irradiation. On the basis of above observations, it may be deduced that the radiation damage in Li_2TiO_3, caused by irradiation with triple ion beams, exhibits a high tolerance for elevated temperatures.

4. Conclusions

The irradiation of Li_2TiO_3 ceramics by H^+, He^+ and O^{2+} ions was found to cause a modification of its surface. The results of Raman spectroscopy and XRD analysis suggest the appearance of anatase layer on the surface of Li_2TiO_3. The formation of the anatase is thought to be due to the simultaneous effect of the displacement damage and electronic energy deposition caused by incident ions. The efficient surface recovery from the traces of anatase was found to start at about 1050 K.

Further studies of radiation damage in Li_2TiO_3 ceramics under ion beam irradiation are desirable at elevated temperatures and high radiation doses for the fundamental understanding of irradiation performance of that material

Acknowledgment

The authors wish to express their thanks to the staffs in the accelerator facilities of Takasaki establishment of JAERI for their invaluable help to the irradiation experiments and to Dr. H. Katsuta for supporting this study and encouragement.

References

1) P. Gierszewski, Review of properties of lithium metatitanate, Report no. CFFTP G-9561, 1995.
2) T. Nakazawa, V. Grisimanovs, D. Yamaki, Y. Katano, T. Aruga and A. Iwamoto, 2000 Int. Conf. on Ion Implantation Technology Proc., (2000) 753.
3) J.F. Ziegler, J.P. Biersack and U. Littmark, The Stopping and Range of Ions in Solids, Pergamon, Oxford, 1985.
4) T. Iwata and T. Nihira, J. Phys. Soc. Japan, 31 (1971) 1761-1783.
5) M. Castellanos and A.R. West, J. Mater. Sci., 14 (1979) 450.

4.6 Damage evolution in high energy multi ion-irradiated BCC metals and the interaction between gas atoms (H and He) and damage defects

Y. Shimomura[1)], I. Mukouda[1)], D. Yamaki[2)], T. Nakazawa[2)], T. Aruga[2)] and S. Jitsukawa[2)]

[1)] Faculty of Engineering, Hiroshima University, [2)] Department of Material Science, JAERI

1. Introduction

For fusion reactor applications, there is an interest in vanadium and its alloys. Hydrogen and helium atoms are generated by nuclear transmutation in the fusion environment. These gas atoms play an important role on the evolution of the damage microstructure. It is well known that helium is active in cavity nucleation. Some studies have been carried out on hydrogen effects. However, it is not extensively characterized. In the present work, quantitative experiments were carried out to study the role of gas atoms (helium and hydrogen) on the evolution of the damage microstructure in irradiated materials. It is possible to control the concentration of gas atoms in irradiated metals by ion irradiation at high energy. We examined void formation in high energy ion irradiated pure vanadium by a single beam (5 MeV Ni) and a dual-beam (5MeV Ni ion and 600 keV He ion) irradiation. The ion energy was selected so that the projected range of the gas ions in copper might coincide with depth of peak damage (1.3 mm) calculated by the TRIM 95 code. Specimens for TEM cross sectional observation were prepared by a FIB (Focused Ion Beam) device. The relation between gas atoms and damage structure was derived from experimental results.

2. Experimental Procedure

The specimen used in this study, pure vanadium

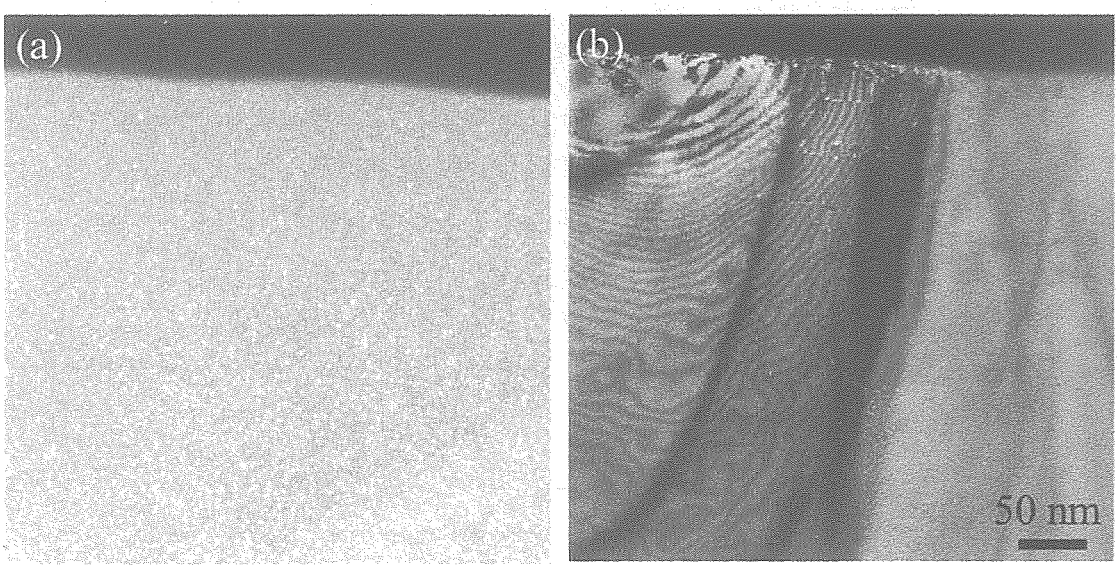


Fig. 1 (a) As thinned specimen with FIB, many dot clusters were observed. (b) After electro-polishing no dot cluster was observed.

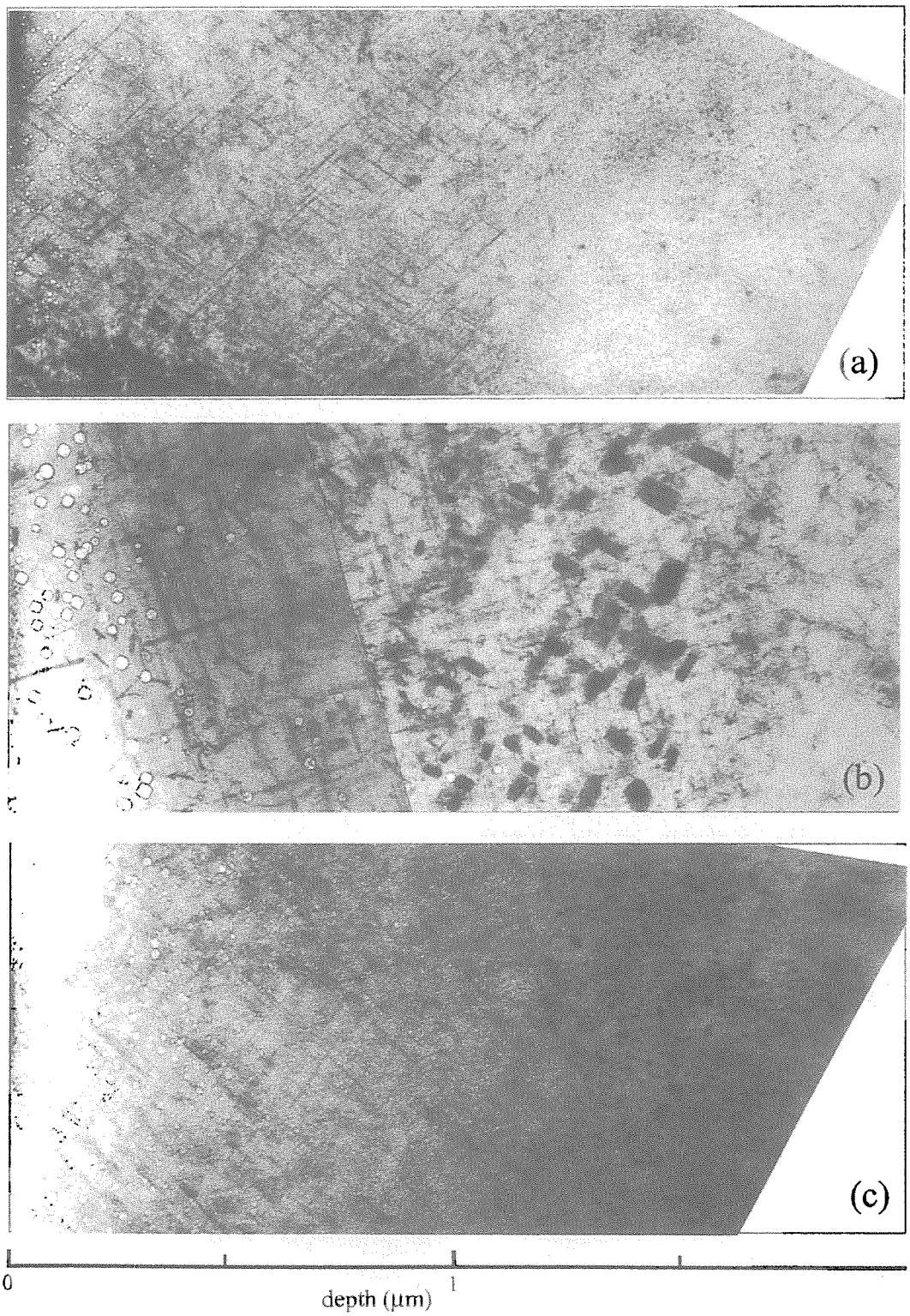


Fig. 2 Damage structure of ion-irradiated pure vanadium.
(a) 5MeV Ni ion irradiation at 500°C, (b) 5MeV Ni ion irradiation at 600°C and (c) 5MeV Ni + 0.6MeV He ion irradiation at 600°C.

had nominal purity of 99.8%. Cut annealed disks of 3mm in diameter and 0.05 mm in thickness was prepared [1-3]. The high energy ion irradiation was carried out with accelerators of TIARA at Takasaki-establishment of JAERI. The ions stop within the depth of a few microns from surface level and damage was formed up to this depth. Pure vanadium was irradiated at 500 and 600°C. For the quantitative investigation, damage structure has to be observed as a function of the depth. We utilized FIB microscopy. To preserve the surface position of ion-irradiated metals, we deposited tungsten on the irradiated surface. In our previous work, it was found that interstitial atoms form their clusters throughout FIB-thinned specimens as shown in Fig. 1(a). To overcome this difficulty, we developed the TEM specimen preparation method which is a combination of FIB thinning and an electro- polishing. The specimens were electro-polished to remove damaged region by FIB, after electro-polishing no dot defects were observed as shown in Fig. 1(b).

3. Results and Discussion

When only nickel ion was irradiated, voids were formed in the region from the surface to the depth of about 0.5 μm irradiated at 500 and 600°C (Fig. 2(a) and 2(b). However in the region of damage peak, voids were not observed. The needle-like precipitate of about 100nm in length was observed for all samples covering the whole penetration depth of ion. It is thought that the precipitate is carbide. Moreover, in the sample irradiated at 600°C, the granular precipitate was observed in the domain of the 1.0 to 1.5 μm depth. While voids formation was observed within the whole ion penetration depth in the sample irradiated with Ni + He ions simultaneously as shown in Fig. 2(c). The needle-like precipitate was observed also in sample irradiated with Ni + He ions.

References

[1] I. Mukouda, Y. Shimomura, T. Iiyama Y. Katano, D. Yamaki, T. Nakazawa and K. Noda, Mat. Res. Soc. Symp. Proc. Vol. **540** (1999) 549-554.

[2] Y. Shimomura and I. Mukouda, Mat. Res. Soc. Symp. Proc. Vol. **540** (1999) 527-532.

[3] I. Mukouda, Y. Shimomura, T. Iiyama, Y. Harada, Y. Katano, T. Nakazawa, D. Yamaki and K. Noda, J. Nucl. Mater. **283-287** (2000) 302-305.

4.7 Dose Rate Effects on Microstructural Evolution in Austenitic Stainless Steels under Ion Irradiation

N. Sekimura[1], T. Okita[1], A. Kurui[1], Y. Hashimoto[1],
S. Jitsukawa[2], T. Sawai[2], Y. Miwa[2], S. Hamada[2], S. Saitoh[2], K. Kikuchi[2]
Department of Quantum Engineering and Systems Science, Univ. of Tokyo [1]
Materials Research Division, JAERI/Tokai [2]

1. Introduction

Most high fluence data needed for fission and fusion application can be derived from accelerated irradiation experiments such as fast reactors and ion accelerators. It has been widely recognized that dose rate is one of the key parameters to influence microstructural evolution and resultant macroscopic changes. To predict the irradiation performance of nuclear materials, it is essential to clarify how to extrapolate higher dose rate data to lower ones.

In this study, systematic ion-irradiation tests at various dose rate are carried out to estimate the effects of dose rate on microstructure evolution in austenitic alloys, which are used as in-core structure materials and thought to be used as the first wall materials of the near future fusion reactor, ITER.

2. Experimental Procedure

Simple model austenitic alloy, Fe-15Cr-16Ni was prepared from high purity Fe, Cr, and Ni. by arc-melting. They were rolled to sheets of 0.2 mm in thickness. Standard 3 mm TEM disks were then punched and annealed for 30 minutes at 1050°C in a high vacuum of 10^{-5} Pa wrapped within Zr foils. Afterwards, they were mechanically and electrically polished.

Irradiation proceeded with 12.0 MeV Ni^{3+} ions in the TIARA (Takasaki Ion Accelerators for Advanced Radiation Application). In this first series of irradiation, no gas atoms were preinjected or simultaneously injected. Irradiation dose ranged from 0.17dpa to 26.1dpa, irradiation dose rate from $1.0x10^{-4}$ dpa/sec to $1.0x10^{-3}$ dpa/sec and irradiation temperature 300, 400, and 500°C. The detailed irradiation conditions are shown in Table 1.

The identical samples were also irradiated with fast neutrons in FFTF/MOTA (Fast Flux Test Facility: Material Open Test Assembly) for one and two cycles. Dose rates ranged from $9.3x10^{-9}$ to $1.7x10^{-6}$ dpa/sec, and irradiation temperatures from 389°C to 444°C.

After irradiation, the ion-irradiated specimens were electrochemically thinned to reach a depth of 700 nm, followed by back-thinning.

Analysis was conducted using a JEOL 200CX transmission electron microscope operating at 200 kV.

3. Results and Discussion

The radiation-induced microstructures are dense, especially at the lower temperatures, but rather simple, being comprised primarily of Frank interstitial loops, some unfaulted perfect loops, some network dislocations and cavities. Cavities can be observed even in the specimens irradiated at 300°C at lowest dose.

Figure 1 shows the dose dependence of irradiation-induced swelling at various dose rates. The swelling of Fe-15Cr-16Ni always increases, as the dose rate is lowered at all three

irradiation temperatures studied. At lower dose rates,, enhanced formation of dislocation loops, as is shown in Figure 2, increases sink strength of interstitials, which enhances cavity nucleation and swelling.

Previous studies show [2-3] that loop density is saturated with the dose rate to the 1/2 power.. However, as shown in Figure 3, at very high dose rate up to 10^{-4} dpa/sec, loop density continues to increases even at a dose higher than 1 dpa. At higher dose rates, much higher dose compared to the neutron cases is required to reach a saturation level of dislocation loop density, because recombination fraction of point defects is larger than sink strength.

Dislocation loops are unfaulted and become network dislocation as it grows and interact with each other. At higher dose rates these processes delay, resulting in suppress of vacancy supersaturaion.

It is only applied in the absence of gaseous atoms that dislocation evolution directly affects cavity nucleation and growth. Gaseous atoms such as He and/or H will also affects microstructural evolution when they are existed. To predict the material behaviors under conditions of high gaseous generation rate, further study is necessary using dual and triple ion irradiation experiments with simultaneous injection of He and/or H.

References

[1] T. Okita, T. Sato, N. Sekimura F. A. Garner, L. R. Greenwood, W. G. Wolfer and Y. Isobe, to be published in the Proceedings of 10th International Conference of Environmental Degradation of Materials in Nuclear Power Systems.

[2] H. Watanabe, A. Aoki, H. Murakami, T. Muroga, and N. Yoshida, Journal of Nuclear Materials 155-157 (1988) 815.

[3] T. Muroga, H. Watanabe and N. Yoshida, Journal of Nuclear Materials 174 (1990) 282.

Table 1 Ion irradiation conditions

Temperature	Dose Rate	Dose
300°C 400°C 500°C	$1x10^{-4}$ dpa/sec $4x10^{-4}$ dpa/sec $1x10^{-3}$ dpa/sec	0.17-0.21 dpa 1.6-1.9 dpa
300°C 400°C 500°C	$4x10^{-4}$ dpa/sec	15.2-17.4 dpa
300°C	$4x10^{-4}$ dpa/sec	26.2 dpa

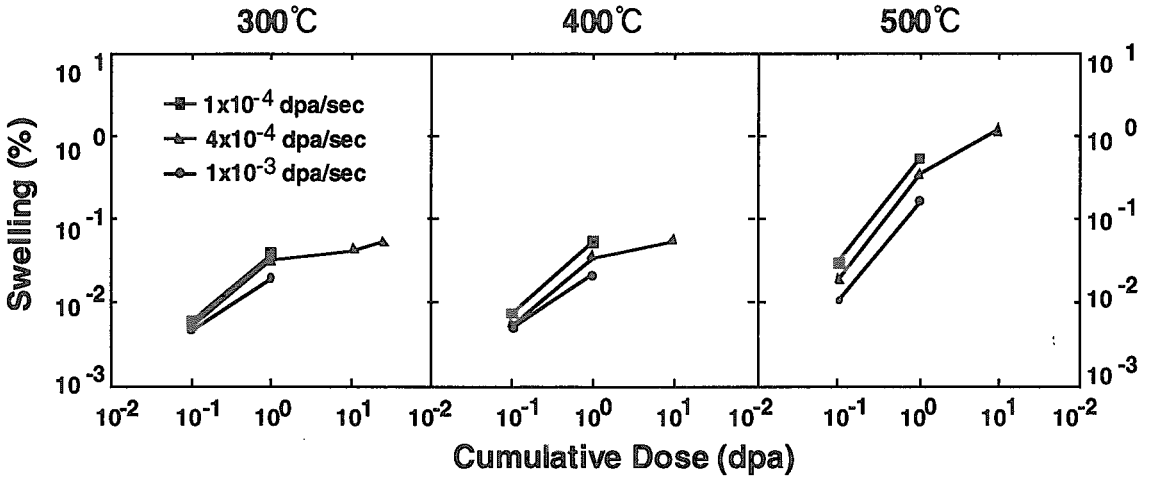


Figure 1 Cumulative dose dependence of swelling in Fe-15Cr-16Ni at various dose rates.

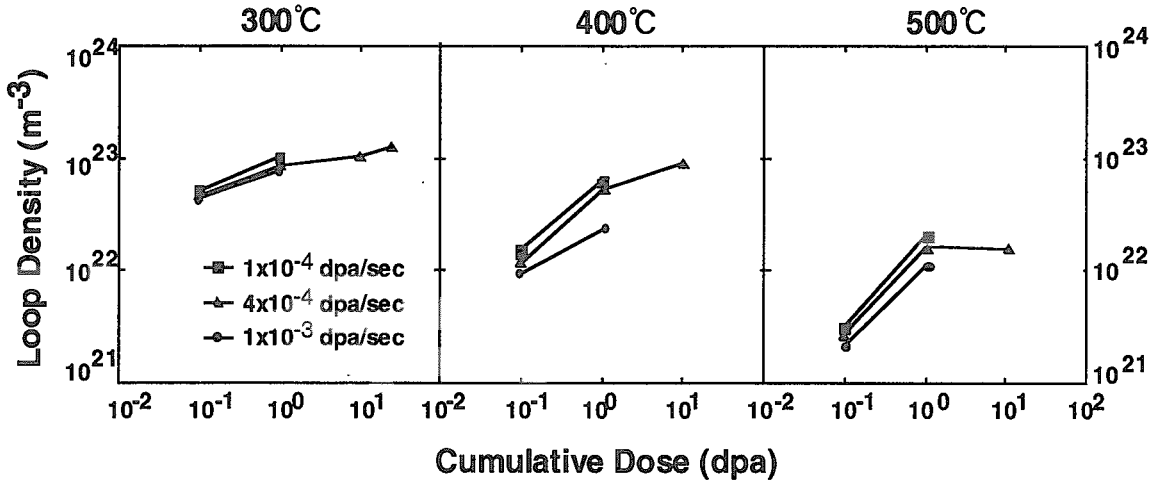


Figure 2 Cumulative dose dependence of interstitial loop density in Fe-15Cr-16Ni at various dose rates.

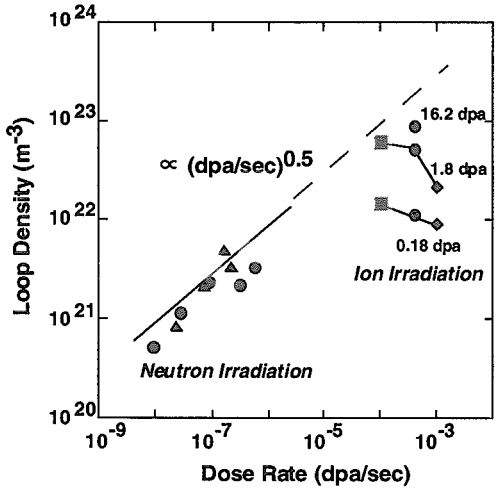


Figure 3 Dose rate dependence of saturated loop density in Fe-15Cr-16Ni irradiatedat about 400°C under wide range of dose rates.

4.8 Effect of Simultaneous Ion Irradiation on Microstructural Change of SiC/SiC Composites at High Temperature

T. Taguchi[1)], E. Wakai[1)], N. Igawa[1)], S. Nogami[2)], A. Hasegawa[2)], L.L. Snead[3)] and S.Jitsukawa[1)]

[1)]Department of Materials Science, JAERI

[2)]Department of Quantum Science and Energy Engineering, Tohoku University

[3)]Metals and Ceramics Division, Oak Ridge National Laboratory

1. Introduction

Ceramic matrix composites show excellent mechanical properties at high temperature and also non-catastrophic failure behavior. The materials, therefore, are expected to be used for structural applications at high temperature. In particular, SiC/SiC composites are expected to be one of the candidate materials for first wall and blanket components in a fusion reactor because of their low residual radioactivity after neutron irradiation. Under the fusion condition, He and H atoms are produced by 14MeV neutron from transmutation reactions of (n,α) and (n,p), respectively. These transmutation rates in SiC are larger than those in the other candidate materials such as ferritic steels and vanadium alloys[1),2)]. The synergistic effect of gas atoms and displacement damage on microstructural change in the SiC/SiC composites had been examined at temperature lower than 800°C[3)]. However, the material will be used at temperature ranging from 800 to 1200°C in a fusion reactor.

In this study, we investigated the effect of simultaneous triple irradiation of He, H and Si ions on microstructural change of SiC/SiC composites at temperature higher than 800°C.

2.Experimental procedure

2.1 Materials and preparation

The 2D plane weave of Tyranno SA SiC fiber fabric was chosen in this study. SiC/SiC composite examined in this study was fabricated by forced thermal gradient chemical vapor Laboratory. The density and porosity of this composite were 2.76 g/cm^3 and 10.8 %, respectively. The fiber volume fraction was about 37%. This composite has the carbon layer as the interface between matrix and fiber and the thickness of the layer was about 150 nm. The surface of the specimen was polished with diamond blade of #8000. The size of specimen was 1mm-width, 5 mm-long and 0.4 mm-thick.

2.2 Irradiation

The simultaneous ion irradiation was carried out at TIARA facility of JAERI/Takasaki. The specimen was simultaneously irradiated at 1000°C by 6.00MeV Si^{2+} ions, 1.2MeV He^+ and 250keV H^+ ions. He^+ ion implantation was performed with using aluminum foil energy degrader in order to control He distribution in the depth range of about 1.5~2.2 μ m from the specimen surface. Figure 1 shows the distributions of He and H concentration and displacement damage as a function of depth from the surface in SiC calculated by TRIM code[4)]. In this study, the displacement threshold energies of Si and C were assumed to be 35 eV and 20 eV[5)], respectively. The irradiation was performed to 10 dpa at the depth of 2 μm as shown in Fig. 1.

2.3 Microstructure observation

The focused ion beam processing was used to prepare a foil specimen for transmission electron microscopy (TEM) observation. The foil specimen contains the fiber, matrix and interface

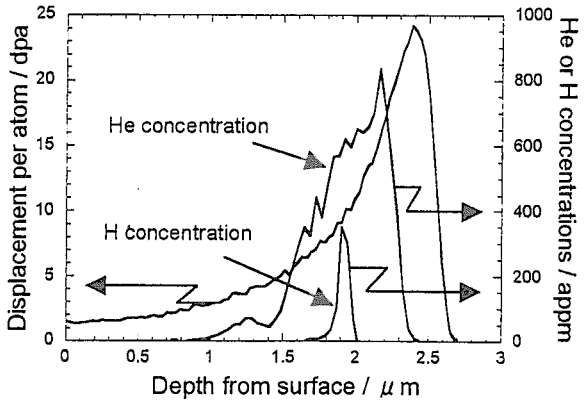


Fig.1 Distribution of He, H concentrations and displacement damage as a function of depth from surface in SiC calculated by TRIM code [4].

regions. Microstructural observation was performed with Hitachi HF-2000 field-emission TEM operated at 200kV.

3. Results

The TEM microphotographs of SiC/SiC composite (Tyranno SA SiC fiber with carbon interface) irradiated at 1000°C with simultaneous triple ion beams are shown in Fig.2. The microstructural change of carbon interface layer was found in the irradiation region. The carbon interface layer was the amorphous structure in non-irradiation region, while the turbostratic carbon structure was formed in the irradiated region. A new phase like SiC was formed in the carbon interface layer of the projected range of Si ions. The weak strain contrast was observed in the irradiated Tyranno SA SiC fiber. The microstructral change in irradiated SiC matrix was not observed.

According to previous report[3], the microstructure observation of the ion irradiated SiC/SiC composites (Hi-Nicalon SiC fiber with carbon interface layer) at 800°C exhibited the debonding at the boundary between carbon interface layer and fibers. This debonding was thought to be the shrinkage of Hi-Nicalon SiC fiber induced by ion irradiation. While, in this study the microstructure observation of the ion irradiated SiC/SiC composite (Tyranno SA SiC fiber with carbon interface) at 1000°C did not exhibit the debonding in the interfaces. It was found that the SiC/SiC composites using Tyranno SA SiC fiber had excellent stability against irradiation.

4. Conclusions

Effect of simultaneous triple irradiation of He, H and Si ions on microstructural change of SiC/SiC composites (Tyranno SA SiC fiber with carbon interface) at 1000°C has been examined. The microstructure of SiC/SiC composite irradiated to 10 dpa was examined by TEM. Microstructure observation showed that SiC/SiC composites using Tyranno SA SiC fiber had excellent stability against irradiation.

References

1) L.L.Snead et al., Journal of Nuclear Materials, **233-237** (1996) 26-36.

2) T.Noda et al., Journal of Nuclear Materials, **233-237** (1996) 1491-1495.

3) S. Nogami et al., Journal of Nuclear Materials, 283-287(2000)268-272.

4) J.F.Ziegler et al., The Stopping and Ranges of Ions in Matter, vol.1, Pergamon Press, New York, 1985.

5) R.Devanathan et al., Journal of Nuclear Materials, **278** (2000) 258-265.

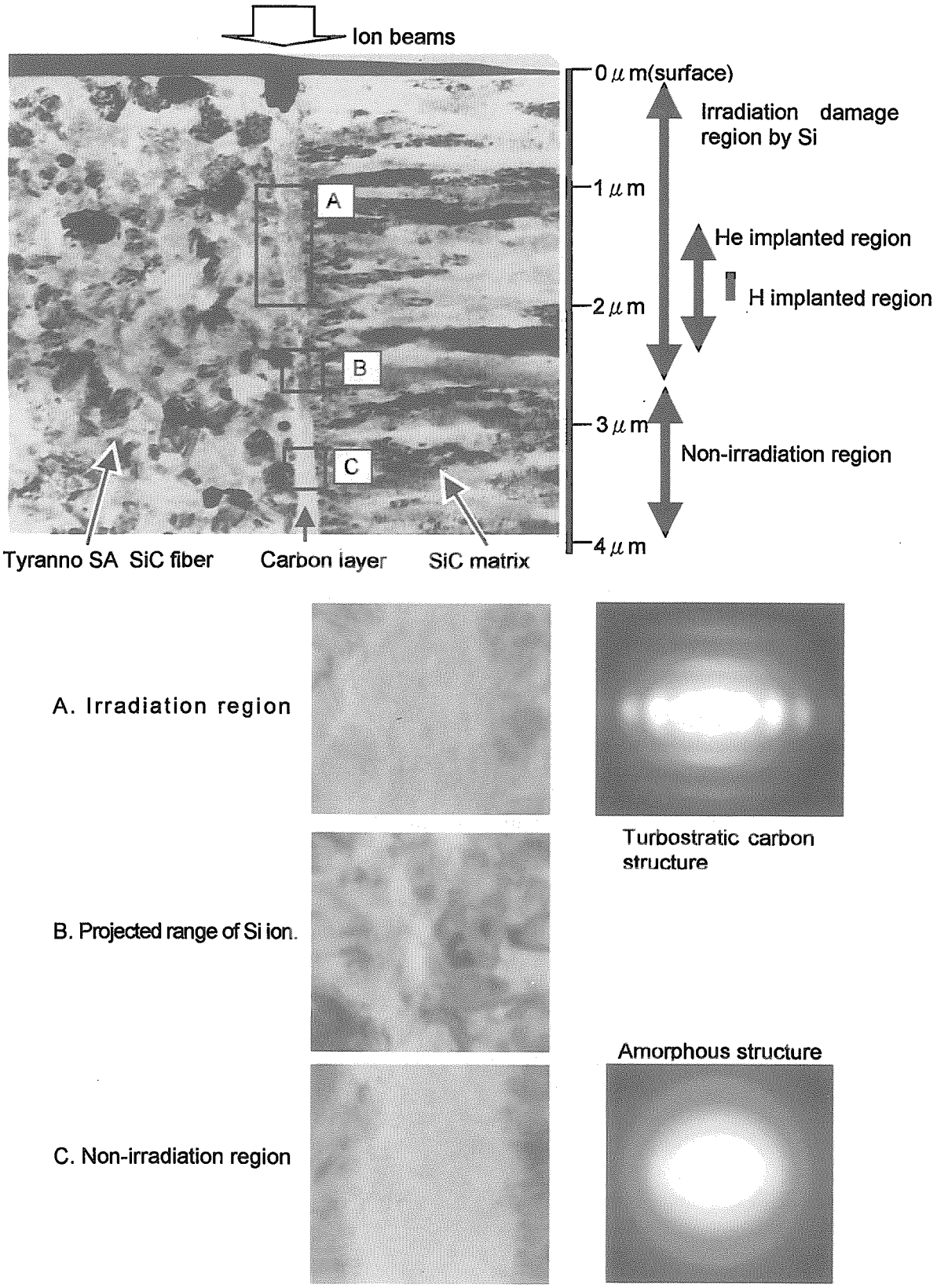


Fig.2 TEM microphotographs of SiC/SiC composite irradiated at 1000°C to about 10 dpa by simultaneous triple ion beams. Cross-section of the irradiated composites is shown in upper figure. This specimen was prepared by FIB. Lower figure shows the magnified micrographs at the interface.

4.9 Radiation Induced Cavity Formation in F82H with various Heat and Mechanical treatments

T. Sawai[1], E. Wakai[1], T. Tomita[2], A. Naito[1] and S. Jitsukawa[1]

[1]Department of Materials Science, [2]Department of Hot Laboratories, JAERI

1. Introduction

Reduced activation ferritic/martensitic (RAF/M) steels are considered as the most promissing materials for the fusion structural applications. A 8Cr-2W-V-Ta steel, F82H, is a leading candidate of this type of alloys. Accumulated knowledge on its radiation behavior makes it also attractive to be used in the structural material in the target of spallation neutron sources.

It has been reported that the co-generated helium appriciably increases the swelling of F82H irradiated by neutrons[1]. This has been confirmed by TIARA experiments, where the alloy-to-alloy differences of swelling were fairly large[2] as experienced in austenitic stainless steels. The neutron irradiation data suggest that the heat treatments would also affect the swelling of F82H that is usually used in a normalized and tempered condition[1].

To evaluated the effects of material conditions on the radiation response of F82H, specimens with various heat and mechanical treatments were irradiated in the TIARA multiple-beam irradiation facility and cavities were observed by a transmission electron microscope (TEM).

2. Experimental

F82H with 8% Cr, 2% W, 0.2% V, 0.04% Ta and 0.1% C (all compositions are in wt%) was normalized at 1040 °C for 40 minutes, followed by tempering at 750 °C or 780 °C. Tempering time was 1 hour or 2 hours. Some of the specimens were cold rolled. Reduction of thickness was 20% or 40%. The conditions of specimens used in this study were summarized in Table 1. In addition to these specimens, TIG weld joints of F82H were irradiated. The conditions of TIG weld are given in Table 2. Further details of weld are given elsewhere[3].

Table 2 TIG welding conditions

Plate Thickness	25mm
Gap width	15mm
Polarity	DC
Travel speed	80 mm/min
Position	Flat
Layer	10-12
Pass	10-20
(Oscillating Electrode method)	

These specimens were irradiated in the TIARA multiple-beam irradiation facility. 10.5 MeV Fe^{3+} beam from the Tandem Accelerator and 1.05 MeV He^{+} beam from the Single-Ended Accelerator were simultaneously irradiated on to the specimens at 450 °C. The He^{+} beam was irradiated through a degrader to widen the implantation depth. Cross-section TEM specimens were obtained using a focused ion beam (FIB) processor with a μ sampling system installed in the Hot Laboratory of JAERI-Tokai. For the weld specimens, preparation of TEM foils from the accurate positions in the heat affected zone was enabled with the FIB system. Further details of irradiation and specimen preparation are given elsewhere[4].

Microstructural data were obtained around the specimen depth of 1 μm, where the displacement damage and concentration profiles of implanted ions change gradually. Irradiation dose rate and He/dpa ratio in dual beam irradiation measured at this depth are about 1.6×10^{-3} dpa/s and 10 appmHe/dpa, respectively.

Table 1 Heat and mechanical treatments of F82H used in this study

normalizing		tempering		As N&T	20% CW	40% CW
1040 °C	40 min	750 °C	1 hr	O		O
			2 hr	O		
		780 °C	1 hr	O	O	

Figure 1 shows the relationship between dislocation density measured by TEM and hardness of the specimens, showing a good proprtionality. Dislocation densities of cold-worked (CWed) specimens were higher than those of as-normalized-and-tempered (as-N&T) ones. Higher tempering temperature results in lower dislocation density, while longer tempering time has limited effects on dislocation density and hardness.

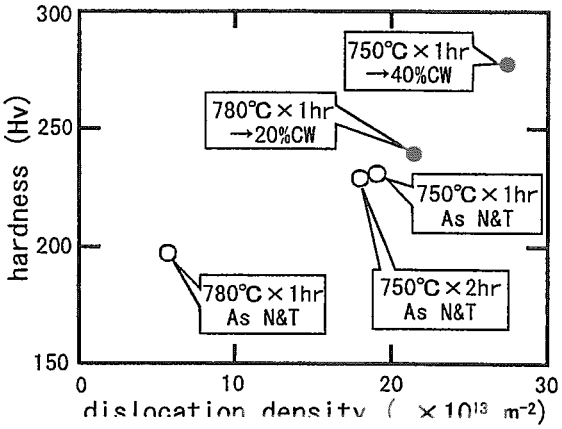


Fig. 1 Hardness vs. dislocation density of used specimens

Figure 2 shows the cavity microstructure in the as-N&Ted and the CWed specimens. These specimens were tempered at 780 °C for 1 hr. Cavities in the CWed specimen were smaller than those in the as-N&Ted specimen. Size distributions of these cavities are given in Fig. 3. Cavity size in the CWed specimen was up to 6 nm, while the as-N&Ted specimen contained cavities up to 13 nm.

The size of the largest cavity contained in F82H specimens with various dislocation density is shown in Fig. 4, where the higher the dislocation density is, the lower the maximum cavity size. Similar results are also obtained with TIARA triple-beam irradiation of spallation simulation[4], where cavities in CWed F82H were smaller than those in as-N&Ted specimens.

In the heat affected zone of F82H weld joint, a marked line appears due to transformation. The inner side of this line was heated above Ac1 temperature during weld. Formed austenitic microstructure was quench-hardended during the cooling after weld. On the other hand, the outer side remains below Ac1 and the heat during weld affects as the additional

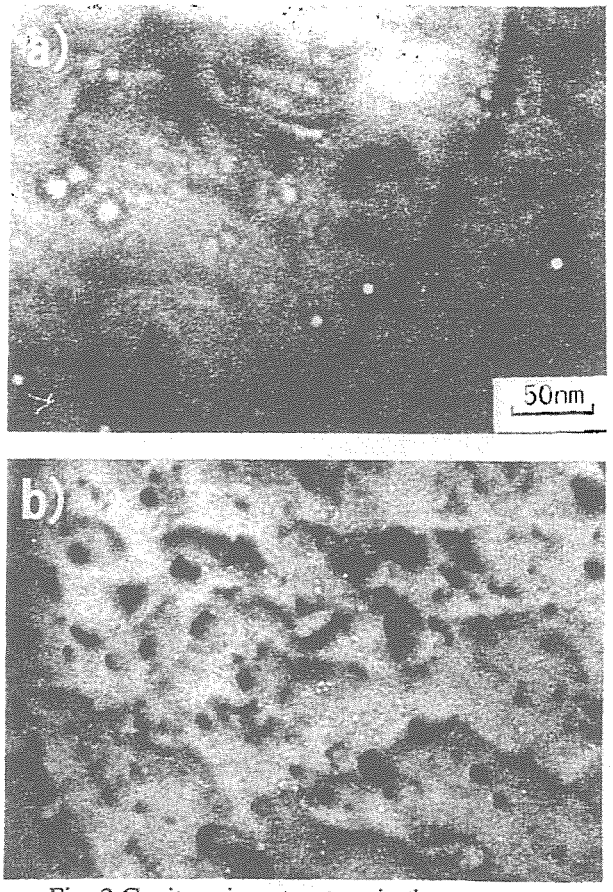


Fig. 2 Cavity microstructure in the as-N&T(a) and the CWed(b) F82H specimens irradiated at 450 °C up to 50 dpa.

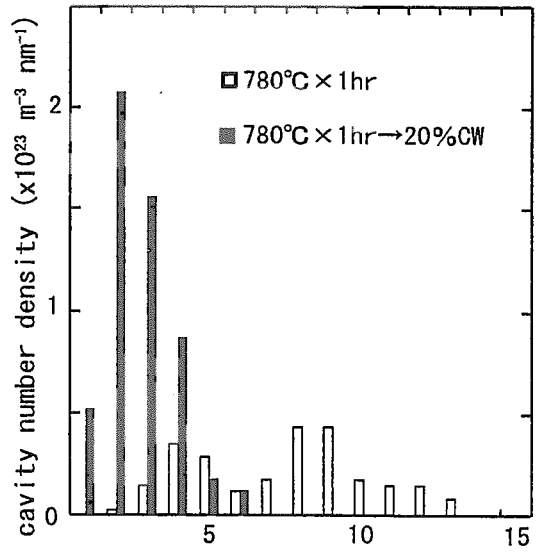


Fig. 3 Cavity size distribution of N&Ted and the CWed F82H specimens irradiated at 450 °C up to 50 dpa.

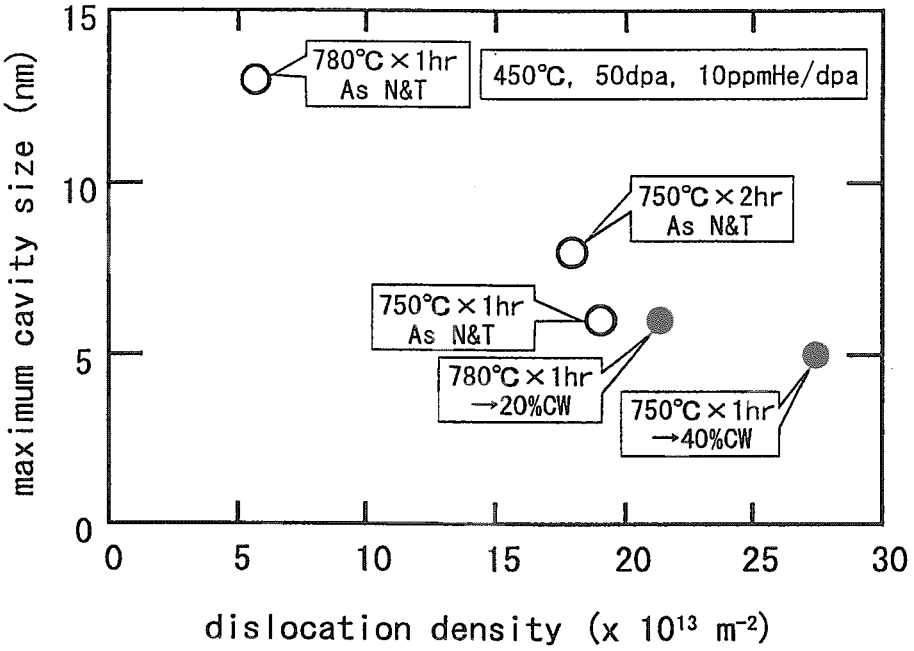


Fig. 4 The maximum cavity size vs. the dislocation density. Open circles represent data obtained with as-N&Ted specimens, and solid ones with CWed ones.

tempering of the martensitic microstructure. Hardness of the inner side is higher than that of the outer side[3], and therefore the dislocation density of the inner side is considered to be higher than that of the outer side. Using the capability of μ sampling of FIB, TEM specimens were obtained 0.5 mm inside and outside of the transformation line from the irradiated weld joint, respectively. Size of cavities in the outer side specimen reaches up to 30 nm. This is the largest cavity size obtained in the present experiment. Size of Cavities in the inner side specimen remains less than 10 nm (Fig. 5). This result is consistent with the results obtained with as-N&Ted and CWed specimens.

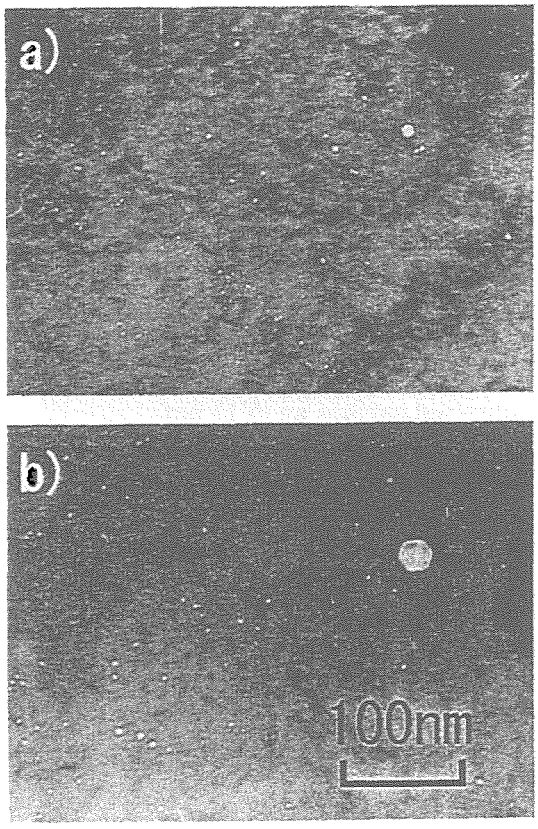


Fig. 5 Cavities formed in the heat affected zone of TIG welded F82H. Cavities in the inner side of the transformation line (a) is smaller than those of outer side of the line(b).

References

1)E. Wakai, N. Hashimoto, Y. Miwa, J. P. Robertson, R. L. Klue, K. Shiba and S. Jitsukawa, J. Nucl. Mater., 283-287(2000)799-805.
2)A. Naito, S. Jitsukawa, E. Wakai, H. Tanigawa I. Ioka, H. Hishinuma and A.Kohyama, JAERI-Review 2000-024 (TIARA Annual Report 1999), pp.128-129.
3)T. Sawai, K. Shiba and A. Hishinuma, J. Nucl. Mater., 283-287(2000)657-661.
4)E. Wakai et al. in this report.

4.10 Comparison of Cavity Formation Behavior in RAF/M Steels Irradiated with Dual Beams of Fe + He ions as Observed in the Depth Dependent Damage Structure

A. Naito, S. Jitsukawa, E. Wakai, T. Sawai, I. Ioka* and H. Tanigawa**
Department of Material Science, JAERI, *Department of Nuclear Energy System, JAERI, **Department of Fusion Engineering Research, JAERI

1. Introduction

Reduced activation ferritic/martensitic (RAF/M) steels have been considered as potential structural materials for the first wall of blanket (FWB) structures. D-T fusion neutrons will produce considerable amount of helium and hydrogen atoms in FWB structural materials by transmutation reactions during service. This may result in the acceleration of void swelling of the materials. The objective of this study is to clarify the effect of helium on cavity formation and swelling in RAF/M steels and to compare depth profiles of cavity formation among those steels by the ion-irradiation experiments with high accuracy.

2. Experimental

The materials used in this study are reduced activation steels, F82H and JLF-1. The chemical compositions are shown in Table 1. The heat treatments given were optimized from the viewpoint of high-temperature strength and fracture toughness. A conventional steel, HT9 is also used as a reference material.

The dual-ion irradiation was carried out at a temperature of 450 °C using the Takasaki Ion Accelerators for Advanced Radiation Application (TIARA) facilities of the Japan Atomic Energy Research Institute (JAERI). Displacement damage was introduced by 11.3 MeV Fe^{3+} ions up to 60 displacement per atom (dpa), and 1.2 MeV He^{+} ions were co-implanted. The microstructure of the irradiated specimens was examined with a JEM-2000FX transmission electron microscope (TEM). The nominal damage rates and He/dpa ratios were 2 x 10^{-3} dpa/s and 20 appm He/dpa, respectively.

The displacement dose, dose rate and helium implantation rate were calculated assuming a 40 eV displacement threshold energy using the SRIM code. This is the ASTM-recommended value. According to the SRIM results, the atomic concentration of injected iron at a depth of 1.9 μm below the specimen surface was 0.07 % at 60 dpa.

3. Results

Unirradiated Microstructure

The microstructures of a region deep enough, i.e. a region that can be regarded as unirradiated range, were observed from the ion-irradiated surface of each steel. The three steels have lath-structure and the width of lath is from 200 to 600 nm. The high-density dislocation and the low-density precipitates consist in each lath. The precipitates are preferentially distributed in the lath boundary with high density. However, components of the precipitates have not been identified.

When lath widths among the three steels are compared, those of JLF-1 and HT9 are almost equal and that of F82H is equivalent to them or somewhat small. As for dislocation density, those of JLF-1 and HT9 are almost equal and that of F82H is higher than they. As for number density of precipitates, as well as dislocation density, those of JLF-1 and HT9

Table 1 Chemical compositions of the materials used.

(wt%)

	C	Si	Mn	P	S	Ni	Cr	V	Ti	Ta	W	Mo	B	Al	N	Fe
F82H	0.10	0.10	0.10	0.005	0.002	-	8.0	0.20	0.05	0.04	2.0	0.001	0.0003	0.01	0.005	Bal.
JLF-1	0.10	0.05	0.45	0.003	0.002	-	8.85	0.20	-	0.080	1.99	-	0.0002	0.003	0.0231	Bal.
HT9	0.19	0.22	0.48	0.018	0.001	0.59	12.0	0.29	-	-	0.51	1.0	-	0.02	0.002	Bal.

are almost equal and that of F82H is higher than they.

Irradiated Microstructure

The damage microstructures produced by ion-irradiation were observed at the range from the ion-irradiated surface to about 3 μm depth. When they are compared with those of unirradiated range, there were no changes in lath structure, dislocation density and the distribution of precipitates for the three steels.

Cavities were formed in the radiation-damaged range for the three steels. In the case of JLF-1 steel, the cavities were observed from the ion-incident surface to the depth of 2.8 μm. The distribution of cavities differs significantly for each lath. Cavity is formed to near the surface in some laths, and no cavity is formed in other laths. The distribution of cavities in each lath is relatively heterogeneous. In every lath, the zone in which cavity is not formed along the lath boundary, i.e. denuded zone is observed by the width about 70 nm.

In the case of HT9 steel, the cavities were observed from the ion incident surface to the depth of 2.4 μm. The differences in the distribution of cavity for each lath observed in JLF-1 steel are hardly observed. The distribution of cavity in each lath is relatively heterogeneous as well as JLF-1 steel. The denuded zone observed in JLF-1 steel was not observed in HT9 steel.

In the case of F82H steel, the cavities were observed from the ion incident surface to the depth of 2.4 μm. The differences in the distribution of cavity for each lath observed in JLF-1 steel are hardly observed similarly to HT9 steel. The distribution of cavity in each lath is relatively heterogeneous similarly to both JLF-1 and HT9 steels. The denuded zone was also not observed in F82H steel.

The depth dependence of the number density of cavity, average cavity size, and the level of swelling is shown in Fig. 1 for each steel. In the case of JLF-1 steel, the depth dependence of number density shows that the formation range of cavity is in a depth of 0.2 to 2.8 μm from the ion incident surface. The peak of number density is located at a depth of 2.0 to 2.2 μm. This peak depth corresponds to a position about 0.2 μm deeper than the peak damage depth and the mean projected range of helium. The half-value width of number density is about 0.3 μm. This value is nearly equal to the half-value width of the implanted helium. Significant bi-modal distribution was shown in the size distributions at 1.6 to 2.0 μm. The average cavity size showed maximum at a depth of 1.2 to 1.4 μm. The swelling level showed a peak at a depth of 1.6 to 2.0 μm. This depth approximately agrees with the peak damage depth, the mean projected range of helium and the depth range in which the bi-modal size distribution are shown.

In the case of HT9 steel, the depth dependence of number density shows that the formation range of cavity is in a depth of 0.2 to 2.8 μm from the ion incident surface. The peak of number density is located at a depth of 2.0 to 2.2 μm. This peak depth corresponds to a position about 0.2 μm deeper than the peak damage depth and the mean projected range of helium. The half-value width of number density is about 0.3 μm. Bi-modal distribution was shown in the size distribution at 1.8 to 2.0 μm. The average cavity size showed maximum at a depth of 1.4 to 1.6 μm. The swelling level showed a peak at a depth of 1.8 to 2.0 μm.

In the case of F82H steel, the depth dependence of number density shows that the formation range of cavity is in a depth of 0.0 to 2.4 μm from the ion incident surface. The peak of number density is located at a depth of 2.0 to 2.2 μm. This peak depth corresponds to a position about 0.2 μm deeper than the peak damage depth and the mean projected range of helium. The half-value width of number density is about 0.8 μm. This value is equivalent to an about 3 times of the half-value width of the implanted helium. The bi-modal

distribution was not shown in the size distribution of every depth region. The average cavity size showed maximum at a depth of 1.0 to 1.2 μm. The swelling level showed a peak at a depth of 1.4 to 1.8 μm. This depth corresponds to a position about 0.3 to 0.7 μm shallow from the peak damage depth and the mean projected range of helium.

When comparison among the steels is carried out for the depth dependence of number density, average diameter of cavity and swelling, the formation range of cavity is comparable with each other for the three steels.

The peak depth of number density is also comparable with each other for the three steels, and is 2.0 to 2.2 μm. Its depth is about 0.2 μm deep from the peak damage depth and the range of helium. The peak is the highest for HT9, and the second for JLF-1 and the third for F82H. The half-value widths of number density in JLF-1 and HT9 are comparable, and that in F82H is smaller than they. The half-value widths in JLF-1 and HT9 are nearly equal to the half-value width of implanted helium, and that of F82H corresponds to three times the half-value width of the implanted helium.

As for the size distribution, the depth region in which the bi-modal distribution is shown exists in JLF-1 and HT9. On the other hand, the depth region in which the bi-modal distribution is not shown, exists in F82H. As for the average diameter, position of the peak is the deepest for HT9, the second for JLF-1 and the third for F82H. The turn of the maximum size of cavity is JLF-1, HT9 and F82H.

As for the peak depth of the swelling, that of HT9 is the deepest, that of JLF-1 is equivalent to it, or it is somewhat shallow, and that of F82H is still shallower. The peak depths of HT9 and JLF-1 are nearly as equal as the peak damage depth, the range of helium and the depth region in which the bi-modal size distribution is shown. The value of peak swelling is large in the order of JLF-1, HT9 and F82H.

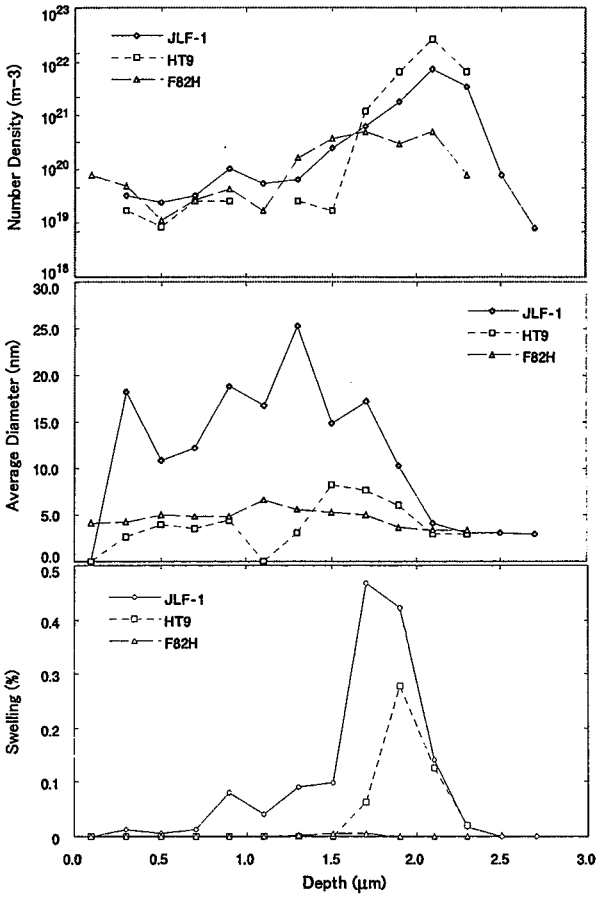


Fig. 1 Depth profiles of number density, average diameter of cavities and swelling in the irradiated specimens.

4. Summary

Cavities were formed in the radiation-damaged range for the three steels. The formation range of cavity was comparable with each other. The peak of cavity number density was the highest for HT9, and the second for JLF-1 and the third for F82H. The turn of the maximum size of cavity was JLF-1, HT9 and F82H. The value of peak swelling was large in the order of JLF-1, HT9 and F82H.

4.11 Investigation of Hardness Changes on Helium-Ion Implanted Iron by Ultra-micro-hardness Testing

H. Tanigawa [1], S. Jitsukawa [2], H. Abe [3], T. Iwai [4], Yutai. Katoh [5]
[1] Office of Fusion Materials Research Promotion, [2] Department of Material Scinece,
[3] Department of Materials Development, [4] Research Center for Nuclear Science and Technology, University of Tokyo, [5] Institute of Advanced Energy, Kyoto University

1. Introduction

A reduced activation ferritic-martensitic steel, F82H (Fe-8Cr-2W-V-Ta), is one of the candidates for the first wall and blanket structural material for a D-T fusion reactor. It has been reported that transmutation-produced helium atoms from (n, α) reactions may play a significant role in the irradiation embrittlement of the alloy during service. There are only a few ways to implant helium into a material, and helium ion implantation using an ion accelerator is the most convenient and accurate method. The main disadvantage of this method is that the helium-implanted region is limited to a few micrometers from the irradiation surface. Because of this, it is generally recognized that helium implantation is not suitable to study mechanical properties. The only way to investigate the mechanical properties of such a small volume is by ultra micro- indentation techniques. Ultra micro-indentation techniques have been developed recently, mainly to measure the mechanical properties of hard thin films on a substrate [1,2] or ion implanted materials' surfaces [3]. This micro-indentation technique has also been applied to ion-irradiated materials [4,5,6]. In this study, the effects of helium on irradiation hardening and embrittlement were investigated by a ultra micro-indentation technique and by microstructural observations in the deformed region.

2. Experimental procedure

The materials used in this study were high purity iron. The impurity content (P, C, S , O, N, B) in the high purity iron was less than a few appm. TEM disks were punched out from sheets of the materials, and polished by the following series: SiC paper up to #4000, 9 and 3 μm diamond powder, 0.3 and 0.05 μm alumina powder, then finished by an electrolytic surface finish.

1 MeV He^+ ions were degraded to 203keV and 317keV to implant helium into a wider range than that for single energy ion implantation. The profile of the implanted helium was calculated with the TRIM code and the results suggest that the helium ions were implanted to a depth between 600 and 800nm from the incident beam surface. Implanted helium concentration was 500 appm at this region. To evaluate the effects of damage simultaneously induced for 0.04 dpa by helium implantation, 2MeV He^+ ion irradiation were performed to induce 0.04 dpa damage in the depth region between 600 and 800 nm. Both helium implanted specimen and damaged specimen were annealed at 673K for 1 hour in vacuum at about 10^{-5} Pa to remove interstitial origin damage structure. With this annealing condition, no cavity or visible bubbles were formed in both specimens.

Ultra micro-indentation was performed using a UMIS-2000 from CSIRO, Australia, with Berkovich-type tips. Measurements were made at loads to penetrate 300 nm, i.e., 6mN for pure Fe and 10 mN for F82H. Typically, indentations of the samples were made using a 5×5 array of indents with a 20 μm interval. The results were analyzed in the manner outlined by Oliver and Pharr[7] with further refinements proposed by Mencik and Swain[8].

For the FIB processing, the implanted surface of a TEM disk was covered with hard adhesive and then the disk was nickel plated on the non-implanted side. A 300 μm thick sheet was sliced in the direction vertical to the disk surface. A half moon TEM disk was drilled out from the sheet using an abrasive slurry disk cutter made by South Bay Technology Inc., and the half moon disk was polished down to 100μm thick. At last, the adhesive cover was removed by acetone, then indentation tests were performed on the disk surface. The thin foil around the impression was made so that they may include the indentation axis by means of FIB micro-processing, using HITACHI FB-2000A focused ion beam system. The details of the FIB micro-processing procedure has been explained elsewhere [9]. Microstructure examination was

carried out using a HITACHI HF-2000 transmission electron microscope operating at 200 kV.

3. Results and discussion

Figure 1 show the normalized hardness on each specimen against non-irradiated specimen, whose hardness is 2.05 GPa on the average. As for as-irradiated specimens, about 23 % increase of hardness compared to the non-irradiated specimen was measured for the helium-implanted specimen, and 36% increase of hardness was measured for the helium-irradiated specimen. On annealed specimens, the helium-irradiated specimen becomes the same hardness level as that of non-irradiated specimen, but 10% increase of hardness was still measured on the helium-implanted specimen. This result suggests that the implanted helium, which may strongly combined with vacancy, would cause the hardening besides irradiation damage.

Bright field TEM images of the region beneath the impression are shown in figure 2. For non-irradiated specimen, induced plastic deformation zone was about 3 μm deep, whereas the maximum indenter depth was about 300 nm. That is, the plastic zone was ten times the size of the indentation depth. On the other hand, the plastic deformation zone was clearly limited to 800 nm from the center of the impression for the 500 appm helium implanted specimen. As for helium-irradiated and annealed specimen, the plastic deformation zone was about 3 μm deep, just as deep as on non-irradiated specimen. On the other hand, the plastic deformation zone on helium-implanted and annealed specimen was clearly limited at the helium implanted region, just as same as on helium implanted specimen. No bubble or cavities were observed at helium implanted region. These observed results quite agree with the results of hardness tests, and suggest that the implanted helium would cause hardening besides irradiation damages.

4. Summary

Ultra micro indentation tests were performed on helium implanted and helium irradiated pure Fe, and microstructures below the impression were examined by means of FIB processing and TEM observation. The following remarks are obtained from the present work;

(1) About 23 % increase of hardness was observed for 500 appm helium implanted specimen and about 36% increase of hardness for helium irradiated specimen.
(2) For annealed specimens, no hardening was detected on helium-irradiated and annealed specimen, but 10% of hardening remained on helium-implanted and annealed specimen. This suggests the possibility that the helium hardening effect was present besides irradiation damages.
(3) The plastic deformation zone of the helium-implanted and annealed specimen was clearly terminated at the helium implanted region; 600 to 800 nm depth from the incident beam surface, but as for the helium-irradiated and annealed specimen, the plastic deformation zone was just the same as that for non-irradiated specimen. These results well agree with the remark (2).
(4) From these results, it could be said that implanted helium would cause hardening besides irradiation hardening.

References

[1] N.G. Chechenin, J. Bottiger, J.P. Krog, Thin Solid Films 261 (1995) 219
[2] M. Wittling, A. Bendavid, P.J. Martin, M.V. Swain, Thin Solid Films 270 (1995) 283
[3] R. Nowak, C.L. Li, M.V. Swain, Mater. Sci. and Eng. A253 (1998) 167
[4] S.J. Zinkle, W.C. Oliver, J. Nucl. Mater. 141-143 (1986) 548
[5] P.M. Rice, R.E. Stoller, B.N. Lucus, W.C. Oliver, Proc. Mater. Res. Soc. Symp. 373 (1995) 205
[6] Y. Katoh, H. Tanigawa, T. Muroga, T. Iwai, A. Kohyama, J. Nucl. Mater. 271&272 (1999) 115
[7] W.D. Oliver and G.M. Pharr, J. Mater. Res. 7 (1992) 1564
[8] J. Mencik and M.V. Swain, Mater. Forum 18 (1994) 277
[9] M. Ando, Y. Katoh, H. Tanigawa, A. Kohyama, J. Nucl. Mater. 271&272 (1999) 111

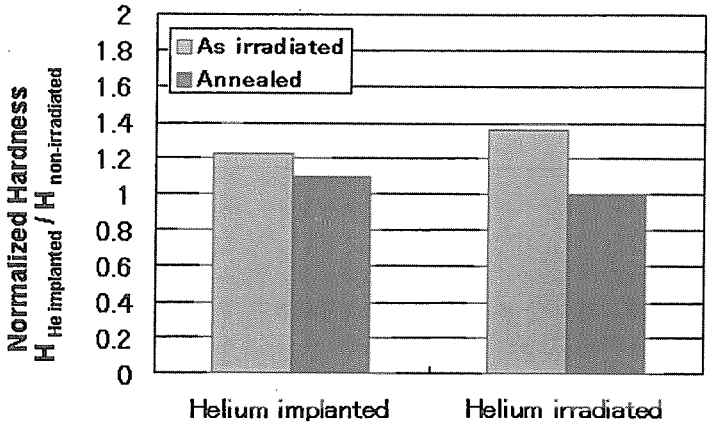


Fig.1 Normalized hardness of helium implanted and helium irradiated specimens

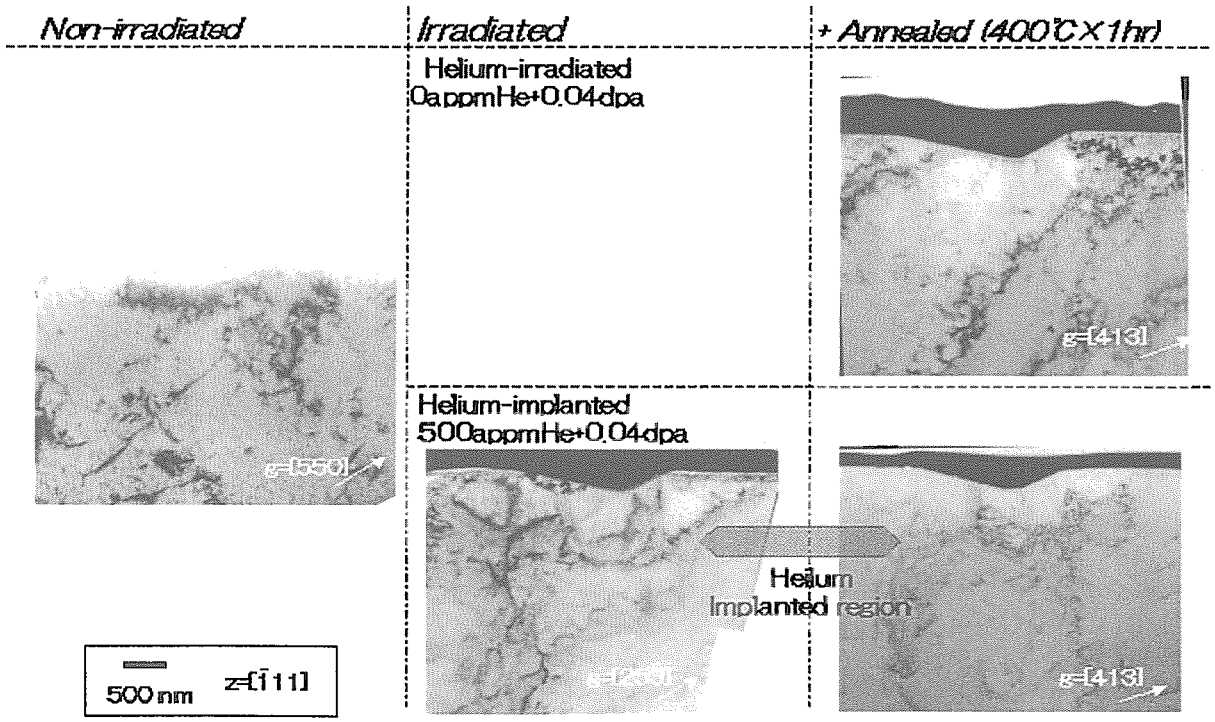


Fig.2 TEM bright field images of the region beneath the impressions.

4.12 Effect of ion irradiation on corrosion behavior of austenitic stainless steel

I.Ioka, S.Hamada, M.Futakawa, A.Naito[1)], K.Kiuchi, S.Kuroiwa[2)], S.Miyamoto[2)] and K.Ogura[2)]
Department of Nuclear Energy System, JAERI,
1) Department of Material Science, JAERI, 2)The Japan Atomic Power Company

1. Introduction

In the upgrading of the power reactor, ultra-high burnup extension of fuel (>100GWd/t) seems to be promising for economy, waste reduction and energy resource security. The realization of the new technology is dependent on the development of high-performance cladding tube. New stable austenitic stainless steel, Fe-highCr-highNi alloy, is developed as a candidate cladding material from the point of neutron economy, irradiation resistance, mechanical property, radioactivity and water-corrosion resistance of practical alloys[1,2]. Irradiation Assisted Stress Corrosion Cracking (IASCC) in the austenitic stainless steel is one of largest problems.

It is believed that inverse segregation of Cr and segregation of impurities (such as P, S, and Si) in grain boundary by the irradiation mainly caused IASCC of the austenitic stainless steel. As quantitative evaluation method of the grain boundary, electro-chemical potentiokinetic reactivation (EPR) test and potentiostatic electrolytic test are being tried in the sensitized stainless steel, the neutron irradiated material and the ion irradiated material[3-6]. However, it is difficult to accurately evaluate the intergranular corrosion in the irradiated material since corrosion resistance in grain itself deteriorates by introduced radiation defects. Then, the development of ISACC resistance evaluation technique, which consists of the ion irradiation and the residual stress by the indentation and the electrochemical corrosion, is advanced. In the report, the change in surface appearance of ion irradiated Type 316 stainless steel (SUS316) which is the comparison material of the candidate cladding material was examined to confirm the capability of this technique.

2. Experimental

Specimen is a disk of 3mm in diameter with 0.2mm thickness. The electrochemically polished specimens were irradiated in triple (12MeV Ni^{3+}, 750keV He^{+} and 290keV H^{+}) ion beam modes at a temperature of 300°C. The TRIM code was used to compute the implanted ion concentration and the displacement dose as a function of depth beneath the specimen surface. The displacement damage in the specimen is mainly attributed to Ni^{3+} ion implantation. The peak dose is about 22dpa around 2μm. The peak values of concentration of Ni, He and H atoms are about 6000appm, 260appm and 2500appm, respectively. The peak positions of implanted He^{+} and H^{+} ions are controlled so that the effect of implanted Ni^{3+} ions can be neglected. The He/dpa and H/dpa ratios of the specimens are about 24 and 230, respectively, at the depth of approximately 1.3μm. In case of the full MOX-ABWR of burn-up 100GWd/t, helium and hydrogen which are created by the nuclear transformation reaction are 120appm and

1100appm for the candidate material, respectively. Displacement damage becomes about 50dpa.

The corrosion test specimen was produced by the cross section method[7] in order to obtain information along the depth direction in the ion irradiated region. The test specimen which drove the indenter near the damage region was also produced.

The analytical result of residual stress which arises around the indentation of the corrosion test specimen is shown in Fig.1. The stress component is reprensented in the direction of y. The part of hatching line in Fig.1 shows a tensile state. The triangular region surrounded by the dotted line is a position of the indentation, and the part bordered by the dotted line on the left hand side is the damage region. It is proved that the tensile stress exists on the surface of damage region.

The corrosion test was carried out in 10% oxalic acid at room temperature (refer to JISG0571). The appearance of the corrosion surface was examined by scanning electron microscope (SEM) and atomic force microscope (AFM).

3. Results and discussion

Surface appearance and surface roughness of the specimen after the corrosion are shown in Fig.2. The upper part of SEM image is the nickel-plated part, and the lower side is the test specimen. Three grains including grain boundary are in the test specimen side, and there is a corrosion-resistant difference by the crystal orientation[6]. Corrosion part of about 2μm corresponding to the damage region was observed in all grains. In line 1 of fig.2, the difference in depth (difference in the corrosion rate) between damage region and non-damage was 50-90nm. Surface roughness was measured along line 2 and 3, which stride over grain, by AFM. Though the intergranular corrosion was confirmed in the non-damage region, it was not confirmed in the damage region. The results of the corroded specimen with indentation by SEM and AFM are shown in Fig.3. From the steeper pile-up around the indentation, it was not possible to confirm the remarkable corrosion in residual stress division of the damage region.

4. Conclusion

After ion irradiated SUS316 with indentation was corroded, the surface appearance was examined to confirm the capability of this technique, and following results were obtained.

1) The difference in corrosion resistance between non-damage region and damage region could be confirmed from the SEM image.
2) The difference in depth between non-damage region and damage region was 50-90nm. The difference was quantitatively recognized by AFM.
3) The intergranular corrosion of non-damage region was confirmed by AFM.
4) It was not possible to confirm the remarkable difference in residual stress division of the damage region.

References

1) K.Kiuchi et al, IAEA Technical Meeting, Argentina, Nov. 25-298(1999).
2) I.Ioka et al, JAERI-Tech 2001-13.
3) W.L.Clarke, NUREG/CR-1095, GEAP-24888, R-5(1981).
4) T.Inazumi et al., Corrosion, 46(1991)786.
5) S.M.Breummer et al., Proc. 4th Int. Conf. on Enviro. Degra. Of Mater. In Nucl.

Power Syst., NACE(1990)14-1.
6) T.Tsukada et al., JAERI-M 92-169.
7) S.Hamada, J. Atomic Energy Soc. of Japan 28 (1986) 1165.
8) S.Yamaguchi, J. Appl. Phys., 22(1951) 983.

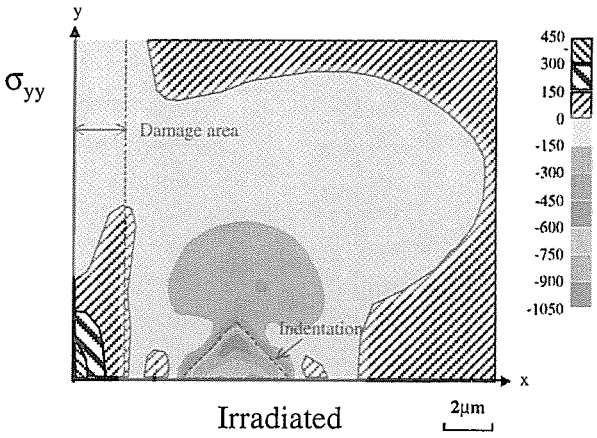


Fig.1 Analytical result of residual stress which arises around the indentation

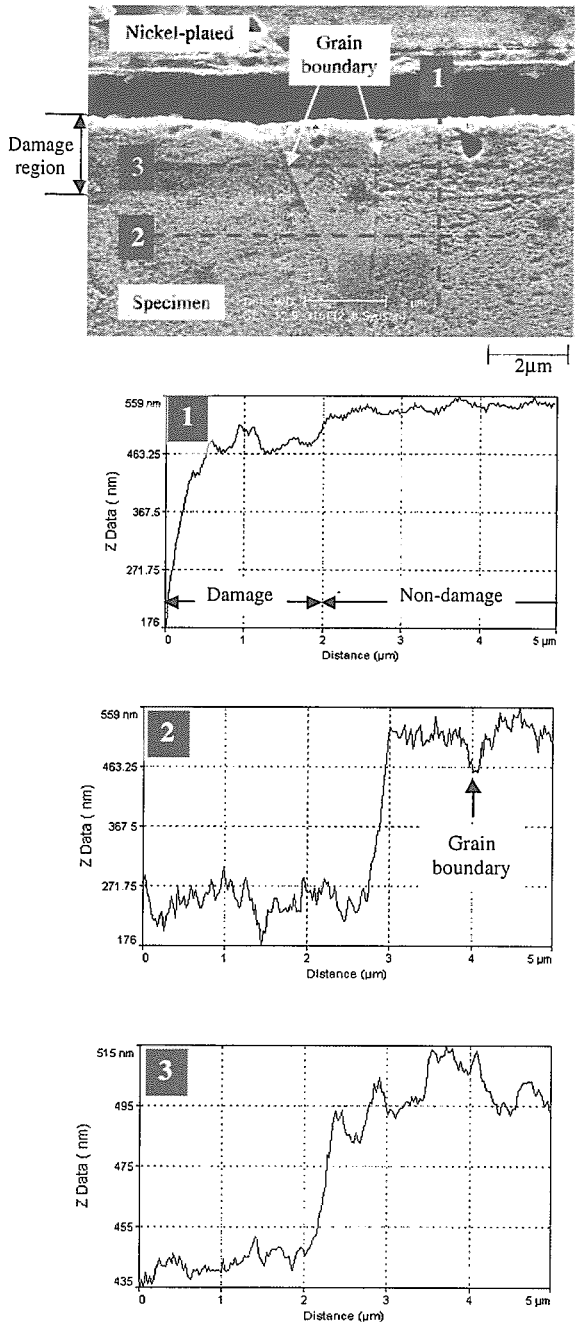


Fig.2 Surface appearance and surface roughness of the specimen after the corrosion observed by SEM and AFM

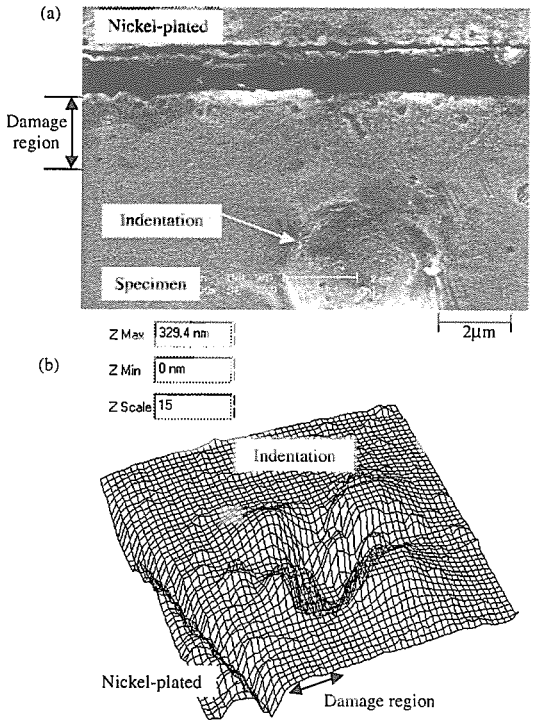


Fig.3 Results of the corroded specimen with indentation by SEM and AFM

4.13 Effect of Radiation on Microstructures and Corrosion Resistance of Austenitic Stainless Steels

S. Hamada, A. Naito, C. Kato, K. Kiuchi

Department of Nuclear Energy System, JAERI

1. Introduction

The study and development of advanced fuel cladding tube materials for light water reactors with ultra high burn-up such as 100GWd/ton started in our laboratory. The characteristic changes of the cladding material irradiated in a reactor have been very influenced by irradiation -induced surface reactions from coolant and fuel sides as well as displacement damage by neutrons, hydrogen and helium atoms produced by nuclear transmutation reactions. Active chemical species such as H_2, O_2 H^+, O^{2-} are produced by radiolysis of water adjacent to the surface of a cladding tube in a light water reactor. Especially, it is reported that hydrogen of them can easily permeate into the material through the surface PDP (Plasma Driven Permeation)[1] at lower temperatures and affects the characteristics of the material. It is predicted that oxygen shows the similar behavior to hydrogen. These atoms will permeate into the cladding material through the surface and accumulate to grain boundaries. As a result, they will lead to ductility loss of a cladding tube without corrosion. Further, promoted diffusion of these atoms under the exposure of neutron and gamma ray would give more ductility loss and decrease of corrosion resistance at grain boundaries might occur.

In order to clear the mechanism of this phenomenon from the viewpoint of microstructural change, which oxygen and hydrogen atoms will induce, and to evaluate corrosion resistance, the ion irradiation experiments were carried out.

2. Experimental

Three types of stainless steels were chosen for irradiation. The chemical composition of each material is shown in Table 1. F3 and F5 were 50% cold worked and F5EBR was SAR treated (Strained – aged – recrystallized: 50%CW + 575C/15hrs + 775C/5hrs) after solution treatment of 1150 C respectively.

The triple beam irradiation apparatus was used for irradiation. In order to obtain the wider depth profile of incident ions, ions with various energies were employed for post experiments. In this study, oxygen ions with 1.0, 1.8 and 3.0MeV and hydrogen ions with 100 through 300keV were irradiated to specimens at about 300C. The depth profiles of oxygen and hydrogen atoms were calculated with TRIM code[2]. In the present study, the content and displacement damage levels were about 3000 appm and 4 dpa for oxygen, respectively. On the other hand, the content of hydrogen was 2500-3000 appm. After irradiation, the layer

Table 1 Chemical composition of used materials (wt%)

	C	Si	Mn	P	S	Ni	Cr	Mo	Ti	N	B
F3	0.009	0.04	0.20	0.001	0.001	24.20	16.50	2.0	0.27	0.002	0.0026
F5	0.011	0.06	0.20	0.001	0.001	34.50	17.40	2.1	0.29	0.001	0.0032
F5EBR	<0.005	<0.10	<0.1	<0.01	<0.002	35.0	18.0	2.2	0.25	<0.001	<0.001

with about 0.5 μm in thickness was removed by sectioning method from the incident surface in the irradiated disks. Then some specimens were corrosion tested by EPR (Electro-chemical potentiokinetic reactivation) method and some were thinned by back thinning method for transmission electron microscopy observation. After the EPR tests, the microstructure on the surface was observed by an optical microscopy.

3. Results and discussions

Fig. 1 shows the depth profiles of oxygen and hydrogen atoms calculated using TRIM code.

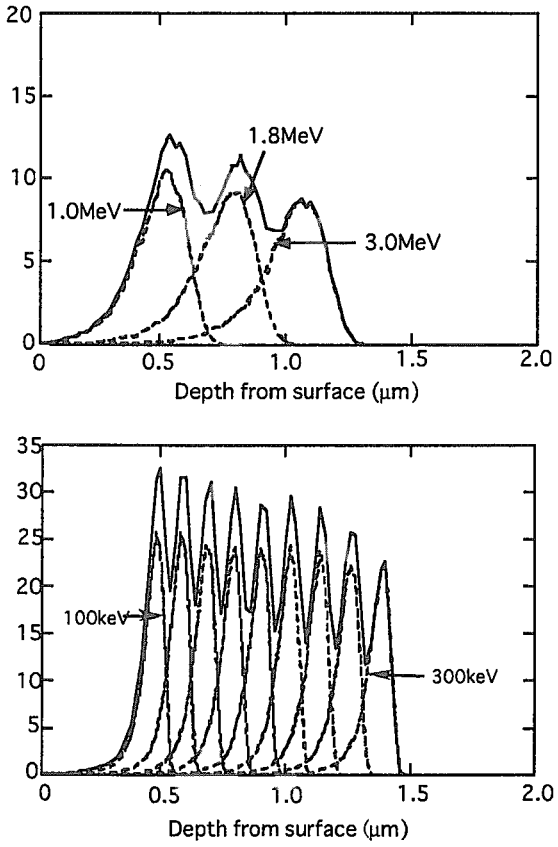


Fig. 1 Depth profiles of oxygen level (upper) and hydrogen level (lower) in stainless steel ($1p\mu A/cm^2$). Each broken line and solid line show depth profile for single energy and synthesis of depth profiles by three energies, respectively.

This shows incident ions deposit in the depth range from 0.5 to about 1.0 μm.

In TEM observation, small dislocation loops with high number density were observed in the only F5 specimen irradiated with oxygen ions as shown in Fig.2. There were hardly microstructural changes in other specimens.

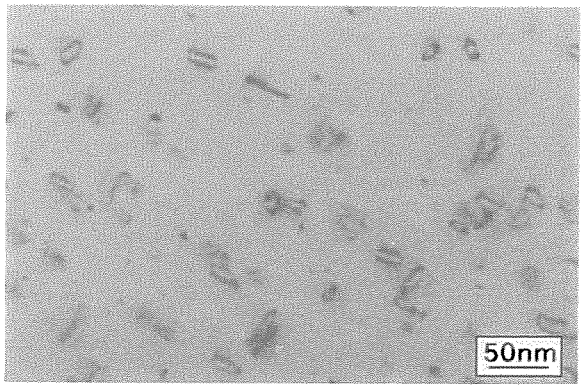


Fig. 2 Dislocation loops observed in F5 irradiated with oxygen ions.

The results of EPR tests are shown in table 2. The effects of ion irradiation on corrosion behavior were studied by observation with an optical microscope of intergranular corrosion crack on the surface of specimens after EPR tests. The change of the specimen surface has been hardly seen by EPR tests in both F3 and F5 irradiated with various ion species and in F5EBR with oxygen ions. On the other hand, the arrayed small etch pits were observed on the surface of F5EBR irradiated with hydrogen ions, and that with oxygen ions after hydrogen irradiation as shown in fig. 3,

Table 2 Results of EPR tests

	H^+ irra.	O^+ irra.	$(H^+ + O^+)$ irra.
F3	—*	—	No change
F5	No change	—	—
F5EBR	many small etch pits	No change	less small etch pits

* untested yet

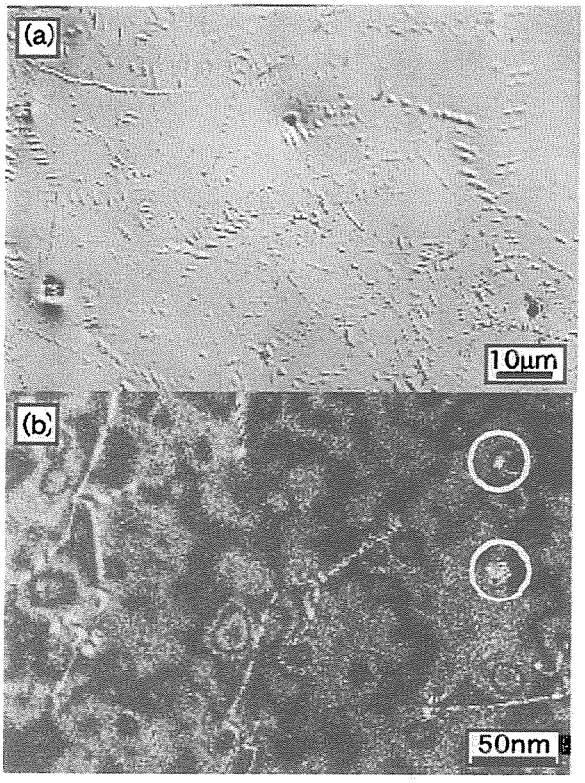


Fig.3 Optical microscope microstructure on the surface (a) and TEM microstructure after EPR test. White circles show small etch pits.

Neither F3 nor F5 irradiated with hydrogen, or hydrogen plus oxygen ions, to which strong cold work were applied, showed a big change of microstructure on the surface after EPR tests. This is considered that high number density of dislocation structures might uniformly spread incident atoms such as hydrogen and oxygen in the matrix and restrain the movement of these atoms onto the grain boundaries at 300C. As a result, intergranular corrosion in these alloys would be inhibited. On the other hand, small etch pits were seen in F5EBR irradiated with hydrogen ions, and with oxygen ions after hydrogen irradiation. F5EBR has the microstructure consisting of fine grains with sub -grain boundaries due to SAR. Fig. 3(b) shows small etch pits are in the region as sub-grain boundary consisting of high number density of dislocations. This might indicate hydrogen atoms trend to be trapped and stored in the region with small strain as a sub-grain boundary and enhance corrosion in the form of etch pits.

4. Summary

The effects of hydrogen and oxygen on microstructural evolution and corrosion resistance in stainless steels, which have been developed in JAERI, were studied using ion irradiation experiment.

(1) With microstructural evolution, no changes were observed in all stainless steels irradiated with hydrogen ions. High number density of small dislocation loops were observed in a stainless steel irradiated with oxygen ions.

(2) After EPR tests, preferential corrosion at the grain boundaries was not found independent of ion and steel species. Small etch pits were seen on the surface of them tests of the steels irradiated with hydrogen ions.

References

1) M. Takizawa et al. Plasma Fusion, 75 (1994) 432.
2) J. F. Ziegler et al. "The Stopping and Range of Ion in Solids" Vol.1, PREGAMON PRESS (1985).

4.14 Nucleation and growth of carbon onions in Cu and Au under ion implantation

Hiroaki Abe, Shunya Yamamoto, Atsumi Miyashita and Hisayoshi Itoh
Department of Materials Development, JAERI

Introduction

A carbon onion is a spherical or ellipsoidal substance that consists of concentric graphitic shells. Based on the spherical morphology and nature, carbon onions are expected as solid lubricants and bearing at nanometer scale. The physical and chemical properties are, however, still unknown because of extremely low production yield. Ion implantation could be the promising method for their mass production. In this work, we performed in-situ transmission electron microscopic observation of microstructural evolution under ion implantation to clarify the formation mechanism of onions [1], as well as their nucleation site and agglomeration at the substrate surface [2].

Experimental Procedure

Annealed polycrystalline copper and gold 3-mm disks were electrochemically perforated to achieve TEM samples. They were, then, implanted with 100-keV C^+ ions with fluxes of 6 x 10^{13} C/cm^{2}s at temperatures from 573 K to 973 K in TEM-Accelerators Facility at TIARA, JAERI. The microstructural evolution was videotaped and image processed in computers.

Results and Discussion

Light or dark circular contrast features, whose size was about 5 nm in diameter, were observed at a fluence of 1.1 x 10^{17} C/cm^2. As shown in Figure 1, they were spherical clusters with both phase and strain contrast, indicating that they were a second phase located inside of specimen. High-resolution electron microscopic observations as well as high-angle tilting and electron energy loss spectroscopy revealed that they were concentric graphitic spheres; carbon onions.

Onions grew in size and number with implantation fluence. The maximum nucleation rate of onions in copper was at 773 K, below which onions were not detected. Significant decrease by the factor of three in the nucleation rate above 823 K was observed. Onions grew 14.3 ± 2.5 nm in diameter by the further implantation to a fluence of 2 x 10^{17} C/cm^2 (about 1hour) in Cu at 773 K. The growth rate of onions was roughly 9 nm/(10^{17} C/cm^2) in the first one hour after nucleation. The maximum growth rate was at 873 K, which is roughly 3 times higher than the one at 773 K. Based on the evaluation of the number of carbon atoms in an onion and equivalent implantation fluence [3], 5 x 10^{16} and 1 x 10^{17} C/cm^2 of carbon atoms agglomerates to form 5- and 14-nm onions in Cu, respectively, both of which corresponds to half of the implantation fluences. On the other hand in gold, the nucleation rate was roughly 10 times higher than in copper at 773 K. Onions in gold grew no more than 4 nm in diameter. The results indicating retarded diffusion of carbon in gold.

Evaporation of Cu substrate due to ion irradiation was observed, which resulted in volume loss at a sample edge roughly in the order of 10^6 atoms/s at a 40nm-length edge. The loss is so high that one can observe its displacement, an example of which is shown in figure 2 together with interaction of the edge with embedded onions. The edge is displaced leftwards in the geometry, though, due to image arrangement, onions embedded in Cu seem to move towards the edge. Onions finally accumulated at the edge. When the edge first reached the embedded onion, half of the onion remains embedded. Thin arc-shape copper layers covers top and bottom surfaces of onions separately as indicated by arrows in the figure. This, as well as their spherical morphology, is the evidence that onions are formed inside of substrate. Neither onion nucleation nor significant growth of carbon onions was detected at an edge. Therefore, surface carbon atoms triflingly contribute to the onion growth or nucleation. Concentration of carbon in the substrate is presumably much higher than that at surface, even in the immiscible system.

Frequently observed at temperatures investigated were mobile dislocations being trapped by carbon onions independent of the size of carbon onions. Figure 3 shows an example of interaction between a dislocation and onions. Trapping of a dislocation by carbon onions is clearly seen, again confirming that the onions nucleate inside of copper samples not at surface. Depth distribution of carbon onions was determined by stereoscopic observations. Onions located mostly at the center of sample cross section, whereas rarely did at roughly near-surface regions. For instance, we hardly detected them at 20-nm-depth regions from top and bottom surfaces of 70-nm-thick TEM samples under 100 keV C^+ implantation in Au at 770 K. Further, we estimate, from their size and depth distributions, 80 % of implanted carbon atoms contribute onion formation in gold.

Summary

Formation of carbon onions and nanocapsules in copper and gold was investigated through simultaneous TEM observation under ion irradiation. Onions nucleate at an implantation fluence of 1 x 10^{17} C/cm^2 in Cu substrates, while they segregate at the surface due to irradiation-enhanced evaporation of the substrate. Dislocation trapping at onions, interaction between onions and sample edges, and localization of onions in depth distribution are strong evidence that onions nucleate inside the sample, not at surface. Once onions agglomerate at surface, they are stable without significant growth.

References

[1] Abe H, Yamamoto S, Miyashita A and Sickafus K E, submitted to J. Appl. Phys.

[2] Abe H, Diamond and Related Materials 10 (2001) 1201.

[3] Cabioc'h T, Riviere J P, and Delafond J, J. Mater. Sci. **30** (1995) 4787.

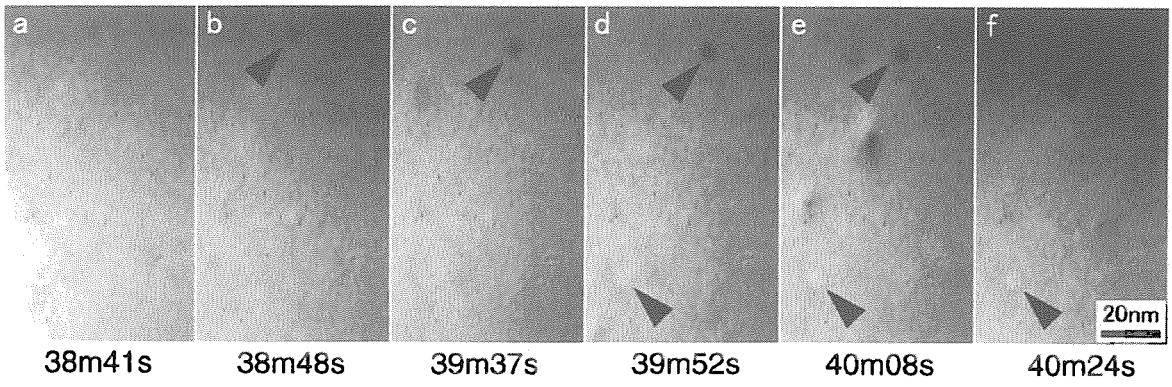


Figure 1. A sequence of videotaped images showing the evolution of light and dark circular contrast in copper implanted with 100 keV C^+ ion fluence of 1.1 x 10^{17} C/cm^2 at 783 K. Each of contrast features corresponds to a carbon onion.

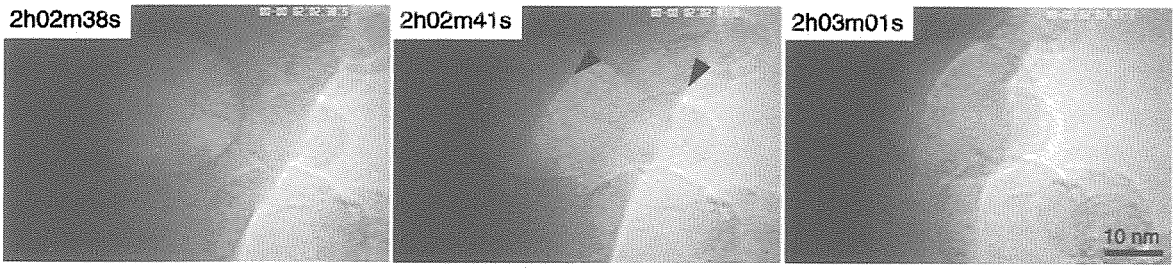


Figure 2. Surface segregation of carbon onions under 100 keV C^+ ion implantation with a flux of 6.8 x 10^{13} C/cm^{2}s at 783 K.

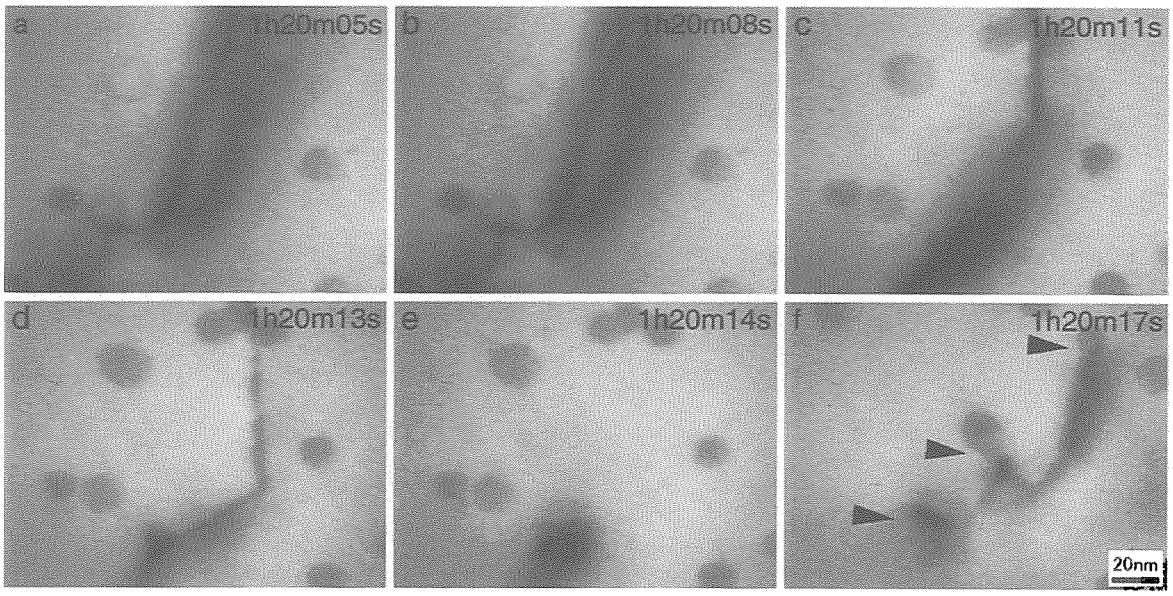


Figure 3. Videotaped bright-field images in copper under 100 keV C^+ ion implantation with a flux of 6.3 x 10^{13} C/cm^{2}s at 783 K. Arrows in (f) indicate that the three of onions trapped a dislocation (W-shape).

4.15 Thermal Response of the Metal/Fullerite Hybrid Assembly

J. Vacik[1], H. Naramoto[1], K. Narumi[1], Y. H. Xu[1], S. Yamamoto[2], H. Abe[2]
[1]Advanced Science Research Center, [2]Department of Materials Development, Japan Atomic Energy Research Institute, 1233 Watanuki, Takasaki, Gunma 370-1292, Japan

1. Introduction

Metal/fullerite (solid C_{60}) thin film packaging provides a new class of fullerene-based materials with interesting transport and structural properties that can be utilized in electronic applications [1-3]. Because of weak van der Waals inter-molecular interactions and the structural vulnerability of the fullerene molecules, the integrated metal/fullerite systems are thermodynamically unstable. A number of disruptive effects, such as annealing or energy beam irradiation, may lead to serious degradation (or entire collapse) of the metal/organic construction. Knowledge of the thermal response of the metal/fullerite systems would help to control their properties eventually to design novel architecture with well-defined parameters.

In this work, the thermal stability of the metal/fullerite sequence was inspected. The hybrid system was prepared as a complex Ni/Ni+C_{60}/C_{60}/Ni superstructure in order to examine the mutual effects of the mixed and mono-componential layers on the structural evolution of the multilayer packaging.

2. Experimental

The Ni/C_{60}/Ni+C_{60}/Ni thin film sequence was deposited onto the MgO(001) single crystal in a four-step procedure using electron beam bombardment of 99.9% Ni pellets and resistive filament heating of 99.9% C_{60} powder. The mixed layer was prepared by co-deposition of both Ni and C_{60} components. Following deposition kinetics was used: the deposition rate of Ni and C_{60} was ~ 5 nm/min, thickness of the layers (measured by quartz microbalance system placed near the sample) was either 150 nm (buried layers) or 50 nm (external layer), and the temperature of the substrate was kept at 500 ºC (buffer Ni layer) or 120 ºC (buried Ni+C_{60}/C_{60} and external Ni layers). The background pressure in the vacuum chamber before and after deposition was ~ $5x10^{-7}$ Torr. The final Ni/Ni+C_{60}/C_{60}/Ni/MgO(001) system was gradually annealed in the Ar (+3% H_2) flow atmosphere between 150 and 600 ºC and the structural evolution of the sample was analyzed in 50 ºC/1 hr steps using several methods, such as Rutherford backscattering (RBS), X-ray diffraction (XRD) or micro-Raman spectroscopy.

3. Results and Discussion

The XRD analysis showed that a) the buffer Ni and intermediate C_{60} layers were growing epitaxially (Ni on MgO with cube-on-cube texturing, fullerite as out-of-plane oriented and in-plane disoriented C_{60}(111) crystallites) and b) the Ni+C_{60}

mixture as amorphous and external Ni as polycrystalline overlayers. Thermal annealing incited an unusual response of the system, different for lower and for elevated temperature regimes. At temperatures below 350 ºC, homo-epitaxial growth of the buried C_{60} layer was observed (see Fig. 1). At temperatures above 350 ºC the multilayer rapidly degraded and collapsed entirely at 600 ºC (the three external layers peeled). A

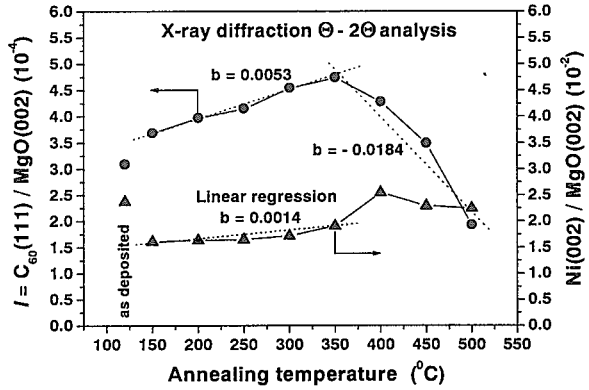


Fig. 1. Evolution of the normalized C_{60}(111) and Ni(002) reflection intensities

key role in the evolution of the metal/ fullerite superstructure was assigned to the Ni+C_{60} interlayer. This amorphous region apparently (at lower temperatures) served as a reservoir of the C_{60} molecules for homo-epitaxial growth of buried fullerite (thermal annealing below T = 350 ºC led to a 50 % increase of the normalized reflection intensity I = C_{60}(111)/MgO(002) with an estimated growth rate $\Delta I / I\Delta T = 0.0023/$ ºC). Above 350 ºC, however, series of processes, such as phase segregation (activated in the mixture region), Ni particle coalescence, C_{60} out-diffusion (through the porous poly- crystalline Ni) and C_{60} decay (to amorphous C, a-C) led to rapid structural degradation of the multilayer packaging (between 350 and 500 ºC the normalized reflection intensity I decreased to 60 % of the original value with an estimated decay rate $\Delta I / I\Delta T = -0.0039/$ ºC). The process of degradation is well demonstrated in Fig. 2 showing a series of RBS spectra of the annealed sample. One can see that above

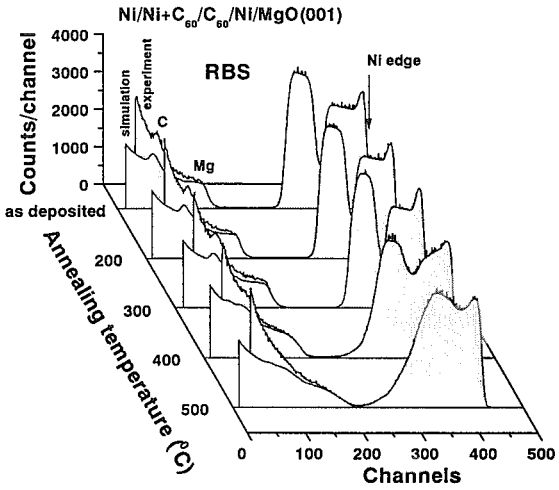


Fig. 2. RBS spectra of the annealed Ni/Ni+C_{60}/C_{60}/Ni/MgO(001) multilayer

300 ºC intermixing of Ni and C_{60} (a-C) appeared, which leads to rapid deterioration of the system and final peeling of the three external layers at 600 ºC.

Surprisingly, the destruction of the three external layers was accompanied by an unusual self-organization of the nanoscopic stripes (buried) in the buffer Ni epilayer. In Fig. 3 a part of the stripe system (revealed after sputtering of a small area with a focus Ga ion beam) can be seen. The stripes were

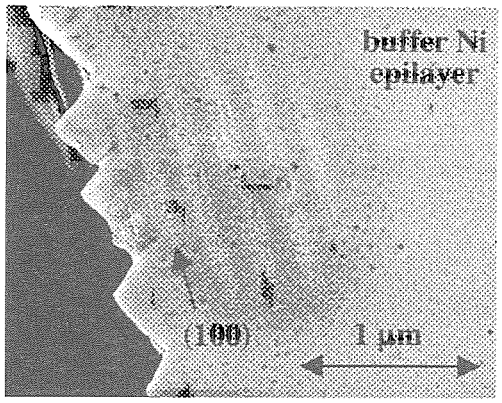


Fig. 3. System of nanoscopic stripes grown buried in the buffer Ni epilayer

grown in parallel with the (100) crystallographic orientation of the MgO(001) substrate in a depth of about 80 nm, with the width and spacing around 100 nm and height estimated to 50 nm.

The self-organization of the buried nanoscopic stripes is a phenomenon that resembles the formation of the mesoscopic stripe waves in a mixture of Ni and C_{60} co-deposited on MgO(001) [4]. The mechanism of this effect was assigned to the drift-and-release propagation of the stress arisen in the mixture due to an accumulation of the C_{60} fragments immiscible with Ni [4]. Similarly, as in the case of the stripe wave system, it is supposed that a-C vs. Ni immiscibility is a driving force of the buried pattern formation. Obviously, during thermal annealing, the C_{60} fragments (from the fullerite overlayer) in-diffuse into the buffer Ni and trigger (at elevated temperatures - supposedly around 500 ºC, when the Ni recrystallization process sets in) the forceful restructuring. The stripe patterning might then arise from the system's tendency to adapt its stressed microstructure to the energetically favorable form. As this tendency (governed by the a-C vs. Ni immiscibility) respects crystalline order of the buffer Ni layer, the growth of the stripes is circumscribed only to directions, which are parallel with the low-index crystallographic orientations of the Ni matrix.

In conclusion, the metal/fullerite thin film construction is very susceptible to thermal processing. Though at low temperature regimes constructive phenomena might occur (e.g., homo-epitaxial growth of buried fullerite), at elevated temperatures a series of disruptive processes (e.g., phase segregation, C_{60} decay and out-diffusion) governs the structural evolution. Destruction might however be accompanied by constructive effects, such as the spontaneous formation of buried stripes that results from the correlated segregation of the immiscible phases confined in the crystalline framework of the Ni matrix.

Reference

[1] K. Hoshimono, S. Fujimori, S. Fujita, Jpn. J. Appl. Phys., 32 (1993) L1070

[2] K. Pichler, M. G. Harrison, R. H. Friend, S. Pekker, Synth. Metals 56 (1993) 3229

[3] R. C. Haddon, A.S. Perel, R. C. Morris, T. T. M. Palstra, A. F. Hebard, and R. M. Fleming, Appl. Phys. Lett. 67 (1995) 121

[4] J. Vacik, H. Naramoto, S. Yamamoto, K. Narumi, K. Myiashita, J. Chem. Phys. 114 (2001) 9115

4.16 Deposition and Characterization of Carbon Films Prepared by Ion-Bombardment-Assisted Method

X. D. Zhu[1], Y. H. Xu[1], H. Naramoto[1], K. Narumi[1], A. Miyashita[2], K. Miyashita[3]
[1] Advanced Sci. Res. Center, [2] Dept. of Materials Development, JAERI
[3] Gunma Pref. Industrial Technology Research Laboratory

1. Introduction

Carbon-based materials with various bonding states present tremendous differences in their materials properties and structures. Great effort has been made to fabricate carbon-based films by employing ion beam methods, because the methods are originally non-equilibrium ones and have several kinds of advantages such as the independent controllability of the ion species, ion energy, and ion current density. The common products obtained by these methods are diamond-like carbon films with the various fraction of sp^3 bonding. It remains far from the strict science even though a few reports have claimed the success of diamond film preparation in ion beam methods [1].

In the present study, the ion beam assisted deposition technique was employed to prepare carbon-based thin films. By optimizing the deposition parameters, we have successfully found the growth conditions to prepare high quality C_{60}, diamondlike carbon, and nanocrystalline diamond films on mirror-polished Si wafers.

2. Experiment

High purity C_{60} power (99.99%) was heated to sublimate C_{60} vapor as carbon source. Growing film was bombarded simultaneously by Ne^+ ions with the incident angle of 60° from the substrate normal. The background pressure in the chamber was less 5×10^{-5} Pa. The working pressure was maintained around 6×10^{-4} Pa. The bonding nature was analyzed with Renishaw 2000 imaging microscope using 514 nm Ar^+ ion laser with the power less than 1mW. For the structural analysis X-ray system (Geiger Flex RAD-III, RIGAKU) equipped with a powder diffraction goniometer was operated at the power of 50kV, 30mA.

3. Results and Discussion

Fig.1 depicts the Raman spectra of the specimen prepared at nearly room temperature with Ne^+ ion bombardments of three different energies. It can be recognized that the quality of C_{60} films can be improved as the Ne^+ ion energy increases up to 500eV, which demonstrates the stable closed-cage structure of C_{60} and its remarkable resilience. With the further increase of Ne^+ ion energy up to 700eV, the deposited films show the typical DLC features in the Raman spectra. The formation of DLC films can be well interpreted by the subplatation model [2]. Under 1.5keV Ne^+ ion bombardment with different substrate temperatures, it is found that the separation between G and D lines in the Raman spectra becomes larger with the substrate temperature increase. This phenomenon is much more pronounced at higher temperatures, indicating that the films become more graphitic. Associated with this change in the Raman spectra, the significant morphological transition from growth mounds to ripple structure occurs in grown

films. This can be interpreted based on the fractal analysis.

An interesting finding is that nano-crystalline diamond can be obtained at the central region of the beam spot with high ratio of Ne^+ ion current density/thermal beam of C_{60} molecules. X-ray diffraction analysis shows that the most diffraction lines correspond closely to those of 2H-, 8H-, 12H- and 20H-hexagonal diamonds. The remaining diffraction lines are from graphite.

Fig.2 shows the Raman spectrum from the same sample as analyzed by XRD. One can observe the slight shift of the first Raman line of diamond from 1332cm^{-1} down to 1326cm^{-1}. This has been confirmed experimentally to be one Raman mode of hexagonal diamond [3]. The weak peak at 1157cm^{-1} is attributed to nano-crystalline diamond. The Raman line centered at 1199cm^{-1} is the convincing evidence of hexagonal diamond, which is fairly well in agreement with the calculated E_{2g} Raman mode of hexagonal diamond at 1193cm^{-1} [4]. This Raman mode has not been reported experimentally before. The broad feature of Raman lines here might be related to nano-size of the crystallites. There appeared big peak shifts centered at 1466 cm^{-1}, 1584cm^{-1} and 1604cm^{-1}, which are assigned to disordered carbon and graphite, respectively. The mechanism involved in the formation of hexagonal diamond at high substrate temperature will be discussed based on the analysis of the combined process between gas phase deposition and ion irradiation effect.

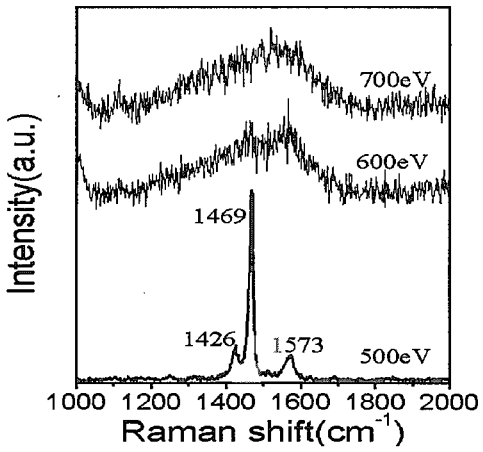


Fig. 1: Raman spectra from the carbon films prepared at nearly room temperature with relatively low ion energies.

References

1) Y. P. Cuo, K. L. Lam, K. M. Lui, R. W. M. Kwok and K. C. Hui, J. Mater. Res. 13 (1998) 2315.

2) Y. Lifshitz, S. R. Kasi and J. W. Rabalais, Phys. Rev. Lett. 62 (1989) 1290.

3) D. S. Knight and W. B. White, J. Mater. Res. 4 (1989) 385.

4) B. R. Wu and J. Xu, Phys. Rev. B 57 (1998) 13355.

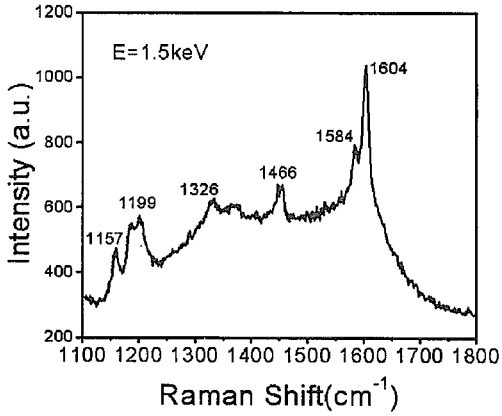


Fig. 2: Raman spectrum from carbon films prepared at 700°C with 1.5keV Ne+ ions.

4.17 Evolution of Co+C_{60} Structures during Co-deposition and Subsequent Annealing

V. Lavrentiev[1,*], H. Abe[2], S. Yamamoto[2], H. Naramoto[1], K. Narumi[1] and K. Miyashita[3]

[1]Advanced Science Research Center; [2]Dept. of Mater. Development, JAERI, [3]Gunma Pref. Industrial Technology Research Lab.

Cobalt has several interesting aspects as magnetic materials, and the magnetic properties can be improved crucially owing to the encapsulation of cobalt nano-particles by some nonmagnetic materials. Since the recent successes for the encapsulation of cobalt by a graphite-like layer, it has been tempting us to perform the similar covering by C_{60} molecules layers. To make the encapsulated structure acceptable for the applications we intended to design it as thin film with the perfect smoothness and the excellent adhesion to the substrate.

To realize our intention we employed an idea to use the mixture between Co and C_{60}. The mixed films were prepared by the simultaneous deposition of cobalt (electron beam evaporation) and C_{60} (thermal sublimation). The co-deposition was made onto α-Al_2O_3 (0001) substrate under 10^{-5} Pa. For TEM analysis the same co-deposition experiment was carried out on cleaved (001) NaCl single crystals. For the characterization of mixed Co+C_{60} films AFM, SEM and Raman spectroscopy were employed.

The optical inspection of co-deposited films shows the metallic gloss on films surface and the excellent adhesion to the α-Al_2O_3 substrate. The detailed analysis on the film surface and the cross section by AFM and SEM permitted us to induce the conclusion about the performance of encapsulation during the co-deposition. The structure of the film deposited at room temperature (RT) looks like the agglomerates of nano-granules with the order of 20-30 nm in diameter (Fig. 1). Moreover, one can see the hilly structure with the height of 20 nm. The density of the hills depends on the thermal conditions in the deposition and the subsequent thermal annealing.

*On leave from Inst. of Applied Physics, Academy of Sciences of Ukraine, Sumy, Ukraine.

Raman spectra from the films deposited at room temperature display several main peaks, which suggest us about the formation of 1D- and 2D-polymerized C_{60} structures. The latter implies the existence of high internal stress in mixed $Co+C_{60}$ films. Small peak nearby 1326 cm^{-1} most probably corresponds to diamond nano-crystals already at room temperature without thermal treatment. Annealing at 300°C under the vacuum induces the big changes in the Raman spectrum of the mixed film.

As in Fig. 2, one can see that the diamond peak at 1330 cm^{-1} becomes more pronounced. Moreover, the strong peak at 1595 cm^{-1} has emerged together. Judging from the spectral features of the 1595 cm^{-1} peak it is reasonably concluded that carbon nano-tubes are prepared by the post-deposition annealing.

TEM observation permits us to discover a complex structure of $Co+C_{60}$ mixture films. The analysis of micro- and nano-diffraction pictures testifies to the fcc structure of cobalt. The large distortion of Co nano-crystals also informs us the accumulation of internal stresses during the co-deposition, which can be the main reason for the diamond formation as evidenced by the electron diffraction analysis. According to the TEM analysis the as-deposited mixed films contain also Co_2C and Co_3C carbides. Through the in-situ annealing analysis under the TEM bright field the transformation from nano-capsules into nano-tubes has been clearly confirmed.

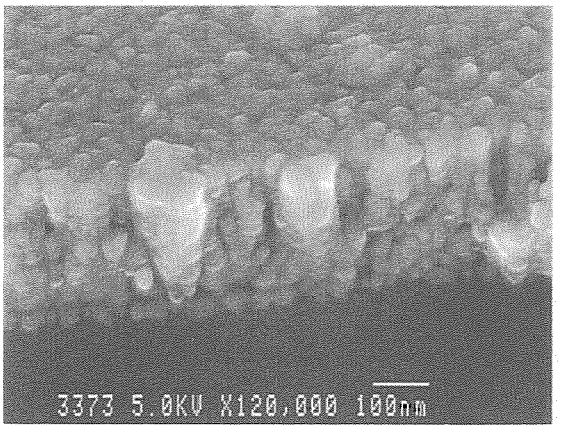


Figure 1: SEM image from cross-sectional area in $Co+C_{60}$ mixed film deposited at RT.

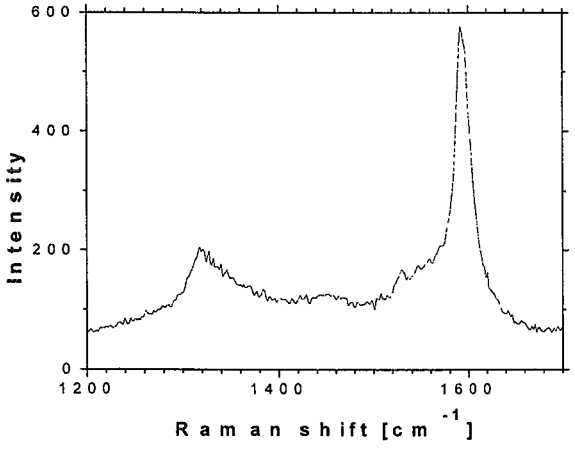


Figure 2: Raman spectrum of $Co+C_{60}$ mixed film after annealing at 300°C for one hour under vacuum.

4.18 Modification of Carbon Related Films with Ion Beams

Hiroshi Naramoto[1], Yonghua Xu[1,*], Kazumasa Narumi[1,+], Xiaodong Zhu[1], Jiri Vacik[1,#], Shunya Yamamoto[2], Kiyoshi Miyashita[3]
[1]Advanced Science Research Center, JAERI
[2]Department of Materials Development, JAERI
[3]Gunma Prefecture Industrial Technology Research Laboratory,

1. Introduction

Carbon atoms condense in different allotropes depending on the preparation conditions, which induces many kinds of approaches to realize new materials. The ion beam techniques have been employed to prepare amorphous carbon films with high sp^3 fraction, and it has been accepted that the ion bombardment is required to facilitate the diamond nucleation [1-2]. However, it has not been successful to obtain large single-crystalline diamond films on different substrates.

In this report the annealing features are shown in sp^3-bonded amorphous carbon films on Si and Ir substrates with IBD techniques. For a comparison, the results from Ne^+ ion-assisted deposition of C_{60} are illustrated.

2. Experimentals

Two kinds of sp^3-bonded amorphous carbon films were prepared on single-crystalline Si and Ir/MgO with 100eV $^{12}C^+$ ions at ambient temperature by employing IBD technique.

Ne ion assisted deposition of C_{60} molecules was made in a different chamber where the vapor pressure of C_{60} was kept constant by setting a Knudsen temperature cell at 450°C. The thermal molecular beam is inclined by 15° off from the surface normal. Ne ions are obliquely incident on substrates by 30°, and the energies were changed from 0.20 to 5keV in the substrate temperature of RT-800°C.

The thin films were examined with micro-Raman spectrometry (Renishaw 2000, and Nano-finder from Tokyo Instruments), and an atomic force microscope (AFM: JSPM-4200 from JEOL).

3. Results and discussion

The heat treatment of amorphous carbon films on Si at 700°C induced the change of sp^3-bonded amorphous state into graphitic one without the change of the surface roughness but the similar treatment of sp^3-bonded amorphous carbon films on Ir(111)/MgO (100) resulted in many circular spots with the loss of amorphous carbon layer after 600°C, and in the remaining areas the sp^3-bonded nature is kept judging from the Raman analysis. This phenomenon can be interpreted to be associated with oxidation of the carbon film by the remaining oxygen in the He gas based on the elemental analysis on that area. It should be also noted that there remains a small dot around the center of the circular spots. This is a totally different situation compared with the carbon film on a Si substrate. After approaching the maximum temperature (700°C), the film was cooled down at a rate of about 10°C /min by a temperature controller. During this cooling process there appeared many small bumps around the boundary of circular spots as shown in Figure 1.

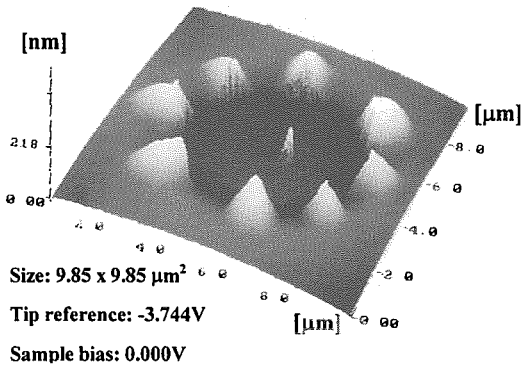


Figure 1. AFM analysis on flower-like pattern in IBD-carbon film on Ir(111)/MgO(100) after heat treatment (700°C, He).

These bumps seem to be small petals attached to a circular spot. The elemental analysis shows less carbon content in the bumps, and the appearance of bumps is probably related to the instability in high-speed-peeling-off caused by the stress accumulation during the rapid cooling process. The typical size of the small dot at the center of the circular spot is less than 500 nm in diameter and around 200 nm in height. The spectroscopic analysis with micro-Raman spectrometry with a 3 μm sized Laser spot

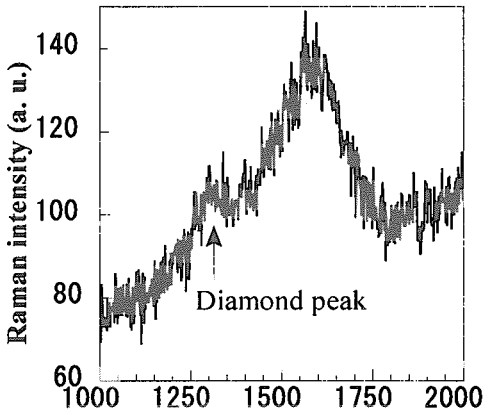


Figure 2. Micro-Raman analysis on the center dot in Figure 1 with 3μm laser spot. No diamond peak around the outer area.

confirmed the existence of diamond nano-particles hidden behind dominant sp^3-bonded amorphous carbon films as in Figure 2. If we look into the details at the bottom of circular spots there exist many crystal imperfections, and all of the nano-particles stem from the imperfections.

The effect of ion bombardments during the deposition of C_{60} was also studied by preparing a specially designed small chamber equipped with a Ne ion gun and a C_{60} evaporator. In this study Ne ions were chosen as bombarding species because those ions do not induce severe sputtering as compared with Ar ions. A set of Raman spectra in Figure 3 illustrates the Ne ion bombarding effect on the quality of the C_{60} film on the Si substrate. The C_{60} deposition was made simultaneously with Ne ion bombardments. The comparison between Figure 3(a) and 3(b) implies that the quality of the C_{60} film is improved with the assist of energetic Ne ions up to 0.5keV. Further increase of Ne energy from 0.6keV to 5.0keV induces the effective decomposition of C_{60} molecules at 60°C. The decomposition rate was dependent on the Ne ion energies, and can be estimated from the intensity of Raman signals. It can be said that the higher the energy, more efficient the C_{60} decomposition. The films obtained have the sp^3-amorphous feature similar to the carbon films prepared with the ion beam deposition

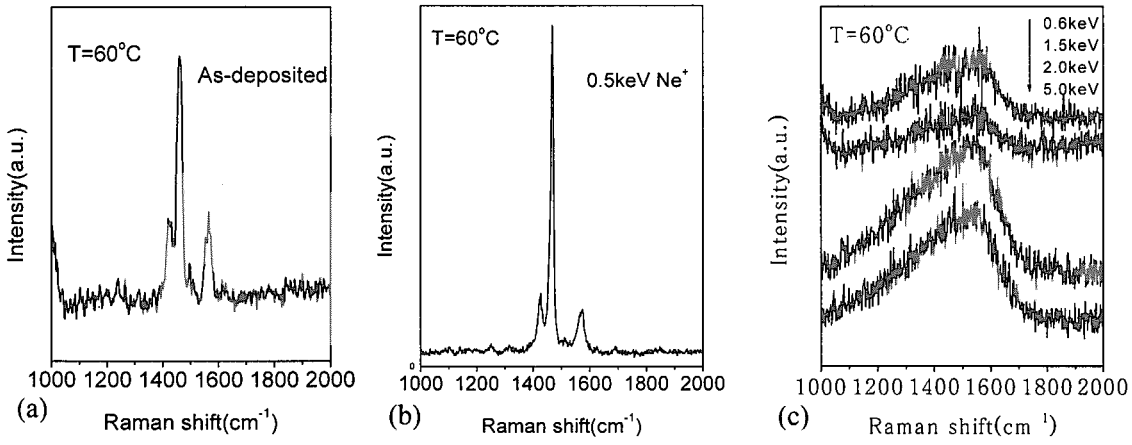


Figure 3. A series of micro-Raman spectra from C_{60} deposited films on Si substrate assisted with different energy Ne ions at 60°C. (a) As-deposited without Ne ion bombardments, (b) Assisted with 0.5keV Ne ions, (c) Assisted with higher energy Ne ions more than 0.6keV.

technique. In these cases the total doses for Ne ion bombardments were kept to be the same roughly.

Further Ne ion assisted deposition studies were performed in the higher temperature region to explore possible formation of crystalline carbon materials. Figure 4 shows a series of Raman spectra from thin carbon films prepared with the same technique described above. A Si substrate temperature of 700°C was chosen after the systematic trials. Spectra in Figure 4(a) are taken from the outer region of the deposited film with different energies, and Figure 4(b) illustrates the spectrum from the center of the same kind of carbon film prepared with 2keV Ne ions. In this experiment the Ne ion beam was not scanned in order to assist the deposition with the higher Ne ion current. One can recognize the significant difference between (a) and (b) in Figure 4.

The spectral features in Figure 4(a) are common among the experiments at higher temperature deposition experiments and can be characterized by the graphite-related structures, and the separation between "D" peak (around 1355cm^{-1}) and "G" peak (around 1581cm^{-1}) becomes better for Ne ions with the energies between 1.5keV and 3keV. On the contrary in Figure 4(b) one can observe many sharp peaks, and two main peaks around 1330 cm^{-1} and 1600 cm^{-1} can be related with the results found in nano-crystalline hexagonal diamond but this interpretation should be assured through further experiment. Micro-structural analysis with SEM and AFM revealed the corrugated structure with densely distributed nano-scale needles. This structure was realized through the combined process between deposition and sputtering under the high ion current. The regularly arranged nano-structure can be utilized for possible electron emission devices. Further effort will be made to find out the critical condition to synthesize the diamond nano-particles without any possible influence of co-existence of graphite.

References

[1] H. Naramoto, Y. Xu, K. Narumi, X. Zhu, J. Vacik, S. Yamamoto, K. Miyashita, Mat. Res. Soc. Proc. 647 (2001) O5.18.1-O5.18.6.

[2] X. D. Zhu, Y. H. Xu, H. Naramoto, K. Narumi and K. Miyashita, J. Phys.: Conden. (2001), to be published.

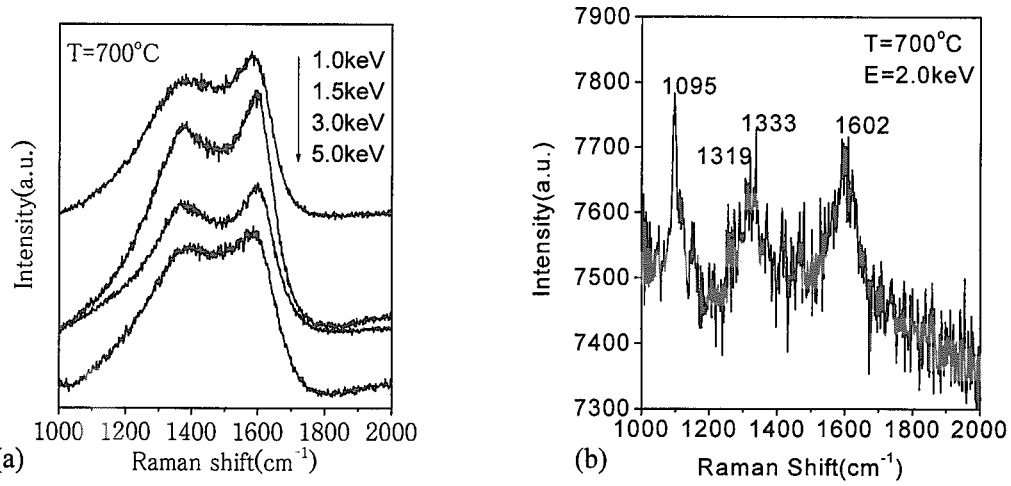


Figure 4. Micro-Raman spectra from C_{60} deposited films on Si substrate assisted with different energy Ne ions at 700°C. (a) is from the outer regions of intense beam spot, and (b) is the typical spectrum found at the central region of the spot with 2.0keV Ne ions at 700°C.

4.19 Formation process and stability of Radiation-induced non-equilibrium phase in silicon

M. Takeda, T. Suda, S. Watanebe, S. Ohnuki, *H. Abe
Dept. Mater. Sci., Fac. Engin., Hokkaido Univ. Sapporo 060-8628, Japan
*JAERI Takasaki, Watanuki-machi, Takasaki 370-1292

1. Introduction

Silicon, a covalent bonding material, easily transforms to amorphous structure during heavy-ion irradiation. The amorphization is enhanced by the irradiation at low temperature and high ion flux. Both of crystallization and amorphization depend strongly on irradiation conditions; temperature and ion flux. It had been reported that the amorphization of polycrystalline silicon (poly-Si) could develop from grain boundary (GB) at the temperature range from 423 to 498 K. The phenomenon is assumed to be a thermodynamically controlled process, which is analogous to grain boundary melting of the solid. On the contrary, it is known that the grain boundary can act as a site for segregation of point defect and for nucleation of second phase. For considering on semiconductor devices, which has been tried to much higher integration and performance, details in GB phenomenon is important. In this study, in-situ observation by transmission electron microscopy (TEM) was carried out under ion-irradiation in JAERI Takasaki facilities, and the effect of ion mass and energy on preferential amorphization is discussed.

1. Experimental

Specimen was poly-Si with the thickness of about 200 nm deposited on SiO_2 substrate by LPCVD method. Poly-Si was annealed at 1223 K for 4 hrs in Ar atmosphere. To obtain poly-Si film, the oxide was resolved by HF solution after the annealing. In-situ TEM observation was performed at IX port by using C^+, N^+ and Ar^+ of 100 – 300 keV, where the ion flux was 3.0 – 4.0 x 10^{17} /m^2s, and the temperature ranged from 104 to 673 K. Table 1 shows the details of irradiation condition. The critical dose was determined by the disappearing of diffraction spots of Si in selected area diffraction (SAD), where halo ring from amorphous phase was revealed. Figure 1 is a schematic illustration of the crystallization from amorphous zone at grain boundary. For measuring the crystallization temperature, as the first step, the preferential amorphous zone was formed by low temperature irradiation at PA. As the second step, the same zone was irradiated by the ion above PA. The

Table 1 Details of irradiation condition

Ion/energy	Temperature, K
100keV C^+	473 – 723
100keV N^+	523 – 673
300keV Ar^+	473 – 773

critical temperature of crystallization was determined by reversed temperature where the movement of c-a interface balanced between amorphization and crystallization under the irradiation. The onset temperature of PA was decided by in-situ TEM observation.

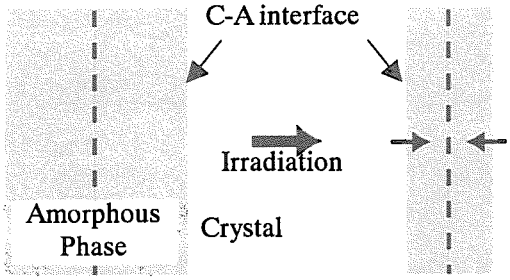


Figure 1 Schematics of the migration of C-A interface under ion-irradiation.

2. Results and Discussion

It is confirmed that the movement of c-a interface depends strongly on the crystallization and amorphization under irradiation at several temperatures. The time dependence of the moving distance of the interface has linearity. The moving rate has temperature dependence. Figure 2 shows the dependence of the moving rate, which includes both of crystallization at high

temperature side and amorphization at low temperature side. The minimum rate means the reverse temperature, T_R. T_R shifted to high temperature side with increasing of ion-mass. Considering the interaction between ions and target materials especially in the thickness of 150 nm, the electronic interaction can be negligible, whereas the elastic collision is preferential in this process. Therefore, the amount of radiation damage could increase with increasing of ion-mass and decreasing of accelerating voltage, where the reverse temperature may shift to high temperature side.

The movement of the interface also depends on irradiation temperature and ion flux. Figure 3 shows the relation between dose rate and temperature, which includes several ion species. In the case of Ar, the activation energy of this process was almost 1.2 eV, which is equivalent for the annihilation of di-vacancy at the c-a interface.

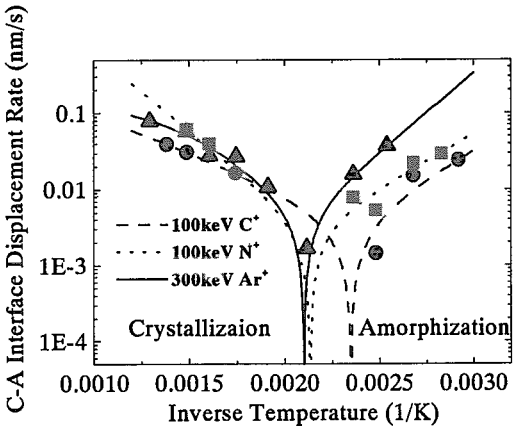


Figure 2. Temperature dependence of C-A interface moving.

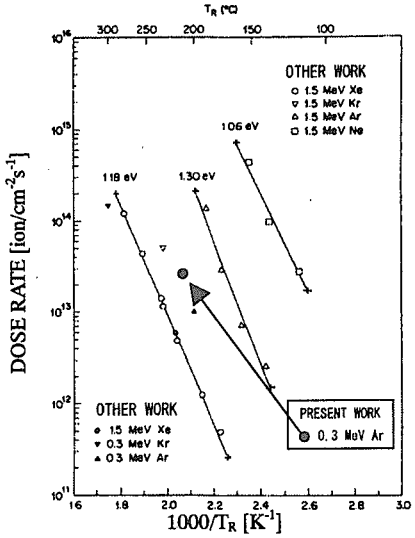


Figure 3. The relationship between ion flux and T_R.

Reference

[1] H.A. Atwater, et al., Appl. Phys. Lett., 56 (1990) 30-32
[2] H.A. Atwater, et al., Nucl. Instr. Meth. and Phys. Rev., B59/60 (1991) 386-390
[3] Abstracts of 9th TIARA, (2000) 74-75
[4] N. Yamauchi, et al., J. Appl. Phys., 75 (1994) 3235-3257
[5] J. Linnros, et al., J. Mater. Res., 3 (1988) 1208-1211

4.20 Improvement in Surface Roughness of Nirogen-Implanted Glassy Carbon by Hydrogen Doping

K. Takahiro[1], N. Takeshima[1], K. Kawatsura[1], S. Nagata[2], S. Yamamoto[3], K. Narumi[4], H. Naramoto[4]

[1]*Department of Chemistry and Materials Technology, Kyoto Institute of Technology,* [2]*Institute for Materials Research, Tohoku University,* [3]*Department of Material Development, JAERI,* [4]*Advanced Science Research Center, JAERI*

1. Introduction

Ion-implanted glassy carbon (GC) exhibits various structural changes depending on damage accumulated in the implanted layer.[1-3] At damage levels up to 0.2 displacements per atom (dpa), the structure displays a reduction in the average graphitic crystalline size. At damage levels between 0.2 and 3 dpa, the implanted layer begins to transform into an amorphous state. During amorphization approximately 15 % of the graphitic bonds are converted into diamond-like bonds, increasing in density from 1.5 to 2.2 g/cm^3. Furthermore, in case of N-implanted GC, the density of the N-implanted layer reduces and surface roughening occurs at higher damage levels.[4] Although the mechanism of surface roughening is not well understood, it is indicated that chemical processes are responsible for it.

In the study of surface roughening of N-implanted GC, we found that the surface roughness depended on a vacuum during implantation. The N implantation in the better vacuum causes the rougher surface. Characterization of the N-implanted GC reveals that a significant amount of hydrogen atoms exists in the implanted layer for implantation in the poor vacuum. Therefore, the hydrogen incorporation may play an important role to prevent surface roughening. In the present work, we study the effect of hydrogen incorporation on surface roughening induced by N implantation. For this purpose, hydrogen atoms are doped by ion implantation prior to N implantation. To examine behavior of the doped hydrogen, D ions instead of H ions are implanted.

2. Experimental procedures

The glassy carbon (GC-30 grade) used were supplied from Tokai Carbon. They were cut into 1 $\times$ 0. 5 $\times$ 0. 1 cm^3 and were polished to mirror surface using 1 μm diamond slurry on a cloth lap. The GC samples were implanted with 10 keV D_2 ions to a dose of 7 $\times$ 10^{17} D$^+$/cm^2, corresponding to the D concentration of approximately 30 at. %. The undoped and the D-doped GC were simultaneously implanted with 100 keV N_2 up to a dose of 12 $\times$ 10^{17} N$^+$/cm^2 at temperature below 100 °C. A vacuum during N implantation was better than 2 $\times$10^{-5} Pa. The projected ranges of 10 keV D_2^+ and 100 keV N_2^+ were calculated by the TRIM code [5] to be ~90 nm and ~120 nm, respectively, assuming the density of GC to be 2.0 g/cm^3. The implanted surface was characterized by means of scanning electron microscopy (SEM), high-energy ion backscattering spectrometry (BS) and elastic recoil detection (ERD) analysis using $^4He^{++}$ beams. The measurements were carried out *ex situ*.

3. Results and discussion

Fig. 1 (a) shows the SEM micrograph taken from the as-polished GC. A collapsed micro-pore of ~3 μm size and many polishing scratches can be seen. Fig. 1 (b) is the photograph taken from the undoped GC sample implanted with N ions to a dose of 4 $\times$ 10^{17} N$^+$/cm^2. This dose is ~20 times as high as the dose at which the N-implanted layer is amorphized. Remarkable surface roughening, which originates in polishing scratches, occurs after N implantation to 4$\times$10^{17} N$^+$/cm^2. Above this dose, however, enhancement in roughness was not observed. For the D-doped GC sample, surface roughening due to N implantation was not recognized in all cases examined, as shown in Fig. 1 (c), indicating that D-doping successfully suppresses surface roughening. Thus hydrogen doping is an effective method to maintain a smooth surface of N-implanted GC.

Fig. 2 shows ERD spectra of the D-doped GC implanted with 100 keV N_2 ions. The maximum D concentration was approximately 30 at. % before N implantation. A part of implanted D atoms was released by N implantation, but hydrogen atoms, which may come from the implantation chamber, were absorbed instead. As a result, total concentration of hydrogen including H and D atoms in

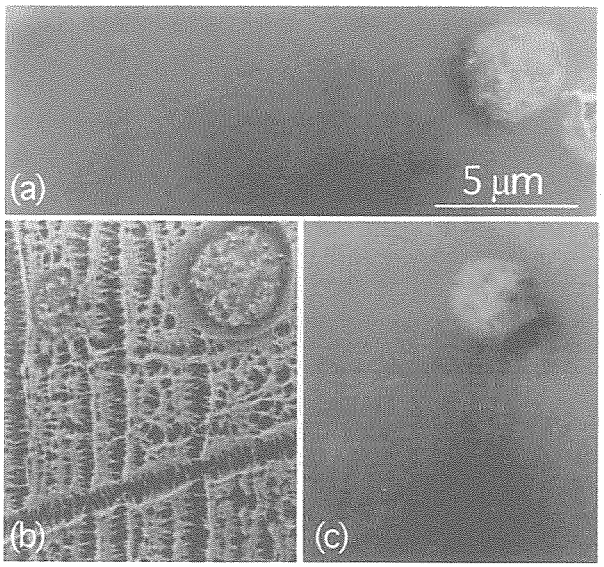


FIG. 1. SEM micrographs of GC surfaces before (a) and after 100 keV N_2^+ implantation to a dose of 4×10^{17} N^+/cm^2 for undoped GC (b) and D-doped GC (c).

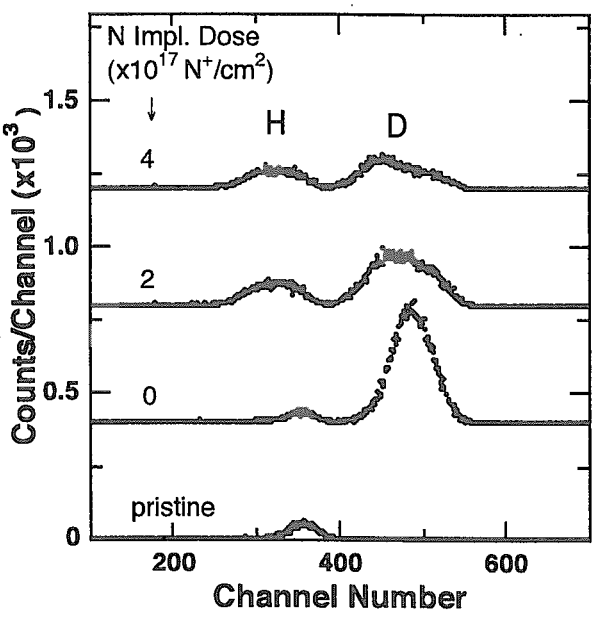


FIG. 2. ERD spectra of the D-doped GC implanted with 100 keV N_2^+. N-implantation doses are given. At the bottom of the figure, ERD spectrum for the as-polished GC (referred to as " pristine") is shown for comparison.

the N-implanted layer exceeds 20 at. % at any doses. As described above, the surface morphology of the D-doped GC is unchanged after N implantation. We conclude, therefore, that the hydrogen atoms in the N-implanted layer improve the surface roughness of the N-implanted GC. In addition, the present results suggest that morphology of the N-implanted GC is influenced strongly by the nature of C-N or C-N-H chemical bonds.

4. Summary

It was demonstrated that the hydrogen doping was an effective method to obtain a smooth surface of N-implanted GC. Our next goal is to make clear relations between surface roughness and chemical bonds formed in the N-implanted layer.

References

1) D. McCulloch, S. Prawer, A. Hoffman and D.K. Sood, Nucl. Instr. Meth. B **80/81**, 1480 (1993).
2) D. McCulloch, A. Hoffman, S. Prawer, J. Appl. Phys. **74**, 135 (1993).
3) D. McCulloch, S. Prawer, A. Hoffman, Phys. Rev. B **50**, 5905 (1994).
4) S.P. Withrow, J.M. Williams, S. Prawer and D. Barbara, J. Appl. Phys. **78**, 3060 (1994).
5) J. F. Ziegler, J. P. Biersack and U. Littmark, "The Stopping and Ranges of Ions in Solids" Vol. 1 (pergamon Press, New York, 1985).

4.21 Temperature Dependence of Growth Process of C_{60} Thin Films on a KBr(001) Surface

Kazumasa Narumi and Hiroshi Naramoto
Advanced Science Research Center, JAERI

1. Introduction

Because of not only its novel shape but also its potential application expected from the molecular structure, C_{60} has fascinated many researchers since the discovery by Kroto et al.[1] The availability of macroscopic quantities of C_{60} and other fullerenes has made it possible to investigate the properties of these novel materials[2] and many studies on C_{60} epitaxial film growth on various types of substrate have been conducted. Growth of C_{60} films on alkali halides has been investigated intensively because of easy preparation of pure substrate surfaces with various lattice constants[3-6]. Although these studies have been done under various deposition parameters, growth process depending on substrate temperature has not been studied intensively yet. In the present study, focusing on dependence on substrate temperature, growth process of C_{60} thin films on a KBr(001) surface has been investigated using an atomic force microscope (AFM)[7].

2. Experimental

Pure C_{60} powder of 99 % was loaded into a Knudsen cell in a deposition chamber whose base pressure was 6×10^{-6} Pa. The deposition was performed under several conditions: The temperature of KBr substrates, which were cleaved along {001} in air, was 45, 85, 125 and 165°C. The deposition time was 1 to 120 min. During the deposition, the K-cell was kept at 450°C, which corresponds to the deposition rate of 2 to 3 nm/min, depending on the substrate temperature. The deposition rate was estimated with an AFM investigation. During the deposition, the pressure in the chamber was better than 3×10^{-5} Pa. After the deposition, surface morphology of the specimens was characterized with AFM (JEOL JSPM-4200) in air and crystallographic orientation was investigated with XRD (Philips X'Pert-MRD).

3. Results and Discussion

Figure 1 shows AFM images of C_{60} thin films on KBr(001). The film shown in Fig. 1(a) was deposited at substrate temperature of 165°C at the rate of 1.9 nm/min and the average thickness was about 10 molecular layers. There are three types of island observed for this film. One is a hexagonal or truncated triangular plate as indicated by the character "A" in the figure. Such a plate-like island shows a well-shaped fcc (111) face. Judging from AFM images, however, the orientation of each plate has no correlation with each other. On the other hand, "B" indicates three-dimensional particles like petals, which seem to have no regular shape. However, a characteristic pentagonal island with multiply twinned structure as indicated by "B' " was sometimes observed[5,8]. The particle consists of five tetrahedra connected with (111) twinning. Imperfect pentagonal islands which lacked one or two tetrahedra existed among them. The other type of island indicated by "C" seems to have both features of "A" and "B": it consists of a plate-like island having a well-shaped fcc (111) face and several three-dimensional islands grown along the plate edges having the <110> directions in an fcc crystal, which look like walls; a good example is indicated by "C' " in the figure. For thin films deposited at 125°C, where AFM

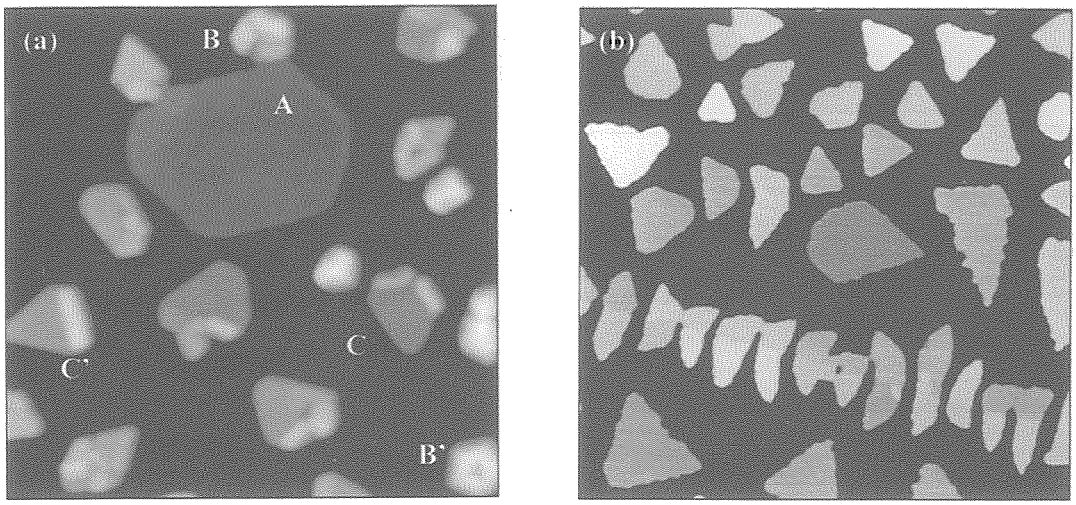


Fig. 1 AFM images of C_{60} thin films on KBr(001); (a) substrate temperature of 165°C and 10 molecular layers at the rate of 1.9 nm/min and (b) substrate temperature of 85°C and 3 molecular layers at the rate of 2.8 nm/min. The scanned area is 2 × 2 μm^2. On the characters in (a), see the text.

images are not shown here, the islands of "A" and "C" were observed, while the petal-like particles "B" were not found on this condition. Figure 1(b) shows an AFM image of a C_{60} thin film on the (001) surface of KBr, which was deposited at substrate temperature of 85°C. The deposition rate was 2.8 nm/min and the average thickness was about 3 molecular layers. As shown in the figure, only plate-like islands "A" were observed and no three-dimensional islands such as "B" and "C" were found. It should be noted that the plate is less-shaped triangles, the sides of which are wavy. The orientation of each plate also has no correlation with each other. For thin films deposited at 45°C, the similar results were obtained.

An AFM image of a C_{60} thick film on the (001) surface of KBr is shown in Fig. 2. The film deposited at substrate temperature of 125°C consists of crystal grains that are a few micrometers in size. Each crystal grain has a mountain-like stepped surface where terraces correspond to the {111} planes in an fcc crystal. Although the shape of the grain is almost irregular, edges in the <110> directions in an fcc crystal can be noticed. As indicated by arrows in the figure, wall-like structures were often observed along such edges independent of film thickness. Judging from features of its appearance, the structure seems to be similar to that of the island "C" shown in Fig. 1(a). Furthermore, they were not observed for the film deposited at substrate temperature lower than 125°C, which was consistent with the results for thin films as shown in Fig. 1. Therefore, it can be concluded that the wall-like structure has the same origin as the type "C" in Fig. 1(a).

In order to investigate the relation between the substrate temperature and the crystallographic orientation of C_{60} films, 2θ-θ scans of X-ray diffraction were measured for C_{60} thick films, which are shown in Fig. 3. The results clearly indicate close-packed C_{60}{111} planes grown parallel to the (001) surface of KBr, which is consistent with the previous reports on C_{60} films on alkali halides[3,6,8-10]. It should be noted that C_{60}{110} planes grow parallel to the KBr(001) surface at substrate temperature higher than 85°C. Comparing the XRD results with the dependence of the film growth on the substrate temperature, we can conclude as follows: The plate-like island grows with the {111} planes parallel to the KBr(001) surface and the C_{60}{110} planes can be attributed to the three-dimensional

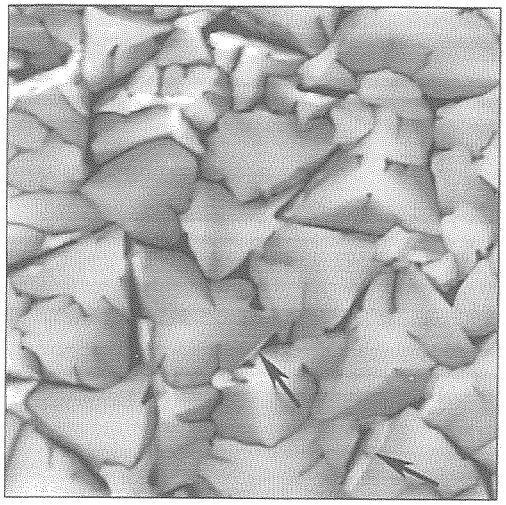


Fig. 2 AFM image of a C_{60} thick film deposited on KBr(001) at substrate temperature of 125°C at the rate of 2.2 nm/min. Average thickness is 260 molecular layers. The scanned area is 5 × 5 μm^2. Arrows indicate the wall-like structure (see the text).

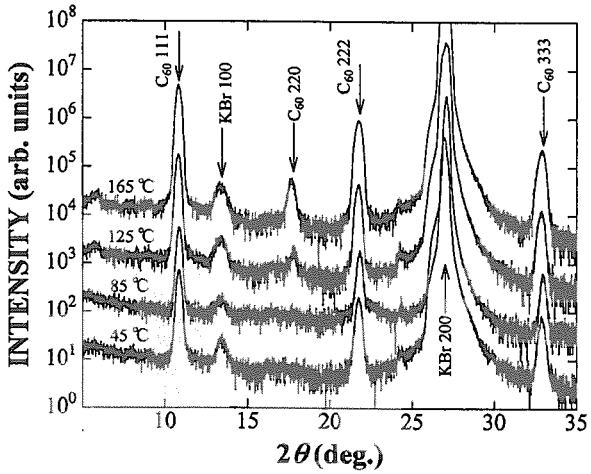


Fig. 3 Temperature dependence of X-ray diffraction results for 2θ-θ scans of C_{60} thick films deposited on KBr(001).

islands such as "B" and "C". However, the crystallographic orientation of the petal-like island and the wall-like structure have not been made clear yet, so that further investigation is necessary.

4. Summary

We have investigated growth process of C_{60} thin films on the (001) surface of KBr using atomic force microscopy. Depending on substrate temperature, three types of island were observed at the initial stage of the growth. The plate-like island growing with the {111} planes parallel to the KBr(001) surface was observed at whole temperature range. Its shape depends on the substrate temperature. The other islands are three-dimensional and observed at substrate temperatures higher than 85°C. XRD measurements revealed that the C_{60}{110} planes, which grew at substrate temperatures higher than 85°C, could be attributed to the growth of the three-dimensional island.

References

1) H. W. Kroto, J. R. Heath, S. C. O'Brian, R. F. Curl and R. E. Smalley, Nature **318** (1985) 162.
2) W. Krätschmer, L. D. Lamb, K. Fostiropoulos and D. R. Huffman, Nature **347** (1990) 354.
3) K. Tanigaki, S. Kuroshima and T. W. Ebbesen, Thin Solid Films **257** (1995) 154.
4) H. Yanagi, S. Doumi, T. Sasaki and H. Tada, J. Appl. Phys. **80** (1996) 4990.
5) Y. Kim, L. Jiang, T. Iyoda, K. Hashimoto and A. Fujishima, Appl. Surf. Sci. **130-132** (1998) 602.
6) K. Yase, N. Ara-Kato, T. Hanada, H. Takiguchi, Y. Yoshida, G. Back, K. Abe and N. Tanigaki, Thin Solid Films **331** (1998) 131.
7) K. Narumi and H. Naramoto, Diamond and Related Materials, **10** (2001) 980.
8) Y. Saito, Y. Ishikawa, A. Ohshita, H. Shinohara and H. Nagashima, Phys. Rev. B **46** (1992) 1846.
9) H. Yanagi, T. Sasaki, Appl. Phys. Lett. **65** (1994) 1222.
10) Z. Dai, H. Naramoto, K. Narumi and S. Yamomoto, J. Phys.: Condens. Matter **11** (1999) 6347.

4.22 Thermal Relaxation of Hydrogen Disordering in Palladium-Hydrogen System Irradiated with Energetic Electrons

K. Yamakawa[1)], Y. Chimi[2)], K. Adachi[1)], N. Ishikawa[2)], A. Iwase[2)]
[1)] Faculty of Engineering, Ehime University
[2)] Department of Materials Science, JAERI

1. Introduction

In Pd-H system, it is well known that an extraordinary behavior occurs near 50K in several properties such as electrical resistivity[1,2)], internal friction[3)], specific heat[4)] and so on. Neutron diffraction measurements have revealed that this anomaly is attributed to the order-disorder transition of hydrogen atoms in interstitial sites of Pd lattice[5,6)]. Irradiation with energetic particles destroys the equilibrium ordered state of hydrogen atoms at low temperatures[7,8)]. In this report, we show the thermal relaxation process of the hydrogen disordering induced by electron irradiation.

2. Experimental Procedure

The specimen used in this study was palladium foil 4μm thick, which was doped with hydrogen up to the atomic ratio of 0.6. First, an ordered state of hydrogen atoms was achieved by cooling the specimen very slowly to 10K. Then, the ordered state was destroyed by irradiating the specimen at 10K with electrons. We chose 0.5MeV as the energy of electrons so that the irradiation did not affect the palladium lattice. During heating the irradiated specimen up to 80K at a constant rate (2K/min), the electrical resistivity was measured as a function of temperature. As the electrical resistivity is well correlated with the state of hydrogen atoms in palladium lattice, we can obtain the thermal relaxation process of hydrogen disordering from the temperature dependence of the resistivity.

3. Results and Discussion

Fig. 1 shows the relaxation of hydrogen atoms from the irradiation-induced state to the thermally equilibrium state (ordered state) as a function of temperature. For comparison, the thermal relaxation behavior for frozen-in disordering, which was obtained by cooling the specimen rapidly from 80K to 10K, is also plotted. As can be seen in the figure, the frozen-in hydrogen disordering relaxes around 55K, while the irradiation-induced disordering relaxes around two temperature regions; around 40K and around 55K. The relaxation process around 55K for irradiation-induced disordering seems to be the same as for frozen-in disordering.

The trend that the relaxation of irradiation-induced disordering starts at lower temperatures than that of frozen-in disordering can also be seen in Fig. 2, where the time variations of the change in resistivity at 10K after electron irradiation and after rapid cooling are plotted. The resistivity after electron irradiation increases more swiftly than after rapid cooling. This result is consistent with that shown in Fig. 1.

The present result can be explained as follows; the state frozen-in from 80K is not a completely disordered state but includes some short-range order (SRO). The relaxation around 55K may correspond to the transition from SRO to the long-range order (LRO). On the other hand, energetic electron irradiation destroys not

only LRO but also SRO. Therefore, the relaxation around 40K may correspond to the transition from the complete disorder to SRO, which subsequently relaxes to LRO at higher temperatures.

The details of the experimental procedure and the data analysis are shown in ref. [8].

References

1) T. Skoskiewicz, B. Baranowski, Phys. Stat. Sol. 30(1968) K33.
2) N. S. Ho, F. D. Manchester, J. Chem. Phys. 51(1969) 5437.
3) J. K. Jacobs, C. R. Brown, V. S. Pavlov, F. D. Manchester, J. Phys. F6(1976) 2219.
4) D. M. Nace, J. G. Aston, J. Am. Chem. Soc. 79(1957) 3623.
5) I. S. Anderson, D. K. Ross, C. J. Carlile, Phys. Lett. 68A(1978) 249.
6) T. E. Ellis, C. B. Satterthwaite, M. H. Mueller, T. O. Brun, Phys. Rev. Lett. 42(1979) 456.
7) P. Vajda, J. P. Burger, J. N. Daou, A. Lucasson, Phys. Rev. B33(1986) 2286.
8) Y. Chimi, K. Adachi, A. Iwase, N. Ishikawa, K. Yamakawa, J. Alloys Compounds, (2001) in press.

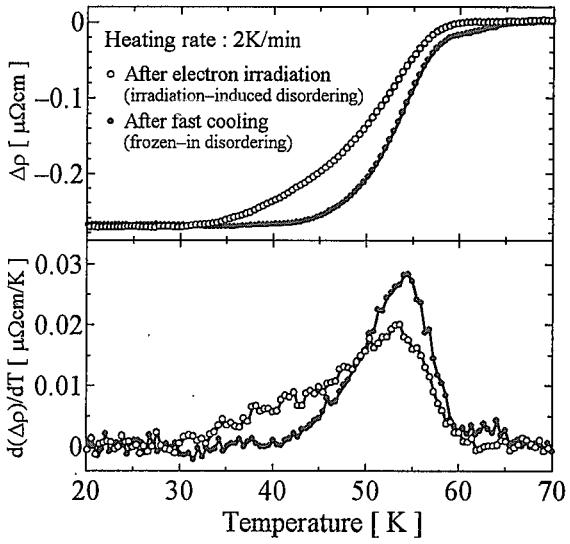


Fig. 1 Thermal relaxation behavior of hydrogen disordering after fast cooling and after electron irradiation as a function of temperature. Heating rate is 2K/min.

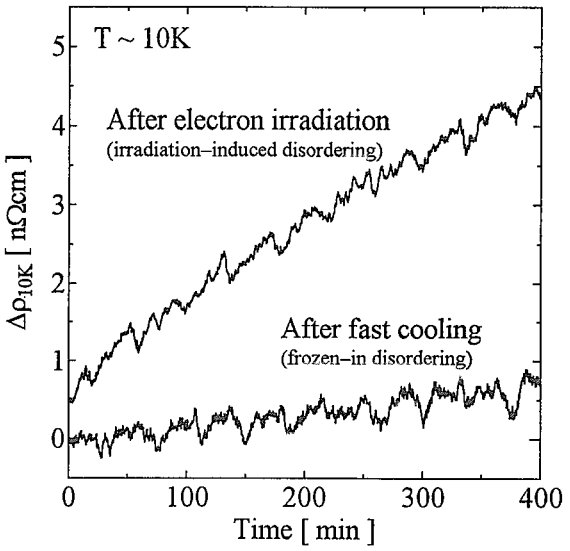


Fig. 2 Change in electrical resistivity at 10K as a function of time after electron irradiation and after fast cooling.

4.23 Anomalous Change in Electrical Resistivity in $EuBa_2Cu_3O_y$ Superconductor Irradiated with Energetic Electrons

N. Ishikawa[1)], Y. Chimi[1)], A. Iwase[1)], H.Wakana[2)], T. Hashimoto[2)], O. Michikami[2)]

[1)]Department of Materials Science, JAERI

[2)]Faculty of Engineering, Iwate University

1.Introduction

In oxide superconductors irradiated with electrons of ~1MeV, point defects are created in lattice system and as a result electrical resistivity increases with increasing electron fluence. In the previous study of electrical resistivity change due to irradiation with electrons and ~1MeV ions, it has been found that the initial slope of electrical resistivity-fluence curve is proportional to energy transfer through elastic collision as shown in Fig.1, indicating that the defect production process is a simple process that can be described as elastic displacements of target atoms[1)]. However, we recently observed small decrease in electrical resistivity with increasing fluence in relatively lower fluence region (~10^{16} electrons/cm^2), although in higher fluence region (~10^{18} electrons/cm^2) monotonic increase is observed. The purpose of this paper is to clarify the origin of this anomalous behavior.

2. Experimental Procedure

A c-axis oriented $EuBa_2Cu_3O_y$ thin film was prepared on MgO substrate. The fluence dependence of electrical resistivity is measured by four-probe method; Gold is deposited on the specimens as electrodes, and Cu wires are glued to the electrodes with silver paste. The specimens were irradiated at low-temperature (100K) with 2MeV electrons from a 3MV single-ended accelerator in TIARA, JAERI-Takasaki. In-situ measurement of fluence dependence of electrical resistivity at 100K was performed.

3.Results and Discussion

Figure 2 shows a small decrease in resistivity due to irradiation and a saturating behavior in the lower fluence region (~10^{16} electrons/cm^2). The problem is how to reconcile the decrease in electrical resistivity in lower fluence region and the increase in higher fluence region. Since not only a specimen but also electrodes are in all the cases irradiated, we measured resistivity in such a condition that only specimen is irradiated. As shown in Fig.3, no change in resistivity is observed in the fluence region of ~10^{16} electrons/cm^2. This result has following implications.

1)Irradiation effect of electrode appears only in low electron fluence region. 2)The effect is small and it saturates, indicating that in higher fluence region irradiation effect of specimen is dominant. 3)The effect of superconductors irradiated with energetic electrons is explained in the framework of elastic displacements. This result of the previous study is not flawed. 4)It should be pointed out that the irradiation effect of

electrode should be clearly separated from other irradiation effect on transport properties such as persistent photoconductivity phenomenon.

Reference

1)N. Ishikawa, Y. Chimi, A. Iwase, K. Tsuru and O. Michikami, J. Nucl. Mater. 258-263 (1998) 1924.

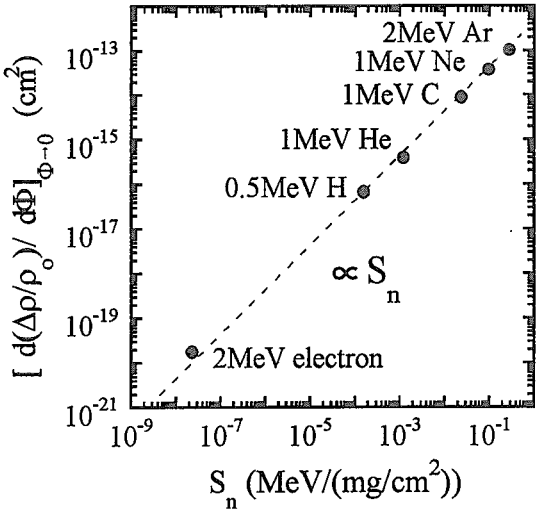


Fig.1 Initial slope of resistivity-fluence curve plotted as a function of nuclear stopping power, S_n. For electron irradiation the damage energy, S_d, is used instead of S_n [1].

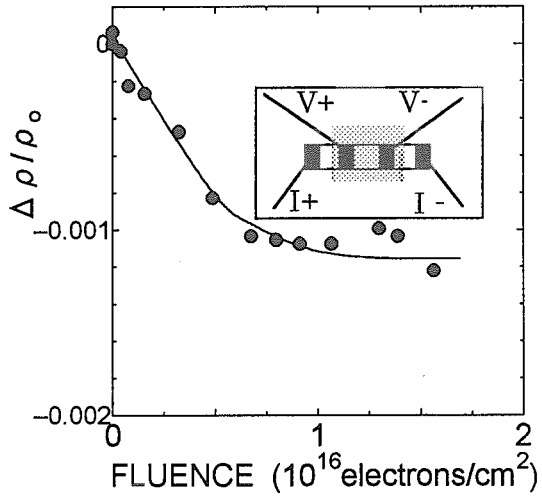


Fig.2 Change in normalized resistivity plotted as a function of fluence. Shaded area corresponds to the irradiated area which includes not only specimen but also electrodes.

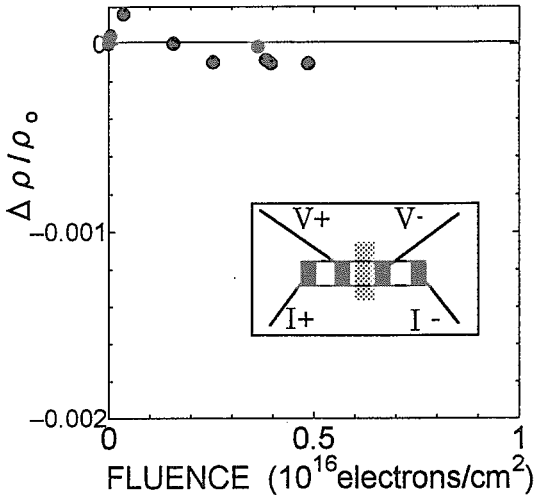


Fig.3 Change in normalized resistivity plotted as a function of fluence. Shaded area corresponds to the irradiated area, which does not include electrodes.

4.24 Defect Accumulation in Nanocrystalline Gold Irradiated with Electrons at Low Temperature

Y. Chimi[1)], A. Iwase[1)], N. Ishikawa[1)], M. Kobiyama[2)], T. Inami[2)], S. Okuda[3)]
[1)] Department of Materials Science, JAERI
[2)] Faculty of Engineering, Ibaraki University
[3)] Tsukuba Institute of Science and Technology

1. Introduction

Nanocrystalline materials have several remarkable properties[1)], which are attributed to nanometer-sized crystal grains, so that they are very attractive for practical use. Moreover, nanocrystalline materials are expected to be irradiation-resistant, because they have a large volume fraction of grain boundaries, which might work as effective sinks for irradiation-produced defects.

In our previous work[2)], we found the irradiation-resistant property in nanocrystalline gold (nano-Au) irradiated with energetic ions at room temperature. On the contrary, in low-temperature irradiation, defect accumulation rate in nano-Au was larger than that in ordinary polycrystalline gold (poly-Au). The contribution of point defects (especially interstitial atoms) can be considered as a reason for the larger accumulation rate.

In the present work, we have studied the defect accumulation in nano-Au during low-temperature irradiation with energetic electrons, which can produce point defects effectively.

2. Experimental Procedure

The specimen was a nano-Au foil (3.4μm thick) prepared by the gas deposition method[3)]. The average grain size of the specimen, which was estimated by X-ray diffraction method[4)], was 23nm. The specimen was irradiated below ~17K with 2.0MeV electrons from a 3MV single-ended accelerator in TIARA, JAERI-Takasaki. The increase in electrical resistivity of the specimen was measured *in situ* at ~10K as a function of electron fluence. For comparison, a poly-Au foil (10μm thick), which had been annealed at 873K for ~1h in vacuum below 2×10^{-7}Torr before irradiation, was placed adjacent to the nano-Au foil, and the same irradiation and measurement were performed simultaneously.

3. Results and Discussion

Figure 1 shows the defect accumulation curves, i.e. the increases in electrical resistivity of the nano- and poly-Au specimens, $\Delta\rho$, as a function of electron fluence, Φ. The defect accumulation rate, $d(\Delta\rho)/d\Phi$, for nano-Au was much larger than that for poly-Au. This result means that defect production increases and/or defect recovery is suppressed in nano-Au. Although this trend could be observed also in ion irradiation, the difference in $d(\Delta\rho)/d\Phi$ between nano- and poly-Au was enhanced in electron irradiation.

For quantitative analysis of the experimental data, the following general rate equation was used

$$\frac{dC}{d\Phi} = \sigma_d - \sigma_r C, \qquad (1)$$

where C is the concentration of the irradiation-produced defects, σ_d the defect production cross-section and σ_r the defect annihilation cross-section. C can be related to $\Delta\rho$ by $\Delta\rho = \rho_F C$, where ρ_F is a resistivity of

unit concentration of Frenkel pairs. In the present analysis, we used ρ_F=250μΩcm[5]. The defect production and annihilation cross-sections for electron and ion irradiations are listed in Tables 1-2.

In electron irradiation, the value of σ_d for nano-Au was 7.8 times larger than that for poly-Au. On the other hand, the multiple for ion irradiation was 2.0. The enhancement of defect production in electron irradiation implies that effective threshold energy for defect production in nano-Au is lower (about in half) than in poly-Au, and/or that point defects are trapped by grain boundaries in nano-Au. The value of σ_r for nano-Au was 2~3 times larger than that for poly-Au in both irradiations. This is consistent with the result of ion irradiation at room temperature, which reveals the irradiation-resistant property.

4. Summary

In order to study the contribution of point defects to the defect accumulation in nano-Au, 2.0MeV electron irradiation was performed at low temperature. The quantitative analysis shows that the defect production cross-section for nano-Au is several times larger than that for poly-Au. By contrast with the result for ion irradiation, it appears that point defects are related to the enhancement of defect production in nano-Au.

References

1) K. Lu, Mater. Sci. Eng. R **16** (1996) 161.
2) Y. Chimi, A. Iwase, N. Ishikawa, M. Kobiyama, T. Inami, S. Okuda, J. Nucl. Mater. **297** (2001) 355.
3) S. Kashu, E. Fuchita, T. Manabe, C. Hayashi, Jpn. J. Appl. Phys. **23** (1984) L910.
4) T. Inami, S. Okuda, H. Maeta, H. Ohtsuka, Mater. Trans. JIM, **39** (1998) 1029.
5) P. Ehrhart, P. Jung, H. Schultz, H. Ullmaier, in *Atomic Defects in Metals, Landolt-Börnstein, Numerical Data and Functional Relationships in Science and Technology*, edited by H. Ullmaier (Springer-Verlag, Berlin, 1991), Group III, vol. 25.

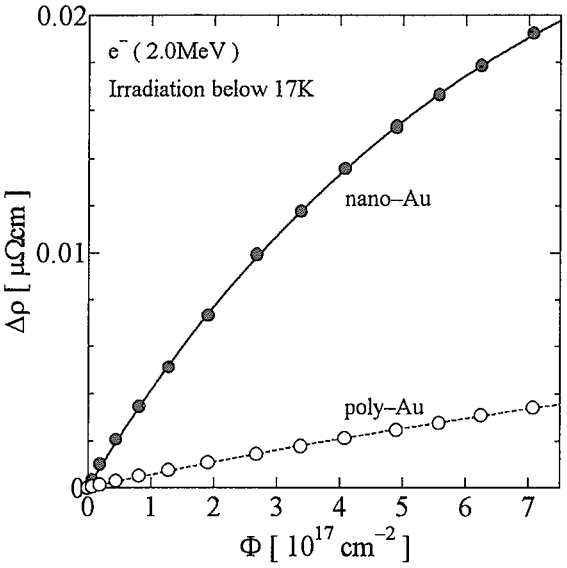


Fig. 1. Defect accumulation curves for nano- and poly-Au specimens.

Table 1. Cross-sections for defect production, σ_d, and annihilation, σ_r, in 2.0MeV electron irradiation.

	nano-Au	poly-Au
σ_d [cm^2]	1.8×10^{-22}	2.3×10^{-23}
σ_r [cm^2]	1.6×10^{-18}	5.6×10^{-19}

Table 2. Cross-sections for defect production, σ_d, and annihilation, σ_r, in 60MeV ^{12}C ion irradiation.

	nano-Au	poly-Au
σ_d [cm^2]	1.4×10^{-18}	7.0×10^{-19}
σ_r [cm^2]	2.0×10^{-15}	8.6×10^{-16}

4.25 Epitaxial Anatase and Rutile TiO_2 Films Prepared by Pulsed Laser Deposition

S. Yamamoto, T. Sumita, T. Yamaki, H. Abe, A. Miyashita, H. Itoh
Department of Materials Development, JAERI

TiO_2 is known to crystallize in three different crystal structures: rutile (tetragonal), anatase (tetragonal) and brookite (orthorhombic). Rutile has been extensively studied and widely used since it is the most stable phase. On the contrary, the anatase has not been well understood in fundamental properties because it is difficult to realize the metastable phase by controlling the stoichiometry. Several of cubic perovskite oxides are good lattice much with anatase TiO_2 (001) plane with square lattice symmetry (lattice constant: 0.3785 nm). Especially single-crystal $LaAlO_3$, (La, Sr)(Al, Ta) O_3 (LSAT) and $SrTiO_3$ were suitable for this purpose. The lattice mismatch of anatase TiO_2 (001) with $LaAlO_3$ (001), LSAT (001) and $SrTiO_3$ (001) are 0.13 %, 2.14 % and 3.06 %, respectively. In this present study, we deposited on the various substrates for epitaxial TiO_2 films by considering the lattice mismatch by pulsed laser deposition (PLD).

The growth of epitaxial TiO_2 films was performed by pulsed laser deposition under the oxygen gas conditions. Various single-crystal substrates were examined for TiO_2 epitaxial growth. The substrates and their orientation are listed in Table 1. For the growth of anatase TiO_2 film, a single-crystal $LaAlO_3$, $SrTiO_3$, LSAT substrates were used. For rutile TiO_2 films, four kinds of different orientation α-Al_2O_3 substrates were used. The substrates with 10 × 10 mm^2 were mirror-polished at both sides. PLD was performed by the second harmonic Q-switched Nd:YAG laser with wavelength of 532 nm, 8 ns in pulse width and 10 Hz in frequency. The laser energy, targets, substrate temperature and oxygen pressure were optimized referring to the crystal quality of anatase film on $SrTiO_3$ (001) substrate and rutile film on α-Al_2O_3 (0001) substrate determined by the X-ray diffraction. For anatase film deposotion, the laser energy was 50 mJ/cm^2 using a titanium (purity: 99.99%) target. For rutile film deposition, the laser energy was 100 mJ/cm^2 using a sintered titanium dioxide (purity: 99.99%). Oxygen gas (purity: 99.99%) was flowed into the chamber through a massflow meter controlled by an absolute pressure gauge (Baratron 626, MKS) under the pumping condition. The epitaxial films were analyzed by Rutherford backscattering spectrometry (RBS) combined with channeling and X-ray diffraction for the crystallographic relationships with the substrates.

The films (200 nm thick) were deposited on the $LaAlO_3$ (001) $SrTiO_3$ (001), LSAT (001) substrates at 500°C under the 35 mTorr O_2 gas pressure. Fig. 1 shows the typical X-ray diffraction pattern from the epitaxial anatase TiO_2 film on the $LaAlO_3$ (001) substrate. Only the reflections from the anatase TiO_2 (004) are observed without any reflection from the substrate, which indicates that the anatase TiO_2 (001) films were epitaxially grown on (001) plane. The orientation relationships between epitaxial TiO_2 films and substrates were summarized in Table 1. It can be seen from the Table that the in-plane orientation relationships between

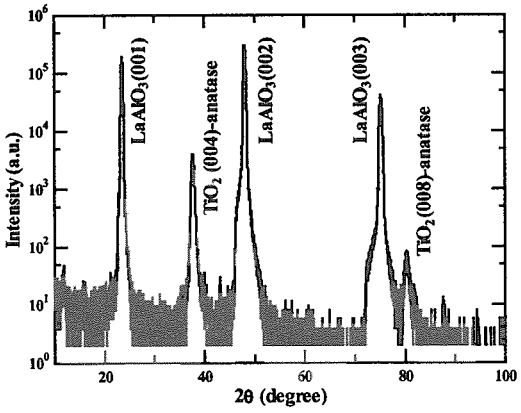


Fig. 1: The X-ray diffraction pattern from the epitaxial anatase TiO_2 films on the $LaAlO_3$ (001) substrate.

anatase (001) films and substrates were the same for the $SrTiO_3$, $LaAlO_3$ and LSAT. Anatase and substrates such as $LaAlO_3$, $SrTiO_3$ and LSAT have the fourfold symmetry and they matches well along their $[100]_{anatase}$ and $[100]_{substrate}$ in-plane direction (mismatch: 0.13 %, 3.06 % and 2.14 %, respectively) As a result, good epitaxial anatase (001) films were obtained on the $LaAlO_3$ (001), $SrTiO_3$ (001) and LSAT (001) substrates. It is reasonably interpreted that these fourfold symmetry of (001) are matched with anatase (001) plane in comparison with the other low index anatase and rutile planes. The lattice mismatch and the substrate structure can play a role in growth of epitaxial anatase films. The best crystal quality of the anatase (001) film was obtained on the $LaAlO_3$ (001), and the FWHM of anatase (004) rocking curves was 0.079°. On the other hand, the substrates with different orientations such as $LaAlO_3$ (110), $SrTiO_3$ (110) were not obtained epitaxial anatase TiO_2 films. These films were polycrystalline and were mixed with the anatase and rutile structures.

The orientation relationships between rutile films and α-Al_2O_3 substrates were also summarized in Table 1. The pole figure analysis was made on the TiO_2 (100) film on α-Al_2O_3 (0001) substrate, and it has become clear that this film consists of three domains rotated by 120° each other around the TiO_2 <100> growth direction. It is considered that the (100) rutile film on the α-Al_2O_3 (0001) substrate is affected by three fold symmetry of the α-Al_2O_3 (0001). At the substrate temperature of 500°C, the best quality rutile film was obtained on the α-Al_2O_3 (0001)

Substrate	Growth film/substrate	In-plane film//substrate	FWHM (deg.)
$LaAlO_3$	(001)/(001)	[100]//[100]	0.079
$SrTiO_3$	(001)/(001)	[100]//[100]	0.794
LSAT	(001)/(001)	[100]//[100]	0.815
α-Al_2O_3	(100)/(0$\bar{0}$01)	[0$\bar{0}$1]//[10$\bar{1}$0]	0.027
	(101)/(1$\bar{1}$20)	[010]//[$\bar{0}$001]	1.684
	(101)/(1$\bar{1}$02)	[010]//[$\bar{2}$110]	0.989
	(001)/(10$\bar{1}$0)	[100]//[0001]	0.461

Table 1: The orientation relationships between TiO_2 films and substrates.

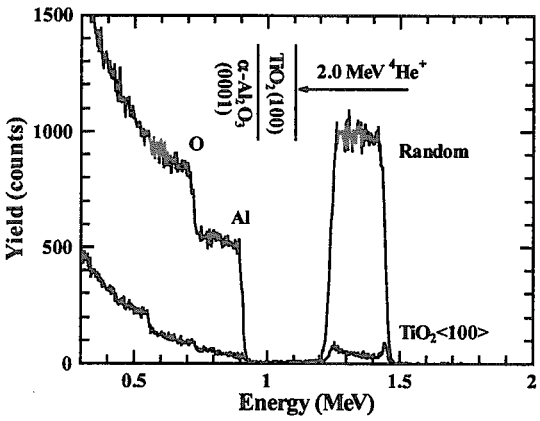


Fig. 2: 2.0 MeV $^4He^+$ RBS/channeling spectra from a deposited rutile TiO_2 film with the thickness of 500 nm on the α-Al_2O_3 (0001) substrate. The aligned spectrum was taken with the beam directed along the <100> axis of the rutile TiO_2 film.

where the FWHM in rutile (200) rocking curve was 0.027°. Fig. 2 illustrates the 2.0 MeV $^4He^+$ RBS spectra from the rutile TiO_2 (100) film on the α-Al_2O_3 (0001) taken under the random and the <100> axial channeling condition. In these RBS spectra, one can recognize the clearly separated peaks from the TiO_2 film and α-Al_2O_3 substrate. The peaks at 1.45 MeV and 0.9 MeV correspond to the Ti component in the TiO_2 film and Al component in the α-Al_2O_3 substrate. Judging from the peaks, the uniform crystal quality TiO_2 film is grown from the interface and the interface is not mixed with each other within the depth resolution (~10 nm) of this technique. The χ_{min} value in the <100> aligned spectrum is 0.028 at the just area behind the surface peak of the Ti component in the TiO_2 film, which suggests that the crystal quality of the rutile film is high enough as in a bulk single-crystal.

The growth of epitaxial anatase and rutile TiO_2 films prepared by PLD was demonstrated successfully. The high quality epitaxial anatase (001) films were grown on the $LaAlO_3$ (001), $SrTiO_3$ (001) and LSAT (001) substrates and the rutile (100) film on the α-Al_2O_3 (0001) substrate by pulsed laser deposition with a Nd:YAG laser under the controlled O_2 atmosphere.

4.26 Effect of Fluorine-Ion Implantation in TiO_2 Rutile Single Crystals

T. Yamaki, T. Sumita, S. Yamamoto, H. Abe, A. Miyashita and H. Itoh
Department of Material Development, JAERI

1. Introduction

Titanium dioxide (TiO_2), a semiconductor with an optical bandgap of 3 eV, i.e., a fundamental absorption edge of 400 nm, is an attractive material for electrochemical solar cells[1] and photocatalysts[2]. Chemical effects in TiO_2 single crystals implanted with metal ions have been extensively studied for many years, using a variety of ions, fluences, and energies[3,4]. This is because doping of various transition metal cations is expected to improve the photoreactivity of TiO_2 and to extend its light absorption into the visible region. Anpo et al.[5] recently prepared the TiO_2 photocatalyst operating effectively under visible-light irradiation by the implantation of chromium or vanadium ions. Their study undoubtedly demonstrates that the metal-ion implantation will provide a good modification of the electronic states to photocatalytic materials.

On the other hand, there have been only a few studies on the anion doping. Subbarao et al.[6] observed an improvement in the photoelectrochemical response of rutile single crystal electrode with doping of F ions by gas-phase HF treatment at high temperatures. A promoting effect on the photocatalytic activity was also found in sol-gel TiO_2 films with a small amount addition of ammonium fluoride into the sol-gel starting solution[7]. In the bulk phase the formal titanium-fluorine single bond energy, 581 kJ mol^{-1}, is the only one higher than that of the titanium-oxygen single bond, 478 kJ mol^{-1} [8]. Thus the fluorination of TiO_2 surfaces possibly leads to an enhancement of chemical and optical stability. In any case, the F ions have the possibilities of acting as promising dopants in the TiO_2 photocatalyst.

In the present work, we implanted F ions in TiO_2 (rutile) single crystals with different fluences and then investigated the effects of subsequent thermal annealing by Rutherford backscattering and channeling (RBS-C) studies, secondary ion mass spectroscopy (SIMS) and X-ray photoelectron spectroscopy (XPS). This is the first report describing the formation of TiO_2 doped highly with F, i.e., $TiO_{2-x}F_x$, by the ion implantation technique, instead of the conventional chemical-doping methods.

2. Experimental

Optically polished single-crystalline TiO_2 (rutile) with the <0 0 1> crystallographic axis was used for our experiments. The size was about 10×10 mm^2 in area and 0.5 mm in thickness. Ion implantations were performed at room temperature using a 400 kV implantor with 200 keV F^+ ions at a nominal fluence of 1×10^{16} to 1×10^{17} ions cm^{-2}. The mean projected range, R_p, and range straggling, ΔR_p, were calculated to be 274 and 72 nm by the TRIM code[9], respectively. An isochronal annealing was carried out in air at 573 and 873 K for 5 h for each step. Helium ions of 2.0 MeV were generated by a 3 MV single-ended accelerator and applied for RBS-C measurements. SIMS was used for probing the F depth profiles in the as-implanted and subsequently annealed TiO_2 crystals. XPS spectra were recorded with a MgKα radiation (hν = 1253.6 eV) to obtain information on the chemical states of the F ions at the surface.

3. Results and Discussion

Fig. 1 shows the RBS-C results obtained for <0 0 1> cut TiO_2 single crystal, implanted with 200 keV F^+ and then annealed at 573 and 873 K. In contrast to the as-implanted state (spectrum (b)), where two damage peaks were found at the surface and near the R_p, these peaks almost disappeared after the annealing as shown in spectrum (c). A comparison between the random and aligned spectra confirms that the pronounced recovery in the Ti and O sublattices can be achieved by a recrystallization within the total thickness of the implanted region. The minimum yield, χ_{min}, the random-to-aligned ratio of backscattering yields, gives a measure of the degree of lattice disorder in crystalline solids. For the Ti sublattice, we obtained the χ_{min} value of < 10% near the surface where a dechanneling contribution to the yield is considered to be the smallest.

In addition to the lattice disorder and recovery, the site location of implanted ions is generally investigated by full angle scans through the crystallographic axial directions in RBS-C analyses. Meyer et al.[10,11] previously performed the angular scan to show that many transition-metal ions occupied substitutional sites by replacing Ti atoms. However, this is not the case with the present analysis; it is not easy to distinguish between the elements with close mass numbers, e.g., O and F atoms. Difficulties also occur in the determination of light element compositions in heavier matrix materials if the signal from the light element is superimposed on the matrix signal. For such reasons, no detailed result regarding the implanted F ions, the very minor constituent in TiO_2, was obtained by our RBS-C studies. We show, therefore, occupation of the F ions on O-lattice sites, i.e., the formation of $TiO_{2-x}F_x$, based on the results of XPS.

In Fig. 2, the SIMS F depth profiles of the implanted rutile single crystals are compared between before and after the two-step annealing. Note that there should be a possible evaporation of F as the volatile components from the TiO_2 surface during the thermal treatments. It is clear that the profile peak position was shifted from the near-R_p depth to the shallower area (around 170 nm) in the sample. In other words, a significant amount of implanted F ions diffused thermally to

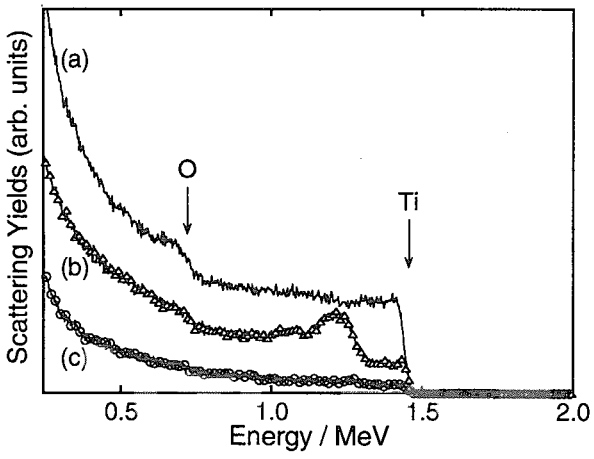


Fig. 1. 2.0 MeV $^4He^+$ <0 0 1> aligned RBS spectra of the TiO_2 rutile single crystal implanted with 200 keV F^+ at room temperature: (b) the as-implanted state and (c) the sample annealed in air at 573 and 873 K after the implantation. The random spectrum of the as-implanted sample (a) is also included in this figure.

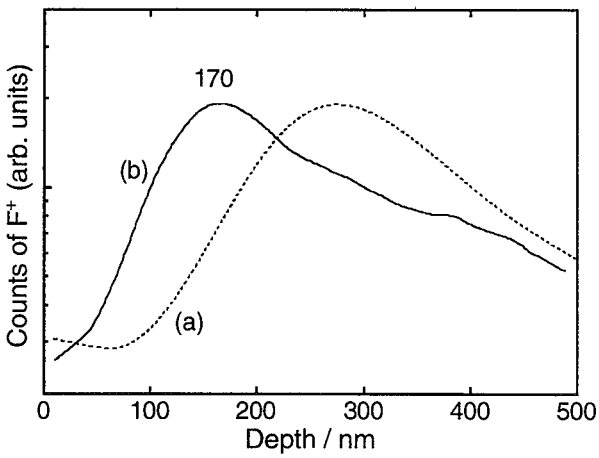


Fig. 2. SIMS F depth profiles of 200 keV F^+ implanted TiO_2 rutile single crystal (a) before and (b) after the thermal treatments at 573 and 873 K. The F^+ secondary ion counts plotted as ordinate are normalized in such a way that the maximum of both profiles is equal.

the outer surface. The implication is that grain boundaries or extended defects are created by the implantation, so that the activation enthalpy for motion of the impurity ions in the lattice effectively decreases. This can induce a preferred outward migration of the F ions at high temperatures, where the above-mentioned damage recovery progresses.

Fig. 3 shows the representative F 1s XPS spectrum of the 1×10^{17} F^+ ions cm^{-2} implanted rutile crystal after the annealing steps. The photoelectron intensity of this spectrum was too low to be measured with a high S/N ratio, and so curve smoothing was applied to the data. The apparent asymmetrical lineshape of the spectrum clearly indicates the existence of at least two different states of the F atoms. The shoulder located around 684.5-685.0 eV is found to correspond to the metal fluoride (F-Ti) by the comparison with spectrum (b) obtained for a commercially-available TiF_4 powder as a standard. The main peak at 683.8 eV may be assigned to structures containing oxyfluoride (F-Ti-O) functional groups.

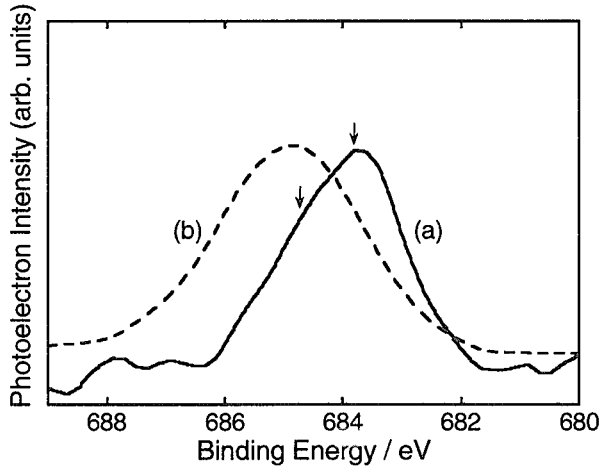


Fig. 3. XPS F 1s spectra of (a) the TiO_2 rutile crystal after the implantation of 1×10^{17} F^+ ions cm^{-2} followed by the two-step annealing in the air and (b) a commercially-available TiF_4 powder for comparison. The asymmetrical lineshape of spectrum (a) reveals the existence of two different chemical states of F (marked with the arrows).

The XPS data were also used for a quantitative estimation of the atomic ratio of F to O, F/O. In this estimation, the elemental ratio was determined from the XPS peak areas of individual elements through correction of the sensitivity factors of these elements. The F/O ratio can be calculated to be 0.0020 from the present spectrum, which means the formation of $TiO_{2-x}F_x$ compounds with x = 0.0039. As a result, TiO_2 doped highly with F was produced by the substitution of O atoms at the top surface (XPS probably probed the first few atomic layers).

References

1) R.H. Wilson, L.A. Harris and M.E. Gerstner, J. Electrochem. Soc. 126 (1979) 844.

2) M.A. Fox and M.T. Dulay, Chem. Rev. 93 (1993) 341.

3) M. Guermazi, P. Thévénard, J.P. Dupin and C.H.S. Dupuy, Radiat. Eff. 49 (1980) 61.

4) M. Guermazi, P. Thévénard, J.P. Dupin and C.H.S. Dupuy, Nucl. Instr. Methods B 182/183 (1981) 397.

5) M. Anpo, Y. Ichihashi, M. Takaushi and H. Yamashita, Res. Chem. Intermed. 24 (1998) 143.

6) S.N. Subbarao, Y.H. Yun, R. Kershaw, K. Dwight and A. Wold, Inorg. Chem. 18 (1979) 488.

7) A. Hattori, M. Yamamoto, H. Tada and S. Ito, Chem. Lett. (1998) 707.

8) O. Kubaschewski, E.L. Evans and C.B. Alcock, in "Metallurgical Thermochemistry 4th Edition" (Oxford, 1967) Table A, p. 304.

9) J.F. Ziegler, J.P. Biersack and U. Littmack, in "The Stopping Range of Ions in Solids" (Pergamon Press, New Tork, 1985).

10) O. Meyer and A. Turos, Mater. Sci. Rep. 2 (1987) 371.

11) R. Fromknecht, I. Khubeis, S. Massing and O. Meyer, Nucl. Instr. Methods B 147 (1999) 191.

This is a blank page.

5. Material Analysis

5.1 In-situ Observation of Growth Processes of Transition Metal Compound Thin Films by Carbon-implantation ····· 207
Y.Kasukabe, Y.Fujino, M.Osaka, Y.Yamada, and H.Abe,

5.2 Development of In-situ Ion Beam Analysis of Adsorbate Atoms at the Solid-liquid Interface ····· 210
J.Yuhara, N.Kishi, H.Suzuki, K.Soda, K.Morita, T.Ohnuki, S.Yamamoto
K.Narumi, H.Naramoto, and K.Saito

5.3 Carbon KVV Auger Electron Emission from HOPG Bombarded by Fast Protons ····· 212
H.Kudo, K.Haruyama, T.Kinoshita, S.Ishii, S.Seki, K.Narumi, and H.Naramoto

5.4 Characterization of Defects and Hydrogen Absorption in Pd Irradiated with Protons ····· 215
H.Abe, A.Uedono, H.Uchida, Z.Q.Chen, S.Okada, and H.Itoh

5.5 Chemical Modifications of Polycarbonate by C_n^+ Cluster Irradiation ····· 218
K.Hirata, Y.Saitoh, K.Narumi, Y.Kobayashi, and K.Arakawa

This is a blank page.

5.1 In-situ Observation of Growth Processes of Transition Metal Compound Thin Films by Carbon-Implantation

Y. Kasukabe, Y. Fujino, M. Osaka[1)], Y. Yamada[1)], H. Abe[2)]
International Student Center/Department of Electronic Engineering, Tohoku University, [1)]Department of Quantum Science and Energy Engineering, Tohoku University, [2)]Department of Materials Development, JAERI.

1. Introduction

It is well known that in transition metals the valence d orbitals are more contracted than valence s and p orbitals, and split in energy by the bonding interaction with the ligand atoms such as carbon (C) and nitrogen (N) ones. The bonding interaction gives rise to transformations of the transition metal sublattice, and to covalent properties as well as metallic and ionic ones. These properties make the compounds interesting for both fundamental researches and technological applications such as hard coatings and diffusion barriers in microcircuits.[1,2] The carbides of titanium (Ti), one of the typical transition metals, are technologically important as corrosion-resistant coatings on cutting tools.[2] It has been revealed that properties of epitaxially-grown Ti compound films are superior to those of polycrystalline ones. Thus, much interest has been focused on the epitaxial films. Recently, it was reported that NaCl-type TiN films were epitaxially grown by the N-implantation into evaporated Ti films.[3] However, the growth process of epitaxial Ti carbide films by C-implantation has not been sufficiently understood.

The purpose of this work is first, to throw light on changes of the crystallographic structure of Ti films by C-implantation, using in-situ transmission electron microscopy (TEM), and then to discuss the epitaxial growth mechanism of Ti carbide films.

2. Experimental

Detailed descriptions of the preparation of evaporated-Ti films were presented in the earlier paper.[3] The 100-nm-thick Ti films were evaporated by an electron-beam heating method in an ultra-high vacuum onto thermally cleaned NaCl substrates held at room temperature (RT). The ultimate pressure in the working chamber was less than 4×10^{-9} Torr. Evaporated Ti films were divided into two kinds of samples: one was separated from the NaCl substrate for TEM observation, and the other remained on the substrate for Rutherford backscattering spectrometry (RBS) using a well-collimated 3.5 MeV $^4He^+$ beam. The implantations of carbon ions (C^+) with 26 keV were performed in the 400 kV analytical and high resolution TEM combined with ion accelerators,[4] and also in the 400 kV ion implantation facility at JAERI-Takasaki. According to the Monte Carlo simulation using the TRIM code, the projected range of C^+ with 26 keV was 54 nm, and thus most of the implanted ions are thought to be retained inside the Ti films. The C-concentrations in Ti films were able to be estimated from the implantation dose measured by a Faraday cage. The maximum dose in this experiment was 3.06×10^{17} ions/cm^2, which corresponded to the C/Ti ratio of 0.54: the average atomic concentration of C in the Ti film.

3. Results and discussion

Typical RBS spectra taken from the unimplanted Ti film and the N-implanted Ti film with N/Ti=0.54 are shown in Fig. 1. It can be seen that after the implantation, the peak of C appears clearly throughout the depth of the Ti film, whereas the height of the Ti peak decreases slightly, owing to the existence of C in the Ti film. These results manifest the carbonizing of evaporated-Ti films by C-implantation. The

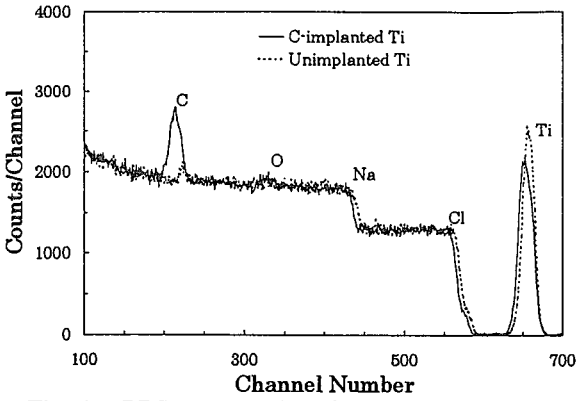


Fig. 1. RBS spectra taken from the unimplanted and C-implanted Ti films with C/Ti=0.54, respectively.

evaluated C/Ti value from the RBS spectrum is 0.53, which is in agreement with the C/Ti value of 0.54 estimated from the implantation dose, within experimental uncertainty. The RBS spectrum taken from the C-implanted Ti film with C/Ti=0.27 estimated from the implantation dose is similar to that with C/Ti=0.54 in Fig. 1. However, the peak of C in the RBS spectra is smaller than that in Fig. 1. The C/Ti value evaluated from the RBS spectrum for the film with C/Ti=0.27 is 0.28. These facts mean that implanted C atoms do not escape from the Ti films during the implantation up to C/Ti=0.54.

The typical result of the TEM observation of the unimplanted Ti film is shown in Fig. 2. An

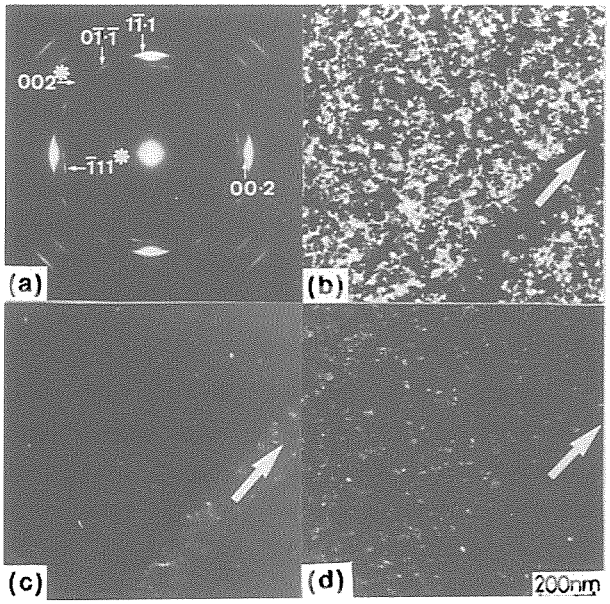


Fig. 2. ED pattern (a), and BF (b) and DF (c), (d) images taken from a 100-nm-thick Ti film. (c) and (d) were taken with the 002* reflection of TiH_x and the 1 1 $\bar{1}$ 1 reflection of hcp-Ti, respectively.

of Fig. 2 (a) indicates that hcp-Ti (lattice constants: a=0.296 nm, c=0.471 nm) and CaF_2-type TiH_x ($x \fallingdotseq 1.5$; lattice constant: a=0.441 nm) mainly exist in this film. The reflection indicated by the three-index system with an asterisk, *, is obtained from TiH_x, whereas those indicated by the four-index system are obtained from hcp-Ti. The bright field (BF) image of Fig. 2(b) shows the band-like contrast indicated by an arrow, elongated in the <110> direction of TiH_x and NaCl. Figures 2(c) and 2(d) are, dark field (DF) images taken from reflections labeled 002* and 1 $\bar{1}$ 1, respectively. The orientation relationships between the hcp-Ti and the NaCl substrate are (03$\bar{5}$)Ti//(001)NaCl and [2$\bar{1}$0]Ti // [$\bar{1}$10] NaCl: (03$\bar{5}$)-oriented hcp-Ti. On the other hand, the orientation relationship between the TiH_x and NaCl is (110)TiH_x//(001)NaCl and [001]TiH_x// [110]NaCl: (110)-oriented TiH_x. Figure 2(c) shows that (110)-oriented TiH_x grows mainly in the band-like contrast region, whereas epitaxial hcp-Ti grows only outside the band-like contrast regions as seen in Fig. 2(d).

Carbon ions with 26 keV were implanted into the evaporated-Ti film which showed such ED pattern as Fig. 2(a). Figures 3(a) and 3(b) show, respectively, a typical ED pattern and BF image taken from the C-implanted Ti film with C/Ti=0.54. The DF image, Fig. 3(c) was taken from the 002 reflection in Fig. 3(a), whereas Fig. 3(d) was taken from the 020 reflection, where the reflections indicated by the three-index system are obtained from NaCl-type TiC_z. An analysis of Fig. 3 indicates that hcp-Ti (lattice constants: a=0.299 nm, c=0.479 nm) and TiC_z (lattice constant: a=0.432 nm) coexist in this film. The orientation relationships between hcp-Ti and NaCl are the same as those in unimplanted Ti films. Crystallites of TiC_z are grown in the two orientations; (110)-oriented TiC_z: (110)TiC_z //(001)NaCl and [001]TiC_z // [110]NaCl, and (001)-oriented TiC_z: (001) TiC_z

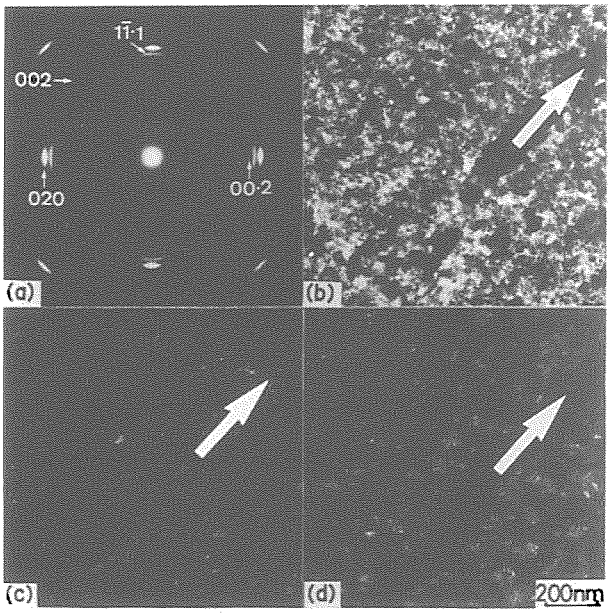


Fig. 3. ED pattern (a), and BF (b) and DF (c), (d) images taken from a C-implanted Ti film (C/Ti=0.54). (c) and (d) were taken with 002 and 020 reflections in (a), respectively.

//(001)NaCl and [100] TiC_z //[100]NaCl. It is noteworthy that reflections of TiH_x cannot be observed. Furthermore, it is revealed from Fig. 3 that (110)-oriented TiC_z crystallites are preferentially grown in the band-like contrast region indicated by an arrow, elongated in the <110> direction of NaCl and TiC_z. These suggest that the C-implantation induces the release of H from evaporated-Ti films containing TiH_x and the occupation of implanted-C atoms in octahedral sites of the H-escaped fcc-Ti sublattice. This process gives rise to the formation of the (110)-oriented TiC_z from (110)-oriented TiH_x without changing the orientation of the fcc-Ti sublattice.

On the other hand, (001)-oriented TiC_z crystallites grow preferentially outside the band-like contrast regions. It can be considered that the C-implantation into the (03 · 5)-oriented hcp-Ti leads to the epitaxial formation of the (001)-oriented TiC_z, as discussed below. Figure 4 shows the rearrangement of Ti atoms during the transformation from (03·5)-oriented hcp-Ti to (001)-oriented fcc-Ti structure. Solid circles represent atoms of hcp-Ti. Note that one of octahedral sites, which lies midway between F and K atoms in Fig. 4 corresponds to an octahedral site in {001} planes of the fcc-Ti. Thus, the occupation of octahedral sites in octahedra such as the GEFJKL in Fig. 4 by C atoms leads to the occupation of octahedral sites of the transformed fcc-Ti by C ones. Therefore, it seems reasonable to conclude that the epitaxial growth of the (001)-oriented TiC_z can be caused by the transformation of hcp-Ti to fcc-Ti during the C-implantation, accompanied with the inheritance of the EFJK square and/or GEFJKL octahedron in Fig. 4, as well as the occupation of C in octahedral sites of the (001)-oriented fcc-Ti.

References

1) K. Sano, M. Oose and T. Kawakubo, Jpn. J. Appl. Phys. **34** (1995) 3266.
2) J. E. Sundgren, Thin Solid Films **128** (1895) 21.
3) Y. Kasukabe, N. Saito, M. Suzuki, Y. Yamada, Y. Fujino, S. Nagata, M. Kishimoto, and S. Yamaguchi, J. Vac. Sci. & Technol. **A16** (1998) 482.
4) H. Abe, H. Naramoto, K. Hojou, and S. Furuno, The TEM-Accelerators Facility at JAERI-Takasaki and its Application to Materials Science, JAERI-Research **96-047** (1996) 1.

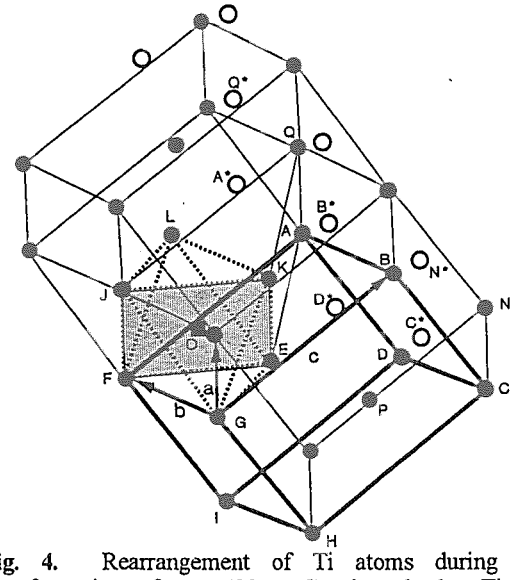


Fig. 4. Rearrangement of Ti atoms during the transformation from (03 · 5)-oriented hcp-Ti to (001)-oriented fcc-Ti structures by a shear. The open circles represent positions of Ti atoms shifted by the shear in order to obtain an fcc structure. The shifted B atom, for example, is represented by the open circle labeled B*. One of octahedral sites is marked by a solid square.

5.2 Development of in-situ Ion Beam Analysis of Adsorbate Atoms at the Solid-Liquid Interface

J. Yuhara [1], N. Kishi [1], H. Suzuki [1], K. Soda [1], K. Morita [1], T. Ohnuki [2], S. Yamamoto [3], K. Narumi [4], H. Naramoto [4], K. Saito [5]
[1] School of Engineering, Nagoya University,
[2] Department of Environmental Sciences, JAERI
[3] Department of Material Development, JAERI
[4] Advanced Science Research Center, JAERI
[5] National Industrial Research Institute of Nagoya

1.Introduction

For the technology for geologic radioactive waste disposal, we have recently developed an in-situ RBS system for measuring heavier nuclides adsorbed at the liquid-solid interface. Silicon windows of 5.5 μm in thickness and of 2.5mm in diameter have been used to detect 9 MeV He^{++} ion backscattered from heavier nuclides [1]. So far, the dissolution rates of Pb layers deposited physically on the SiO_2 surface into water solutions with different pH values have been measured using the in-situ RBS system[2]. However, the thickness of silicon windows is not thin enough to detect sub-monolayer (~10^{14} atoms/cm^2) nuclides such as Sr-90, Cs-137, and Ce-144 because of its low scattering cross-section comparison to heavier nuclides, although they are also important nuclides for the geologic radioactive waste.

The purpose of this study is to develop the low background in-situ ion beam analysis of adsorbate atoms at the solid-liquid interface by using thinner silicon window thickness and lower energy He^{++} ion beam to prevent Si substrate and C slit from nuclear reactions.

2.Experimental

The window of the silicon specimen was fabricated using preferentially slow etching of heavily B-implanted silicon as in the previous study. The substrate materials were (100)-oriented silicon disks of 0.3 mm in thickness and of 10 mm in diameter, one face being mirror-finished. 2.4 MeV B^+ ions with the projected range of 3.2 μm, were uniformly implanted from the mirror-finished face to a dose of $1x10^{16}$ ions/cm^2 at a random direction. The implanted disks were annealed at 950°C for an hour to reduce damage produced by the implantation, and to form an oxide layer of about 0.25 μm on the surface. The thinning process was described elsewhere[3]. A drop of 10^{-2} cc $NdNO_3$ solution of 10^{-3} M Nd (decay products of Ce-144) was deposited on the window surface and was dried out. The detection limit of Nd concentration was tested by in-situ RBS analysis. The energies of He^{++} ion beams used were 9 MeV, 5 MeV, and 4 MeV. It was required for 30 min to obtain each spectrum.

3. Results and Discussion

All RBS spectra have been obtained at solid-gas (air) interface, not solid-liquid interface, using the in-situ RBS analysis chamber. Typical RBS spectra are shown in Fig.1. The incident energies of He^{++} ion beams

are 9 MeV (a), 5 MeV (b), and 4 MeV (c). It is clearly shown from Fig.1 (a) that there exist two sharp nuclear reaction peaks, from the silicon window, at the channels between 440 and 520. Another sharp nuclear reaction peak from carbon slit is also seen at the channel below 130. From peak area of Nd peak around 740 ch in the 9 MeV He^{++} spectrum, Nd concentration has been calculated to be $5x10^{16}$ atoms/cm^2. Using background counts, the detection limit of Nd estimated is calculated to be ~$4x10^{15}$ atoms/cm^2. The detection limit is also calculated to be be ~$4x10^{15}$ atoms/cm^2 using the data in the 5 MeV He^{++} spectrum. The detection limits are caused by a pileup effect in these normal RBS measurements for the short period, since the nuclear reaction cross sections (σ_n) of Si substrate are 25 times larger than Rutherford backscattering cross sections (σ_R) [4]. If the thickness of the window is even thinner than that of the present window, which is 3.2 μm, the detection limit will be improved. However, such a thinner window is too weak in strength to use in the solid-liquid interface RBS experiments. The detection limit might be improved, if we measured for several hours to obtain a RBS spectrum using a very low intensity ion beam in the present system.

Therefore, it is concluded that it is impossible to measure the dissolution and adsorption rates of sub-monolayer nuclides such as Sr-90, Cs-137, and Ce-144 in the present in-situ RBS system. It might be helpful to use (p,γ) reaction to perform high sensitivity ion beam solid-liquid interface analysis.

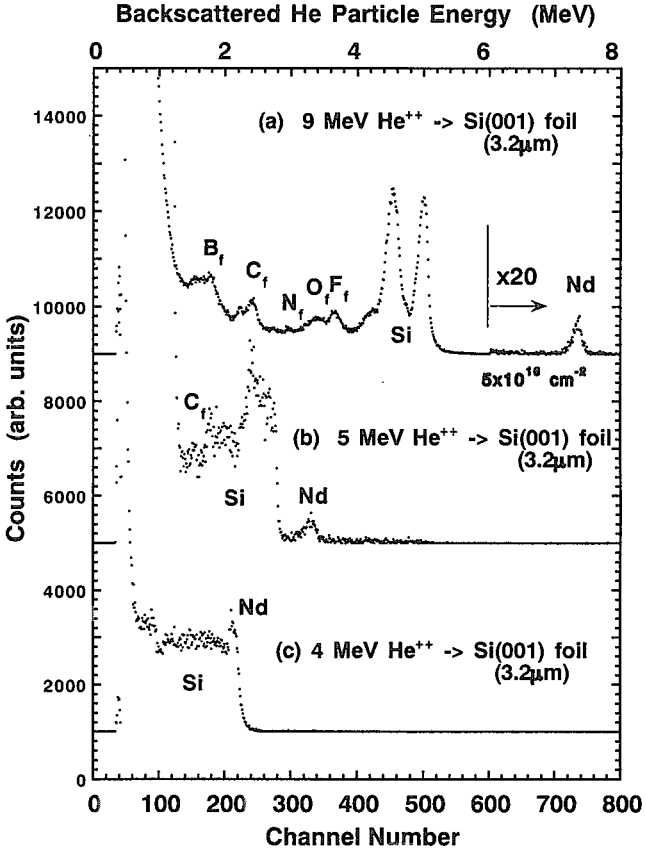


Fig.1 Typical RBS spectra of (a) 9 MeV, (b) 5 MeV, and (c) 4 MeV He^{++} ion beam from the silicon window of the sample with Nd layers deposited on the back-surface.

References

1) K. Morita, J. Yuhara, R. Ishigami, B. Tsuchiya, K. Saitoh, S. Yamamoto, P. Goppelt-Langer, Y. Aoki, H. Takeshita, and H. Naramoto, Rad. Phys. and Chem., 49, No.6 (1997) pp603-608

2) K. Morita, J. Yuhara, R. Ishigami, B. Tsuchiya, K. Soda, K. Saitoh, T. Ohnuki, S. Yamamoto, Y. Aoki, K. Narumi, and H. Naramoto, to be published.

3) K. Saitoh, H. Niwa, S. Nakao, and S. Miyagawa, Proc. 10th Int. Conf. on Ion Implantation Technology, ed. by S. Coffa *et al.*, 1995, pp.998-1001.

4) Handbook of modern ion beam materials analysis, ed. By J. R. Tesmer and M. Nastani, Materials Research Society (MRS) (1995)

5.3 Carbon KVV Auger Electron Emission from HOPG Bombarded by Fast Protons

H. Kudo[1)], K. Haruyama[1)], T. Kinoshita[1)], S. Ishii[2)], S. Seki[3)], K. Narumi[4)], H. Naramoto[4)]
[1)]Institute of Applied Physics, Univ. of Tsukuba, *Advanced Science Research
[2)]Tandem accelerator center, Univ. of Tsukuba
[3)]SSL, Tsukuba
[4)]Advanced Science Research Center, JAERI

1. Introduction

We have studied ion-induced Auger electron emission under the condition that Auger yields depend on a layered structure of the target material, so that the commonly used macroscopic treatment of Auger yields must be modified. Since Auger peaks are superposed on the continuum energy spectrum, precise analysis of such structure-sensitive yields requires knowledge on the continuum (background) yield, which results mainly from the binary-encounter processes.[1)] A recently established technique, i.e. 180° ion-induced electron spectroscopy, has a characteristic feature that the continuum energy spectrum is independent of the tilt angle of the surface of a solid target.[2, 3)] The 180° electron spectroscopy therefore allows direct comparison of the electron spectra measured under oblique incidence conditions on the surface.

2. Experiment

We have used highly oriented pyrolytic graphite (HOPG) as a sample, which has a typical layer structure of hexagon network of carbon atoms. The bond length in the carbon network is 1.42 Å and the layer spacing is 3.35 Å. A fresh and flat surface of HOPG(0001) was obtained by peeling of the surface layer using an adhesive tape. Observations by an atomic force microscope in air assured that the fresh (0001) surface is atomically flat except for steps of a few monolayers, which are separated from each other typically by a micronmeter. The HOPG samples were bombarded by 1 MeV H^+. Under the present experimental conditions, the critical angle of HOPG(0001) planar channeling (~0.42°) is much less than the values of the incidence angle θ relative to the surface, so that specular reflection of the ions does not occur.

We have measured energy spectra of carbon KVV Auger electrons (kinetic energy E_A=260 eV) which are emitted at 180° with respect to the beam direction, while it is bombarded by 1 MeV H^+. The electron measurements have been carried out using a 45° parallel-plate spectrometer of the double deflection type under the pressure of 3×10^{-7} Pa. For a geometrical reason, the influence of scattering of the emitted electrons by the steps must be minimized for observations at 180°. When the HOPG surface is oblique to the ion beam, i.e., to the spectrometer direction, the Auger electron produced inside the target moves towards the surface and is emitted from the surface in the 180° direction after they are refracted at the surface, owing to the work function of ~5 eV.

3. Results and discussion

The Auger peak height can commonly be

related to the mean free path for inelastic scattering λ, which characterizes the attenuation of the elastically scattered Auger yield as $\exp(-z/\lambda)$, where z is the escape length of the electron. For the geometry illustrated in Fig. 1, the relative intensity of the Auger yield $Y(\theta)$ is written

$$\begin{aligned} Y(\theta) &= (1/\sin\theta)[1+\exp(-d/\lambda\sin\theta_1) \\ &\quad + \exp(-2d/\lambda\sin\theta_1) + \exp(-3d/\lambda\sin\theta_1)+....] \\ &\quad \times \exp(-t/\lambda\sin\theta_2) \\ &= (1/\sin\theta)\,[1-\exp(-d/\lambda\sin\theta_1)]^{-1} \\ &\quad \times \exp(-t/\lambda\sin\theta_2), \end{aligned} \qquad (1)$$

where θ_1 is related to θ by $\cos\theta_1=(1-e\varphi/E_A)^{1/2}\times\cos\theta$, and t is the effective thickness of the electron distribution above the HOPG surface. θ_2 is the average emission angle at the surface, which can be approximately given by $(\theta_1+\theta)/2$. The term $1/\sin\theta$ represents geometrical enhancement of the irradiated surface area. It is also assumed that the valence Auger electrons are produced on the atomic sites.

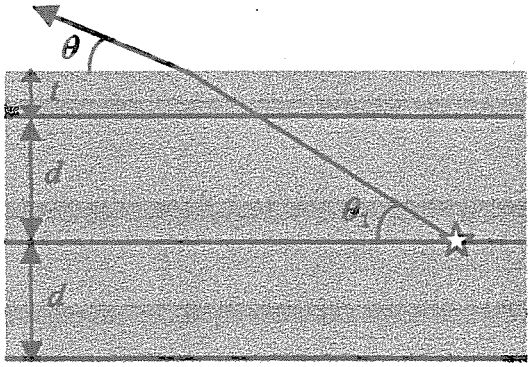


Fig. 1. Emitting direction of the Auger electron.

Figure 2 shows the values of $R=Y(\theta)/Y(90°)$ as a function of λ, calculated from eq. (1), for θ=5.7 and 10°, which correspond to θ_1=9.8 and 12. 8°, respectively. In this case, we have assumed that t=0.6d , and d. Generally, $R\geq0$ for t=0. Also, R approaches $\sin\theta_1/\sin\theta$ as $\lambda\rightarrow\infty$, which corresponds to the macroscopic treatment of the Auger peak height.

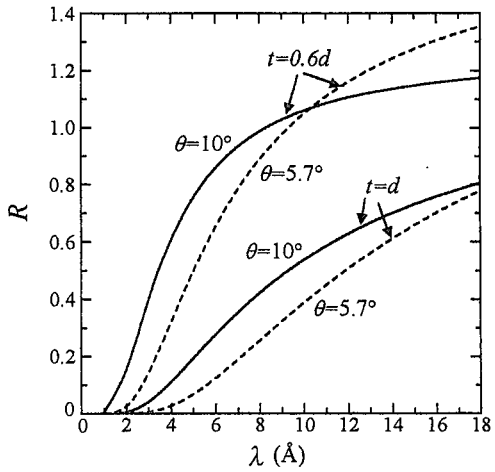


Fig. 2. $R=Y(\theta)/Y(90°)$ as a function of λ.

The measured electron spectra for θ=5.7, 10, and 90° are shown in Fig. 3. These three spectra are plotted after they are normalized so that the continuum yields at 300–350 eV are equal. This assumption seems to be valid for the 180° electron spectroscopy, mentioned earlier. Furthermore, it is anticipated that the smooth continuum spectrum should be less influenced by the scattering by valence electrons above the surface, as noted earlier.

We see in Fig. 3 that the normalized Auger peak becomes lower with decreasing θ. The experimental values of R for θ=5.7 and 10° are 0.52±0.03 and 0.68±0.03, respectively. These values can be compared with the calculated results, shown in Fig. 2, taking into account an estimated value of $\lambda\approx$10 Å.[4] In the preasent analysis, t may be regarded as an adjusting parameter. The observed values of R can be well reproduced for $\lambda\approx0.8d$=2.7 Å. It is important to note that t=0 must

be assumed in eq. (1), if the production sites of KVV Auger electrons are uniformly distributed in HOPG, i.e. not localized near the carbon nuclei. In this case, R=Y(θ) should increase with decreasing θ from 90°, contrary to the observation. The experimental results therefore indicate that production sites of the KVV Auger electron are localized near the carbon nuclei, rather than uniformly distributed over the layered lattice.

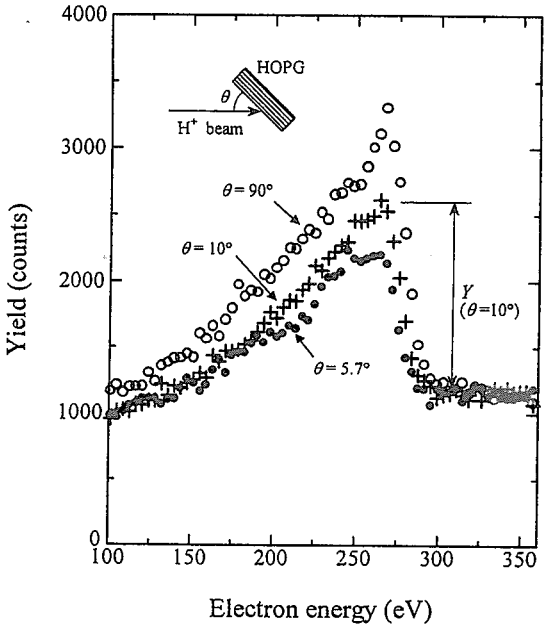


Fig. 3. Energy spectra of electrons measured for θ=5.7, 10, and 90°.

The analysis model used here is rather qualitative. However, essential aspects of the phenomenon have been revealed from the present experiments, i.e.,

(i) the degraded KVV Auger peaks for emission in the oblique directions are due to the elastic and inelastic collisions with valence electrons distributed above the surface. Also, the Auger peak height reflects the layered structure of HOPG.

(ii) $R\geq 0$ for any θ if the Auger electrons are produced uniformly in HOPG. However, the experiments indicate $R<1$, implying localized production of the valence Auger electrons.

Detailed analysis of the experimental results should provide location of the preferential production sites of the valence Auger electrons in the layered structure.

References

1) M. E. Rudd, Y.-K. Kim, D. H. Madison, T. J. Gay, Rev. Mod. Phys. 64 (1992) 441.
2) H. Kudo, A. Tanabe, T. Ishihara, S. Seki, Y. Aoki, S. Yamamoto, P. Goppelt-Langer, H. Takeshita, and H. Naramoto, Nucl. Instr. and Meth. B 115 (1996) 125, and references therein.
3) H. Kudo, *Ion-Induced Electron Emission from Crystalline Solids* (Springer, Berlin, Heidelberg, 2001), in press as a volume of *Springer Tracts in Modern Physics*.
4) M. P. Seah, W. A. Dench, Surf. Interface Anal. 1 (1979) 2.

5.4 Characterization of defects and hydrogen absorption in Pd irradiated with protons

H. ABE[1], A. UEDONO[2], H. UCHIDA[3], Z. Q. CHEN[2], S. OKADA[4] and H. ITOH[1]

[1] Department of Material Development, JAERI

[2] Institute of Applied Physics, University of Tsukuba

[3] Faculty of Engineering, Tokai University

[4] Advanced Science Research Center, JAERI

1. INTRODUCTION

For practical use of palladium (Pd) as a hydrogen storage, it is indispensable to improve the hydrogen absorptivity in the material. Regarding the hydrogen storage in metals, it was reported that the absorption concentration and hydrogen reaction rate depend strongly on the surface state of metals[1]. For surface modification of materials, low energy ion irradiation, i.e., ion implantation is known to be a quite useful method. These facts give the possibility that the hydrogen absorptivity in Pd is improved by surface modification due to ion irradiation. In order to examine the effects of ion irradiation on the hydrogen absorption process in Pd, we have performed proton irradiation into the material. Defects introduced in Pd by ion irradiation was investigated using positron annihilation spectroscopy[2]. Hydrogen absorption in ion irradiated Pd was also evaluated. Based on the obtained results, we discuss the correlation between ion irradiation and hydrogen absorption in Pd.

2. EXPERIMENTAL

The samples used in this study were Pd sheets (99.99% purity) with a size of 10 x 10 x 0.1 mm^3. Prior to irradiation, all Pd samples were annealed at 1073 K in a flowing pure N_2 gas (99.9998% purity). Ion irradiation was made with 100 keV protons up to a dose of 1 x 10^{16} /cm^2.

Positron annihilation measurements were performed for the samples before and after irradiation. Doppler-broadening profiles of annihilation γ-rays for the unirradiated and irradiated samples were obtained at room temperature by using monoenegetic positron beams with energies (E) up to 30 keV[3]. The obtained spectrum of annihilation γ-rays was characterized by the S-parameter, which is defined as the ratio of the counts in an energy range of 511 ± 0.75 keV to the total counts (5 x 10^5 photons). For the analysis of the S-E relation, a computer code VEPFIT[4] was used. In the analysis, we assumed a square depth distribution of defects in the irradiated Pd samples.

Hydrogen absorption measurements were also performed for the irradiated and

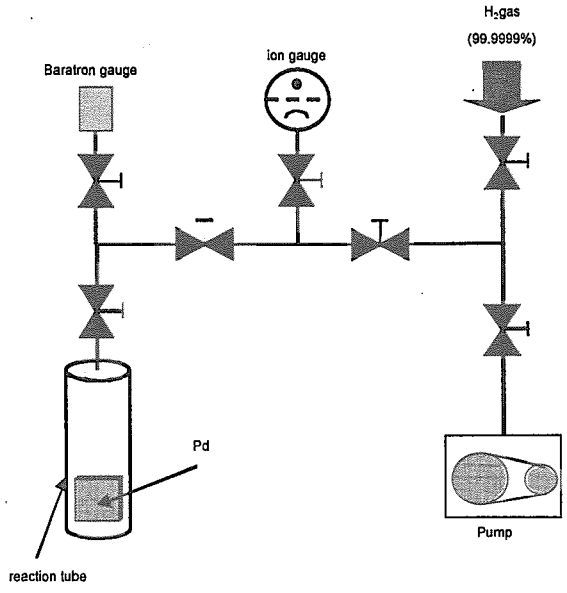


Fig. 1. Sieverts' type apparatus

unirradiated samples. A Sieverts' type apparatus, which is shown in Fig.1, was used to characterize hydrogen storage of the samples[5]. After each sample was placed into a reaction tube, inner gas was exhausted to a vacuum level of 1 x 10^{-5} Torr at room temperature. Next, pure H_2 gas (99.99999% purity) was introduced into the reaction tube to a pressure of 2 atm. To obtain the reaction rate of hydrogen in the samples, a change in the hydrogen pressure in the reaction tube was monitored. The total hydrogen storage concentration of the irradiated and unirradiated Pd samples were derived from the saturated value of the hydrogen pressure.

3. RESULTS AND DISCUSSION

Figure 2 shows the *S*-parameter as a function of *E* for the proton irradiated and unirradiated Pd samples. In the unirradiated sample, the *S*-parameter increased with decreasing *E*. This result is attributed to out diffusion of positrons and their annihilation at the surface. As a result of fitting using VEPFIT, the positron diffusion length in the unirradiated sample was obtained to be 162 ± 1 nm.

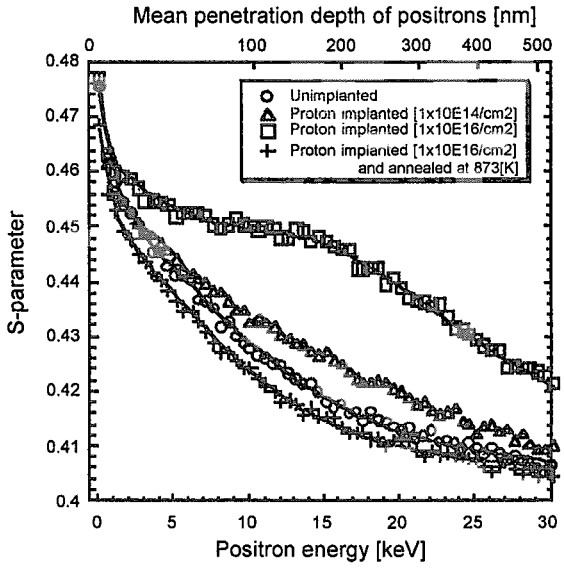


Fig. 2. *S*-parameter as a function of incident positron energy for the unirradiated and irradiated Pd samples. The fluences of protons were 1 x 10^{14} and 1 x 10^{16} /cm^2. Data for the sample irradiated at 1 x 10^{16} /cm^2 and subsequently annealed at 873 K is also plotted.

In the proton irradiated samples, large values of the *S*-parameter were obtained in comparison with those of the unirradiated sample. The *S* value increased with irradiation fluence of protons. These results indicate that vacancy type defects are produced by irradiation and that their size and concentration increase with proton fluence. In the sample irradiated at 1 x 10^{16} /cm^2, it was derived from the fitting that vacancy type defects were formed to a depth of 400 ± 10 nm, which is in good agreement with the calculated range of defect production using TRIM[6]. The characteristic *S*-parameter and positron diffusion length in a defective region were also estimated to be 0.4509 ± 0.0001 and 37 ± 2 nm, respectively. After annealing of the sample at 873 K, the *S* values decreased to a level similar to those of the unirradiated sample. This result suggests that almost all vacancy type defects are removed by the annealing.

Figure 3 shows the results of hydrogen storage in the unirraidated and proton irradiated samples. The hydrogen reaction rate (*r*) can be determined from a temporal change in the *[H]/[Pd]* value in a liner region. The value of *r* for the unirradiated sample was estimated to be 2.41 x 10^{-3} /sec, and that for the proton irradiated one was 1.61 x 10^{-3} /sec. The hydrogen reaction rate of the unirraidated sample was higher than that of the irradiated one. This result can be explained by the hydrogen blocking and/or trapping at vacancy type defects.

The total hydrogen storage ratio *[H]/[Pd]* (after about 900 sec in Fig.3) in the irradiated sample is almost the same as that in the unirradiated one. The value of *[H]/[Pd]* = 0.7 was obtained for both samples. The result can be interpreted by the fact that the

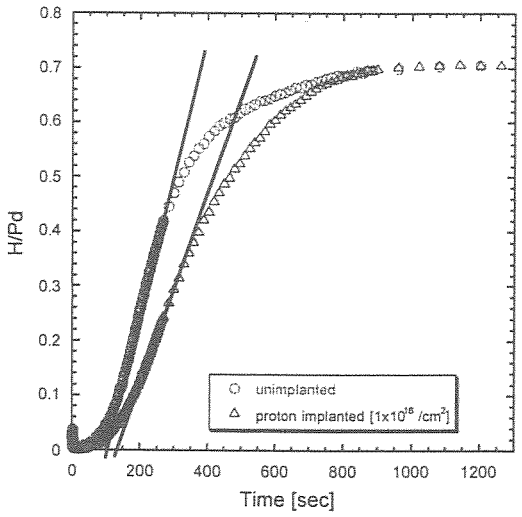


Fig.3. Change in the ratio of absorbed hydrogen atoms to Pd atoms (*[H]/[Pd]*) for the unirradiated and irradiated samples. The absorption reaction rate *r* for each sample is determined from an increase of *[H]/[Pd]* in a linear region, which is shown by solid lines.

volume of the irradiated region is much smaller than the total volume. Figure 4 shows SEM images (x 600) of the unirradiated sample before and after hydrogen absorption. SEM images (x 600) of the proton irradiated sample before and after hydrogen absorption are also shown in Fig. 5. In the SEM images, no significant difference was observed between the unirradiated and irradiated samples, while an increase of cracks was observed after hydrogen absorption. To clarify the effects of ion irradiation on hydrogen storage properties of Pd, further investigations are necessary.

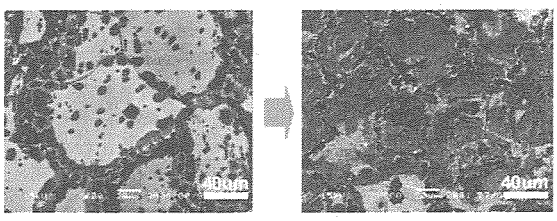


Fig. 4. SEM images (x 600) of the unirradiated Pd before (left) and after (right) hydrogen absorption.

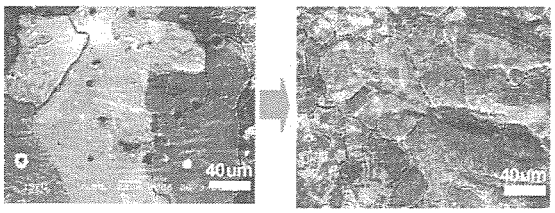


Fig. 5. SEM images (x 600) of the proton irradiated (1 x 10^{16} /cm^2) Pd before (left) and after (right) hydrogen absorption.

References

1) H. Uchida, Int. J. Hydrogen Energy 24 (1999) p.861.
2) P. Asoka-Kumar et al,. Appl. Phys. Lett. 57 (1990) p.1634.
3) A. Uedono et al., J. Appl. Phys. 87 (2000) p. 4119.
4) A. van Veen et al.,: AIP Conf. Proc. 218 (1990) p.171.
5) H. Uchida et al., J. Alloys Comp. 293-295 (1999) p. 30.
6) J. F. Ziegler, *Handbook of Ion Implantation Technology* (Elsevier, Amsterdam 1992), p. 1.

5.5 Chemical modifications of polycarbonate by C_n^+ cluster irradiation

K. Hirata, Y. Saitoh*, K. Narumi*, Y. Kobayashi, and K. Arakawa*

National Institute of Advanced Industrial Science and Technology (AIST), Tsukuba, Ibaraki 305-8565, Japan

*Advanced Radiation Technology Center, JAERI, Takasaki, Gumma 370-1292, Japan

1. Introduction

Implanted ions passing through a matter are slowed down by electronic and nuclear interaction with target atoms. On this slowing down process of implanted ions, irradiation damage is inevitably produced. Recent studies of cluster ion implantation revealed that the interactions of implanted cluster ions are different from those of single ions [1-3]. In this paper, we present results of FTIR measurements for single-ion and cluster-ion irradiated polycarbonate (PC). The measurements were carried out to study chemical modification by the irradiations.

2. Experimental

The C_n^+(n=1-8) ion irradiation to amorphous polycarbonate (PC) films with a thickness of 100 μ m and a density of 1.2 g/cm^3, which were supplied by Mitubishi Chemical Co. Ltd., was carried out at JAERI/Takasaki [4]. Singly negative cluster ions were produced in a conventional Cs sputter ion source and injected into a 3MV tandem accelerator after mass separation. A small fraction of the negative cluster ions was stripped to singly positive ions and then accelerated at the second stage of the tandem accelerator, although most of the clusters were dissolved into the separated atoms by collision with a stripper N_2 gas in the terminal. The accelerated ions were analyzed by a separating magnet to obtain singly positive cluster ions. The implantation energy and dose of cluster ions were 0.19 - 0.3 MeV/atom and 3×10^{13} atoms/cm^2, respectively.

Information on chemical changes in PC by the irradiations was obtained by attenuated total reflectance (ATR) Fourier-transform infrared (FTIR) spectroscopy. All measurements were carried out on a Bio-Rad FTE-40 spectrometer at a resolution of 4 cm^{-1} employing a 45° cut ZnSe internal reflection element. 128 scans were collected and the signals were averaged to reduce spectral noise.

3. Results and discussion

Typical ATR-FTIR spectra, for unirradiated and 0.19 MeV/atom-C_n^+(n=1, 8)-irradiated PC, are shown in Fig. 1. The spectra are normalized to the intensity of the 1504 cm^{-1} band (due to aromatic C-C), which is little affected by ion irradiation [5]. One can see in the figure that the absorbance intensity for carbonyl (C=O) stretching vibration at 1770 cm^{-1} is reduced after the irradiation. This is commonly observed for ion irradiated PC and indicates that the weak carbonyl bond between the phenyl rings in the chemical structure of PC is dominantly decomposed. Other characteristic changes in Fig. 1 are: (a) formation of the broad band between 2500 and 3650 cm^{-1}, with a peak around 3420 cm^{-1}, for the irradiated samples, (b) enhancement in the intensity at 2930 cm^{-1} for the

C_8^+-irradiated sample. The broad band (a) mainly corresponds to hydroxyl O-H species and the peak at 2930 cm^{-1} (b) is assigned to CH_2 stretching mode.

The spectra for irradiated PC around the wavenumber region, where the characteristic changes (a) and (b) were observed, consist of the several band contributions. We paid attention to three major peaks due to O-H, CH_2 asymmetric stretching and CH_3 asymmetric stretching and evaluated these peak intensities, $I_{\nu(OH)}$, $I_{\nu as(CH2)}$, $I_{\nu as(CH3)}$, by the following way; (I) the broad O-H intensity $I_{\nu(OH)}$ was determined as the peak intensity at 3420cm^{-1} and (II) the peak intensities of $I_{\nu as(CH2)}$ and $I_{\nu as(CH3)}$ were calculated based on least-squares analysis by approximating the band between 2900 – 3000 cm^{-1} with two Lorentzian functions (for CH_2 asymmetric stretching at 2930 cm^{-1} and CH_3 asymmetric stretching at 2968 cm^{-1}) after subtraction of the broad OH band contribution from the spectrum.

Figs. 2 and 3 show the peak intensities, $I_{\nu(OH)}$, $I_{\nu as(CH2)}$, $I_{\nu as(CH3)}$, versus the number of atoms in one cluster n for the 0.19MeV/atom-C_n^+(n=1-8) and 0.3MeV/atom-C_n^+(n=1-6) irradiated samples, respectively. It is seen in both the figures that $I_{\nu(OH)}$ increases and $I_{\nu as(CH3)}$ decreases with increasing the cluster size. These indicate that the OH bond formation and the CH_3 dissociation are related to the cluster size.

In contrast to the case of $I_{\nu(OH)}$ and $I_{\nu as(CH3)}$, $I_{\nu as(CH2)}$ is nearly independent of the cluster size up to 6 and 4 for the 0.19MeV/atom-C_n^+ and 0.3MeV/atom-C_n^+ irradiated samples, respectively. Interestingly, anomalously sharp increases in $I_{\nu as(CH2)}$ are observed in going from 0.19MeV/atom-C_6^+ to 0.19MeV/atom-C_8^+ and from 0.3MeV/atom-C_4^+ to 0.3MeV/atom-C_6^+. As the cluster number n is increased, accumulated energy density around ion track becomes higher by simultaneous impacts of several ions to small area. Higher energy density by 0.19MeV/atom-C_8^+ and 0.3MeV/atom-C_6^+ irradiation seems to activate chemical reaction for the CH_2 formation and then the enhancement of $I_{\nu(CH2)}$ occurs.

References

[1] K. Narumi, K. Nakajima, K. Kimura, M. Mannami, Y. Saitoh, S. Yamamoto, Y. Aoki and H. Naramoto: Nucl. Instr. and Meth. in Phys. Res. B **135**, 77 (1998).

[2] K. Hirata, Y. Saitoh, Y. Kobayashi, A. Kawasuso, S. Okada and M. Saidoh: JAERI-Review **99-025**, 193 (1999).

[3] K. Hirata, Y. Saitoh, K. Harumi, Y. Kobayashi, A. Kawasuso, S. Okada and K. Arakawa: JAERI-Review **2000-024**, 193 (2000).

[4] Y. Saitoh, K. Mizuhashi and S. Tajima: JAERI-Review **97-015**, 240 (1997).

[5] D. Fink, R. Klett, W. H. Chung, R. Grunwald, M. Dobeli, F. Ames, L. T. Chadderton, J. Vacik, and V. Hnatowicz: Rad. Eff. Def. Solids **140**, 3 (1996).

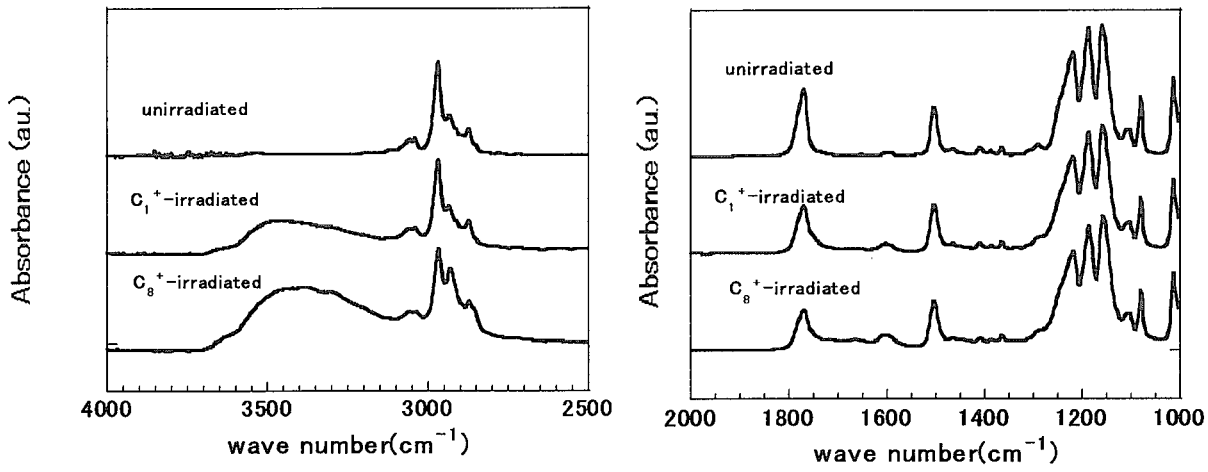


Fig. 1 ATR-FTIR spectra for unirradiated and 0.19 MeV/atom-C_n^+(n=1, 8)-irradiated PC.

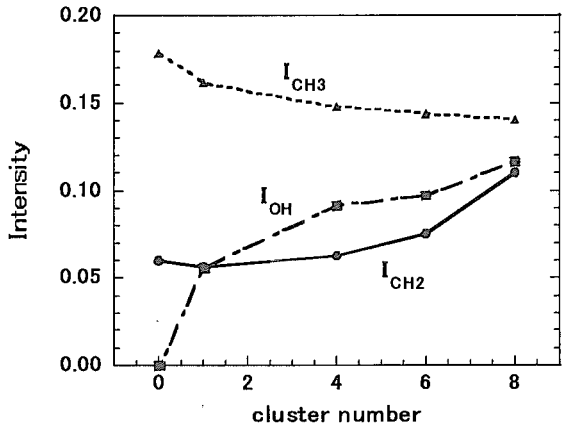


Fig. 2 Peak intensities, $I_{\nu(OH)}$, $I_{\nu as(CH2)}$, $I_{\nu as(CH3)}$, as a function of the number of atoms in one cluster n for 0.19MeV/atom-C_n^+(n=1-8).

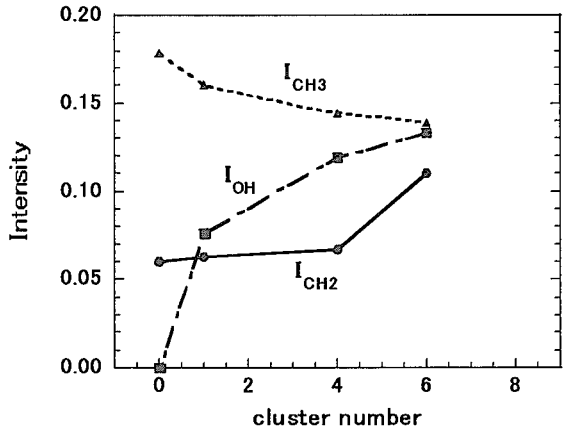


Fig. 3 Peak intensities, $I_{\nu(OH)}$, $I_{\nu as(CH2)}$, $I_{\nu as(CH3)}$, as a function of the number of atoms in one cluster n for 0.3MeV/atom-C_n^+(n=1-6).

6. Nuclear Science and RI Production

6.1 Development of a Laser Ion Source with an Ohmic-heating Ionizer for the TIARA-ISOL ····· 223
M.Koizumi, A.Osa, M.Oshima, T.Sekine, and H.Miyatake

6.2 Internal Conversion Electron Measurements in the Decay of the Proton-rich Isotope ^{126}Ce using an On-line Mass Separator ····· 226
M.Shibata, T.Shindou, H.Yamamoto, K.Kawade, A.Taniguchi, A.Osa, M.Koizumi, and T.Sekine

6.3 Synthesis of Endohedral ^{133}Xe-fullerene by Ion Implantation ····· 228
S.Watanabe, N.S.Ishioka, T.Sekine, A.Osa, M.Koizumi, H.Muramatsu, H.Shimomura, and K.Yoshikawa

6.4 Excitation Functions of Rhenium Isotopes on the ^{nat}W(d,xn) Reactions and Production of No-carrier-added ^{186}Re ····· 230
N.S.Ishioka, S.Watanabe, A.Osa, M.Koizumi, H.Matsuoka, and T.Sekine

This is a blank page.

6.1 Development of a laser ion source with an ohmic-heating ionizer for the TIARA-ISOL

Mitsuo KOIZUMI[1)], Akihiko OSA[1)], Masumi OSHIMA[1)], Toshiaki SEKINE[1), 2)], Hiroari MIYATAKE[3)]
[1)]Department of Materials Science, JAERI, [2)]Department of Radiation Research for Environment and Resources, JAERI, [3)]KEK

1. Introduction

In spectroscopic study of nuclei far from stability with an isotope separator on-line (ISOL), a mass-separated unstable isotope is usually accompanied by its isobars. Because of the low yield of the mass-separated isotope of interest, signals from the isotope are often obscured by the background due to the decay of its isobars. In order to reduce the background, an element selective process should be introduced into the isotope separation.

Resonance photoionization is highly element selective because atoms are excited and ionized through atomic transitions specific to the element.[1)] We, therefore, have been developing a laser ion source for an ISOL,[2-4)] modifying a surface-ionization ion source used at the TIARA-ISOL. The efficiency of the laser ion sources, however, was not so sufficient as we expected. It seemed that photoions produced in the ionizer were not extracted efficiently.

An ohmic-heating laser ion source was proposed by Alkhazov et al to extract photoions efficiently.[5)] The ionizer of this ion source was heated by a dc current flowing along the ionizer, while that of our laser ion sources was heated by electron bombardment. The dc heating current produces an electric field inside the ionizer, which pushes ions toward the exit hole of the ionizer. This may improve the efficiency of our laser ion source, althogh our target-catcher system is much different with that of Alkhazov et al.

In this report, we describe a new laser ion source equipped with an ohmic-heating ionizer.

2. Laser Ion Source with an Ohmic-heating Ionizer

Heated up to about 2000 °C, a hot-cavity type laser ion source also ionizes atoms with a low ionization potential through surface ionization. Accordingly, even though the photoionization process is element selective, the surface ionization reduces the element selectivity of a laser ion source.

In order to suppress the effect of surface ionization, two methods have been proposed. Firstly, surface ionization can be reduced if one applies an ionizer made of a material with a low work function.[6)] Secondly, the beam of surface-ionized ions can be brocked by putting a time gate with a fast deflector system:[7)] this device deflects and obstructs ion beams unless a bunched photoion beam passes. For this system to work effectively the pulse width of photoion beam should be short enough.[7)]

The newly introduced ohmic-heating laser ion source developed for the TIARA-ISOL is shown in Fig. 1. The radius of the ionizer was 3 mm and the length of that 30 mm. The ionizer consisted of two layers of rolled metallic foils: the outside layer of a W-film and the inside layer of a Ta- or Nb-foil. The size of the foil was 10 X 30 mm with a thickness of 15 μm. The rolled

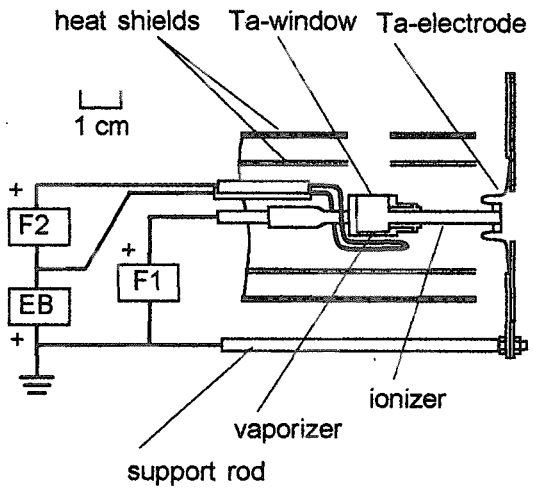


Fig. 1. A schematic drawing of the ohmic-heating laser ion source. The vaporizer is heated by electron-bombardment. F1, F2, and EB are power supplies.

metal sheets having a tendency to unroll were fastened by two Ta rings, which were 3 mm in radius, about 0.5 mm in length, and 0.1 mm in thickness. The ionizer was inserted into the vaporizer and was attached to the Ta-electrode. The electrode was a ring of 3 mm in radius, 2 mm in length and 0.1 mm in thickness. The radius of the exit hole of the electrode was 1.5 mm or 3 mm. The part of the ionizer heated by a dc current was about 20 mm in length. The dc heating current used in the present experiments was about 50 A, and formed an electric potential of 4-5 V/cm inside the ionizer.

The pulse shape of photoion beam was measured off-line with a Faraday cup equipped with an amplifier (Ultra-Low-Noise Current Amplifier LCA-400K-10M, FEMTO). The output signal was recorded with a digital oscilloscope. Figure 2 shows time distributions of Ba^+ photoions from two different laser ion sources, a previously developed electron-bombardment-heating laser ion source and an ohmic-heating laser ion source. We observed the sharp first peak and the broad second peak. It can be explained as follows. Photoions near the exit hole of the ionizer were drawn swiftly out of the ionizer by a strong extraction electric field; and then the rest were extracted after drifting in the ionizer. They formed the first and second peaks, respectively. From comparison of the pulse shapes of the photoion beams from the two ion sources, it can be pointed out that the pulse width of the second peak obtained from the ohmic-heating laser ion source was narrower than that from the electron-bombardment-heating laser ion source. This means that the electric field produced by the dc heating current effectively transported phtoions toward the exit hole. Consequently, the second peak of the ion beam from the ion source was narrow and intense.

3. On-line ^{25}Al separation with the ohmic-heating laser ion source

An on-line experiment of the laser ion source has been carried out with ^{25}Al ($T_{1/2}$ = 7.2 s) produced through the ^{12}C (^{16}O, p 2n) reaction. The energy of $^{16}O^{4+}$ beam was 100 MeV, and the typical beam current was 1 eμA. A carbon target, working also as a catcher, was placed inside the vaporizer. The dominant products at A = 25 were ^{25}Na ($T_{1/2}$=59.6 s) and ^{25}Mg (stable), together with ^{25}Al.

For the photoionization of Al, the transition process given in Fig. 3 was used. Since the energy of $3s^2(^1S)3p\ ^2P^0_{3/2}$ metastable state is 0.014 eV, the population of the metastable state is about 1.8 times larger than that of the $3s^2(^1S)3p\ ^2P^0_{1/2}$ ground state at a temperature of about 2000°C. We, therefore, photoionized Al atoms in the $^2P^0_{3/2}$ metastable state. The $3s3p^2\ ^2P_{3/2}$ and $3s3p^2\ ^2P_{1/2}$ states are both autoionization states. The light sources were dye lasers pumped by an excimer laser, the repetition rate of which was 300 Hz.

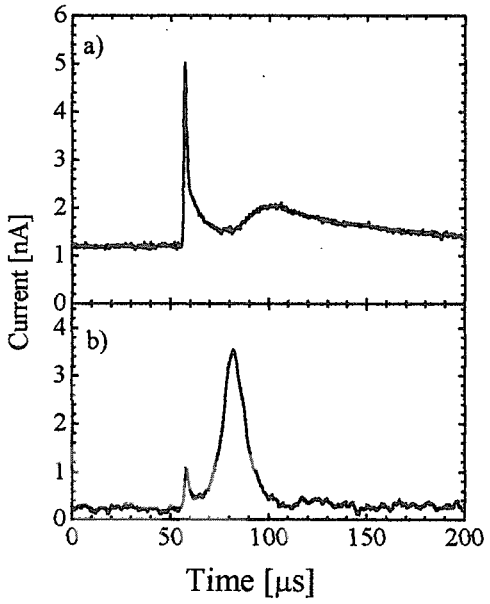


Fig. 2. Time distributions of Ba^+ ions from two different laser ion sources: (a) an electron-bombardment-heating laser ion source and (b) an ohmic-heating laser ion source. The exit hole of the ionizers was 1.5 mm in radius. The walls inside the ionizers were a Nb foil.

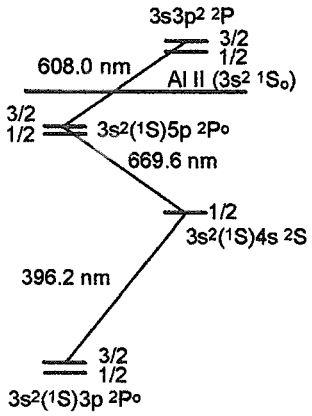


Fig. 3. A partial level scheme of Al relevant to the resonance photoionization used for the laser ion source experiments.

After mass-separation, γ-ray spectra at A = 25 were measured with a tape transport system set at the end of the ISOL beam line. Because of the low ionization potentials of Na (5.138 eV) and Al (5.984 eV), surface-ionized ^{25}Na and ^{25}Al was observed as shown in Fig. 4(a): the 511-keV annihilation γ-rays coming from the β^+ decay of ^{25}Al and the other γ-peaks coming mainly from the β^- decay of ^{25}Na. When laser beams were sent to the laser ion source, the yield of ^{25}Al increased by a factor of about two as shown in Fig. 4(b). Figure 4(c) shows that the fast deflector system, which let photoions pass during 56 μs, reduced the background γ-ray peaks of ^{25}Na to 1/50 of those without it. It also reduced the total yield of ^{25}Al to 1/5 of that without it and the photoion yield to 2/5 of that without it. This high reduction in the photoion yield can be explained as follows. The ^{25}Al observed in Fig. 4(b) were probably photoionized in the ionizer and vaporizer. But, the photoions in the vaporizer might not be transferred by the electric field produced by dc current; they therefore, came after the second peak of the ion beam, forming a broad tail; consequently, they were obstructed by the deflector system.

Applying an average nuclear reaction cross section of 12 mb calculated with the ALICE-code and an effective target thickness of 12 mg/cm^2, we estimated the photoionization efficiency of the laser ion source to be about 0.1%. This efficiency was almost the same as that of the conventional surface ion source used at the TIARA-ISOL.

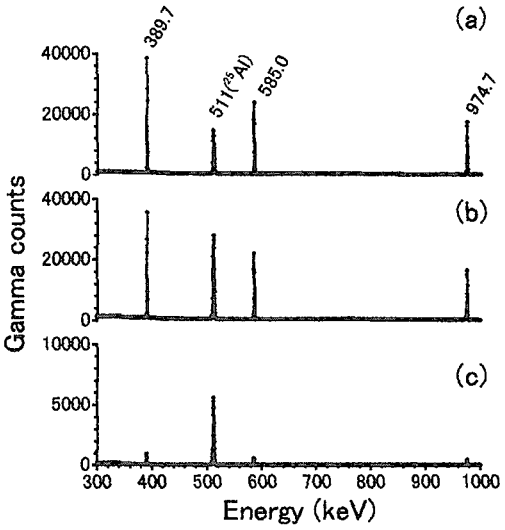


Fig. 4. γ-ray spectra at A = 25 measured with a tape transport system. The radius of the exit hole of the laser ion source was 3 mm. The inside layer of the ionizer was a Ta foil. The numbers indicate peak energies in keV. (a) Laser beams were not introduced. (b) Laser beams were introduced. (c) A fast deflector system was used.

4. Summary

We have developed an ohmic-heating laser ion source with a thin ionizer, which can form an electric field of 4-5 V/cm inside the ionizer. The pulse width obtained was narrower than that from an electron-bombardment-heating laser ion source. With a pulse gate system, the γ-peak ratio of ^{25}Al and ^{25}Na was improved by a factor of 10. Although the photoionization efficiency of 0.1% for ^{25}Al with a laser ion source seems low for some experiments, it can be improved if a high frequency laser system is available. This ion source combined with a pulse gate system supplies an ion beam containing less isobars and would be useful not only for the study of nuclear structure but also for astrophysical experiments such as the study of nuclear synthesis.

References

1) V.S. Letokhov, Laser photoionization spectroscopy, Academic Press, INC., 1987.
2) M. Koizumi, A. Osa, T. Sekine, and M. Kubota, Nucl. Instr. and Meth. B126 (1997) 100.
3) A. Osa, M. Koizumi, T. Sekine, H. Katsuragawa, W.G. Jin, T. Wakui, TIARA Annual Report 1998, p203.
4) M. Koizumi, A. Osa, T. Sekine, H. Katsuragawa, W.G. Jin, T. Wakui, Y. Ishida, J. Sun-chan, H. Ishiyama, H. Miyatake, TIARA Annual Report 1999, p213.
5) G.D. Alkhazov E.Ye. Berlovich and V.N. Panteleyev, Nucl. Instr. and Meth. A280 (1989) 141.
6) V.I. Mishin, V.N. Fedoseyev, H.-J. Kluge, V.S. Letokov, H.L. Ravn, F. Scheerer, Y. Shirakabe, S. Sundell, O. Tengblad, and ISOLDE Collaboration, Nucl. Instr. and Meth. B73 (1993) 550.
7) Y. Jading, R. Catherall, V.N. Fedoseyev, J. Jokinen, O.C.Jonsson, T. Kautzsch, I. Klöckl, K.-L. Kratz, E. Kugler, J. Littry, V.I. Mishin, H.L. Ravn, F. Scheerer, O. Tengblad, P. Van Duppen, W.B. Walters, A. Wöhr, and the ISOLDE Collaboration, Nucl. Instr. and Meth. B126 (1997) 76.

6.2 Internal Conversion Electron Measurements in the Decay of the Proton-rich Isotope ^{126}Ce using an On-Line Mass Separator

M. Shibata, T. Shindou, H. Yamamoto, K. Kawade, A. Taniguchi*, A. Osa**, M. Koizumi**, T. Sekine***

Graduate School of Engineering, Nagoya University, *Research Reactor Institute, Kyoto University, **Department of Materials Science, JAERI, ***Department of Radiation Research for Environment and Resources, JAERI

1. Introduction

Spins and parities of excited states are important information for nuclear structure far from the stability line. When differences of spin values between isomers are large, internal conversion electron (ICE) measurement is an effective method to identify isomeric states. Concerning the doubly odd nuclide ^{126}La, the Q_β and γ-γ angular correlation have been already measured and the level structure of its daughter nuclide of ^{126}Ba have been studied well by using the on-line mass separator installed at the AVF cyclotron in JAERI, Takasaki (TIARA-ISOL). From the data, Asai *et al.*[1] and Kojima *et al.*[2] proposed the decay scheme with low-spin and high-spin isomeric states whose half-lives of 50 s and 54 s, respectively. Kojima *et al.*[3] also deduced the Q_β values to be 7910(400) and 7700(100) keV, respectively. This result predicts an isomeric state of about 200 keV, although the Q_β values have large uncertainties. In this region, other proton-rich lanthanum isotopes have isomeric states similarly, while their level orderings are also unknown. In order to identify the isomeric state, we already measured not only β-γ delayed coincidences but also β-γ anti coincidences for ^{126}Ce decay, however, we could not observed it. The spin differences between the two isomers are expected to be large enough to observe the ICEs according to Kojima *et al.*[2] In this experiment, we tried to identify the isomer by measuring the ICE in the decay of ^{126}Ce by using a cooled Si(Li) detector installed at the TIARA-ISOL.

2. Experiment

An Argon beam ($^{36}Ar^{8+}$, 195MeV) from the AVF cyclotron was irradiated on 93.9% enriched ^{94}Mo targets for production of ^{126}Ce. The fusion-evaporation reaction products of ^{126}Ce were ionized by a surface ionization technique in Ce monoxide (CeO^+) and mass-separated by the TAIRA-ISOL. The mass-separated beams were implanted into a computer-controlled aluminized Mylar tape and transported to the counting position every 100 s of about 2 times the half-life of ^{126}Ce ($T_{1/2}$ = 54 s).

At the counting position, a Si(Li) detector (300 $mm^2 \times 5\ mm^t$, provided by Eurisys Co.) for ICEs. For γ-ray measurements, an LEPS (50 $mm^\phi \times 10\ cm^t$, Low Energy Photon Spectrometer, provided by ORTEC Co.) was adopted in order to measure the low energy region below 820 keV carefully. Singles and e^--γ coincidence measurements were carried out for 16 hours totally by setting the detectors in 180° geometry.

3. Results and Discussion

A portion of the singles ICE spectrum associated with the decay of ^{126}Ce obtained

with the Si(Li) detector is shown in Fig.1 together with the γ-ray spectrum obtained with the LEPS. This electron spectrum was obtained from the decay of ^{126}Ce for the first time. The deduced k internal conversion coefficients (α_k) are shown in Fig.2 together with the theoretical values[4]. These values were deduced from the peak intensity ratios of electrons to γ-rays normalized to that of the pure E2 ($2^+ \rightarrow 0^+$) 256 keV γ-ray in ^{126}Ba. Almost all the transitions were assigned to M1/E2 transitions as shown in Fig.2. The 346 keV γ-ray has an apparently large conversion coefficient (Fig.2) compared to the 321.7 and 427.0 keV γ-rays. In the γ-ray spectrum in Fig.1, there are no other intensive γ-rays around 346 keV. This γ-ray is possibly an isomeric transition, however, this result is not consistent with the results obtained from the γ-γ coincidence measurement. The decay scheme of ^{126}Ce is now under construction, including the results of γ-γ and β-γ delayed coincidence measurements. So far, it is considered that the low-spin isomeric state of ^{126}La probably decays to ^{126}Ba directly and the isomeric transition could not be observed. The origin of the intensive electron peak is still unclear. It should be checked carefully in comparison to the other coincidence results.

4. Conclusions

The k conversion coefficients for 15 transitions in ^{126}La were deduced from the decay of ^{126}Ce for the first time. Precise analysis is in progress in order to construct the decay scheme and identify isomeric states. In understanding the property of the isomeric states, the complicated structures of doubly odd proton-rich La isotopes will be made clear.

References

1) M. Asai et al., Phys.Rev.,C56, 3045, 1997.
2) Y.Kojima, Ph.D theses, Nagoya University.
3) Y.Kojima et al., Appl. Radiat. Isot., 49, 829, 1998.
4) F. Rösel et al., At. Data and Nucl. Data Tables, 21, 91, 1987.

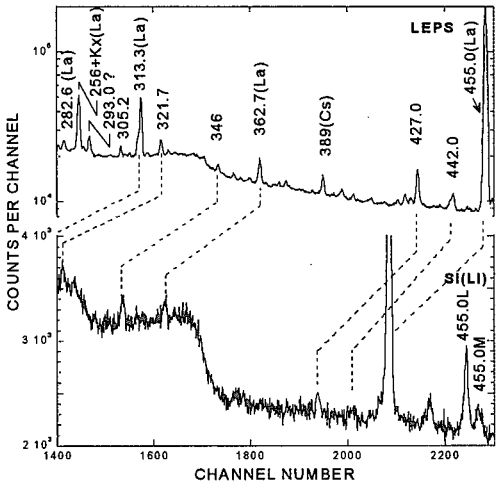


Fig.1 Gamma-ray (up) and internal conversion electron (down) spectra associated with the decay of ^{126}Ce obtained with a Si(Li) detector and an LEPS, respectively.

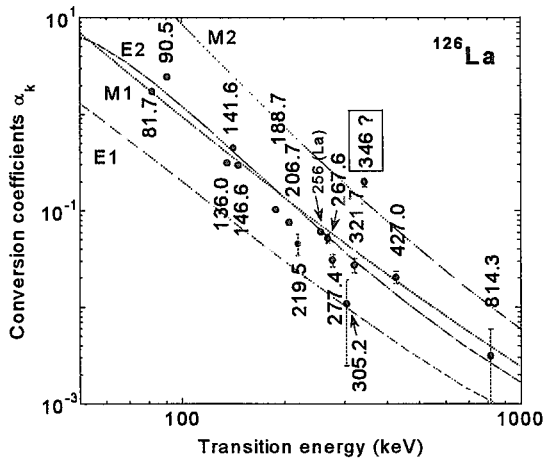


Fig.2 Experimental and theoretical conversion coefficients for the transitions in ^{126}La.

6.3 Synthesis of Endohedral ^{133}Xe-Fullerene by ion implantation

S. Watanabe[1], N. S. Ishioka[1], T. Sekine[1], A. Osa[2], M. Koizumi[2], H. Muramatsu[3], H. Shimomura[3], K. Yoshikawa[3]
[1]Department of Radiation Research for Environment and Resources, [2]Department of Materials Science, [3]Faculty of Education, Shinsyu University

1. Introduction

Endohedral fullerene, which encapsulates one, two or three atoms within a fullerene cage, has been produced by using arc-discharge, laser-vaporization and nuclear-reaction processes. The products by these methods are mixtures of different species of fullerenes, e.g., C_{82} and C_{84}, with different encapsulated atoms. To obtain a product containing one species of endohedral fullerene in high purity, ion-implantation may be a promising process, in particular for radioisotopes. In the literature, however, light elements such as He and Li have been encapsulated into fullerene by ion-implantation. In the present paper, we describe the production of endohedral ^{133}Xe-fullerene by implantation of ^{133}Xe ions into a fullerene target.

2. Experimental

The targets used for ion-implantation were made by vacuum evaporation of 1 mg of C_{60} or C_{70} on Ni foils in an area of 25mmϕ. Implantation of ^{133}Xe ions was carried out with an isotope separator at an acceleration energy of 40 keV. After ion implantation, the targets were dissolved in o-dichlorobenzene. The target solutions were filtered through a millipore filter to remove insoluble materials. The filtrates were injected into a column of 5PBB, 5PYE or Buckyprep supplied by Cosmosil and eluted with o-dichlorobenzene at a flow rate of 1 ml/min. The concentration of fullerene in the effluent was continuously monitored by a UV detector. The effluent from the UV detector was collected for 0.5 min interval and the ^{133}Xe radioactivity in each fraction was measured by γ-ray spectrometry.

3. Results and Discussion

Figure 1 shows the elution curves of ^{133}Xe radioactivity and C_{60} concentration obtained by using Buckyprep column. The peak of the UV chromatogram at 4 min corresponds to C_{60}, as determined at the calibration run. The strong correlation observed between the C_{60} and ^{133}Xe peaks corroborates the formation of ^{133}Xe@C_{60}, although the ^{133}Xe peak was followed by a tail. The same strong correlation was observed between C_{60} and ^{127}Xe by Otsuki *et al.*[1] using a nuclear reaction for production of ^{127}Xe@C_{60}, and also between C_{60} and Ar by DiCamello *et al.*[2] applying high-pressure and high-temperature for production of Ar@C_{60}, although their column materials were not the same as ours. Similar HPLC data obtained for the ^{133}Xe-implanted C_{70} samples corroborate the formation of ^{133}Xe@C_{70}.

Our chromatograms are much simpler than those reported by Otsuki et al[1]. From their chromatograms they reported that dimers (C_{60}-C_{60}, ^{127}Xe@C_{60}-C_{60}) were produced, while no distinct peak possibly corresponding to a dimer was observed in the present work. This difference indicates that our ion-implantation process was much milder than the process involving a nuclear reaction.

As mentioned above, the ^{133}Xe peak was followed by a tail. Similar tails were observed for the other column materials

used. The tailing in the elution of ^{133}Xe suggests a possibility of isolation of endohedral ^{133}Xe fullerene from empty fullerene.

References

1. T. Otsuki *et al.*, *Phys. Rev. Lett.*, 81, 967 (1998).
2. B. A. DiCamello *et al.*, *J. Phys. Chem.*, 100, 9197 (1996).

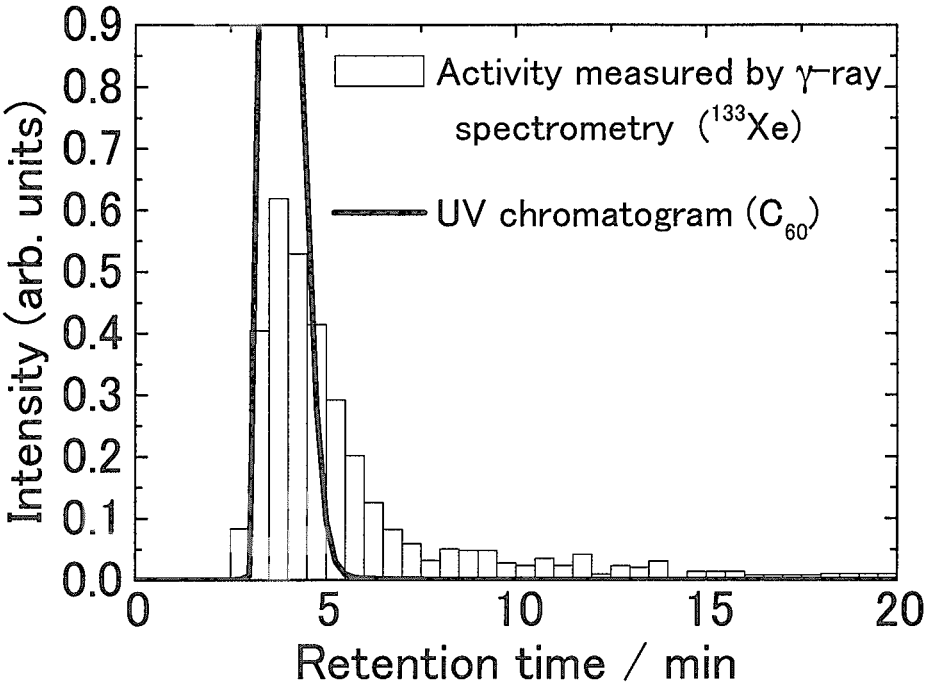


Fig. 1. HPLC elution curves of ^{133}Xe and C_{60} obtained by using Cosmosil Buckyprep column.

6.4 Excitation Functions of Rhenium Isotopes on the $^{nat}W(d,xn)$ Reactions and Production of No-Carrier-Added ^{186}Re

N. S. Ishioka[1], S. Watanabe[1], A. Osa[2], M. Koizumi[2], H. Matsuoka[3], T. Sekine[1]
[1]Department of Radiation Research for Environment and Resources, JAERI, [2]Department of Materials Science, JAERI, [3]Department of Research Reactor, JAERI

1. Introduction

Rhenium-186 is regarded as one of the best radionuclides used for radiotheraphy and radioimmunotherapy due to its attractive properties which include emission of high-energy β -rays ($E_{\beta,max}$=1.07 MeV) and decay to stable daughter with an appropriate half-life ($T_{1/2}$ = 3.8 d). Especially for radioimmunotherapy, the ^{186}Re product is required to have very high specific activity. Our earlier work illustrated that no–carrier-added ^{186}Re can be produced using the $^{186}W(p,n)^{186}Re$ nuclear reaction on highly isotopically enriched ^{186}W.[1)] However, the available physical yield of this reaction is rather low (520 MBq/μA using an enriched ^{186}W (100%) target at proton energies 13.6→0 MeV).

Exploring the feasibility of the production of no-carrier-added ^{186}Re using the $^{186}W(d,2n)^{186}Re$ nuclear reaction, several authors have measured its excitation function at deuteron energies up to 21 MeV.[2,3,4,5)] They have reported that the maximum cross section value is at least four times of that measured on the $^{186}W(p,n)^{186}Re$ reaction. However, there are considerable differences between the reported excitation functions. In addition, excitation functions for other deuteron-induced reactions on tungsten isotopes, which are needed for evaluation of the radiochemical purity of the product, are scarce.

2. Experimental

The excitation functions were measured using the stacked-foil technique. Natural-composition tungsten foils of 28.5 mg/cm^2 were used as a target material. The stacked targets consisting of tungsten, aluminum and copper foils were irradiated with a 35 MeV deuteron beam at the AVF cyclotron in TIARA. Irradiations were carried out with a 1 μA beam for 10 min. The incident beam energies at each tungsten foil were calculated according to the OSCAR code[7)] which is made on the basis of Zieglers's formulas[8)]. The averaged beam current was determined from the radioactivity produced in the copper foils. After irradiation, radioactivities in the foils were assayed by γ-ray spectrometry using a calibrated Ge detector.

3. Results and Discussion

Cross sections of the reactions $^{186}W(d,2n)^{186}Re$, $^{nat}W(d,xn)^{181-184}Re$ and $^{186}W(d,p)^{187}W$ were deduced from the $^{181-186}Re$, ^{187}W and ^{65}Zn radioactivities by reference to the nuclear data[9)] and the cross sections of the $^{65}Cu(d,2n)^{65}Zn$ reaction reported by Fulmer *et al.*[10)]

Fig.1 shows the excitation functions of the $^{186}W(d,2n)^{186}Re$ reaction obtained in the present work together with the previously reported ones and a theoretical one. The present excitation function curve reaches its maximum of 450 mb at 13 MeV, which is in good agreement with the result of Szelecsényi *et al.*[5)] Although the cross section values given by Zhenlan *et al.*[4)] are in agreement with ours concerning the magnitude of the maximum, their curve shows a slight energy shift, as noted by

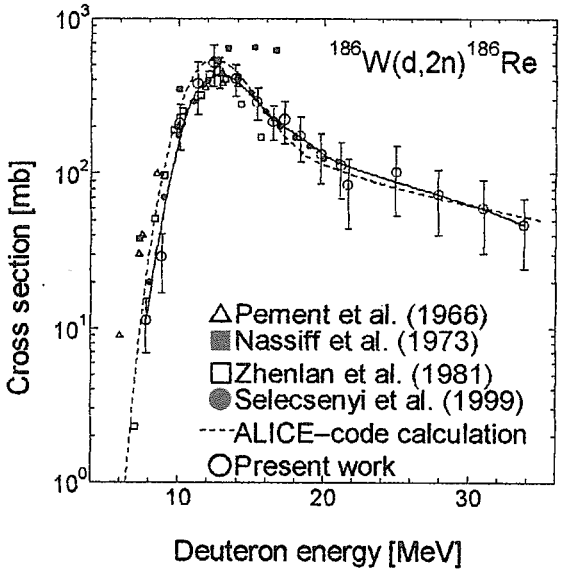


Fig.1 Excitation functions of the ^{186}W(d,2n)^{186}Re reaction

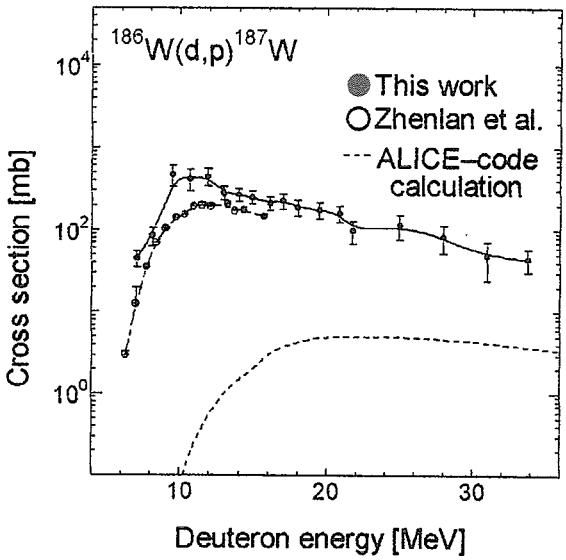


Fig.2 Excitation functions of the ^{186}W(d,p)^{187}W reaction

Szelecsényi *et al.* The theoretical excitation function was obtained using the hybrid model of the ALICE code.[6] One can note that the present experimental excitation function is found to be reproduced by the ALICE calculation.

Table 1 Radioactive products and energetics of deuteron induced reactions on ^{nat}W targets

Radio-Nuclide	Half-life	Contirbuting reaction	Q-value (MeV)
^{187}W	23.85 h	^{186}W(d,p)^{187}W	+3.2
^{186}Re	90.64 h	^{186}W(d,2n)^{186}Re	-3.6
^{184}Re	38.0 d	^{183}W(d,n)^{184}Re	+2.9
^{184m}Re	169 d	^{184}W(d,2n)^{184}Re	-4.5
		^{186}W(d,4n)^{184}Re	-17.5
^{183}Re	71 d	^{182}W(d,n)^{183}Re	+2.6
		^{183}W(d,2n)^{183}Re	-3.6
		^{184}W(d,3n)^{183}Re	-11.0
		^{186}W(d,5n)^{183}Re	-23.9
^{182}Re	64.0 h	^{182}W(d,2n)^{182}Re	-5.8
^{182m}Re	12.7 h	^{183}W(d,3n)^{182}Re	-12.0
		^{184}W(d,4n)^{182}Re	-19.4
^{181}Re	19.9 h	^{182}W(d,3n)^{181}Re	-12.9
		^{183}W(d,4n)^{181}Re	-19.1

For the theoretical excitation functions of $^{181-184}$Re, the contributing reactions as listed in Table 1 were taken into account based on the isotopic compositions of natural tungsten. Reasonable agreement is obtained between these experimental and theoretical excitation functions except for the ^{186}W(d,p)^{187}W reaction, as shown in Fig.2. The large experimental cross sections for the ^{186}W(d,p)^{187}W reaction can be ascribed to the contribution of the Oppenheimer and Phillips process.

References

1) N. Shigeta *et al.* , J. Radioanal. Nucl. Chem., **205**, 85 (1996).
2) S. J. Nassiff and H. Munzel, Radiochim. Acta., **19**, 97 (1973).
3)F. W. Pement and R. L. Wolke, Nucl. Phys., **86**, 429 (1966).
4) T. Zhenlan *et al.*, Chinese J Nucl. Phys., **3**, 242 (1981) (in Chinese).
5) F. Szelecsényi *et al.*, J Labelled Cpd. Radiopharm. **42**, *S*912 (1999).
6) M. Blann, Report C00-3494-29 (1975) University of Rochester, NY.
7)K. Hata and H. Baba, JAERI-M 88-184 (1988).
8)J. F. Ziegler *et al.*, "The stopping and range of ions in solids, Volume 1 of the stopping and ranges of ions in matter", Pergamon Press (1985).
9)C. M. Lederer and V. S. Shirley, "Table of isotopes seventh edition", John Wiley & Sons, Inc. (1978).
10)C. B. Fulmer and I. R. Williams, Nucl. Phys., **A155**, 40 (1970).

This is a blank page.

7. Microbeam Application

7.1 Evaluation of Three Dimensional Microstructures on Silica Glass Fabricated by Ion Microbeam ····· 235
H.Nishikawa, T.Souno, M.Hattori, Y.Nishihara, Y.Ohki, T.Yamaguchi, E.Watanabe, M.Oikawa, T.Kamiya, K.Arakawa, and M.Fujimaki

7.2 Development of High Performance Buffer Materials —Sorption Mechanism of Europium by Apatite and Smectite Mixture using RBS and Micro-PIXE— ····· 238
T.Ohnuki, N.Kozai, M.Samadfam, S.Yamamoto, K.Narumi, H.Naramoto, T.Kamiya, T.Sakai, S.Oikawa, T.Sato, and T.Murakami

7.3 Development of In-air Micro-PIXE System for High-efficiency Elemental Analyses ····· 241
T.Kamiya, T.Sakai, M.Oikawa, K.Ishii, S.Matsuyama, T.Satoh, and A.Tanaka

7.4 Fluoride Uptake Measurement using Microbeam PIGE ····· 244
M.Nomachi, Y.Sugaya, M.Yoshifuku, K.Yasuda, H.Yamamoto, Y.Iwami, S.Ebisu, T.Kamiya, T.Sakai, and M.Oikawa

7.5 Application of In-air Micro-PIXE Camera to Bovine Aortic Endothelial Cells and Human Leukemia Cells ····· 247
A.Tanaka, K.Ishii, T.Satoh, S.Matsuyama, H.Yamazaki, M.Satoh, S.Harada, T.Kamiya, T.Sakai, M.Oikawa, K.Arakawa, and M.Saidoh

7.6 Application of Micro-PIXE to the Analysis of Single Fog Droplets ····· 250
M.Kasahara, C.J.Ma, Y.Inokuchi, T.Kamiya, T.Sakai, M.Oikawa, and T.Sato

7.7 In-air Micro-PIXE Analysis of Ascitic Hepatoma Tissue Slices ····· 253
A.Tanaka, K.Kubota, K.Ishii, H.Fukuda, T.Akaizawa, T.Satoh, Y.Oishi, S.Matsuyama,H.Yamazaki, T.Kamiya, T.Sakai, M.Oikawa, K.Arakawa, and M.Saidoh

7.8 Redistribution of Elements between Minerals in Rocks —Analysis of Uranium Distribution in Rocks by μ-PIXE— ····· 256
T.Ohnuki, N.Kozai, M.Samadfam, R.Yasuda, T.Kamiya, T.Sakai, S.Oikawa, T.Sato, and T.Murakami

7.9 Radiation Damage in Si PIN Diodes Induced by Heavy Ion Microbeam Single Hits ····· 259
T.Kamiya, T.Sakai, M.Oikawa, and T.Hirao

7.10 Development of a High-energy Microbeam Single Ion Hit Technique for Bio-medical Applications ····· 262
T.Kamiya, W.Yokota, Y.Kobayashi, M.Oikawa, M.Taguchi, and M.Cholewa

This is a blank page.

7.1 Evaluation of Three Dimensional Microstructures on Silica Glass Fabricated by Ion Microbeam

H. Nishikawa [1], T. Souno [1], M. Hattori [2], Y. Nishihara [2], Y. Ohki [2], T. Yamaguchi [3], E. Watanabe [3], M. Oikawa [4], T. Kamiya [4], K. Arakawa [4], M. Fujimaki [5]

[1] Department of Electrical Engineering, Shibaura Institute of Technology

[2] Department of Electrical, Electronics, and Computer Engineering, Waseda Univ.

[3] Department of Electrical Engineering, Tokyo Metropolitan University

[4] Advanced Radiation Technology Center, JAERI

[5] Japan Science and Technology Corporation

1. Introduction

Silica glass is an important material for optical communications. Much attention has been paid to the radiation effects induced by high-energy particles and photons on silica glass over the past several decades, since they have capabilities in modifying the structures and properties of the silica-based optical devices[1]. It is therefore important to understand the changes in silica glass induced by MeV order ion implantation.

Refractive-index changes can be induced by ion implantation for almost all kinds of silica glass. Since the control of the refractive index is possible by this technique, the ion implantation is expected to be applied to the fabrication of optical fiber gratings[2]. This effect was mainly determined by nuclear stopping power and can be utilized for the fabrication of optical fiber gratings.

The objective of this research is to understand radiation effects on silica glass induced by ion microbeam. Especially, aiming at the formation of three dimensional microstructures with modified optical and topological properties, the present study focuses on the spatial distribution of radiation effects involved in the modification of various properties of silica glass.

In this report, radiation effects on silica induced by ion microbeam were investigated by means of combined photoluminescence (PL) - Raman microspectroscopy and atomic force microscopy (AFM). We focused on the electronic energy loss by which most defects are induced, since it accounts for most of the total energy loss in the case of MeV order ion implantation. Irradiation of optical fibers using ion microbeam was also performed for the fabrication of optical fiber gratings.

2. Experimental Procedures

Ions (H^+, He^{2+}, or Si^{5+}) with energies in the range of 2 to 18 MeV were implanted into high-purity silica substrates with various OH contents (<1 ppm to 1200 ppm) using a microbeam line (TIARA, JAERI Takasaki, beam diameter: ~1 μm). Some of the samples were implanted with H^+ at an energy of 4 MeV using a tandem accelerator at the University of Montreal.

Radiation effects by ion implantation were investigated using a micro PL-Raman spectrometer (JASCO) equipped with an Ar ion

laser. Topographic images of the ion implanted surface were investigated by AFM.

3. Results and Discussion

3.1 Photoluminescence and Raman Spectra

A PL band at 650 nm, which is associated with nonbridging oxygen hole centers (NBOHCs) induced by ion implantation, was observed at room temperature under excitation by a 488 nm or 514.5 nm laser, as shown in Fig.1.

From the observation of the depth profile of the PL intensity, it is found that the electronic excitation rather than the nuclear stopping power creates the NBOHCs. A Possible effect of the concentration quenching was discussed by comparing the PL profile with the depth profiles of electronic excitation predicted by TRIM code.

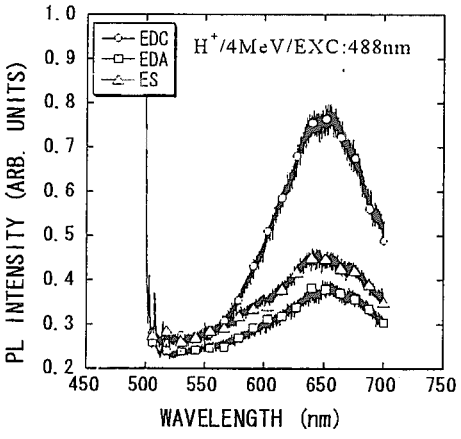


Fig. 1 Typical PL spectra obtained for silica irradiated by H^+ with an energy of 4 MeV.

Radiation effects along with the tracks of ions were also evaluated by the mapping of the PL intensity at the 1 μ m-microbeam irradiated regions, as shown in Fig. 2. The spread of the distribution of the PL intensity increases by a factor of two to three with the ions penetrating into silica glass. It is considered that the PL distribution reflects the distribution of the electronic excitation along with the tracks of implanted ions.

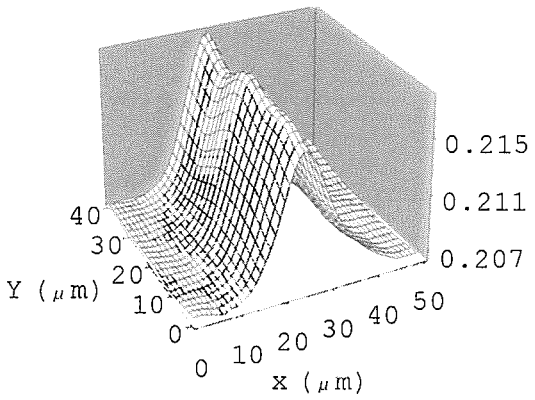


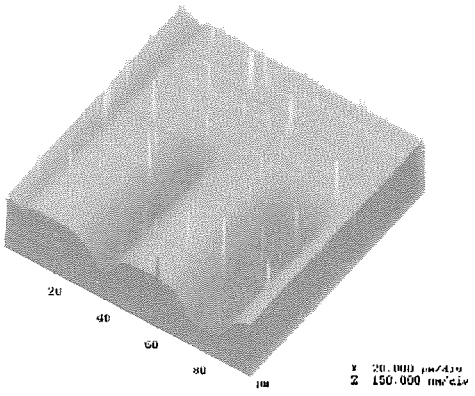
Fig. 2 Distribution of PL intensity of the 1-μ m-width microbeam-irradiated (H^+, 2.2 MeV, 1.0×10^{15} cm^{-2}) area observed at the depth of 30 μ m for 650 nm PL under excitation at 488 nm.

Raman spectra were also measured. While compaction of silica is observed at the region around the projected range of the ions, no distinctive change was observed for the D_1 and D_2 bands associated with small ring structures in silica even after the ion implantation.

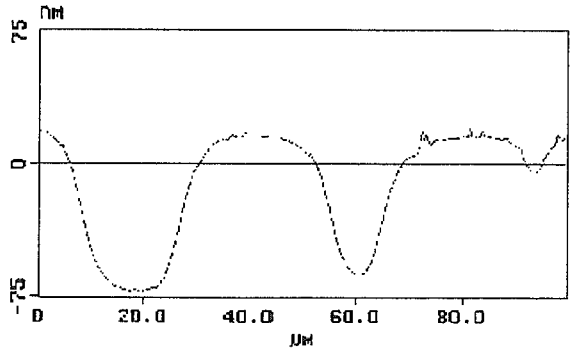
3.2 Atomic Force Microscope

Shown in Figs. 3 are the AFM image and the profile of the microbeam-irradiated (Si^{5+}, 18 MeV, fluence: 1.0×10^{14} cm^{-2}) regions. The surface structures measured by the AFM indicate the formation of a shallow channel with depths of up to ~80 nm along with the microbeam-irradiated rectangular shaped regions, depending on the implanted areas. Since the width of the channel is larger than the implanted area by a factor of

2 to 4, it is suggested that the formation of the shallow channel along with the implanted regions was mainly due to the radiation effects under the silica surface rather than sputtering. Correlation of the surface deformation with radiation effects is



(a)



(b)

Figs. 3 (a) AFM image and (b) the profile of the microbeam-irradiated regions (Si^{5+}, 18 MeV, fluence: 1.0×10^{14} cm^{-2}) .

under investigation.

3.3 Implantation into Optical Fibers

Irradiation of optical fibers using ion microbeam was also carried out with H^+ ions with an energy of 2.47 MeV through a Mylar film with a thickness of 4 μm. Under this condition, the formation of a bright arc region, which overlaps with the core of the optical fiber,

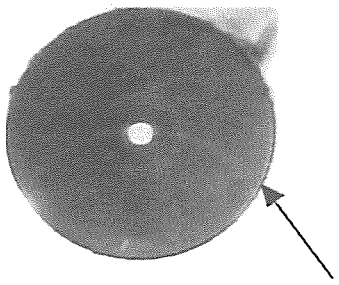


Fig. 4 Cross-sectional image of the optical fiber irradiated through a Myler film with H^+-microbeam at an energy of 2.47 MeV.

can be seen in the cross-sectional microscopic image of the fiber, as shown in Fig. 4. The bright arc region is located at a depth from the fiber surface, which is in good agreement with the projected range calculated by TRIM code.

4. Summary

Silica glass implanted by ion microbeam was characterized by means of combined micro-PL Raman spectroscopy and AFM. These techniques were shown to be highly useful to observe the micro-scale distribution of the radiation effects induced by the ion microbeam.

Three dimensional distributions of both optical and topological properties are informative for the future application of ion microbeam to the fabrication of the microstructures on silica glass.

References

1) H. Nishikawa, in "Silicon-Based Materials and Devices" Vol. 2, ed. by H. S. Nalwa, pp.93-123 (Academic Press, 2001)

2) M. Fujimaki et al., Optics Letters, Vol.25, No.2, pp.88-89 (2000).

7.2 Development of High Performance Buffer Materials -Sorption Mechanism of Europium by Apatite and Smectite Mixture Using RBS and micro-PIXE-

Toshihiko OHNUKI*,[1], Naofumi KOZAI*, Mohammad SAMADFAM*, Shunya YAMAMOTO**, Kazumasa NARUMI***, Hiroshi NARAMOTO***, Tomihiro KAMIYA****, Takuro SAKAI****, Shoichi OIKAWA****, Takahiro SATO**** and Takashi MURAKAMI*****

Department of Environmental Science, JAERI*, Dept. of Material Development, JAERI**, Avanced Science Research Center, JAERI***, Advanced Radiation Technology Center, JAERI****, Mineralogical Institute, The University of Tokyo*****

1. Introduction

The sorption behaviors of trivalent actinides and lanthanides on the components of geosphere are debated subjects because of their relevance to potential migration from radioactive wastes to biosphere. A major question relating to sorption studies on soil and rock (mixture of components) is how the sorption behavior on soil and rock can be estimated from the behaviors on the individual components. It has been reported that each component in a mixture equally contributes to the sorption of cesium and strontium[1]. On the other hand, cobalt is preferentially sorbed by Mn oxides/hydroxides for the sorption by Mn oxides/hydroxides and smectite mixture[2]. It is still question on the sorption behavior of trivalent elements on a mixture of the components.

We here propose the methodology using a thin film of powdered components to clarify the sorption behavior of Eu on the mixture. Due to very low solid/solution ratio, use of the thin film has the following advantages: (i) The solution of low Eu concentration can be used in the sorption experiment, (ii) The solution pH is constant during the sorption experiment, and (iii) Decrease of the Eu concentration in the solution is very low. However, if Eu is only sorbed on the surface of the thin film, the sorption behavior of Eu on the thin film may be different from that of the powdered mixture of components.

Rutherford backscattering spectroscopy (RBS) and proton-induced X-ray emission (PIXE) techniques are sensitive methods to detect elements in ppm level. The depth profiles and the spatial distributions of Eu are directly obtained by RBS and micro-PIXE (μ-PIXE) analyses, respectively. In the present study, the thin film containing apatite and smectite are provided for the sorption experiments. Apatite and smectite are selected as the components by their high sorption performance[3-5].

2. Experimental

2.1 Sorption experiments

The single crystals of fluoroapatite ($Ca_5(PO_4)_3F$) from Cerro de Marcado, Durango, Mexico, were used. Powdered samples of apatite were prepared by grinding to less than approximately 0.05 mm in diameter. Smectite ($Na_{0.33}(Si_{3.67}Al_{0.33})Al_2O_{10}(OH)_2$) was obtained from Kunimine Kogyo Co. Ltd., Japan, and originated from Tsukinuno, Japan. X-ray diffraction patterns of the apatite and the smectite showed that they did not contain measurable impurities.

All solutions were prepared with ultrapure deionized distilled water (DDI) water and reagent-grade chemicals. Eu solutions were prepared by diluting a $Eu(NO_3)_3$ stock solution in the DDI water to obtain Eu concentrations of between $1.0x10^{-5}$ and $1.0x10^{-3}$ mol·L^{-1}. The Eu solutions were adjusted to be in pH 4.5 with a 1 M NaOH or 1 M HCl solution.

A 60 μl solution of 1 g smectite·L^{-1} with 1 g apatite·L^{-1} was placed on a glassy carbon plate. A thin film of the mixture of smectite and apatite was made by drying the above sample for overnight at room temperature. The RBS

analysis indicated that the thickness of the thin film was approximately several μm at the region of smectite.

The thin film was immersed in the 20 ml Eu solution of $1.0x10^{-5}$, $1.0x10^{-4}$ or $1.0x10^{-3}$ mol·L^{-1} for 2 days at 25 °C. After the thin film separated from the solution, the thin films were washed with the DDI solution, followed by drying for overnight at room temperature. The thin film was not changed after contacting the Eu solution.

2.2 Analysis by RBS and μ-PIXE

The depth profiles of Eu, Al, Si, Ca, P and O in the thin film were obtained by the 2.0 MeV ^{4}He RBS system developed in the TIARA facility of JAERI. The beam size of ^{4}He ions was approximately 5mm in diameter. The elemental depth profile in the thin film of fresh smectite (not contacted with the Eu solution) was also measured as a reference case.

The spatial distributions of Eu, P, Si were determined by μ-PIXE system developed in the TIARA facility. The beam size was approximately 1 μm in diameter. The scanning area of μ-PIXE system was 740 x 740 μm in maximum.

3. Results and discussion

3.1 RBS analysis of depth profile of Eu in film

Figure 1 shows RBS spectra of the thin film of the mixture contacted with the Eu solution of $1.0x10^{-3}$ mol·L^{-1} and of the thin film of fresh smectite. A plateau of Ca (one of the major elements in apatite) is observed in the RBS spectrum of the Eu sorbed thin film. This indicates the existence of apatite in the thin film. On the other hand, no peak for Ca is observed in the RBS spectrum of the thin film of fresh smectite (Fig. 1). A plateau of Eu is observed in the RBS spectrum of the Eu sorbed thin film, where the intensity of the plateau decreases at around 1.2 MeV. This indicates that Eu was not only sorbed on the surface of the thin film, but also penetrates deeper from the surface.

3.2 Micro-PIXE analysis of spatial distribution of Eu

Micro-PIXE analysis shows that the distribution of Eu does not correspond to that of smectite, but to apatite. This indicates that most of Eu sorbed on the thin film is associated with apatite. Even when the thin film is contacted with Eu solution of $1.0x10^{-4}$ mol·L^{-1}, good correspondence in the distributions

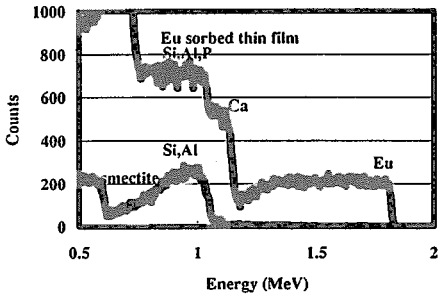


Fig. 1 RBS spectra for the thin film of the mixture contacted with the $1.0x10^{-3}$ mol·L^{-1} Eu solution, and for the thin film of fresh smectite.

between Eu and P is observed.

The peaks of Eu as well as P and Ca are observed in the PIXE spectrum detected at the region of apatite. The intensity ratios of the peak area for Eu to P are 0.11, 0.094 and 0.025 for the Eu concentrations of $1.0x10^{-3}$, $1.0x10^{-4}$ and $1.0x10^{-5}$ mol·L^{-1}, respectively. Note that the intensity ratios are average values in the regions of apatite. The intensity ratio of Eu to P for the original apatite is measured by μ-PIXE to be 0.02. This indicates that small amount of Eu is contained in the original apaptite. The amount of Eu sorbed on apatite for the Eu solution of $1.0x10^{-5}$ mol·L^{-1} is considered to be similar to the background level of the original apatite.

In the PIXE spectrum detected at the regions of smectite, the intensity ratios of Eu to Si are 0.041 and 0.046 for the Eu concentrations of $1.0x10^{-3}$ and $1.0x10^{-4}$ mol·L^{-1}, respectively. And, peak for Eu is not recognized for the Eu solution of $1.0x10^{-5}$ mol·L^{-1}. This indicates that the amount of Eu sorbed on smectite for the Eu solution of $1.0x10^{-5}$ mol·L^{-1} is

considered to be below the detection limit. Note that simple comparison of the intensity ratio between apatite and smectite should not be made because of different efficiencies for elements by μ-PIXE and different mole fractions in different minerals. And the intensity ratios are average values in the regions of smectite.

The μ-PIXE results indicate that the amounts of Eu sorbed on either apatite or smectite is constant, when the concentration of Eu is higher than $1.0x10^{-4}$ mol·L^{-1}.

3.3 Sorption behavior of Eu on smectite and apatite

More than 90 % of Eu is determined to be taken up by the powdered smectite. This indicates that smectite has high performance to sorb Eu. Because the sorbed Eu onto smectite is desorbed by a 1 M KCl solution, the Eu sorption by smectite is reversible. More than 90 % of Eu is sorbed by the powdered apatite, and thus apatite has also high performance to sorb Eu. The sorbed Eu is not desorbed by a 1 M KCl solution. This indicates that Eu is irreversibly sorbed on apatite.

3.4 Sorption mechanism of Eu on the thin film of the mixture

The constant intensity ratio of Eu to Si in the region of smectite indicates that the sorption sites of smectite for Eu are saturated for Eu concentrations more than $1.0x10^{-4}$ mol·L^{-1}. Cation exchange capacity (CEC) of smectite is measured to be 1 meq·g^{-1}. Since the amount of smectite in the thin film is 60 μg, 0.02 μmole Eu can be sorbed on smectite. When Eu concentrations in the solution are higher than $1.0x10^{-4}$ mol·L^{-1}, total amount of Eu in 20 ml solutions is higher by 100 times than the CEC of smectite. This is the reason for the saturation for the sorption site of smectite in the thin film.

Most of Eu sorbed on the thin film is associated with apatite. This suggests that the sorption capacity of apatite is higher than smectite. Xu et al[5] have clarified that the sorption capacity of the surface of apatite are approximately 0.6 mmol·g^{-1} for Zn and Cd. Similar sorption capacity has been reported by Takeuchi et al.[6]. Even though the apatite used in the present study is different from those in their work, the sorption capacity of the apatite used in the presnt study is within the same order. The capacities reported are similar to CEC of smectite. If Eu is sorbed by ion exchange reaction, Eu should be equally associated with both apatite and smectite in the thin film. This disagrees with the result by μ-PIXE.

Ohnuki et al.[3] have shown by RBS analysis that some fraction of Eu is penetrated deeper from the surface of the single crystal specimen of apatite. This suggests that Eu is not only sorbed on the surface of apatite, but also penetrated in the crystal structure of apatite. This penetration uptake apparently causes the increase of sorption capacity and the irreversible sorption. Thus, the penetration uptake causes that most of Eu sorbed on the thin film are associated with apatite.

References

1)D.A. Palmer, S.Y. Shiao, R.E. Meyer, J.A. Wethington, J. Inorg. Nucl. Chem., 43, (1981) 3317.

2) T. Ohnuki, N. Kozai, Radiochimica Acta, 68, (1995) 203.

3] T. Ohnuki, N. Kozai, H. Isobe, T. Murakami, S. Yamamoto, Y. Aoki, H. Naramoto., J. Nucl. Sci. Tech., 34, (1997) 58.

4) J.O. Nriagu, Geochim. Cosmochim. Acta, 38, (1974) 887.

5) Y. Xu, D., F. W. Schwartz, S. J. Tralna, Environ. Sci. Technol., 28, (1994)1472.

6) Y. Takeuchi, H. Arai, J. Chem. Eng. Japan, 23, (1990) 75.

7.3 Development of In-air Micro-PIXE System for High-efficiency Elemental Analyses

T.Kamiya, T.Sakai, M.Oikawa, K.Ishii*, S.Matsuyama*, T.Satoh* and A.Tanaka*,
Advanced Radiation Technology Center, JAERI,
*The School of Engineering, Tohoku University.

1. Introduction

A technique of micro-PIXE is a powerful tool for local area elemental mapping of various kinds of samples with a high-spatial resolution microbeam system. In TIARA, the atmospheric micro-PIXE analyzing technique was established for biological and environmental applications at the light ion microbeam system[1-3]. Now a large solid angle X-ray detection system is under development for higher efficiency and shorter time analyses of large number of biological cells or other samples.

By setting a sample in the atmosphere, the variety of analyzable samples is larger than that by setting it in the vacuum in physical, chemical and also geometrical allowance. Furthermore, larger tolerance to ion beam heating can also be expected from cooling effect of surround air or gas flow. In order to irradiate sample in the atmosphere by microbeams with a beam spot size of less than 1 μm, a 5-μm thick polymer (polyethylene terephthalate, PET) film is used not only as a beam exit window but also as a sample backing, to which the samples are attached from the atmospheric side. So PET film needs to be investigated on its physical and chemical change of property by high-intensity microbeam irradiation.

This paper describes details of the new detection system, and shows results of microbeam irradiation test for beam exit windows.

2. Development of a large solid angle X-ray detector

A large solid angle Si(Li) detector has a space of pentagonal pyramid facing to the sample to detect X-rays from it through the beam exit window efficiently as shown in Fig. 1. In order to detect lower energy X-rays from light elements like Al or Mg, thinner Be window is used for the detector. However, the thin window allows high-energy backscattering protons to pass through it on to the high-efficiency detector, which generates high-count rate and large charge pulse signals. Therefore, the detector is divided into many small cells to prevent the detection system from too high dead time ratio due to charge reset signals from the pre-amplifiers.

3. Irradiation Test of Beam Exit Windows

In the experiments, 4-μm thick PET films attached on to window holding disks were irradiated by 2.2 MeV H ion microbeams with an about 300-nC dose in 20 x 20 μm^2 areas. The condition of the atmospheric gas was tested air and dry helium.

In physical point of view, reduction of the thickness and change of color were were observed for those irradiated area using a laser three-dimensional profile microscope (model VK-8500, Keyence, Japan) from the atmospheric side.

On the other hand, in order to investigate change of the chemical bond in film by irradiation irradiated and non-irradiated area of the film was analyzed by a Fourier transform infrared (FT-IR) spectrometer of Gunma Prefectural Industrial Technology Research Laboratory. FT-IR spectra are shown in Fig. 2. A 1720 cm^{-1}-peak in the non-irradiated area resulting from elastic oscillation of carbonyl bonds was shifted to 1710 cm^{-1} in irradiated area. This seems to show some change of chemical bonds of the carbonyl neighbor. A 1609 cm^{-1}-peak in the irradiated area, which is never in non-irradiated area, seems to result from

increase of freedom of phenyl group due to cutting of the combination happened by the irradiation. In the comparison of the irradiation atmosphere, the level of phenyl group peak by in-air irradiation is equaler to the carbonyl peak than that by in-He gas. This seems to show that the in-air irradiation progresses on the radiation damage more with equivalent radiation value. A broad peak of 3600-2600, resulting from the hydroxyl group for in-air irradiation is much larger than that for in-He gas. This seems to show difference of the humidity in the atmosphere. The moisture in the air seems to form many hydroxyl groups active site, which was created by the irradiation by the attack of water molecule in the environment approach. From these results, the prospect which quantitatively examined the damage of the window application from peak of the phenyl group and absorption of the hydroxyl group by the micro FT-IR analysis was formed.

References

1)T.Kamiya, T.Sakai, T.Hamano, T.Suda and T.Hirao, Nucl. Instr. and Meth. B130 (1997) 285.
2)T.Kamiya, T.Suda and R.Tanaka, Nucl. Instr. and Meth. B118 (1996) 423.
3)A.Sugimoto, K.Ishii, S.Matsuyama, T.Satoh, K.Gotoh, H.Yamazaki, C.Akama, M.Sato, T.Sakai, T.Kamiya, M.Oikawa, M.Saidoh and R.Tanaka, Int. J. PIXE, 9 (1999) 151.

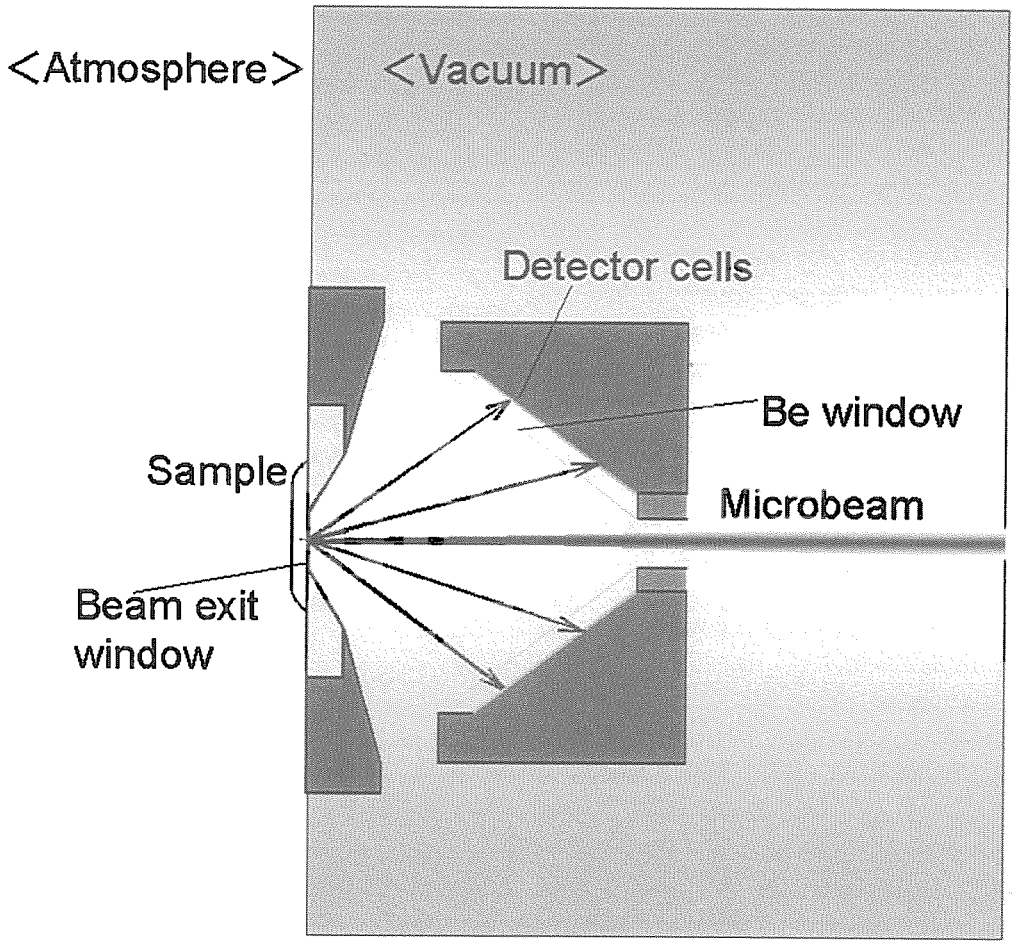


Fig. 1 Schematic illustration of a large solid angle X-ray detector

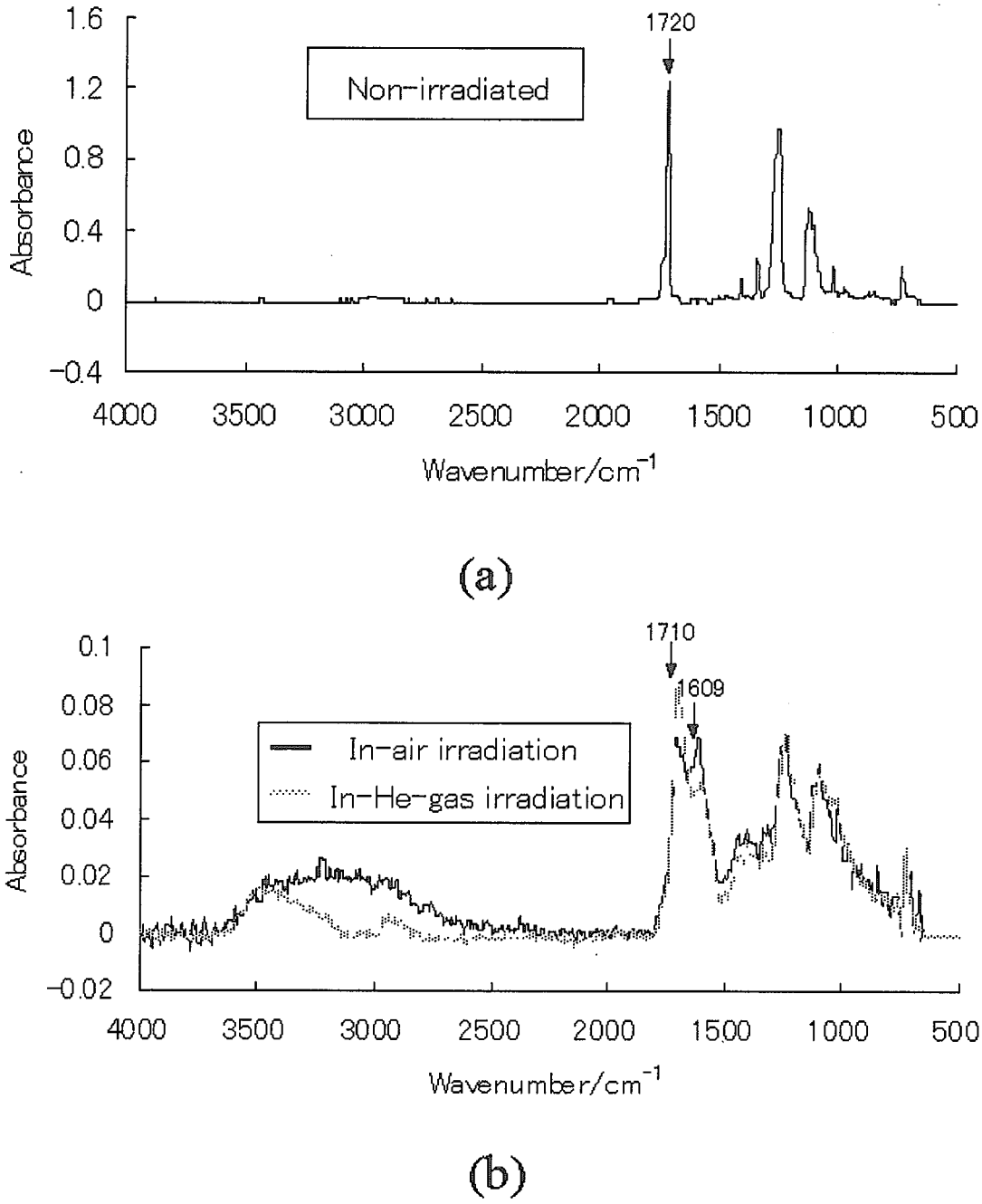


Fig. 2 Micro-FT-IR spectra of (a) non-irradiated and (b) irradiated regions of 5-μm thick PET film with 2.2 MeV H^+. In (b), solid line and dashed line indicate spectra of in-air and in-He-gas irradiations, respectively.

7.4 Fluoride Uptake Measurement using Microbeam PIGE

M. Nomachi, Y. Sugaya, M. Yoshifuku, K. Yasuda*, H. Yamamoto**,
Y. Iwami**, S. Ebisu**, T. Kamiya***, T. Sakai***, and M. Oikawa***
Graduate school of Science, Osaka University
Wakasa-wan Energy Research Center*,
Graduate school of Dentistry, Osaka University**,
Advanced Radiation Technology Center, JAERI***

1. Introduction

At the fluoride relating research in the dental field, the fluoride distribution in a tooth is one of the criteria for evaluation of the cariostatic properties of fluoride. Though the uptake of fluoride in a tooth has been intensively studied, the suitable fluoride concentration for the preventing caries has not been determined yet. For establishing the quantitative measurement of the fluoride, we have reported the method using proton induced gamma-ray emission (PIGE) of TIARA. In this report, we present the fluoride distribution both in the part of around a cavity wall in a tooth and the fluoride-releasing material filled in the cavity, and also the fluoride distribution at the interface between the tooth and the fluoride-releasing material. All of the fluoride releasing-materials in the measurements are being used in the conventional dental clinic.

2. Experimental set-up

The 1.7 MeV proton beam accelerated by the TIARA single-ended accelerator at JAERI-Takasaki, was injected in an ion micro-beam facility[1]. The proton beam bombarded specimens in air. The beam spot size was about 1μm with a beam current of about 100pA. The area of 1100μm by 1200μm was scanned at maximum[2].

We have used a nuclear reaction $^{19}F(p,\alpha\gamma)^{16}O$ for measuring fluoride concentration. The gamma rays of this reaction were detected with a 5" NaI (Tl) detector. It was replaced later by a 3" BGO detector to obtain higher full peak efficiency. The gamma-ray detector was placed 15 mm to 30 mm behind the specimen. The gamma rays energy of the reaction is much higher than the energy of background gamma rays generated by natural radioactivity, because the reaction has a large Q-value. The measurement using the nuclear reaction has, therefore, high signal to noise ratio. Concentration of calcium was measured by the X-rays. Proton induced X-rays were simultaneously detected with a Si (Li) detector.

The specimens' thickness was larger than the range of 1.7 MeV protons. Gamma-ray yield depends on the number of fluorine nuclei in the proton range. It is proportional to fluoride concentration in the case of similar chemical components. Gamma-rays yield from four reference materials $Ca_{10}(PO_4)_6(OH)_{2-2x}F_{2x}$ (x=0, 0.1,0.5,1.0), which have similar chemical compounds to those of a tooth, were measured. X-rays yields were also measured for the reference targets.

The measurement of the beam current is indispensable for quantitative analysis. In the case of thick targets like teeth, however, direct measurement of the beam current is not possible. We, therefore, monitored the beam current periodically. X-ray intensity from a 20 μm copper foil next to the scanned area was measured as shown in Figure 1. The copper foil was bombarded for three seconds in every 30 seconds.

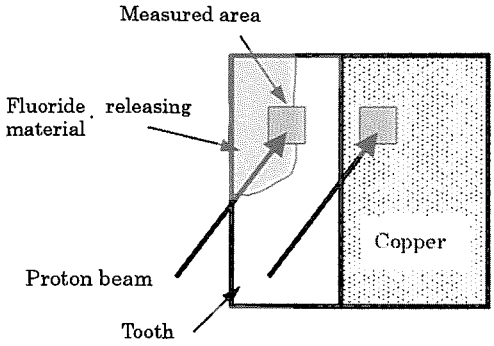


Fig.1. Schematic view of the 500 μm x 500 μm scanned area. The fluoride concentration and calcium concentration were measured in the 80 μm x 80 μm rectangular area. The beam was shifted to the copper for 3 seconds in every 30 seconds.

3. Specimens

Class V cavities were prepared in the buccal face of extracted human teeth and the cavities were filled with the following fluoride-releasing dental materials; a) conventional glass-ionomer cement, b) resin-modified glass-ionomer cement, c) compomer, d) fluoride-releasing composite resin. The teeth were immersed in a plastic capsule filled with 10ml of normal saline solution at 37°C. After one-month immersion, the specimens were removed from the saline and bisected longitudinally perpendicular to the cavity floor with a precision saw (Isomet, Buehler Ltd., Lake Bluff, ILL USA). The fluoride concentration was measured at the

around cavity of the bisected surface. A thin copper foil was glued on the surface of specimens. The specimens with copper foil were glued on a 4 μm thick aramid foil used as vacuum window (φ2 mm). In addition, the tooth applied NaF and the natural tooth as a reference specimen were also measured. The tooth applied NaF is that the buccal surface of tooth was applied with 2% NaF 4 times at an interval of a week. After one-month immersion, a tooth applied NaF and a natural tooth were cut perpendicularly in the buccal surface. On cut off face, fluoride distribution was measured from the buccal surface to the inside

4. Results

Figure 2-7 show the fluoride distribution both in the part of around a cavity in a tooth and fluoride-releasing material in the cavity. The data were obtained in a continuous measurement from tooth to fluoride-releasing material in the cavity in an experimental procedure.

The figure shows continuous fluoride distribution data from the tooth to fluoride-releasing material through the interface. The continuous fluoride distribution between two phases is observed at the first time in this experiment. Fluoride concentration was not uniform in a material. The non-uniformity was different from one kind of a material to another material. It suggests material was various kinds of composite materials. Around a cavity wall fluoride distribution showed location dependence as previously reported[3], but no direct co-relation between the fluoride distribution in the fluoride-releasing material and that of the tooth was observed both in terms of concentration and penetration depth.

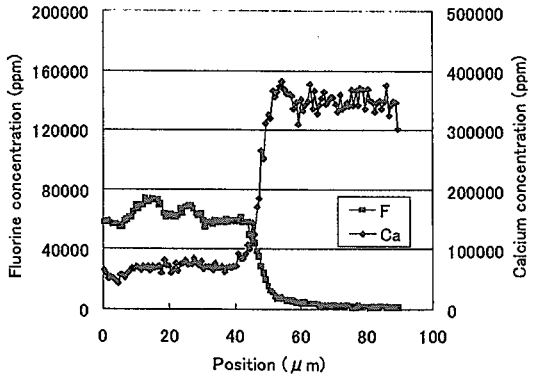


Fig.2 Fluoride distribution of the part of around a cavity in a tooth and the conventional glass-ionomer cement filled in the cavity. The position is relative distance in the scanned area. The cement contains fluoride necessarily included through the fabrication process, and releases the fluoride gradually after hardening in acid-base reaction. The hardening takes time.

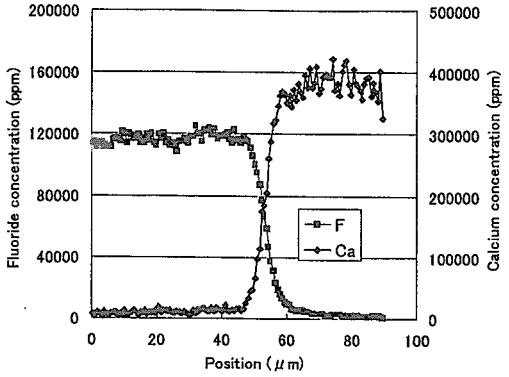


Fig.3 Fluoride distribution of the part of around a cavity in a tooth and the resin-modified glass-ionomer cement filled in the cavity. The position is relative distance in the scanned area. In order to reduce water sensitivity in the hardening of the conventional glass-ionomer cement and increase the hardness, composite resin, which cures by the visible ray, is mixed in the conventional glass-ionomer cement. The hardening of the surface layer is early.

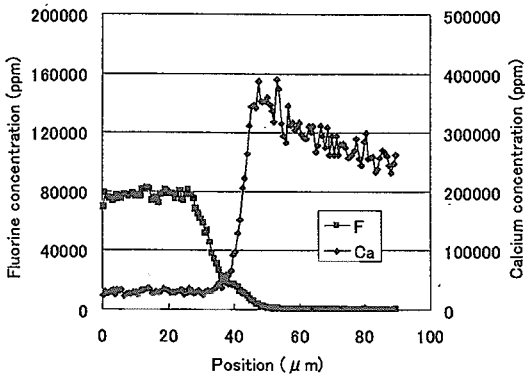


Fig.4 Fluoride distribution of the part of around a cavity in a tooth and the compomer filled in the cavity. The position is relative distance in the scanned area. In order to add the characteristic of fluoride releasing in the conventional glass-ionomer cement, the part of conventional glass-ionomer cement is included for the composite resin that cures by the visible ray.

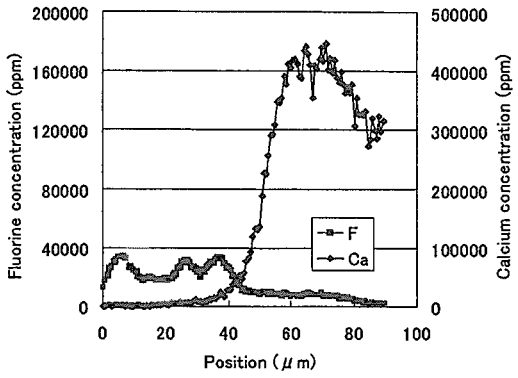


Fig.5 Fluoride distribution of the part of around a cavity in a tooth and the fluoride-releasing composite resin filled in the cavity. The position is relative distance in the scanned area. Fluoride releasing composite resin, which intentionally added the fluoride in various forms in order to release the fluoride gradually after hardening.

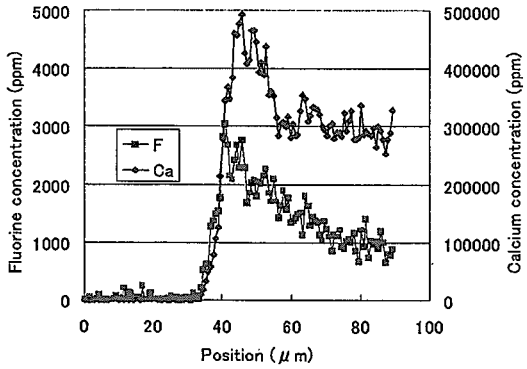


Fig.6 Fluoride distribution on the cut face of a tooth from the buccal surface to the inside. The position is relative distance in the scanned area. The tooth was applied with 2% NaF 4 times at an interval of a week.

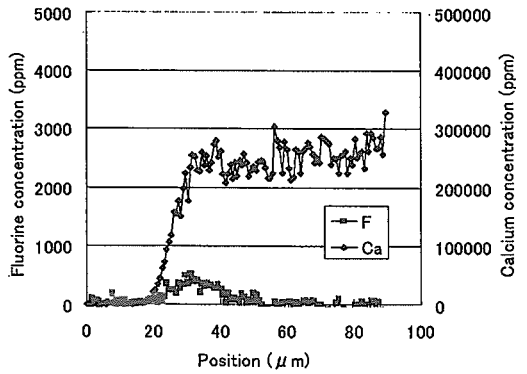


Fig.7 Fluoride distribution on the cut face of a natural tooth from the buccal surface to the inside. The position is relative distance in the scanned area.

5. Summary

Both fluoride distribution in a fluoride-releasing material filled in the cavity and the part of around the cavity in a tooth are simultaneously observed at the first time in this experiment. The data is useful for application of fluoride-releasing material in conventional dental clinic. The experiment requires the measurement in the micro region and only becomes possible by PIGE of TIARA.

As fluoride uptake showed location dependence reported, further accumulation of data may be necessary for statistical treatment to characterize the property of fluoride-releasing material. Moreover, by measuring the fluoride distribution in the material in micro region, the possibility to clarify the dynamic phase of the fluoride in dental material in future has been coming out.

6. Acknowledgements

We would like to thank the members of TIARA for operating the accelerator facility. This work was supported by JSPA, grant-in-aid for scientific research.

References

1) T. Sakai et al., *Biological Trace Element Research*, p77-82 Vols. 71-72, (1999)

2) T. Sakai et al, *Nucl. Instr. And Meth.* B136, 1 (1998)

3) H.Yamamoto et al., Oper. Dentistry 25,104~112,2000.

7.5 Application of In-Air Micro-PIXE Camera to bovine aortic endothelial cells and human leukemia cells

A.Tanaka, K.Ishii, T.Satoh, S.Matsuyama, H.Yamazaki, M.Satoh*,
S.Harada**,T.Kamiya***, T.Sakai***, M.Oikawa***, K.Arakawa***,M.Saidoh***
Department of Quantum Science and Energy Engineering, Tohoku Univ.
Department of Mechatronics and Precision Engineering, Tohoku Univ.*
School of Medicine, Iwate Medical University**
Advanced Radiation Technology Center, JAERI***

1. Introduction

We are developing a micro-PIXE system at the Division of Takasaki Ion Accelerators for Advanced Radiation Application (TIARA) in JAERI. It consists of a micro-beam system combined with a 3MV single-ended electrostatic accelerator, a beam position control, and several X-ray detectors [1-3] and the target is settled in air. We call this system In-Air Micro-PIXE camera since it takes a picture of the elemental. The micro-beams always scan on an interesting region of the target. When an x-ray is detected, the x-ray energy and the beam position are simultaneously measured for each event[3] and the elemental maps can be obtained.

The cellular sample is easily damaged, deformed or destroyed by the beam irradiation in vacuum, and the elements contained are sometimes evaporated. In the case of In-Air Micro-PIXE, the target sample can be analyzed in the atmospheric pressure and can be cooled with the helium gas. This cooling was very effective for keeping the good condition of the cellular samples. If the target of biological sample is in vacuum, the sample shrinks due to beam irradiation and it results in the increase in the density of elements in a beam spot[4], but such phenomenon was not observed in the In-Air micro-PIXE[5].

We apply here the In-Air Micro-PIXE to examine the DNA synthesis in the nucleus of bovine aortic cell and an irradiation effect in the human leukemia cells.

2. DNA synthesis in the nucleus of bovine aortic endothelial cell

We incubated the bovine aortic endothelial cells in the culture medium in which bromodeoxyuridin (BrdU) (1:1000 for culture medium) was supplemented, and in incubation times for 6, 12, and 24 hours respectively. We prepared the targets of cultured bovine aortic endothelial cells by the technique described in the previous report[6] and analyzed them by the In-Air Micro-PIXE.

Major elements contained in the cells, P, S, and K were observed and a trace amount of Br could be clearly recognized. The distribution of S agreed almost with the shape of the cell observed by the microscope. The elements of P, S, and K are concentrated in the central regions

of the cells corresponding to their nuclei. The existence of Br in the nucleus proves that BrdU was used in the DNA synthesis of the nucleus.

Based on the quantitative formula for Micro-PIXE[7], we calculated the quantities of Br and P with respect to each the cell in the incubation times for 6, 12, and 24 hours, respectively. The quantities of Br and P were in the order of 10^{-13}g/cell and 10^{-11}g/cell respectively. Figure 1 shows the histograms of frequency on the concentration of Br per cell. The distributions are different in the cases of 6, 12 and 24 hours. In the case of the incubation time for 6 hours, 50% of the cells took in the bromine in their cycle and almost all the cells took in the bromine in the case of the incubation time for 12 hours. It means that the period of the cell cycle was about 12 hours. In the case of the incubation time for 24 hours, two peaks appear in the histogram. The second peak presents the cells which performed the DNA synthesis two times.

3. Irradiation Effect in the Human Leukemia cells

The human leukemia cells(MOLT-4) received 5 or 10 Gy irradiation using ^{60}Co gamma rays. After the irradiation for 6, 9, and 12 hours, the elemental maps in the cell for the trace elements (Fe, Ca, Zn) were obtained by the In-Air Micro-PIXE Camera. Six hrs after irradiation, the strong point accumulation of Fe was observed in the cell stroma (See Fig.2). From 9 to 12 hours after irradiation, Fe accumulation was diminished; instead, Ca accumulation increased in the nucleus. As Ca accumulates in the nucleus, the Zn accumulation in nucleus decreased. These phenomena may be related to the apoptosis induced by irradiation.

4.Conclusion

In this work, the behavior of BrdU in the DNA synthesis of the bovine aortic endothelial cells could be studied by using the images of the In-Air Micro-PIXE Camera and also the irradiation effect was observed as the strong accumulation of Fe in the human leukemia cell.

It is helpful for the study of mechanism of metabolism of the cell and also gives the possibility of quantitative diagnosis by micro-PIXE camera in the clinical application. Our cellular target preparation in which the cells are cultivated on the thin Mylar film is very appropriate for the In-Air micro-PIXE. In this method, since the cells are not required to be completely freeze-dried, the distributions of elements in the cell, which are similar to those in vivo, can be obtained. Actually, the cells did not shrink and the quantities of elements in the cells did not change during beam irradiation. Thus, the In-Air micro-PIXE camera was very useful for biomedical study.

References

1) T. Kamiya, T. Suda, and R. Tanaka, Nucl. Instr. and Meth. B104 (1995)43.
2) S. Matsuyama, K. Ishii, A. Sugimoto, T. Satoh, K. Gotoh, H. Yamazaki, S.Iwasaki, K. Murozono, J. Inoue, T. Hamano, S. Yokota, T. Sakai, T. Kamiya, and R. Tanaka, Int. J. PIXE 8 (1998)203.
3) T. Sakai, et al., Nucl. Instr. and Meth. B136/138 (1998)390.
4) M.Maetz,W.J.Przybylowicz,J.Mesjasz-Przybylowicz, A. Schussler, Kurt Traxel, Nucl. Instr. and Meth. B158 (1999)292.
5) K. Ishii et al., Nucl. Instr. and Meth. B (2001)(in press).

6) A. Sugimoto, K. Ishii, S. Matsuyama, T. Satoh, K. Gotoh, H. Yamazaki, C. Akama, M. Sato, T. Sakai, T. Kamiya, R. Tanaka, and M. Oikawa, Int. J. PIXE 9 (1999)151.

7) A.Sugimoto et al. JAERI-Review 2000-024, p224-p226.

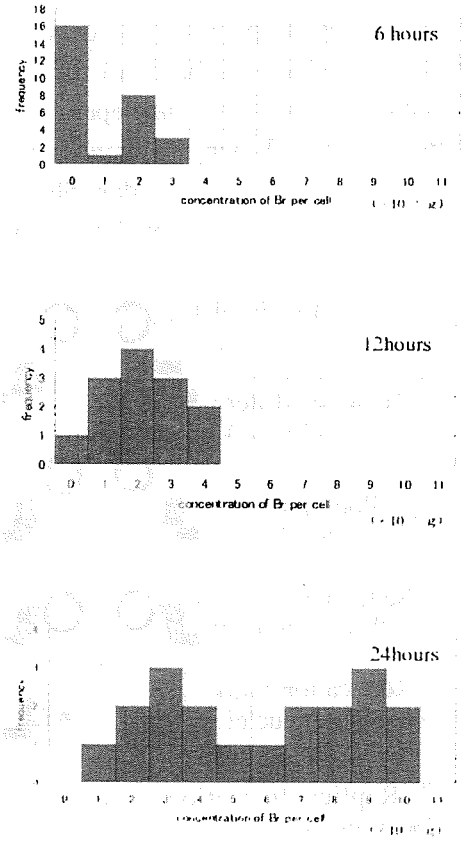


Fig.1. The frequency histogram for the concentration of Br in the cells cultured in the medium containing BrdU for 6, 12, and 24 hrs.

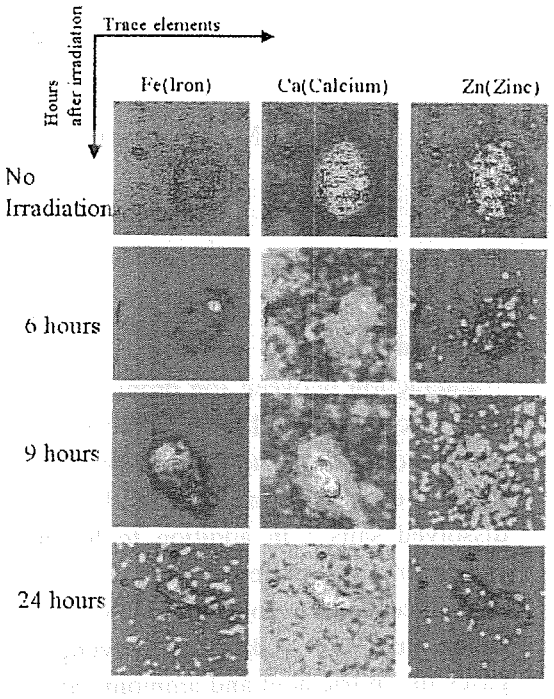


Fig.2. Time change of elemental maps of Ca, Fe and Zn in the irradiated human leukemia cells.

7.6 Application of micro-PIXE to the Analysis of Single Fog droplets

M. Kasahara, C.- J. Ma, Y. Inokuchi, T. Kamiya*, T. Sakai*,
M. Oikawa* and T. Sato*
Graduate School of Energy Science, Kyoto University
*Advanced Radiation Technology Center, JAERI

1. Introduction

Interaction between fog droplets and materials is a complex multiphase process which can lead to corrosion and dissolution, as well as, during evaporation, to the deposition of dissolved salts.[1] In addition to having solute concentration differences that arise from differences in the composition of the condensation nuclei, fog droplets scavenge soluble gases like nitric acid and ammonia and act as a medium for various aqueous phase reactions, including the oxidation of absorbed SO_2 to sulfate.[1] A lot of determinations of the chemical components in fogwater have been made. The analysis was carried out nearly always with bulk sample. But detailed information cannot be obtained by this bulk sample analysis because the chemical content of fog droplets depends on the drop size. Fortunately, however, recent Tenberken and Bächmann's capillary zone electrophoresis (1998) and Ma's polymeric water absorbent film technologies (2000) have provided new methods by which chemical analysis of single and classified-fog droplet can be carried out. The investigation of the characteristics of individual fog droplets is primary importance for both the explanation of fog formation processes and the modeling of acid deposition processes. In this study, thin collodion film method was proposed to collect the individual fog droplets, and also the micro-PIXE method was applied to the chemical analysis of individual fog droplets.

2. Experiments

For the purpose of forming the fog droplets replica, thin collodion film was prepared. Collodion solution can be made by dissolving the nitrocellulose involving 11-12 % of nitrogen into the mixed solution of ether and alcohol. Fig.1 illustrates the replica formation process of individual fog droplets on the collodion film. 200 $\mu\ell$ of collodion solution (3 %) was mounted onto the non-hole nuclepore filter just before sampling. When fog droplets fall freely onto the thin layer of the collodion film (130±10 μm) they gently settled without bounce-off.

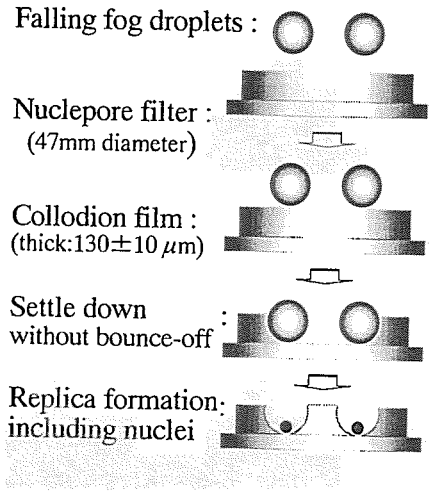


Fig. 1 Replica formation process of individual fog droplets.

Before the sampling of fog droplets, the plate sampling stage consisted of four-Petridish (8.5 cm diameter), which was designed in this study, was set up outside and pre-conditioned to the ambient outdoor temperature. Samplings were performed at Kyoto University in Kyoto, Japan from the end of February to the end of April, 2000.

To analyze the individual fog droplet replicas, micro-PIXE (Particle Induced X-ray Emission) analysis was performed at the facilities of the Japan Atomic Energy Research Institute, Takasaki.

3. Results and Discussion

When droplet was deposited too early onto the surface of the collodion film, the replica of original shape of droplet could not be formed because of the reaction between droplet and collodion solution. It was found that the most adequate time for getting the successful replica was 15-30 seconds after making the collodion film. The replicas of individual fog droplets were formed separately on the thin collodion film as shown in Photo 1.

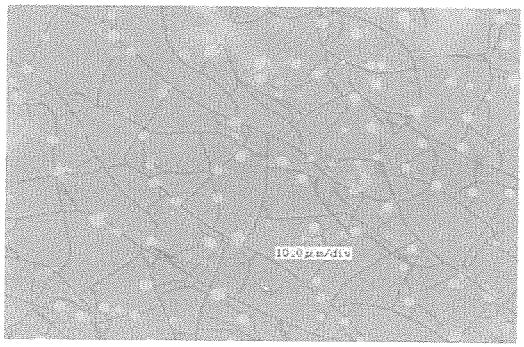


Photo 1 Digital microscopic image of individual fog droplet replicas formed on the collodion film.

It is necessary to know the accurate size distribution of fog droplets to study theoretically on the scavenging of atmospheric pollutants by fog droplets. In this study, the number size distribution of individual fog droplets was successfully determined by measuring the replica diameter. The size ranges of fog droplet during two fog events were 0.9-21 μm with 0.14 g m^{-3} liquid water content (W_L) and 1.5-13 μm in diameter with 0.11g m^{-3} W_L. Fig. 2 shows the number size distributions of fog droplets during two different fog events. The number size

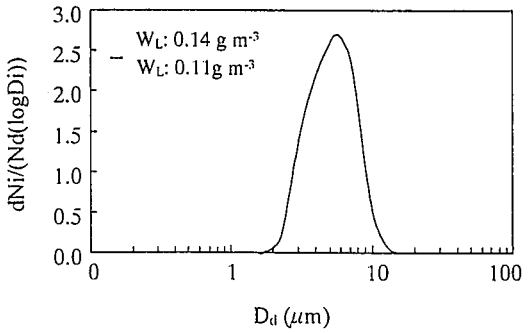


Fig. 2 Number size distributions of individual fog droplets.

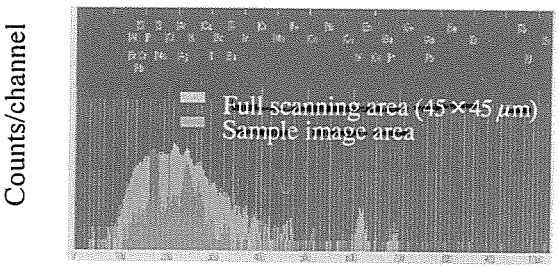


Fig. 3 Micro-PIXE spectrum of a single fog droplet collected on the collodion film.

distribution is bimodal showing positive skewness with a long tail toward the larger sizes at the 1st fog event. In the case of the 2nd event, the number of fog droplets rises from a low value to a maximum, and then decreases toward larger sizes. In comparison with other researches[1], small size fog droplets and low W_L were measured in this study. According to Pandis (1990), one may distinguish among three stages during a fog event. In the formative stage, the droplet number concentration increases with time resulting in increasing W_L while the mean drop size may remain the same or may increase slightly. During the mature stage, the number concentration, W_L and mean drop size fluctuate rather strongly around generally constant values. The final dissipative stage is a period of decreasing drop concentration, drop size, and W_L. Our results can be explained well on the ground of Kunkel's viewpoint because every fog event was several hours old when samplings were done. The application of micro-PIXE method to the chemical analysis of individual fog droplets was attempted. The non-volatile components existent in individual fog droplet replicas were the target of micro-PIXE analysis. Fig. 3 shows the micro-PIXE spectrum of a single fog droplet. White and gray color spectra mean total net counts corresponding to each channel number in full scanning area and those of only in sample image area, respectively. More detailed spectrum can be obtained by the re-scanning of micro beam on the surface of single fog droplet image. Several elements including sulfur were successfully analyzed. In

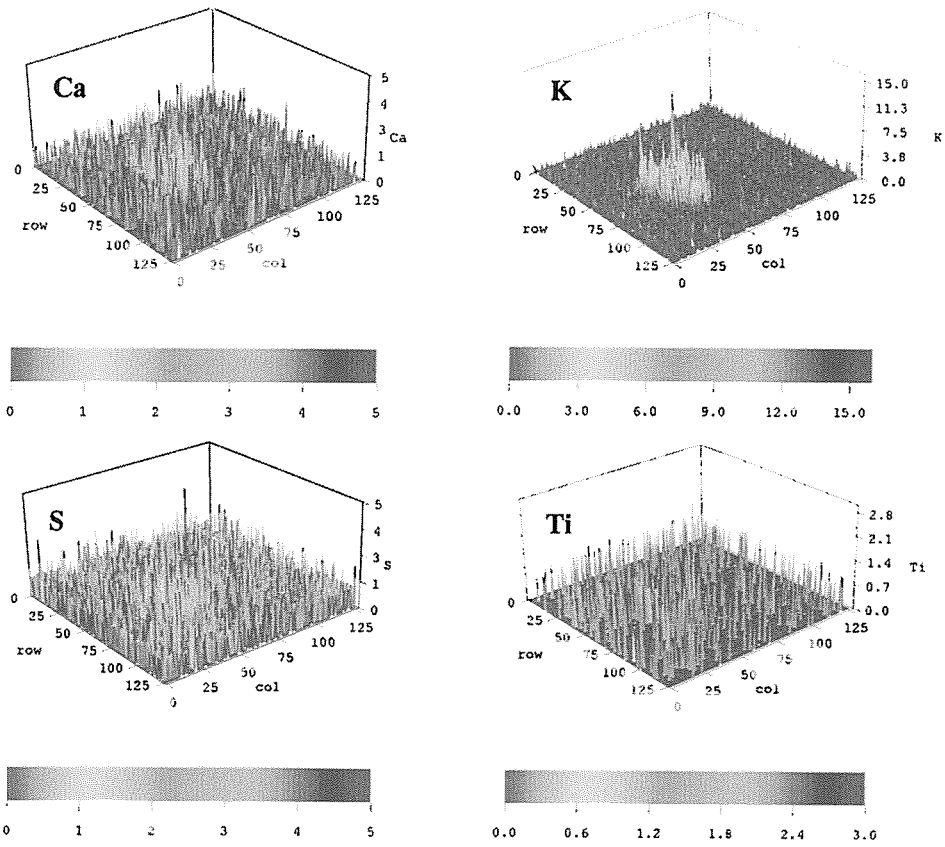


Fig. 4 Micro-PIXE elemental maps taken on the single fog droplet collected on the collodion film (scanning area : 45 × 45 μm).

particular, potassium and calcium were detected as overwhelming majority. Each elemental map can be drawn on the 128 × 128 pixels by scanning of about 1 μm small hydrogen beam on the sample surface. Elemental maps shown in Fig. 4 were formed on a 45 × 45 μm scanning area including a single fog droplet replica. Row and col are pixels corresponding beam scan area and the scale bar is the peak count of characteristics X-ray. Soil components such as calcium, potassium, and titanium were distributed in the range from 50 to 80 and from 30 to 60 row and column pixel axes, respectively. Sulfur was distributed at the same portion. From the results of elemental maps taken by micro-PIXE analysis, we can presume the inner-structure and mixing stage in individual fog droplets.

4.Conclusion

The replicas of individual fog droplets were formed successfully on the thin collodion film without bounce-off. The number size distribution of individual fog droplets was successfully determined by this method. The size ranges of fog droplet during two fog events were 2.2-10.5 μm in diameter with 0.11g m^{-3} W_L and 1.1-23 μm with 0.14 g m^{-3} W_L. Several elements including sulfur in individual fog droplets were successfully analyzed. In particular, potassium and calcium were detected as overwhelming majority. Individual fog droplets existed as the mixing state of soil components and sulfur. It should be said that the proposed sampling and analysis methods of individual fog droplets in this study are effective to obtain more detailed information on fog droplets.

References

1) Pandis, S.N. et al. Atmos. Environ., 24A, 1957,1990.
2) Tenberken, B. and K. Bächmann, Atmos. Environ., 32, 1757, 1998.
3) Ma, C.J. et al. 17th Symp. on Aero. Sci. and Tech. Japan, 122, 2000.

7.7 In-Air Micro-PIXE Analysis of Ascitic Hepatoma Tissue Slices

A.Tanaka, K. Kubota*, K.Ishii, H.Fukuda*, T.Akaizawa*, T.Satoh, Y. Oishi, S.Matsuyama, H.Yamazaki, T.Kamiya**, T.Sakai**, M.Oikawa**, K.Arakawa**, M.Saidoh**

Department of Quantum Science and Energy Engineering, Tohoku Univ.

Institute of Development, Aging and Cancer, Tohoku Univ.*

Advanced Radiation Technology Center, JAERI**

1. Introduction

The PIXE method is high sensitive in the analysis of trace metal elements in a biological sample. We are now developing a PIXE analysis method using proton micro-beams for cellular samples at the Division of Takasaki Ion Accelerator for Advanced Radiation (TIARA) in JAERI[1 - 3]. By this PIXE method, spatial distributions of trace elements in a cell can be obtained as images with a spatial resolution of <1μm and the cell can be analyzed in atmospheric pressure. We call this system In Air Micro-PIXE camera[3]. In the In-Air Micro-PIXE camera, the target sample can be cooled with the helium gas. This cooling was very effective for keeping the good condition of the cellular samples, while, in vacuum, the sample is easily damaged, deformed or destroyed by the beam irradiation and the elements contained are sometimes evaporated.

As described in the previous JAERI annual report[4, 5], we analyzed trace elements both in a cultured cell and the tissue slice. The experimental results of the cultured cells presented the usefulness of this method to the clinical application. In the case of tissue slices, we could not obtain anything meaningful and it was required to improve the technique of target preparation in target thickness and drying method.

2. Target preparation

The tumor cells of AH109A were subcutaneously planted into the back of Donryu rat. A week after planting, cisplatin (CDDP)(0.25mg/rat) were administrated into the rat 3 times with the interval for 6 hours. CDDP was used to examine the effect of anti-cancer drug and also to recognize the nuclei of the cell because CDDP is uptaken into the nucleus[6,7]. The rats were sacrificed by over dose of anesthesia, immediately the tumor tissue and liver were taken and were frozen with liquid N_2. Since the size of the cell is 10~20μm, the frozen sections were cut into 30 μm thick slices with a microtome under –25℃. The slices were placed on the 4μm thick Mylar film. In the previous work, the thickness of slice was 10μm and the tissue slices were dried in air. We tested three methods of drying for the tissue slices of 30μm; drying in air, drying in vacuum, and freeze drying in vacuum.

3. Results and Discussion

Figures 1, 2, and 3 show the elemental maps (45μm×45μm) of the tissue slices of AH109A dried in air, dried in vacuum, and freeze-dried in vacuum, respectively. In the case of drying in air, elements seems to be uniformly distributed in the tissue. On the other hand, elements are strongly localized in the case of drying in vacuum. It is very difficult to obtain specific information from these images. We show the elemental images of P, S, Cl, K, Ca, Fe, and Zn in the figures. The element of Pt which are contained in CDDP, was not detected in the present experiment. This result presents that the quantity of Pt is very trace and it might be less than 10^{-13}g/cell. Therefore, an X-ray detection system with a large solid angle is desired to analyze the tissue slices by the micro-PIXE method.

References

1) T. Kamiya, T. Suda, and R. Tanaka, Nucl. Instr. and Meth. B104 (1995)43.
2) S. Matsuyama, K. Ishii, A. Sugimoto, T. Satoh, K. Gotoh, H. Yamazaki, S.Iwasaki, K. Murozono, J. Inoue, T. Hamano, S. Yokota, T. Sakai, T. Kamiya, and R. Tanaka, Int. J. PIXE 8 (1998)203.
3) T.Sakai, et al., Nucl. Instr. and Meth. B136/138 (1998)390.
4) A.Sugimoto et al. JAERI-Review 2000-024, p224-p226.
5) A.Tanaka et al., JAERI-Review 2000-024, p230-p232.
6) R.Ortega, Ph.Morreto, A.Fajac, J.Bernard, Y.Llabador, and M.Simonoff, Cellular and Morecular Biology 42(1996)77-88.
7) A. Sugimoto, K. Ishii, S. Matsuyama, T. Satoh, K. Gotoh, H. Yamazaki, C. Akama, M. Sato, T. Sakai, T. Kamiya, R. Tanaka, and M. Oikawa, Int. J. PIXE 9 (1999)151.

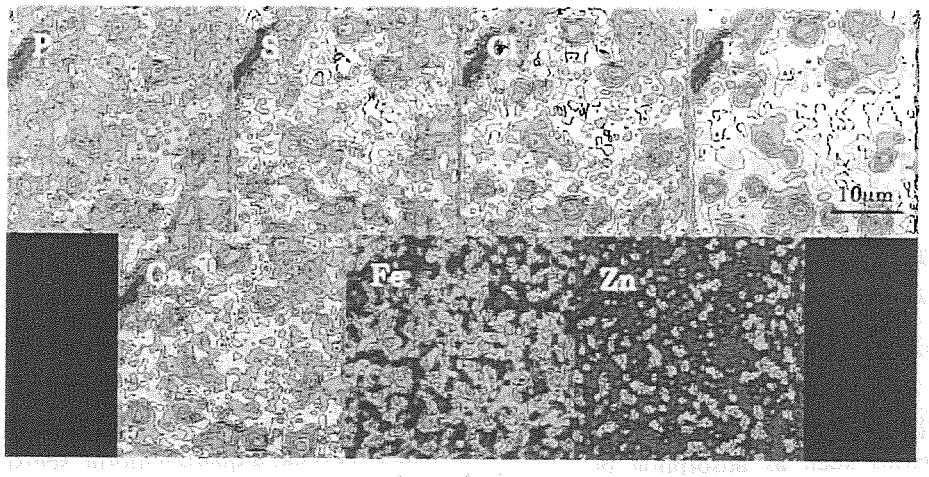


Fig.1. Elemental maps of P, S, Cl, K, Ca, Fe, and Zn in the tissue slice of AH109A tumor. The tissues slice were dried in air.

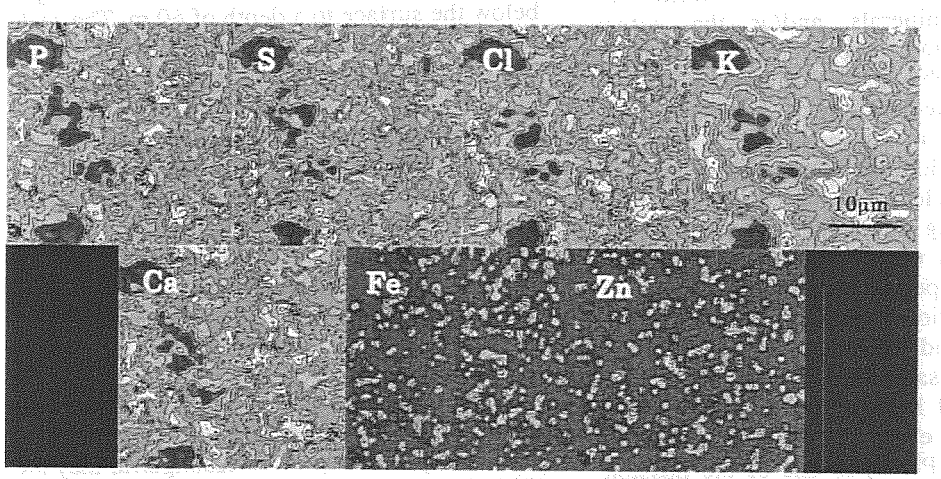


Fig.2. Same as Fig.1 except for in vacuum.

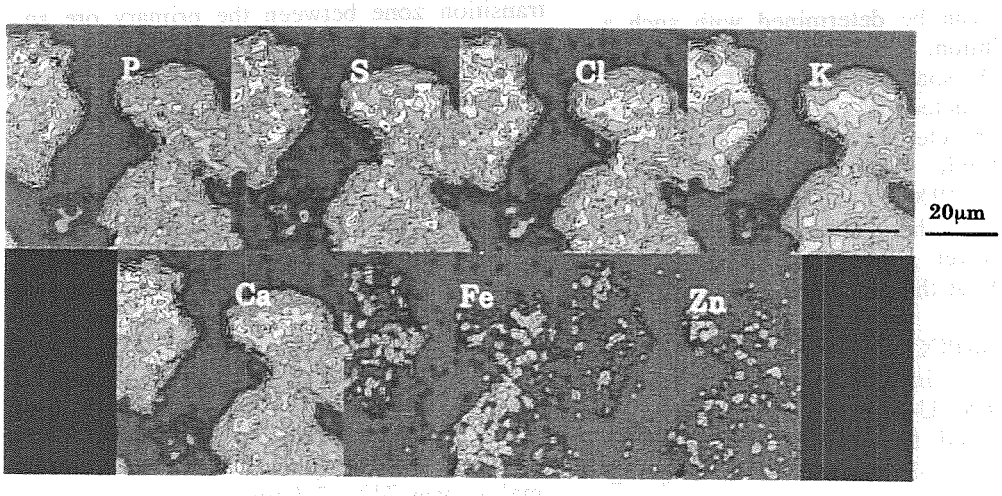


Fig.3. Same as Fig.1 except for freeze-dried in vacuum.

7.8 Redistribution of Elements between Minerals in Rocks -Analysis of Uranium Distribution in Rocks by μ-PIXE-

T. Ohnuki*, N. Kozai*, M. Samadfam*, R. Yasuda**, T. Kamiya***, T. Sakai***, Shoichi Oikawa****, Takahiro Sato**** and T. Murakami****

Department of Environmental Science, JAERI*, Department of Hot Laboratories, JAERI**, Advanced Radiation Technology Center, JAERI***, Mineralogical Institute, The University of Tokyo****

1. Introduction

The mobility of dissolved U in natural water is affected by processes such as adsorption or desorption of U ions and precipitation or dissolution of U-bearing minerals[1]. Thus, oxidation states and chemical forms of U-sorbed on minerals and/or the nature U-bearing minerals should be clarified to understand the behavior of U in environment.

The electron technology is introduced into mineralogical science in the 60's and early 70's. By employing this technique, mineralogical analysis using electron microprobe analysis (EMPA), scanning electron microscopy (SEM) and transmission electron microscopy (TEM) have been developed. Today SEM and EMPA are used as traditional methods to determine U concentrations and the nature of U-minerals at μm-scale in rock samples.

Application of high-energy ion beams also goes back to the early 70's. Particle induced X-ray emission (PIXE) is one of the possible methods for detecting the elements in the level of ppm[2]. If we use the probe beams of μm order or less in diameter, U distribution in a rock sample can be determined with such a spatial resolution. A light ion microbeam system with the spatial resolution of less than 1 μm was constructed on a beam line of 3 MV single-ended accelerator in the TIARA facility at Japan Atomic Energy Research Institute (JAERI). A μ-PIXE analyzing system was developed for chemical analysis with a sub-micron level spatial resolution[3]. Thus, mapping of U at the ppm level is available by μ-PIXE.

Using μ-PIXE, we examined the distribution of U in rock samples collected at the Koongarra U-deposit, Australia. We finally compared the relative advantages of μ-PIXE and SEM-EDS analyses for mapping of U in rock samples.

2. Geological setting

Koongarra is located in a tropical monsoon climate. The host rock, a quartz-chlorite schist, and the primary U mineral, uraninite, have been weathered at the Koongarra U ore deposit. The primary ore deposit extends from just below the surface to a depth of 60 m. The rocks currently at and near the surface have probably been subjected to weathering for more than one million years[4,5]. In the "primary" ore deposit, uraninite has been partly altered to uranyl-lead oxides and uranyl silicates[6,7]. In the "secondary" ore deposit, extending to 20 m below the surface and formed by weathering of the primary ore deposit, the U(VI) oxides and silicates are further weathered and U is found as uranyl phosphates, mostly saléeite[6,8,9].

3. Experimental

The rock samples were collected from diamond-drill cores drilled upstream from the "secondary" ore deposit at Koongarra; they are, DDH65-97 (22.7 m depth from the surface) and DDH65-100 (23.5 m), respectively. The two samples analyzed obtained from the transition zone between the primary ore and the weathered zone. Petrological thin sections of about 30 μm thick were made from the collected rock samples. The thin sections were initially checked by optical microscopy (OM). After the observation by OM, cores of 6 mm in diameter were drilled in interesting region of some of the thin sections for the μ-PIXE analysis. After the μ-PIXE analysis, SEM-EDS analysis on the same sample was carried out.

A Proton beam with the energy of 2.6 MeV from the single-ended machine was used for μ-PIXE analysis. The beam spot was approximately 1 μm in diameter. The maximum scanning area for the μ-PIXE analysis was 740 x 740 μm^2.

4. Results and Discussion

4.1 SEM and EPMA analysis

A backscattered electron image (BEI) of the rock sample DDH65-97 shows that several U-bearing minerals are observed. These U bearing mineral surround apatite which is an accessory mineral of the host rock at Koongarra deposit. EPMA analysis of the bright regions shows that the chemical composition of the U bearing mineral is expressed by $Mg(UO_2)_2(PO_4)_2 \cdot nH_2O$. This formula corresponds to saléeite.

The primary apatite observed in the DDH 65-100 thin section, which is located slightly deeper than DDH 65-97, contains no detectable U. These indicate that U migrated from the primary ore reacts with P dissolved from the primary apatite at the rim of the primary apatite to be mineralized to form saléeite.

Comparison of the BEI with the distributions of Ca, P and U obtained by SEM-EDS indicates that the distribution of U is in good agreement with that in the bright region in BEI. The distribution of P shows that P is present in both apatite and saléeite. The distribution of Ca shows that Ca is present in apatite, but not in saléeite. Note that the spatial resolution of the X-ray image obtained with an accelerating voltage of 15 kV is about 7 μm^2.

4.2 μ-PIXE analysis

The distributions of Si, P, K and Fe of DDH65-97 are shown in Fig. 1(a), (b), (c) and (d), respectively. The distribution of U determined by L-X-ray line of U is shown in Fig. 2(a). The distribution of the element determined by the peak around 3.16 KeV, which is the same energy for U M-line peak, is also presented in Fig. 1(b). The distribution of U determined by L-X-ray line of U corresponds to that of P (Fig. 2(b)). On the other hand, the distribution of U determined by L-X-ray line of U does not correspond to that of K (Fig. 1(c)).

The regions where we detect P, Si and Fe in Fig. 1 are called a saléeite, clay and

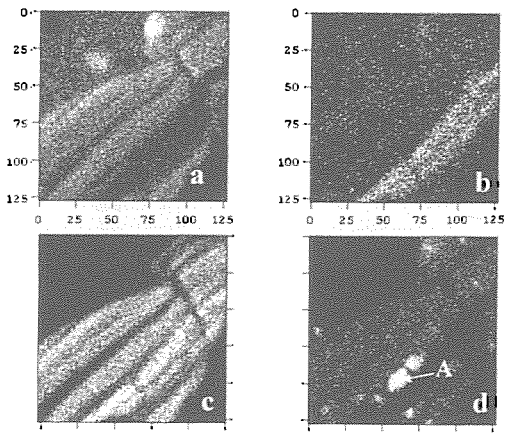


Fig. 1 Distributions of Si (a), P (b), K (c) and Fe (d) obtained by μ-PIXE in the rock sample of DDH 65-97.

Fe-mineral regions, respectively. The PIXE-EDS spectra of the above regions show that both M- and L- X-ray lines of U are observed in the saléeite region. The peak position of M-line X-ray of U (3.16 KeV) is very close to that of K-X-ray line of K (3.31 KeV). On the other hand, no other peaks are observed around L-X-ray line of U.

In the PIXE-EDS spectrum of the Fe-mineral region, no uranium peak appears. No correlation between U and Ti is observed. These indicate that the amount of U sorbed on the Fe-mineral and Ti-bearing mineral is quite lower than that of U precipitated to form saléeite around apatite. Murakami et al. have reported that micro-crystallization of U is the dominant retardation mechanism for U migration at Koongarra[10], which is in good agreement with our results.

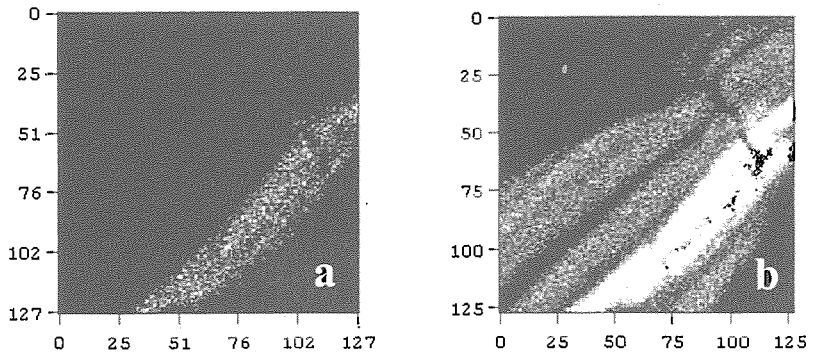


Fig. 2 Distributions of U determined by M-line (a) and L-line (b) X-ray of U at the same region in Fig. 1. A brighter region shows higher concentration of U.

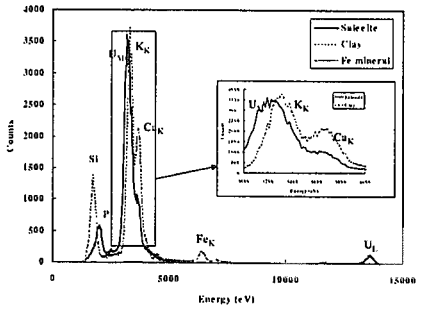


Fig. 3 PIXE-EDS spectra of the P, Si, and Fe regions in Fig. 1. Enlarged PIXE-EDS spectra of the saleeite (P) and clay (Si) regions between 3000 and 4000 eV in energy are also shown.

4.3 Comparison of SEM-EDS and μ-PIXE

Both SEM-EDS and μ-PIXE give the uranium distribution at the rim of apatite. The contrast of the U distribution obtained by μ-PIXE is clearer than that by SEM-EDS. The difference in mole fraction of P between apatite and saléeite appears more clearly by μ-PIXE rather than by SEM-EDS. This clear contrast in elemental distribution is one of the advantages of μ-PIXE.

The grains of saléeite are more clearly separated in μ-PIXE than in SEM-EDS. In SEM-EDS the X-ray generating area with an accelerating voltage of 15 kV is about 3 μm in size. On the other hand, the X-ray generating area in quartz and saléeite of 30 μm in thickness with 2.6 MeV proton beam is calculated by SRIM code[11] to be the same as the spatial beam size saléeite. Since beam spot in the μ-PIXE system in TIARA is 0.8 μm^2, spatial resolution in U distribution by μ-PIXE is higher than by SEM-EDS. Thus, the spatial resolution of μ-PIXE is higher than that of SEM-EDS.

When a clay mineral containing K is present, the U distributions differ between M- and L-X-ray line of U (Fig. 2). In the clay region in Fig. 1a where we detect Si, an overlap of M-line X-ray of U and K-line X-ray of K occurs in the EDS spectrum. However, no peak around 3.16 KeV is recognized in the X-ray spectrum of the clay region. These indicate that U in the clay region is quite low. Thus, the distribution of U obtained by the L-X-ray line is more reliable than that obtained by the M-X-ray line. Detection of L-X-ray line of U by μ-PIXE is an advantage with respect to the analysis of a geological sample containing clay mineral.

Therefore, it is concluded that μ-PIXE is one of the best techniques that allows U to be accurately analyzed and mapped in K-bearing minerals, using its L-line.

References

1) J.K Osmond and M. Ivanovich, in: M. Ivanovich and R. S. Harman (eds.), Uranium series disequilibrium: Application to earth, marine, and environmental science (2nd Ed.) Oxford University Press, Oxford,1992, p259.
2) S. Sueno, Eur. J. Mineral., (1995), 1273.
3) T.Kamiya, T.Suda and R.Tanaka, Nuclear Inst. Method B 118 (1996) 447.
4) P.L. Airey, P. L., Chemical Geology, 55, (1986) 255.
5) T. Murakami, H. Isobe, T. Sato, T. Ohnuki, Clays and Clay Minerals, 44, (1996) 244.
6) A.A. Snelling, in: J. Ferguson and A. B. Goleby (eds.), Uranium in the Pine Creek Geosyncline, International Atomic Energy Agency, Vienna (1980) p.487.
7) H. Isobe, T. Murakami, R.C. Ewing, Journal of Nuclear Materials 190, (1992) 174.
8) H. Isobe, R.C. Ewing, R. C., T. Murakami, in Materials Research Society Symposium Proceedings, 333, (1994) 653.
9) T. Murakami, et al., in Alligator Rivers Analogue Project Final Report Vol. 9, DOE/HMIP/PR/92/079, 138 p. Australian Nuclear Science and Technology Organisation, Sydney (1992).
10) T. Murakami, T. Ohnuki, H. Isobe, T. Sato, American Mineralogist, 82, (1997) 888.
11) SRIM code is developed by IBM. The code is open at website.

7.9 Radiation Damage in Si PIN Diodes Induced by Heavy Ion Microbeam Single Hits

T.Kamiya, T.Sakai, M.Oikawa and T.Hirao*
Advanced Radiation Technology Center, JAERI
*Department of Material Development, JAERI

1. Introduction

The single ion hit system [1-3] combined with the heavy ion microbeam system was designed to study SEU, malfunction caused by high dense charge generation induced by single ion injections [4]. However, this phenomenon consists not only of the charge generation and collection but also of radiation damage in the devices due to a large energy transfer in a confined area of the device. We utilized the single ion hit technique to induce radiation damages onto micron areas of a Si PIN diode and to evaluate the lateral extent of the charge collection by analyzing the radiation damage effects using a Weibull function[5]. Computer simulation of this irradiation experiment has been made based on a simple model describing the damage and charge collection process, which we assumed [6].

The next step of the development of the single ion hit technique is real time position sensitive single ion detection using a thin film. A thin and strong enough film is required to extract single ions out to the atmosphere for living biological cell irradiation. The film should also be a single ion detector, emitting secondary electrons or photons by ion's passing through it. Our aim is to obtain positional information as well as a detection signal.

This paper will describe the result of the simulation compared with the measurement, and the result of a preliminary experiment of microbeam irradiation onto a diamond film.

2. Simulation of single ion hit on to a Si PIN diode

Charge collection and radiation damage induced by single-ion injections to a diode using 1 μm diameter (FWHM) microbeams were simulated by applying a simple model using a Monte Carlo method. Single-ion hits to the number of about 10,000 were simulated on the imaginary field with areas varying from 1 x 1 to 50 x 50 μm^2. A schematic illustration of the simulation is shown in Fig. 1. Simulations were made on a field divided into many small unit pixels. Initially each pixel is given a capacity of charge generation in number, which are reduced by ion hits until a lower limit. In the simulations, the followings were assumed; (1) the microbeam has the Gaussian profile, (2) both radiation damage and charge generation per injection per pixel are uniform within their own regions, (3) the damages accumulated by single-ion hits affect to the next charge collection, and (4) the output of pulse height is evaluated as the total balance of the generated charge against the extinguished one in all corresponding pixels in the charge collection region. The statistical error was considered to every output.

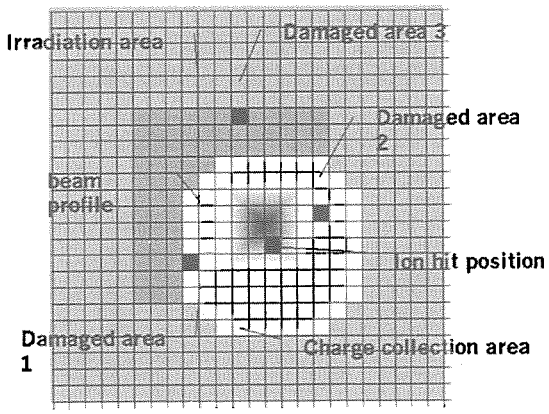
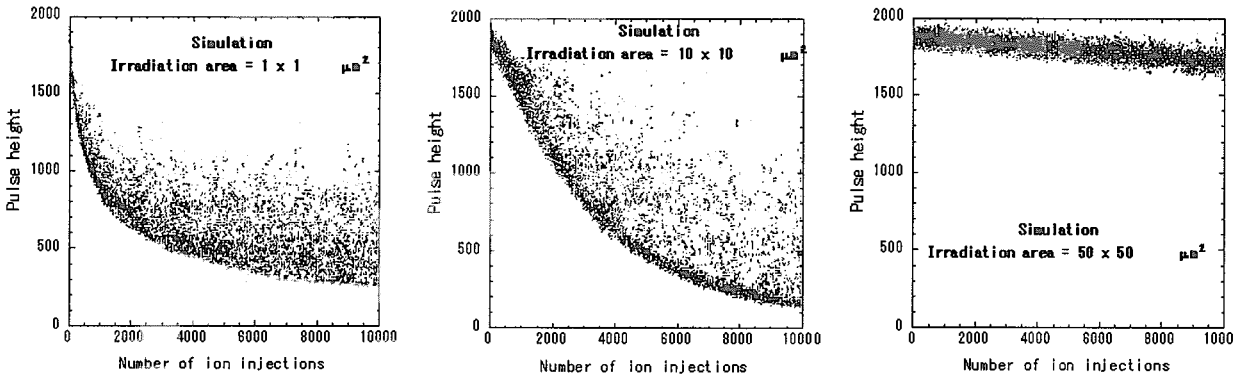


Fig. 1. Schematic illustration of the simulation for single ions to hit Si PIN diode to introduce radiation damage and charges to be collectd by electrodes.

Simulations were performed for irradiation areas from 1 x 1 to 50 x 50 μm^2. Numerical calculations were iterated until simulation results could reproduce measurements with 15 MeV Ni microbeams in parameters of the Weibull function. Eventually, the numbers of 10 and 20 were respectively selected for the charge generation and the charge extinction per injection per pixel, and 1 for the lower limit of charge collection in a pixel. The number of pixels for the 1 μm beam size, the width of an irradiation area, the lateral radius of individual charge collection and that of radiation damage were also selected to be 10, 10, 20 and 1, respectively. This means that lateral extent of the charge collection and the radiation damage are 2 μm and 0.1 in radius, respectively. Figure 2 shows three cases of the simulation results, for the irradiation areas of 1 x 1 μm^2, 10 x 10 and 50 x 50. Results of analyses, which are the changes of scale and shape parameters α and m as the function of width of irradiation area b, as shown in Fig. 3, can reproduce for measured data. Although the model for the simulation seems to be too simple to reproduce all the data absolutely for various micro area of the PIN photodiode, the simulation could reproduce the tendency of TC pulse height reduction depending on the area of single-ion hit.

3. Microbeam irradiation onto a diamond film

A 2-μm thick CVD multi-crystalline diamond film was irradiated by 10.5 MeV Au ion microbeams with a beam size of 2-3 μm and a scan size of 36 x 41 μm^2. Irradiation dose was changed in 5 steps from 9.4 to 56 $pC\mu m^{-2}$. After irradiations, an optical microscope and a secondary electron imaging were obtained for irradiated region of the diamond film as shown in Fig. 4 (a) and (b), respectively. 10 MeV Au ions stop in the film to transfer their whole energy to it. Therefore, radiation damage can easily seen optically and also by SEI. Analysis of damage effect will be in further investigation.



(a) (b) (c)

Fig. 2 Three simulated results to reproduce measured one in analysis with a Weiull disribution function. (a), (b) and (c) relate to irradiation areas of 1 x 1, 10 x 10 and 50 x 50 μm^2, respectively.

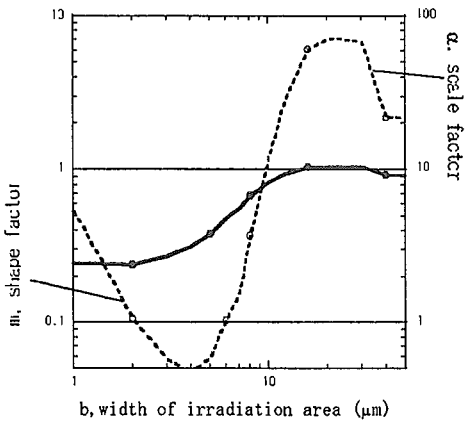
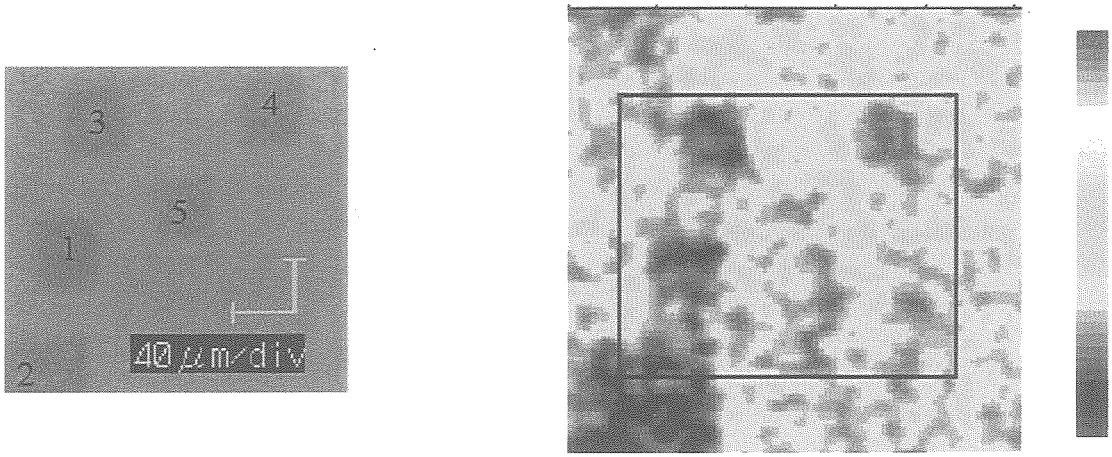


Fig. 3 Shape parameters *m* (rigid line) and scale parameter α (dashed) versus *b* by Weibull analysis for simulated results of 15 MeV Ni irraiation.

References

1)T.Kamiya, T.Sakai, T.Hamano, T.Suda and T.Hirao, Nucl. Instr. And Meth. B130 (1997) 285.
2)T.Kamiya, T.Suda and R.Tanaka, Nucl. Instr. And Meth. B118 (1996) 423.
3)T.Sakai, T.Hamano, T.Suda, T.Hirao and T.Kamiya, Nucl. Instr. And Meth. B130 (1997) 498.
4).Nashiyama, T.Hirao, T.Kamiya, H.Yutoh, T.Nishijima and H.Sekiguchi, IEEE Trans. On Nucl. Sci. 40, No.6 (1993) 1935.
5)T.Kamiya, T.Sakai, Y.Naitoh and T.Hirao, Nucl. Instr. And Meth. B158 (1999) 255.
6)T.Kamiya, T.Sakai, T.Hirao and Y.Naitoh, TIARA Ann. Rep. 1998, JAERI-Review, 99-025 (1999) 220.



(a) (b)

Fig. 4 Observation of 10 MeV Au microbeam irradiated areas of the diamond film by (a) optical microscope and (b) secondary electron imaging with the same Au microbeam.

7.10 Development of a High-Energy Microbeam Single Ion Hit Technique for Bio-Medical Applications

T.Kamiya, W.Yokota, Y.Kobayashi*, M.Oikawa, M.Taguchi* and M.Cholewa**
Advanced Radiation Technology Center, JAERI
*Department of Radiation Research for Environment and Resources, JAERI
**The School of Physics, The University of Melbourne, Australia

1. Introduction

A single ion hit technique is useful to introduce large radiation effect to specific local area of various biological cells. This technique has been introduced to the high-energy microbeam system on a vertical beam line of the AVF-cyclotron [1]. While similar techniques have been developed at several facilities to hit individual cells in the atmosphere for bio-medical applications [2-4], the advantage of our system is using high-energy (more than 10 MeV/u) heavy ions, which can induce single damages in biological cells, respectively. A fundamental technology of single ion hit was established at the heavy ion microbeam system connected to a 3 MV tandem accelerator [5,6].

An automated beam positioning technique, on the other hand, is required for individual irradiation of large number of cells in a crowd of those, which may be spread on a holder randomly in practical use. An automatic cell recognition system that consists of an optical microscope, sample stages and a computer system has been introduced to get information of positions of adequate cells to be hit in a shorter period.

This paper outlines the total system combined with a single ion hit system. It also shows experimental results obtained with this system.

2. Automated Cell Recognition and Beam Positioning System

A fully automated cell recognition and beam positioning system, which consists of an off-line and an on-line system. Pictures of sample stages for those systems and a schematic illustration of the system function are shown in Fig. 1.

The off-line system recognizes cell samples to be irradiated using a software package (AUTOSCOPE) [7], which has image processing functions to obtain positional data from a CCD camera image. The samples, which have been processed by the off-line system, are transferred to the on-line system together with the sample holder having a couple of fiducial marks on it. The on-line system combined with the single ion hit system can irradiate samples using a software package IRRADIATE [7] according to the database obtained by the off-line system.

3. Preliminary test

In order to demonstrate the performance of this system, an automated pattern drawing with single ion hit was made using 460 MeV Ar ions and a CR-39 plate. A 'daruma' pattern, which was shown in Fig. 2 (a) schematically, was printed tenuously by an ink jet printer on transparent film, so that every ink dot can be isolated to each other. A database for ink dots, which is shown in Fig. 2 (b) as a plotted image, was obtained and stored by AUTOSCOPE in the off-line system. A CR-39 plate set on the on-line stage was irradiated with 460 MeV Ar ions microbeams by IRRADIATE according to the database. As shown in Fig. 2 (c), a whole 'daruma' image could be transferred to the CR-39 film by the automated drawing as a etch pit pattern. A zoomed image of a region enclosed by a square in Fig. 2 (c) shows etch pits formed by single ion injections (ten ions per point) followed by chemical etching with 60 °C, 6 N (normal) NaOH solution for six hour.

4. Summary

An automated single cell irradiation

system combined with a high-energy heavy ion microbeam system was developed on the vertical microbeam line of the AVF cyclotron in TIARA. Reliability of the automated sample recognition and beam positioning system was tested using a printed 'daruma' pattern as a sample and a CR-39, a nuclear track detector, as an irradiation target instead of real cells. A 'daruma' shaped single ion hit patterns was drawn successfully in this experiment. This was the first step to utilize the high-energy heavy ion microbeam and single hit system. The next will be observation of individual radiation effect in real biological cells.

References

1) Y.Kobayashi, M.Taguchi, T.Shimizu, S.Okumura and H.Watanabe, J. Radiat. Res. 36(4) (1996) 290.

2) M.Folkard, B.Vojnovic, G.Schettino, M.Forsberg, G.Bowey, K.M.Prise, B.D.Michael, A.G.Michette and S.J.Pfauntsch, Nucl. Instr. And Meth. B130 (1997) 270.

3) C.R.Geard, D. J. Brenner, G. Randers-Pehrson, and S. A. Marino, Nucl. Instr. and Meth. B54, 411-416 (1991).

4) L.A.Braby, Scanning Microscopy, 6, 167-175 (1992).

5) T.Kamiya, T.Sakai, T.Hamano, T.Suda and T.Hirao, Nucl. Instr. And Meth. B130 (1997) 285.

6) T.Kamiya, T.Suda and R.Tanaka, Nucl. Instr. And Meth. B118 (1996) 423.

7) M.S.Krochmal, G.Laken, I.D.Larsen, L.Fiddes, G.Parkhill, K.Dowse, Autoscan Systems Pty. Ltd., Australia.

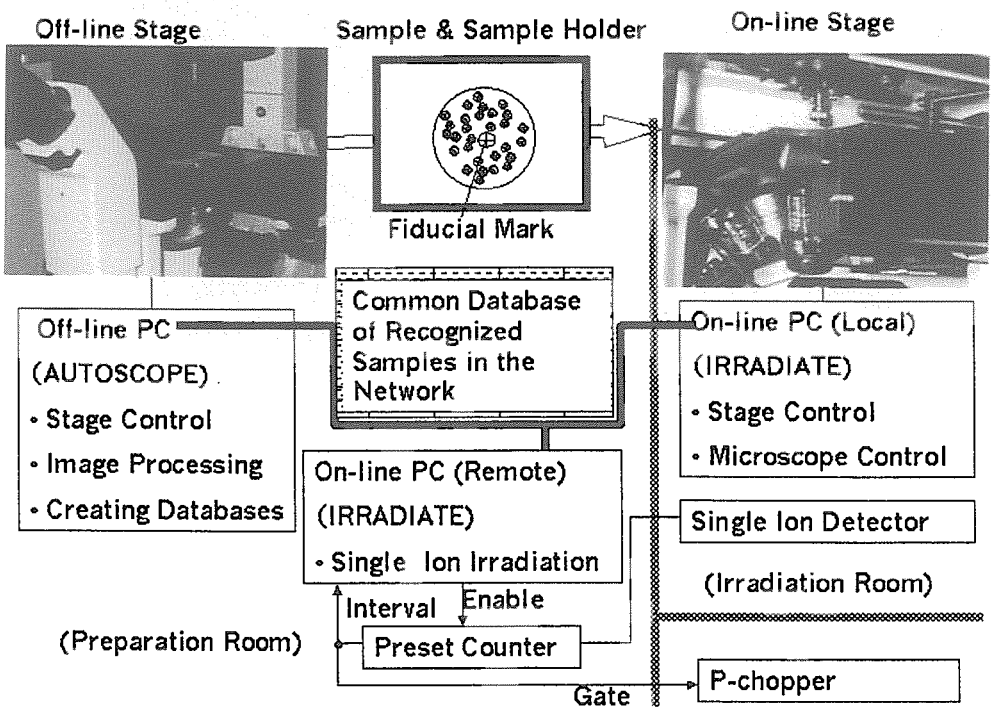


Fig. 1 Pictures of sample stages for the off-line system (left) and the on-line one (right) and a schematic illustration of the system functions. A micro-aperture can be seen in the picture of the on-line stage. The common database of the recognized samples created by AUTOSCOPE on the off-line system can be accessed through the network by the on-line system for IRRADIATE.

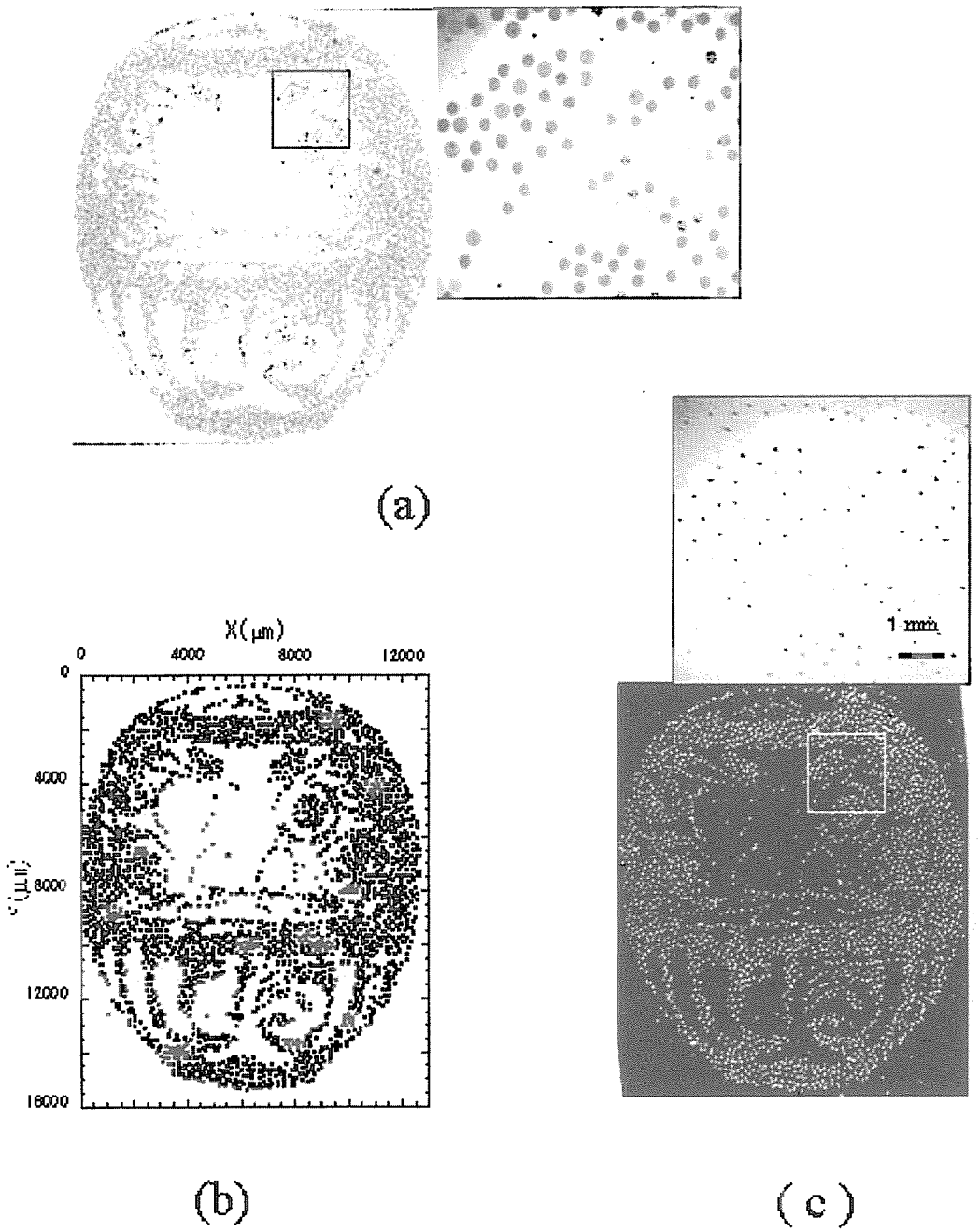


Fig. 2 (a) A 'daruma' image printed on a transparent film to be set at the off-line stage. 'Daruma' is a Japanese doll (a symbol of luck). A magnified image for the region enclosed by a square shows dots created by an ink jet printer. (b) A plotted image according to the database, in which about 2,500 points were recognized and stored by the off-line system. (c) A whole 'daruma' pattern on CR-39 drawn with etch pits by 460 MeV Ar ions (10 ions per point) at the on-line stage according to the 'daruma' pattern. Each dot looks dilating more than a real size of a etch pit, due to light scattering at taking picture. A magnified picture by an optical microscope for the same region as (b) shows real size of it.

8. Radiation Shielding for Accelerator Facilities

8.1 Study of Particle Size Distribution of Radioactive Aerosols Formed by Irradiation of 65 MeV Quasi-monoenergetic Neutrons 267
A.Endo, H.Noguchi, S.Tanaka, Y.Kanda, Y.Oki, T.Iida, K.Sato, and S.Tsuda

8.2 Measurement of Neutron Dose behind Iron Shield with Tissue Equivalent Proportional Counter 270
Y.Nakane, Y.Sakamoto, Y.Harada, S.Tanaka, and T.Nunomiya

8.3 Development of Neutron Monitor Using a Liquid Scintillator 273
E.Kim, A.Endo, S.Tsuda, F.Takahashi, M.Yoshizawa, Y.Yamaguchi, S.Tanaka, T.Shiomi, T.Nunomiya, R.A.H.Danielle, and T.Nakamura

This is a blank page.

8.1 Study of Particle Size Distribution of Radioactive Aerosols Formed by Irradiation of 65 MeV Quasi-monoenergetic Neutrons

A. Endo[1)], H. Noguchi[1)], Su. Tanaka[2)], Y. Kanda[3)], Y. Oki[3)], T. Iida[4)], K. Sato[1)] and S. Tsuda[1)]

[1)]Department of Health Physics, [2)]Advanced Radiation Technology Center, JAERI

[3)]Radiation Science Center, KEK

[4)]Graduate School of Nuclear Engineering, Nagoya University

1. Introduction

Radiation protection against induced airborne radionuclides is one of the key issues for radiation safety in the development of an intense spallation neutron source using a high-power proton accelerator.[1)] In estimating the internal dose due to the intake of airborne radionuclides, their physicochemical properties, such as particles size of aerosol and chemical form of gas, are significant factors.

The purpose of the present study is to clarify formation mechanism and size distribution of radioactive aerosol particles generated in high-energy radiation fields for the internal dose evaluation. The size distributions of ^{38}Cl, ^{39}Cl and ^{84}Br aerosols formed from irradiation of argon and krypton containing di-octyl phthalate (DOP) aerosols by 65 MeV quasi-monoenergetic neutrons were measured. The formation mechanism of the radioactive aerosols is discussed on the basis of the attachment reaction of the radioactive atoms to the DOP aerosols.

2. Experimental

The experiment was carried out using the quasi-monoenergetic neutron source facility of TIARA. Fig. 1 shows a block diagram of experimental setup. It consists of an irradiation chamber, an aerosol generator and two particle size analyzers. The irradiation chamber made of stainless steel (27 cm diameter and 100 cm length) equipped with acrylic windows was placed in the beam axis of the LC0 course.

Argon gas containing the DOP aerosols was used as the irradiation samples. First, the irradiation chamber was filled with high-purity argon (purity > 99.995 %). The DOP aerosols were generated from liquid DOP dissolved in 2-propanol using an atomizer and a dryer. After confirming with the scanning mobility particle sizer that the particle size distribution to be lognormal, the DOP aerosols were introduced into the argon-filled irradiation chamber. The prepared sample was irradiated with the 65 MeV quasi-monoenergetic neutron beam for 60–120 min. The neutron fluence rate at the acrylic window of the irradiation chamber was 2.3×10^4 cm^{-2} s^{-1} in the monoenergetic peak (61.0–69.0 MeV).

After the irradiation, γ-ray spectroscopy and particle size analysis were carried out for the sample. The γ-ray spectrum was measured for aerosol particles collected with a membrane filter. The size distribution of the aerosol particles was measured using the electrical low-pressure impactor (Model ELPI-2000, Dekati). For the number size distribution, an electrical current from the charged particles collected in each impactor was recorded by the respective electrometer. For the activity-weighted size distribution, the collection substrates of the impactor stages were removed after the sampling, and their radioactivities were measured using a gas-flow counter.

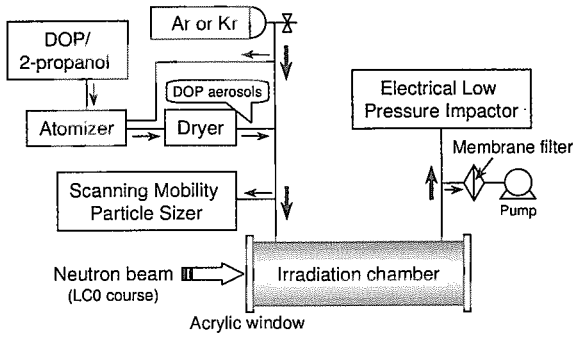


Fig. 1 Block diagram of the experimental setup.

Irradiation using krypton gas containing the DOP aerosols was also carried out in order to see nuclide dependence for the particle size distribution of radioactive aerosols.

3. Results and Discussion

For irradiation of the argon gas with the DOP aerosols, the radioactive aerosols of ^{38}Cl and ^{39}Cl, formed from the (n, 2np) and (n, np) reactions of ^{40}Ar, were found as shown in Fig. 2(a). On the other hand, these aerosols were not observed after the irradiation of argon for the same irradiation time and the neutron fluence rate (Fig. 2(b)). It was confirmed that the production of non-radioactive aerosols was not found in the argon atmosphere under the present beam and irradiation conditions. These results indicate that the formation of radioactive aerosols requires the presence of the non-radioactive aerosol particles.

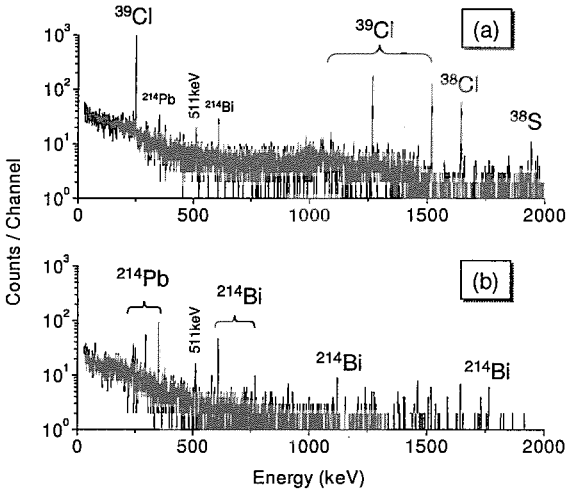


Fig. 2 Gamma-ray spectra of the membrane filters. (a) Irradiation of argon gas with the DOP aerosols; (b) irradiation of argon gas only.

Fig. 3 shows the number size distribution and the activity-weighted size distribution of the irradiated sample of the argon gas with the DOP aerosols. The activity-weighted size distribution was obtained from the total activity of ^{38}Cl and ^{39}Cl. It was found that the activity-weighted size distribution is greater than that of the number size distribution. This result is similar to those found in the previous study dealing with the ^{7}Be, ^{24}Na and ^{38}S aerosols in the proton accelerator tunnel.[2–4)]

The radionuclides formed through the nuclear reactions by high-energy particles would have large kinetic energies and/or charges at their birth and interact with the surrounding as hot atoms. After completion of these hot atom reactions, part of them is likely to attach to the surrounding non-radioactive aerosols in order to form radioactive aerosols with a certain particle size. Thus, the size distributions shown in Fig. 3 could be analyzed on the basis of the simple attachment model.

The particle size distribution of the radioactive aerosols formed by the attachment could be determined by multiplying the size distribution of the non-radioactive aerosols, $N(r)$, by the attachment coefficient, $\beta(r)$, where r is the particle radius. $N(r)$ was determined from a fitting of the experimental data assuming the lognormal distribution. The values of $\beta(r)$ was calculated from the following equation.[3,5)]

$$\beta(r) = \frac{\pi r^2 \bar{\nu}}{1 + (\bar{\nu} r / 4D)}$$

where $\bar{\nu}$ is the average velocity and D is the diffusion coefficient.

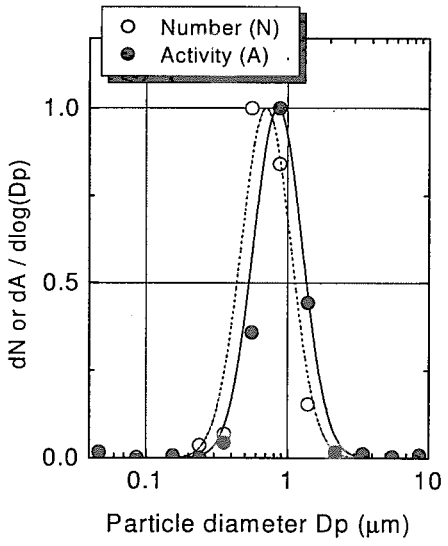


Fig. 3 Particle size distributions obtained using the ELPI. ○: Number size distribution; ●: activity-weighted size distribution. Dotted line: fitted distribution of the DOP aerosols assuming the lognormal distribution; solid line: computed distribution of the radioactive aerosols.

Fig. 3 also shows the computed size distributions of the DOP aerosols and the radioactive aerosols. The geometric mean diameter and the standard deviation of the DOP aerosols deduced from the fitting of the experimental data were 0.7 μm and 1.5, respectively. It is shown from the figure that the calculated size distribution of the radioactive aerosols based on the size distribution of the DOP aerosols agrees with the experimental data.

For irradiation of the krypton gas with the DOP aerosols, the formation of the ^{84}Br aerosols were observed. The activity-weighted size distribution of the ^{84}Br aerosols agreed with that expected from the number size distribution of the DOP aerosols and the attachment model, as discussed for the ^{38}Cl and ^{39}Cl aerosols.

In the 12 GeV proton accelerator tunnel, most of the aerosol particles in the air are of sub-micron size, produced through the radiation-induced reaction during the machine operation, and their main components have been identified as sulfate and nitrate aerosols.[2,6] It was suggested that the radioactive aerosols of ^{7}Be, ^{24}Na and ^{38}S are formed by the attachment of the radioactive atoms, produced by the nuclear spallation, to the non-radioactive aerosols.[2–4] It was found from the present study that the size distribution of the ^{38}Cl, ^{39}Cl and ^{84}Br aerosols formed by the 65 MeV quasi-monoenergetic neutron irradiation can be explained by this simple attachment model. These results indicate that the radioactive aerosols generated in high-energy radiation fields are formed by the simple attachment process of the radioactive atoms to the surrounding aerosol particles, independent of the kind of aerosols and radioactive atoms.

4. Summary

The particle size distribution of ^{38}Cl, ^{39}Cl and ^{84}Br aerosols formed from the irradiation of argon and krypton containing the DOP aerosols by high-energy neutrons was studied using the quasi-monoenergetic neutron source of TIARA. The activity-weighted size distribution of the radioactive aerosols can be well explained by the simple attachment model of the radioactive atoms to the DOP aerosols. The result of the present study indicates that the particle size distribution of the radioactive aerosols formed in the air of high-energy accelerator facilities can be estimated from the size distribution of the non-radioactive aerosols and the attachment model.

References

1) The Joint Project Team of JAERI and KEK. JAERI-Review 99-020 (1999).

2) K. Kondo, H. Muramatsu, Y. Kanda and S. Takahara. Int. J. Appl. Radiat. Isot. 35, 939-944 (1984).

3) H. Muramatsu, K. Kondo and Y. Kanda. Appl. Radiat. Isot. 39, 413-419 (1988).

4) Y. Oki, K. Kondo, Y. Kanda and T. Miura. J. Radioanal. Nucl. Chem. 239, 501-505 (1999).

5) L. Lassen and G.Rau. Zeit. Phys. 160, 504-519 (1960).

6) A. Endo, Y. Oki, Y. Kanda, T. Oishi and K. Kondo. Radiat. Prot. Dosim. 93, 223-230 (2001).

8.2 Measurement of Neutron Dose behind Iron Shield with Tissue Equivalent Proportional Counter

Y. Nakane[1], Y. Sakamoto[2], Y. Harada[1], S. Tanaka[3] and T. Nunomiya[4]
[1]Center for Neutron Science, JAERI, [2]Department of Health Physics, JAERI,
[3]Advanced Radiation Technology Center, JAERI,
[4]Department of Quantum Science and Energy Engineering, Tohoku University

1. Introduction

Because of lacking of experimental data for neutron dose evaluations above 20 MeV, the calculation code used for shielding design of accelerator facilities has not been validated efficiently from the viewpoint of dose evaluation. The neutron spectra behind iron and concrete shields have been measured for 40- and 65-MeV quasi-monoenergetic neutrons with a liquid scintillation detector at TIARA of JAERI, and compared with the calculated ones[1-3]. Calculated spectra were in good agreement with measured ones. In the present study, dose distribution and microdosimetric spectra were measured on and inside a plastic phantom placed behind iron shield with a tissue equivalent (TE) detector for the 65-MeV quasi-monoenergetic neutrons at TIARA.

2. Experiments

Figure 1 shows a cross sectional view of the experimental arrangement. Quasi-monoenergetic source neutrons of about 65-MeV were produced in 5.2-mm thick ^{7}Li-target (99.9% enriched) bombarded with 68-MeV protons. Source neutrons emitted in the forward direction were introduced to a 10.9-cm-diameter x 220-cm-long iron collimator embedded in a shielding wall and a 10.9-cm-diameter x 85-cm-long additional collimator on a movable stand, while proton beam penetrating through the target was bent down by a clearing magnet to a Faraday cup. A 20-cm-thick iron test shield was placed for the present work at the exit of the additional collimator. The 30 x 30 x 30 cm^3 slab phantom made of polymethyl methacrylate (PMMA) was placed after the test shield at the position of 558

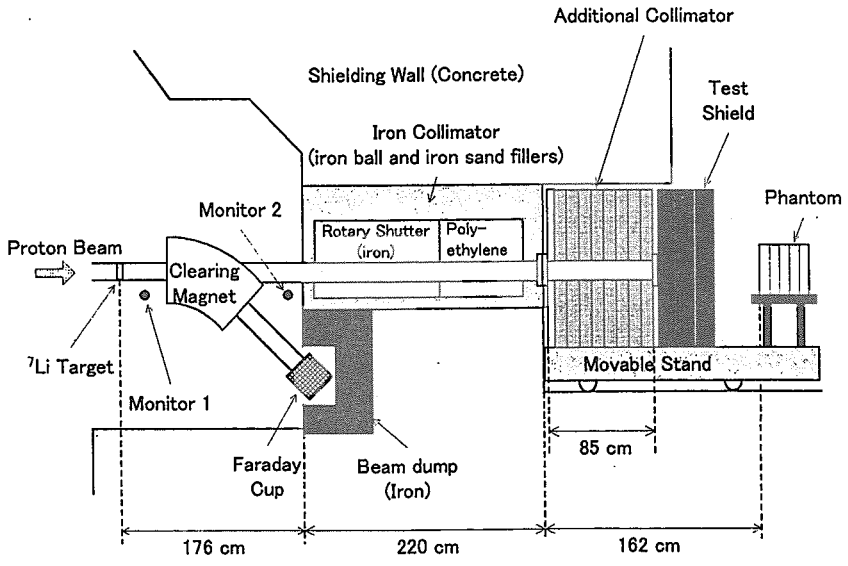


Fig. 1 Cross sectional view of the experimental arrangement

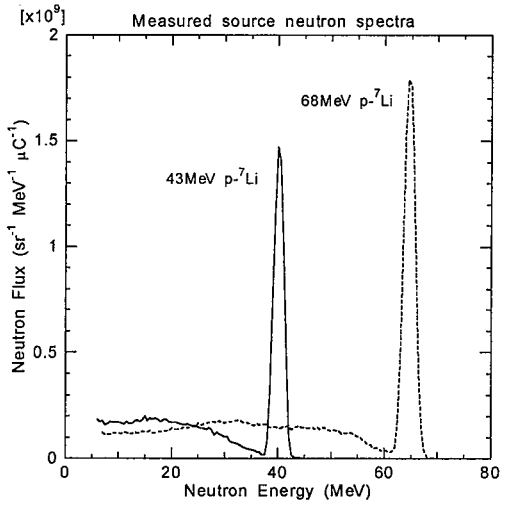


Fig. 2 Measured spectra of source neutrons by using the BC501A detector [1)]

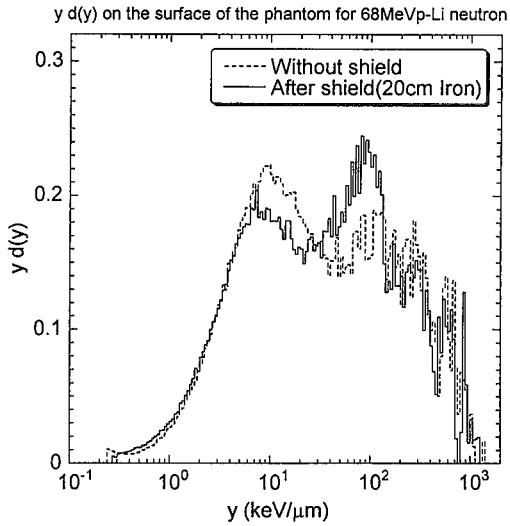


Fig. 3 Microdosimetric spectra measured by the TEPC

cm from the Li target.

Source neutron spectra above 10 MeV have been measured[1)] by the TOF method with a 12.7-cm-diameter x 12.7-cm-long BC501A liquid scintillation detector as shown in Fig. 2. The intensity of neutrons at the irradiating position was monitored with the proton beam Faraday cup and two fission counters placed near the target and the collimator, of which efficiencies had been calibrated from the measurement[4)] of absolute intensities by using a proton-recoil-counter-telescope (PRT). Error of neutron intensity monitoring was estimated to less than 7%.

Dose distribution and microdosimetric spectra on the surface and at the depth of 2, 3.5, 5 and 15 cm in the phantom were measured along the center line of the phantom by using a tissue equivalent proportional counter (TEPC) (Far West Technology Inc., Model LET-SW1/2). The counter consists of a 1.27-cm-diameter TE plastic sphere, a collecting wire of stainless steel and an 2.0 cm outer diameter aluminum shell outside the TE sphere used as a vacuum tight container. The counter was filled with a propane-based TE gas at the pressure of 9.03 kPa.

3. Results and discussion

Figure 3 shows the microdosimetric spectrum on the surface of the phantom measured behind the iron shield and without the shield, where the d(y) is normalized to unity. The figure shows that the discrepancy between the two results is found for the y region from 5 to 130 keV/μm. A peak position of about 80 keV/μm measured behind the shield is higher than that of about 9 keV/μm measured without the shield because the energy of neutrons penetrating through the shield is lower than that without the shield, and large dE/dx for low-energy protons in MeV region. The contribution of each particle to the absorbed dose can be roughly estimated from the spectra. The contribution of low-energy protons with deposition energy from 40 to 130 keV/μm is large to the absorbed dose for the measurement behind the shield, while that of recoil protons by 65 MeV neutrons with deposition energy from 5 to 30 keV/μm is large for the measurement without the shield.

Figure 4 shows absorbed dose distributions in the phantom measured behind the shield and without the shield. The ratio of absorbed dose measured behind the shield to that measured without the shield is shown in Figure 5. It is found from the figure, the value of absorbed

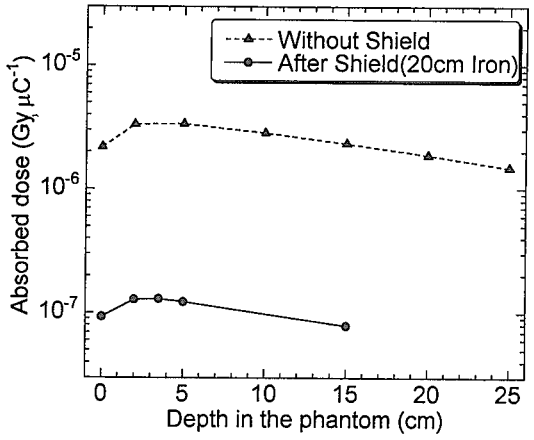


Fig. 4 Absorbed dose measured in the phantom

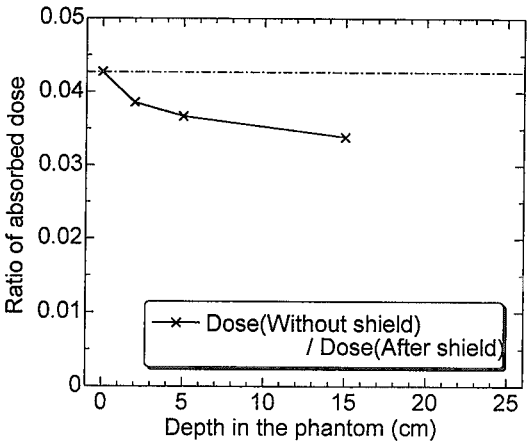


Fig. 5 Ratio of absorbed dose

dose measured behind the shield is attenuated from that measured without the shield to the factor of 1/23 to 1/30. Because neutron energy is lower for the measurement behind the shield, the tendency of attenuation in the phantom is larger for the measurement behind the shield than that without the shield.

Average quality factor in the phantom was obtained from the microdosimetric spectra measured by the TEPC and the quality factor, Q(y), given in ICRU-40[4]. Figure 6 shows average quality factors measured behind the shield and without the shield. It is found that the discrepancy between the two results is small.

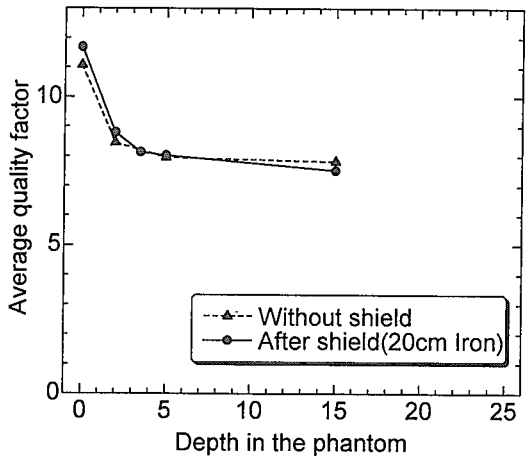


Fig. 6 Average quality factor measured in the phantom

Average quality factor rapidly decreases at the depth up to 3.5cm, while that is almost constant at the deeper position of the phantom. This may be ascribed to the attenuation of low-energy component of source neutrons.

References

1) N. Nakao, H. Nakashima, T. Nakamura, Sh. Tanaka, Su. Tanaka, K. Shin, M. Baba, Y. Sakamoto and Y. Nakane, Ncul. Sci. Eng., 124 (1996) 228-242.
2) H. Nakashima, N. Nakao, Sh. Tanaka, T. Nakamura, K. Shin, Su. Tanaka, H. Takada, S. Meigo, Y. Nakane, Y. Sakamoto and M. Baba, Ncul. Sci. Eng., 124 (1996) 243-257.
3) N. Nakao, M. Nakao, H. Nakashima, Su. Tanaka, Y. Sakamoto, Y. Nakane, Sh. Tanaka and T. Nakamura, J. Nucl. Sci. Technol. 34(4) (1997) 348-359.
4) ICRU Report 40 (1986).

8.3 Development of Neutron Monitor Using a Liquid Scintillator

E. Kim[1], A. Endo[1], S. Tsuda[1], F. Takahashi[1], M. Yoshizawa[1], Y. Yamaguchi[1], Su.Tanaka[2], T. Shiomi[3], T. Nunomiya[3], R.A.H. Danielle[3] and T. Nakamura[3]
[1] Department of Health Physics, [2] Advanced Radiation Technology Center, JAERI
[3] Department of Quantum Science and Energy Engineering, Tohoku University

1. Introduction

Intense neutron sources using high-power proton accelerator have been developed for various fields of study, such as nuclear physics, material physics, radiotherapy. Radiation monitoring of the neutrons in these facilities is very important for radiation safety management for workers and the members of public.

The purpose of this study is to develop a neutron monitor that can evaluate dose of neutrons in the energy range from thermal energy to 100 MeV. In this work, a spectrum weight function (G function) method[1,2] is applied to a liquid scintillator and boron-loaded liquid scintillator that are usually used as a neutron spectrometer. This paper describes the principle of the G function method and the calculation method of the G function. Next, the measurement method of pulse height spectrum is presented. Applicability of the present method for neutron dose evaluation is discussed.

2. Calculation of spectrum weight function

Neutron dose, H, in a radiation field is evaluated by Equation (1) using neutron energy spectrum, which is obtained by unfolding of pulse height spectrum.

$$H = \int h(E) \cdot \phi(E) dE, \qquad (1)$$

where $h(E)$ is the dose conversion coefficient and ϕ(E) is the neutron energy spectrum.

Assuming an operator, $G(E_R)$, that correlates response function of detector with dose per unit neutron fluence, $h(E)$ is expressed as Equation (2) using $G(E_R)$

$$h(E) = \int R(E,E_R) \cdot G(E_R) dE_R, \qquad (2)$$

where $R(E,E_R)$ is the response function of detector. Using Equations (1) and (2), H can be written as follows:

$$H = \int \left(\int R(E,E_R) \cdot G(E_R) dE_R \right) \cdot \phi(E) dE$$
$$= \int P(E_R) \cdot G(E_R) dE_R, \qquad (3)$$

where $P(E_R)$ is the pulse height spectrum of detector. Therefore, using the operator $G(E_R)$, H can be directly evaluated from the pulse height spectrum by multiplying the $G(E_R)$ using Equation (3).

To calculate the $G(E_R)$ in Equation (2), it is necessary to obtain the response function of the detector and the dose conversion coefficients. A set of response functions[3] of the liquid scintillator was calculated by the SCINFUL-R code[4] for incident neutron energies up to 80MeV and by the CECIL code[5] above 80MeV. The response function of the boron-loaded liquid scintillator was evaluated using the pulse height spectra measured in the neutron field. The ambient dose equivalent conversion coefficients were taken from ICRP Publ. 74 [6].

The $G(E_R)$ in Equation (2) was determined by an unfolding method using successive approximation[7]. On calculating the $G(E_R)$ function, maximum iteration frequency was set to be 20 to avoid oscillation by more iterations.

3. Experiment

To verify the response function of the scintillator and the neutron dose evaluated by the G function, measurements of the pulse height distribution were carried out using some different neutron sources which have continuous energy spectra, mono-energetic spectra and quasi mono-energetic spectra. The experiment in the neutron field having the continuous energy spectra was performed using the neutron sources ^{252}Cf and ^{241}Am-Be of FRS at JAERI[8]. The pulse height spectra for the mono-energetic neutrons and quasi mono-energetic neutrons were measured at FNL in Tohoku University[9] and at TIARA in JAERI[10], respectively.

Figure 1 shows the experimental arrangement at TIARA. In order to evaluate the response function of the boron-loaded liquid scintillator, measurements of pulse height spectra of this scintillator were carried out using quasi mono-energetic neutrons of 41MeV and

65MeV produced by the ^{7}Li(p, n) reaction and a white neutron source by the Cu(p, n) reaction.

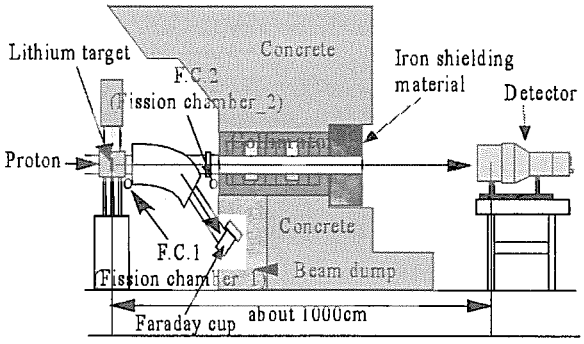


Figure 1 Experimental arrangement at TIARA.

4. Results and discussion

Figure 2 shows the G functions of the liquid scintillator and the boron-loaded liquid scintillator for ambient dose equivalent estimation. The G function below 0.1MeVee of the boron-loaded liquid scintillator was obtained from the light output of alpha particles produced by the ^{10}B(n, α) reaction.

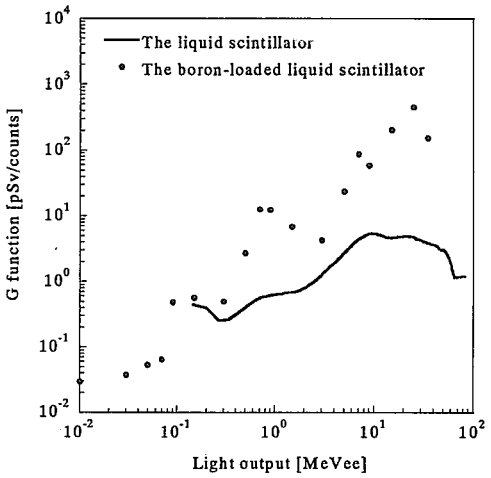


Figure 2 G functions of the liquid scintillator and the boron-loaded liquid scintillator calculated for ambient dose equivalent estimation.

Table 1 shows the neutron ambient dose equivalent that was directly evaluated by pulse height spectrum using the G function of the liquid scintillator. This table shows also the neutron dose obtained from neutron energy spectrum in order to confirm validity of dose evaluation by the G function. Doses for neutrons above 15MeV are in very good agreement with those by energy spectrum as ratios of 0.9 to 1.1. On the other hand, for ^{252}Cf, ^{241}Am-Be and 2MeV neutrons, the ratios of the dose evaluated by the G function to that by the neutron energy spectrum are 0.63, 0.74 and 0.45, respectively. This is because the contribution of dose by pulse height below threshold level, which was set to remove noise component and to reduce the dead time in measurements, is high in the neutron sources of the ^{252}Cf, ^{241}Am-Be and 2MeV. The discrepancies shall be improved by adjusting the threshold level during measurement and the extrapolation of low light components. From these results, it was found that neutron dose in the energy range from a few MeV to 100MeV can be obtained directly from the pulse height spectrum of the liquid scintillator by the G function method.

In the case of the boron-loaded liquid scintillator, neutron events below 1MeV were discriminated using the alpha particles produced by the thermal capture reaction of ^{10}B(n, α) reaction. The response function of the alpha particles was distributed around 0.06MeVee[11]. However, in the radiation field that gamma back-ground is high, neutron events below 1MeV couldn't be discriminated because of the low light output components of electron produced by gamma. It was concluded from this reason that the G function method cannot be applied to the boron-loaded liquid scintillator.

5. Summary

An evaluation method of neutron dose in the energy range from a few MeV to 100MeV has been developed using the liquid scintillator combination with the G function. The validity of the G function for the liquid scintillator was confirmed from comparison of the dose obtained by G function and the dose calculated from energy spectrum.

On the other hand, the boron-loaded liquid scintillator was found to be unsuitable as monitor for neutron in the energy range from thermal energy to 100MeV because the discrimination for neutron events below 1MeV was very difficult due to the low light output of the alpha particle. However, by using the response function evaluated from experimental results, boron-loaded liquid scintillator is available as a neutron spectrometer. As the next step of this study, a hybrid neutron detector consisting of a liquid scintillator and a lithium glass scintillator was designed to detect the thermal neutron by the ^{6}Li(n, α) reaction. This hybrid neutron detector will be tested in the neutron field of TIARA.

Table 1 Comparison of ambient dose equivalent by the G function and the energy spectrum

Neutron source (Facility)	Dose by the G function (G) [pSv/fluence]	Dose by the energy spectrum (D) [pSv/fluence]	Ratio (G/D)
^{252}Cf_FRS	1.57E-03	2.48E-03	0.63
^{241}AmBe_FRS	2.10E-03	2.83E-03	0.74
2MeV_FNL	1.88E+02	4.20E+02	0.45
15MeV_FNL	5.71E+02	5.40E+02	1.06
41MeV_TIARA	8.41E+02	9.67E+02	0.87
64MeV_TIARA	1.08E+03	1.08E+03	1.00

References

1) S. Moriuchi, JAERI 1209 (1998) (in japanese)
2) Y. Oyama, K. Sekiyama and H. Maekawa, Paper for Eleventh Topical Meeting in the Technology of Fusion Energy, June 19-23, 1994, New Orleans, Lousiana, U.S.A.
3) E. Kim, A. Endo, Y. Yamaguchi, M. Yoshizawa, T. Nakamura and T. Shiomi, Proc. 10th International Congress of The International Radiation Protection Association, May 14-19, 2000, Hiroshima, Japan.
4) S. Meigo, Nucl. Instrum. Methods A401, 365-378 (1997)
5) R. CECIL, B. Anderson and R. Madey, Nucl. Instrum. Methods 161,439 (1979)
6) International Commission on Radiological Protection. ICRP Publication 74 (Oxford: PERGAMON Press) (1997)
7) W.N. McElroy, S. Berg and T. Crockett, AFWL-TR-67- 41. Vol. I-IV (1967)
8) J.P. Dumais, M. Yoshizawa and Y. Yamaguchi, JAERI-Tech 98-005 (1998) (in japanese)
9) M. Baba, M. Takada, T. Iwasaki, S. Matsuyama, T. Nakamura, H. Ohguchi, N. Nakao, T. Sanami and H. Hirasawa, Nucl. Instrum. Methods A376, 115-123 (1996)
10) M. Baba, Y. Nauchi, T. Iwasaki, T. Kiyosumi, M. Yoshioka, S. Matsuyama, N. Hirakawa, T. Nakamura, Su. Tanaka, S. Meigo, H. Nakashima, Sh. Tanaka and N. Nakao, Nucl. Instrum. Methods A428, 454-465 (1999)
11) M.C. Miller, R.S. Biddle, S.C. Bourret, R.C. Byrd, N. Ensslin, W.C. Feldman, J.J. Kuropatwinski, J.L. Longmire, M.S. Krick, D.R. Mayo, P.A.Russo, M.R. Sweet et al. Nucl. Instr. and Meth. A422, 89-94 (1999)

This is a blank page.

9. Accelerator Technology/TIARA General

9.1 Beam Energy Measurement by the Time-of-flight Technique ····· 279
S.Okumura, K.Arakawa, M.Fukuda, I.Ishibori, H.Tamura, T.Agematsu, T.Nara, W.Yokota, S.Kurashima, and T.Ishimoto

9.2 Study of Beam Energy Spreads for the Single-ended Accelerator using Nuclear Resonance Reactions (II) ····· 281
Y.Ishii, A.Chiba, I.Takada, and S.Tajima

9.3 Measurement of MeV Energy Cluster Ion Beam Current ····· 283
Y.Saitoh, and Y Nakajima

9.4 Development of Transparent-type Beam Current Monitor ····· 285
Y.Nakajima, Y.Saitoh, and S.Tajima

9.5 Development of the Sub-micron Ion Beam System at keV Range ····· 287
Y.Ishii, A.Isoya, K.Arakawa, T.Kojima, and R.Tanaka

9.6 Temperature Control of Cyclotron Magnet for Stabilization of Magnetic Field Strength ····· 290
S.Okumura, S.Kurashima, T.Ishimoto, W.Yokota, K.Arakawa, M.Fukuda, Y.Nakamura, I.Ishibori, T.Nara, T.Agematsu, and H.Tamura

9.7 Present Status of JAERI AVF Cyclotron System ····· 293
Y.Nakamura, T.Nara, T.Agematsu, I.Ishibori, H.Tamura, S.Kurashima, W.Yokota, M.Fukuda, S.Okumura, K.Akaiwa, To.Yoshida, S.Ishiro, A.Matsumura, Y.Arakawa, Tu.Yoshida, S.Kanou, A.Ihara, and K.Takano

9.8 Renewal of Computer Control System of the 3MV Tandem Accelerator ····· 296
K.Mizuhashi, S.Uno, A.Chiba, R.Kitchen, and S.Tajima

This is a blank page.

9.1 Beam Energy Measurement by the Time-of-flight Technique

S. Okumura, K. Arakawa, M. Fukuda, I. Ishibori, H. Tamura, T. Agematsu, T. Nara, W. Yokota, S. Kurashima, T. Ishimoto*
Advanced Radiation Technology Center, JAERI
*Department of Material Development, JAERI

1. Introduction

We have developed a movable time-of-flight (TOF) counter system[1-2] for precise measurement of the absolute energy and the energy width of a beam extracted from the cyclotron. Especially, the energy width is a very important parameter for production of a micro beam, which is constructing now. We are developing a flat-top acceleration system to provide a beam with small energy width enough for the micro beam production.

A TOF method is easier way to determine the absolute energy for the variety of ion species with high precision than the other energy measurement method such as the crossover technique and analyzing magnet. The precision of the energy measurement depends on uncertainty in measurement of the flight path length and the flight time. In order to achieve 10^{-3} precision of energy measurement, uncertainty less than 10^{-3} in both measurements of the flight path length and the flight time is needed. The flight path length can be obtained easily with uncertainty less than 10^{-3}, because a normal digital scale has enough precision. On the other hand, it is difficult to obtain enough precision in the flight time measurement, because the time accuracy of a normal time analyzing system is around 100ps, which is not enough for the flight time of a few ten nano seconds in a flight length of a few meters.

We have applied a time analyzer, pTA(ORTEC, model 9308), to measurement of the flight time, because its time resolution is superior to normal time analyzers.

2. Experimental Setup

The system, shown in Fig.1, has two ion detectors: one is a transmission detector, a start detector, using a thin foil and an electron multiplier for production of a start signal when an ion pass through the detector, and the other, a stop detector, for production of a stop signal.

To achieve precise measurement of the beam energy, we adopted relative measurement of the length and the time difference, which eliminates inaccuracy of decision of the time and the length criteria. Using this system, the length and the time difference can be obtained by moving the stop detector.

The detectors are installed in different vacuum chambers connected with bellows. The chamber for the stop detector can be moved at the maximum distance of 2 m. The relative change of the length can be measured with a magnetic scale with a precision less than 0.1 mm. The relative change of the time difference is obtained as a shift of the time spectrum peak measured with the pTA by using timing signals from the start and stop detectors.

3. Measurements and Results

We measured the beam energies of a cocktail beam M/Q = 2 (heavy ions), in which we can change ion species quickly, and a 50 MeV (nominal) proton beam. The accuracy of the energy measurement system was almost achieved within 0.1 %, but in case of the cocktail beam, energy loss of the beam at foil transmission of the start detector is more than 0.1% of the energy. We measured the beam energies of cocktail M/Q = 2, 108.1, 323.7, and 431.9 MeV, corresponding to $^{4}He^{2+}$, $^{12}C^{6+}$, and $^{16}O^{8+}$, respectively. In the measurement of the 50 MeV proton beam, we obtained the beam energy and the beam width. Figure 2 shows the relation between the flight length and the flight time. The beam energy, calculated from the data in the maximum flight length of 2 m, is 48.19 MeV. The beam width was evaluated from the relation between the flight length and the increase of the width of the time spectra, as shown in Fig. 3. From the ratio of 8 ps/2m, the beam width ratio, dE/E, was estimated to be 0.1 %.

References

1) S.Okumura et. al., JAERI Review 99-025, 249-250.
2) S.Okumura et. al., The 12th Sympo. on Accel. Sci. and Tech., Wako, Japan (1999) 471-472.

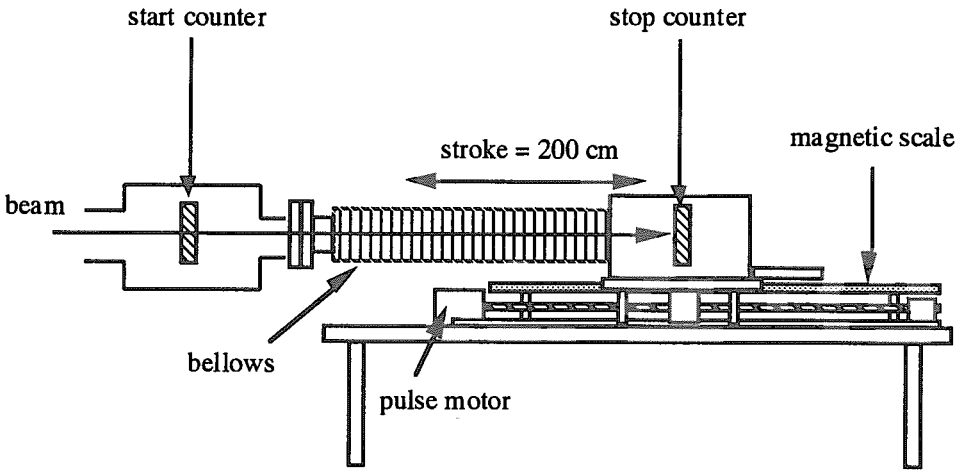


Fig. 1 Layout of the movable TOF counter system.

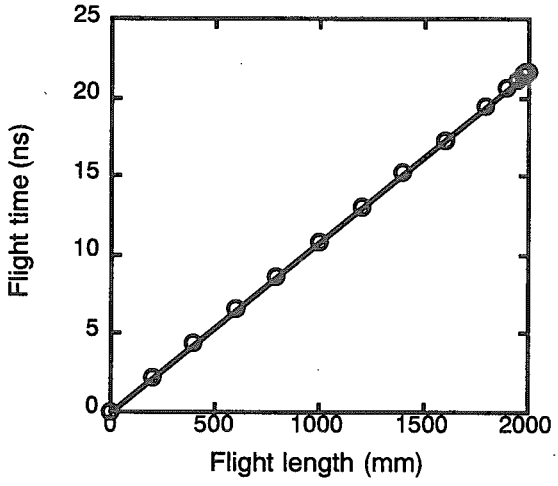


Fig. 2 Relation between the flight length and the flight time for 50 MeV proton beam.

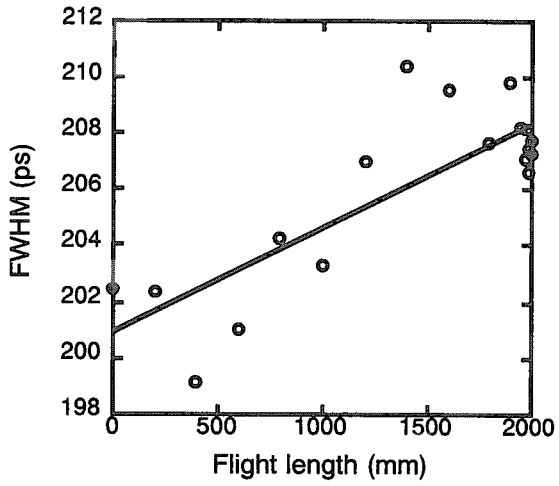


Fig. 3 Relation between the flight length and the increase of the width of time spectra for 50 MeV proton beam.

9.2 Study of beam energy spreads for the single-ended accelerator using nuclear resonance reactions (II)

Yasuyuki Ishii, Atuya Chiba, Isao Takada and Satoshi Tajima
Advanced Radiation Technology Center, JAERI

1 Introduction

The beam energy spread produced from the single-ended accelerator with the voltage stability of $\pm 1 \times 10^{-5}$ has been measured using nuclear resonance reactions in its accelerator voltage range from 1 MeV to 3 MeV. The resonance nuclear reactions of $^{27}A\ell(p,\gamma)^{28}Si$ and $^{24}Mg(p,\gamma)^{25}A\ell$ with the narrow resonance reaction widths were selected in order to achieve the hight energy resolution of 10^{-5} order; The former resonance widths are the 100 eV and 50 eV at the 0.992 MeV and 1.317 MeV proton beams, respectively and the latter ones are the 150 eV and 300 eV at the 2.010 MeV and 2.400 MeV ones, respectively [1].

This measurement method of the beam energy spread is required the direct injection of the H^+ beam in the target, because the beam energy spread depends on the energy resolution of an analyzing magnet. The thin foil targets of $A\ell$ and Mg were placed in the 0-degree beam line in order to measure the bean energy spread by means of directly injecting the H^+ beam into their targets with H_2^+ and H_3^+ beams.

The beam energy spreads at the 0.992 MeV and 1.317 MeV have already been measured in the previous studies [2, 3]. The measurement of the energy spreads using the $^{24}Mg(p,\gamma)^{25}A\ell$ was, however, difficult of detections of the γ-rays from its reaction. The difficulty lay on the detection of the the same energy γ-ray produced from the reactions at injedcted different energy nuclei. When the H^+ and H_2^+ beams at about 2.4 MeV were injected into the targets, each nucleus energy of those beams were about 2.4 MeV and 1.2 MeV, respectively. The same 1.317 MeV γ-ray was emitted, because each nucleus reacted to the Mg target at 2.4 MeV and 1.2 MeV.

H^+ ion analyzed in the 0-degree line was obtained by winding the beam trajectory in the acceleration tube by means of four removable magnets to eliminate electrons in its tube. The resonance nuclear reactions of $^{24}Mg(p,\gamma)^{25}A\ell$ at 2.010 MeV and 2.400 MeV were clearly detected by the reduction of noise γ-ray using the H^+ beam. Thereby, the beam energy spreads were measured at four different energies employing the two kinds of reactions. The average beam energy spread was about 4×10^{-4}.

2 Experimental

The experimental chamber was connected with the 0-degree line. The both thin $A\ell$ and Mg foils of about 600 Å thick with 0.3 mm Ta backing were used as the targets to reduce the γ-ray noise from the other reactions. Although control resolution of the acceleration voltage is at 1 kV step, the suppression voltage up to 5 kV was applied at the target to control the beam energy less than 1 keV.

The beam was analyzed in the 0-degree line using the removable magnets attached on the acceleration tube and optimizing the condition injecting the beam into the acceleration tube from the the RF-ion source. The analyzed beams, shown in

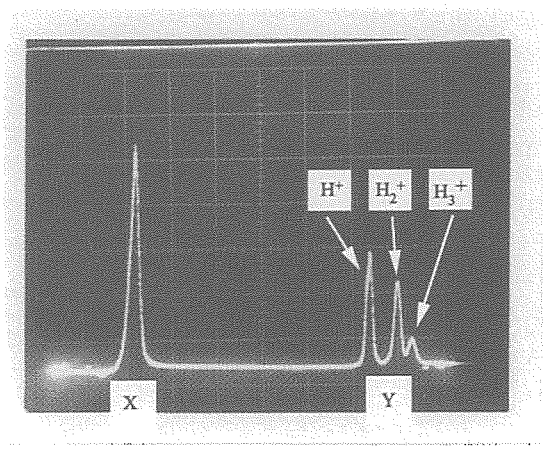


Figure 1: Picture of beam profile analyzed at the beam monitor

the fig.1, were checked by the beam profile moni-

tor placed in about 3 m from the exit of the accelerator. The accelerator energy was calibrated within the rate of the energy deviation of $(\frac{\Delta E}{E} =)1 \times 10^{-4}$ before starting the measurement of the beam width in order to detect the fine beam energy width less than 1 keV. The yields of γ-ray were detected by the 2 inch NaI detector. The detected γ-ray energies of the $^{27}Al(p,\gamma)^{28}Si$ were 1.77 MeV at the both beam energies of 0.992 and 1.317 MeV and those of the $^{24}Mg(p,\gamma)^{25}Al$ were 3.77 and 3.65 MeV at γ-ray energies of at 2.010 and 2.400 MeV, respectively. The number of ions injected in the target was normalized by counting the back scattered H^+ using the SSD (silicon surface detector).

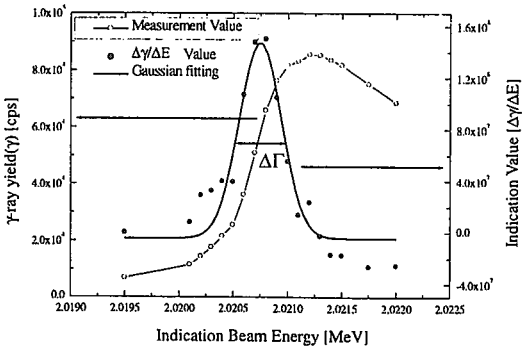
3 Results and summary

The measurement results of the beam energy spreads between the beam energy based on the accelerator controller (indication energy) and γ-ray yield on using Mg targets were shown in Fig.2 (A). The differential values of γ-ray yield at the indication value are also shown in fig.2 (B). The differential values were fitted using Gaussian distribution as considering the beam energy spreads to be nearly equal to its distribution in these measurement results. The beam energy spread was defined as Full Width Half of Maximum (FWHM, Γ) of the Gaussian distribution. The beam energy spreads were listed in Table-1 with the beam spread results of $^{27}Al(p,\gamma)^{28}Si$. The average beam energy spread was about 4×10^{-4}.

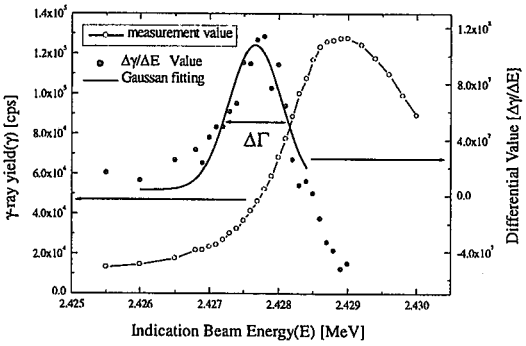
Table 1: Result of beam energy spread using the nuclear resonance reaction

Beam energy (E) [MeV]	Beam energy spread ($\Delta\Gamma$) ($\times 10^{-4}$) [MeV]	$\frac{\Delta\Gamma}{E}(\times 10^{-4})$
0.992	4.16	4.52
1.317	5.33	4.05
2.010	6.49	3.23
2.400	12.7	5.29

The beam energy spreads over 2.0 MeV were measured by using the method of analyzing the beam in 0-degree line. The the method of nuclear resonance reactions using the analyzing beam enables us to measure the beam energy spreads with the resolution of less than 1×10^{-4} in the acceleration voltage range from about 1 MeV to 2.4 MeV.



(A)



(B)

Figure 2: The γ-ray yield and the differential values $\frac{\Delta\gamma}{\Delta E}$ depended on the indication beam energy.(A):resonance energy is 2.010 MeV. (B):resonance energy is 2.400 MeV.

References

[1] J.W.Mayer and E.Rimini, "Ion Beam Handbook for Matirial Analysis", ACADEMIC PRESS, 1977, P.205

[2] Y.Ishii et. al. JAERI-Review 97-015, P.242

[3] Y.Ishii et. al. JAERI-Review 99-025, p.268

9.3 Measurement of MeV Energy Cluster Ion Beam current

Y. Saitoh, Y. Nakajima
Advanced Radiation Technology Center, JAERI Takasaki

1. Introduction

Interaction of high energy molecular or cluster ions to materials has attracted attention in points of fundamental research such as non-liner effects at the surface of a target. Recently, a small enhancement in energy loss was obtained for carbon and boron cluster ions comparing to their single ions at the same velocity [1, 2]. Large enhancement for metal sputtering yield by irradiation of gold cluster ions was also reported[3]. It is expected that the massive energy deposition introduced by cluster ion irradiation in a very small volume will lead to non-linier phenomena[4]. We have developed various kinds of MeV energy cluster and molecular ions with mass-separated beam current of nano ampere order by the TIARA 3 MV tandem accelerator. We can propel not only study of fundamental interactions mentioned above but also that of materials modification with the cluster ion beam.

Appling the cluster ion beam to materials modification, we must control the implanted ion dose into a target with measuring the accurate beam current. However, we observed that the value of measured beam current depended on materials of the target and irradiation time shown in the fig.1. This phenomenon was not observed for single ion irradiation. It suggests that the amount of secondly charged particles from a target irradiated by a cluster ion beam be different from that irradiated by a single ion beam because of the non-linier phenomena. Therefore, it is important to investigate the non-linier phenomena on secondly particles from a target

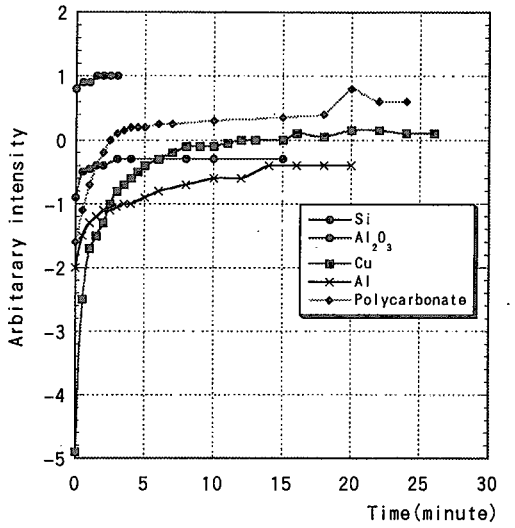


Fig.1 Measured beam currents of 6 MeV C_8 in various targets.

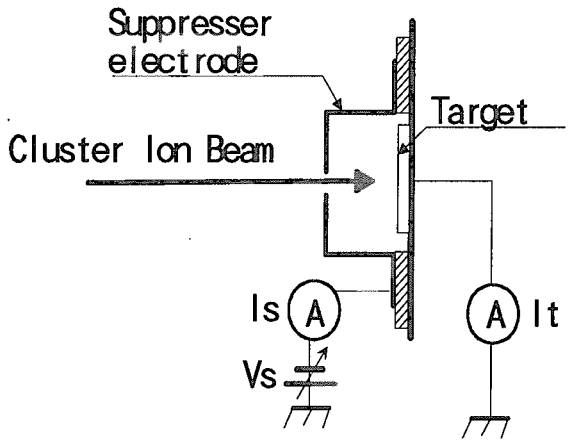


Fig. 2. Schematic drawing of a beam current monitor.

such as electrons and ions for each cluster in MeV energy region. In a preliminary study, we simultaneously measured a target beam current and a secondary charged particle current detected by a suppresser electrode that covered the target.

2. Experimental setup

The schematic drawing of a beam current monitor is shown in the fig. 2. The target current I_t and the suppresser current I_s are measured with digital pico-ampere meters (Advantest 8800) for the single carbon (C_1) ion irradiation and the cluster ion (C_8) irradiation, respectively. The voltage of the suppresser electrode is changed from –500 V to 500 V in the measuring.

3. Results

The beam current of the I_t and the I_s versus the voltage of suppresser electrode are plotted in the fig. 3 and the fig. 4 for C_1 and C_8 beam irradiation, respectively. In the case of C_1 irradiation, the I_s current is negligible comparing to that of the I_t. It means the most of secondary charged particles emitted from a target are electrons, and the negatively biased suppresser electrode repels them to the target. That is the usual function of a Faraday cup. In the case of C_8 irradiation, the negative value of the I_t was observed in the voltage of –50 V to –100 V. And, the I_s always indicates a positive value, which has the maximum value in the voltage between –50 V and –100 V. It implies that the amount of secondary positive ions from a target is not negligible in the C_8 irradiation, and some of the positive ions are run away from the beam monitor, being accelerated by the negative voltage of the suppresser electrode. Therefore, the measured beam current by a usual Faraday cup should indicate a smaller value than that of true beam current in large cluster ion irradiation.

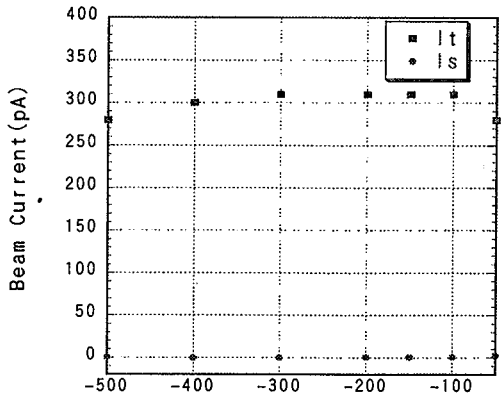


Fig. 3. Measured beam current of C_1.

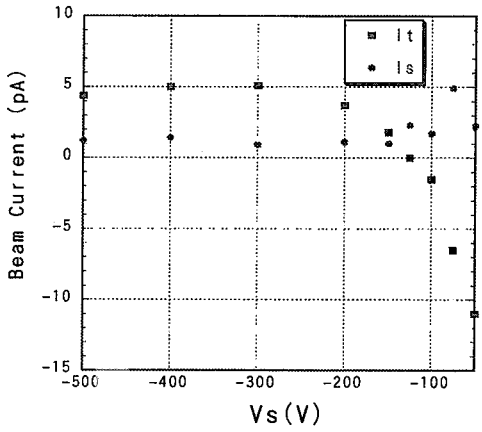


Fig.4. Measured beam current of C_8

References

1) K.Baudin, A.Brunelle, M.Chabot, S.Della-Negra, J.Depauw, D.Gardès, P. Håkanoss, y. Le Beyec, A. Billebaud, M. Fallavier, J. Remillieux, J.C. Poizat, J. P. Thomas, Nucl. Instrum. and Methods. B 94 (1994) 341-344.

2) K. Narumi, K. Nakajima, K. Kimura, M. Mannami, Y. Saitoh, S. Yamamoto, Y. Aoki, H. Naramoto, Nucl. Instrum. and Methods. B 135 (1998) 77-81.

3) H. H. Andersen, A. Brunelle, S. Della-Negra, J.Depauw, D. Jacquet, and Y. Le Beyec, Phys. Rev. Lett. Vol. 80 No. 24 (1998) 5433-5436.

4) Ch.Tomaschko, D. Brandl, R. Kügler, Schurr, H. Voit, Nucl. Instrum. and Methods. B 103 (1995)407-411.

9.4 Development of Transparent-type Beam Current Monitor

Y.Nakajima, Y.Saitoh and S.Tajima
Advanced Radiation Technology Center, JAERI

1. Introduction

We are developing a transparent-type beam current monitor which is required measuring beam current for multiple coincide irradiation in TIARA facility.

There are two methods to continuously monitor the beam intensity during irradiation, one is the method measuring the secondary electrons emitted from wire probe, and other is that measuring the current collected on the probe. The former gives information of relative beam intensity depending on the ion species and the energy. The latter is able to measure the absolute beam current by completely suppressing the secondary electrons.

We measured some characteristics of secondary electron emitted from wire mesh using the test device, and we confirmed following facts.

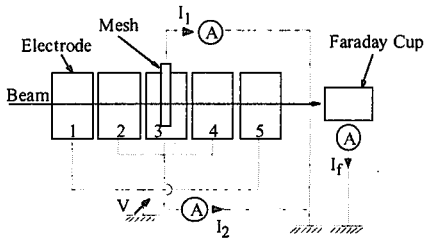
(1) Almost of secondary electrons emitted from the wire mesh are distributed to backward and they are increased with the beam energy.
(2) Sum of mesh current and secondary electron current is depended on suppressor voltage.

In this time, we measured the relationship between suppressor voltage and the sum of secondary electron current and mesh current using test device with Carbon, Oxygen and Gold ions of energy from 1 to 21MeV.

2. Experimental

Fig.1 shows measuring circuit of the test device consisted of five electrodes and the tungsten wire mesh. Five electrodes can use not only collector electrode to measure secondary electron current but also use as suppressor.

In this measurement, 2,3 and 4 electrodes were used as secondary electron collector and 1 and 5 as suppressor. When the mesh is inserted into the beam, the mesh collects a part of beam current (defined by the mesh size as the sampling ratio, δ) and also emits a lot of secondary electrons. Therefore the mesh current is negative at without suppressor voltage. The sampling ratio of the mesh was evaluated to be 0.069 by the geometrical calculation.



I_1:Mesh Curent
I_2:Secondary Electron at No.2,3 and 4 Electrode
I_f:Beam Current at Faraday Cup
V:Suppressor Voltage

Fig.1 Measuring circuit of the device

The current measurements were curried out by changing the suppressor voltage from –700V to +700V for various energy beams of C, O and Au ions. The standard beam current was measured by a Faraday cup installed at just behind beam line of the device.

3. Result

Fig.2 shows the mesh current, I_1, secondary electron current, I_2, and sum of them, I_m', as a function of suppressor voltage with 18MeV Au^{5+}. In this figure,

I_m' reaches to the plateau region at –200V. It suggests that almost secondary electrons emitted from the mesh are returned to the mesh or captured to the collector electrodes of the device. So, sum of the mesh current and the secondary electron current, I_m', can be treated as the full suppressed mesh current. The expected mesh current, I_m , was calculated from standard current, I_f ,and δ as follows; $I_m=I_f \cdot \delta$.

Expected mesh current, the suppressed mesh current and the ratio of them, I_m'/I_m, measured with various beam conditions are listed in Table.1. In the Table, I_m'/I_m, were not equal to 1.0 and distribute from 1.5 to 3.6. And also they depend on charge state of the beams, that is, they tend to decrease with charge state. Since, the number of secondary electron emitted from the material by ion bombardment does not depend on charge state of ion, these suggest that the difference from 1.0 of the ratio was caused by escaping the some secondary electrons from the device.

In the next step, we are going to improve the suppressor electrodes to capture all of the secondary electrons. And also it is important to define the accurate sampling ratio by the measurement with various beam condition.

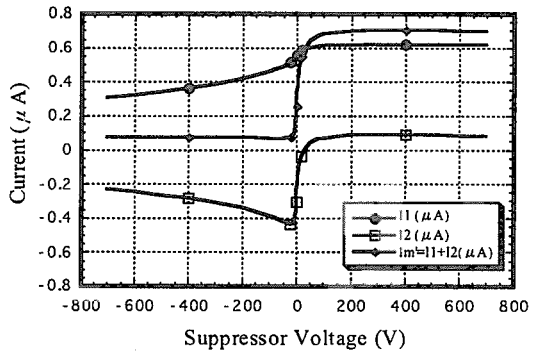


Fig.2 Mesh current, secondary electron current and sum of them as a function of suppressor

Reference
1) S.Tajima, I.Takada, et al., JAERI Tech 96-029(1996)
2) Y.Nakajima, Y. Saitoh, S.Tajima, TIARA Annual Report 1998 (JAERI-Review 99-025), 262-263
3) Y.Nakajima, Y.Saitoh, S.Tajima, TIARA Annual Report 1999 (JAERI-Review 2000-024), 280-281

Table.1 List of expected mesh current, suppressed mesh current and ratio of them

Ion Species	Beam Energy (MeV)	Standard Beam Current If(A)	Expected Current Im (A)	Suppressed Mesh Current Im' (A)	Ratio (Im'/Im)
C	1 (1+)	7.08E-7	4.93E-8	1.12E-7	2.27
	3 (1+)	3.50E-7	2.44E-8	6.38E-8	2.62
	6 (1+)	3.85E-7	2.68E-8	6.27E-8	2.34
	9 (2+)	1.94E-6	1.35E-8	2.37E-7	1.76
	12 (3+)	3.49E-6	2.43E-8	3.75E-7	1.54
	15 (4+)	1.45E-6	1.01E-7	1.63E-7	1.62
O	1 (1+)	2.84E-7	1.98E-8	4.58E-8	2.32
	3 (1+)	4.06E-7	2.83E-8	6.47E-8	2.29
	6 (1+)	1.69E-7	1.18E-8	4.12E-8	3.50
	9 (2+)	8.26E-7	6.24E-8	1.63E-7	2.61
	12 (3+)	2.47E-7	1.72E-7	3.87E-7	2.25
	15 (4+)	1.96E-6	1.36E-7	2.59E-7	1.90
Au	1 (1+)	3.29E-7	2.29E-8	5.23E-8	2.28
	3 (1+)	1.30E-7	9.05E-9	2.53E-8	2.80
	6 (1+)	1.03E-7	7.17E-9	2.59E-8	3.61
	9 (2+)	5.50E-7	3.83E-8	8.57E-8	2.24
	12 (3+)	9.36E-7	6.51E-8	1.27E-7	1.95
	15 (4+)	5.30E-7	3.69E-8	6.70E-8	1.82
	18 (5+)	2.84E-7	1.98E-8	4.29E-8	2.17
	21 (6+)	2.10E-7	1.46E-8	2.64E-8	1.81

9.5 Development of the Sub-micron Ion Beam System at keV Range

Y. Ishii[a], A. Isoya [a]*, K. Arakawa [a] T. Kojima [a] and R. Tanaka [b]
[a] Advanced Radiation Technology Center, JAERI
[b] Ion Beam Irradiation Service Co. Ltd.

1 Introduction

The sub-micron ion beam system has been developed using the original duoplasmatron-type ion source with the narrow energy spread of about 1eV and low energy of about 100 eV, and the focusing lens system with the magnification in the order of 10^{-4} to generate gas ion of about 100 keV with the beam width of 0.1 μm, e.g. H_2^+ or Ar^+ [1)-4)]. The focusing lens system consists of two acceleration lens in series along the beam trajectory: each lens has double functions of single aperture lens and beam acceleration in the uniform electric field. The beam width measurement device consisting of a sharp-edge, a Faraday cup and a detector of the position of sweeping edge with the resolution of less than 0.05 μm, was developed to estimate the beam width from the relation between sharp-edge position and the beam current[5)].

The 30 keV hydrogen ion microbeam was used as the first step to approach the 100 keV microbeam because it has bigger allowance in depth of focusing. The preliminary results demonstrate the production of 0.43 μm beam width. However, the beam width was about 2.5 times larger than the width estimated from the beam transport calculation. On the other hand, the slow drifting of the final beam focusing point from right to left in the fig.2 was observed during about 10 min. Two improvements of the system were: (1) additional voltage was applied to avoid perturbation electric field caused by secondary electrons in the drift space between two acceleration lenses, (2) the beam injection system, connecting upstream of the focusing lens system, was introduced to reduce the divergence angle of the incident beam in its lens system as shown in Fig.1. The later improvement enabled us to achieve the 0.28 μm beam and slightly beam drift within 0.3 μm. The microbeams

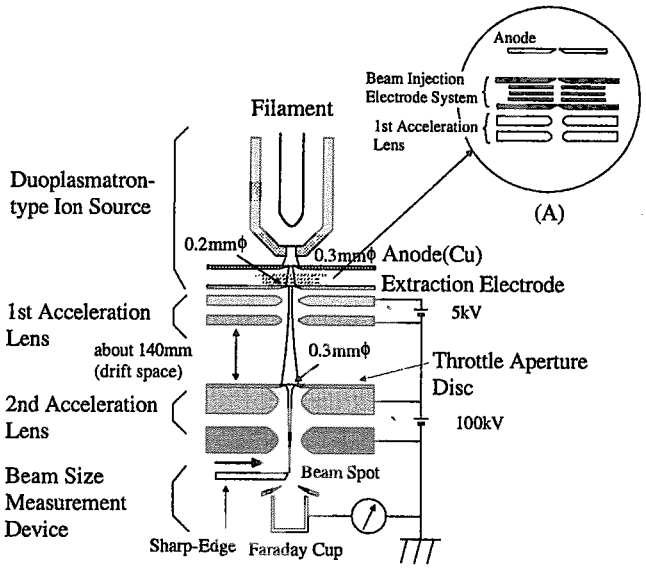


Figure 1: Schmatic diagram of the sub-microm ion beam system. The focusing lens system consists of the 1st and 2nd acceleration lenses. Inserted Drawing (A): the introduced electrode system

having the width down to 0.1mm and the beam position drift within their widths should be formed by the further improvement of the incident beam condition at the beam focusing system.

2 Preliminary Results on the Beam Width

The preliminary beam width measurement was carried out using the 30 keV hydrogen ion beam after sufficient warming up of the ion source. The beam current of about 10 μA was extracted from the anode aperture of 0.3 mmϕ after applying the voltage of about 100 V. The beam current of about 30 nA at the focusing lens system was measured on the throttle aperture disc in front of the second acceleration lens. The beam width at the throttle aperture disc

*An emeritus professor of Kyushu University, Hakozaki, Higashi-ku, Fukuoko-shi, Fukuoka, 812-8581 Japan and an invited researcher of Japan Atomic Energy Research Institute.

was estimated to be about 5 mmϕ from the spot colored by irradiation. The beam current of the tens pA was measured by the Faraday cup at the beam spot in Fig.1. The ion distribution at the beam spot was considered to be nearly uniform after passing through the small throttle aperture since the beam spot having 0.3 mmϕ width is defined into the center part of the 5 mmϕ defocused beam at the throttle aperture disc. The beam width measurements were repeated by five times scans of the shape-edge under the same condition during about 10 min. The relation between the sharp-edge position and the beam current is shown in Fig.2. The broken line and the dotted line were

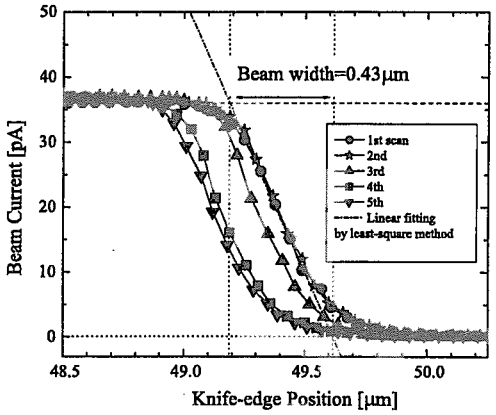


Figure 2: Preliminary result on the relation between the sharp-edge position and the beam current for 5 repeated the sharp-edge scans under the same condition. The beam energy was about 32keV. The beam width was estimated from the abscissa values of two intersection points of the three lines drawn by the least squire method. The minimum beam width value was also shown for discussion.

drawn at the plateau part of about 36 pA and the base line (0 pA) parallel to the x-axis. The dash-doted linear line was fitted by the least square method in the beam current decreasing part. The beam width was estimated from the abscissa values at the two intersection points of above three lines by assuming the uniform ion distribution. The beam width is 1.1 times wider than the one estimated assuming Gaussian ion distribution, which is on the over-estimation side. The maximum and minimum beam width were 0.44 μm and 0.41 μm, respectively. The average beam width values were 0.43 $\pm$ 0.05 μm. These values were about 2.5 times larger than the calculated one at 30 keV. The slow drift of the beam spot position within 0.3 μm was observed during about 10 min. It was practically negligible for beam width estimation, because the total time for the sharp-edge scanning across the beam spot was less than 20 s.

3 Improvement of the Beam Width and Beam Spot Drift

The dominant reasons of the increase of the beam width and the drift of the beam spot could be as follows: (1) the error in the electric field may be caused by the secondary electrons in the drift space between the first and the second acceleration lens, or (2) the beam divergence angle at the plasma lens which is formed between the lasma beam sheath and the extraction electrode may be different from the one pre-estimated by the beam transport calculation and/or fluctuate as the function of time. The drift of the beam spot within the range of some-micrometers might be caused by the change of the divergence angle of the order of 2×10^{-3} rad. The following experiments were tried to check these assumptions. The drift space was electrically independent of the between the two acceleration lenses in this improvement. Beam irradiation-induced secondary electrons at the throttle aperture disc were accumulated in the drift space. The voltage difference was made in the drift space to avoid the error electric field. The increase of beam width and the drift of the beam spot were still observed even applying voltages of 200 to 300 V to the two acceleration lenses. It suggests that (1) is not the dominant reason. The divergence angle at the first acceleration lens was re-adjusted to the designed one. The injection electrode system to set the parallel electric field between the anode and the extraction electrode was introduced for the adjustment of the divergence angle, as shown in the inserted figure (A) in Fig.2. The beam width of 0.28 μm was ultimately obtained as shown in Fig.3. The average beam width values were 0.33 $\pm$ 0.02 μm, though the drift of the beam spot was observed. The beam width was still about 1.6 times larger than the calculation one. This beam width is over-estimated width as mentioned in the above section. However, the result suggests that the beam width of less than 0.2 μm should be theoretically achievable by applying the voltage of about 100 kV to the second acceleration lens and accurate setting of the beam spot within the depth of focus. The further improvement of the beam injection condition at the beam focusing system is in progress aiming to achieve 0.1 μm beam

width and less the drift of the beam position within the limit of its beam width.

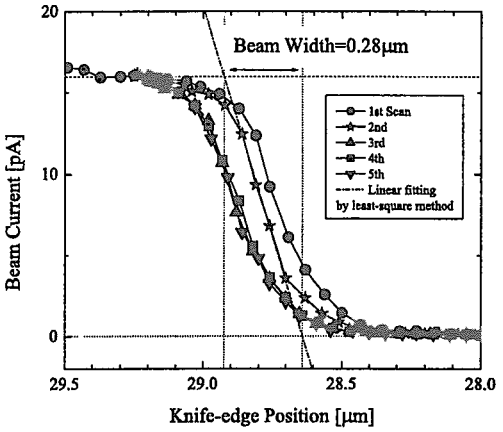


Figure 3: The result on the relation between the sharp-edge position and the beam current for 5 repeated the sharp-edge scans under the same condition after introduction of the injection electrode system. The beam energy was about 33 keV. The beam width was estimated from the abscissa values of two intersection points of three lines drawn by the least squire method. The minimum beam width value was shown for discussion.

References

1)Y. Ishii. et.al., JAREI-Reciew 98-016, P.257.
2)A. Isoya, Ulvac Technical Journal No.44(1996) p.42.
3)Y. Ishii et. al, Nucl. Instr. and Meth. B113(1996) 75.
4)Y. Ishii, R. Tanaka and A. Isoya, Nucl. Instr. and Meth. B113(1996)75.
5)Y.Ishii. et. al, JAERI-Review 99-025, P.25.

9.6 Temperature Control of Cyclotron Magnet for Stabilization of Magnetic Field Strength

S. Okumura, S. Kurashima, T. Ishimoto[1)], W. Yokota, K. Arakawa, M. Fukuda, Y. Nakamura, I. Ishibori, T. Nara, T. Agematsu, H. Tamura
Advanced Radiation Technology Center, JAERI,
[1)]Department of Material Development, JAERI

1. Introduction

It is known for many cyclotrons in the world that beam intensity gradually decreases when they are operated at a high magnetic field. Since the start of the cyclotron routine operation at TIARA in 1991, we have experienced a strong decrease of beam intensity during two days after the cyclotron magnet is excited at the main coil current higher than 500 A. In the typical case of 195 MeV $^{36}Ar^{8+}$ acceleration by the JAERI cyclotron at 820 A (1.6 T average magetic field), beam currents reduced to zero within ten hours after the cyclotron magnet was excited as shown in Fig.1. The magnetic field needed to be corrected every few hours by adjusting current of the outermost trim coil in order to recover the beam intensity.

This recovery process clearly showes that decrease in the magnetic field strength gave rise to the beam intensity decrease. On the other hand, the reason why the magnetic field drifted was unknown for a long time. We had a suspicion in 1995 that change in temperature of the cyclotron magnet might be a cause of the beam decrease. Therefore we accumulated the data of magnetic field strength of the cyclotron and temperature at 60 points on the cyclotron magnet yoke for more than two years. A clear correlation was found between the magnetic field strength and the temperature. We further carried out thermal conduction simulation by using the thermal analysis code "NASTRAN"[1)]. The simulation explained the temperature data well by tuning a parameter of thermal conductivity between the main coil and the yoke. As a result, it became apparent that the beam decrease was induced by temperature rise of the magnet yoke and the heat sources were the main coil (primary) and the trim coils (secondary). But its mechanism has not been made clear yet[2)],. We think that the cause of the beam decrease might be a complex of thermal expansion of the pole gap and the yoke volume and thermal change in magnetization of iron of the yoke and the pole.

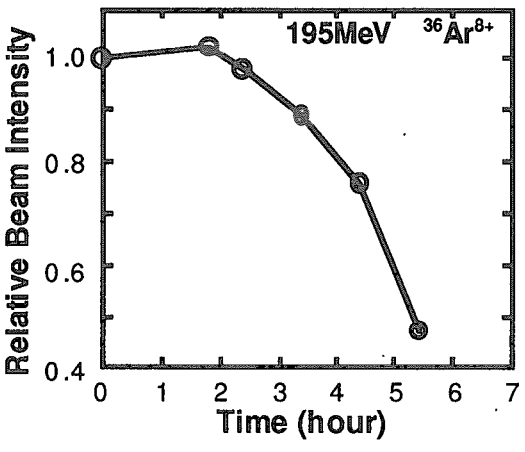


Fig. 1 Beam intensity decrease with time.

We decided to adopt a temperature control system to stabilize the magnetic field. The stabilization will provide us with great advantages in use of acceleration or irradiation techniques as well as in beam intensity stability. For example, in addition to the beam decrease, single-pulse beams, formed after two-hour tuning of the cyclotron and the chopping system, spread out to multi-pulse beams in twenty minutes. The stabilization will realize the steady single-pulse formation. Furthermore, the cocktail beam acceleration of M/Q=2 and 4 requires high stability of the magnetic field strength to keep low ratio of impurity ions. A heavy ion microbeam system, which will be constructed in 2002, also needs the high stability.

In the following sections, the outline of the stabilization system and the results of stability tests with the system are described.

2. Outline of Temperature Control System

The temperature control system was designed to reduce the temperature rise over the whole yoke less than 0.5°C 50 hours after excitation of the cyclotron magnet start. It consists of following two parts, each of which insulates heat conduction from the main coils and controls the trim coil temperature, respectively.

1) Thermal insulation between the main coil and the yoke by inserting temperature-controlled copper plates. The temperature of the plates is kept constant by water circulation in the hollow conductors embedded in them.
2) Temperature control of cooling water for the trim coils to keep temperature of the magnet pole surface constant. The water temperature is controlled so that the average of the inlet and the outlet temperatures is kept constant independently of the coil currents.

A new additional cooling unit controls three water loops independent of the existing cooling system: one is for the temperature-controlled copper plates and the others are for twelve trim coils. Since the trim coil #11 generates more than 50% of the total heat of the trim coils, the trim coil water loops are divided into two loops: for the trim coil #11 and for the other eleven trim coils, respectively. In each loop, average temperatures of the inlet and the outlet water can be controlled with an accuracy of ± 0.5°C.

3. Test Operation of Temperature Control System

The beam stabilization test was carried out under two different operating conditions of the temperature control system.

In the test under the first condition, the coolant temperature for the copper plates and the trim coils was set at 24°C, the yoke temperature before the cyclotron magnet was excited. The temperature of the yoke rose by 2 to 3°C in 50 hours, the rising rate was a half of the case without the temperature control system. The time, in which the beam intensity halved, was extended from 5 to 20 hours. The intensity decreased to 10 % of the initial intensity after 40 hours.

Although we had appreciable improvement, the temperature rise is several times as large as that designed. The rise of the yoke temperature in spite of the thermal insulation indicates that influence of other minor heat sources such as air in the cyclotron vault or conduction paths such as the gap between the main coil and the pole has became relatively larger.

Taking the results into account, the second condition described below was examined in order to further reduce the temperature rise without additional devices:

* Raising the yoke temperature at the start of the cyclotron operation up to about 26° C by keeping the temperature control system operated while the cyclotron is stopped, or during a weekend.
* Lowering temperature of the copper plates to absorb the heat conduction from the main coil to the pole through the gap.

As a result of the test, the temperatures rise of the yoke was less than 1°C after 50 hours. Figure 2 shows the change in the beam intensity with time. The decrease was about 10% of initial intensity. The magnetic field was also stabilized well as shown in Fig. 3.

4 Summary

The 195 MeV $^{36}Ar^{8+}$ beam was satisfactorily stabilized using the temperature control system. In order to meet various operation condition of the cyclotron, accumulation of operation data of

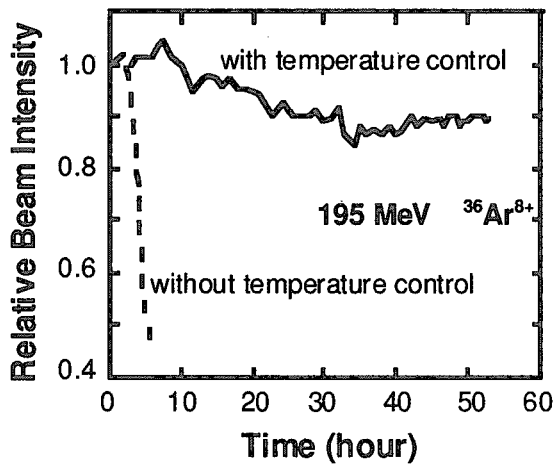


Fig. 2 Change in beam intensity with time comparing with and without the temperature control.

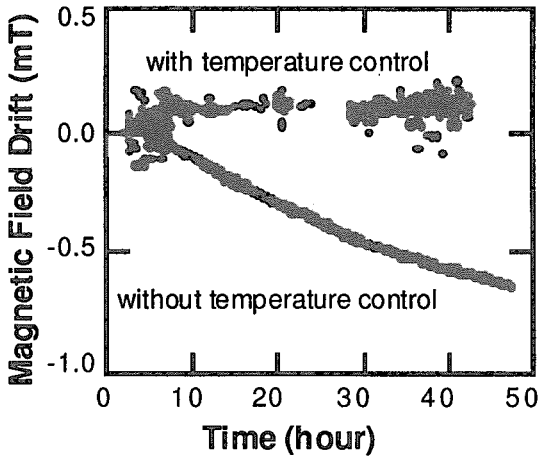


Fig. 3 Magnetic field drift. Data points with temperature control are scattered because of noise for an NMR probe.

the temperature control system is indispensable as well as more careful optimization of the system parameters.

Monitoring the magnetic field is one of the most useful tools for the stabilization. It is very difficult, however, to use an NMR probe in the acceleration space because of poor uniformity of the magnetic field and noisy environment. Monitoring the beam phase may be a good substitution to get information of an average change in the magnetic field at each radius.

Since the major conduction paths from the big heat sources were cut off, influence of the miner heat path of air gap between the main coils and the yoke has been relatively enhanced. In addition we sometimes observed influence of changing air temperature of the cyclotron vault. Therefore tight heat shields over a wide surface of the cyclotron yoke will be necessary for higher stability.

References

1)Y.Nakamura, S.Okumura, M.Sano, T.Nara, T.Ishimoto, S.Kurashima, W.Yokota, K.Arakawa, K.Saitoh, T.Fukuda, J.Kanakura, M.Fukuda, I.Ishibori, H.Tamura, T.Agematsu, JAERI TIARA Annual Report 1999, JAERI-Review 2000-024, 282-284.

2)M.Fukuda, K.Arakawa, S.Okumura, I.Ishibori, T.Nara, Y.Nakamura, W.Yokota, T.Agematsu, H.Tamura, A.Matsumura, JAERI TIARA Annual Report 1998, JAERI-Review 99-025, 251-253.

9.7 Present Status of JAERI AVF Cyclotron System

Y. Nakamura, T. Nara, T. Agematsu, I. Ishibori, H. Tamura, S. Kurashima, W. Yokota, M. Fukuda, S. Okumura, K. Akaiwa*, To. Yoshida*, S. Ishiro*, A. Matsumura*, Y. Arakawa*, Tu. Yoshida*, S. Kanou*, A. Ihara* and K. Takano*

Advanced Radiation Technology Center, JAERI
* Beam Operation Service, Co., Ltd.

1. Introduction

The JAERI AVF cyclotron system in TIARA facility has been operated smoothly without serious troubles since the first beam extraction in March, 1991 [1), 2)]. A cumulative operation time of the cyclotron system amounted to 29500 hours at the end of March in 2001. Yearly operation time is about 3200 hours on an average for last eight years as shown in Fig. 1.

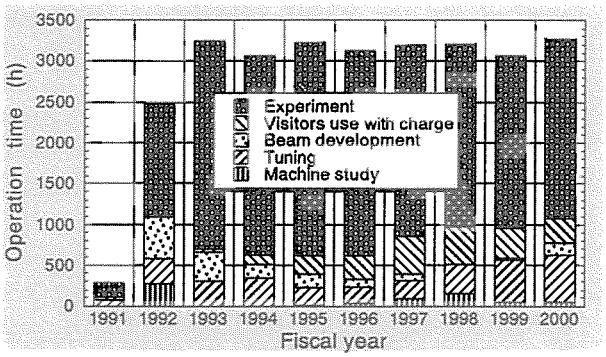


Fig. 1 Statistics of operation time and its utilization since 1991.

2. Present Status

2.1 Development and Improvement

The measures for the stabilization of the cyclotron beam were already carried out in March, 2000 [3)]. As an additional measure, the surface on the cooling pipe laid in the cyclotron pit room was almost covered with adiabatic layer so called "thermo-belt" because of the reduction of heat dispersion in the room.

At the present stage, we confirmed that the decrease of cyclotron beam was improved within 10 % by continuous operation of the exclusive cooling system [4), 5)].

A flat-top (FT) acceleration system for the JAERI AVF cyclotron has been designed to minimize the energy spread for the micro beam formation. The fifth harmonic of the main RF frequency will be used to construct the FT system.

We investigate carefully the structure, characteristics, power consumption and so on for the FT system using a MAFIA code [6)].

The control system consisting of personal computers for cyclotron was renewed completely in March, 1999 [7)]. A pair of liquid crystal displays were connected with the SCU to always monitor the operating condition on each control console. One set of the two control units on the console is shown in Fig. 2. The right display of the three is new one.

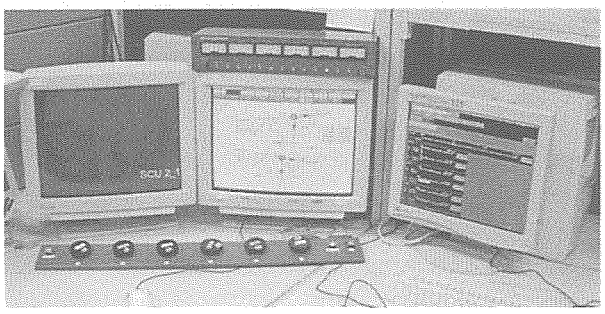


Fig. 2 New third (right) display connected with the SCU.

It had been pointed out that the beam trajectory just after the cyclotron was shifted upward. As a result of measurement, several magnets along the trunk beam transport line had sunk below maximum about 3 mm as illustrated in Fig. 3. These magnets were aligned again in original positions within the precision of 0.2 mm for the sake of guarantee of the good beam transportation.

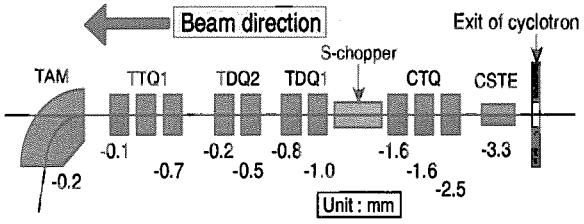


Fig. 3 The measurement data at several magnets along the trunk beam transport line. Numbers below the magnets show the vertical displacement of the sinkage.

Five controllers for TMP's installed in the switching magnet room on the first floor were moved to the cyclotron pit room in the basement where the radiation level is lower, because they had to be sometimes repaired so far owing to the accumulated radiation damage.

A new control rack was installed at the cable distribution area in the pit room as shown in Fig. 4. Of course, a lot of cables and wires for the controllers were also renewed and penetrated through the bent sleeves between two floors.

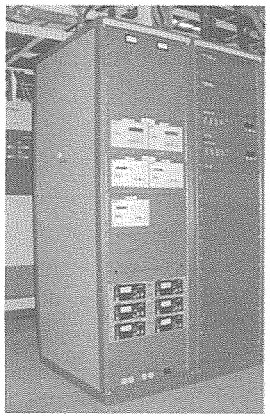


Fig. 4 New control rack for TMP's.

In order to improve the uniformity of beam fluence for the scanner, the phase control of triangular scanning wave in three beam scanners was made possible so that the scanning pitch on the target plane became to be narrower.

New scanning frequency of 0.25 Hz was added on the scanner equipped with LD course.

2.2 Maintenance and Repair

Four mechanical-seal pumps with electric motors for the circulation of cooling water were renewed preventively. The manufacturing period for these pumps is more than three months since they are usually begun to make after the order from a customer. These pumps had been operated for about 35000 hours since the installation in 1990.

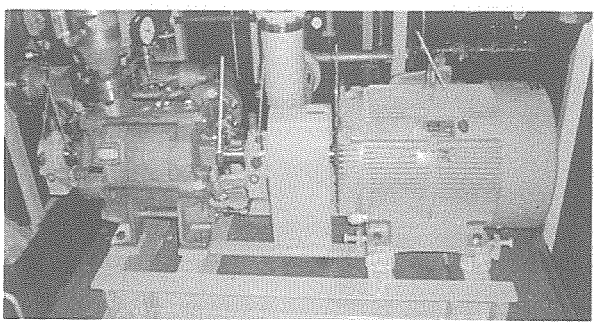


Fig. 5 An appearance of mechanical-seal pump. The rated flow rate of this pump is 56 m^3/h and the range of lift is 150 m.

An appearance of the pump for cyclotron system, when the factory test was done, is shown in Fig. 5.

Furthermore, the control mode for cooling tower on the building roof was also modified to the continuous operation using an inverter from the intermittent ON-OFF motion.

Serious water leakage from the magnetic channel occurred at the "Vebeo" fitting for the introduction of coil current. The metal fitting contacted directly with neighbor one because the shrinkable tube covering the fitting suffered from deep damage by heating for a long-term operation. Therefore, the meltdown was caused by rare-shortening of the metal fitting through large coil current.

We examined the difference of surface temperature between stainless steel and brass material for the metal fitting. A measurement result of saturated temperature is shown in Fig. 6. As the surface temperature on the shrinkable plastic tube was restrained below 70 ℃ with maximum coil current of 1430 A, finally we chose the "Swagelok" fitting made of brass.

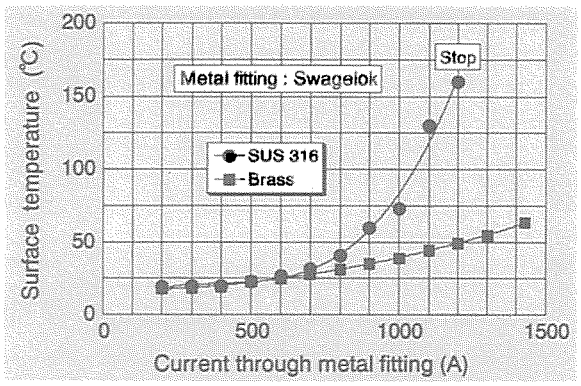


Fig. 6 A comparison of surface temperature between stainless steel and brass fitting.

The vacuum chamber of the OCTOPUS was filled fully with cooling water on account of the serious leakage. The OCTOPUS was disassembled completely for internal cleaning, polishing and replacement of gaskets. The HYPERNANOGAN was operated for the experiments about two weeks instead of the OCTOPUS.

In the periodical maintenance in last summer, principal items were performed as followings:

(1) Addition on several digital flow switches in the exclusive cooling system for the stabilization of cyclotron beam,

(2) Adjustment of the height and gradient of the dee electrodes,
(3) Replacement of main O-ring for the vacuum chamber of the cyclotron,
(4) Inspection of RF system and evaluation of RF characteristics,
(5) Periodical inspection for three beam scanners,
(6) Routine maintenance for four cryogenic pumps, each of which is the capacity of 4.0 m^3/s,
(7) Exchange of lubrication oil for about 50 rotary pumps.

In addition, several power supplies were periodically taken care of their performances and conditions.

3. Beam Acceleration Test

Two kinds of metallic ion species of 200 MeV $^{40}Ca^{9+}$ and 500 MeV $^{197}Au^{31+}$ were accelerated successfully using the HYPER-NANOGAN. The 25 MeV $^{2}D^{+}$ was newly developed with good transmission by the same manner as the acceleration of cocktail beam based on 50 MeV $^{4}He^{2+}$.

These ion species have been already delivered for various experiments in last fiscal year.

A number of ion species accelerated by JAERI AVF cyclotron so far are summarized in Table 1.

Table 1 The list of ion species accelerated by JAERI AVF cyclotron. The symbol of "T_{ext}" in Table 1 is defined by a ratio of the beam current at the Faraday cup just after the cyclotron to that at 900 mm of the cyclotron radius. The "T_{all}" is a ratio of the beam current extracted from the cyclotron to that injected into.

Ion species	Energy (MeV)	Intensity (eμA)	Text (%)	Tall (%)
H^+	10	12	80	27
	20	5	77	23
	30	5	67	22
	45	30	79	14
	50	5	44	14
	55	5	63	14
	60	5	57	22
	65	7	62	12
	70	5	42	12
	80	3	47	13
	90	10	48	7.7
D^+	10	11	29	3.7
	20	5.6	80	16
	25	11	88	30
	35	40	59	13
	50	20	49	7.2
$^{4}He^{2+}$	20	5.5	69	12
	30	10	42	10
	50	20	62	22
	100	10	32	10
	108	1.6	M/Q=2	
$^{12}C^{3+}$	75	2	M/Q=4	
$^{12}C^{5+}$	220	0.25	77	22
$^{12}C^{6+}$	320	0.0025	M/Q=2	
$^{14}N^{3+}$	67	4	43	10
$^{15}N^{3+}$	56	0.70	M/Q=5	5.0
$^{16}O^{4+}$	100	5	M/Q=4	22
$^{16}O^{5+}$	100	4	34	21
$^{16}O^{6+}$	160	1.9	58	21
$^{16}O^{7+}$	225	1	82	13
$^{16}O^{7+}$	335	0.1	41	6
$^{16}O^{8+}$	430	0.0045	M/Q=2	
$^{20}Ne^{4+}$	75	1.5	M/Q=5	6.6
$^{20}Ne^{5+}$	125	0.01	M/Q=4	
$^{20}Ne^{6+}$	120	1.6	53	18
$^{20}Ne^{7+}$	260	0.33	70	19
$^{20}Ne^{8+}$	350	1.5	63	23
$^{20}Ne^{10+}$	540	10^5 cps	M/Q=2	
$^{36}Ar^{8+}$	195	2.5	73	13
$^{36}Ar^{10+}$	195	0.1	43	1.2
$^{36}Ar^{18+}$	970	10^5 cps	M/Q=2	
$^{40}Ar^{8+}$	150	2.4	M/Q=5	6.2
	175	3	73	15
$^{40}Ar^{10+}$	250	0.2	M/Q=4	
$^{40}Ar^{11+}$	330	0.7	86	22
$^{40}Ar^{13+}$	460	0.03	63	24
$^{40}Ca^{9+}$	200	2	61	11
$^{56}Fe^{15+}$	400	0.55	66	23
$^{84}Kr^{17+}$	320	0.08	M/Q=5	5.0
$^{84}Kr^{18+}$	400	0.04	60	2
$^{84}Kr^{20+}$	520	0.06	72	22
$^{84}Kr^{21+}$	525	0.0032	M/Q=4	
$^{129}Xe^{23+}$	450	0.2	72	11
$^{197}Au^{31+}$	500	0.022	49	3

M/Q = 2, 4 and 5 : Cocktail beams
Woven pattern : added ion species on previous table

References

1) Y. Nakamura, T. Nara, *et al.*, TIARA Annual Report 1999 (JAERI-Review 2000-024)
2) Y. Nakamura, T. Nara, *et al.*, Proc. 16th Int. Conf. Cyclo. Their Applic., East Lansing, MI, USA (2001)
3) Y. Nakamura, S. Okumura, *et al.*, TIARA Annual Report 1999 (JAERI-Review 2000-024)
4) S. Okumura, K. Arakawa, *et al.*, Proc. 16th Int. Conf. Cyclo. Their Applic., East Lansing, MI, USA (2001)
5) W. Yokota, S. Okumura, *et al.*, in this annual report
6) S. Kurashima, M. Fukuda, *et al.*, Proc. 16th Int. Conf. Cyclo. Their Applic., East Lansing, MI, USA (2001)
7) T. Agematsu, K. Arakawa, *et al.*, TIARA Annual Report 1999 (JAERI-Review 2000-024)

9.8 Renewal of computer control system of the 3MV tandem accelerator

K. Mizuhashi[1], S. Uno[1], A. Chiba[1], R. Kitchen[2] and S. Tajima[1]
[1] Advanced Radiation Technology Center, JAERI
[2] National Electrostatics Corp. USA

1.Introduction

The 3MV tandem accelerator has been operating for over ten years since 1990. We had many troubles on the computer control system of the tandem accelerator so far. For example, the old system had five operation terminals and three terminals had broken for the last few years. These became serious problems since the computer maker would not support our computer control system providing the replaced parts any more. So we make plan to renew the computer control system. This was timely planned, because the main computer broke at just before the completion of the renewal work plan. A basic construction of new computer control system is the same as the previous system [1]. The general-purpose computers were used on the new system to keep the support of the maker for long term and also some new software functions were introduced to make machine operation easy.

2. New computer control system

A new computer system consists of six personal computers. Each computer is connected by the Ethernet network and runs a Linux operating system. This networked computer system controls the devices through the five CAMAC interfaces. The CAMAC system was out of the renewal, so that the existing equipments were reused. New personal computer installing 800 MHz Pentium processor, 250MB RAM and 9GB hard disk, is remarkable powerful machine as compared with previous one installed 25MHz processor, 4MB RAM and 390MB hard disk.

New computer control system succeeds the ability of the previous one, so it has the old and new function of operation. In order to smoothly operate the accelerator using the computer system, it is necessary for the system to respond quickly and to handle easily. A response speed of the new system is so over 10Hz that is enough for the congruity operation. The operator is able to operate easily the accelerator with the graphic page on CRT (Fig.1) using mouse and keyboard. In addition to above feature, new system has new functions as follows.

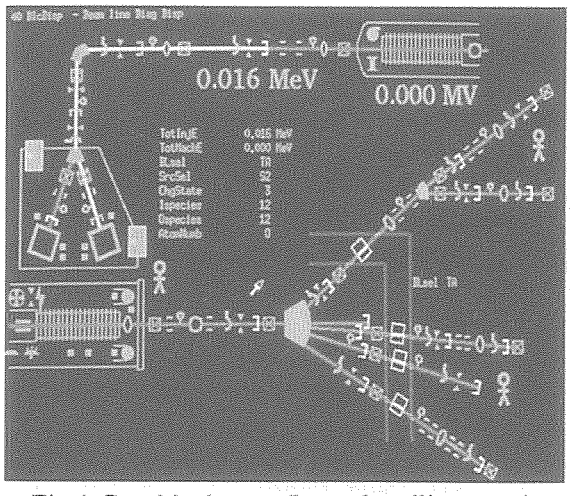


Fig.1 Graphical page (beam handling page)

3. New functions

The new functions are introduced for the saving of operating work. Main functions are described below.

3-1. Watching

New system watches the read back data of the important devices of the accelerator instead of the operator. It makes alarm for the operator with sound when the read back data is out the permissive range. This function can watch seven parameters and continuously write them on the CRT at the same time (Fig.2). The full range of the time-axis is 5 minutes when the sampling time of data is 0.5 seconds.

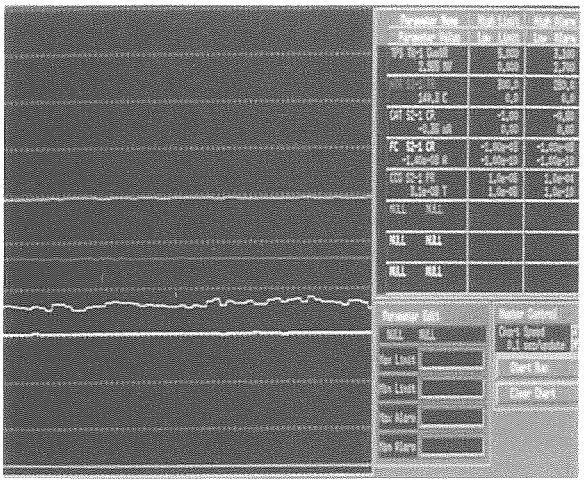


Fig.2 Watching window of parameter

3-2. Scaling

This function scales new control value of the magnetic and electrostatic devices and it automatically changes about twenty-five parameters to scaled them for the new ion conditions (energy, mass, charge state). So the operator does not need to make the new parameter about many devices to control an ion beam but only need to finely adjust them. The main scaling equations are noted below.

$$B_n = B_b \cdot (M_n/M_b)^{1/2} \cdot (E_n/E_b)^{1/2} \cdot (Q_b/Q_n) \quad (1)$$

$$V_n = V_b \cdot (E_n/E_b) \cdot (Q_b/Q_n) \quad (2)$$

Where, B is magnetic field of the magnetic devices, M is mass of ion, E is energy of accelerated ion, Q is a charge state, V is voltage of the electrostatic device. Suffix n is new data and b is based data for scaling.

3-3. Calculating

This function calculates the mass and energy of accelerated ion by using calibrated bending radius and magnetic field of the bending magnet.

When we accelerate element or molecular ions by the tandem accelerator, there are so many kinds of ion species and conditions at the some points of the accelerator. For example, many isotopes and combinations at the injection line and many masses and charge numbers at the post acceleration line, that operator was sometime confused. This function supports for operator on objective ion.

4.Summary

The TIARA tandem accelerator is operating from 8:30 a.m. to 11 p.m. every day. So it is difficult for the operator to keep the watching of the parameter for long time during operation. The beam trouble sometime happened such as beam escape and decrease during experiment. By using the control system with new function, the handling performance is improved and the saving of operating work is achieved. Further, the performances of safety operation are improved, because the computer watches the important parameters during operation of the accelerator.

Reference:

1) R. D. Rathmell, R. L. Kitchen, T. R. Luck and M. L. Sundquist, Nuclear Instruments and Methods in Physics Research B56/57 (1991) 1072 - 1075

This is a blank page.

10. Status of TIARA 2000

10.1 Utilization of TIARA Facilities ····· 301
Utilization and Coordination Division
10.2 Operation of the Electrostatic Accelerators ····· 303
I.Takada, K.Mizuhashi, S.Uno, K.Ohkoshi, Y.Nakajima, A.Chiba, Y.Saitoh, Y.Ishii, T.Kamiya, and T.Sakai
10.3 Operation of JAERI AVF Cyclotron System ····· 304
Y.Nakamura, T.Nara, T.Agematsu, I.Ishibori, H.Tamura, S.Kurashima, W.Yokota, M.Fukuda, S.Okumura, K.Akaiwa, To.Yoshida, S.Ishiro, A.Matsumura, Tu.Yoshida, Y.Arakawa, S.Kanou, A.Ihara, and K.Takano
10.4 Radiation Control & Radioactive Waste Management in TIARA ····· 305
Safety Division & Utilities and Maintenance Division
Department of Administrative Services, JAERI.

This is a blank page.

10.1 Utilization of TIARA Facilities

Utilization and Coordination Division,

Advanced Radiation Technology Center, JAERI

1. Introduction

TIARA is a center of the ion accelerator facilities composed of four ion accelerators, the AVF cyclotron, the 3MV tandem accelerator, the 3MV single-ended accelerator, and the 400kV ion implanter. These accelerators have been fully served for ion beam applications since January 1994.

2. Utilization System

TIARA is opened for public use: it receives applications of the experimental subjects in wide areas once a year from outside users as well as JAERI staffs. The subjects and these own utilizable beam times are approved after the official investigation by Subcommittee for TIARA under Advisory Council for JAERI's Research Facilities, which are both publicly organized since 1999. To attain an effective outcome of the research program, the utilization time of each accelerator is fairly allotted to the subjects three times in a year based on the approved beam time.

Charges for the utilization are remitted in the case that a contract of the joint research between JAERI and a university or a company or that of the projective joint research between JAERI and universities is made. The results of research have to be published at the TIARA Research Review Meeting and in the JAERI TIARA Annual Report. There is another system of visitor use with charges but without the publication duty.

3. Experimental subject approved

Number of subjects using cyclotron approved in FY2000 for the experiment was 55 while the total number using three electrostatic accelerators was 47 as shown in Table 1. Table 2 shows the number allotted to users under various contracts.

Table 1 Number of experimental subjects at various research fields.

Accelerators / Fields of research	Number of subjects	
	Cyclotron	Electrostatic accelerators
Materials for space	5	5
Materials for fusion	3	11
Biotechnology	30	2
Functional material	1	18
RI & nuclear sci.	2	0
Radiation chemistry	7	2
Basic technology	7	9
Total	55	47

Table 2 Number of experimental subjects at various relations with users.

Accelerators / Relations with visitors		Number of subjects	
		Cyclotron	Electrostatic accelerators
JAERI only	Takasaki Establishment	11	12
	Others	3	11
Cooperative research with university		18	11
Projective joint research between JAERI and universities		8	9
Joint research with private company or governmental institute		15	4
Total		55	47

4. Allotted time to users

The cyclotron has been continuously operated from Monday to Friday. The utilization time for the cyclotron is allotted by the hour. In case of the electrostatic accelerators, on the other hand, the utilization time is allotted by the day either from 9 a.m. to 6 p.m.: (A mode), or from 9 a.m. to 10 p.m.: (B mode).

As shown in Table 3, the cyclotron was used at the various research fields, while the electrostatic accelerators were mainly used in the field of functional material and material for fusion. The ratios of allotted time to JAERI staffs were 30% in the cyclotron utilization and 53% in the utilization of other electrostatic accelerators as shown in Table 4.

Table 3 Utilization of the accelerators in FY2000 at various research fields.

Accelerators / Fields of research	Utilization time at each period															
	Cyclotron (hours)				Tandem accelerator (days)				Single-ended accelerator (days)				Ion implanter (days)			
	00-1	00-2	00-3	total	00-1	00-2	00-3	total	00-1	00-2	00-3	total	00-1	00-2	00-3	total
Material for space	130	153	184	467	17	6	12	35	-	-	-	-	13	10	6	29
Material for fusion	22	50	12	84	14	18	14	46	11	15	10	36	8	13	14	35
Biotechnology	300	286.5	164	750.5	2	1	1	4	-	-	-	-	-	-	-	-
Functional material	0	0	6	6	11	14	12	37	19	14	18	51	18	20	18	56
RI & nuclear science	67	61	54	182	-	-	-	-	-	-	-	-	-	-	-	-
Radiation chemistry	39	48.5	34	121.5	0	2	2	4	-	-	-	-	-	-	-	-
Basic technology	290	208	116	614	9	10	8	27	22	19	18	69	3	2	2	7
Total	848	807	570	2225	53	51	49	153	52	48	46	146	42	45	40	127

Table 4 Utilization of the accelerators in FY2000 at various relations with users.

Relation with visitors / Accelerators		Utilization time at each period															
		Cyclotron (hours)				Tandem accelerator (days)				Single-ended accelerator(days)				Ion implanter (days)			
		00-1	00-2	00-3	total	00-1	00-2	00-3	total	00-1	00-2	00-3	total	00-1	00-2	00-3	total
JAERI Only	Takasaki Establishment	323	254	133	710	29	19	23	71	12	12	9	33	23	20	19	62
	others	11.5	50	0	61.5	5	3	4	12	14	8	17	39	4	5	6	15
Cooperative research with universities		167.5	155.5	125.5	448.5	7	7	5	19	8	5	2	15	10	11	6	27
Projective joint research between JAERI and universities		189.5	158	113	460.5	9	15	10	34	18	23	18	59	4	8	8	20
Joint research with company or governmental institute		16.5	189.5	198.5	544.5	3	7	7	17	-	-	-	-	1	1	1	3
Visitors use with charges		95	145	75	315	-	-	-	-	-	-	-	-	7	1	3	11
Total		945	952	645	2540	53	51	49	153	52	48	46	146	49	46	43	138

10.2 Operation of the Electrostatic Accelerators

I. Takada, K.Mizuhashi, S. Uno, K. Ohkoshi, Y.Nakajima,
A.Chiba,Y. Saitoh, Y. Ishii, T. Kamiya and T. Sakai

Advanced Radiation Technology Center, JAERI

1. Operation

The Electrostatic accelerators except the tandem were operated smoothly for various experiments in FY 2000. The operation of the tandem accelerator was suspended by trouble of control system for eighteen days. The total operation time for each accelerator in this fiscal year was 1,916 hours for the tandem accelerator, 2,282 hours for the single-ended accelerator and 1,859 hours for the 400kV ion implanter, respectively. Monthly and yearly operation time for each accelerator are shown in Fig.1 and Fig.2.

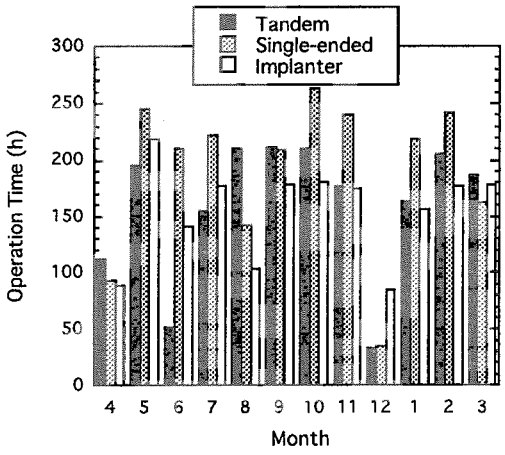


Fig. 1 Monthly operation time for each accelerator in FY 2000.

2. Maintenance

The maintenance for the accelerators were carried out in April, August and December. During these terms several improvement and renewals were performed as follows;

For the tandem accelerator; 1) A control system was renewed in January because the trouble of it increased by operating for about ten years . The function of new system was extended in consideration of establishment a second heavy ion source .

For the single-ended accelerator; 2) The bearing used Motor Generator rod were replaced with new ones because the grease of them were deteriorated by radiation. 3) The Thermo Mechanical Leak valve which was made pin-hole by SF6 decompositions was exchanged twice with new one.

For the 400kV ion implanter ; 4) A damaged insulator by sparks was exchanged with new one in May. 5)The Control method for the ECR ion source on the high-voltage terminal was improved so that it could adjust the source parameter at the control room.

3. Development

We made the multiply charged ions generating test for O and Kr ions,and succeeded in the generation of Kr^{+5}beam of $2e\mu A$ and O^{+3}beam of $3e\mu A$,respectively. In order to develop the on-line beam monitor,we made a measurement system consisted of five electrodes and tungsten wire mesh,and examined the relation between suppressor voltage and sum of secondary electron and mesh current using C,O,Ni and Au ions.

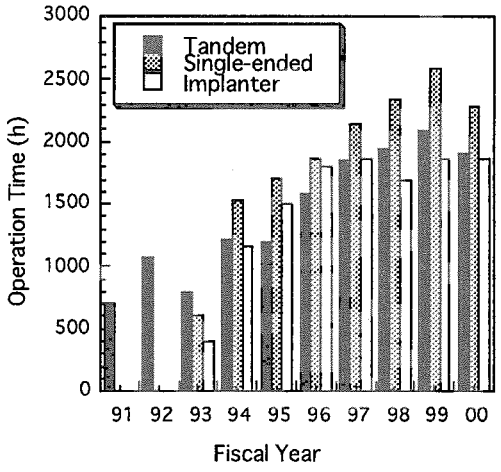


Fig.2 Yearly operation time for each accelerator since 1991

10.3 Operation of JAERI AVF Cyclotron System

Y. Nakamura, T. Nara, T. Agematsu, I. Ishibori, H. Tamura, S. Kurashima, W. Yokota, M. Fukuda, S. Okumura, K. Akaiwa*, To. Yoshida*, S. Ishiro*, A. Matsumura*, Tu. Yoshida*, Y. Arakawa*, S. Kanou*, A. Ihara* and K. Takano*

Advanced Radiation Technology Center, JAERI
*Beam Operation Service, Co., Ltd.

The JAERI AVF cyclotron system was steadily operated according to a beam time schedule. The total operation time through FY 2000 amounted to 3286 hours.

The operation time for every month is shown in Fig.1. The ratios of operation time used for experiments including visitor's use, tuning, beam development and machine study were 76.7%, 17.8% and 5.5%, respectively. Thirty kinds of ion species, almost the same as last year, were delivered for various research experiments.

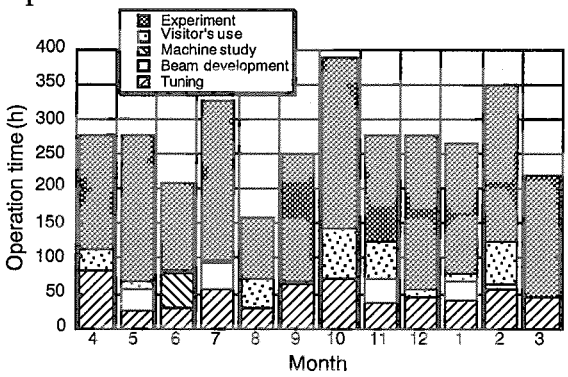


Fig. 1 Monthly operation time in FY 2000.

A regular yearly overhaul was performed for four weeks in summer.

The stabilization of the cyclotron beam was confirmed certainly by the measurement of various quantities under the practical operation of the cyclotron after the measures of reconstruction. The designing for the flat-top acceleration system is in progress. The FT system will be installed in next March, 2002.

In last March, four circulation pumps for cooling system were renewed preventively in consideration of long-term operation. An operation method for the cooling tower was also improved to continuous operation using an inverter from ON-OFF mode. Several controllers for TMP's were moved to the cable distribution area on the basement from the switching magnet room on the first floor to reduce the radiation damage. A pair of liquid crystal displays for the SCU were added further on the control system to reinforce the monitoring functions on the console.

Figure 2 shows the percentages of accelerated ions. The summed rate of heavy ions and cocktail occupies about 70 % of total time, while the beam time for light ions is 28 % as shown in Fig. 2.

Especially, some metallic ions such as 400 MeV $^{56}Fe^{15+}$, 200 MeV $^{40}Ca^{9+}$ and 500 MeV $^{197}Au^{31+}$ were used for about 140 hours for research experiments.

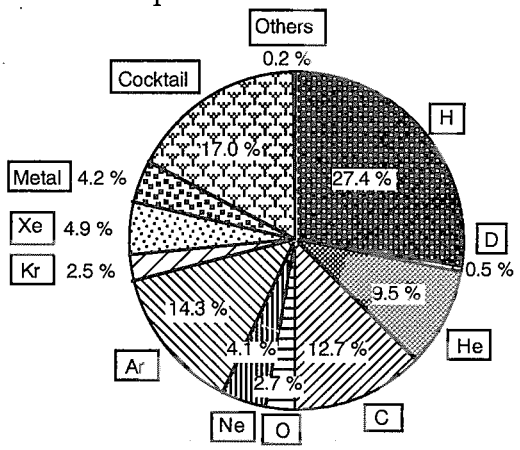


Fig. 2 The percentages of accelerated ion species in FY 2000.

The frequency of the change for particle, energy and beam course is shown in Fig. 3. This figure was revised so as to add the new beam development on the previous data. The number of the change for beam course amounts to 268, which is the largest so far. And the frequency of particle and energy change also increases gradually year by year.

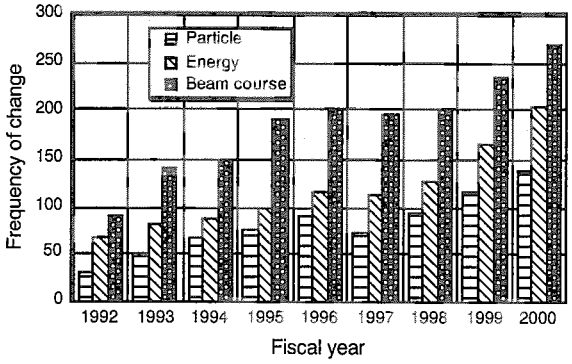


Fig. 3 Frequencies of the change for particle, energy and beam course since 1992.

10.4 Radiation Control & Radioactive Waste Management in TIARA

Safety Division & Utilities and Maintenance Division
Department of Administrative Services, JAERI

1. Radiation Control

1.1 Individual monitoring

(1) Individual monitoring for the radiation workers

Table 1 shows a distribution on effective dose equivalent of the radiation workers in FY 2000. The effective dose equivalent values of almost workers were less than 0.2 mSv (minimum detectable dose equivalent).

Maximum dose equivalent was 1.1 mSv/y due to the overhauling of the cyclotron.

(2) Individual monitoring for the visitors and others

Table 2 shows number of persons who have been temporally entered the radiation controlled areas. The effective dose equivalent of all persons was less than 0.1 mSv.

Table1. Distributions on the effective dose equivalent in FY 2000.

Items \ Persons / Periods		Number of persons			
		1st quarter	2nd quarter	3rd quarter	4th quarter
Distribution range on effective dose equivalent HE:Effective dose equivalent*1 (mSv)	HE < 0.2	509	530	545	554
	0.2 ≦HE ≦ 1.0	2	6	3	2
	1.0 <HE ≦ 5.0	0	0	0	0
	5.0 <HE ≦ 50.0	0	0	0	0
	50.0 <HE	0	0	0	0
Persons for radiation control(A)		511	536	548	556
Exposure above 1 mSv	Persons(B)	0	0	0	0
	(B)/(A)×100(%)	0	0	0	0
Mass effective dose equivalent (Person・mSv)		0.7	2.6	1.3	0.8
Mean dose equivalent (mSv)		0.00	0.00	0.00	0.00
Maximum dose equivalent (mSv)		0.4	0.8	0.3	0.3

*1 Not detected according to internal exposure.

Table 2. Number of temporary entrance persons to radiation controlled areas in FY 2000.

Persons / Periods / Temporary entrance persons	Number of persons				
	1st quarter	2nd quarter	3rd quarter	4th quarter	Total
	287	307	404	264	1262

1.2 Monitoring of radioactive gases

Table 3 shows the maximum radioactive concentrations and total activities for radioactive gases released from TIARA's stack, during each quarter of FY 2000.

The least amount of ^{41}Ar and ^{11}C were detected for some time during operation of the cyclotron, but the pulverized substance (^{65}Zn, etc) were not detected.

Table 3. Monitoring results of released gaseous radioactivity in FY 2000.

Nuclide	Items / Periods	1st quarter	2nd quarter	3rd quarter	4th quarter	Total
^{41}Ar	Maximum concentration (Bq/cm^3)	3.2×10^{-4}	2.5×10^{-4}	$<5.4\times10^{-4}$	1.3×10^{-4}	3.2×10^{-4}
	activity (Bq)	1.6×10^{9}	9.5×10^{8}	4.3×10^{7}	6.9×10^{8}	3.3×10^{9}
^{11}C	Maximum concentration (Bq/cm^3)	$<5.4\times10^{-5}$	$<5.4\times10^{-5}$	$<5.4\times10^{-5}$	$<5.4\times10^{-5}$	$<5.4\times10^{-5}$
	activity (Bq)	3.6×10^{7}	1.2×10^{8}	1.5×10^{8}	3.7×10^{7}	3.4×10^{8}
^{65}Zn	Maximum concentration (Bq/cm^3)	$<4.8\times10^{-10}$	$<8.4\times10^{-10}$	$<8.7\times10^{-10}$	$<6.7\times10^{-10}$	$<8.7\times10^{-10}$
	activity (Bq)	0	0	0	0	0

1.3 Monitoring for external radiation and surface contamination

External radiation monitoring was routinely carried out in/around the radiation controlled areas and surface contamination monitoring was also carried out. Neither unusual value of dose equivalent rate nor surface contamination were detected.

Figure 1 displays a typical example of distribution of the dose equivalent rate at the radiation controlled area in the cyclotron building.

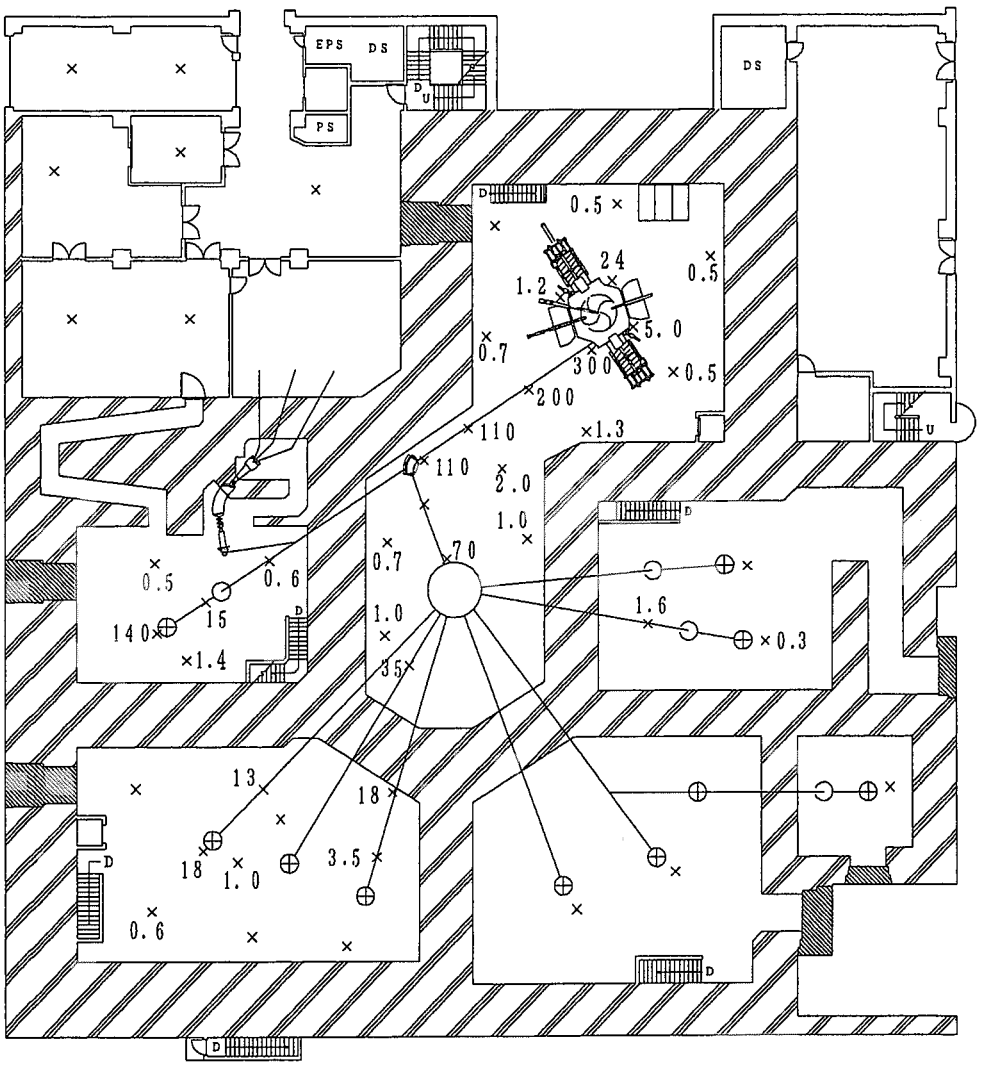


Fig.1 Dose rate distribution at the radiation controlled area in the cyclotron building.
Date measured : March 29, 2001
Measuring position : Indicated with × above 1m from floor
Unit : μSv/h(numeric less than 0.2 μSv/h are not indicated)

2. Radioactive Waste Management

2.1 Solid wastes

Table 4 shows the amounts of solid wastes at various properties and kinds generated in each quarter of FY 2000. All wastes were combustible matter such as rubber gloves, compressible matter such as thin metals, and incompressible matter such as contaminated components. Compressible wastes were generated mainly by the cyclotron maintenance.

2.2 Liquid waste

Liquid waste was almost waste water ("inorganic" in Table 5) generated with chemical experiments and operation of air conditioning units installed in each room of the first class radiation controlled area. Larger quantities of the wastewater in summer season (2nd quarter) are mainly due to condensed water, which is treated by evaporation, and condensed water is reused in the controlled area. Only small amounts of residue are generated by the evaporation because the waste quality is very pure.

The evaporation residue and sludge are solidified by cement in a stainless steel drum. The residue and sludge of ca. 100 liter makes cement solidify of 200-litter drum.

Table 4. Radioactive solid wastes generated in FY 2000.

Amounts / Items	Amounts of generation in each periods (m^3)					Number of package /drum
	1st quarter	2nd quarter	3rd quarter	4th quarter	Total	
Category A*	0.82	0.60	0.58	0.44	2.44	
1)Combustible	0.50	0.24	0.40	0.32	1.46	9**
2)Incombustible	0.32	0.36	0.18	0.12	0.98	0
Compressible	0.12	0.16	0.18	0.12	0.58	4**
Filters	0	0	0	0	0	0
Incompressible	0.20	0.20	0	0	0.40	2
Ion exchange resin	0	0	0	0	0	0
(Cement solidify)	0	0	0	0	0	0
Category B*	0	0	0	0	0	
1)Incombustible	0	0	0	0	0	0

* defined by dose at the outer surface of container : (A) < 2 mSv/h ≦ (B)

** 200-liter drum

Table 5. Radioactive liquid waste generated in FY 2000.

Amounts / Items	Amounts of generation in each periods (m^3)					Number of package /drum
	1st quarter	2nd quarter	3rd quarter	4th quarter	Total	
Category A*	15.26	18.06	6.66	3.23	43.21	
1)Inorganic	15.26	18.06	6.66	3.13	43.11	treatment
2)Organic	0	0	0	0	0	0
Organic	0	0	0	0	0	0
Oil	0	0	0	0	0	0
3)Sludge	0	0	0	0.10	0.10	1
Category B*	0	0	0	0	0	
1)Inorganic	0	0	0	0	0	0
2)Organic	0	0	0	0	0	
Organic	0	0	0	0	0	0
Oil	0	0	0	0	0	0
3)Sludge	0	0	0	0	0	0
Evaporation residue	0	0	0	0.10	0.10	1

* defined by concentrations in $Bq/cm^3(\beta,\gamma)$: (A) $< 3.7\times10 \leqq$ (B) $< 3.7\times10^4$

Appendix

Appendix 1. List of Publication 311
A1.1 Publications in Journal 311
A1.2 Publications in Proceeding 318
Appendix 2. Type of Research Collaboration 325
Appendix 3. Organization and Personnel of TIARA 327

This is a blank page.

Appendix 1. LIST OF PUBLICATION

A 1.1 Publications in Journal

10J01
T. Hirao, H. Itoh, S. Okada, and I. Nashiyama.,
Studies of single-event transient current induced in GaAs and Si diodes by energetic heavy ions
Radiat. Phys. Chem., **60**, 269-272 (2001)
T SCS 02001

10J02
T. Hirao, J.S. Laird, H. Mori, S. Onoda, and H. Itoh.,
The investigation of charge transport properties of SOI semiconductor devices using a heavy ion microbeam
Solid State Phenomena, **78-79**, 395-400 (2001)
T SCS 02001

10J03
J.S. Laird, T. Hirao, H. Mori, S. Onoda, and H. Itoh,
A system for ultra-fast transient ion and pulsed laser current microscopies as a function of temperature
Solid State Phenomena, **78-79**, 401-406 (2001)
T SCS 02001

10J04
H. Mori,T. Hirao, S. Onoda, H. Itoh, S. Okada, and Y. Okamoto,
Profiling of collimated swift ion micro-beam using 16Mbit DRAM
Radiat. Phys. Chem., **60**, 273-276 (2001)
C SCS 01001

10J05
T. Ohshima, K. Abe, H. Itoh, M. Yoshikawa, K. Kojima, I. Nashiyama, and S. Okada,
Electrical Activation of Phosphorus-Donors Introduced in 6H-SiC by Hot-implantation
Appl. Phys., A 71, 141-145 (2000)
I SCS 02003

10J06
A. Uedono, S. Tanigawa, T. Ohshima, H. Itoh, M. Yoshikawa, I. Nashiyama, T. Frank, G. Pensl, R. Suzuki, T. Ohdaira, and T. Mikado,
Crystallization of an amorphous layer in P^+-implanted 6H-SiC studied by monoenergetic positron beams
J. Appl. Phys., **87**, 4119-4125 (2000)
I SCS 02003

10J07
T. Ohshima, M. Yoshikawa, H. Itoh,
Effect of gamma-ray irradiation on the characteristics of 6H Silicon Carbide Metal-Oxide-Semiconductor Field Effect Transistor with hydrogen-annealed gate oxide
J. Appl. Phys., (in press.)
I SCS 02003

10J08
T. Tanaka, T. Ohshima, H. Itoh, S. Okada, A. Wakahara and A. Yoshida,
Effect of electron irradiation on properties of CuInSe2 thin films
Jpn. J. Appl. Phys., **39** (Suppl.39-1), 192-193 (2000)
I SCS 02004

10J09
M. Taguchi, K. Hayano, Y. Xu, M. Moriyama, Y. Kobayashi, H. Hiratsuka, and S. Ohno,
Yields of tyrosine isomers in the radiolysis of aqueous phenylalanine solution by energetic heavy ions
Radiat. Phys. Chem., **60**, 263-268(2001)
C RCO 01008

10J10
M. Taguchi, M. Moriyama, H. Namba, and H. Hiratsuka,
Yield of acridine C-rafical produced by irradiation with energetic heaby ions
Radiat. Phys. Chem., (submitted)
C RCO 01008

10J11
Y. Hase, A. Tanaka, T. Baba, and H.Watanabe,
Frill is required for petal and sepal development in Arabidopsis

Plant J., **24**(1), 24-32 (2000). Supplement (2001), p.53
C BIT 01012

10J12
M. Kawai, Y. Kobayashi, A. Hirata, Y. Oono, H. Watanabe, and H. Uchimiya,
Ion beam as a noble tool to induce apoptosis-like cell death in roots of maize (Zea mays L.)
Plant Biotech., 7, 305-308 (2000)
C BIT 01029

10J13
Y. Kobayashi, M. Taguchi, and H. Watanabe,
Use of a collimated heavy ion Microbeam for irradiating cells individually
Ext. abstract: Radiat. Res., **153**, 228-229 (2000)
C BIT 01026

10J14
S. Matsuhashi, H. Uchida, and T. Kume,
Positron imaging for plant study using positron emitting tracer imaging system(PETIS) and imaging. Plate(IP)
Radioisotopes, **49**, 558-570(2000)
C BIT 1032

10J15
S. Matsuhashi and T. Kume,
Development of positron imaging method for plant study
Radiat. Chem., **70**, 20-25(2000)
C BIT 1032

10J16
N. Ohtake, T. Sato, H. Fujitake, K. Sueyoshi, T. Ohyama, N.S. Ishioka, S. Watanabe, A. Osa, T. Sekine, S. Matsuhashi, T. Ito, T. Mizuniwa, T. Kume, S. Hashimoto, and A. Tsuji,
Rapid N transport to pods and seeds in N-deficient soybean plants
J. Exp . Bot., 277-283(2001)
C BIT 01033

10J17
S. Mori, S. Kiyomiya, H. Nakanishi, N.S. Ishioka, S. Watanabe, A. Osa, S. Matsuhashi, S. Hashimoto, T. Sekine, H. Uchida, S. Nishiyama, H. Tsukada, and A. Tsuji,
Visualization of ^{15}O-water flow in tomato and rice in the light and dark using a positron-emitting tracer imaging system(PETIS)
Soil Sci. Plant Nutr., **46**, 975-979(2000)
C BIT 01034

10J18
S. Kiyomiya, H. Nakanishi, H. Uchida, A. Tsuji, S. Nishiyama, M. Futatsubashi, H. Tsukada, N.S. Ishioka, H. Tsukada, and A. Tsuji,
^{13}N-Translocation in rice under different environmental conditions using positron emitting tracer imaging system
Plant Physiol., **125**, 1743-1753(20001)
C BIT 01034

10J19
N. Bughio, H. Nakanishi, S. Kiyomiya, S. Matsuhashi, N.S. Ishioka, S. Watanabe, H. Uchida, A. Tsuji, A. Osa, T. Kume, S. Hashimoto, T. Sekine, and S. Mori,
Real-time[^{11}C]methionine translocation in barley in relation to mugineic acid phytosiderophore biosynthesis
Planta, (2001), (in press.)
C BIT 01034

10J20
J. Furukawa, H. Yokota, K. Tanoi, S. Ueoka, S. Matsuhashi, N.S. Ishioka, S. Watanabe, H. Uchida, A. Tsuji, T. Itoh, T. Mizuniwa, A. Osa, and T.M. Nakanishi,
Vanadium uptake manner and an effect of vanadium treatment on water movement in a cowpea plant by PETIS
J. Radioanal. Nucl. Chem., (in press.)
C BIT 1036

10J21
T.M. Nakanishi, J. Furukawa, K. Tanoi, H. Yokota, S. Ueoka, N. Ishioka, S. Watanabe, A. Osa, T. Sekine, T. Itoh, T. Mizuniwa, S. Matsuhashi, S. Hashimoto, H. Uchida, and A. Tsuji,
Water uptake and transport imaging of soybean

plant by PETIS (Positron emitting tracer imaging system)
J. Radioanal. Nucl. Chem., (in press.)
C BIT 1036

10J22
T.M. Nakanishi, H. Yokota, K. Tanoi,
J. Furukawa, N. Ikeue, Y. Ohkuni, H. Uchida, and A. Tsuji,
Circadian rhythm in ^{15}O-labeled water uptake manner of a soybean plant by PETIS (Positron emitting tracer imaging system)
Radioisotopes, **50**, 163-168 (2001)
C BIT 1036

10J23
T.M. Nakanishi, H. Yokota, K. Tanoi, N. Ikeue,
Y. Ohkuni, J. Furukawa, N.S. Ishioka,
S. Watanabe, A. Osa, T. Sekine, S. Matsuhashi,
T. Itoh, T. Kume, H. Uchida, and A. Tsuji,
Comparison of ^{15}O-labeled and ^{18}F-labeled water uptake in a soybean plant by PETIS (Positron emitting tracer imaging system)
Radioisotopes, **50**, 265-269(2001)
C BIT 1036

10J24
Y. Nakayama, K. Imagawa, M. Tagashira,
M. Nakai, H. Kudoh, M. Sugimoto, N. Kasai, and T. Seguchi,
Evaluation and analysis of thermal control materials under ground simulation test for space environment effects
High Perform. Polym., (in press.)
C, T RCO 01041, 02037

10J25
L.O. Peng,P.Y. Apel,Y. Maekawa and
M. Yoshida,
Conductometric study of the radial track etch rate:Free shape analysis
Nucl. Instr. Meth. Phys. Res., **B168**, 527-532 (2000)
C RCO 1042

10J26
H. Koizumi, M. Taguchi, Y. Kobayashi, and
T. Ichikawa,
Crosslinking of polydimethylsiloxane in heavy ion tracks
Nucl. Instr .Meth., B, (in press.)
C RCO 01046

10J27
S. Ohno, K. Furukawa, M. Taguchi, T. Kojima, and H. Watanabe,
An ion-track model based on experimental measurements and its application to calculate radiolysis yields
Radiat. Phys. Chem., **60**, 259-262(2001)
C RCO 01045

10J28
M. Taguchi, M. Moriyama, H. Namba, and
H. Hiratsuka,
Yield of acridine C-radical produced by irradiation with energetic heavy ions
Radiat. Phys. Chem., (in press.)
C RCO 01008

10J29
E. Wakai, T. Sawai, A. Naito, and S. Jitsukawa
Microstructural development and swelling behavior of F82H steel irradiated by dual beams
J. Electron. Microscopy, (to be printed in 2001.)
T, I, S IOM 01007/02011

10J30
E. Wakai, T. Sawai, K. Tomita, K. Furuya,
A. Naito, S. Yamashita, S. Ohnuki,
S. Yamamoto, H. Naramoto, and S. Jitsukawa,
Radiation effects of ferric steel irradiated by dual/triple ion beams
J. Nucl. Mater., (accepted)
T, I, S IOM 01007/02011

10J31
K. Furuya, E. Wakai, T. Sawai, M. Ando,
S. Jitsukawa, and H. Takeuchi,
Microstructural and hardness examinations of HIP jointed F82H steel irradiated by simultaneous triple ion beams
J. Nucl. Mater., (accepted)
T, I, S IOM 01007/02011

10J32

T. Sawai, E. Wakai, K. Tomita, A. Naito, and S. Jitsukawa,
Radiation-induced cavity formation in F82H with various heat and mechanical treatment
J. Nucl. Mater., (accepted.)
T, I, S IOM 01007/02011

10J33
Y. Shimomura and I.Mukouda,
Development of vacancy clusters in neutron-irradiated copper at high temperature
J. Nucl. Mater., **283-287**, 249-254(2000)
T, I, S IOM 02008

10J34
I. Mukouda, Y. Shimomura, T. Iiyama, Y. Harada, Y. Katano, T. Nakazawa, D. Yamaki, and K. Noda,
Microstructure in pure copper irradiated by simultaneous multi-ion beam of hydrogen, helium and self ions
I. Nucl. Mater., **283-287**, 302-305(2000)
T, I, S IOM 02008

10J35
N. Sekimura, S. Yonamine, T .Sawai, Y. Arai, A. Naito, Y. Miwa, and S. Hamada,
Synergistic effects of hydrogen and herium on microstructural evolution in vanadium alloys by triple ion beam irradiation
J. Nucl .Mater., **283-287**, 224-228(2000)
T, S, I IOM 02009

10J36
T. Okita, T. Kamada, and N. Sekimura,
Effects of dose rate on microstructural evolution and swelling under neutron irradiation
J. Nucl. Mater., **283-287**, 224-228(2000)
T, S, I IOM 02009

10J37
T. Taguchi, E. Wakai, N. Igawa, L.L. Snead, and S. Jitsukawa,
Effect of simultaneous ion irradiation on microstructural change of SiC/SiC composites at high tempereture
J. Nucl. Mater., (ICFRM-10, accepted)
T, I, S IOM 02010

10J38
H. Abe,
Nucleation of carbon onions and nanocapsules under ion implantation at high temperature
Diamond and Related Mater., **10**, 1201(2001)
I IOM 2019

10J39
H. Tanigawa, H. Abe, S. Jitsukawa, T. Iwai, H. Serizawa, and Y. Katoh,
Role of local melting on intergranular fracture of Fe-P binary alloy
Mater. Transact., **JIM** , (submitted)
I IOM 2014

10J40
E. Wakai, A. Hishinuma, H. Abe, S. Takagi, and K. Abiko,
Microstructural evolution of Fe-50Cr-xW model alloys during Fe+ ion Irradiation
Mater. Transact., **JIM 41**, 1176-1179(2000)
I IOM 2012

10J41
Y. Kasukabe, H. Tani, H. Abe, and Y. Yamada,
In-situ transmission electron microscopy and electron energy loss, Spectroscopy observation of TiN grown by N-implantation
Jpn. J. Appl. Phys., **39**, 4395-4399(2000)
I IOM 2021

10J42
I. Vacik, H. Naramoto, J. Cervena, V. Hnatowicz, I. Peka, and D. Fink,
Absorption of molten fluoride salts in glassy carbon, pyrographite and Hastelloy B
J .Nucl. Mater., **289**, 308-314(2001)
O IOM

10J43
J. Vacik, H. Naramoto, S. Yamamoto, and K. Narumi,
Patern formation induced by co-deposition of Ni and C_{60} on MgO(100)
J. Chem. Phys., **114**, 9115-9119 (2001)
O, I IOM

10J44

J. Vacik, V. Hnatowicz, J. Cervena,
H. Naramoto, S. Yamamoto, and D. Fink,
Energy loss and energy straggling of light ions in fullerite
Fullerence Sci. and Techn., **9**(2), 67-79 (2001)
T IOM 02026

10J45
J. Vacik, S. Yamamoto, H. Naramoto, and K. Narumi,
Epitaxial recrystallization of the Ni film on the MGO(001) substrate
J. Crystal Growth, (submitted)
T IOM 02026

10J46
J. Vacik, H. Naramoto, S. Yamamoto, K. Narumi, H. Abe, and Y.H. Xu,
Thermally incited degradation of the $Ni/C_{60}/Ni/MgO(100)$ sequence
Surface Sci., (submitted)
O IOM 02026

10J47
J. Vacik, H. Naramoto, S. Yamamoto, K. Narumi, Y. Xu, and K. Miyashita,
Thermal response of the $Ni/Ni+C_{60}/Ni/MgO(100)$ system
Surface Science, (submitted)
O IOM

10J48
X. Xu, Y. Xu, H. Naramoto, K. Narumi, and K. Miyashita,
Role of simultaneous Ne^+ ion bombardments in preparing carbon films from C_{60} vapor
Thin Solid Film, (submitted)
O IOM

10J49
H. Naramoto, S. Yamamoto, and K. Narumi,
RBS/Channeling analysis of implanted immisible species
Nucl. Instr. Meth., **B161-163**, 534-538 (2000)
I, S IOM 02026

10J50
J. Vacik, H. Naramoto, V. Hnatowicz, J. Cervena, I. Peka, and D. Fink,
Absorption of molten Fuloride salts in Glassy carbon, Pyrographite and Hastelloy B
J .Nucl. Mater., **289**, 308-314(2001)
S IOM 02026

10J51
Z. Tang, Z.J. Zhang, K. Narumi, Y. Xu, H. Naramoto, and S. Nagai,
Effect of mass-selected ion species on structure and properties of diamond-like carbon films
J. Appl .Phys., **89**, 1959-1964(2001)
O IOM 02026

10J52
Y. Chimi, K. Adachi, A. Iwase, N. Ishikawa, and K.Yamakawa,
Thermal relaxation of hydrogen disordering in Pd-H system irradiated with high-energy particles
J. Alloys and Compounds (2001), (in press.)
S IOM 02028

10J53
S. Yamamoto, T. Sumita, and A. Miyashita,
Preparation of TiO_2-anatase films on Si(001) substrate with TiN and $SrTiO_3$ as buffer layers
J. Phys. Condens. Matter, **13**, 2875(2001)
S IOM 02022

10J54
T. Yamaki, and K.Asai,
Alternate multiplayer deposition from ammonium amphiphiles and titanium dioxide crystalline nanosheets using the Langmuir-Blodgett technique
Langmuir, **17**, 2564(2001)
I, S, O IOM 02036

10J55
S. Sumita, T. Yamaki, S. Yamamoto, and A. Miyashita,
A new characterization method of photocatalytic activity in semiconductorphotocatalysts
Japn. J. Appl. Phys., Pt.1, **40**, 4007(2001)
I, S, O IOM 02036

10J56

T. Yamaki, R. Shinohara, and K. Asai,
Formation of hybrid monolayers and Langmuir-Blodgett-typemultilayers from ammonium cations and TiO_2 crystalline nanosheets
Thin Solid Films, (in press.)
I, S, O IOM 02036

10J57
Y. Kasukabe, H. Tani, H. Abe, and Y. Yamada,
In-situ transmission electron microscopy and electron energy loss spectroscopy observation of TiN grown by N-implantation
Japn. J. Appl. Phys., **39**, 4395-4399 (2000)
I IOM 02021

10J58
H. Kudo, N. Nakamura, K. Shibuya, K. Narumi, S. Yamamoto, H. Naramoto, K. Sumitomo, and S. Seki,
Ion-induced electron emission from Si crystal targets covered with noncrystalline Si layers
Nucl. Instr. & Meth., **168**, 181-191(2000)
I MAN 02023

10J59
H. Kudo, T. Kumaki, K. Haruyama, Y. Tsukamoto, S. Seki, and H. Naramoto,
Structural analysis of bent KCl and NaCl crystals with ion-induced electron spectroscopy
Nucl. Instr. Meth., **B174**, 512-518(2001)
O MAN 02023

10J60
A. Uedono, S. Tanigawa, T. Ohshima, H. Itoh, Y. Aoki, M. Miyashita, and I. Nashiyama,
Oxygen-related defects in O^+-implanted 6H-SiC studied by Monoenergetic positron beams
J. Appl. Phys., **86**, 5392(1999)
I IOM 02032

10J61
S. Watanabe, N.S. Ishioka, A. Osa, I. Koizumi, T. Sekine, S. Kiyomiya, H. Nakanishi, and S. Mori
Production of positron emitters of metallic elements to study plant uptake and distribution
Radiochim. Acta. (in press.)
C NRI

10J62
T. Ohnuki, N. Kozai, M. Samadfam, S. Yamamoto, K. Narumi, H. Naramoto, T. Kamiya, T. Sakai, and T. Murakami,
Study on uptake of europium by the thin film of apatite and smectite mixture using RBS and micro-PIXE
Nucl. Instr. And Meth. B, (in press.)
T, C IOM 02035

10J63
H. Yamamoto, Y. Iwai, T. Unezaki, Y. Tomii, And Y. Tsuchitani,
Fluoride uptake around cavity walls; Two-dimentional mapping by electron probe microanalysis
Oper. Dentistry, **25**, 104~112(2000)
S ACT 02040

10J64
C.J. Ma, M. Kasahara, K.C. Hwang, K.C.Choi, S.B.Choi, and J.J.Lee,
Physicochemical characteristics of single Asian dust storm particles
J. Kor. Soc. Atmos. Envir., 16/E, 29-38 (2000)
S ACT 02043

10J65
C.J. Ma, M. Kasahara, R. Höller and T. Kamiya,
Characteristics of single particles sampled in Japan during the Asian dust-storm period
Atmos. Envir., 35/15, 2707-2714 (2001)
S ACT 02043

10J66
T. Ohnuki, N. Kozai, M. Samadfan, T. Kamiya, T. Sakai, and T. Murakami,
Analysis of uranium distribution in rocks by μ-PIXE
Nucl. Instr. Meth., B, (in press.)
T, C IOM 02046

10J67
Y. Nakane and Y. Sakamoto,
Measurement of absorbed dose distributions in a

plastic phantom, irradiated by 40- and 65-MeV
quasi-monoenergetic neutrons
Nucl. Instr. Meth., **A459**, 552 (2001)
C RSH 01053

A 1.2 Publications in Proceeding

10C01
N. Nemoto, H. Shindou, S. Kuboyama,
S. Matsuda, H .Itoh, S. Okada, and
I. Nashiyama,
Relationship between single-event upset immunity and fablication processes of recent memories
5th Europian Conference Radiation and its Effects on Components and System (RADECS99)
C SCS 01002

10C02
N. Nemoto, H. Shindou, S. Kuboyama,
S. Matsuda, K. Sugimoto, I. Nashiyama, and
H. Itoh,
Development of 1M gate CMOS gate array
Europian Space Components Conference
C SCS 01002

10C03
A. Makihara, H. Shindou, N. Nemoto,
S. Kuboyama, S. Matsuda, T. Ohshima, T. Hirao,
H. Itoh, S. Buchner, and A.B. Campbell
Analysis of single-ion multiple-bit upset in high-density DRAMs
The IEEE Nuclear and Space Radiation Effects Conference(NSREC 2000)
C SCS 01002

10C04
J.S. Laird, T. Hirao, H. Mori, S. Onoda, and
H. Itoh,
The development of a new data collection system and chamber for transient ion beam and laser beam induced current measurements as a function of temoerature
The 4th International Workshop on Radiation Effects of Semiconductor Devices for Space Application, pp.97-102, Tsukuba, Oct. 11-13, (2000)
T SCS 02001

10C05
H. Mori,T. Hirao, S. Onoda, H. Itoh, S. Okada, and Y. Okamoto,
Profiling of collimated swift ion micro-beam using 16Mbit DRAM
International Symposium on "Prospects for Application of Radiation towards the 21th century" (Japan)
C SCS 01001

10C06
T .Ohshima, H. Itoh, and M. Yoshikawa,
Enhancement of electrical activation of aluminum acceptors in 6H-SiC by Co-implantation of carbon ions
Proceedings of the 3rd European Conference on Silicon Carbide and Related Materials (ECSCRM 2000), Kloster Baanz (Germany), September 2000, Materials Science Forum, Vols. 353-356, 575-578 (2001)
I SCS 02003

10C07
L .Hae-Seok, H. Okada, A. Wakahara,
A. Yoshida, T. Ohshima, H. Itoh, S. Kawakita,
M. Imaizumi, and S. Matsuda,
Effect of proton irradiation on electrical properties of $CuInSe_2$ thin films
12th International Photovoltaic Science and Engineering Conference, JEJU, June 11-15, p.91-92(2001)
I SCS 02004

10C08
Y. Hase, and A. Tanaka,
Analysis of *frill* mutant that affects petal and sepal development in Arabidopsis
Plant Cell Physiology, **Vol.42**, Supplement(2000), p.53
C BIT 01012

10C09
Y. Sasuga, Y. Kami, M. Ooshima, G. Takata,
Y. Kobayashi, Y. Sakata, Y. Oono, Y. Kobayashi,
S. Tanaka, and H. Takenagaka,
Isolation of response deficient mutants to

environments from plant seeds irradiated with ion-beam
Abs. of 10th TIARA Research Review Meeting(Takasaki, June 18-19), 153-154(2001)
C BIT 01030

10C10
T. Funayama, Y. Kobayashi, M. Taguchi, H. Watanabe, and K. Yamamoto,
Irradiation of collimated heavy ion beam on individual cells:The method for detecting ion Tracks at irradiation time
Abstracts of the 5th International Workshop on Microbeam Probes of Cellar Radiation Response (Stresa,Italy, May 26-27), (2001) p.27-28
C BIT 01026

10C11
Y. Kobayashi, T. Funayama, S. Wada, M. Tanaka, T.Kamiya, W. Yokota, H. Watanabe, and K. Yamamoto,
The effect of single ion irradiation on mammalian cells
Abstract of the 10th TIARA Research Review Meeting(Takasaki, June 18-19,2001), p.145
C BIT 01026

10C12
Z.L. Tu, K. Shirai, R. Kanekatsu, K. Kiguchi, Y. Kobayashi, M. Taguchi, and H. Watanabe,
Radiosurgery by heavy ion beams for biological study of the silkworm, *Bombyx mori*
Proc. of 4th China Inter. Silk Conf., May 2000 (China), p.13-17
C BIT 01027

10C13
T.M. Nakanishi, T. Kataoka, J. Furukawa, K.Tanoi, H. Yokota, S. Ueoka, N.S. Ishioka, S. Watanabe, A. Osa, T. Sekine, T. Itoh, T. Mizuniwa, S. Matsuhashi, S. Hashimoto, H. Uchida, and A. Tsuji,
Water uptake and transport imaging of Cowpea Plant by PETIS (Positron emitting tracer imaging system)
Proc. of 5th International Conference on Methods and Applications of Radioanalytical Chemistry-MARC V, April 9-14, 2000 (Hawaii), p.158
C BIT 1036

10C14
J. Furukawa, H. Yokota, K. Tanoi, S. Ueoka N.S. Ishioka, S. Watanabe, A. Osa, T. Sekine, T. Itoh, T. Mizuniwa, S. Matsuhashi, S. Hashimoto, H. Uchida, A. Tsuji, and T.M. Nakanishi,
Vanadium uptake manner and an effect of vanadium treatment on water movement in a cowpea plant by PETIS
Proc. of 5th International Conference on Methods and Applications of Radioanalytical Chemistry-MARC V, April 9-14 , 2000 (Hawaii), p.157
C BIT 1036

10C15
T.M. Nakanishi, J. Furukawa, K. Tanoi, H. Yokota, S. Ueoka, N.S. Ishioka, S. Watanabe, A. Osa, T. Sekine, T. Itoh, T. Mizuniwa, S. Matsuhashi, S. Hashimoto, H. Uchida, and A. Tsuji,
Water uptake and transport imaging of Cowpea Plant by PETIS (Positron emitting tracer imaging system)
Proc. of 12th Conference of the Federation of European Societies of Plant Physiology, August 21-25 2000 (Budapest), p.57
C BIT 1036

10C16
Y. Nakayama, K. Imagawa, M. Tagashira, M. Nakai, H. Kudoh, M. Sugimoto, N. Kasai, and T. Seguchi,
Evaluation and analysis of thermal control materials under ground simulation test for space environment effects
Proc. 8th ISMSE & 5th ICPMSE, 2000 (Arcachon, France)
C, T RCO 01041, 02037

10C17
H. Kudoh, M. Sugimoto, N. Kasai, T. Seguchi, K. Imagawa, Y. Nakayama, M. Tagashira, and

M. Nakai,
On-ground radiation resistant tests on polymer based space materials - Thermal control film and flame resistant wire -
Proc. 8th ISMSE & 5th ICPMSE, 2000 (Arcachon, France)
C, T RCO 01041, 02037

10C18
Y. Maekawa, M. Yoshida, M. Asano and H. Koshikawa,
Thermally stable and highly sensitive polymer membrances for ion and electron beam radiation
International Application, Beijing-Chaina, Novermber 6-10(2000)
C RCO 1042

10C19
N. Sekimura,
Modeling of radiation effects in fission and fusion reactor materials
Proceedings of the Fifth Japan-Chaina Symposium on Materials for Advanced Energy Systems and Fission and Fusion Engineering (1999), p.221
T, S, I IOM 02009

10C20
T. Sawai,
Cavity formation in irradiated F82H
IEA Workshop on reduced activation ferritic /martensitic steels, Nov, 2000, JAERI-Conf. 2001-007, pp.162-179
T, I, S IOM 02012

10C21
E. Wakai, T. Sawai, A. Naito, and S. Jitsukawa,
Microstructual development and swelling behavior of F82H steel irradiated by dual ion beams
Eighth Conference on Frontiers of Electron Microscopy in Materials Science, (October, 2000, J. Electron Microscopy. (in press)
T, I, S IOM 02012

10C22
H. Abe, S. Yamamoto, A. Miyashita,
In-situ TEM observation of nucleation and growth of spherical graphitic clusters under ion implantation
Eighth Conference on Frontiers of Electron Microscopy in Materials Science (FEMMS 2000)
I IOM 2019

10C23
J. Vacik, S. Yamamoto, H. Naramoto, K. Narumi, and H. Abe,
Thermal stability of buried C_{60} epitaxial layers
Proc. of the 17th Fullerene General Symposium, August 9-10, 1999(Gifu). p.137
O IOM

10C24
J. Vacik, S. Yamamoto, H. Naramoto, K. Narumi, and K. Miyashita,
Mesoscopic patterning induced by co-deposition of C_{60} and Ni on MgO(100)
Proc. of the 18th Fullerene General Symposium, January 13-14, 2000 (Okazaki), p.124
O IOM

10C25
J. Vacik, H. Naramoto, S. Yamamoto, K. Narumi. Y. Xu, and T. Tanabe,
Growth of faceted crystal drolets from the mixture of Ni and C_{60} co-deposited on the MgO(100)
Proc. of the 19th Fullerene General Symposium, July 27-28, 2000 (Kiryu), p.34
T IOM

10C26
J. Vacik, H. Naramoto, S. Yamamoto, and K. Narumi,
Non-equilibrium growth of Ni + C_{60} on MgO(100)
TIARA Annual Report 1999,p.160, Advanced Radiation Technology Center, JAERI, October 2000
O IOM

10C27
J. Vacik, H. Naramoto, S. Yamamoto, and

K. Narumi,
Epitaxial re-crystallization of the Ni/MgO(100) interface
TIARA Annual Report 1999, p.157, Advanced Radiation Technology Center, JAERI, October 2000
T IOM 02026

10C28
J. Vacik, H. Naramoto, S. Yamamoto, K. Narumi, and Y.H. Xu,
Effect of energetic beam irradiation on the thermal evolution of the Ni-C_{60} systems
Abstracts of the 1st Open Symposium of Quantum Science and Engineering Center, Kyoto University, p.80, October 28, 2000, Kyoto
T IOM 02026

10C29
J. Vacik, H. Naramoto, S. Yamamoto,
K. Narumi, and H. Abe,
Structural variations of the Ni-C_{60} systems induced by energetic beam bombardment and thermal annealing
Proc. of the 11th Symposium on Beam Engineering of Advanced Material Syntheses-Including Bio-Medical
Materials and Treatments BEAMS 2000, p.135-138, November 21-22, 2000, Tokyo
T IOM 02026

10C30
J. Vacik, H. Naramoto, S. Yamamoto, K. Narumi, and K. Miyashita,
Mesoscopic patterning induced by Co-deposition of C_{60} and Ni on the MgO(100) single crystal
Proc. of Fall Meeting of Materials Research Society, Abstracts, p.349, Nov.27-Dec.1, 2000, Boston, U.S.A.
O IOM

10C31
J. Vacik, H. Naramoto, S. Yamamoto, K. Narumi, and Y.H. Xu,
Thermally incited structural variations of the Ni-C_{60} systems
Proc. of the 20th Fullerene General Symposium, p.92, oral/poster contribution January, 22-23, 2001, Okazaki
O IOM

10C32
J. Vacik, H. Naramoto, S. Yamamoto, and K. Narumi,
Fabrication of mesoscopic stripes based on self-organization, The 4th International Symposium on Inter. Materials Nanoscopic Structure and Dynamics for New Functional Materials and Devices
Invited poster,p.18, Februry 6-7, 2001, Osaka University, Osaka(The Best International Prize)
O IOM

10C33
J. Vacik, H. Naramoto, S. Yamamoto,
K. Narumi, and Y.H. Xu,
Thermal response of the metal/fullerite hybrid assembly
Abstracts of the Tenth TIARA Research Review Meeting, **1P37**, p.84, June 18-19, 2001,Takasaki
O IOM

10C34
J. Vacik, H. Naramoto, S. Yamamoto,
K. Narumi, and Y.H. Xu,
Unusual thermal response of the metal/fullerite superstructure
Proc. of the 21th Fullerene General Symposium, p.92, oral/poster contribution, July 25-27, 2001, Tsukuba
T IOM 02026

10C35
J. Vacik, H. Naramoto, S. Yamamoto, and
K. Narumi,
Epitaxial recrystallization of the Ni films on the MgO(100) substrate
Proc. of the 13th International Conference on Crystal Growth Doshisha University Kyoto, Japan, 30 July-4 August, 2001
O IOM

10C36
H. Naramoto, Y. Xu, K. Narumi, X. Zhu,
J. Vacik, S. Yamamoto, and K. Miyashita,

Modification of carbon related films with energy beams
Proc. of MRS Fall-Meeting (Boston, 2000)
O IOM

10C37
H. Naramoto, X. Zhu, J. Vacik, Y. Xu,
K. Narumi, S. Yamamoto, V.I. Lavrentiev, and K. Miyashita,
Allotropic conversion of carbon-ralated films by using energy beams
Proc. Int. Symposium on Fullerene and Clusters 2001 (St. Petersburg, July 2-6, 2001), (to be published)
O, T IOM

10C38
H. Naramoto, Y. Xu, K. Narumi, X. Zhu,
J. Vacik, S. Yamamoto, and K. Miyashita,
Modification of C_{60} carbon-lerated films with energy beams
Mat. Res. Soc. Symp. Proc.,647,
O5.18.1-O5.18.6 (2001)
I IOM 02026

10C39
K. Narumi, and H. Naramoto,
AFM investigation of growth process of C_{60} thin films on a KBr(001) Surface
Diamond and Related Materials 10, 980-983 (2001)
O IOM, MAN 02027

10C40
S. Yamamoto, T. Sumita, and A. Miyashita,
Hydrogen analysis of extaxial Cu(111)/Nb(110) Multilayer using MeV ion beams
Proc. of sixteenth international conference on the application of accelerators in research and industry, November 2000(Denton Texas, USA), (in press.)
I IOM 02022

10C41
T. Yamakim, T. Sumita, S. Yamamoto, and A. Miyashita,
Surface modification of TiO_2 single crystals by Nonmetal-ion implantation
Proceedings of the Eleventh Symposium on Beam Engineering of Advanced Materials Synthesis, p.131, (November, 2000, Tokyo)
I, S IOM 02036

10C42
A. Arai, K. Hirata, T. Sekiguchi, A. Kawasuso,
Y. Kobayashi, and S. Okada,
Effect of radiation damage on luminescence of erbium-implanted SiO_2/Si studied by slow positron beam
6th International Workshop on Positron and Positronium Chemistry, June 1999
I IOM 02032

10C43
T. Ohshima, A. Uedono, H. Itoh, M. Yoshikawa,
K. Kojima, I. Nashiyama, S. Okada, and K. Abe,
Relationship between donor activation and defect annealing in 6H-SiC hot-implanted with phosphorus ions
Materials Science Forum, **338-342**(2000), p.857
I IOM 02032

10C44
H. Abe, A. Uedono, H. Uchida, A. Komatsu,
S. Okada, and H. Itoh,
Positron annihilation studies of defects in ion implanted Palladium
Materials Science Forum, **363-365**(2001), p.156
I IOM 02032

10C45
T. Yamaguchi, E. Watanabe, T. Souno,
H. Nishikawa, M. Fujimaki, and Y. Ohki,
Evaluation of silica implanted by high-energy ions using microspectroscopy (II)
The 61st Autumn Meeting, 2000; The Japan Society of Applied Physics, **6a-B-10**, p.814, Sep. 2000
O IOM 02034

10C46
T. Souno, H. Nishikawa, T. Yamaguchi,
E. Watanabe, M. Fujimaki, and Y. Ohki,
Characteristics of defects in silica implanted by

high-energy ions during thermal treatment
The 61st Autumn Meeting, 2000; The Japan Society of Applied Physics, **6a-B-8**, p .813, Sep. 2000
O IOM 02034

10C47
T. Souno, H. Nishikawa, T. Yamaguchi, E. Watanabe, Y. Nishihara, M. Hattori, M. Fujimaki, Y. Ohki, M. Oikawa, T. Kamiya, and K. Arakawa,
Microscopic Characterization of Ion-Implanted Silica Glass
Proc. of the 32nd Symposium on Electrical and Electronic Insulating Materials and Applications in Systems, **Pb-7**, pp.269-272, Nov. 2000
T, S IOM 02034

10C48
T. Souno, H. Nishikawa, T. Yamaguchi, E. Watanabe, Y. Nishihara, M. Hattori, M. Fujimaki, Y. Ohki, M. Oikawa, T. Kamiya, and K. Arakawa ,
Microspectroscopic Evaluation of Silica Glass Implanted by Ion Microbeam
The 48th Spring Meeting, 2001; The Japan Society of Applied Physics and Related Societies, **29a-ZL-3**, p.940, Mar. 2001
T, S IOM 02034

10C49
M. Hattori, Y. Nishihara, M. Fujimaki, Y .Ohki, T. Souno, H. Nishikawa, T. Yamaguchi, E. Watanabe, M. Oikawa, T. Kamiya, and K. Arakawa,
Densification of silica glass induced by ion implantation, using ion microbeam
The 48th Spring Meeting, 2001; The Japan Society of Applied Physics and Related Societies, **29a-ZL-7**, p.941, Mar. 2001
TS IOM 02034

10C50
T. Yamaguchi, E. Watanabe, T. Souno, H. Nishikawa, Y. Nishihara, M. Hattori, M. Fujimaki,Y. Ohki, M. Oikawa, T. Kamiya, and K.Arakawa,
Evaluation of silica implanted with high－energy ions using UV－excited microspectroscopy
The 48th Spring Meeting, 2001; The Japan Society of Applied Physics and Related Societies, **29a-ZL-9**, p.942, Mar. 2001
O IOM 02034

10C51
M. Hattori, Y. Nishihara, M. Fujimaki, Y. Ohki, T. Souno, H. Nishikawa, T. Yamaguchi, E. Watanabe, M. Oikawa, T. Kamiya, and K. Arakawa,
Characterization of ion-implanted silica glass by vacuum UV spectroscopy
Technical Meeting on Dielectrics and Insulating *Materials*, **DEI-01-79**, IEEJ, Mar. 2001
IOM 02034

10C52
K. Ishii, A. Sugimoto, T. Satoh, A. Tanaka, S. Matsuyama, C. Akama, M. Sato, T. Kamiya, T. Sakai, M. Saidoh, R. Tanaka, and M. Oikawa,
Elemental analysis of cellular samples by air micro-PIXE
Proc. of 7th Int.Conf. on Nuclear Microprobe Technology and Applications(Bordeaux, France, 10-15 Sep.2000) to be published in Nucl. Instrr. and Meth., B
S ACT 02045

10C53
M. Kasahara, S. Akashi, C.-J. Ma and S. Tohno,
Fixation and chemical analysis of single liquid particle
Am. Inst. of Phys., AIP Conf. Proc., 534, 15th International Conference on Nucleation and Atmospheric Aerosols, August 2000 (Missouri, USA) ,p.736-739
S ACT 02043

10C54
M. Kasahara, C.-J. Ma, T. Kamiya and T. Sakai,
Applications of micro-PIXE to atmospheric aerosol studie,
Proc. Intern. Conf. on Nuclear Microprobe Technology and Applications, Sept.2000 (Bordeaux)

S ACT 02043

10C55
T. Kamiya, T. Sakai, M. Oikawa, and T. Hirao,
Observation of individual radiation damage using an automated single ion hit technique at the JAERI heavy ion Microbeam system
Proc. of 7th Int. Conf. on Nuclear Microprobe Technology and Applications(Bordeaux, France, 10-15 Sep.2000)(to be published in Nucl. Instrr. and Meth., B)
T ACT 02039

10C56
T. Kamiya, W. Yokota, Y. Kobayashi,
M. Cholewa, M.S. Krochmal, G. Laken,
I.D. Lasen, L. Fiddes, G. Parkhill, K. Dowsey,
Development of an automated single cell irradiation system combined with a high-energy ion Microbeam system
Proc. of 7th Int. Conf. on Nuclear Microprobe Technology and Applications(Bordeaux, France, 10-15 Sep. 2000) (to be published in Nucl. Instr. and Meth., B)
S ACT 01051

10C57
E. Kim, A. Endo, Y. Yamaguchi, M. Yoshizawa,
T. Nakamura, and T .Shiomi,
Design of neutron monitor for wide energy range from thermal to 100MeV
Proc. 10th Intern. Congr. of The Intern.Radiat. Protec. Assoc., May 14-19, 2000, Hiroshima, Japan
C RSH 1054

10C58
W. Yokota, K. Arakawa, S. Okumura,
M. Fukuda, T. Kamiya, and Y. Nakamura,
Topics and Future Plans of Ion Beam Facilities at JAERI
Proc. of the 4th International Workshop on Radiation Effects on Semiconductor Devices for Space Application (Tsukuba, 2000), p.179
C SCS, ACT

Appendix 2. Type of Research Collaboration

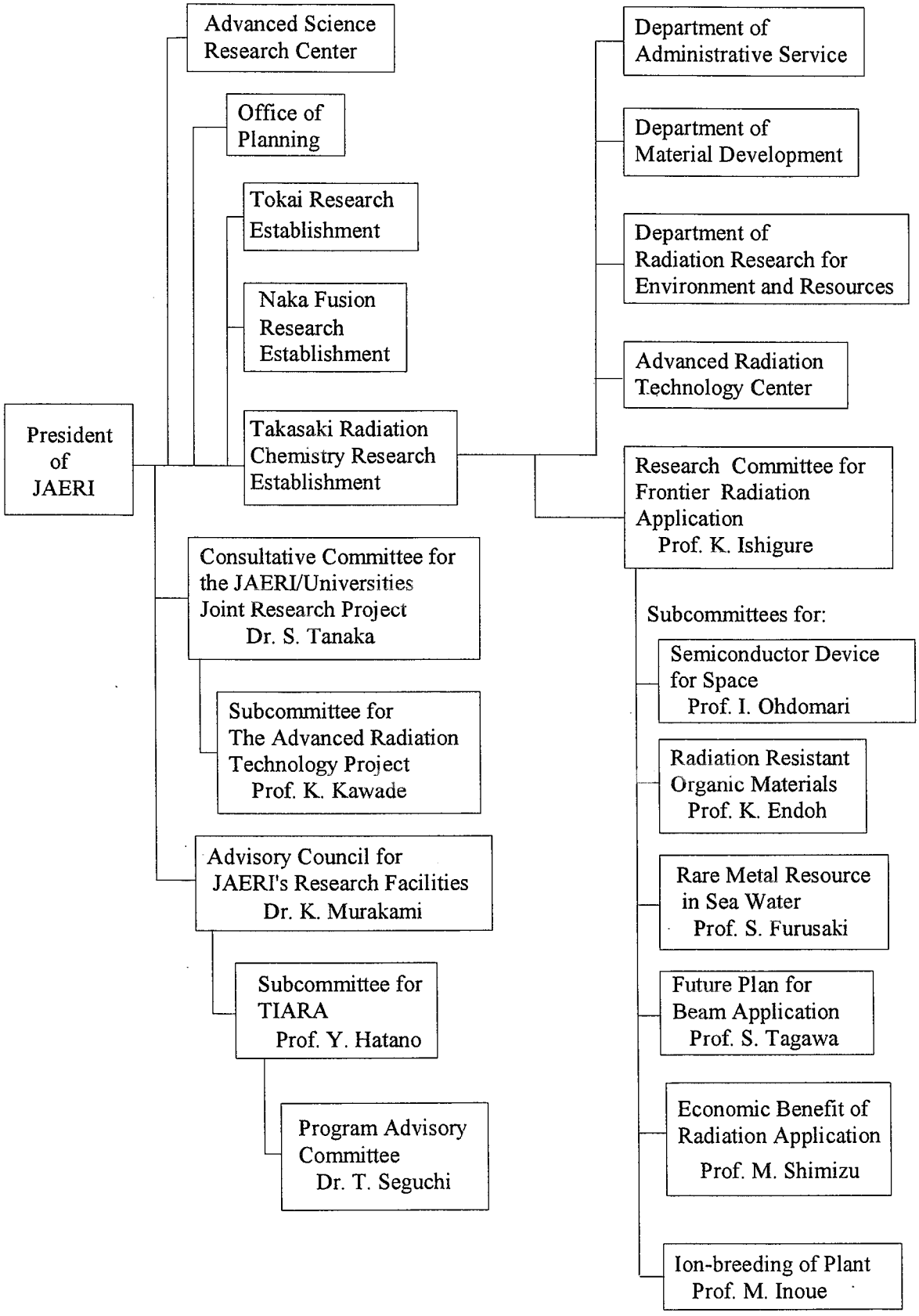
Section of this Report	Research Program Number	Type of Research Collaborations*	Section of this Report	Research Program Number	Type of Research Collaborations*
1.1	01003/02002	Joint.Res.	3.5	01044	Coop.Res.Univ.
1.2	01002	Joint.Res.	3.6	01047	Coop.Res.Univ.
1.3	02001	JAERI	3.7	01045	JAERI
1.4	01001	JAERI			
1.5	01004/02005	Joint.Res.	4.1	01005	JAERI
1.6	02003	JAERI	4.2	01006	JAERI
1.7	02004	Coop.Res.Univ.	4.3	01007/02011	Proj.Res.Univ
1.8	01038/02031	Coop.Res.Univ.	4.4	02006	JAERI
			4.5	02007	Proj.Res.Univ
2.1	01008	JAERI	4.6	02008	Proj.Res.Univ
2.2	01013	Joint.Res.	4.7	02009	Proj.Res.Univ
2.3	01010	Joint.Res.	4.8	02010	Proj.Res.Univ
2.4	01009	Coop.Res.Univ.	4.9	02012	JAERI
2.5	01023	Joint Res.	4.10	02013	JAERI
2.6	01020	Coop.Res.Univ.	4.11	02014	JAERI
2.7	01011	Joint Res.	4.12	02015	JAERI
2.8	01012	JAERI	4.13	02016	JAERI
2.9	01014	Joint.Res.	4.14	02019	JAERI
2.10	01015	Joint.Res.	4.15	off line	JAERI
2.11	01018	Joint.Res.	4.16	off line	JAERI
2.12	01019	Coop.Res.Univ	4.17	off line	JAERI
2.13	01021	Joint Res.	4.18	02026	JAERI
2.14	01022	Coop.Res.Univ	4.19	02020	Coop.Res.Univ.
2.15	01025	Coop.Res.Univ.	4.20	02024	Coop.Res.Univ.
2.16	01029	JAERI	4.21	02027	JAERI
2.17	01030	Coop.Res.Univ.	4.22	02028	Coop.Res.Univ.
2.18	01026	JAERI	4.23	02029	JAERI
2.19	01027	Coop.Res.Univ.	2.24	02030	JAERI
2.20	01016	Coop.Res.Univ.	4.25	02022	JAERI
2.21	01017	Joint.Res.	4.26	02036	JAERI
2.22	off line	JAERI			
2.23	02018	JAERI	5.1	02021	Coop.Res.Univ.
2.24	02017	Coop.Res.Univ.	5.2	02025	Coop.Res.Univ.
2.25	01032	JAERI	5.3	02023	Coop.Res.Univ.
2.26	01033	Proj.Res.Univ.	5.4	02032	JAERI
2.27	01034	Proj.Res.Univ.	5.5	02033	Joint.Res.
2.28	01035	Proj.Res.Univ.			
2.29	01036	Proj.Res.Univ.	6.1	01039	Coop.Res.Univ.
2.30	01037	Joint.Res.	6.2	01040	Coop.Res.Univ.
2.31	01028	Coop.Res.Univ.	6.3	off line	JAERI
2.32	01031	Coop.Res.Univ.	6.4	off line	JAERI
3.1	01041/02037	Joint.Res.	7.1	02034	Coop.Res.Univ.
3.2	01042	Coop.Res.Univ.	7.2	02035	JAERI
3.3	01050	JAERI	7.3	02045	Proj.Res.Univ.
3.4	01046	Coop.Res.Univ.	7.4	02040	Coop.Res.Univ.

Section of this Report	Research Program Number	Type of Research Collaborations*
7.5	02042	Proj.Res.Univ
7.6	02043	Proj.Res.Univ
7.7	02044	Proj.Res.Univ
7.8	02046	JAERI
7.9	02039	JAERI
7.10	01051	JAERI
8.1	01052	Proj.Res.Univ
8.2	01053	Proj.Res.Univ
8.3	01054	Proj.Res.Univ
9.1	01048	JAERI
9.2	off line	JAERI
9.3	02047	JAERI
9.4	off line	JAERI
9.5	off line	JAERI
9.6	01049	JAERI
9.8	off line	JAERI

*Joint Res.: Joint research with private company or governmental institution
Coop. Res. Univ.: Cooperative research with a university or universities #
Proj. Res.Univ.: The JAERI-Universities Joint Research Project #
#For administration of these programs, we appreciate the cooperation of:
Research Center for Nuclear Science and Technology, The University of Tokyo.

Appendix 3. Organization and Personnel of TIARA (FY 2000)

1) Organization for the Research and Development of Advanced Radiation Technology



2) Personnel for the Administration, Operation and Control of TIARA

Advanced Radiation Technology Center

Director	M. Saidoh

Administration Division

General Manager	T. Sekino
Staff Member	K. Morishita, M. Nakata

Utilization and Coordination Division

General Manager	Su. Tanaka
Staff Member	K. Nishimura, M. Hosono

Ion Accelerator Operation Division

General Manager	S. Tajima

Group of Cyclotron Operation

Staff Member	Y. Nakamura, T. Nara, T. Agematsu, I. Ishibori, H. Tamura, S. Kurashima

Group of Electrostatic Accelerators Operation

Staff Member	I. Takada, K. Mizuhashi, S. Uno, K. Ohkoshi, Y. Nakajima, A. Chiba

Ion Beam Engineering Division

Head	K. Arakawa
Staff Member	T. Kojima, W. Yokota, H. Tachibana, M. Fukuda, T. Kamiya, S. Okumura, Y. Saito, Y. Ishii, T. Sakai, S.Oikawa

Irradiation Service Division

General Manager	H.Sunaga
Staff Member	T. Kanazawa, H. Kaneko, T. Haneda Y. Haruyama, H. Takizawa, H.Hanaya

Department of Administrative Services

Safety Division

Staff Member	Y.Ohi, H. Miyauchi

(Radiation Monitoring and Control in TIARA)

Utilities and Maintenance Division

Staff Member	S. Kaneko, Y. Takayama

(Radioactive Waste Management and Utility Control in TIARA)

国際単位系 (SI) と換算表

表1　SI基本単位および補助単位

量	名称	記号
長さ	メートル	m
質量	キログラム	kg
時間	秒	s
電流	アンペア	A
熱力学温度	ケルビン	K
物質量	モル	mol
光度	カンデラ	cd
平面角	ラジアン	rad
立体角	ステラジアン	sr

表2　SIと併用される単位

名称	記号
分，時，日	min，h，d
度，分，秒	°，′，″
リットル	l，L
トン	t
電子ボルト	eV
原子質量単位	u

1 eV=1.60218×10^{-19} J

1 u=1.66054×10^{-27} kg

表5　SI接頭語

倍数	接頭語	記号
10^{18}	エクサ	E
10^{15}	ペタ	P
10^{12}	テラ	T
10^{9}	ギガ	G
10^{6}	メガ	M
10^{3}	キロ	k
10^{2}	ヘクト	h
10^{1}	デカ	da
10^{-1}	デシ	d
10^{-2}	センチ	c
10^{-3}	ミリ	m
10^{-6}	マイクロ	μ
10^{-9}	ナノ	n
10^{-12}	ピコ	p
10^{-15}	フェムト	f
10^{-18}	アト	a

表3　固有の名称をもつSI組立単位

量	名称	記号	他のSI単位による表現
周波数	ヘルツ	Hz	s^{-1}
力	ニュートン	N	m·kg/s^2
圧力，応力	パスカル	Pa	N/m^2
エネルギー，仕事，熱量	ジュール	J	N·m
工率，放射束	ワット	W	J/s
電気量，電荷	クーロン	C	A·s
電位，電圧，起電力	ボルト	V	W/A
静電容量	ファラド	F	C/V
電気抵抗	オーム	Ω	V/A
コンダクタンス	ジーメンス	S	A/V
磁束	ウェーバ	Wb	V·s
磁束密度	テスラ	T	Wb/m^2
インダクタンス	ヘンリー	H	Wb/A
セルシウス温度	セルシウス度	℃	
光束	ルーメン	lm	cd·sr
照度	ルクス	lx	lm/m^2
放射能	ベクレル	Bq	s^{-1}
吸収線量	グレイ	Gy	J/kg
線量当量	シーベルト	Sv	J/kg

表4　SIと共に暫定的に維持される単位

名称	記号
オングストローム	Å
バーン	b
バール	bar
ガル	Gal
キュリー	Ci
レントゲン	R
ラド	rad
レム	rem

1 Å= 0.1 nm=10^{-10} m

1 b=100 fm^2=10^{-28} m^2

1 bar=0.1 MPa=10^5 Pa

1 Gal=1 cm/s^2=10^{-2} m/s^2

1 Ci=3.7×10^{10} Bq

1 R=2.58×10^{-4} C/kg

1 rad=1 cGy=10^{-2} Gy

1 rem=1 cSv=10^{-2} Sv

（注）

1. 表1－5は「国際単位系」第5版，国際度量衡局 1985年刊行による。ただし，1 eVおよび1 uの値はCODATAの1986年推奨値によった。
2. 表4には海里，ノット，アール，ヘクタールも含まれているが日常の単位なのでここでは省略した。
3. barは，JISでは流体の圧力を表わす場合に限り表2のカテゴリーに分類されている。
4. EC閣僚理事会指令ではbar，barnおよび「血圧の単位」mmHgを表2のカテゴリーに入れている。

換　算　表

	N(=10^5dyn)	kgf	lbf
力	1	0.101972	0.224809
	9.80665	1	2.20462
	4.44822	0.453592	1

粘度　1 Pa·s(N·s/m^2)=10 P(ポアズ)(g/(cm·s))

動粘度　1 m^2/s=10^4St(ストークス)(cm^2/s)

圧力	MPa(=10 bar)	kgf/cm^2	atm	mmHg(Torr)	lbf/in^2(psi)
	1	10.1972	9.86923	7.50062×10^3	145.038
	0.0980665	1	0.967841	735.559	14.2233
	0.101325	1.03323	1	760	14.6959
	1.33322×10^{-4}	1.35951×10^{-3}	1.31579×10^{-3}	1	1.93368×10^{-2}
	6.89476×10^{-3}	7.03070×10^{-2}	6.80460×10^{-2}	51.7149	1

エネルギー・仕事・熱量	J(=10^7 erg)	kgf·m	kW·h	cal(計量法)	Btu	ft·lbf	eV
	1	0.101972	2.77778×10^{-7}	0.238889	9.47813×10^{-4}	0.737562	6.24150×10^{18}
	9.80665	1	2.72407×10^{-6}	2.34270	9.29487×10^{-3}	7.23301	6.12082×10^{19}
	3.6×10^6	3.67098×10^5	1	8.59999×10^5	3412.13	2.65522×10^6	2.24694×10^{25}
	4.18605	0.426858	1.16279×10^{-6}	1	3.96759×10^{-3}	3.08747	2.61272×10^{19}
	1055.06	107.586	2.93072×10^{-4}	252.042	1	778.172	6.58515×10^{21}
	1.35582	0.138255	3.76616×10^{-7}	0.323890	1.28506×10^{-3}	1	8.46233×10^{18}
	1.60218×10^{-19}	1.63377×10^{-20}	4.45050×10^{-26}	3.82743×10^{-20}	1.51857×10^{-22}	1.18171×10^{-19}	1

1 cal = 4.18605 J(計量法)

= 4.184 J　(熱化学)

= 4.1855 J　(15 °C)

= 4.1868 J(国際蒸気表)

仕事率　1 PS(仏馬力)

= 75 kgf·m/s

= 735.499 W

放射能	Bq	Ci
	1	2.70270×10^{-11}
	3.7×10^{10}	1

吸収線量	Gy	rad
	1	100
	0.01	1

照射線量	C/kg	R
	1	3876
	2.58×10^{-4}	1

線量当量	Sv	rem
	1	100
	0.01	1

（86年12月26日現在）

R100
古紙配合率100%
白色度70%再生紙を使用しています